Lecture Notes in Electrical Engineering 341

Jiadong Sun
Jingnan Liu
Shiwei Fan
Xiaochun Lu
Editors

China Satellite Navigation Conference (CSNC) 2015 Proceedings: Volume II

Springer

Lecture Notes in Electrical Engineering

Volume 341

About this Series

"Lecture Notes in Electrical Engineering (LNEE)" is a book series which reports the latest research and developments in Electrical Engineering, namely:

- Communication, Networks, and Information Theory
- Computer Engineering
- Signal, Image, Speech and Information Processing
- Circuits and Systems
- Bioengineering

LNEE publishes authored monographs and contributed volumes which present cutting edge research information as well as new perspectives on classical fields, while maintaining Springer's high standards of academic excellence. Also considered for publication are lecture materials, proceedings, and other related materials of exceptionally high quality and interest. The subject matter should be original and timely, reporting the latest research and developments in all areas of electrical engineering.

The audience for the books in LNEE consists of advanced level students, researchers, and industry professionals working at the forefront of their fields. Much like Springer's other Lecture Notes series, LNEE will be distributed through Springer's print and electronic publishing channels.

More information about this series at http://www.springer.com/series/7818

Jiadong Sun · Jingnan Liu
Shiwei Fan · Xiaochun Lu
Editors

China Satellite Navigation Conference (CSNC) 2015 Proceedings: Volume II

Springer

Editors
Jiadong Sun
China Aerospace Science
and Technology Corporation
Chinese Academy of Sciences
Beijing
China

Jingnan Liu
Wuhan University
Wuhan
China

Shiwei Fan
China Satellite Navigation Office
Beijing
China

Xiaochun Lu
Chinese Academy of Sciences
Beijing
China

ISSN 1876-1100 ISSN 1876-1119 (electronic)
Lecture Notes in Electrical Engineering
ISBN 978-3-662-46634-6 ISBN 978-3-662-46635-3 (eBook)
DOI 10.1007/978-3-662-46635-3

Library of Congress Control Number: 2014937269

Springer Heidelberg New York Dordrecht London

Printed on acid-free paper

Springer-Verlag GmbH Berlin Heidelberg is part of Springer Science+Business Media (www.springer.com)

Editorial Board

Preface

BeiDou Navigation Satellite System (BDS) is China's global navigation satellite system which has been developed independently. BDS is similar in principle to the global positioning system (GPS) and compatible with other global satellite navigation systems (GNSS) worldwide. The BDS will provide highly reliable and precise positioning, navigation and timing (PNT) services as well as short-message communication for all users under all-weather, all-time and worldwide conditions.

China Satellite Navigation Conference (CSNC) is an open platform for academic exchanges in the field of satellite navigation. It aims to encourage technological innovation, accelerate GNSS engineering and boost the development of the satellite navigation industry in China and in the world.

The 6th China Satellite Navigation Conference (CSNC 2015) was held during May 13–15, 2015, Xian, China. The theme of CSNC2015 is Opening-up, Connectivity, Win–win, which covers a wide range of activities, including technical seminars, academic exchanges, forums, exhibitions and lectures. The main topics are as follows:

1. BDS/GNSS Navigation Applications
2. Satellite Navigation Signal System, Compatibility and Interoperability
3. Precise Orbit Determination and Positioning
4. Atomic Clock Technique and Time-Frequency System
5. Satellite Navigation Augmentation and Integrity Monitoring
6. BDS/GNSS Test and Assessment Technology
7. BDS/GNSS User Terminal Technology
8. Satellite Navigation Models and Methods
9. PNT System and New Technologies of Navigation
10. Policies and Regulations, Standard and Intellectual Property

The proceedings (Lecture Notes in Electrical Engineering) have 197 papers in ten topics of the conference, which were selected through a strict peer-review process from 513 papers presented at CSNC2015. In addition, another 251 papers were selected as the electronic proceedings of CSNC2015, which are also indexed

by “China Proceedings of Conferences Full-text Database (CPCD)” of CNKI and Wan Fang Data.

We thank the contribution of each author and extend our gratitude to the 215 referees and 49 session chairs who are listed as members of the editorial board. The assistance of the organizing committees of CNSC2015 and the Springer editorial office is highly appreciated.

Jiadong Sun
Chair of CSNC2015

The 6th China Satellite Navigation Conference (CSNC 2015)

Scientific Committee

Chairman

Jiadong Sun, China Aerospace Science and Technology Corporation

Vice-Chairman

Rongjun Shen, China
Jisheng Li, China
Qisheng Sui, China
Zuhong Li, China Academy of Space Technology
Shusen Tan, Beijing Satellite Navigation Center, China

Executive Chairman

Jingnan Liu, Wuhan University
Yuanxi Yang, China National Administration of GNSS and Applications
Shiwei Fan, China

Committee Members: (By Surnames Stroke Order)

Xiancheng Ding, China Electronics Technology Group Corporation
Qingjun Bu, China
Liheng Wang, China Aerospace Science and Technology Corporation
Yuzhu Wang, Shanghai Institute of Optics and Fine Mechanics, Chinese Academy of Sciences
Guoxiang Ai, National Astronomical Observatories, Chinese Academy of Sciences
Shuhua Ye, Shanghai Astronomical Observatories, Chinese Academy of Sciences

Zhaowen Zhuang, National University of Defense Technology
Qifeng Xu, PLA Information Engineering University
Houze Xu, Institute of Geodesy and Geophysics, Chinese Academy of Sciences
Guirong Min, China Academy of Space Technology
Xixiang Zhang, China Electronics Technology Group Corporation
Lvqian Zhang, China Aerospace Science and Technology Corporation
Junyong Chen, National Administration of Surveying, Mapping and Geoinformation
Benyao Fan, China Academy of Space Technology
Dongjin Luo, China
Guohong Xia, China Aerospace Science and Industry Corporation
Chong Cao, China Research Institute of Radio Wave Propagation (CETC 22)
Faren Qi, China Academy of Space Technology
Sili Liang, China Aerospace Science and Technology Corporation
Shancheng Tu, China Academy of Space Technology
Rongsheng Su, China
Zhipeng Tong, China Electronics Technology Group Corporation
Ziqing Wei, Xi'an Institute of Surveying and mapping

Organizing Committee

Secretary General

Haitao Wu, Navigation Headquarters, Chinese Academy of Sciences

Vice-Secretary General

Wenhai Jiao, China Satellite Navigation Office Engineering Center
Yuehu Hu, The 20th Research Institute of China Electronics Technology Group Corporation
Weina Hao, Navigation Headquarters, Chinese Academy of Sciences

Committee Members: (By Surnames Stroke Order)

Qun Ding, Xi'an Institute of Navigation Technology
Miao Yu, Beijing Institute of Space Science and Technology Information
Jun Lu, China Satellite Navigation Office Engineering Center
Yintang Yang, Xidian University
Xiuwan Chen, Peking University
Mingquan Lu, Tsinghua University

Xiang'an Zhao, China Defense Science and Technology Information Center
Jing Zhao, Ministry of Science and Technology National Remote Sensing Center
Guangzhou Ouyang, Academy of Opto-Electronics, Chinese Academy of Science
Gang Hu, Beijing Unicore Communications Inc.
Yamin Dang, Chinese Academy of Surveying and Mapping, China
Zhong Dou, National Time Service Center of Chinese Academy of Sciences

Contents

Part II Satellite Navigation Augmentation and Integrity Monitoring

Part I
Satellite Navigation Signal System, Compatibility and Interoperability

Chapter 1
Optimization Selection of the HRC Correlator Spacing for Different Navigation Signals

Song Li, Jing Lv, Jiang Chang, Xiang Tian and Kaixiang Tong

Abstract Multipath effect is the major factor which influences the precision of navigation and positioning. EML is the method which realized easily, it is still used by many receivers to mitigate multipath in the loops. But HRC performs better in multipath mitigation and will be used in the engineering practice, but the researches by now mostly focus on the ordinary characteristics or only for BPSK signals, and lack of deep and system research, and the application in practice should select different correlator spacing for different signals. To solve the problems above, this paper mainly researches the scope of code phase discrimination and performance of multipath mitigation, and proposes the methods of optimization selection of the HRC correlator spacing, and gains the scope to select. Simulation results show that, the HRC correlator spacing should be selected different for different signals, the phase discrimination scopes become wider as the correlator spacing increases, the performance of multipath mitigation increases as the correlator spacing decreases, and the performance of multipath mitigation does not improve distinctly as the correlator spacing decreases in a small correlator spacing and narrow baseband, and the correlator spacing should be selected wider in a certain extent in order to increase the scope of discrimination. The researches in the paper are innovative and practically valuable and have important theory values and can perform an important director meaning for engineering practice.

Keywords HRC · Phase discrimination · Correlator spacing · Multipath mitigation

S. Li (✉) · J. Lv · J. Chang · X. Tian · K. Tong
College of Communications Engineering, PLAUST, Nanjing, China
e-mail: lisong2008hust@163.com

J. Sun et al. (eds.), *China Satellite Navigation Conference (CSNC) 2015 Proceedings: Volume II*, Lecture Notes in Electrical Engineering 341,
DOI 10.1007/978-3-662-46635-3_1

1.1 Introduction

Multipath effect cannot be mitigated by difference technology and is need to be mitigated specially by some technologies by the receivers. As the precision of navigation and positioning improves, a higher demand is needed for phase discrimination and multipath mitigation. Traditional receivers usually use the EML [1] (Early Minus Late) to discriminate and mitigate multipath effect, HRC [2] (High Resolution Correlator) is enhanced compared with EML, it is also called Double-delta [3], Strobe Correlator [4] and Pulse Aperture Correlator (PAC) [5] are both the realization styles, HRC owns one pairs of correlators than EML and uses the slopes of correlations to discriminate code phases. HRC performs better in the precision of discrimination and multipath mitigation, but the discrimination scope of HRC is smaller. The key point to use HRC is to select a proper correlator spacing to meet the demand of discrimination and multipath mitigation. Researches in papers [2, 4, 5] by now mainly focus on the performance of multipath mitigation in infinite bandwidth, and different navigation signals and correlator spacing are not considered. The literature [6] did a research on the precision of range measures in the conditions of small spacing and the finite bandwidth, but it did not research the performance of multipath mitigation. The literature [3] did a research on the performance of multipath mitigation of BPSK signals in the conditions of the finite bandwidth and some correlator spacing, but it only made some commonly analysis and did not consider other navigation signals. In fact, different navigation signals have different performance of anti-multipath and the correlator spacing are different, and the analysis recently cannot meet the demand of applications. As the precision improves and different navigation signals are used gradually, HRC will be used more in receivers, and the deep research of HRC in different signals has an important meaning.

BPSK signal is used in traditional GPS L1CA, L2C and Galileo E6 and so on; BOC(1,1) signal is used in modernized GPS L1C and Galileo OS (Opening Service) [7]. OS signal in B1C of BeiDou-2 is TMBOC and the data part is BOC(1,1), the pilot part is BOC(1,1) and BOC(6,1) with the proportion of 29:4 [8], TD-BPSK is used in BeiDou. The paper analyzes the optimization selection of correlator spacing of HRC in different signals by comparing the scope of discrimination and performance of multipath mitigation, and points out the proper selection scope of correlator spacing for BPSK, TDDM-BPSK, BOC(1,1), and TMBOC.

1.2 Code Tracking of Satellite Navigation Signals and HRC

1.2.1 Code Tracking of Navigation Signals

The two important processes after receiving satellite navigation signals are capturing and tracking. The aim of capturing is to identify the PRN numbers to get the estimation values of carrier Doppler shift and code phase to initialize the tracking

mode [7]. There are carriers and code tracking in tracking process and HRC is used in code tracking. The principle of code tracking to copy the pseudorandom code which is almost the same as the received signal and multiply each other to peel off the pseudorandom code of signals, then the receivers will get important values associated with the calculation of pseud-range [9].

1.2.2 HRC Discriminator

There are two pairs of early and late correlators in HRC and the correlator spacing is d and 2d chips symmetrically located beside the prompt correlator, the principle is shown in Fig. 1.1.

The difference value of early and late correlator is used in code tracking, namely

$$\begin{aligned} Dis &= (E1 - L1) - \frac{1}{2}(E2 - L2) \\ &= R\left(\tau + \frac{d}{2}\right) - R\left(\tau - \frac{d}{2}\right) - \frac{1}{2}[R(\tau + d) - R(\tau - d)] \end{aligned} \tag{1.1}$$

In the equation E1, L1, E2, L2 are the correlate values between the reproduction code and the received signals. Then E1, L1, P, E2, L2 are the five sample values of $R(\tau)$. If we assume the prompt reproduction code is τ_0 earlier than the early code, then code delay of the E1 is $\tau_{E1} = \tau_0 - d/2$, and the code delay of the E2 is $\tau_{E2} = \tau_0 - d$, the code delay of the L1 is $\tau_{L1} = \tau_0 + d/2$, and the code delay of the L2 is $\tau_{L2} = \tau_0 + d$.

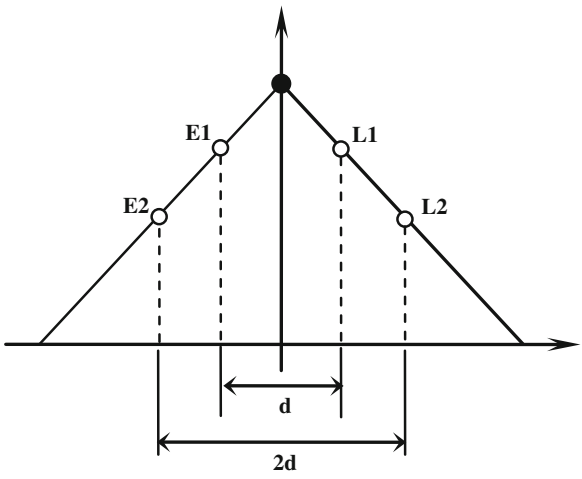

Fig. 1.1 Discrimination curve of HRC

1.3 Characteristics of Different Navigation Signals and the Derivation of HRC

The main meaning of BOC is to make the spectrum divided into two parts to avoid the interface with BPSK signals [10]. The reproduction codes of TD-BPSK are produced at the rate of 5.115 Mcps and will make correlation with received signals after transforming into a NRZ (Return to Zero) code at the duty rate of 1/2. The data part of TMBOC is BOC(1,1) and BOC(6,1) with the proportion of 29:4, and the correlation should be the summation of the two kind of signal with the proportion of 29:4. The curves of correlation of the four kinds of signals are shown in Fig. 1.2. The spectrum density of BPSK and BOC(1,1) is shown in Fig. 1.3, and we can see that the spectrum is divided with BPSK.

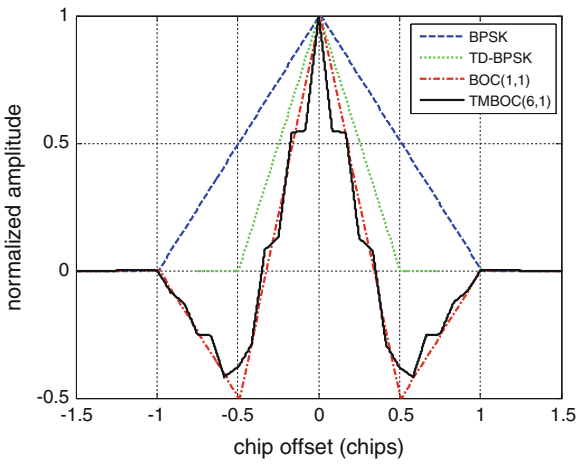

Fig. 1.2 Autocorrelation curve of the four signals

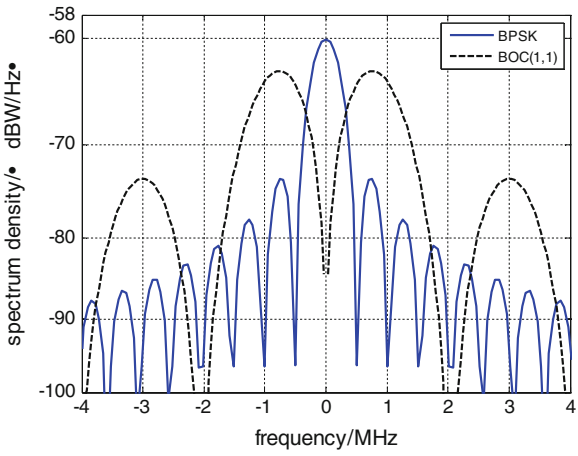

Fig. 1.3 Spectrum density of BPSK and BOC signals

Take the example of BOC(1,1) to deprive the discrimination function of HRC, and the other signals are almost the same except the different slope SL.

When $\tau \in [-0.5, 0.5]$,

$$R(\tau) = \begin{cases} A + SL \cdot \tau & -0.5 < \tau < 0 \\ A - SL \cdot \tau & 0 \le \tau < 0.5 \end{cases} \tag{1.2}$$

$SL = 3 \cdot A$, A is the correlation value of R(0).

When $-d/4 \le \tau_0 < d/4$, τ_E is always smaller than 0, and τ_L is always larger than 0, so

$$E1 = R\left(\tau - \frac{d}{2}\right) = A + SL \cdot \left(\tau - \frac{d}{2}\right) = A + SL \cdot \tau - SL \cdot \frac{d}{2} \tag{1.3}$$

$$E2 = R(\tau - d) = A + SL \cdot (\tau - d) = A + SL \cdot \tau - SL \cdot d \tag{1.4}$$

$$L1 = R\left(\tau + \frac{d}{2}\right) = A - SL \cdot \left(\tau + \frac{d}{2}\right) = A - SL \cdot \tau - SL \cdot \frac{d}{2} \tag{1.5}$$

$$L2 = R(\tau + d) = A - SL \cdot (\tau + d) = A - SL \cdot \tau - SL \cdot d \tag{1.6}$$

Then

$$E1 - L1 - \frac{1}{2}(E2 - L2) = 3A \cdot \tau \tag{1.7}$$

And

$$E1 + L1 = 2A - 3dA = (2 - 3d)A \Rightarrow A = \frac{E1 + L1}{(2 - 3d)} \tag{1.8}$$

Or

$$E1 + L1 - \frac{1}{2}(E2 + L2) = A \tag{1.9}$$

And we will get that,

$$\begin{aligned} \tau &= \frac{E1 - L1 - \frac{1}{2}(E2 - L2)}{3A} = \frac{E1 - L1 - \frac{1}{2}(E2 - L2)}{3\frac{E1+L1}{(2-3d)}} \\ &= \frac{E1 - L1 - \frac{1}{2}(E2 - L2)}{E1 + L1} \cdot \frac{2 - 3d}{6} \end{aligned} \tag{1.10}$$

Or

$$\tau = \frac{E1 - L1 - \frac{1}{2}(E2 - L2)}{3A} = \frac{E1 - L1 - \frac{1}{2}(E2 - L2)}{3[(E1 + L1) - \frac{1}{2}(E2 + L2)]} \tag{1.11}$$

1.4 Curve of HRC Discrimination and the Simulation of Multipath Mitigation

1.4.1 Curve of HRC Discrimination

We will select different correlator spacing when analyze the four kinds of navigation signals. And the curve of discrimination in the ideal condition of no multipath, no noise and infinite bandwidth is shown is Figs. 1.4, 1.5, 1.6 and 1.7.

As we can see in Figs. 1.4, 1.5, 1.6 and 1.7, the scope of discrimination is better when d is larger in some extent. For BSPK signals, there will be a turn point of discrimination zero point when d = 0.5 chip for HRC and when the correlator spacing is smaller than 0.5 chip, the scope of discrimination becomes better when d becomes larger and it will be meaningless as two pair correlators when d is larger than 0.5 chip. For TD-BSPK, the turn point of discrimination zero point is 0.25 chip, when the correlator spacing is smaller than 0.25 chip, the scope of discrimination becomes better when d becomes larger and it will be meaningless as two pair correlators when d is larger than 0.25 chip. BOC(1,1) is almost the same as TD-BPSK. For TMBOC when we use the pilot part only, the curve of discrimination is turned around when d is larger than 4/24 and we should avoid select values in that scope, and we can select 0–1/24, 2/24–3/24, and if we want to get a better scope of discrimination, we can select the correlator spacing between 2/24–3/24.

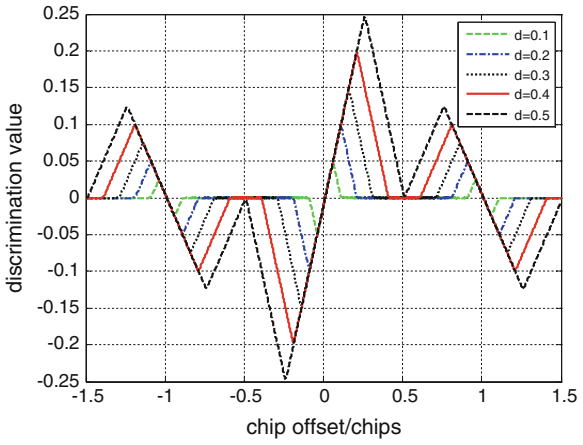

Fig. 1.4 Different d of HRC discrimination of BPSK

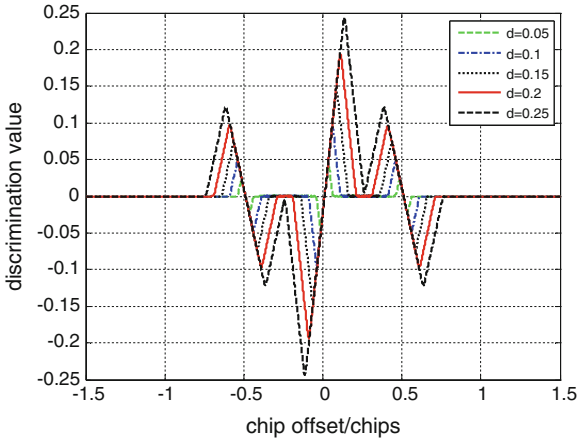

Fig. 1.5 Different d of HRC discrimination of TD-BPSK

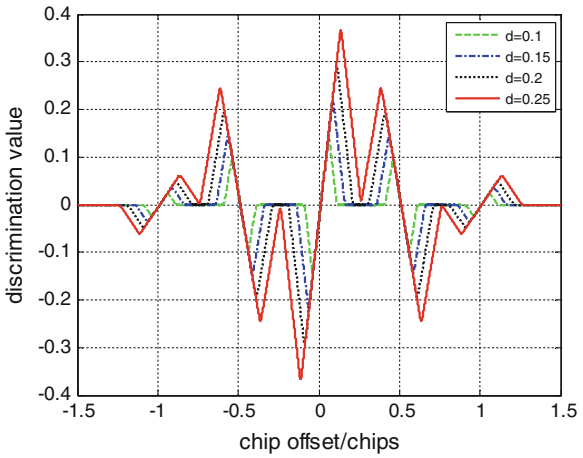

Fig. 1.6 Different d of HRC discrimination of BOC(1,1)

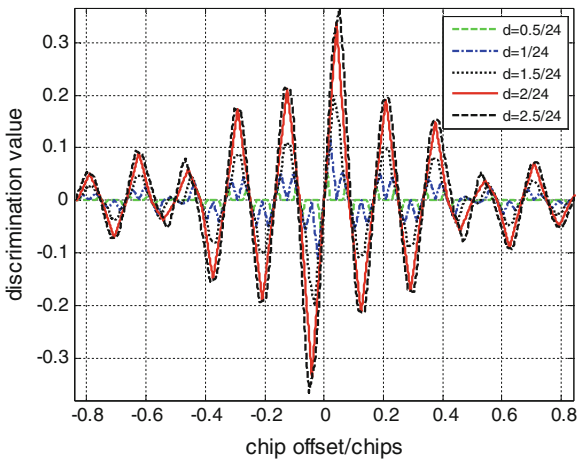

Fig. 1.7 Different d of HRC discrimination of TMBOC

1.4.2 Simulation of HRC for Different Kinds of Navigation Signals

Multipath signals are received after reflecting and refraction, and they will make the correlations between the compose signals and the reproduced code aberrant, this will bring errors for the calculation of position, speed and time [11], so measures should be taken to mitigate them. Simulation conditions in this paper are set as: the amplitude eclipse is 1/2, the rank of low pass filter is 31, and the front bandwidth is 2 MHz for BSPK and TD-BPSK, 4 MHz for BOC(1,1) and 16 MHz for TMBOC, and different correlator spacing will be selected, the simulations results are shown in Figs. 1.8, 1.9, 1.10 and 1.11.

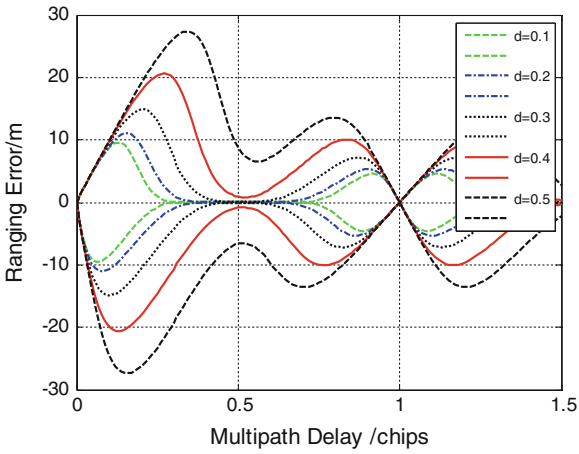

Fig. 1.8 Multipath tracking error envelope BPSK with HRC

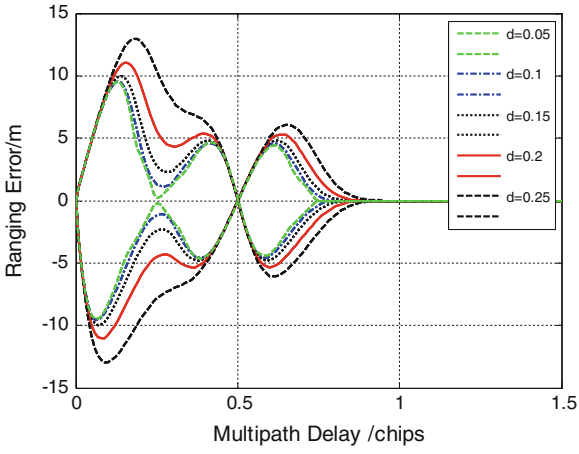

Fig. 1.9 Multipath tracking error envelope TD-BPSK with HRC

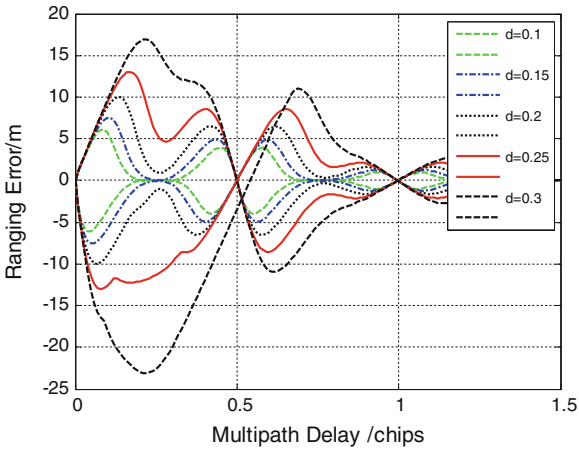

Fig. 1.10 Multipath tracking error envelope BOC(1,1) with HRC

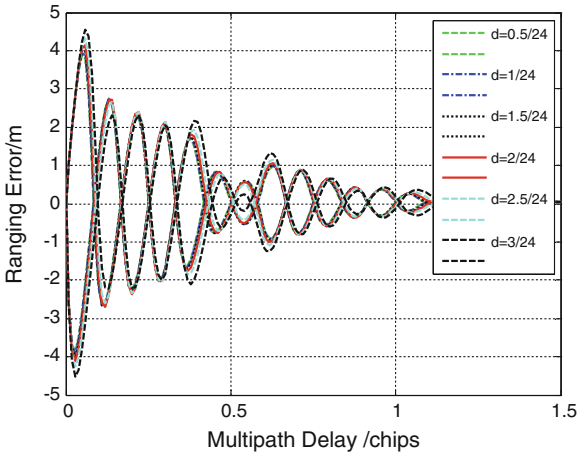

Fig. 1.11 Multipath tracking error envelope TMBOC with HRC

As we can see in Figs. 1.8, 1.9, 1.10 and 1.11, the performances of multipath mitigation are different for different signals. When multipath signals exist, the error envelops of multipath error become larger as the correlator spacing become larger, but the speed of variation are different. When the baseband is narrow, and the correlator spacing is small, the performance of multipath mitigation does not improve evidently any more when we select smaller spacing.

To take account of both the scope of discrimination and performance of multipath mitigation, the suggestion for BPSK is to select d smaller than 0.5 chip and we can select 0.25 chip to consider the both factors and we can adjust the spacing to meet the demand of scope of discrimination and performance of multipath mitigation. The suggestion for TD-BPSK is to select d smaller than 0.25 chip and we can select 0.15 chip in narrow baseband, the performance of multipath mitigation

does not improve evidently any more when we select smaller spacing of 0.1 chip. The suggestion for BOC(1,1) is almost the same with TD-BPSK. For TMBOC when we only use pilot part, the multipath errors do not different evidently in different correlator spacing, but if d is larger than 4/24, the multipath error will become large immediately, from Sect. 4.1 in this paper we know that when the spacing is larger than 4/24, the curve of discrimination will turn around which brings the bad effect for multipath mitigation, to consider the scope of discrimination this paper suggest to select the correlator spacing as 3/24 and can adjust beside it.

1.5 Conclusions

The selection of HRC will affect the scope of discrimination and the performance of multipath mitigation, and the key point is to make a balance between them and select optimize. This paper analyses the scope of discrimination and the performance of multipath mitigation, and gets the conclusions that when the correlator spacing is larger, the scope of discrimination is wider but the performance of multipath mitigation is worse, and the method of optimization selection is to balance both in different bandwidths. This paper points out the maximum of correlator spacing of HRC for different signals, for BPSK it is 0.5 chip, for TD-BPSK and BOC(1,1) it is 0.25 chip, for TMBOC it is 3/24 chip. When the baseband is narrow, the performance of multipath mitigation does not improve evidently any more when we select smaller spacing, in order to make the scope of discrimination wider, the correlator spacing should be selected larger to some extent. If other technologies of multipath mitigation are applied in different navigation signals, similar research can be done referent to this paper.

Acknowledgments This work is supported by National Natural Science Foundation of China (61032004 and 91338201), National High Technology Research and Development Program of China (“863” Program) (2012AA121605, 2012AA01A503, 2012AA01A510).

References

1. Van Dierendonck AJ et al (1992) Theory and performance of narrow correlator spacing in a GPS receiver. J Inst Navig 39(3):265–283
2. McGraw MB (1999) GNSS multipath mitigation using high resolution correlator concepts. ION NTM 1999:333–342
3. Liu H, Cheng X, Wang F (2011) The multipath mitigation performance of double-delta technique in band-limited receiver channel. Geomatics Inf Sci Wuhan Univ 2011:1231–1235
4. Lionel G (1996) Strobe and edge correlator multipath mitigation for code. ITM, Kansas City, pp 657–664
5. Jason J, Fenton P, Smith B (2011) Theory and performance of the pulse aperture correlator. http://www.novatel.com/Doucuments/Papers/PAC.pdf

6. Morrissey TN, Shallberg KW, Townsend B (2006) Code tracking errors for double delta discriminators with narrow correlator spacing and band limited receivers. The Institute of Navigation NTM, Monterey
7. Dong X, Tang B, Jiang D (2008) Principle and design of satellite software receiver. National Defense Industry Press, Beijing, pp 59–76
8. Li B, Xu J, Cao K, Zhu Y (2012) Analysis and simulation on anti-multipath performance of BeiDou2 navigation. J Chin Inertial Technol 20(3):339–347
9. Kaplan ED, Hegarty CJ (2012) Understanding GPS principles and applications, 2nd edn. pp 210–215
10. Qiu Z (2005) BOC modulation of GPS M code signal. Navigation 3(1):1–18
11. Xie G (2009) Principles of GPS and receiver design. Publishing House of Electronics Industry, Beijing, pp 336–337

Chapter 2
The Key Questions Discussing of the Inter-Satellite Link (ISL) Signal Design Based on Earth-Moon System

Jianjun Fan, Yang Yang and Min Li

Abstract There are four kinds of inter-satellite link (ISL) based on Earth-Moon Lagrange navigation system. The much larger difference in transfer distance leads to large signal level dynamic range. Therefore signal design has much difficulty. In order to simplify the complexity of satellite payload, an integrative ISL signal scheme based on CDMA technique is proposed. The question of signal frequency selection and near-far effect have been analyzed in this article. The scheme's feasibility is justified by theoretical modeling and simulation calculation in the end.

Keywords Inter-satellite link · Near-far effect · Frequency selection

2.1 Introduction

The Earth-Moon Lagrange navigation system which arranges a plurality of space navigation station at Lagrange libration points networks construction with near earth satellite navigation to meet navigation and positioning requirements such as autonomous operation of near earth satellite navigation and deep space exploration. There are four kinds of inter-satellite link which is between Lagrange navigation satellites, between navigation satellites near the earth, between Lagrange navigation satellites and navigation satellites near the earth, and between Lagrange navigation satellite and spacecraft users. Links are at the distance of 70,000–400,000 km, dynamic range for received signal level is large, and there are higher accuracy requirement and a large quantity of information transmission. The signal design is difficult, particularly to avoid in large dynamic signal condition signal interference problem [1–3]. In this paper, 4 links are designed that is based on the basic

J. Fan (✉) · Y. Yang · M. Li
Beijing Satellite Navigation Center, Beijing 100094, Beijing, China
e-mail: fjjgps@163.com

J. Sun et al. (eds.), *China Satellite Navigation Conference (CSNC) 2015 Proceedings: Volume II*, Lecture Notes in Electrical Engineering 341,
DOI 10.1007/978-3-662-46635-3_2

requirements and characteristics of the Lagrange navigation system. The signal designed is fully and rationally utilizing spectrum with the space tracking and navigation of spacecraft users sharing the same channel, namely the system using the orbit determination and time synchronization link also providing radio ranging service for all customer spacecraft, which greatly simplifies the load on the satellite design complexity but increases of signal design difficulty, including signal frequency selection and modulation mode selection, coding scheme, especially considering the effect of signal near-far effect for longer transmission distance. This paper will focus on above problems with analysis and discussion.

2.2 Analysis of Inter Satellite Link Characteristics

On the basis of the Earth-Moon Lagrange navigation system mainly consists of 3–5 navigation satellites (located in L1, L2, L3, L4, L5 navigation satellite) and near earth navigation constellation (24 satellite). Lagrange navigation satellite can transmit navigation signal, the construction of inter satellite link between each other, distance observation and communication, and inter satellite link observation and communication with near navigation constellation composed of observation and communication system link, orbit determination and time synchronization processing system, and provides the Earth Moon space navigation application service. Between the Lagrange navigation satellite and near earth navigation satellite each constitute a relatively independent navigation system, through the construction of measurement and communication link between the Lagrange navigation satellites and near earth navigation satellite, can run autonomously to solve the near earth satellite navigation system is very good when the satellite constellation rotation problem. Signal integration design of 4 link, convenient device configuration is simple and uniform, and can avoid because of the different terminal to realize the kinds of system error and random error, is a basic principle of this inter satellite link signal design follow.

The inter-satellite link signal of the Earth-Moon Lagrange navigation system has the following characteristics: (1) large signal dynamic range. Four kinds of links are at the distance of 70,000–400,000 km, and the received signal level dynamic range is more than 8 dB. (2) The communication rate and measuring accuracy is limited. Because the satellite resources is limited, it is difficult to use a larger power to realize high speed data transmission. At the same time, long distance communication also has large space transmission loss, so generally ranging accuracy and data transmission rates are not high. The Lagrange system operation and navigation service requirements on ranging precision is about 0.3–3 ns and data transmission rate is not less than 500 bps, and even up to 5 kbps. System for spacecraft is not less than 25 bps to provide the transmission rate of the navigation message. (3) High

transmission delay. Transmission distance of 400,000 km has the transmission delay 1.3 s. Therefore, for deep space communications and navigation, real-time operation, control and communication is not possible.

According to the Consultative Committee for Space Data Systems (CCSDS) radio frequency and modulation proposal, there is no high bit rate transmission data transmission and ranging signals at the same time advice. The following will be integrated into communication and measurement requirements, equipment implementation ability and the future development trend of technology, planning the design of inter satellite link signal.

2.3 Design of Inter Satellite Link Signal

2.3.1 Frequency Selection

Frequency selection involves the following several problems: (1) frequency band selection. It is not only to meet the allocation rule of International Telecommunication Union (ITU), but also to consider the service demand for the comprehensive implementation of the ability, the influence of spatial transmission error and technology; (2) the two-way communication and measuring system working mode selection. The full duplex or half duplex communication mode decides the number of frequencies or band; (3) the multi access method selection for multi user signal. Selecting communication mainstream TDMA, FDMA or navigation field mainstream CDMA mode decides signal number in the single channel.

(1) Frequency band selection

Signal frequency band selection is mainly based on available carrier frequency ITU distribution. Frequency selection also comprehensively considers of several aspects such as the service demand, propagation effects and technology needs.

According to the radio regulations, VHF, UHF, L, S, Ka band and above Ka band can be used for the inter satellite link communication. In the navigation system, satellite ground links using L, S band, from the system electromagnetic compatibility perspective, inter satellite link is mainly selected from VHF, UHF and Ka bands.

In fact, the performance of millimeter wave active device determines the whole millimeter wave system performance to a great extent, but also limits the choice of working frequency band. Foreign technology is more advanced. The antenna, transmitter and receiver can be integrated in a MMIC chip which has the advantages of small volume, light weight, good consistency. At present the foreign has more than 100 GHz reports. According to the current level of millimeter wave active device which can realize the transceiver module under 35 GHz. For the current equipment implementation capacity, using the 32.3 GHz 33 GHz band is more suitable.

(2) Work mode selection

TDD and FDD belong to two different duplex mode. TDD stands for time division duplex, and belongs to half duplex. That is to say on the up and down link in the same frequency band according to the allocation of time for the cross. FDD represents a full duplex that the up and down link are in different frequency band at the same time. The two types of their respective advantages and disadvantages is that, TDD for uplink and downlink in the same frequency band, so it can better use of spectrum resources, easy to layout; and FDD for uplink and downlink at the same time, in different frequency bands act as one pleases, so the data transmission capacity is more. As mentioned earlier, data space transmission delay can reach to 1.3 s for the big link space transmission distance between satellites. Then considering the signal acquisition, tracking and stabilization time, half duplex TDD is low efficiency, and should not be selected. The choice of a two frequency band at the same time, two-way data transmission and signal measurement of continuous is the ideal way of working.

(3) The multiple access mode selection

The signal must be designed to avoid interference between different satellite signals, so as to ensure that the receiver can distinguish between different signal. FDMA, TDMA and CDMA is the most commonly used several multiple access modes in currently the radio communication and navigation system.

Using orthogonal CDMA code sequence for implementing different satellite access, different satellite signal overlap in the frequency spectrum and time domain. The current navigation field and recent development of 3G system and CDMA2000 just use code division multiple access.

The separation of different satellite signal spectrum access is realized by FDMA, and different signal overlap in time domain and code domain. Frequency division multiple access allocates a single channel to individual users, such as the GLONASS of each satellite using a band only. In a large number of users, the system cost is higher than that of TDMA system. The main reason is the need for RF front end terminal unit with ultra wide band, also need to configure the expensive bandpass filter.

TDMA is to launch a satellite signal at the different time to avoid interference in the system. A major feature of TDMA is the data transmission or location is not continuous, and the demand for bandwidth is smaller. For the 400,000 km of transmission distance, inter satellite link signal space transmission time reached about 1.3 s, so the signal chain building time is too long and the signal acquisition and tracking is very difficult. Therefore it does not recommend the application of the multiple access mode.

Based on the above analysis, CDMA is proposed mode of multiple access.

According to the choice of frequency selection, working mode and multiple access mode, the 2 bands in the 32.3 GHz 33 GHz frequency range is chosen. Considering the transmitter receiver isolation, we selected the center frequency of 43.50103 GHz/43.56241 GHz, bandwidth of send and receive pairing, respectively

44 MHz. The bit rate of 20.46 Mcps is chosen. The code length is tentatively scheduled for 10,230 bit, and it can be extended according to the equipment to realize the ability.

2.3.2 Modulation Mode Selection

Any communication system or a navigation system in the selection of modulation mode, power efficiency and bandwidth efficiency are the two most important factors. The frequency band and the power performance have the good performance, and can simultaneously carry out the modulation data transmission and ranging from QPSK/OQPSK, MSK/GMSK. MSK has a characteristics of constant envelope and small power out of band. But zero bandwidth of MSK is 1.5 times of that of BPSK, and the realization of the receiver in the satellite has difficulties. In fact, for the effective mode power, CCSDS first proposed a QPSK modulation. QPSK has good error performance, and main lobe of signal modulation spectral is narrow. Because of the existence of the envelope fluctuation problem, QPSK is mainly applied to linear channel. Through reducing the envelope fluctuations and increasing RF power amplifier, frequency spectrum after this amplifier can be limited to the allowed range. QPSK envelope fluctuation is mainly due to symbol from two orthogonal branch with common starting time, and jumping ±180° in the phase symbol at conversion time. OQPSK solves these problems. OQPSK is deformation of QPSK through the shift of half a symbol, which makes the phase mutation maximum ±90°, and reduce the signal envelope fluctuation. But the BER performance and bandwidth efficiency are same with QPSK. In fact, UQPSK is another kinds of deformation for QPSK with I/Q channel power regulation. UQPSK error performance and bandwidth efficiency are same with QPSK. It helps to improve the signal design flexibility, and balance the anti-interference ability of I/Q channels. The demodulation processing is simple, but the processing complexity is slightly higher than QPSK.

A comprehensive comparison of the spectral efficiency, error rate performance, the ranging performance and implementation complexity and so on many factors, OQPSK and UQPSK modulation (U-OQPSK) are suggestion choice as the inter satellite link system modulation, which can better balance the threshold difference for the ranging signal and digital signal, wherein the I branch is for ISL ranging, end users ranging and the information demodulation, Q branch is for inter satellite communication link.

2.3.3 Coding Mode Selection

The traditional coding methods, such as convolutional codes, linear block codes with short code length, RS and convolutional concatenated code, the coding gain is low. High gain channel coding scheme is used as far as possible, such as LDPC

Table 2.1 Scheme of inter satellite link signal for Lagrange navigation system

Parameters	Content
Center frequency	43.50103 GHz/43.56241 GHz (Transceiver pairs)
Work width	50 MHz
Modulation	UQPSK
The multiple access	CDMA
Code rate	20.46 Mcps
Code length	10,230
I channel data rate	25 bps
Q channel data rate	500 bps
I channel code mode	Convolutional code
Q channel code mode	½ LDPC

code [4]. LDPC codes are block codes, the packet length is strictly limited by information timeliness requirements and inter satellite link payload hardware resource constraints. In the condition of aging demand is not high, the length may be 1000 or 2000. Packet length should not be too long, so the I channel is chosen as 1024. In accordance with the coding gain and spreading gain, 1/2 LDPC code is selected as the Q channel coding scheme. I channel information rate is low, so simple convolutional code is used.

In summary, link signal scheme between the satellites is seen in Table 2.1.

2.3.4 Link Budget

I channel signal is to be used as ranging and message broadcasting to meet the end user ranging and navigation requirements, the orbit determination and time synchronization ranging needs. Because the message rate were significantly lower than those of Q channel, the desired signal carrier to noise is lower than the threshold. So the carrier to noise ratio threshold of I channel mainly depends on the ranging threshold. Noncoherent discriminator ranging error calculation formula in accordance with BPSK modulation:

$$\sigma_\tau = T_c \sqrt{\frac{2d^2 B_n}{C/N_0}\left[2(1-d) + \frac{4d}{TC/N_0}\right]} \tag{2.1}$$

Table 2.2 Different ranging demands of the carrier to noise ratio threshold

Ranging demands (ns)	Carrier to noise ratio threshold (dB-Hz)
0.3	34.9
1	28.2
10	18.8

Assuming that the receiver loop noise bandwidth of Bn is 0.1 Hz, the relevant interval of d is 1 chip, and the cumulative integral time T is 0.005 ms. According to the above formula, the ranging accuracy is to be achieved better than 0.3, 1 and 10 ns (1Sigma) of the carrier to noise ratio threshold as shown in Table 2.2.

Q channel signal is mainly used for data transmission. Considering the signal-to-noise ratio and the carrier to noise ratio between the coding gain:

$$\left[\frac{C}{N_0}\right] = \left[\frac{E_b}{N_0}\right] + 10\log(\mathrm{R_b}) + [L] - [G] \tag{2.2}$$

$\left[\frac{C}{N_0}\right]$ is carrier to noise ratio; $\left[\frac{E_b}{N_0}\right]$ is signal to noise ratio; $\mathrm{R_b}$ is data rate; $[L]$ is realization loss, the general is under 2 dB; $[G]$ is code gain.

Modulation mode is BPSK, the BER requirements is for 10^{-6}, and using coherent demodulation requires $\mathrm{E_b/N_0}$ to 10.6 dB. Assuming the processing loss is 2 dB and Q channel coding gain is 9 dB, the carrier to noise ratio at receiving antenna aperture requirements is 30.6 dB-Hz.

In short, when the ranging precision is 0.3 ns, the signal carrier to noise ratio requirements is 34.9 dB-Hz. When the ranging accuracy requirements is 10 ns, the signal carrier to noise ratio requirements to Q channel is prevail of demodulation threshold, namely 30.6 dB-Hz.

Antenna gain has been achieved can reach 35 dBic, and emission EIRP of 40 dBW can be achieved. Therefore, the carrier to noise of the near earth navigation satellite received from Lagrange navigation satellite is such as shown in Table 2.3.

It can be seen from Table 2.3, the antenna gain under 35 dBic cannot satisfy the ranging accuracy 0.3 ns requirements, but the other needs can be satisfied. It is able to meet the Q channel data transmission and I channel 1 ns pseudorange measurements and 25 bps message broadcasting. When the antenna gain is increased above 3 dB, according to the link calculation, it can meet the requirements of 0.3 ns ranging accuracy obviously.

Table 2.3 The actual received carrier to noise ratio (a distance of 400,000 km)

Parameters	Result
Transmitting power (dBW)	5
A transmitting antenna gain (dBic)	35
Transmitting EIRP (dBW)	40
The path loss (dB)	243.3
Pointing, polarization loss (dB)	2.0
Receiving antenna gain (dBic)	36
The actual received carrier to noise ratio (dB-Hz)	32.6

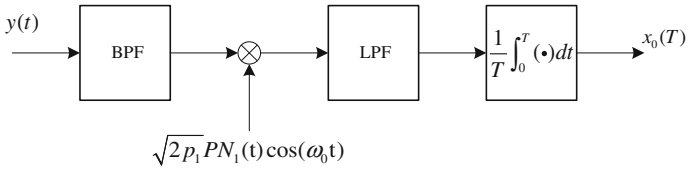

Fig. 2.1 The received CDMA signal model

2.4 Analysis of Near-Far Effect

Relative to other multiple access methods, CDMA is the most sensitive to the near far problem, and need to be carefully treated. In the near earth satellite navigation system of autonomous operation stage, the satellite can receive signals from Lagrange navigation satellite, also receive signals from other near navigation satellite. Signal level differences is above 8 dB. The weak signal receiving ability is needed to study. Assuming near navigation satellite with reference to the GPS constellation design, each near navigation satellite has also received 8 other near earth navigation satellite signal and the 2 Lagrange navigation satellite signal ability. Combined signal through the antenna and channel equipment after reference signal correlation demodulation, low pass filter, integral accumulation, the received model is shown in Fig. 2.1 [5].

The received signal plus interference and thermal noise model is shown below:

$$y(t) = \sum_{i=1}^{N} \sqrt{2p_i} d_i(t) PN_i(t) \cos(\omega_0 t) + \sqrt{2} n_c(t) \cos(\omega_0 t) + \sqrt{2} n_s(t) \sin(\omega_0 t)$$

In the formula, p_i is the signal power, N = 10, p_1 is Lagrange navigation satellite signal power, the other is near earth navigation satellite signal power; $d_i(t)$ is a baseband signal data; $PN_i(t)$ is spreading code applied in signal; The last two items is thermal noise which is modeled as Gauss random process.

Assumed that baseband equivalent filter function is $H_{BB}(f)$, and the bandwidth is B Hz. The output of the signal after the correlation demodulation with reference signal, low pass filter, integral accumulation is:

$$\begin{aligned} x_0(T) &= \sqrt{p_1} \int_{-\infty}^{\infty} H_{BB}(f) S_{d1}(f) df + \frac{1}{T} \sum_{i=2}^{N} \sqrt{p_i} \int_0^T d_i(t) PN_i(t) PN_1(t) dt + \frac{1}{T} \int_0^T n_c(t) PN_1(t) (dt) \\ &= s_0(T) + n_0(T) \end{aligned}$$

The noise part n_0 (T) is thermal noise plus other user interference signal, and its variance:

$$Var(n_0(T)) = \frac{1}{T}\int_{-\infty}^{\infty} S_{n_c}(f)S'_{PN_1}(f)df + \frac{1}{T}\sum_{i=2}^{N}\frac{P_i}{2}\int_{-\infty}^{\infty} S'_{PN_1}(f)S'_{PN_1}(f)df$$

where $R'_{PN}(\tau)$ is the unit power self-correlation function of $PN_i(t)$. Among them, $S_{n_C}(f)$ is a bilateral noise spectral density; $S'_{PN_i}(f)$ is signal unit power spectral density.

Considering the front-end bandpass filter restriction, it can get:

$$Var(n_0(T)) = \frac{N_0}{2T}\int_{-\infty}^{\infty} |H_{BB}(f)|^2 S'_{PN_1}(f)df + \frac{1}{T}\sum_{i=2}^{N}\frac{P_i}{2}\int_{-\infty}^{\infty} |H_{BB}(f)|^2 S'_{PN_1}(f)S'_{PN_1}(f)df$$

Equivalent noise spectrum density N'_0 is defined as below:

$$N'_0 = 2TVar(n_0(T))$$

Therefore, the equivalent noise spectrum density:

$$N'_0 = N_0\int_{-\infty}^{\infty} |H_{BB}(f)|^2 S'_{PN_1}(f)df + \sum_{i=2}^{N} P_i\int_{-T}^{T} |H_{BB}(f)|^2 S'_{PN_1}(f)S'_{PN_i}(f)df$$

The above formula is simplified as:

$$N'_0 = \upsilon N_0 + \sum_{i=2}^{N} P_i I_0$$

Among them, $\upsilon = \int_{-\infty}^{\infty} |H_{BB}(f)|^2 S'_{PN_i}(f)df$,

$$I_0 = \int_{-T}^{T} |H_{BB}(f)|^2 S'_{PN_1}(f)S'_{PN_1}(f)df$$

υ is usually very close to 1, I_0 is the spectral separation coefficient. In this case,

$$N'_0 = N_0 + \sum_{i=2}^{N} P_i I_0$$

According to the equivalent definition of carrier to noise ratio:

$$\frac{P_1}{N_0'} = \frac{P_1}{N_0 + \sum_{i=2}^{N} P_i I_0} = \frac{\frac{P_1}{N_0}}{1 + \sum_{i=2}^{N} \left(\frac{P_i I_0}{N_0}\right)} \tag{2.3}$$

The conventional BPSK (10) of the spectral separation coefficient is about −70.0 dB. Because the signal bandwidth and the rate are wide, on this signal design conditions spectral separation coefficient calculated is −74.0 dB.

According to the formula (2.3), in the spectral separation coefficient is −74.0 dB, the corresponding equivalent carrier to noise ratio is 32.6 dB-Hz, the receiving effect that other near navigation satellite signal to Lagrange navigation satellite signal can be ignored; in the spectral separation coefficient is −70.0 dB, the corresponding equivalent carrier to noise ratio is still about 32.6 dB-Hz. Thus, in this paper the assumption that the signal received quantity condition, smaller effect of strong signal of receiving weak signals, can be ignored.

Considering the theoretical limit, when the spectral separation coefficient of −74.0 dB, change the near earth satellite navigation signal number reached 1400, equivalent carrier to noise ratio reached 30.6 dB-Hz; and when the spectral separation coefficient of −70.0 dB, change the near earth satellite navigation signal number reached 570, carrier to noise ratio reached 30.6 dB-Hz equivalent. As can be seen, the influence of spectral separation coefficient of the user capacity is very big still, and illustrates the requirements of PN code correlation properties of the signal design is very necessary.

2.5 Conclusion

In this paper, the thorough research on the inter satellite link signal design is based on the Earth Moon system Lagrange navigation system. A design scheme based on CDMA multiple access is proposed from the aspects of frequency selection, modulation, the rate and coding method, and the ability of the future technology development trend considered communication and measurement requirements, equipment. The problem focuses on the work mode selection, multiple access near-far effect selection that CDMA system is sensitive to. Negligible influence on weak signal with receiving strong signal system is proved through theoretical modeling, simulation, so the signal design plan is feasible. Finally, the theoretical limit of the user capacity of the system is given, and that the spectral separation coefficient affect user capacity is pointed out, which is determined as a basic principle for pseudo code optimization.

References

1. Kaplan ED, Hegarty CJ (2007) Understanding GPS principles and applications. Artech House, Boston
2. Roger LP, Rodger EZ, David EB (2006) Introduction to spread spectrum communications. Publishing House of Electronics Industry, Beijing
3. Sanchez M, Pulido JA (2008) The ESA "GNSS+" Project Inter-satellite ranging and communication links in the frame of the GNSS infrastructure evolutions. In: Proceedings of the 21st international technical meeting of the satellite division of the institute of navigation. The Institute of Navigation, Georgia, pp 2538–2546
4. MacKay DJC (1999) Good error-correction codes based on very sparse matrices. IEEE Trans Inf Theor 45(2):399–431
5. Jack KH, Jun C, Yi L, Zhuo T (2013) Translation. Spread spectrum system for GNSS and wireless communication. Electronic Industry Press, Beijing

Chapter 3
Application Study of a Phase-Optimized Constant-Envelope Transmission (POCET) Optimization Algorithm for BDS B1 Signal

Minggui Cai, Jun Xie and Gang Wang

Abstract Firstly we describe an improved POCET algorithm and design a multiplexing plan for B1 signals using it. At B1 frequency, binary complex subcarrier is chosen to implement the center frequency difference between regional and global navigation systems. Regional BPSK(2) OS signal and global TMBOC signal are combined and the best multiplex efficiency is −1.010 dB. Regional BPSK(2) AS signal and global BOC signal are combined and the best multiplex efficiency is −1.593 dB. And then, we analyze the signal in band-limited systems from three aspects: multiplex efficiency, constellation diagram and signal's peak to average power ration (PAPR). And then, we analyze the multiplex signal in band-limited system from three aspects: multiplex efficiency, constellation diagram and signal's peak to average power ration (PAPR). The ideal constant-envelope signal has become nonconstant-envelope of which constellation has changed and PAPR has increased. Also the multiplex efficiency has decreased, and it has decreased more after 30 MHz filter by almost 0.55 dB. The results of this paper provide the constant-envelope multiplex scheme at B1 frequency and the multiplex efficiency, and the analysis in band-limited system which is of significance in engineering practice.

Keywords Constant-envelope multiplex · BDS · POCET · Multiplex efficiency · Band limit

M. Cai (✉) · G. Wang
Xi'an Branch, China Academy of Space Technology, Xi'an, China
e-mail: 850139631@qq.com

J. Xie
China Academy of Space Technology, Beijing, China

J. Sun et al. (eds.), *China Satellite Navigation Conference (CSNC) 2015 Proceedings: Volume II*, Lecture Notes in Electrical Engineering 341,
DOI 10.1007/978-3-662-46635-3_3

3.1 Introduction

With the continuous development of GNSS (Global Navigation Satellite Systems), the number of service signals is increasing fast [1]. But the navigation frequency resource is limited, so the multichannel ranging code should be modulated compositely on the limited carriers in order to deal with GNSS signal spectrum congestion. POCET (Phase-Optimized Constant-Envelope Transmission) is a kind of phase modulation technique. It computes the phase and amplitude of the modulation signal to maximize the multiplex efficiency by optimization algorithm on the premise of the power and phase relationship between the signals [2]. The multiplex efficiency of POCET is high and the implementation is quite simple. The GPS signals using POCET has been verified in semi-physical simulation [3], and the Aerospace has been studying the POCET modulation for multi-frequency signals [4].

3.2 POCET Algorithm

3.2.1 Theory of POCET

The multiplex efficiency of N-signals multiplex can be defined as the ration between total power of all sub signals to power of compound signal:

$$\eta = \frac{\sum_{n=1}^{N} |\mathrm{corr_n}|^2}{A^2} \tag{3.1}$$

where $P_{dn} = |\mathrm{corr_n}|^2$ is the power of nth sub signal from correlation receiver, and A^2 is the power of compound signal with A is the amplitude, and $\mathrm{corr_n}$ is the correlation of the nth sub signal:

$$\mathrm{corr_n} = \frac{A}{2^N} \sum_{k=0}^{2^N-1} [1 - 2b_n(k)] \exp(j\theta_k) \tag{3.2}$$

where $b_n(k)$ is the binary code of nth signal, and θ_k is the phase corresponding to the kth codes group.

POCET is an optimization problem with the constraints of the phase and power relationship between sub signals, and usually penalty function is used to change this constrained optimization into an unconstrained one.

3.2.2 Constrained Optimization Algorithm

An improved algorithm without amplitude A is given in 5, but it still uses the penalty function for optimization. In fact, the penalty factors will affect the solutions when using penalty function. But there is no simple liner relationship between them and the factors will affect each other. So to find the optimal solution, the factors should be continuously readjusted according to the last solutions which increases the optimization time.

Therefore we provide a constrained optimization algorithm. Firstly normalized correlation $\mathrm{corr_n}$ and expected power $\mathrm{p_n}$ is defined as:

$$\mathrm{corr_n} = \frac{1}{2^N}\sum_{k=0}^{2^N-1}[1-2b_n(k)]e^{j\theta_k} \tag{3.3}$$

$$\mathrm{p_n} = \eta\frac{(\mathrm{corrd_n})^2}{\sum_{i=1}^{N}(\mathrm{corrd_n})^2} \tag{3.4}$$

where $(\mathrm{corrd_n})^2$ is the expected power of the nth sub signal, and $\eta = \sum_{n=1}^{N}|\mathrm{corr_n}|^2$, that is the multiplex efficiency.

The power error and phase error can be written as:

$$\begin{aligned}\Delta P &= \sum_{n}^{N}\left||\mathrm{corr_n}|^2 - \mathrm{p_n}\right| \\ \Delta\varphi &= \sum_{m=1}^{N}\sum_{l=m+1}^{N}\left|\mathrm{imag}(e^{j\varphi_{ml}}\frac{\mathrm{corr_m corr_l^*}}{|\mathrm{corr_m}||\mathrm{corr_l}|})\right|\end{aligned} \tag{3.5}$$

Then the optimization problem can be written as:

$$\min f(\bar{\theta}) = 1-\eta, \quad \text{s.t.}\begin{cases}\Delta P \le \delta_1 \\ \Delta\varphi \le \delta_2\end{cases} \tag{3.6}$$

where δ_1 and δ_2 is the maximum power and phase error which can be set according to the practical requirements. The complex method is used to search the optimal solution.

3.3 Multiplex Design for B1 Signals

For BDS B1 frequency band, there is OS (Open Service) signal using MBOC (1,6,1/11) modulation and AS (Authorized Service) signal using BOC(14,2) modulation [5]. We choose TMBOC modulation for OS signals, and set the power ratio of pilot signal to data signal as 3:1.

3.3.1 Smooth Transition for B1 Signals

The complex subcarrier shown as follows is taken to modulate the QPSK(2) at L1 frequency band (1575.42 MHz), to move down the center frequency:

$$\begin{aligned} SC_{cos}(t) &= \text{sign}(\cos 2\pi f_{sc} t) \\ SC_{sin}(t) &= \text{sign}(\sin 2\pi f_{sc} t) \\ SC(t) &= SC_{sin}(t) + jSC_{cos}(t) \end{aligned} \tag{3.7}$$

where $f_{sc} = 14.322\,\text{MHz}$.

3.3.2 POCET Phase Solution

3.3.2.1 Multiplex of Four B1 OS Signals

The power ratio between $S_{B1I\_I}(t)$, $S_{B1I\_Q}(t)$, $S_{B1C\_p}(t)$ and $S_{B1C\_d}(t)$ is set as 1:1:1.717:0.572. And there is 90° phase difference between $S_{B1I\_I}(t)$ and $S_{B1I\_Q}(t)$, and 0° phase difference between $S_{B1C\_p}(t)$ and $S_{B1C\_d}(t)$. The phase is worked out based on Eq. (3.6) with $\delta_1 = \delta_2 = 10^{-3}$. The optimized phase is shown in Table 3.1, and because of the symmetry of the codes value, the rest phases have 180° phase difference between the ones shown.

The multiplex efficiency is −1.010 dB, and PAPR is 1 which means that the compound signal is ideally constant-envelope. The constellation of the compound signal is shown in Fig. 3.1 from which we can visually denote all the phase points locate on the unit circle. The power error and phase error of the optimal phase solution is 10^{-3} and 10^{-7}.

3.3.2.2 Multiplex of Three B1 AS Signals

The power ratio between $S_{B1Q\_I}(t)$, $S_{B1Q\_Q}(t)$ and $S_{B1A}(t)$ is set as 1:1:2. And there is 90° phase difference between $S_{B1Q\_I}(t)$ and $S_{B1Q\_Q}(t)$.

Table 3.1 Phase of 4-signals multiplex

SB1C_d	SB1I_I	SB1I_Q	SB1C_p	$\theta_k(°)$
0	0	0	0	0
0	0	0	1	−55.4
0	0	1	0	112.2
0	0	1	1	−23.1
0	1	0	0	242.1
0	1	0	1	291.7
0	1	1	0	127.2
0	1	1	1	−100.1

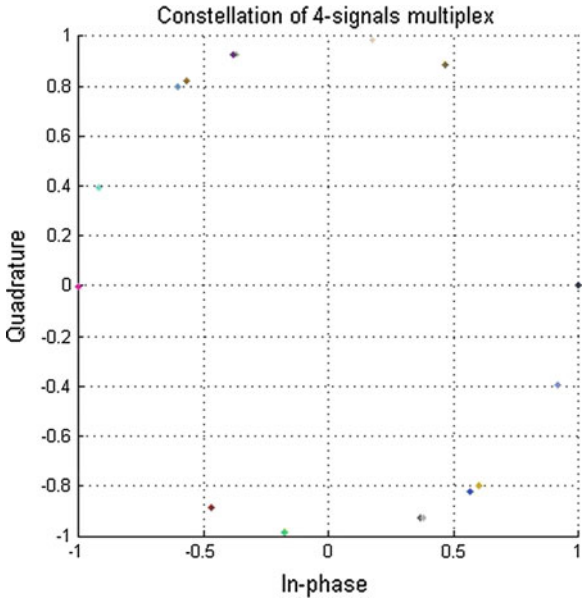

Fig. 3.1 Constellation of 4-signals multiplex

The phase is worked out based on Eq. (3.6) with $\delta_1 = \delta_2 = 10^{-3}$. The optimized phase is shown in Table 3.2.

The multiplex efficiency is −1.593 dB, and PAPR is 1. The constellation is shown in Fig. 3.2.

3.4 Simulation and Analysis in Band-Limited System

There has been much research about constant-envelope multiplex techniques for navigation signals. For example, the BDS B1 4-codes multiplex plan proposed by Zhang Kai using optimized POCET [6] and the BDS B1 4-codes multiplex plan proposed by Zhu Liang et al. using asymmetric AltBOC [7], both of which multiplex efficiency reaches −1 dB. But the bandwidth limit in real satellite navigation

Table 3.2 Phase of 3-signals multiplex

SB1Q_I	SB1Q_Q	SB1A	$\theta_k(°)$
0	0	0	0
0	0	1	−226.1
0	1	0	113.4
0	1	1	−193.7

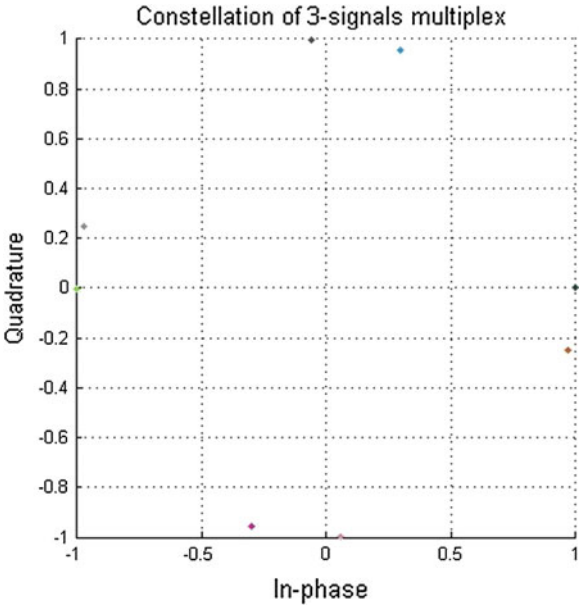

Fig. 3.2 Constellation of 3-signals multiplex

systems was not considered in all these multiplex plans. So in this chapter the multiplex performance in band-limited system is further simulated and analyzed.

According to Eq. (3.1), the multiplex efficiency in band-limited system can be written as:

$$\eta = \frac{\sum_{n=1}^{N} |\mathrm{corr}_{\mathrm{real\_n}}|^2}{\bar{A}^2} \tag{3.8}$$

where $\bar{A}^2$ is the compound signal's power, and $\mathrm{corr}_{\mathrm{real\_n}}$ is the correlation of the compound signal and the nth sub signal:

$$\mathrm{corr}_{\mathrm{real\_n}} = \frac{\sum_{k=0}^{N_s-1} s(k)b_n(k)}{N_s} \tag{3.9}$$

where $s(k)$ is the compound signal, N_s is the length of the signal, and $b_n(k)$ is the nth ideal sub signal.

3.4.1 Baseband Equivalent Model

The baseband equivalent model for simulation is shown in Fig. 3.3 [8]. The filter is 8th order low-pass elliptic filter, and the HPA (high-power amplifier) adopts normalized Saleh model [9]. Two groups of band-limited signals with 30 MHz bandwidth and 60 MHz bandwidth are simulated separately for comparison.

3.4.2 Analysis of Multiplex Performance

We focus on the multiplex of four B1 OS signals with band limit. The constellation of the compound signal after pre-filter is shown as Figs. 3.4 and 3.5.

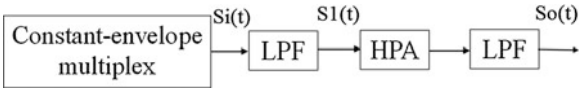

Fig. 3.3 Baseband equivalent model

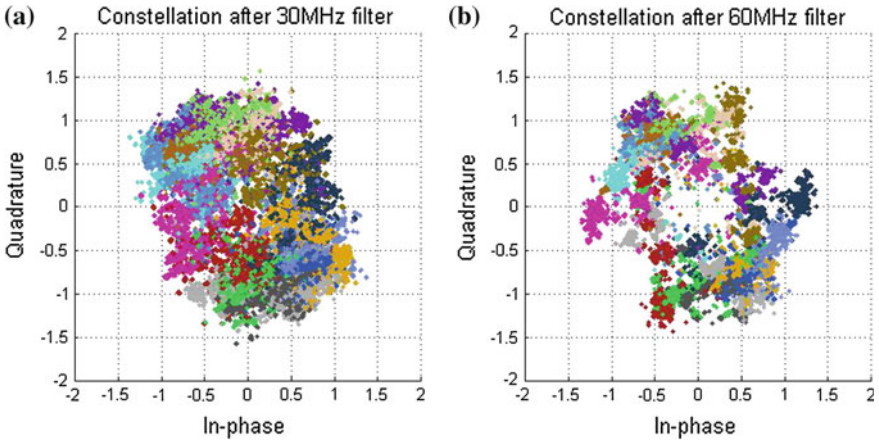

Fig. 3.4 Contrast of constellation after pre-filter

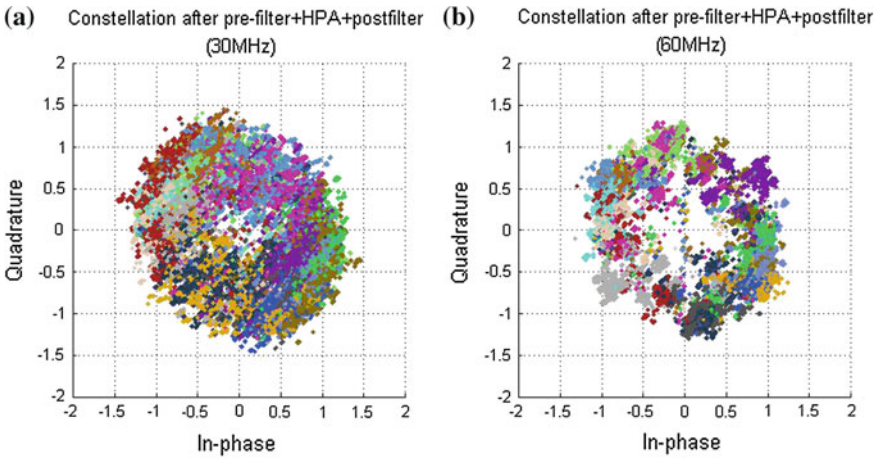

Fig. 3.5 Contrast of constellation after pre-filter, HPA and post-filter

We can see that band limit will break the constant-envelope feature: the amplitude is not constant anymore and the phase points spread. Comparing Fig. 3.4a with b, we can see that the deformation of the signal with 30 MHz bandwidth limit is severer, and overlapping region of phase points is lager. Also Quadrature branch varies more than In-phase branch for 30 MHz band-limited signal, while the fluctuations of both branches are basically the same for the 60 MHz one. Multiplex efficiency is −1.430 dB after 30 MHz bandwidth filter, 0.4 dB less than in ideal conditions, which is an obvious loss. And PAPR of it is 2.8386, which shows the signal is no longer constant-envelope and the amplitude range is relatively wide. For 60 MHz band-limited signal, multiplex efficiency is −1.234 dB, 0.2 dB less than in ideal conditions. PAPR of it is 2.3947.

The constellation of the compound signal after pre-filter is shown as Fig. 3.4.

Comparing with the constellation only after pre-filter, we can see that deformation of signal becomes severer, and overlapping region of phase points becomes lager. Especially with the phase characteristic of HPA, the constellation has rotated. With 30 MHz bandwidth limit, the multiplex efficiency turns into −1.542, 0.55 dB less than in ideal conditions and 0.1 dB less than only after pre-filter. And PAPR is 2.4007. For 60 MHz band-limited signal, the multiplex efficiency turns into −1.334, 0.3 dB less than in ideal conditions and 0.1 dB less than only after pre-filter. And PAPR is 1.9544. Although the PAPR of both signals has decreased a little, we can see from the constellation obviously that phase points spread much more seriously and overlapping region is lager, especially for 30 MHz band-limited signal, the phase points in close proximity mostly overlap.

3.5 Conclusions

POCET computes the phase of the modulation signal on the premise of the power and phase relationship between the signals to maximize the multiplex efficiency, so it can reach the highest efficiency in theory. In traditional POCET, penalty function is used to change constrained optimization into unconstrained optimization. But finding appropriate penalty factors will cause an extra increase in solving iterations which takes much time. While the constrained optimization algorithm presented in this article can simplify resolution process and reduce iterations. Besides, the form of setting power and phase errors is more suitable for practical use.

We provide a constant-envelope multiplex plan for B1 signals using the improved POCET algorithm: multiplex efficiency of four OS signals is −1.010 dB and of three AS signals is −1.593 dB. And according to the simulation results of 4-signals multiplex, the given power and phase constrains can be satisfied perfectly using the improved POCET. The improved algorithm greatly simplifies the process of searching for optimal solution.

At present, there have been lots of studies of constant-envelope multiplex techniques of satellite navigation signal, but the bandwidth limit in navigation systems is not considered in all of them. Thus we simulate the multiplex of four B1 OS signals in band-limited system. With bandwidth limit, the constant-envelope signal becomes nonconstant and multiplex efficiency decreases: multiplex efficiency decreases to −1.542 dB in 30 MHz band-limited system and −1.334 dB in 60 MHz system. The influence of band limit is quite obvious, thus analysis of the multiplex performance in band-limited system is of more significance in engineering practice.

References

1. Kaplan ED, Hegarty CJ (eds) (2005) Understanding GPS: principles and applications, 2nd edn. Artech House, Boston
2. Dafesh PA, Cahn CR (2001) Phase-optimized constant-envelope transmission (POCET) modulation method for GNSS signals. In: Proceedings of the 22nd international technical meeting of the satellite division of the Institute of Navigation (ION GNSS 2009)
3. Dafesh PA, Bow R et al (2011) Receiver compatibility of POCET signal combining. In: Proceedings of the 2011 international technical meeting of the institute of navigation
4. Dafesh PA, Cahn CR (2011) Application of POCET method to combine GNSS signals at different carrier frequencies. In: Proceedings of the 2011 international technical meeting of the institute of navigation
5. Current and Planned Global and Regional Navigation Satellite Systems and Satellite-Based Augmentations Systems. http://www.oosa.unvienna.org/pdf/publications/icg_ebook.pdf. Accessed 15 Jan 2011
6. Zhang K, Wang F (2011) Application of phase-optimized constant-envelope transmission method in compass signal design in the presence of finite DA word-length effects. In: The 2nd China satellite navigation conference

7. Zhu L, Yao Z, Feng Z (2012) Non-symmetrical ALTBOC multiplexing for Compass B1 signal design. Tsinghua Univ (Sci & Tech) 6:869–873
8. Ran Y, Hu X, Ke T (2010) Analysis of nonlinear and compatibility of satellite navigation modulation. Chin Space Sci Technol 5:39–46
9. Xie G (2009) The research of linearization technology of RF power amplifier. Dissertation, Fudan University
10. Xie Z, Li J, Chen Z (eds) (2010) Nonlinear optimization theory and methods. Higher Education Press, Beijing

Chapter 4
Nonlinear Equalization with Symbol Error Aided in Beidou Satellite Navigation Communication System

Chengkai Tang, Baowang Lian and Yi Zhang

Abstract With consider of nonlinear interference in Beidou satellite channel and the higher transmission frequency is adopted in Beidou satellite system, the traditional equalization cannot satisfy the requirement. This paper proposed a novel nonlinear blind equalization algorithm. The algorithm utilizes the third-order Volterra model to obtain the revised nonlinear error by symbol error. Then the parameters of equalization are updated by the revised nonlinear error to track the model of satellite channel and remove the nonlinear interference. The simulation result shows that our proposed nonlinear equalization have lower symbol error ratio and quicker convergence speed than the neural network blind equalization algorithm and channel detection aided equalization algorithm and has a good application value in the field of engineering.

Keywords Beidou · Nonlinear interference · Symbol error aided · Blind equalization

4.1 Introduction

With development of Beidou satellite navigation communication system both in military and commercial field. The inter-symbol interference (ISI) and inter-channel interference (ICI) become larger due to the high order modulation techniques were utilized in Beidou satellite navigation communication system [1]. The distortion of

C. Tang (✉) · B. Lian · Y. Zhang
School of Electronics and Information, Northwestern Polytechnical University, Xi'an, 710072, China
e-mail: tangchengkai99@163.com

B. Lian
e-mail: bwlian@nwpu.edu.cn

Y. Zhang
e-mail: zhangyi@nwpu.edu.cn

J. Sun et al. (eds.), *China Satellite Navigation Conference (CSNC) 2015 Proceedings: Volume II*, Lecture Notes in Electrical Engineering 341,
DOI 10.1007/978-3-662-46635-3_4

amplitude and phase caused by ISI and ICI will degraded the communication performance of Beidou satellite navigation communication system [2]. Specially, the inter satellite channel have the nonlinear feature which produced nonlinear interference. The nonlinear ISI and ICI which combined the nonlinear interference and ISI or ICI is further increasing the difficulty of decoding. How to degrade the nonlinear ISI and nonlinear ICI is hot point in research of Beidou satellite navigation communication system [3].

The equalization is the most effective method to remove the nonlinear interference in current techniques. The traditional equalization utilizes the feature of satellite communication channel to compensate ISI and ICI. The equalization is divided into the self-adaptive trained equalization algorithm and self-adaptive blind equalization algorithm. The self-adaptive trained equalization algorithm require the transmitter send a series symbols which are known by receiver of satellite and train the equalization by them. This algorithm has higher accuracy because the training symbol is perfect correct. But the training time which is built the equalization will waste the satellite communication time and the equalization need be trained in every link establishment. The self-adaptive blind equalization algorithm utilized the seeker symbol to update the parameter of equalization in small range and adjust the parameter by data symbol.

Literature [4] proposed a self-adaptive blind equalization with minimum mean square error standard. Literature [5] proposed a self-adaptive blind equalization with recursive least squares standard. Both algorithms of [4, 5] are convenient to realize and the receiver of satellite didn't need the known signal to train the parameters of equalization. But both algorithms can't abate nonlinear ISI and ICI and are unsuitable for the satellite communication. Literature [6] proposed a neural network blind equalization algorithm which cans fully approximation for all of nonlinear satellite channel by the construction of multilayer neural network. But the neuron of neural network will produce small fluctuation error near zero due to the minimum interval of neuron's value. Literature [7] proposed a multimode blind equalization algorithm, the algorithm build an aim function which constructed by many kinds of values. The algorithm is convenient to implement and has better robustness. But the slower convergence is the main drawback of this algorithm. Literature [8] proposed a channel detection aided equalization algorithm. The algorithm utilizes maximum likelihood estimation, Bias estimation and the minimum error probability criterion estimation to detect satellite channel and decoding directly. But the error will enlarge by the decoding methods, so it is also unsuitable for satellite communication.

In view of the above equalization algorithms have higher calculation complexity, lower convergence speed and weak ability of nonlinear interference reducing [9]. But the satellite channel of Beidou satellite navigation communication system has obvious nonlinear characteristics and the distance of satellite channel is far away than the wireless communication channel [10]. It means every communication time of the satellite link is limited due to the satellite is moving, so keeping the convergence speed of equalization parameter quickly to save the time of equalization establishing [11]. In this paper, we proposed a symbol error revised nonlinear blind

equalization algorithm. In Beidou satellite navigation communication system, the channel mainly has nonlinear feature and memory feature. Memory feature is close to multipath interference but is different from multipath interference. The multipath interference signal didn't overstep the main signal. Our proposed algorithm utilize the decision symbol to establish the nonlinear revised error based on the third-order Volterra model, then update the parameters of blind equalization by revised error. The construction of blind equalization just have feedback module due to the memory of satellite channel. Our proposed algorithm can degrade nonlinear ISI and ICI quickly and has the advantages of accurate, stable and efficient in Beidou satellite navigation communication system.

4.2 System Model

In Beidou satellite navigation communication system, the modulation of transmitter signal and coding rule are certain [12], but the satellite channel will change due to the environment alter. So we focus on the blind equalization of receiver to degrade nonlinear ISI and ICI form the satellite channel. In this paper, the blind equalization system model is shown on Fig. 4.1.

In Fig. 4.1, $y(n)$ represents receiver's signal which pass by the match filter and downsample to remove out of band interference. $s(n)$ represents the interference signal which produced by blind equalization. $r(n)$ represents the interference cancelation signal which is processed by blind equalization. $w_1, w_2, \ldots, w_{N_b-1}, w_{N_b}$ represent the parameters of blind equalization, N_b represents the length of feedback module, $\hat{X}(n)$ represents the decision symbol, n is sample time.

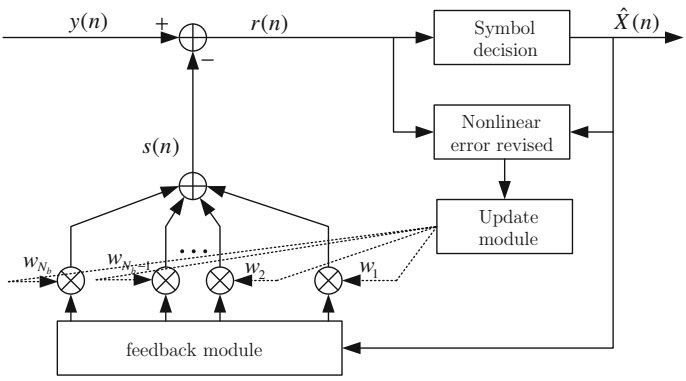

Fig. 4.1 The blind equalization system model

4.3 Blind Equalization Algorithm

We utilized the feedback module to obtain the current decision symbol and delay decision symbol, then multiply the parameters of blind equalization respectively and accumulate all of results to get the interference signal $s(n)$ as follow:

$$s(n) = \sum_{j=1}^{N_b} w_j \hat{X}(n-j) \tag{4.1}$$

The interference cancelation signal $r(n)$ can be obtained by signal $y(n)$ subtract the interference signal $s(n)$.

$$r(n) = y(n) - s(n) \tag{4.2}$$

Then the interference cancelation signal $r(n)$ though the symbol decision module to obtain the decision symbol $\hat{X}(n)$. The decision rule adopts the minimum distance criterion.

$$\begin{aligned} \hat{X}(n) &= \arg\min_{X(n)}(|r(n) - X(n)|) \\ X(n) &\in C \end{aligned} \tag{4.3}$$

C represents the data symbol set. The current error is obtained from the interference signal $r(n)$ and decision symbol $\hat{X}(n)$ as follow:

$$e(n) = r(n) - \hat{X}(n) \tag{4.4}$$

4.4 Nonlinear Error Revised Model

Multiple amplitude and multiple phase modulation will be widely applied in Beidou satellite navigation communication system and other satellite communication system. In order to simplify the calculation, the error is complex number. Due to the satellite channel have nonlinear feature, so we should establish the nonlinear error model. The mainly nonlinear model includes the memory polynomial model and Volterra model. Volterra model is greater adaptation and higher accuracy. With large enough order of Volterra model, it can eliminate all kinds of nonlinear interference, and it is superior in the precision than memory polynomial model. Truncate of the Volterra filter model at a certain length derived by the required accuracy will ensure the fast signal pre-distortion. Volterra series are memory expansion of Tyler series, and it can be written as

$$z(t) = \sum_{k=0}^{\infty} \int_{-\infty}^{\infty} \int_{-\infty}^{\infty} \cdots \int_{-\infty}^{\infty} g_k(\tau_1, \tau_2, \ldots, \tau_k) \prod_{i=1}^{k} [v(t-\tau_i) d\tau_i] \tag{4.5}$$

where $g_k(\tau_1, \tau_2, \ldots, \tau_k)$ is the kth order continual Volterra kernel. $v(t)$ represents the input signal of Volterra model, $z(t)$ represents the output signal of Volterra model. And τ_k is the corresponding delay at the kth time slot. Equation (4.4) represents the continual time domain and it's hard to achieve in practice, so we rewritten the Eq. (4.4) in discrete domain as follow:

$$z(n) = \sum_{k=0}^{(P-1)/2} \sum \cdots \sum g_k(m) |v(n)|^{2k} v(n-m) \tag{4.6}$$

where $z(n)$ and $v(n)$ represent the discrete input and output of Volterra model respectively, and $g_k(m)$ is the discrete Volterra Kernel, P denotes the nonlinear order. Beidou satellite navigation communication system will focus on wide-band and high-frequency data transmission, so the equalization requires higher coefficients updating speed. The truncated Volterra model also can track the nonlinear feature of satellite channel, so we utilize the error and third-order Volterra model to establish the symbol error revised model as follow:

$$\begin{aligned} z(n) = & \sum_{m=-M}^{M} g_1(m) v(n-m) \\ & + \sum_{m=-M}^{M} \sum_{i=-M}^{M} \sum_{j=-M}^{M} g_3(m,i,j) v(n-m) v^*(n-i) v(n-j) \end{aligned} \tag{4.7}$$

where $2M+1$ denotes the memory length. $g_1(m)$ represents the first-order Volterra kernel and $g_3(m,i,j)$ represents the third-order Volterra kernel. m is the corresponding delay. M represents the length of delay. The first-order part describes the linear interference and the third-order part describes the nonlinear interference. The value of kernels adopts the decrease model based on literature [2] which describe the memory effect of different kernel.

$$g_1(m) = 1/2^{|m|} \tag{4.8}$$

$$g_3(m,i,j) = 1/2^{|m|+|i|+|j|} \tag{4.9}$$

Then we obtained the nonlinear error revised model as follow:

$$\begin{aligned} \hat{e}(n) = & \sum_{m=-M}^{M} g_1(m) e(n-m) \\ & + \sum_{m=-M}^{M} \sum_{i=-M}^{M} \sum_{j=-M}^{M} g_3(m,i,j) e(n-m) e^*(n-i) e(n-j) \end{aligned} \tag{4.10}$$

$\hat{e}(n)$ represents the revised nonlinear error.

In Beidou satellite navigation communication system, communication transmission speed mainly depends on the equalization parameter updating speed. So we adopt the current sampling time of received signal instead of the vector of received signal to save the computation. The minimum mean square error (MMSE) is adopted to build the different value function $\Delta(n)$ as follow:

$$\Delta(n) = \frac{\partial[\hat{e}^2(n)]}{\partial w(n)} = -\hat{e}(n)\hat{X}^*(n) \tag{4.11}$$

where, the $\hat{X}^*(n)$ represents the Conjugate signal of decision symbol $\hat{X}(n)$. The parameter updating function of equalization is obtained as follow:

$$w_i(n) = w_i(n-1) + \mu\hat{e}(n)\hat{X}^*(n) \tag{4.12}$$

where, μ represents the convergence factor and the range of it is from 0 to 1. The larger value of μ will accelerate convergence speed of equalization but the fluctuation of error is larger. The smaller value of μ will produce the little fluctuation of error but the convergence speed is slower. So we set the value is 10^{-2} in this paper.

4.5 Simulation and Analysis

In Beidou satellite navigation communication system, the signal modulations include BPSK, QPSK, BOC, AltBOC and so on. The QPSK have good transmission feature and be utilized in this paper. The pulse shaping filter and match filter both adopt 64 samples (or 8 symbols). The roll off factor of filter is 0.25. The training symbol length is 10^5 and the transmitted symbol length is 10^7.

4.5.1 Symbol Error Ratio

We first treat the case of symbol error ratio. The length of equalization has larger effect on the symbol error ratio (SER). So the different lengths of equalization were adopted to test the performance and result is shown on Fig. 4.2.

Form Fig. 4.2 we can see, the length of equalization become longer, the performance of SER is better. The reason is that longer equalization will cover the more nonlinear ISI and ICI. But the SER curve of length of equalization is 15 and the SER curve of length of equalization is 17 are close to each other. The result indicates the length is 15 can cover most of nonlinear ISI and ICI, so we adopt the length of equalization is 15 in the later simulation.

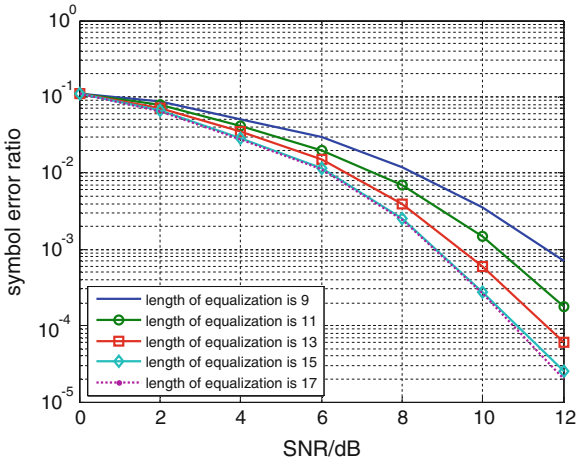

Fig. 4.2 SER curve with different length of equalization

The performance of our blind nonlinear equalization algorithm compare with the neural network blind equalization algorithm was proposed by literature [6], channel detection aided equalization algorithm was proposed by literature [8] and linear equalization algorithm. The results of the comparison can be seen as Fig. 4.3.

Form the Fig. 4.3 we can see, the linear equalization algorithm have a higher error floor due to the nonlinear ISI and ICI are remained in satellite channel. The channel detection aided equalization algorithm is mainly effected by channel parameter accuracy of satellite channel estimation. So when the SNR is lower, the performance of channel detection aided equalization is bad, for example, the SNR is 8 dB, the SER is about 7×10^{-3} and is higher than the other nonlinear equalization.

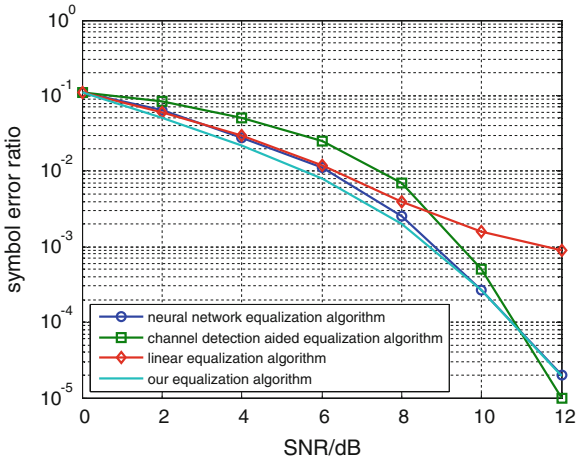

Fig. 4.3 SER curve with different equalization algorithm

When the SNR is higher, the performance of channel detection aided equalization is better than other nonlinear equalization, for example, the SER is close to 10^{-5} with the SNR is 12 dB. Our equalization algorithm is better than network blind equalization algorithm. When the SER is 10^{-3}, the SNR of both algorithms are 8.5 dB. It means our proposed algorithm can remove nonlinear ISI and ICI perfectly.

4.5.2 Convergence Speed

In Beidou satellite navigation communication system, the convergence speed will affect the communication link building time. The convergence speed mainly focus on the iteration times and fluctuation of mean square error (MSE). We also compare our algorithm with the neural network blind equalization algorithm was proposed by literature [6] and channel detection aided equalization algorithm was proposed by literature [8]. The results of the comparison can be seen as Fig. 4.4.

Form Fig. 4.4 we can see, the convergence speed of channel detection aided equalization algorithm is slower than other algorithms due to the channel detection need more iteration times to have accuracy and the MSE is also higher than other algorithms. Neural network blind equalization algorithm have higher convergence speed due to the neuron have good nonlinear feature but it bring the fluctuation caused by itself factor. Our proposed equalization algorithm has quickly convergence speed and lower MSE due to the nonlinear error model can track all kinds of nonlinear ISI and ICI.

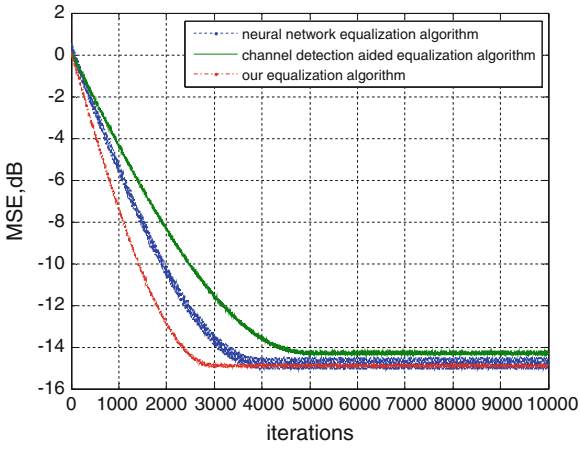

Fig. 4.4 Convergence speed with different equalization algorithms

4.6 Conclusions

Aim to satellite channel of Beidou satellite navigation communication system has strong nonlinear ISI and ICI, so the traditional wireless channel equalization algorithm isn't satisfied in satellite channel. Beidou satellite communication's frequency and capacity are larger than the wireless communication; it means the equalization algorithm should have higher updating speed to track the frequency and code. This paper proposed a nonlinear blind equalization algorithm. The algorithm utilized the symbol error to construct the third-order nonlinear revised error, and then we update the parameter of equalization by the revised error under MMSE standard. From the simulation results we can see, our proposed equalization algorithm has good value in application field.

References

1. Tang C, Lian B, Zhang L (2015) Self interference cancelation algorithm with bidiretional relay for satellite communication system. J Xi'an Jiaotong Univ 49(2)
2. Mestre X, Majoral M, Pfletschinger S (2013) An asymptotic approach to parallel equalization of filter bank based multicarrier signals. IEEE Trans Signal Process 61(14):3592–3606
3. Tang C, Lian B, Zhang L (2014) Post predistortion of 16APSK modulation with memory and nonlinear effect in satellite communication. J Northwest Polytech Univ 32(6):34–39
4. Kim K, Kalantarova N, Kozat SS (2013) Linear MMSE-optimal turbo equalization using context trees. IEEE Trans Signal Process 61(12):3041–3055
5. Nafta A, Johannisson P, Shtaif M (2013) Blind equalization in optical communications using independent component analysis. J Lightwave Technol 31(12):2043–2049
6. Sun Y, Zhang L, Zhang J (2013) Neural network blind equalization algorithm applied in medical CT image restoration. Math Probl Eng 3(1):1–6
7. Wang X, Liu B, Li H (2014) An equalization algorithm based on constellation matched phase error for M-ary phase shift keying signals. J Comput Inf Syst 10(3):895–902
8. Zhang J, Ye Z, Feng Q (2014) A dual-mode blind equalization algorithm for improving the channel equalized performance. J Commun 9(5):433–440
9. Tang C, Lian B, Zhang Y (2013) Dual loop feedback pre-distortion in satellite communication. J Syst Eng Electron 24(4):586–591
10. Tang C, Lian B, Zhang L (2015) Post nonlinear interference cancelation algorithm in satellite communication. J Xidian Univ 42(1)
11. Tang C, Lian B, Zhang L (2013) Doppler-aided channel estimation in satellite communication base on frequency-domain equalization [C]. ICNS2013, USA, pp 1–4
12. Melgarejo MA, Albarracin LF (2013) Channel equalization using quasi type-2 fuzzy strategies. J Intell Fuzzy Syst 25(4):989–999

Chapter 5
GCE-BOC Modulation: A Generalized Multiplexing Technology for Modern GNSS Dual-Frequency Signals

Xinming Huang, Xiangwei Zhu, Xiaomei Tang, Hang Gong and Gang Ou

Abstract For the purpose of structural enhancement and backwards compatibility, more than two binary signals on one carrier frequency are required to emit. In order to maximize the power efficiency, constant-envelope modulation is adopted. Alt-BOC and ACE-BOC modulations, the constant-envelope modulation that multiplexes four binary spreading codes as two QPSK signals at two different carrier frequencies, are proposed by Galileo and BeiDou respectively. A constraint of these new modulations is that the number of signals to be multiplexed must be no larger than four signal channels. In this paper, a generalized dual-frequency constant-envelope multiplexing technology, named generalized constant envelope BOC (GCE-BOC) modulation, is presented. The modulation can be regarded as the extended form of Alt-BOC and ACE-BOC modulations and provides a solution to dual-frequency constant envelope multiplexing problem for worldwide GNSS.

Keywords GNSS · Dual-Frequency · Constant envelope · GCE-BOC

5.1 Introduction

For the purpose of structural enhancement and backwards compatibility, more than two binary signals on one carrier frequency are required to emit [1]. In order to maximize the power efficiency, constant envelope modulation is adopted. Several multiplexing techniques, including Interplex, CASM, majority signal voting and phase-optimized constant envelope transmit (POCET) technology, are proposed in

X. Huang · X. Zhu · X. Tang · H. Gong · G. Ou (✉)
Satellite Navigation R&D Center, National University of Defense Technology, Changsha 410073, China
e-mail: ougang_nnc@163.com

J. Sun et al. (eds.), *China Satellite Navigation Conference (CSNC) 2015 Proceedings: Volume II*, Lecture Notes in Electrical Engineering 341,
DOI 10.1007/978-3-662-46635-3_5

order to solve the problem of constant envelope transmitting several signals in a center frequency [2–4]. While for some applications, signals on dual-frequency are required to transmit with constant envelope. The typical dual-frequency constant envelope modulation technologies include Alt-BOC modulation, which is the constant-envelope modulation adopted by Galileo to multiplex four codes with equal power on E5 band [5], and ACE-BOC modulation, which is the optional constant-envelope modulation preferred by BeiDou system to multiplex four codes with unequal power on B2 band [6]. Both Alt-BOC and ACE-BOC modulations can solve the problem of constant envelope transmitting dual-frequency signals. A constraint of Alt-BOC and ACE-BOC is that the number of signals to be multiplexed must be no larger than four signal channels, which is not always the very constraint for some transmission applications. A more generalized problem is to multiplex arbitrary number of signals on two sidebands into a signal with constant envelope.

Dual-frequency constant envelope modulation technology has wide applications prospects. For example, for backward compatibility of BeiDou B1 signals, a regional signal and two global signals with 14.322 MHz center frequency difference must be multiplexed, which is a typical dual-frequency multiplexing problem. A proposed application to GPS III is to combine the L2C, L2-P(Y), and L5 signals into a constant-envelope signal transmitted by a single power amplifier, which is also a typical dual-frequency multiplexing problem [7]. Moreover, GLONASS system has an attempt to constant envelope transmit the traditional FDMA signal with a CDMA signal in dual frequencies [7, 8].

In order to solve the problem of multiplexing arbitrary number of signals on two sidebands into a signal with constant envelope, we present a generalized dual-frequency constant envelope modulation named GCE-BOC modulation. Then its application on BeiDou B1 band is discussed. The paper is organized as follows: In Sect. 5.2, the principle of GCE-BOC modulation is introduced. Secondly, the applications of GCE-BOC modulation on Beidou B1 band are presented and analyzed in Sect. 5.3. Finally conclusions are drawn in Sect. 5.4.

5.2 GCE-BOC Modulation

Assume the generalized dual-frequency multiplexing problem as combining several signals on two sidebands into an integrated signal in which $s_k(t)\, k = 1, 2, 3 \ldots N$ are located on the lower sideband, $\tilde{s}_j(t) j = 1, 2, 3 \ldots M$ are located on the upper sideband. On each sideband the signals are modulated into a constant envelope signal, with the center frequencies of two sidebands $2f_{sc}$ apart. Any multiplexing technology can be chosen, including Interplex, CASM, majority signal voting and phase-optimized constant envelope transmit (POCET) technology. The signals on the lower sideband modulated as a constant envelope signal by the chosen multiplexing technology can be expressed as

$$\begin{cases} s_{up}(t) = s_{up}^{r}(t) + js_{up}^{i}(t) \\ s_{down}(t) = s_{down}^{r}(t) + js_{down}^{i}(t) \end{cases} \tag{5.1}$$

where $s_{up}^{r}(t)$ and $s_{up}^{i}(t)$ are real and imaginary parts of the constant envelope signal located on the upper sideband, $s_{down}^{r}(t)$ and $s_{down}^{i}(t)$ are real and imaginary parts of the constant envelope signal located on the lower sideband.

The dual-frequency baseband signal modulated as a constant envelope signal by the Interplex modulation can be expressed as

$$\begin{aligned} s_{\Sigma}(t) &= (s_I(t) + js_Q(t))e^{-j2\pi f_{sc}t} + (\tilde{s}_I(t) + j\tilde{s}_Q(t))e^{j2\pi f_{sc}t} \\ &= \alpha_1 \sin(2\pi f_{sc}t + \varphi_1) + j\alpha_2 \sin(2\pi f_{sc}t + \varphi_2) \end{aligned} \tag{5.2}$$

where

$$\begin{cases} \alpha_1 = \sqrt{(s_I(t) + \tilde{s}_I(t))^2 + (s_Q(t) - \tilde{s}_Q(t))^2} \\ \alpha_2 = -\sqrt{(s_Q(t) + \tilde{s}_Q(t))^2 + (s_I(t) - \tilde{s}_I(t))^2} \end{cases} \tag{5.3}$$
$$\begin{cases} \varphi_1 = \operatorname{atan} 2[s_I(t) + \tilde{s}_I(t), s_Q(t) - \tilde{s}_Q(t)] \\ \varphi_2 = -\operatorname{atan} 2[s_Q(t) + \tilde{s}_Q(t), s_I(t) - \tilde{s}_I(t)] \end{cases}$$

And atan 2(•,•) is four-quadrant arctangent.

By employing a 2-level waveform like the BOC subcarrier as the subcarrier [8], we can get the constant envelope modulation baseband signal as GCE-BOC modulated signal, which can be expressed as

$$s(t) = \alpha_1 \operatorname{sgn}[\sin(2\pi f_{sc}t + \varphi_1)] + j\alpha_2 \operatorname{sgn}[\sin(2\pi f_{sc}t + \varphi_2)] \tag{5.4}$$

GCE-BOC modulation is expressed as the form of GCE-BOC$_{(m,n)}$ in the paper, where m denotes the number of signals in the lower sideband, and n denotes the number of signals in the upper sideband.

Considering multiplexing four signals into an integrated signal in which $s_1(t)$ and $s_2(t)$ are located on the lower sideband, $s_3(t)$ and $s_4(t)$ are located on the upper sideband, with the center frequencies of two sidebands $2f_{sc}$ apart. QPSK is the most widely used modulation for traditional navigation signals. The quadrature phase relationship provides good cross-correlation protection between the two spreading codes. Thus we adopt QPSK as the constant envelope modulation method for each sideband. Consequently, the dual-frequency constant envelope modulation baseband signal can be expressed as

$$s(t) = \alpha_1 \operatorname{sgn}[\sin(2\pi f_{sc}t + \varphi_1)] + j\alpha_2 \operatorname{sgn}[\sin(2\pi f_{sc}t + \varphi_2)] \tag{5.5}$$

where

$$\begin{cases} \alpha_1 = \sqrt{(s_1(t)+s_3(t))^2+(s_2(t)-s_4(t))^2} \\ \alpha_2 = -\sqrt{(s_1(t)-s_3(t))^2+(s_2(t)+s_4(t))^2} \end{cases} \quad (5.6)$$
$$\begin{cases} \varphi_1 = \arctan[(s_1(t)+s_3(t)),(s_2(t)-s_4(t))] \\ \varphi_2 = -\arctan[(s_2(t)+s_4(t)),(s_1(t)-s_3(t))] \end{cases}$$

As can be seen, the special case of GCE-BOC modulation for four signals has the same analytical expression as ACE-BOC modulation, thus the GCE-BOC modulation can be regarded as the extended form of ACE-BOC modulation.

By combing the constant envelope signals on the both sidebands, the multiplexing efficiency can be expressed as

$$\eta = \left(\frac{\sum_{k=1}^{N} P_{s_k} + \sum_{j=1}^{M} P_{\tilde{s}_j}}{\alpha_1^2 + \alpha_2^2} \right) \quad (5.7)$$

where P_{s_k} is the power of $s_k(t)$, $P_{\tilde{s}_j}$ is the power of $\tilde{s}_j(t)$.

As the fraction of fundamental harmonic in square wave is 81.06 %, thus the signal power in main lobes can be expressed as

$$\eta_m = \eta \times 81.06\,\% \quad (5.8)$$

As the application of the special case of GCE-BOC modulation for four signals on BeiDou B2 band is discussed in detail in [7], we will choose the multiplexing problem on BeiDou B1 band as an example to illustrate the effectiveness of GCE-BOC modulation in solving the dual-frequency multiplexing problem.

5.3 Application for B1 Band

5.3.1 Multiplexing Model of BeiDou B1 Band

The baseline of BeiDou B1 signals contains a traditional BPSK(2) signal at 1561.098 MHz and MBOC(6,1,1/11) signals and BOC(14,2) modulated Authorized Service (AS) signals at 1575.42 MHz [9]. BeiDou baseline options use MBOC(6,1,1/11) as global B1 Open Service (OS) signals, which are a mixture of BOC(1,1) and BOC(6,1) with a power ratio of 10:1. MBOC modulation has three different implementations: Composite BOC (CBOC), Time Multiplexed BOC (TMBOC) and Quadrature Multiplexed BOC modulations (QMBOC). CBOC modulation linearly combines BOC(1,1) and BOC(6,1) sub-carriers, and the waveform has four different levels, which leads to greater combining difficulty with

other signals. In this paper TMBOC and QMBOC are chosen as the candidates for the BeiDou B1 signal. With different implementations of MBOC(6,1,1/11), different multiplexing tragedies will be adopted.

Summarizing the multiplexing problem on BeiDou B1 band, there might exist two multiplexing schemes. In the first scheme, TMBOC is chosen as the implementation of MBOC modulation, and there are five signals, as shown in Table 5.1, to be multiplexed.

The pilot and data channels of BOC(14,2) are realized by time division data multiplexing (TDDM), thus the waveform has only two levels, and there are only four signals to be multiplexed. B1I signal is located on the lower sideband, and B1A and B1C signals are located on the upper sideband. Thus the multiplexing problem on BeiDou B1 band is how to constant envelope transmit an asymmetric dual-frequency signal.

In the second scheme, QMBOC is chosen as the implementation of MBOC modulation, and there are six signals, as shown in Table 5.2, to be multiplexed.

The pilot and data channels of BOC(14,2) are realized by time division data multiplexing (TDDM), thus the waveform has only two levels, and there are five signals to be multiplexed. B1I signal is located on the lower sideband, and B1A and B1C signals are located on the upper sideband. Thus the multiplexing problem on BeiDou B1 band is how to constant envelope transmit an asymmetric dual-frequency signal.

The Interplex/CASM technology, a particular phase modulation combining multiple signals into a phase modulated composite signal, was preferred by GPS and Galileo systems because it provides good power efficiencies. Thus the Interplex/CASM modulation is chosen as the method to multiplexing the signals on each sideband into a constant envelope signal.

Table 5.1 Signals need to be multiplexing in BeiDou B1 band

Signal	Frequency (MHz)	Modulation	Service
B1I	1561.098	BPSK(2)	OS
B1Cp	1575.42	TMBOC(6,1,4/33)	OS
B1Cd	1575.42	BOC(1,1)	OS
B1Ap	1575.42	TDDM-BOC(14,2)	AS
B1Ad	1575.42		AS

Table 5.2 Signals need to be multiplexing in BeiDou B1 band

Signal	Frequency (MHz)	Modulation	Service
B1I	1561.098	BPSK(2)	OS
B1Cp	1575.42	BOC(1,1)	OS
		BOC(6,1)	OS
B1Cd	1575.42	BOC(1,1)	OS
B1Ap	1575.42	TDDM-BOC(14,2)	AS
B1Ad	1575.42		AS

5.3.2 The First Multiplexing Scheme with GCE-BOC Modulation

The four signals that need to be multiplexed are B1I signal, time-multiplexed B1A signal, B1Cp signal and B1Cd signal. We denote $s_1(t)$ as B1I signal, $s_2(t)$ as B1A signal, $s_3(t)$ and $s_4(t)$ as B1Cp signal and B1Cd signal respectively. The power constraints between $s_3(t)$ and $s_4(t)$ are set as the ratio of 3:1 as the GPS L1C signal, and the three signals are assumed as having equal power. Thus the power ratios between the four signals are 2:4:3:1.

The signals on the upper sideband modulated as a constant envelope signal by the CASM modulation by the same method as above can be expressed as

$$\begin{aligned} s_{up}(t) = &\left(\sqrt{P_I}s_3(t)\cos(m) - \sqrt{P_Q}s_4(t)\sin(m)\right) \\ &+ j\left(\sqrt{P_Q}s_2(t)\cos(m) + \sqrt{P_I}s_2(t)s_3(t)s_4(t)\sin(m)\right) \end{aligned} \tag{5.9}$$

where P_I and P_Q are powers of in-phase and quadrature-phase channels, m is the coefficient that decides the power constraint between the signals, which can be defined as

$$m = \tan^{-1}\sqrt{\frac{P_{s_4}}{P_{s_2}}} \tag{5.10}$$

where the power of $s_2(t)$ and $s_4(t)$ are P_{s_2} and P_{s_4}.

Consequently, the constant envelope baseband signal acquired by GCE-BOC modulation can be expressed as

$$s(t) = \alpha_1 \operatorname{sgn}[\sin(2\pi f_{sc}t + \varphi_1)] + j\alpha_2 \operatorname{sgn}[\sin(2\pi f_{sc}t + \varphi_2)] \tag{5.11}$$

where

$$\begin{cases} \alpha_1 = \sqrt{\begin{array}{l}\left(\sqrt{P_{s_1}}s_1(t) + \left(\sqrt{P_Q}s_2(t)\cos(m) + \sqrt{P_I}s_2(t)s_3(t)s_4(t)\sin(m)\right)\right)^2 \\ +\left(\sqrt{P_I}s_3(t)\cos(m) - \sqrt{P_Q}s_4(t)\sin(m)\right)^2\end{array}} \\ \alpha_2 = -\sqrt{\begin{array}{l}\left(\sqrt{P_{s_1}}s_1(t) - \left(\sqrt{P_Q}s_2(t)\cos(m) + \sqrt{P_I}s_2(t)s_3(t)s_4(t)\sin(m)\right)\right)^2 \\ +\left(\sqrt{P_I}s_3(t)\cos(m) + \sqrt{P_Q}s_4(t)\sin(m)\right)^2\end{array}} \end{cases}$$

$$\begin{cases} \varphi_1 = \operatorname{atan2}\left[\dfrac{\sqrt{P_{s_1}}s_1(t) + \left(\sqrt{P_Q}s_2(t)\cos(m) + \sqrt{P_I}s_2(t)s_3(t)s_4(t)\sin(m)\right)}{\sqrt{P_I}s_3(t)\cos(m) - \sqrt{P_Q}s_4(t)\sin(m)}\right] \\ \varphi_2 = -\operatorname{atan2}\left[\dfrac{\sqrt{P_I}s_3(t)\cos(m) + \sqrt{P_Q}s_4(t)\sin(m)}{\sqrt{P_{s_1}}s_1(t) - \left(\sqrt{P_Q}s_2(t)\cos(m) + \sqrt{P_I}s_2(t)s_3(t)s_4(t)\sin(m)\right)}\right] \end{cases} \tag{5.12}$$

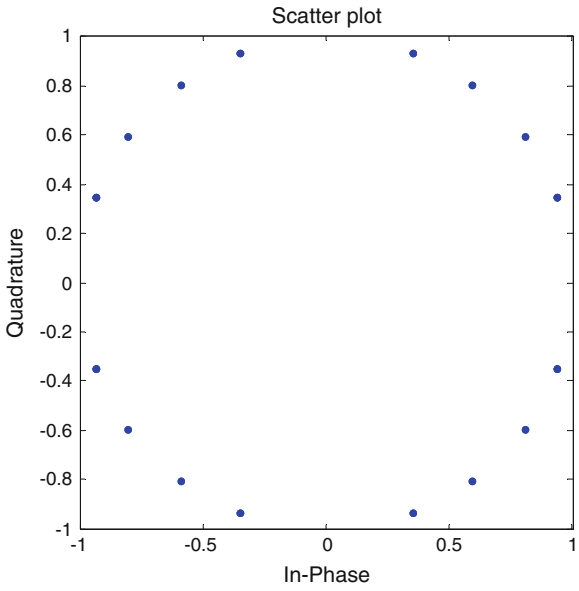

Fig. 5.1 Constellation of GCE-BOC$_{(1,3)}$

The constellation of GCE-BOC$_{(1,3)}$ modulation used in the first multiplexing scheme is shown in Fig. 5.1.

It is required that the multiplexing technology brings no obvious influence on signals receiving separately, which means that constant envelope multiplexing ought to be transparent to receivers. Users do not need to know which multiplexing technology is used, and only need to generate the replica of the desired component.

The power loss can be expressed as

$$\eta = \sum_{i=1}^{4} |R_i|^2 = \left| \frac{1}{T} \int_T \overline{s(t) s_i(t) e^{j2\pi f_{sc} t} dt} \right|^2 + \sum_{i=1}^{3} \left| \frac{1}{T} \int_T \overline{s(t) s_i(t) e^{-j2\pi f_{sc} t} dt} \right|^2 \quad (5.13)$$

where R_i is the average output of the correlator for $s_i(t)$.

The power loss calculated according to (5.13) is about 1.2496 dB. As the fundamental harmonic efficiency for square wave subcarrier is 0.8106, the efficiency of the desired signal power in main lobes is about 92.52 %.

5.3.3 The Second Multiplexing Scheme with GCE-BOC Modulation

The five signals that need to be multiplexed are B1I signal, time-multiplexed B1A signal, B1Cp signal and B1Cd signal. We denote $s_1(t)$ as B1I signal, $s_2(t)$ as B1A signal, $s_3(t)$ and $s_4(t)$ as BOC(6,1) and BOC(1,1) signals in quadrature

respectively, which compose B1Cp signal, and $s_5(t)$ as B1Cd signal. The power constraints between B1Cp signal and B1Cd signal are set as the ratio of 3:1 as the GPS L1C signal, and the three signals are assumed as having equal power. Thus the power ratios between the five signals are 22:44:4:29:11.

Consequently, the constant envelope baseband signal acquired by GCE-BOC modulation can be expressed as

$$s(t) = \alpha_1 \operatorname{sgn}[\sin(2\pi f_{sc} t + \varphi_1)] + j\alpha_2 \operatorname{sgn}[\sin(2\pi f_{sc} t + \varphi_2)] \tag{5.14}$$

where

$$\begin{cases} \alpha_1 = \sqrt{\left(\sqrt{P_{s_1}} s_1(t) + \tilde{s}_1(t)\right)^2 + \left(\tilde{s}_2(t)\right)^2} \\ \alpha_2 = -\sqrt{\left(\sqrt{P_{s_1}} s_1(t) - \tilde{s}_1(t)\right)^2 + \left(\tilde{s}_2(t)\right)^2} \\ \varphi_1 = \arctan[\tilde{s}_1(t), \tilde{s}_2(t)] \\ \varphi_2 = -\arctan[\tilde{s}_2(t), \tilde{s}_1(t)] \end{cases}$$

$$\begin{cases} \tilde{s}_1(t) = \sqrt{P_{s_2}} s_2(t) - \sqrt{P_{s_3}} s_3(t) - \sqrt{\frac{P_{s_3} P_{s_5}}{P_{s_4}}} s_3(t) s_4(t) s_5(t) - \sqrt{\frac{P_{s_2} P_{s_5}}{P_{s_4}}} s_2(t) s_4(t) s_5(t) \\ \tilde{s}_2(t) = \sqrt{P_{s_4}} s_4(t) + \sqrt{P_{s_5}} s_5(t) + \sqrt{\frac{P_{s_3} P_{s_4}}{P_{s_2}}} s_2(t) s_3(t) s_4(t) - \sqrt{\frac{P_{s_3} P_{s_5}}{P_{s_2}}} s_2(t) s_3(t) s_5(t) \end{cases} \tag{5.15}$$

The constellation of GCE-BOC$_{(1,4)}$ modulation used in the second multiplexing scheme is shown in Fig. 5.2.

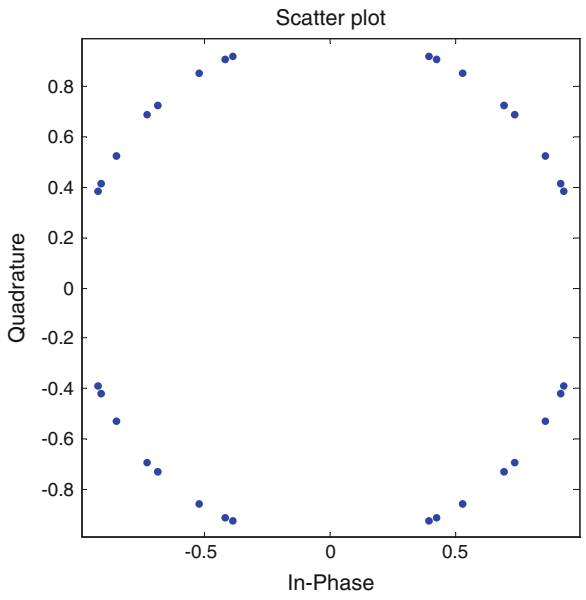

Fig. 5.2 Constellation of GCE-BOC$_{(1,4)}$

The power loss calculated according to (5.13) is about 1.6987 dB. As the fundamental harmonic efficiency for square wave subcarrier is 0.8106, the efficiency of the desired signal power in main lobes is about 83.43 %.

5.4 Conclusions

In order to solve the problem of multiplexing arbitrary number of signals on two sidebands into a signal with constant envelope, we present a generalized dual-frequency constant envelope modulation named GCE-BOC modulation. The modulation can be regarded as the extended form of Alt-BOC and ACE-BOC modulations. The application of GCE-BOC modulation on BeiDou B1 band is chosen as an example to illustrate the effectiveness of GCE-BOC modulation in solving the dual-frequency multiplexing problem. The generalized dual-frequency constant envelope modulation proposed not only gives some suggestions to BeiDou signal designs, but also provides a solution to dual-frequency constant envelope multiplexing problem for worldwide GNSS.

Acknowledgments The authors are thankful to Professor Kou Yanhong for her valuable remarks and suggestions.

References

1. Avila-Rodriguez JA (2008) On generalized signal waveforms for satellite navigation. University FAF Munich, Munich
2. Dafesh PA, Nguyen TM (1999) Coherent adaptive subcarrier modulation (CASM) for GPS modernization. In: Proceedings of the 12th national technical meeting of the institute of navigation, San Diego, CA, 25–27 Jan, pp 649–660
3. Butman S, Timor U (1972) Interplex-an efficient multichannel PSK/PM telemetry system. IEEE Trans Commun 20(3):415–419
4. Dafesh PA, Cahn CR (2009) Phase-optimized constant-envelope transmission (POCET) modulation method for GNSS signals. In: Proceedings of the 22nd international technical meeting of the satellite division of the institute of navigation, Savannah, GA, 22–25 Sept, pp 2860–2866
5. Lestarquit L, Artaud G, Issler J (2008) AltBOC for dummies or everything you always wanted to know about AltBOC. In: Proceedings of the 21st international technical meeting of the satellite division of the institute of navigation, Savannah, GA, 16–19 Sept, pp 961–970
6. Yao Z, Lu M (2013) ACED multiplexing and its application on BeiDou B2 band. In: Proceeding of 4th China satellite navigation conference, Wuhan, China
7. Dafesh PA, Cahn CR (2011) Application of POCET method to combine GNSS signals at different carrier frequencies. In: Proceedings of the international technical meeting of the institute of navigation, San Diego, CA, 24–26 Jan, pp 1201–1206
8. Kharisov V, Povalyaev A (2011) Optimal aligning of GNSS navigation signals sum. In: Proceedings of the 24th international technical meeting of the satellite division of the institute of navigation. Portland, Oregon, pp 3141–3155
9. Zhang K, Zhou H, Wang F (2011) Multiplexing performance assessment of POCET method for compass B1/B3 signals. J Navig 64:41–54

Chapter 6
Research of Novel BCC Signal Structure

Ying Xu, Zhili He, Maoshu Zeng, Hong Yuan and Weina Hao

Abstract Aimed at possibility of deep fusion in signal layer of navigation and communication, we analyze basic characteristics of communication signal, and put forward a novel signal structure with basic characteristics of communication signal —BCC (Burst Compound Carrier) signal. In the paper, basic performance of the signal (such as ranging precision and autocorrelation etc.) is analyzed, followed by mapping model from signal performance to signal parameters. Moreover, the design of its synchronous algorithm is studied. Due to its time-division property, the proposed signal can't be tracked continuously. To solve the problem, methods based on fitting, two-dimensional refinement and long-time filter are brought forward to achieve high-precision pseudo-code acquisition. Then, to test and verify the performance, a prototype is developed. Analysis shows that BCC signal is possessed of great compatibility, capable of co-existing with normal TDD communication signal. Test result indicates that single carrier BCC signal's ranging precision is 6.06 m, position precision is 10.8 m, which is sufficient for users basic positioning demands, and worthy of further researches.

Keywords Complex carrier · Time-division · Communication signal · Signal synchronization

Y. Xu (✉) · Z. He · M. Zeng · H. Yuan · W. Hao (✉)
Academy of Opto-Electronics, Chinese Academy of Sciences, Beijing, China
e-mail: nadinexy@aoe.ac.cn

W. Hao
e-mail: weinahao@163.com

M. Zeng
University of Chinese Academy of Sciences, Beijing, China

J. Sun et al. (eds.), *China Satellite Navigation Conference (CSNC) 2015 Proceedings: Volume II*, Lecture Notes in Electrical Engineering 341,
DOI 10.1007/978-3-662-46635-3_6

6.1 Introduction

With prominent advantages of high precision, fast speed and low cost, satellite navigation and positioning technologies have become the world's most widely used navigation and positioning system. Navigation signal, as the data transmission carrier of satellite navigation and positioning system, carries navigation message and related ranging and correction information. Signals received from several navigation satellites are used for data synchronization, and a user will be able to obtain pseudo-range and carrier phase observation value based on synchronized navigation message and pseudo-code phase, which in turn are used to calculate the user's speed and location information, thus realizing navigation and positioning [1].

Design of satellite navigation system mainly considers constellation, signal system, time benchmark and other factors. Among them, signal system design is the key technology and directly determines performance of navigation system, and therefore, it plays an important role in GPS, GLONASS, Galileo and the BDS satellite navigation system China is building [2].

GPS and Galileo are common satellite navigation systems used abroad. GPS signal format evolved from initial BPSK-modulated C/A code and P code to the latest BOC-modulated M code. BOC signal initially proposed by BetZ is able to achieve spectral separation when navigation frequency band resources are constrained [3]. Moreover, BOC-modulated signals have better correlation function performance than BPSK-modulated signals. Its correlation function is much steeper compared with BPSK-modulated signals of the same bit rate, which means higher code tracking accuracy and better multipath resolution capability [4]. As a result of this, Galileo system also adopts navigation signals based on BOC modulation to ensure navigation accuracy and meanwhile achieve compatibility and interoperability with GPS system.

With the development of BDS satellite navigation system, China has carried out in-depth research on signals based on BOC modulation, and plans to apply a signal system based on BOC modulation in BDS global system. Besides navigation, China's Beidou system also possesses communication function.

Along with the development of navigation technology, design of navigation signal system has evolved from realizing original single function of navigation to considering compatibility between various navigation systems and improving positioning accuracy. Satellite navigation is becoming perfect, however, it also has some inherent shortcomings: first, due to its low message data rate, initial positioning time of cold start (TTFF, Time to First Fix) is too long to satisfy the need of fast positioning; second, when satellite navigation signals reach the ground, they are already very weak, only 160 dBW in normal situation [5], and their signal strength will decline sharply in indoor and sheltered environment, so it is very difficult to receive signals for positioning; third, the positioning principle of satellite navigation requires to simultaneously calculate XYZT four parameters, so there must be at least four satellites available to complete positioning algorithm, this requirement

often cannot be met in case of sheltered environment or interference, furthermore, it is impossible to receive satellite signals in indoor environment.

As dependence on navigation in daily lives is increasing, people are having higher requirements on navigation performance. Inherent shortage of satellite navigation results in the fact that solely relying on satellite navigation system has been unable to meet individual requirements on navigation speed, continuity, accuracy and reliability.

Mobile communication network is characterized by wide coverage and strong signal strength, and it can also provide location services to users, even in complex environments such as indoor and sheltered environment where satellite navigation fails to provide independent positioning, but its accuracy is relatively low. Therefore, using communication signals to support satellite navigation and positioning and achieve deep fusion of navigation and communication has attracted widespread attention, and this is also the focus of interdisciplinary of navigation and communication. The common method used by the study of deep fusion of navigation and communication is based on communication link assisted satellite navigation technology (A-GNSS, Assisted-GNSS) [6, 7], which uses wireless networks to transmit enhanced information, such as navigation message and differential correction information, to quickly search for satellites and improve positioning accuracy. GPSOne technology uses mobile communication network in combination with satellite navigation system for positioning, which integrates navigation and communication at observation level and realizes single satellite positioning [8–10].

In spite of the above methods, it is still difficult to fully meet people's rapidity, continuity, accuracy and reliability requirements on navigation and the above-proposed solutions are mainly based on information domain, observation domain, and platform level to integrate navigation and communication, instead of exploring deep fusion of communication and navigation in signal layer.

Under the background of navigation and communication signal fusion, this paper analyses the basic characteristics of communication signals, and puts forward the novel BCC (Burst Composite Carrier) signals characterised by deep fusion of navigation and communication, followed by BCC signal performance analysis and synchronization algorithm design based on the analysis. Finally, this paper conducts simulation analysis, and to carry out desktop-level test and validation, a principle sample machine is developed.

6.2 Basic Features of Communication Signals

There are a variety of existing mobile communication systems, in which the most common ones include 3G mobile communication [11, 12], 4G mobile communication [13, 14], CMMB [15, 16] and so on. Signal systems in all communication systems are generally similar to navigation signals with pseudo-code spread spectrum system structure, and therefore can be used for ranging. In addition,

communication signal also has the following characteristics compared with normal navigation signal:

① Existing high rate information transmission channel. The main purpose of communication signal is to satisfy communication needs, its rich channel resources are able to provide two-way, real-time voice and data service at a much higher communication rate than the existing satellite navigation system, so it can be used to transfer navigation message and precise ephemeris and other navigation information.
② High signal transmit power. Transmit power of communication signal is generally much higher than signal power of satellite navigation. Apart from that, base station and users are also close to each other. Therefore, when used for navigation, it is much easier for users to receive relatively higher SNR.
③ Wide signal bandwidth, more frequency resources available. Spectrum range dedicated to satellite navigation is relatively narrow, so with the increase of satellite navigation systems, bandwidth resources will be increasingly strained. Communication signals are of wider bandwidth and more frequency resources relative to those of navigation signals, and can have hundreds of megabytes of bandwidth in a single frequency band.
④ Time-division characterized signal structure. Time-division signal has been in use in terrestrial communication network since 2G and 3G till today, and serves different users in different time slots. Time-division signal is the basic means to ensure multiple user access to communication network, and the basic framework of communication signals.
⑤ Multi-carrier characterized signal structure. Current mainstream communication signal systems are generally based on multi-carrier characterized OFDM system (for example, 4G, 5G, CMMB system, etc.). With higher spectral efficiency and good anti-multipath performance, OFDM system has been widely used in ground communication [17].

6.3 Introduction to BCC Signal System

Through combining the characteristics of and achieving compatibility between communication signal and navigation signal, this novel signal system integrates navigation and communication by using bursts compound carrier modulation to construct compound carrier time-division signal (BCC). N subcarriers are modulated on a single frequency point in each ranging channel, with fixed subcarrier frequency interval, and bursts characterized signal duration can be regulated. All subcarriers modulate the same pseudo codes, and meanwhile all subcarriers' signal power can be regulated as needed. Finally, signal of N subcarriers will be combined together for transmission, using different pseudo codes to represent different signal sources. Its design principle is as follow: in terms of frequency domain, divide frequency bandwidth of a single transmitted frequency point in a ranging channel

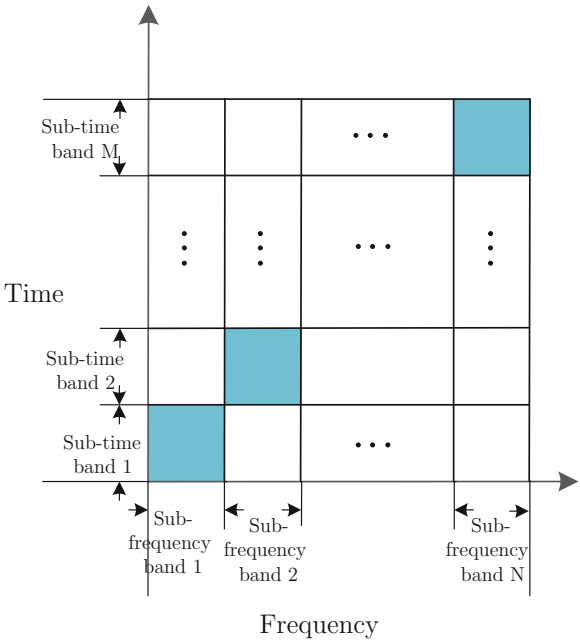

Fig. 6.1 BCC signal's time-domain and frequency domain

into N sub-frequency bands; in terms of time domain, period of the signal is divided into M sub-time bands, duration of all subcarriers follows the pre-set duration in the subcarriers, and meanwhile, all subcarriers have the same frequency interval, and its width is multiples of pseudo code rate. Its signal distribution in terms of time frequency is shown in Fig. 6.1.

6.3.1 BCC Signal Format

As can be seen from the above description, signal system uses code division to distinguish signal sources, and burst compound carrier to form single frequency point navigation signal, so the transmitted signal of signal source number j can be expressed as:

$$\begin{aligned} S_j(t) &= \sum_{l=1}^{N} A_l \cos[2\pi(f_0 + l\Delta f)t + \phi_l] C_{ij}(t) g_{sum}(t) \\ &= \begin{cases} \sum_{l=1}^{N} A_l \cos[2\pi(f_0 + l\Delta f)t + \phi_l] C_{ij}(t), & (i-1)T_w < t \le (i-1)T_w + \sigma T_w \\ 0 & (i-1)T_w + \sigma T_w < t \le iT_w \end{cases} \end{aligned} \tag{6.1}$$

where, $g_{sum}(t) = \sum_{n=-\infty}^{+\infty} g(t-nT)_b$, $g(t) = \begin{cases} 1 & 0 < t \le \sigma T_w \\ 0 & \sigma T_w < t \le T_w \end{cases}$, $l = 1, 2, \ldots, N$ stands for the subcarrier serial number of BCC signal; A_l is the transmit signal amplitude of subcarrier l; ϕ_l refers to modulation phase of subcarrier l; i is non-zero integer, representing signal is currently in cycle i; Tw refers to signal cycle; σ is signal's duty cycle; C_{ij} refers to the modulated pseudo code of signal j in cycle i, with bit rate of f_c and chip width of T_c; Δf represents subcarrier interval.

It can be seen from the above expression that in BCC signal duration period $[(i-1)T_w \quad (i-1)T_w + \sigma T_w]$, the existing signal is a multicarrier signal consists of N carriers; in signal non-continuous period $[(i-1)T_w + \sigma T_w \quad iT_w]$, signal does not exist, while BCC signal from other signal sources may exist. Receiving terminals receive BCC signals from different channels in different time slots, and thus realizing navigation signal enhancement.

6.3.2 Preliminary Analysis of Signal Performance

6.3.2.1 Power Spectral Density

It can be concluded from expression (6.1) that BCC signal's power spectrum equals to the sum of subcarrier power, which can be expressed as

$$P_{BCC}(f) = \sum_{l=1}^{N-1} p_l(f) \tag{6.2}$$

where, p_l stands for signal power of subcarrier l, according to the carrier's expression, its power spectrum equals to the convolution of continuous signal's power spectrum and power spectrum of gate function whose duty cycle is σ. Continuous signal's power spectrum can be expressed as:

$$pc_l(f) = T_c |\sin c(T_c(f - (f_0 + l\Delta f)))|^2 \tag{6.3}$$

Subcarrier power spectrum of gate function whose duty cycle is σ can be expressed as

$$p_g(f) = \sigma^2 \sum_{k=-\infty}^{\infty} \left| \frac{\sin(\pi\sigma T_w f)}{\pi T_w f} \right|^2 \delta(f - kf_0) \tag{6.4}$$

So subcarrier signal power spectrum can be expressed as

$$p_l(f) = pc_l(f) * p_g(f) \tag{6.5}$$

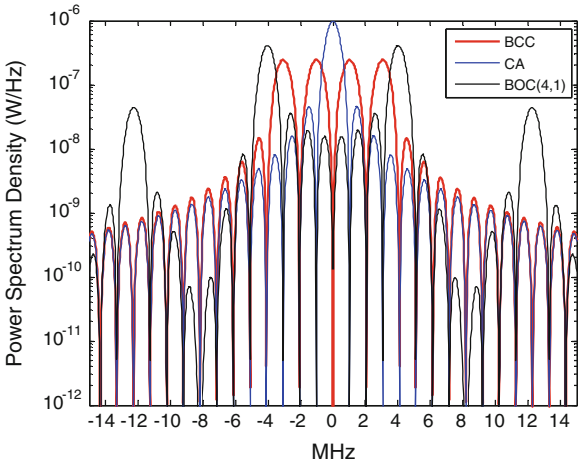

Fig. 6.2 Signal power spectral densities

According to Eq. (6.5), if N = 4, code rate f_c = 1.023 MHz, subcarrier frequency interval $\Delta f = 2.046$ MHz, all subcarriers have the same amplitude of 1, and they have the same initial phase of 0, signal cycle Tw = 10 ms, duty cycle $\sigma = 0.1$. It can be seen from the expression that signal bandwidth of BCC signal is wider relative to that of continuous signal, and its value is co-determined by pseudo-code rate, number of subcarrier, frequency interval, duty cycle and signal cycle. Power spectrum of BCC signal is shown in Fig. 6.2.

As can be seen from the diagram, BCC signal power spectrum and power spectrum of BOC modulated signal share the characteristic of multi-peak, and the expression shows that BCC signal's signal bandwidth is also affected by signal duration. The number of subcarriers determines the number of BCC multi-peak, and its performance is related to pseudo-code rate, number of subcarriers, frequency interval, duty cycle and signal cycle.

6.3.2.2 Autocorrelation Function

According to stochastic process principle, autocorrelation function is the Fourier inversion of power spectrum, which can be expressed as

$$R_{BCC}(\tau) = IFFT(P_{BCC}) \tag{6.6}$$

According to Eq. (6.6), BCC signal's autocorrelation function is shown in Fig. 6.3.

As can be seen from above, BCC signal has good correlation performance, the steepness of its main peak is slightly lower than that of BOC(4,1) signal but higher than that of C/A code; amplitude of peaks near the main peak is smaller than that of BOC(4,1) signal, which is more conducive to signal detection and estimation, and

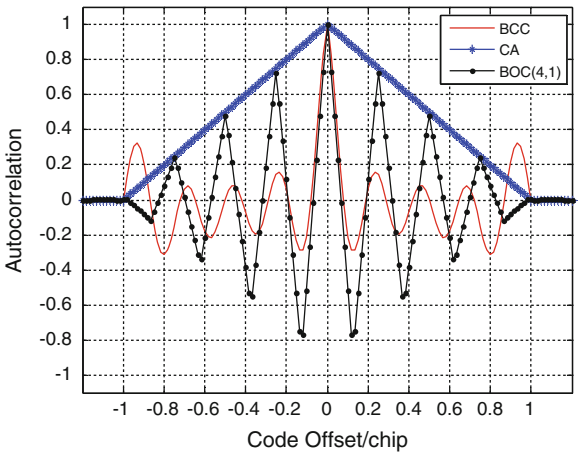

Fig. 6.3 Signal's autocorrelation

obtain of accurate pseudo-code phase information. So BCC signal has better ranging and navigation performance.

6.3.2.3 RMS Bandwidth

RMS bandwidth is the power weighted average of useful signal in transmitting bandwidth. Weight at centre frequency is 0 and reaches maximum on both sides, which directly reflects peak sharpness. B_{rms}, RMS bandwidth of BCC, can be expressed as

$$B_{rms} = \sqrt{\frac{\int_{-B_r/2}^{B_r/2} P_{BCC}(f) f^2 df}{\int_{-B_r/2}^{B_r/2} P_{BCC}(f) df}} \tag{6.7}$$

where, B_r stands for signal's transmitting bandwidth. It can be seen from Eq. (6.7) that the higher of frequency, the greater of RMS bandwidth and the higher of the sharpness of the signal's autocorrelation peak. This also proves that BCC signal's autocorrelation function is sharper than that of CA code, and slightly less sharp than that of BOC(4,1).

6.3.2.4 Ranging Accuracy in Theory

After analysing BCC signal's theoretical ranging accuracy, the lower bound of its pseudo-code's theoretical ranging accuracy can be expressed as

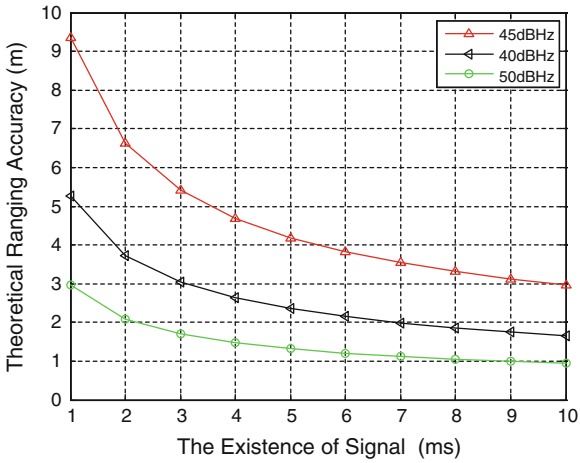

Fig. 6.4 Theoretical ranging accuracy

$$\begin{aligned} \mathrm{std}(\hat{\theta}) &\geq \frac{\sigma_n^2}{\sum_{n=0}^{N-1}\left(\frac{ds(t)}{dt}\Big|_{t=nT_s}\right)^2} \\ &= \frac{N_0 \cdot 2B_r}{\frac{1}{T_s}\int_0^{\sigma T_w}\left(\frac{ds(t)}{dt}\right)^2 dt} \\ &= \frac{\sqrt{2B_r T_s}}{\sqrt{\sigma T_w \cdot CNR \cdot (2\pi B_{rms})^2}} \end{aligned} \tag{6.8}$$

where, N_0 stands for density of noise power, Ts stands for sampling intervals and CNR refers to carrier to noise ratio. Equation (6.8) shows that theoretical ranging accuracy is related to sampling interval of the signal, signal continuous duty cycle, signal cycle, carrier to noise ratio and RMS bandwidth. As in other similar cases, the longer the existence of signal (the signal's duty cycle times signal cycle), the higher of the theoretical ranging accuracy, and meanwhile, the higher of the carrier to noise ratio, the higher of the theoretical ranging accuracy. The theoretical ranging accuracy can be seen in Fig. 6.4, where 1/Ts is 50 MHz.

6.4 Signal Synchronization Algorithm Study

BCC signals, due to its non-continuous characteristic and generally short signal duration, cannot use existing navigation receiver's continuous-signal based synchronization algorithm. The purpose of adopting continuous-signal based navigation signal for synchronization is to obtain accurate pseudo-code phase and navigation message, and finally pseudo range and signal transmission time. In BCC

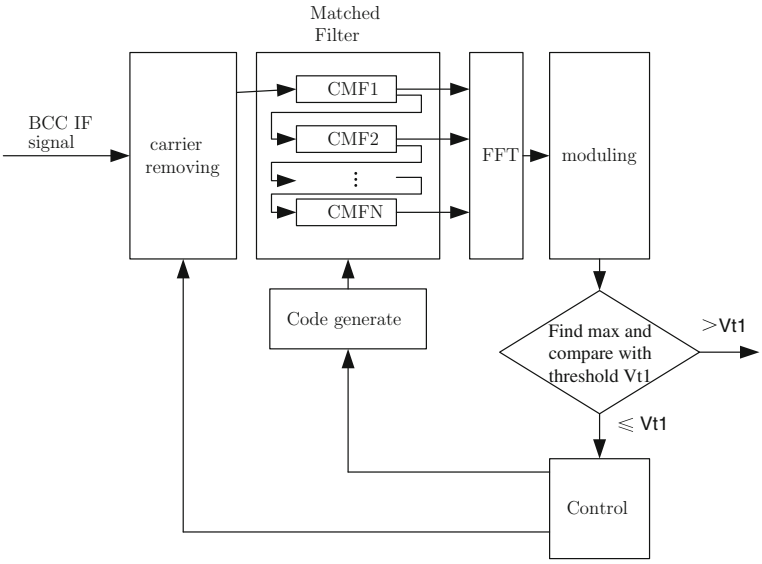

Fig. 6.5 Coarse acquisition structures

navigation signal system, since non-continuous signal is not suitable for information dissemination, its signal does not come with modulated navigation message, so the navigation message has to be obtained via other means; while accurate pseudo-code phase is acquired through the following three methods. These three methods all consist of coarse acquisition and fine acquisition stages. In coarse acquisition stage, due to BCC signal's multi-frequency, the proposed method is to use matched filtering together with FFT algorithm [18], and its capture structure is shown as follow. There are three methods to acquire accurate pseudo-code phase based on the rough pseudo-code phase provided by coarse acquisition, which are two-dimensional refine algorithm [19], curve-fitting algorithm and long-term filter algorithm (Fig. 6.5).

6.4.1 Two-Dimensional Refine Algorithm

Two-dimensional refine algorithm is to apply finer pseudo-code step-by-step search method and Doppler frequency-shift step-by-step method in refined search around rough pseudo-code phase and Doppler frequency following below steps.

Step 1. For received signals, use matched filtering and FFT algorithm to obtain coherent integration, and compare the maximum value with threshold, record code phase and Doppler frequency of maximum value's location as

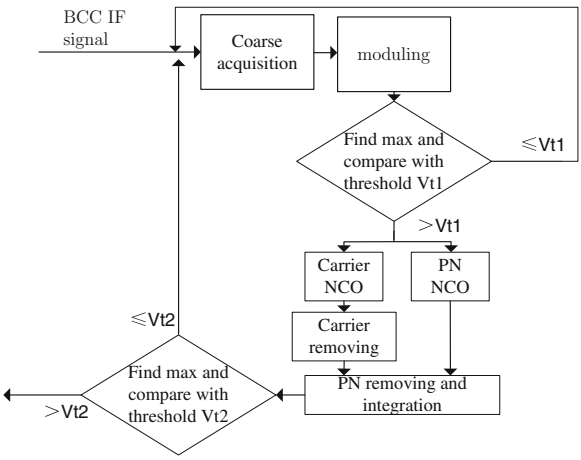

Fig. 6.6 Two-dimensional refine algorithm

the result of coarse acquisition if the maximum value is greater than the threshold, otherwise repeat step 1.

Step 2. On the basis of coarse acquisition, use the Doppler frequency shift acquired through coarse acquisition as centre, refine the search of Doppler frequency with length one stepping value of that of coarse acquisition, which means the refined stepped frequency is smaller. Centred by the code phase acquired by coarse acquisition, the refined code phase search scope is the stepped value of coarse acquisition FFT, so refined code phase is finer step value, which is used in serial search.

Step 3. In different Doppler frequency offset, obtain coherent integration under different pseudo-code phases and find the maximum point, and then compare it with threshold, export the Doppler frequency offset and pseudo-code phase of maximum point's location if the maximum point is greater than the threshold, otherwise return to step 1 (Fig. 6.6).

6.4.2 Curve-Fitting Algorithm

Curve-fitting algorithm is based on the characteristic of code autocorrelation. Due to limited bandwidth, pseudo-code autocorrelation function has no peak in real signal, but similar to smooth parabola-like shape. Extreme point of the parabola, or maximum correlation value's corresponding phase, is refined pseudo-code phase, so curve fitting is used to calculate correlation function parabola's extremes, which is the basis of obtaining fine pseudo-code phase. The steps are as follows.

Step 1. For received signals, use matched filtering and FFT algorithm to obtain coherent integration, and compare the maximum value with threshold, record the code phase and Doppler frequency of maximum value's location

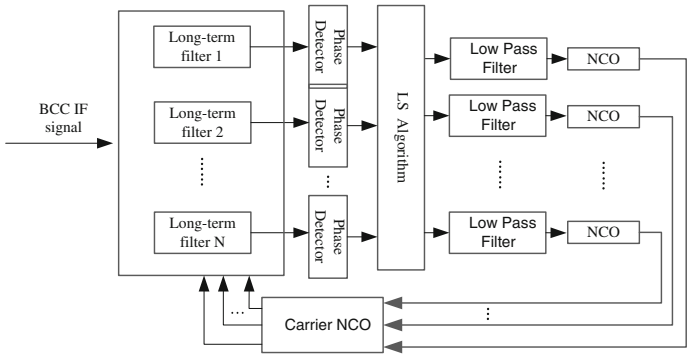

Fig. 6.7 Long-term filter tracking algorithm

as the result of coarse acquisition if the maximum value is greater than the threshold, otherwise repeat step 1.

Step 2. Course acquisition results will produce corresponding lead, lag and instant local pseudo codes and carriers, with corresponding lead, lag and instant coherent integration results, which will serve as inputs of curve fitting. After calculation, extreme points of the curve fitting will be obtained with fine pseudo-code phase based on corresponding filter.

6.4.3 Long-Term Filter Algorithm

In light of the multicarrier and non-continuous characteristics of BCC signal system, multi-channel combined with long-term filter algorithm is adopted to track BCC signals. Signal correlation time in tracking algorithm is a pseudo-code cycle, which can increase signal correlation time, cover a cycle of BCC signal's subcarrier signal and offset the impact of discontinuity on signal tracking, due to discontinuity of BCC signal. Results of algorithm are shown in Fig. 6.7.

6.5 Performance Simulation

(1) Correlation integral FFT acquisition algorithm simulation

Simulation criteria: 4 subcarriers for each signal source; pseudo-code rate of 1.023 MHz; CA code as pseudo code; subcarrier frequency interval of 2.046 MHz; carrier frequency of 10.5 MHz; sampling rate of 45.714 MHz; time of correlation integral is 1 ms; number of simulation is 1000 Monte Carlo simulations. In a single

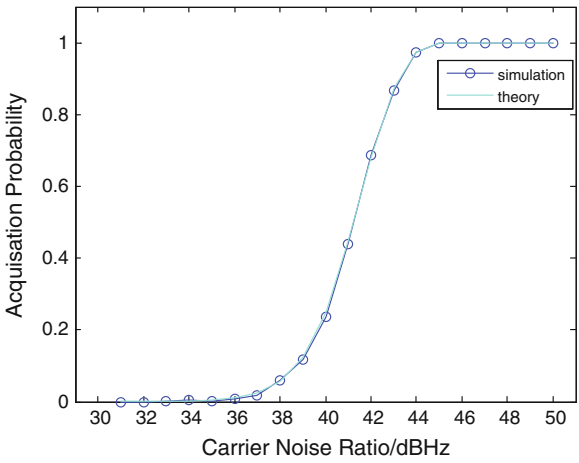

Fig. 6.8 Acquisition probabilities

detection probability, results of detection probability of constant false alarm with 10-6 false alarm probability are shown in Fig. 6.8.

The simulation results show that this algorithm can effectively capture BCC signal and the results coincide with the theoretical results.

(2) Long-term filter joint tracking algorithm simulation

Simulation conditions: 4 subcarriers for each signal source; pseudo-code rate of 1.023 MHz; CA code as pseudo code; subcarrier frequency interval of 2.046 MHz; carrier frequency of 10.5 MHz; sampling rate of 45.714 MHz; time of correlation integral is 2 ms; duty cycle of 50 %; carrier Doppler changes at 0.5 Hz/s; second order phase locked loop is adopted; signal correlation integral time is 2 ms; pseudo-code bandwidth of 2 Hz; carrier bandwidth of 20 Hz; 0.2 loop gain. The simulation results of Doppler frequency change obtained are shown in Fig. 6.9.

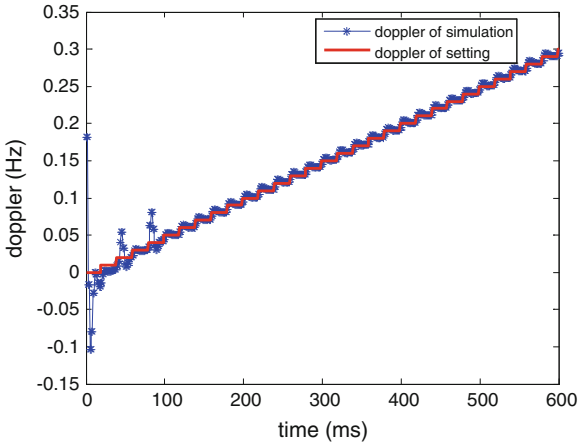

Fig. 6.9 Long-term filter joint tracking Doppler results

The Fig. 6.9 demonstrates that at duty cycle of 50 %, preliminary simulation results prove that long-term filter combined with joint tracking algorithm is able to effectively track BCC signal with above parameters.

6.6 Test Verification

Existing experimental conditions can produce navigation signals under the existing signal system through IFEN simulator, but not multicarrier BCC signals. With the help of MATLAB post-processing, single carrier BCC navigation signals can be obtained. Principle sample machine has been developed to test and verify key algorithm of this signal system through receiving single-carrier BCC intermediate frequency signal.

In this test, IFEN simulator produces navigation signal at GPS L1 frequency point, signal's carrier to noise ratio is 43 dBHz, and user receiver is static. First sampling intermediate frequency of the navigation signal in MAX2769 module, and then collect GPS L1 digital intermediate frequency signal in the sample via M2i.7011 acquisition card, after that, use the signal synchronization algorithm introduced here to obtain fine pseudo-code phase in MATLAB, the final measurement error of pseudo-range is shown in Fig. 6.10 and positioning errors in three directions are shown from Figs. 6.11, 6.12, 6.13. After 150 times of positioning, measurement error of pseudo-range under 1 is 6.06 m, range errors in X, Y and Z directions are 3.75, 6.97 and 7.3 m respectively, so its positioning error is 10.8 m. Although this study did not fully adopt multi-carrier BCC signal for testing, its positioning accuracy for single carrier can reach 10.8 m, so it is expected that theoretical analysis of multi-carrier positioning accuracy is

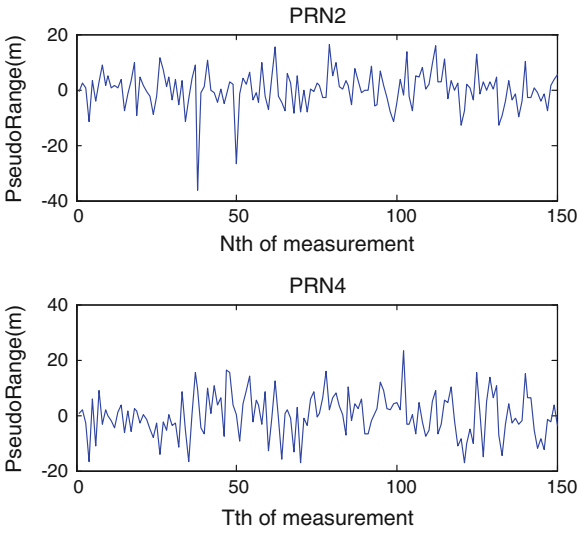

Fig. 6.10 BCC signal ranging accuracy

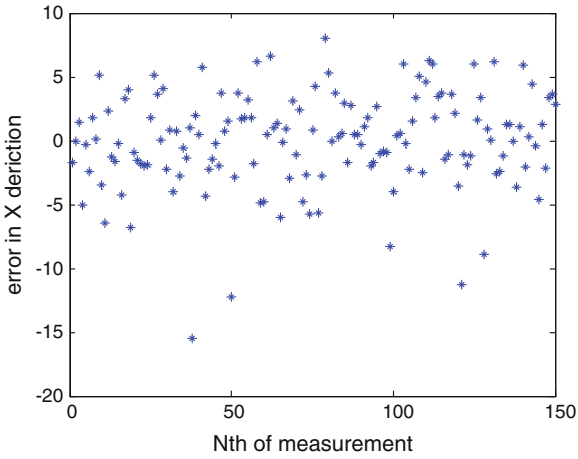

Fig. 6.11 Positioning errors at X direction

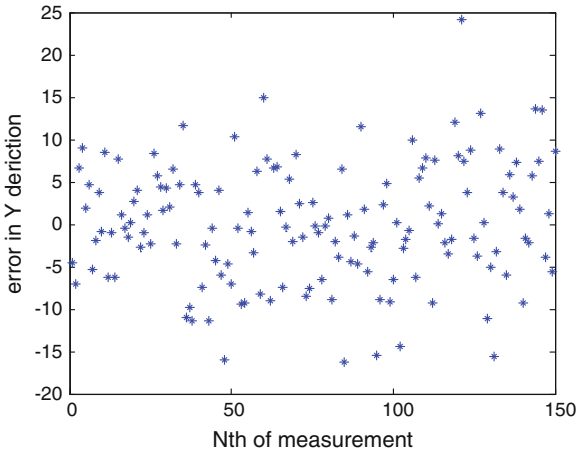

Fig. 6.12 Positioning errors at Y direction

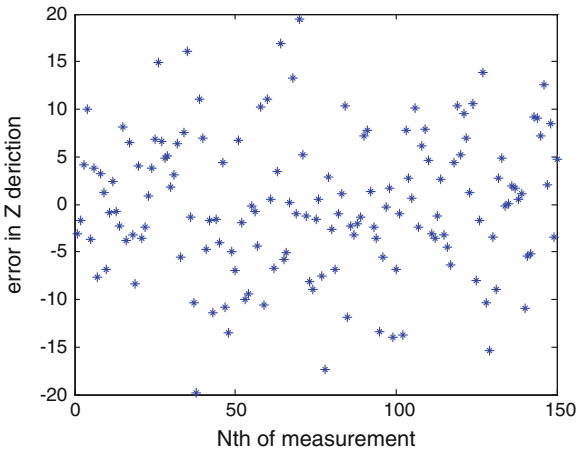

Fig. 6.13 Positioning errors at Z direction

less than 10.8 m; meanwhile, this experiment tests and verifies key algorithm of BCC signal, and proves that synchronization algorithm is very effective in positioning resolve. This study fully explains that BCC signal has the potential for further exploration.

6.7 Feasibility Analysis of Fusion with Communication

There is a high similarity between BCC navigation signal system's intrinsic characteristics of multi-carrier and time-division signal and the characteristics of OFDM and TDD signal systems of existing communication systems. So it is possible to employ communication network to transmit navigation message by adding spread spectrum pseudo-code sequence in OFDM and TDD communication signals for ranging, and thus achieving navigation and positioning. Since communication signals have wider bandwidth, pseudo-code rate and number of subcarrier can be regulated to adapt to different environments as needed; communication signals' strong signal power ensures effective signal receiving in both the indoor and outdoor environment, and also the continuity of navigation and positioning. In addition, potential improvement of positioning accuracy of BCC navigation signal could meet the accuracy requirement of indoor/outdoor environment. Existing TD-LTE communication signal system has already adopted OFDM and TDD combination method, and therefore is fully capable to integrate navigation and communication by adding BCC navigation signals in GP time-slot of TD-LTE. So it can be concluded that BCC navigation signals and communication signals can be integrated very well, and future design of 5G signals is sure to consider compatibility with 4G signals, so navigation and communication fusion model of TE-LTE provides reference for future 5G-signal design.

6.8 Conclusion

This paper analyses basic characteristics of navigation signal and communication signal, and proposes a novel signal system bearing basic features of communication signal, aiming at realizing deep fusion in signal layer. In this paper, the new signal's correlation function, power spectrum density, RMS bandwidth and positioning accuracy are studied, followed by comparative analysis of the new signal and BPSK modulated C/A code signal and BOC modulated BOC(4,1) signal, with the conclusion that BCC signal has better of navigation and positioning performance. Moreover, this study also puts forward signal synchronization algorithm based on signal features, simulates signal performance and tests and verifies key algorithm. The result indicates that single-carrier BCC signal's ranging accuracy is 6.06 m, and positioning accuracy is 10.8 m. The ranging and positioning accuracy will be better in multi-carrier conditions, which will be sufficient for users' basic

positioning requirements. The analysis of communication signals confirms that the signal is able to integrate with existing communication signals, which is worthy of further in-depth study.

References

1. Understanding GPS: principles and applications. Artech house (2005)
2. Tang Z (2009) Research on relevant theory for GNSS signal design and evaluation. Huazhong University of Science and Technology, Wuhan
3. Betz JW (2001) Binary offset carrier modulations for radionavigation. Navigation 48(4):227–246
4. Ries L, Legrand F, Lestarquit L et al (2001) Tracking and multipath performance assessments of BOC signals using a bit-level signal processing simulator, In: Proceedings of the 16th international technical meeting of the satellite division of the institute of navigation (ION GPS/GNSS 2003) pp 1996–2010
5. Spilker JJ (1996) Global positioning system: theory and applications
6. Anwar A, Loannis G, Pavlidou F (2009) Indoor Location tracking using AGPS and Kalman Filter, WPNC, Hannover, 19 March 2009
7. Li J, Liu J (2013) Improving availability of AGPS positioning algorithm with fuzzy theory, ICIST, China, 23–25 March 2013
8. Soliman S, Agashe P, Fernandez I (2000) gpsOneTM: a hybrid position location system, In: IEEE sixth international symposium on spread spectrum techniques and applications, Parsippany, 20 Sept 2000
9. Kedong W, Lei Y, Hui W, et al (2004) GpsOne: a new solution to vehicle navigation. In: IEEE position location and navigation symposium (), pp 341–346
10. Shaobin Z, Yongsheng L, Yuefang G, et al (2010) On researching the key algorithm of dual-mode vehicle positioning system. In: 3rd International conference on computer science and information technology, vol 4, pp 659–662
11. Dahlman E, Parkvall S, Skold J, et al (2010) 3G Evolution: HSPA and LTE for Mobile Broadband. Academic press, Oxford
12. Salkintzis AK (2004) Interworking techniques and architectures for WLAN/3G integration toward 4G mobile data networks. IEEE Wirel Commun 11(3):50–61
13. Khan AH, Qadeer MA, Ansari JA et al (2009) 4G as a next generation wireless network. In: IEEE international conference on future computer and communication, ICFCC 2009, pp 334–338
14. Govil J (2007) 4G mobile communication systems: turns, trends and transition. In: IEEE international conference on convergence information technology, pp 13–18
15. Park JY, Chung KS (2011) Overlapped message passing technique with resource sharing for high speed CMMB LDPC decoder. IEEE Trans Consum Electron 57(4):1564–1570
16. Huang C, Hu Y, Zhang H et al (2013) Research on pseudo-range measurement technique for CMMB system. In: Joint IEEE European frequency and time forum and international frequency control symposium (EFTF/IFC), pp 356–359
17. Nee R, Prasad R (2000) OFDM for wireless multimedia communications, Artech House, Norwood
18. XU Y, Yuan H (2011) Navigation signal structure based on complex carrier modulation. Sci China Phys Mech Astron 54(6):1035–1045
19. He Z-L, Xu Y, Yuan H, Wei D-Y (2014) A two-dimensional refinement algorithm for signal acquisition. J Electron Inform Stechnol 36(10):2450–2455

Part II
Satellite Navigation Augmentation and Integrity Monitoring

Chapter 7
Research on Multi Satellite Failure Detection and Recognition Method of Satellite Navigation RAIM

Zhixin Deng, Jun Li and Mengjiang Liu

Abstract Satellite Navigation Receiver Autonomous Integrity Monitoring (RAIM) is developed for detection and recognition of satellite faults using the redundant observation values of receiver itself. This article first makes a comparative analysis to the conventional and recently proposed RAIM fault detection and identification methods, and then points out that the conventional fault identification methods have such weakness as low fault detection probability and high false alarm probability in the situation of simultaneous multiple faulty satellites, while the recently proposed multi-satellite fault identification methods require excessive computation work though enjoy a higher detection probability. To solve these problems, a new RAIM multiple satellite fault detection and recognition method is proposed in this paper, which is characterized by high detection probability, low false alarm probability and low computation load, practicable for project implementation. Based on a simulation analysis, it turns out that this method has a higher detection probability without false alarm at all. This method requires so low computation work that it only needs 2 m times of least squares residuals fault detection and m times of fault identification in m ($m > 0$) faulty satellites situation, showing a very promising application value.

Keywords RAIM · Multi satellite fault detection · Multi satellite fault recognition · Multi epoch smoothing

Z. Deng (✉) · J. Li · M. Liu
The 54th Research Institute of CETC, Shijiazhuang, China
e-mail: chinadengzhixin@139.com

Z. Deng · J. Li · M. Liu
Satellite Navigation Technology and Equipment Engineering Technology Research Center of Hebei Province, Shijiazhuang, China

J. Sun et al. (eds.), *China Satellite Navigation Conference (CSNC) 2015 Proceedings: Volume II*, Lecture Notes in Electrical Engineering 341,
DOI 10.1007/978-3-662-46635-3_7

7.1 Introduction

Satellite navigation integrity is one of important service performance in satellite navigation system. It is users' requirement to detect and exclude the faulty satellite (s) timely in case that any navigation satellite goes wrong, thus to acquire continuous and correct positioning service. Receiver Autonomous Integrity Monitoring (RAIM) is developed to carry out quick monitoring of satellite faults in a satellite navigation system. Essentially, RAIM must answer two questions: is there any satellite in trouble and which one if any?

The early developed RAIM algorithms include Kallman filtering algorithm and positioning-solution maximum interval algorithm. The Kallman filtering algorithm may improve the solution accuracy using the past observed quantities if the apriori error characteristics are known in advance. However, the actual error characteristics are very difficult to foresee accurately. It might degrade the solution accuracy in case of inaccurate forecast. The positioning-solution maximum interval algorithm needs a complicated mathematical analysis process and it is not easy to determine the alarm threshold of fault detection. Relatively good RAIM algorithms are "snapshot" algorithms using the pseudo-range observation values at the current epoch, including pseudo-range comparison algorithm, least square residual algorithm and parity vector algorithm. These three algorithms show good and equivalent performance in the conditions that only one fault is present. However, these three algorithms behave very poor in fault recognition performance when a number of faults are present, with the recognition rate only up to 40 % through 60 %. The reason is these algorithms are all based on comparison of the detection statistical quantities with a fixed threshold for fault recognition. When several faults come up, the faults cause divergence of detection statistical vectors, making it difficult to correctly identify faults.

In September 2008, Zhang Qiang et al. proposed a fault recognition workflow that is based on hypothesis verification. It assumes k satellites among n satellites go wrong, and then works out the projection observed quantities of every assumed combination. However, this algorithm is impossible to predetermine the number of faulty satellites; therefore, the larger is the k, the more times of hypothesis verification have to be made, leading to a very huge computation amount. In December 2011, Chen Canhui et al. proposed a fault exclusion algorithm based on a fault detection function that carries out a random search among all the satellites to ultimately find out the constellation containing the maximum fault-free satellites. This algorithm requires to initialize a fault-free constellation at random in advance before making any attempt to include more fault-free satellites. Although this algorithm provides a high detection probability, it requires to try various fault-free combinations at random repeatedly for fault detection. The computational complexity is impracticable for the case of high data updating rate. In June 2011, Sun Shu-guang proposed a detection algorithm based on stratified integrity detection. By comparing the statistical quantity calculated from all the observed quantities with the statistical quantity calculated from partial observed quantities, it indicates

the presence of a fault if the difference exceeds a threshold. After the fault is taken care, a similar flow will go on for fault exclusion. To select the partial observed quantities, computational attempts must be made continually. When the number of faulty satellites grows, the computational complexity of this algorithm increase in geometric series. Therefore, it is relatively suitable for the fault recognition when only two satellites in a constellation are in trouble at most.

Conclusively, the conventional techniques are low in detection probability and high in false alarm probability for multiple satellite RAIM fault detection and recognition. The recently proposed techniques require too much computation, inapplicable to extensive applications, especially impracticable for the receivers with high data updating rate.

7.2 RAIM Fault Detection and Recognition Using Least Square Residual Algorithm

7.2.1 Least Square Residual Model

It is a GNSS pseudo-range observation model containing n observation satellites.

$$Y = G \cdot X + \varepsilon \tag{7.1}$$

where,

- Y represents the n-dimension vector of the difference between the observation pseudo range and the computed pseudo range;
- X represents a 4-dimension unknown vector, containing three position corrections and one receiver clock-error correction;
- ε represents the observation noise vector of n-dimension pseudo range; and
- G represents a n × 4-dimension coefficient matrix, as expressed below:

$$G = \begin{bmatrix} -\boldsymbol{I}_x^{(1)}(x_{k-1}) & -\boldsymbol{I}_y^{(1)}(x_{k-1}) & -\boldsymbol{I}_z^{(1)}(x_{k-1}) & 1 \\ -\boldsymbol{I}_x^{(2)}(x_{k-1}) & -\boldsymbol{I}_y^{(2)}(x_{k-1}) & -\boldsymbol{I}_z^{(2)}(x_{k-1}) & 1 \\ & \cdots & & \\ -\boldsymbol{I}_x^{(n)}(x_{k-1}) & -\boldsymbol{I}_y^{(n)}(x_{k-1}) & -\boldsymbol{I}_z^{(n)}(x_{k-1}) & 1 \end{bmatrix},$$

$$-\boldsymbol{I}_x^{(i)} = \frac{\partial r^{(i)}}{\partial x} = -\frac{x^{(i)} - x}{r^{(i)}}$$

$$-\boldsymbol{I}_y^{(i)} = \frac{\partial r^{(i)}}{\partial y} = -\frac{y^{(i)} - y}{r^{(i)}}$$

$$-\boldsymbol{I}_z^{(i)} = \frac{\partial r^{(i)}}{\partial y} = -\frac{z^{(i)} - z}{r^{(i)}}$$

$$r^{(i)} = \sqrt{(x^{(i)} - x)^2 + (y^{(i)} - y)^2 + (z^{(i)} - z)^2},$$

where,

$[x^{(i)},\ y^{(i)},\ z^{(i)}]^T$	represents the position coordinate vector of satellites i;
$[x,\ y,\ z]^T$	represents the calculated user's position coordinate vector; and
$r^{(i)}$	represents the observation range between user and the satellite

The least square residual RAIM algorithm uses χ^2 test that is based on square sum of residuals for satellite integrity fault detection and uses Gauss test to residual elements for satellite fault recognition, thereby to complete satellite integrity monitoring.

The least squares solution of Eq. (7.1) is $\hat{X} = (G^T \cdot G)^{-1} G^T Y$; therefore, $\hat{Y} = G \cdot \hat{X}$. And then, the pseudo-range residual is expressed as below:

$$v = Y - \hat{Y} = (I - G(G^T G)^{-1} G^T) Y \tag{7.2}$$

Let's assume the association factor matrix of pseudo-range residual vector is $Q_v = I - G(G^T G)^{-1} G^T$, then $v = Q_v Y$. Vector v contains the error information of satellite ranging, which may be used as reference to evaluate whether a satellite goes wrong. The statistical test quantity in fault detection is expressed as below:

$$\hat{\sigma}_d = \sqrt{v^T v/(n-4)} = \sqrt{SSE/(n-4)} \tag{7.3}$$

where, SSE represent the Sum of the Squares of range residual Errors. It appears χ^2 distribution that the degree of freedom is correlated to the number of navigation system.

7.2.2 Fault Detection and Recognition

To evaluate whether a satellite is in trouble, a dualism hypothesis can be made, that is:

The fault-free hypothesis is H_0:$E(\varepsilon) = 0$, then $\frac{SSE}{\sigma_0^2} \sim \chi^2(n-4)$, i.e., $\frac{SSE}{\sigma_0^2}$ is subject to χ^2 distribution at n-4 degrees of freedom.

The faulty hypothesis is H_1:$E(\varepsilon) \neq 0$, then $\frac{SSE}{\sigma_0^2} \sim \chi^2(n-4,\ \lambda)$, i.e., $\frac{SSE}{\sigma_0^2}$ is subject to χ^2 distribution at n-4 degrees of freedom when the non-centralization parameter is λ and $\lambda = E(SSE)/\sigma_0^2$.

At this moment, if the false alarm probability P_{FA} is given, it is possible to work out the test threshold T using the probability equation $P_r(SSE/\sigma_0^2 < T^2) = \int_0^{T^2} f_{\chi^2(n-4)}(x)dx = 1 - P_{FA}$, and then figure out the detection threshold $\sigma_T =$

$\sigma_0 \times T/\sqrt{n-4}$ of $\hat{\sigma}_d$. Because this threshold is only related to the false alarm rate and the degrees of freedom of the chi square distribution function, σ_T is possible to be given in advance. In navigation calculation, the $\hat{\sigma}_d$ computed in a real time manner is compared with σ_T. If $\hat{\sigma}_d > \sigma_T$, then it represents that a fault is detected and the user will be warned before starting fault recognition; otherwise, it is assumed that no satellite is in trouble.

If only one fault is present, it is preferable to identify the faulty satellite with the maximum likelihood algorithm. The fault recognition statistical quantity $d_i = v_i^2/Q_{vii}$ of every satellite is worked out and compared one another, the satellite i corresponding to the maximum d_i is the faulty satellite. Where, v_i is the ith element of the pseudo-range residual vector v.

7.2.3 Usability of RAIM Algorithm

In the process of RAIM fault detection, because of satellite geometric distribution, the positioning error might go over the limit and the statistical detection quantity becomes less than the threshold, i.e., missing detection. Therefore, it is necessary to evaluate whether the present satellite geometric distribution is suitable for integrity monitoring. The usual criterion is to evaluate the usability of satellite geometric distribution with the ARP (Approximated Radial-Error Protected) value. The ARP principle is demonstrated in the figure below (Fig. 7.1).

In the diagram above, the X axis represents the magnitude of detection statistical quantity and the Y axis represents the horizontal radial error. Each satellite has its corresponding slope. The larger is the slope, the more probably occurs missing detection. Accordingly, if no missing detection takes place when the satellite of the

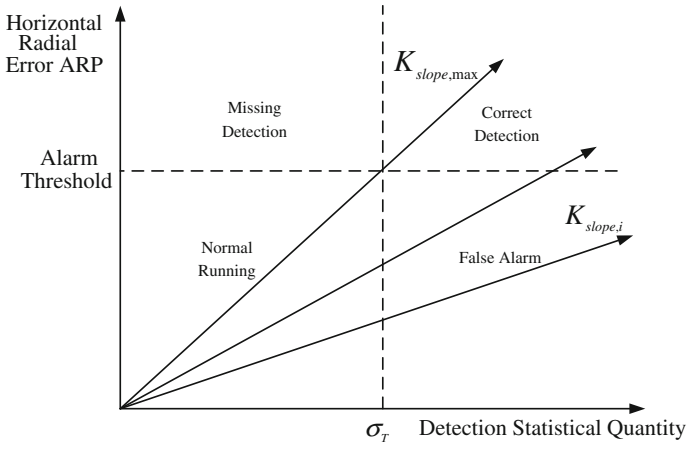

Fig. 7.1 Diagram of usability analysis of fault detection

maximum slope goes wrong, then neither do the other satellites. Therefore, it is possible to evaluate the usability of RAIM fault detection by following the procedure below.

Define the matrix $A = (G^T G)^{-1} G^T$, and then calculate the slope $K_{slope,i} = \sqrt{(A_{1i}^2 + A_{2i}^2)(n-4)/Q_{vii}}$ of every satellite before work out the horizontal protection level $HPL = K_{slope,\max} \cdot \sigma_T$.

Before start the fault detection using the least square RAIM algorithm, compare the calculated HPL value with the given HAL(n) value (acquired from the empirical data of the associated industry, where n represents the number of visible satellites). RAIM fault detection is adaptable only when HPL ≤ HAL(n). The RAIM algorithm is unusable if HPL > HAL(n).

7.3 A Novel RAIM Detection and Recognition Method for Simultaneous Multiple Satellite Faults

The above-mentioned RAIM fault detection and recognition method of least square residual has mainly the following weakness:

(1) In case of multiple faulty satellites, it is very easy to cause divergence of gross error in the detection statistical quantities of fault recognition, consequently leading to missing detection or false alarm. Even if the maximum likelihood estimation method is adopted in case of single satellite failure, it would also lower the detection probability and raise the false alarm probability.
(2) Since no abrupt change will take place within a certain period whether a satellite is in trouble or not, the detection result based on a single epoch is unreliable. In case of missing detection or false alarm, the service performance provided to users will be affected more or less.

Considering the above problems with the conventional RAIM fault detection and recognition method of least square residual, a novel RAIM fault detection and recognition method is proposed on that basis. Its workflow is as follows:

(1) At every epoch, keep detecting fault and estimating faulty satellite step by step with the least square residual algorithm and the maximum likelihood algorithm until a fault-free constellation is determined, thereby to get the initial fault detection result, including whether a fault is present and the SVN of faulty satellite.
(2) Based on the initial fault-free constellation, verify the detected faulty satellite(s) one by one, thereby to confirm if the satellite(s) is really in trouble and to obtain the verified fault detection result at the current epoch.
(3) Smooth the verified fault detection result at the current epoch and the fault detection results at the latest two past epochs to obtain the final fault detection result at the current epoch.

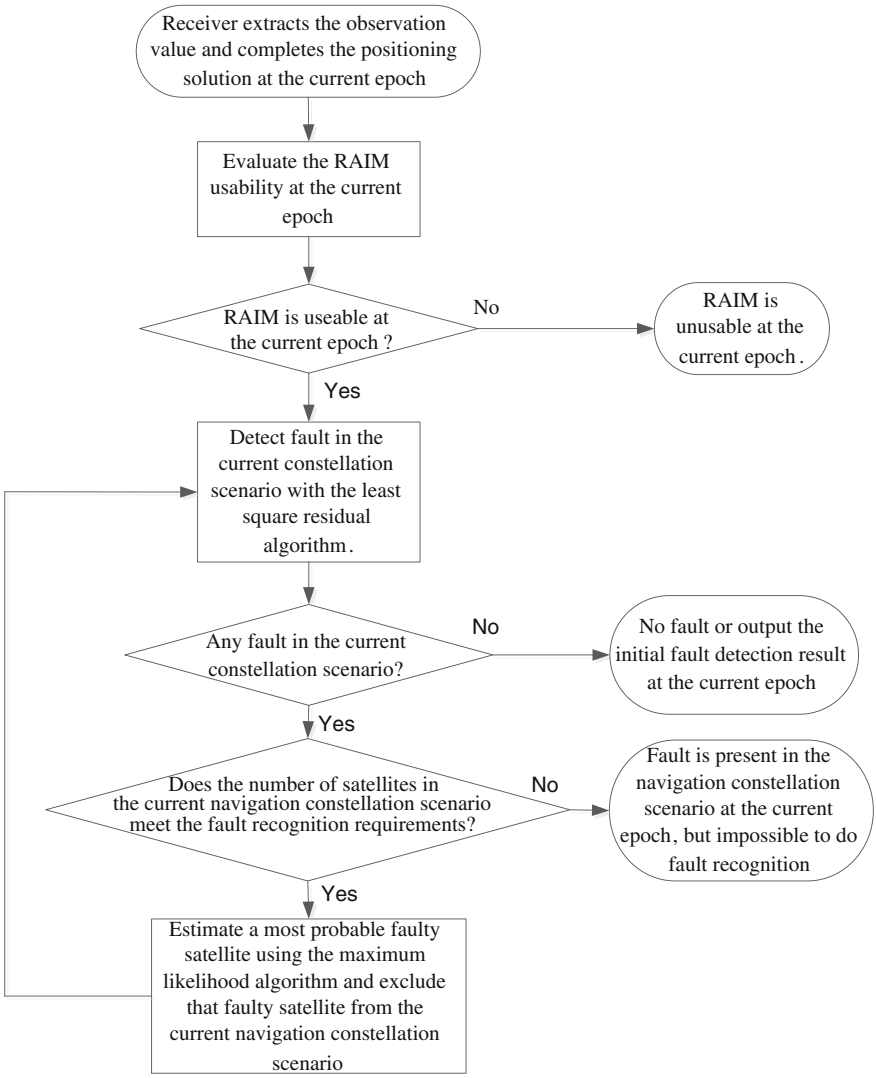

Fig. 7.2 Flow chart of single epoch initial fault detection

The workflow for the initial fault detection at an epoch in Step (1) is as shown in Fig. 7.2, and its specific procedure is as follows:

(1) The receiver evaluates the RAIM usability. If RAIM is usable, then go on to Step (2); otherwise, output the initial fault detection result that RAIM is unusable at that epoch.
(2) The receiver checks the current navigation constellation for any fault with the least square residual algorithm. If a fault is detected, then go on to Step (3); otherwise, skip to Step (4).

(3) If the number of satellites in the current navigation constellation scenario at this epoch meets the fault recognition requirements, then estimate a most probable faulty satellite using the maximum likelihood algorithm and exclude that faulty satellite from the current navigation constellation scenario before go back to Step (2). If fails to meet the fault recognition requirements, then go on to Step (4).
(4) If a fault is present in the current navigation constellation scenario and the satellite number in the scenario meets the fault recognition requirements, then output the initial fault detection result at that epoch. If a fault is present in the current navigation constellation scenario, but the satellite number in the scenario fails to meet the fault recognition requirements, then output the initial fault detection result at that epoch that a fault is present in the current navigation constellation scenario, but impossible to start fault recognition. If no fault is present in the current navigation constellation scenario, then output the initial fault detection result that no fault is detected at that epoch.

The workflow to verify the suspect faulty satellites one by one in Step (1) is as shown in Fig. 7.3, and its specific procedure is as follows:

(1) Evaluate if there is any faulty satellite pending for verification, and select one if any. Put the original observation information of that faulty satellite into the current fault-free constellation scenario and go on to Step (2). If there is no faulty satellite pending for verification, then skip to Step (3).
(2) Carry on fault detection again in the newly established constellation using the least square residual algorithm. If no fault is detected, then attribute that satellite to fault-free satellite. If a fault is detected, then attribute that satellite to faulty satellite and exclude the observation information of that satellite from the current constellation scenario before go back to Step (1).
(3) Output the verified fault detection result at that epoch, including whether a fault is present in the current scenario and the SVN of every faulty satellite.

The workflow for smoothing the fault detection results at several epochs in Step (3) is as shown in Fig. 7.4, and its specific procedure is as follows:

(1) Carry out fault detection and verification for the kth epoch.
(2) Save the fault detection result at the kth epoch, which will be used in three groups of different fault detection smoothing schemes. They are separately the smoothing scheme for the fault detection results from the $k - 2$th epoch through the kth epoch, that from the $k - 1$th epoch through the $k + 1$th epoch and that from the kth epoch through the $k + 2$th epoch.
(3) Complete the smoothing process for the fault detection results from the $k - 2$th epoch through the kth epoch and output the final fault detection result.

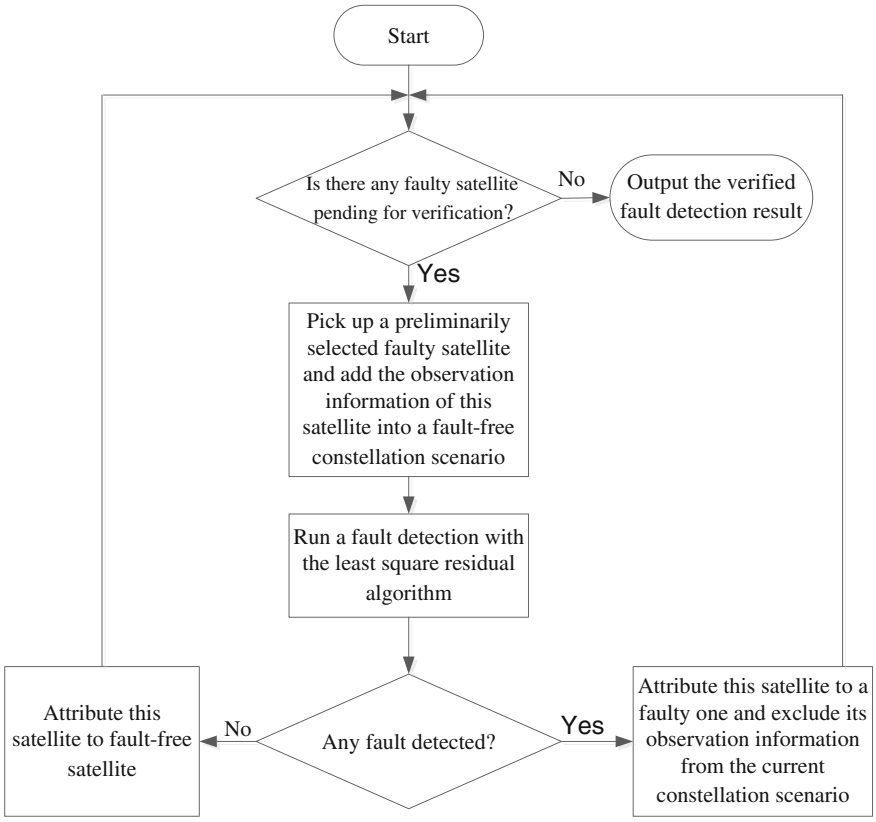

Fig. 7.3 Flow chart of validating the faulty satellites one by one

The specific smoothing process of multi-epoch fault detection is as follows:

(1) Evaluate whether there are two or more unusable fault detection results at the corresponding epoch in the fault detection results at the latest three epochs.
(2) If yes, then take that result as the final fault detection result at the current epoch; if not, then check if there are two or more fault detection results that a fault is present at the epoch in the navigation constellation scenario in the fault detection results at the latest three epochs but impossible to do fault recognition.
(3) If yes, then take that result as the final fault detection result at the current epoch; if not, then check if there are two or more completely identical in the fault detection results at the latest three epochs.
(4) If yes, then take that identical result as the final fault detection result at the current epoch; if not, then take the result that a fault is present at the epoch in the navigation constellation scenario but impossible to do fault recognition as the final fault detection result at the current epoch.

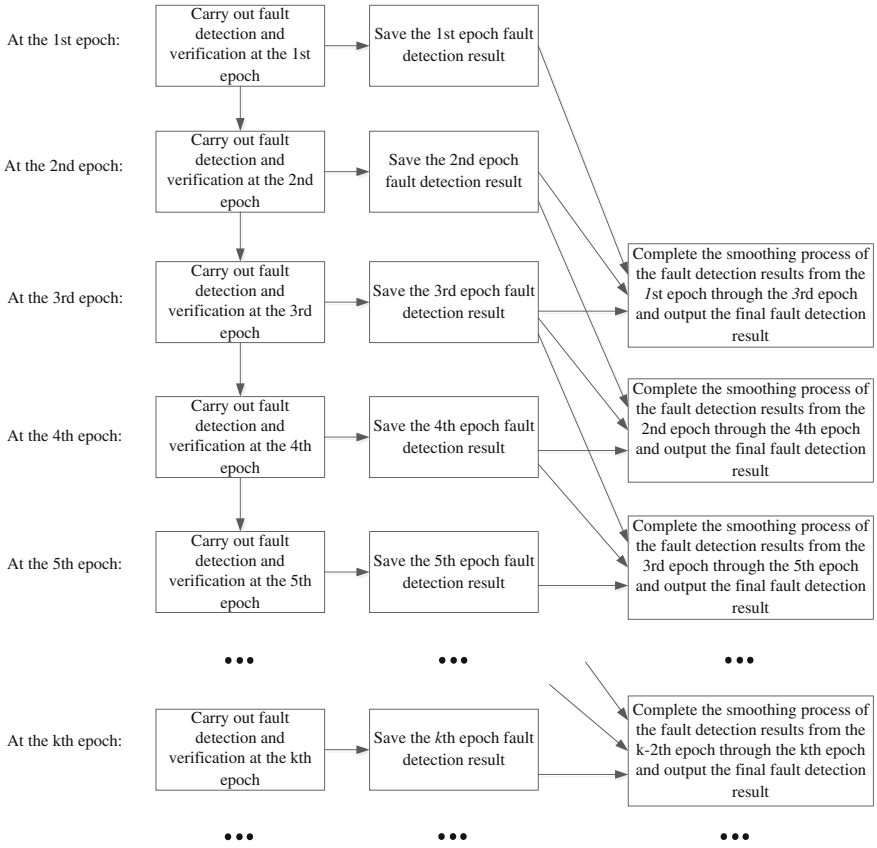

Fig. 7.4 Flow chart of multi epoch fault detection results smoothness

7.4 Simulation Validation of Algorithm Performance

The performance of the novel RAIM detection and recognition method for simultaneous multiple satellite faults was validated by means of simulation under the following conditions. In a 12-satellite scenario, the scenario GDOP is 1.6055, the false alarm probability of RAIM fault detection is 0.001, the positioning solution precision is set to 0.001 m, the simulation validation times is 1000 for probability statistics and set faulty satellites at random with reference to the preset satellite number in each sampling. Unless otherwise specified, then the pseudo-range noise of receiver is 0.25 m and the pseudo-range error of satellite is a random quantity ±10 m. If the fault detection result of every satellite is completely consistent with the preset result (faulty or fault-free), then the detection result will be regarded as correct; otherwise, incorrect. This evaluation mechanism considers both missing detection and false alarm.

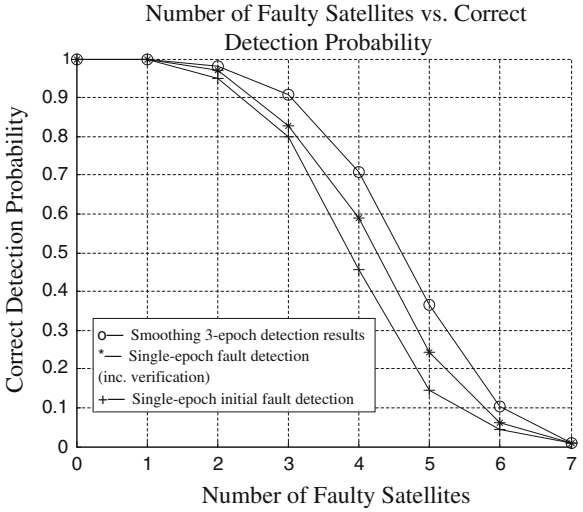

Fig. 7.5 Performance of different RAIM fault detection algorithm

Figure 7.5 shows the relation between the number of faulty satellites and the correct detection probability without false alarm using different RAIM fault detection and identification algorithms. Three situations are simulated for the fault detection and recognition performance, which are separately the single-epoch initial fault detection (only inc. Step (1)), single-epoch fault detection (inc. verification, i.e., both Steps (1) and (2)) and three-epoch fault detection result smoothing (inc. Steps (1), (2) and (3)). As shown in the figure, the single-epoch initial fault detection method already considerably improved the recognition probability of simultaneous multiple satellite faults. After adding faulty satellite verification in Step (2) and then multi-epoch detection result smoothing in Step (3), the recognition probability of simultaneous multiple satellite faults further advanced effectively. The performance using the novel method is noticeably upgraded especially in the scenario that three, four and five satellites go wrong respectively.

According to the specific detection probabilities exported from the simulation program, Steps (1), (2) and (3) of RAIM fault detection and recognition were taken. In the cases that there was no faulty satellite and one faulty satellite, the correct detection probability was both 100 %. In the case that there were two faulty satellites, the correct detection probability was greater than 98 %. In the case that there were three faulty satellites, the correct detection probability was 90 % around. In the case that there were four faulty satellites, the correct detection probability was 65 % through 70 % around.

Figure 7.6 shows the relation between the times of fault pseudo range relative to the standard deviation of pseudo-range noise and the correct detection probability without false alarm under the condition of different numbers of faulty satellites. As shown in the figure, the correct detection probability and the algorithm performance is both maximized when the fault pseudo range is 8 through 9 times or more than the pseudo-range noise.

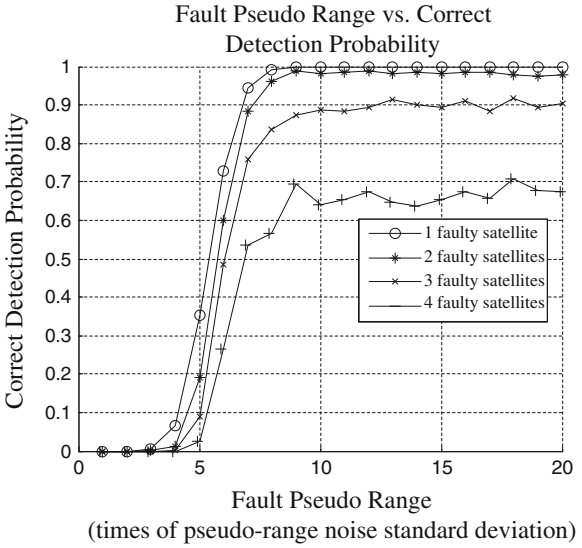

Fig. 7.6 Relationship between fault pseudo-range and detection probability without false alarm

Figure 7.7 shows the relation between the pseudo-range noise and the correct detection probability without false alarm when the fault pseudo range is 10 m around under the condition of different numbers of faulty satellites. As shown in the figure, the fault detection performance starts going down when the pseudo-range noise is above 1.2 m (1/8.3 of 10 m), which is consistent with the conclusion drawn from Fig. 7.6.

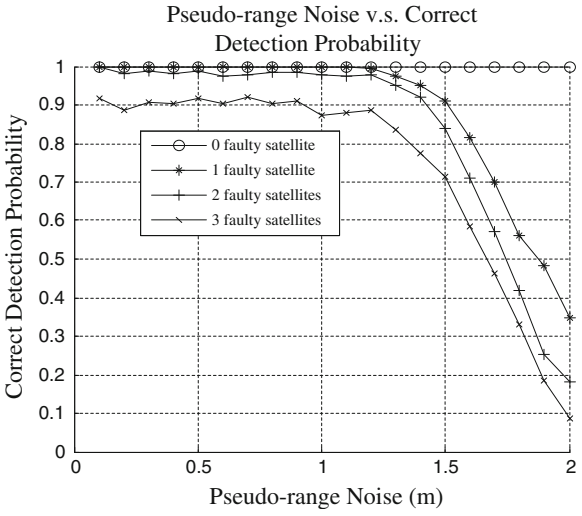

Fig. 7.7 Relationship between pseudo-range noise and detection probability without false alarm

7.5 Conclusion

Conclusively, the RAIM detection and recognition method for simultaneous multiple satellite faults proposed in this paper has the following advantages.

The detection probability is effectively upgraded by means of step-by-step detection using conventional fault recognition methods like the least square residual algorithm and the maximum likelihood algorithm in the event of multiple faulty satellites. The false alarm probability of the RAIM algorithm is considerably lowered by verifying the initially selected faulty satellites one by one, which consequently increases the number of satellites in fault-free constellation. The smoothing process to multi-epoch fault detection results further improves the fault detection probability and lowers the false alarm probability.

In comparison with the conventional satellite fault detection and recognition methods introduced in the previous sections, the RAIM fault detection and recognition method for simultaneous multiple satellite faults proposed in this paper requires very low computational workload. In the situation that m ($m > 0$) satellites are in trouble, it only needs 2 m times of least squares residuals fault detection and m times of fault identification, showing a very promising application value.

Acknowledgments Funding information: This paper was funded by the Research and Development of Simulation Test System for Multi-mode Navigation Service Quality Monitoring (2012AA1218 01) project, which was among the 863 Hi-tech Projects of the 12th China National Five-Year Plan.

References

1. Sun S (2011). RAIM algorithm for detection of multiple fault satellites based on maximum likelihood ratio. J Chin Inert Technol 19(3)
2. Chen C, Zhang X (2011) Novel method of multiple-satellite faults exclusion for global navigation satellite system. J Beijing Univ Aeronaut Astronaut 37(12)
3. Zhang Q, Zhang X, Chang X (2008) New method for satellite navigation identifying simultaneous multi-faulty satellites. Acta Aeronautica Et Astronautica Sinica 29(5)
4. Chen X, Teng Y (2008) Study of receiver autonomous integrity monitoring algorithm. J Univ Electron Sci Technol China 37(2)
5. Hwang PY, Brown RG (2005) RAIM FDE revisited: a new breakthrough in availability performance with NIORAIM. In: Proceedings of the ION NTM. SanDiego, CA, pp 654–665
6. Macabiau C, Gerfault B, Nikiforov I et al (2005) RAIM performance in presence of multiple range failures. In: Proceedings of the ION NTM. San Diego, CA, pp 779–791
7. Blanch J, Ene A, Walter T, Enge P (2007) An optimized multiple hypothesis RAIM algorithm for vertical guidance. In: Proceedings of ION GNSS. Fort Worth, TX, pp 2924–2933
8. Ene A (2006) Further development of Galileo-GPS RAIM for vertical guidance. In: Proceedings of ION GNSS. Fort Worth, TX, pp 2597–2607
9. Lee YC (2004) Performance of receiver autonomous integrity monitoring (RAIM) in the presence of simultaneous multiple satellite faults (60th annual meeting of the institute of navigation. Institute of Navigation, Dayton, pp 687–697
10. Hewitson S, Wang J (2006) GNSS receiver autonomous integrity monitoring (RAIM) performance analysis. GPS Solutions 10(3):155–170

Chapter 8
Ionospheric Threat Model Methodology for China Area

Dun Liu, Li Chen, Liang Chen and Weimin Zhen

Abstract The ionosphere is the largest remaining error source affecting GNSS regional augmentation system. The situation could be more serious when there is no enough measurement in a limited areas monitored by the network. The spatial threat model is constructed to restrict the ionospheric behavior under these under-sample scenarios for a more stringent bound. In this work two ionospheric spatial threat model, namely 'blob' and 'wall' models are constructed. In the 'blob' model, ionospheric delay increase with radius of 'blob' until the saturation is reached at a distance of 500 km. In the 'wall' model, ionospheric delay increase with the distance of ionospheric grids to 'wall'. Different ionospheric behavior during the storm for China area and North America area is responsible for the different model variation.

Keywords GNSS · Ionosphere · Integrity · Spatial threat model

8.1 Introduction

Ionospheric grid model is generally used for ionospheric delay correction and its error bounding in GNSS regional augmentation system. The essence of grid model is a planner fitting of ionospheric delays at fixed grid points with measured delays at ionospheric pierce points (IPPs). Spatial correlation model is used in the grid model to depict the spatial behavior of the ionospheric delays for effective error over-bounding [1, 2, 3].

Based on its utilization, three kinds of ionospheric spatial correlation model could be made, namely zero-order spatial correlation model, first-order spatial correlation and spatial threat model. The zero and first order model is used to depict the ionospheric error and its residual characteristics of the planner fitting in

D. Liu (✉) · L. Chen · L. Chen · W. Zhen
No.22nd Research Institute, CETC, 266107 Qingdao, China
e-mail: dun.l@163.com

J. Sun et al. (eds.), *China Satellite Navigation Conference (CSNC) 2015 Proceedings: Volume II*, Lecture Notes in Electrical Engineering 341,
DOI 10.1007/978-3-662-46635-3_8

ionospheric grid model, while the spatial threat model is used to describe the effects caused by under-sampled ionospheric measurements to grid model.

Steep ionospheric delay gradient exists in ionospheric storms, degrading the grid model performance. The situation is more serious when there are no enough IPP measurements [4–7]. A spatial threat model is used to increase the GIVEs (Grid Ionospheric Vertical Error) to over-bound the ionospheric residuals.

In this paper the ionospheric spatial threat model methodology is presented. Two kinds of models namely "blob" and 'wall' spatial threat model are studied for China area. Comparison of models in China and North America area is made also.

8.2 Data and Preprocessing in Model Construction

8.2.1 Data Used in Model Construction

Data used in the spatial thread model construction includes:

(1) GPS dual-frequency measurements
GPS dual-frequency data from stations (Fig. 8.1) in and around China areas are used to retrieve ionospheric delay.

(2) Solar terrestrial space environment data
The data such as Kp index are used for judgment of ionospheric disturbance.

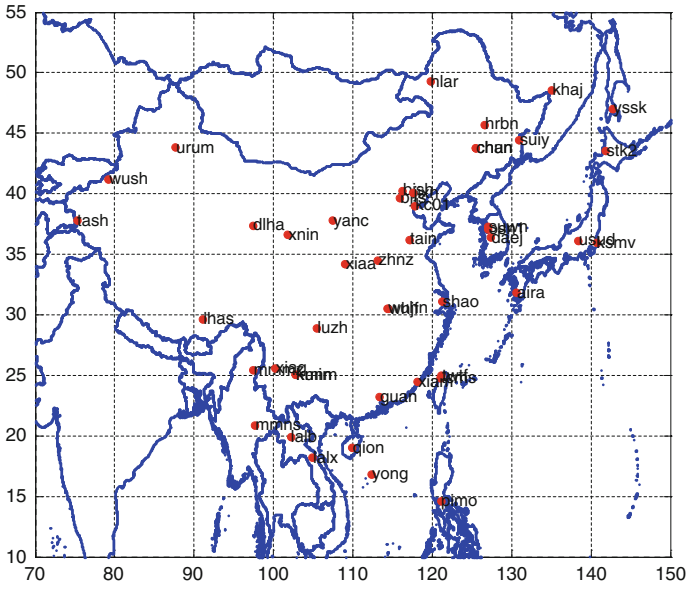

Fig. 8.1 GPS network in China and around area

8.2.2 Pre-process of GPS Data

The following procedure is used to retrieve ionospheric delay precisely.

(a) Ionospheric delay is calculated with the carrier phase smoothed pseudo-range measurements.
(b) DCB (Differential code bias) of GPS satellites from CODE (Center for Orbit Determination in Europe) is used.
(c) GPS receiver hardware bias is estimated with data before and after stormy days and averaged to improve the accuracy. Comparison with IGS published data shows an accuracy of better than 0.5 ns.

With these data ionospheric delays are retrieved in stormy days for modeling.

8.3 Ionospheric Spatial Threat Model Construction

Two kinds of spatial threat model are constructed, namely the 'blob' model and the 'wall' model.

8.3.1 'Blob' Spatial Threat Model

When unevenly distributed IPPs measurements are used to estimate ionospheric delays on grids, there may be the possibility that an un-sampled area exists leading to errors in the estimation. Figure 8.2 is a schematic drawing for "blob" model.

In the modeling of this scenario, a region of 'blob' can be formed by removing IPPs stepwise. Then the ionospheric delay at the grid point is estimated with the measurements at the remaining pierce points. The estimated delays are compared with the real ionospheric delay at the grid point. With this method, residual variation of the estimated ionospheric delays at the grid point with the extension of the 'blob' region can then be studied, consequently with 'blob' spatial threat model constructed.

Figures 8.3 and 8.4 shows the result of the 'blob' spatial threat model with GPS data of 2011/04/01 when a strong ionospheric storm occurred. Figure 8.3 is the histogram for ionospheric delay residual with 'blob' radius, while Fig. 8.4 is plot for statistical ionospheric delay residual with 'blob' radius. It can be seen that when the radius of the 'blob' is less than 250 km, ionospheric delay residual increase with the radius; when the radius is more than 500 km, little variation of the residual happens, i.e. saturation reached.

'Blob' spatial threat model shows that measurements within the distance of 250 km to the grid point have the most effects in the grid ionospheric delay estimation. As the distance increase, contribution to the ionospheric delay estimation at

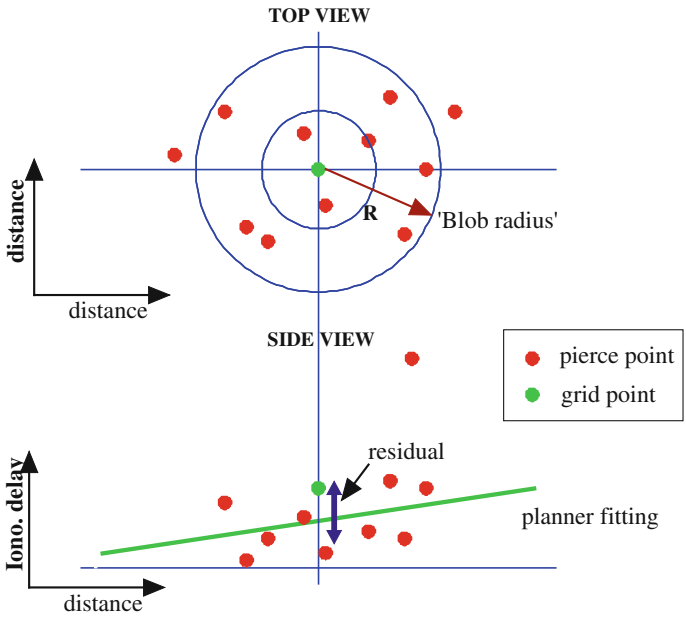

Fig. 8.2 Schematic drawing for 'blob' spatial threat model

the grid point decrease for measurements far from the grid. That is, as the distance increasing, only a rough ionospheric planar fitting can be made with the measurements far from the grid point, and variation of the ionospheric delay, especially the large gradient in the 'blob' cannot be detected.

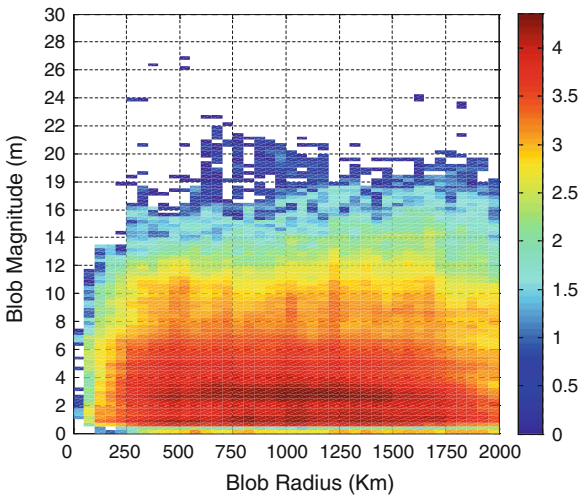

Fig. 8.3 Histogram for ionospheric delay variations with 'blob' radius

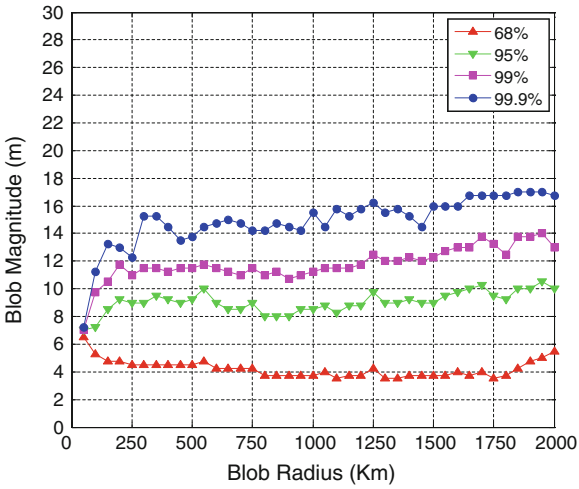

Fig. 8.4 Plot for ionospheric delay statistical variations with 'blob' radius

8.3.2 'Wall' Spatial Threat Model

In the 'wall' spatial threat model, ionospheric IPPs locate on the same side of the grid point, large residual of the ionospheric delay at the grid point will be caused with measurements at these IPPs. It describes an extreme scenario which occurs often near the border of the regional augmentation system. Schematic drawing for 'wall' spatial threat model is shown in Fig. 8.5.

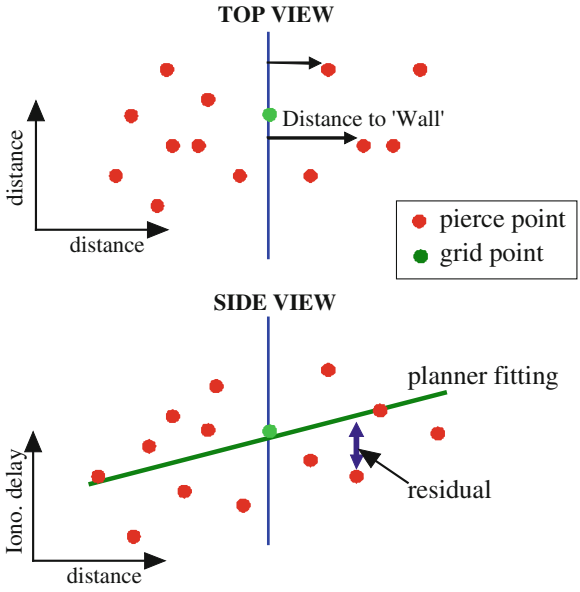

Fig. 8.5 Schematic drawing for 'wall' spatial threat model

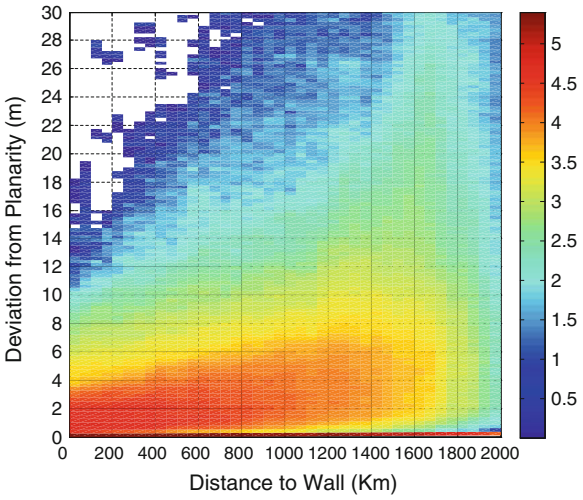

Fig. 8.6 Histogram for ionospheric delay variations with distance to the 'wall'

In the 'wall' spatial threat modeling, a region formed by removing pierce points on one side of the 'wall'. Then the ionospheric delay at the grid point can be estimated with the measurements at the remaining pierce points. The estimated delays are compared with the real ionospheric delay at the grid point. With this method, residual variation of the ionospheric delay at the grid point with the distance from the grid point to the 'wall' can be studied.

Figures 8.6 and 8.7 show the result of the 'wall' spatial threat model with GPS data of 2011/04/01. Figure 8.6 is histogram for ionospheric delay residual with distance to the 'wall', while Fig. 8.7 is plot for statistical ionospheric delay residual variations with distance to the 'wall'. It can be seen that residual of the ionospheric delay always increase with the distance from the grid points to 'wall'.

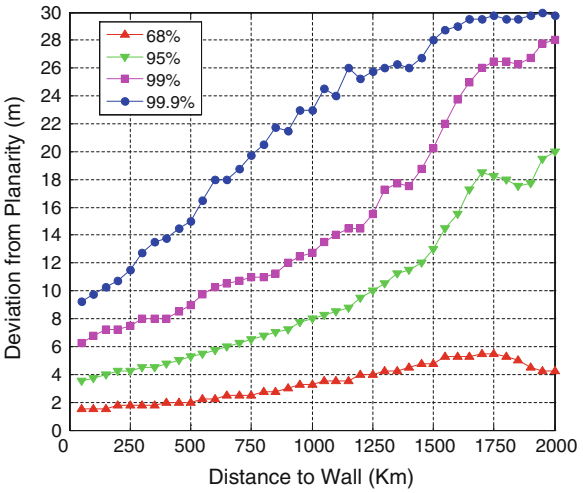

Fig. 8.7 Plot for ionospheric delay statistical variations with distance to the 'wall'

'Wall' spatial threat model shows that residual of the ionospheric delay increase with the distance from the 'wall' to the grid point. The measurements at the pierce points used for grid ionospheric delay estimation cannot describe the overall spatial variation of the ionosphere since they are all located at one side of the grid point. When the grid model is constructed with the measurements at one side of the 'wall' and extended to the area on the other side, large error arise as only information on one side of the 'wall' could be used.

8.4 Comparison of Ionospheric Threat Model in China and North America Areas

Spatial threat model in China area and that in North America are compared to show their characteristics [5–7].

Significant difference exists in two 'blob' spatial threat models. In China area residual of the ionospheric delay increase with the radius less than 250 km, and saturation is reached when the radius of the 'blob' is more than 500 km. While in North America, residual of the ionospheric delay increases always with increase of the radius [7].

No much difference exists in two 'wall' spatial threat model. For the model in North America areas given by Raytheon Corp, residual of the ionospheric delay varies mild when the distance is small, but increase abruptly when the distance is large [7]. For China areas, residual varies mild when the distance is less than 500 km, but increase fast when the distance is more than 500 km (see the 1σ ionospheric delay residual variation). This trend is more evident for the 2σ ionospheric delay residual.

Difference in the spatial threat model in China and North America is analyzed with GIM TEC map. Figures 8.8 and 8.9 shows the typical variation of ionospheric delay respectively in these two regions during the ionospheric storm occurred at 2003/10/29.

During the storm, gradient of ionospheric delay extended from south-east to north-west in North America. That is, big gradient occurs in a narrow and small region while in other part the ionospheric delay varies mild. Similar characteristics also be found in other storm events in years of 2000–2003. This characteristic of gradient variation in the ionospheric delays makes the error in the planar fitting with IPPs ionospheric delays increase as the 'blob' radius increase or the number of IPPs use for grid delay estimation decrease.

For China region steep gradient existed from south to north while small variation existed from east to west in the ionospheric delays during storm. The gradient lies between the belt with the maximum ionospheric delays where Guangzhou, Hainan and Kunming locate and the belt of mild ionospheric delays where Shanghai, Wuhan and Chongqing locate.

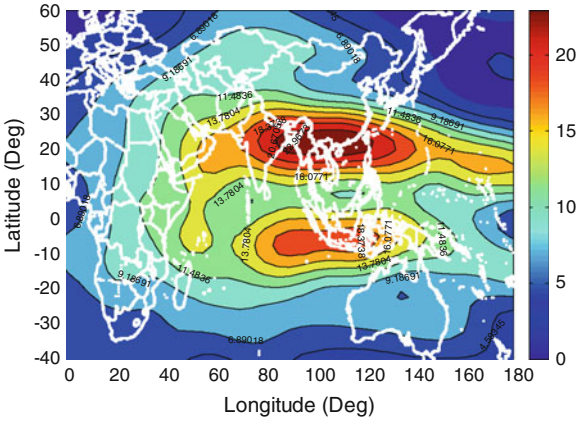

Fig. 8.8 Ionospheric delay distribution during the storm of 29th October 2003 for China area

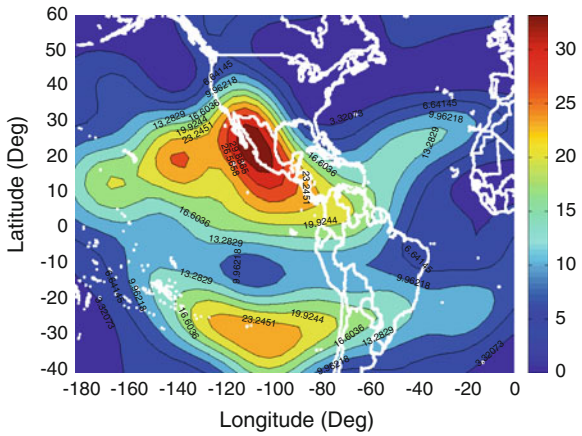

Fig. 8.9 Ionospheric delay distribution during the storm of 29th October 2003 for North America area

The gradient of ionospheric delay in the south-north direction has great effect to the 'blob' model while that along the east-west direction contribute little. When the 'blob' radius is less than the distance of the steep gradient variation from south to north (about 500 km), the ionospheric delay error increases fast with the increasing of the radius of the 'blob'. When the radius is larger than that distance, the ionospheric delay errors reach the maximum, i.e. the saturation state reached.

China region covers the low and mid latitude areas, in which complicated ionospheric delays variation happen during storms. The situation is even more complicated with the effects of ionospheric anomaly superposed. The North America locates in mid latitude region, large ionospheric delays gradients are caused mainly by storms extended from the low latitude areas. Different characteristics the ionospheric storms in these two regions are responsible for the difference of the spatial threat models.

8.5 Conclusion

Under-sampled observations in GNSS regional augmentation system will cause large error in the ionospheric grid model and failure of integrity. The condition becomes much more serious when ionospheric storms happen. The ionospheric spatial threat model is constructed to set up a more stringent bound of the ionospheric delay residuals.

Two type of spatial threat models namely the 'blob' model and the 'wall' model are studied and constructed with GNSS data during the ionospheric storm in China region. 'Blob' model shows an increasing ionospheric delay residual with the 'blob' radius until saturation state reached at the distance about 500 km. In the 'wall' model the ionospheric delay residual increases with the distance to the wall monotonously.

The spatial threat model for China areas and North America areas shows difference which is caused by the different characteristics of ionospheric delays during ionospheric storms in these two regions.

Acknowledgments This work is sponsored by the International Technological Cooperation Projects (No.2011DFA22270).

References

1. Hansen A, Peterson E, Walter T, Enge P (2000) Correlation structure of ionospheric estimation and correction for WAAS. In: ION NTM 2000, pp 454–463
2. Hansen A, Walter T, Blanch J, Enge P (2000) Ionospheric spatial and temporal correlation analysis for WAAS: quiet and stormy. In: ION GPS 2000, pp 634–642
3. Liu D, Zhen W, Chen L (2013) Ionospheric spatial correlation analysis for China area, In: CSNC, Guangzhou
4. Walter T, Hansen A, Blanch J, Enge P et al (2000) Robust detection of ionospheric irregularities. In: ION GPS 2000, pp 209–218
5. Blanch J, Walter T, Enge P (2002) Ionospheric threat model methodology for waas. Navigation 49(2):103–107
6. Blanch Juan, Walter Todd (2001) Per Enge. Ionospheric threat model methodology for WAAS, ION AM
7. Altshuler ES, Robert M (2001) Fries and Lawrence sparks, The WAAS ionospheric spatial threat model. In: ION GPS 2001, pp 2463–2467
8. Liu D, Zhen W (2012) The effects of china regional ionosphere on satellite augmentation system. Chin J Radio Sci 27(1):195–203

Chapter 9
Real-Time Cycle Slip Detection and Repair Algorithm for SBAS Airborne Receiver

Jie Chen, Zhigang Huang and Rui Li

Abstract SBAS improves performance of GNSS by providing timely corrections and integrity monitoring to meet the requirement for civil aviation. Single frequency SBAS augments GPS L1 signal, such as WAAS and EGNOS, providing APV-I service. Receiver uses GIVD to correct ionosphere delay, in which way the impact of ionosphere storm cannot be eliminated. Thus, SBAS performance is limited. Dual frequency SBAS receiver directly mitigates ionosphere delay. However, receiver will suffer considerably larger noise, proposing a higher demand for carrier smoothing techniques. Cycle slip is frequent in airborne receiver's carrier measurement, which makes smoothed measurement pulsing, thereby reducing the positioning accuracy. This paper presents a real-time cycle slip detection and repair method, including chi-square detection algorithm and sequence-sum repair algorithm based on the statistical property of fourth order differential of carrier measurement, and its repair error variance. According to the measured data analysis, the algorithm shows good performance in cycle slip detection and repair and is sufficient for carrier smoothing techniques for SBAS airborne receiver.

Keywords SBAS · Carrier smoothing · Cycle slip detection and repair · Fourth order differential

9.1 Introduction

Satellite-based augmentation system (SBAS) broadcasts augmentation information frequently to support precision approach operations using global navigation satellite system (GNSS).

WAAS and EGNOS have been put into use, augmenting GPS L1 C/A only, providing APV-I service within their service areas respectively. The main reason

J. Chen (✉) · Z. Huang · R. Li
Beihang University, Beijing, China
e-mail: chenjieee@buaa.edu.cn

J. Sun et al. (eds.), *China Satellite Navigation Conference (CSNC) 2015 Proceedings: Volume II*, Lecture Notes in Electrical Engineering 341,
DOI 10.1007/978-3-662-46635-3_9

why single frequency SBAS cannot provide a higher level of service is that the airborne receiver uses grid ionosphere vertical delay to correct ionosphere delay, in which case the impact of ionosphere storm cannot be eliminated. In the future, dual-frequency multiple-constellation (DFMC) SBAS will provide augmentation information for core GNSS constellations, including GPS, GLONASS, Galileo and BeiDou. The use of two signals at two distinct frequencies enables the airborne receiver to mitigate ionosphere delay directly. However, the airborne receiver will suffer considerably larger pseudorange noise [3].

Carrier smoothing technique is an efficient way to reduce pseudorange noise [1]. Single-frequency SBAS receiver minimum operational performance standards (RTCA DO-229) requires that a receiver must perform carrier smoothing to improve ranging accuracy, and the carrier smoothing equation is clearly given, namely single-frequency carrier smoothing (SFS) filter. Although DFMC SBAS specification is still under developing, it is reasonable to assume that iono-free smoothing (IFree) shall be performed to obtain iono-free pseudorange [2].

Cycle slip in the carrier measurement is common for airborne receivers, which leads to smoothed pseudorange pulsing, thereby positioning accuracy and integrity may be affected. Thus, airborne receivers should have the ability to perform cycle slip detection and repair before carrier smoothing.

There are four typical methods for cycle slip detection and repair, namely polynomial fitting method and high-order differential method for single-frequency receivers, ionosphere residual method and combination method of pseudorange and carrier phase for dual-frequency receivers. These methods have a common problem that the detection threshold is dependent on engineering experience, and is not applicable for different cases. Another common problem is that these methods cannot provide integrity parameters of corrections. In addition, the high-order differential method can't be used in real-time cycle slip detection, and dual-frequency methods have high computing cost to determine cycle slips on each frequency. Thus, these methods are incapable of cycle slip detection and repair for SBAS airborne receiver. Cycle slip detection and repair using triple-frequency measurements has also been researched [4]. But the plan for utilization of a third frequency hasn't been proposed by aviation community yet.

Based on the statistics characteristic of fourth order differential of carrier measurement, a real-time cycle slip detection and repair method is proposed, including chi-square detection algorithm and sequence-sum repair algorithm. This method also gives the variance of cycle slip estimated error for integrity calculation.

9.2 Requirements Analysis

Assuming that sampling interval is one second, the smoothed pseudorange of SFS filter can be written as:

$$\hat{\rho}(t) = \frac{1}{\tau}\rho(t) + \frac{\tau - 1}{\tau}[\hat{\rho}(t-1) + \lambda\varphi(t) - \lambda\varphi(t-1)] \tag{9.1}$$

where, $\hat{\rho}$ is the smoothed pseudorange in meters; ρ is the raw pseudorange in meters; φ is the carrier measurement in cycles; λ is the carrier wavelength in meters; τ is the time constant of 100 s.

The smoothing error with cycle slip occurring at time t can be expressed as:

$$\begin{aligned} \Delta\hat{\rho}(\mathrm{t}) &= \frac{\tau - 1}{\tau}\lambda\Phi \\ \Delta\hat{\rho}(\mathrm{t}+\mathrm{k}) &= -\frac{(\tau-1)^{k-1}}{\tau^k}\lambda\Phi, k \geq 1 \end{aligned} \tag{9.2}$$

where, $\Delta\hat{\rho}$ is the smoothing error in meters; Φ is the cycle slip in cycles.

The smoothed pseudorange on L1 of IFree filter can be written as:

$$\begin{aligned} \hat{\rho}_{L1}(t+1) = \frac{1}{\tau}\left[\rho_{L1}(t+1) - \frac{1}{\alpha}(\rho_{L1}(t+1) - \rho_{L5}(t+1))\right] + \frac{\tau-1}{\tau}\left[\hat{\rho}_{L1}(t)\right. \\ \left. + \lambda_{\varphi 1}\left(1 - \frac{1}{\alpha}\right) \times (\varphi_{L1}(t+1) - \varphi_{L1}(t)) - \frac{\lambda_{\varphi 5}}{\alpha}(\varphi_{L5}(t+1) - \varphi_{L5}(t))\right] \end{aligned} \tag{9.3}$$

The smoothing error with cycle slip occurring at time t can be expressed as:

$$\begin{aligned} \Delta\hat{\rho}_{L1}(\mathrm{t}) &= \frac{\tau-1}{\tau}\left[\left(1 - \frac{1}{\alpha}\right)\lambda_{\varphi 1}\Phi_{L1} - \frac{1}{\alpha}\lambda_{\varphi 5}\Phi_{L5}\right] \\ \Delta\hat{\rho}_{L1}(\mathrm{t}+\mathrm{k}) &= -\frac{(\tau-1)^{k-1}}{\tau^k}\left[\left(1 - \frac{1}{\alpha}\right)\lambda_{\varphi 1}\Phi_{L1} - \frac{1}{\alpha}\lambda_{\varphi 5}\Phi_{L5}\right], k \geq 1 \end{aligned} \tag{9.4}$$

According to Eqs. (9.2) and (9.4), small cycle slip affects the smoothed pseudorange the time it occurs, and has an ignorable effect on the later smoothed pseudoranges.

Assuming that code-tracking noise is a hundredth of code length, and smoothing error threshold is one-tenth of code-tracking noise. Thus, the cycle slip thresholds for SFS filter and IFree filter are 1.56 cycles and 0.688 cycles respectively.

It is necessary to provide not only corrections but also corresponding integrity parameters for SBAS airborne receiver. The alert time for precision approach operations is no more than 10 s, and civil aircraft is in a high-speed motion, so that cycle slip detection and repair shall be real-time.

9.3 Cycle Slip Detection and Repair Algorithm

In this section, the algorithm is described in detail, and the flowchart is given.

9.3.1 Fourth Order Differential

Carrier phase measurement can be expressed as:

$$\lambda\varphi = r + c\left(-t_{iono} + t_{trop} + t_u - t_s\right) + N + \eta \tag{9.5}$$

where, r is the geometrical distance in meters; c is the speed of light in meters per second; t_{iono} is the ionosphere delay in seconds; t_{trop} is the troposphere delay in seconds; t_u is the receiver clock error in seconds; t_s is the satellite clock error in seconds; N is the carrier ambiguity; η is the carrier-tracking noise.

The fourth order differential of carrier measurement at time k is:

$$\Delta^4\varphi_k = \varphi_k - 4\varphi_{k-1} + 6\varphi_{k-2} - 4\varphi_{k-3} + \varphi_{k-4} \tag{9.6}$$

Assuming that the noises of carrier measurements are independent and normally distributed with the same variance, $\Delta^4\varphi_k$ is normally distributed and the variance of $\Delta^4\varphi_k$ is:

$$\sigma^2_{\Delta^4\varphi} = \frac{70}{\lambda^2}\sigma^2_{\varphi} \tag{9.7}$$

9.3.2 Chi-Square Detection Algorithm

As $\Delta^4\varphi_k$ is normally distributed, chi-square test can be used to detect cycle slip.

The slide-window sequence is constructed as follows:

$$z = [\,z_1 \quad z_2 \quad \ldots \quad z_n\,]^T = \left[\,\Delta^4\varphi_1 \quad \Delta^4\varphi_2 \quad \ldots \quad \Delta^4\varphi_n\,\right]^T \tag{9.8}$$

To detect the cycle slip, the following hypothesis is proposed:

$$\begin{aligned} H_0 &: \sigma_z^2 = \sigma_0^2 \\ H_1 &: \sigma_z^2 \neq \sigma_0^2 \end{aligned} \tag{9.9}$$

where, σ_z^2 is the variance of the sequence z.

The chi-square statistic is given by:

$$T = z^T z / \sigma_z^2 \tag{9.10}$$

The calculated value T is compared with the threshold value Td of the chi-square distribution, which depends on the allowed error probability P_{FA} and sequence length n as described below:

$$\int_0^{Td} f_n(x)dx = P_{FA} \tag{9.11}$$

where, $f_n(x)$ is the probability density function with n degrees of freedom.

If T is larger than Td, the hypothesis is rejected and cycle slip is detected, otherwise it is accepted and there is no cycle slip.

9.3.3 Sequence-Sum Repair Algorithm

Fast Fourier transform is defined by the formula:

$$Z(k) = \sum_{j=1}^{n} z_j w_n^{(j-1)(k-1)}, \; w_n = e^{(-2\pi i)/n} \tag{9.12}$$

The fourth order differential with cycle slip can be expressed as:

$$z_n = z_{0,n} + \Phi \tag{9.13}$$

where, z_0 is the fourth order differential without cycle slip.

Consequently, Z(1) can be expressed as:

$$Z(1) = \sum_{j=1}^{n} z_j = \sum_{j=1}^{n} z_{0,j} + \Phi \tag{9.14}$$

The expectation of cycle slip can be expressed as:

$$E[\Phi] = E\left[\sum_{j=1}^{n} z_j\right] - E\left[\sum_{j=1}^{n} z_{0,j}\right] \tag{9.15}$$

where, $E[\cdot]$ is mathematical expectation.

Considering that z_0 is normally distributed with zero mean and that Φ is an integer, the estimated value of cycle slip is:

$$\hat{\Phi} = Round\left[\sum_{j=1}^{n} z_j\right] = Round\left[\sum_{j=1}^{n} \Delta^4 \varphi_j\right] \tag{9.16}$$

where, $Round[\cdot]$ rounds the number to the nearest integer.

The estimated error can be expressed as:

$$\Delta\Phi = \Phi - \hat{\Phi} \tag{9.17}$$

In order to evaluate the repair accuracy, some latest samples are selected to calculate the variance of cycle slip estimated error defined as follows:

$$\sigma^2_{\Delta\Phi} = \frac{1}{N-1}\sum_{i=1}^{N}\left(\Delta^4\varphi_i - \Delta^4\bar{\varphi}\right)^2 \tag{9.18}$$

where, N and $\Delta^4\bar{\varphi}$ are the number and the mean value of the samples respectively. N is a variable integer, which increases with time and is set to zero when cycle slip is detected. Considering the correlation of samples, the maximum number of N is set to sixty.

When this method is applied, the variance of smoothed pseudorange is:

$$\sigma^2_{\hat{\rho}} = \sigma^2_0 + \lambda\sigma^2_{\Delta\Phi} \tag{9.19}$$

where, σ^2_0 is the variance of smoothing filter output pseudorange.

9.3.4 Algorithm Flow

The flowchart in Fig. 9.1 describes the algorithm flow. The maximum number of sequence is 6, and the allowed error probability is 10^{-3}.

1. Empty sequence z. Start cycle slip detection and repair after four continuous samples.
2. If there is a new measurement, go to step 3, otherwise terminate the procedure of cycle slip detection and repair.
3. Calculate fourth order differential $\Delta^4\varphi_k$.
4. Calculate cycle slip estimated error $\sigma^2_{\Delta\Phi}$.
5. Insert $\Delta^4\varphi_k$ into sequence. If the sequence length is smaller than six, $z_k = \left[z_{k-1,1}, z_{k-1,2}, \ldots, z_{k-1,n}, \Delta^4\varphi_k\right]$, otherwise $z_k = \left[z_{k-1,2}, z_{k-1,3}, \ldots, z_{k-1,n}, \Delta^4\varphi_k\right]$.
6. Detect cycle slip using chi-square detection algorithm. If cycle slip is detected, go to step 7, otherwise go to step 2.

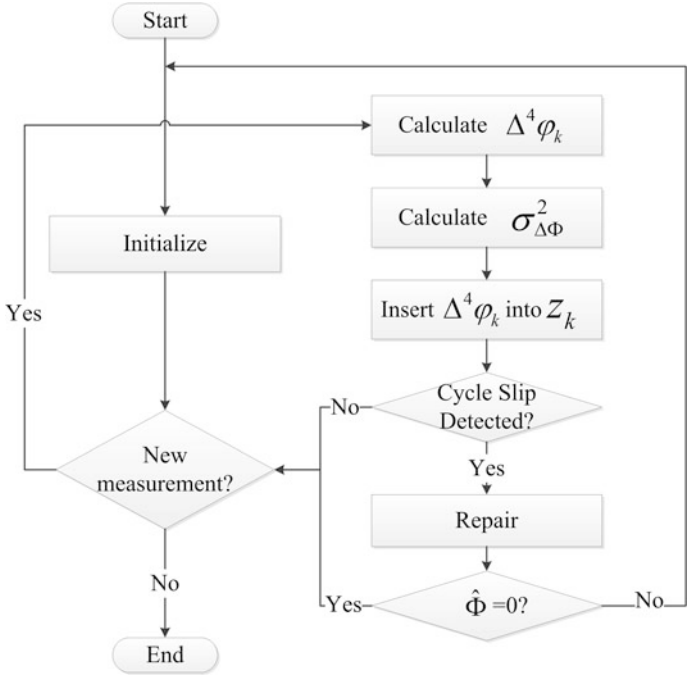

Fig. 9.1 Flowchart of real-time cycle slip detection and repair algorithm for SBAS airborne receiver

7. Estimate cycle slip using sequence-sum repair algorithm. If estimated value of cycle slip is zero, go to step 2, otherwise go to step 1.

9.4 Performance and Analysis

In this section, carrier phase is measured by receiver UR370, whose nominal clock stability is 5×10^{-7}.

9.4.1 Statistical Property

The carrier measurements were statically collected at July 27, 2014. The sampling interval is one second. There are 357,076 fourth order differential samples. It's reasonable to assume that fourth order differential without cycle slip is smaller than 10. After excluding those larger than 10, there are 357,072 samples left, of which the mean value is 4.176×10^{-5} cycles and the standard deviation is 0.7657 cycles.

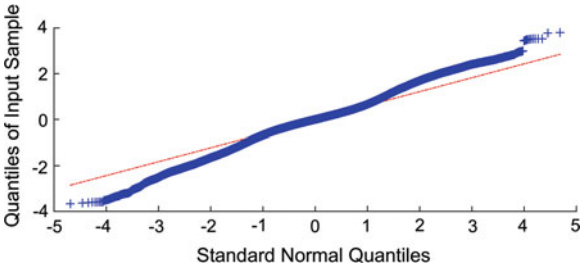

Fig. 9.2 Q-Q plot of 357,072 samples. The *blue cross* represents the sample quantiles and the *red dashed line* represents the theoretical quantiles from a normal distribution

The Q-Q plot of 357,072 samples is showed in Fig. 9.2, indicating that fourth order differential can be treated as normally distributed.

9.4.2 Detection Performance

In this section, the performance of chi-square detection algorithm has been analyzed and evaluated using 20054 carrier phase samples of GPS PRN 1.

The detection result of raw data is showed in Fig. 9.3. The detection function has been performed 20,046 times, and cycle slip has been detected in the 17115th sample. Assuming that there is no cycle slip in raw data, the probability of false detection is about 0.00499 %.

Then, cycle slips are manually added to the raw data every 60 s. Cycle slip value is generated as follows:

$$\Phi_k = Round[randn_k \times 50] \tag{9.20}$$

where $randn_k$ is a standard normally distributed random variable.

The detection result of data with cycle slips is showed in Fig. 9.4. The detection function has been performed 18,878 times, and cycle slip has been detected 22

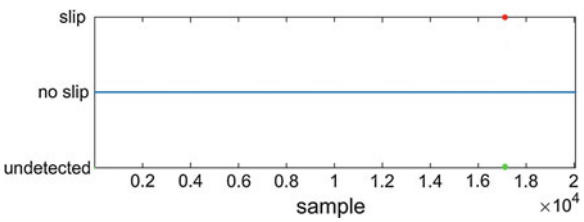

Fig. 9.3 Detection result of GPS PRN 1 raw data. The *red dot* represents the sample with cycle slip detected, the *blue dot* represents the sample with no cycle slip detected, and the *green dot* represents the sample undetected during initialization

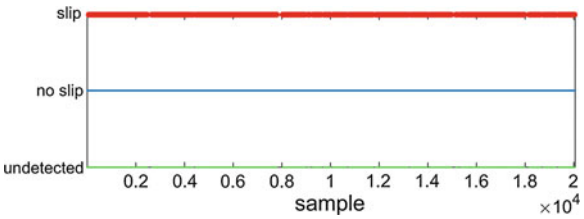

Fig. 9.4 Same as Fig. 9.3 but the detection result of GPS PRN 1 data with manually added cycle slips

times. No cycle slip is added but cycle slip is detected in the 9497th, 11281st, 11551st, 17115th and 17531st samples, thus the probability of false detection is about 0.0265 %. Cycle slip is added but no cycle slip is detected in the 2526th, 2595th, 4407th, 7849th, 7913rd, 7975th, 9012nd, 9207th, 9670th, 10053rd, 11804th, 13240th, 14020th, 15090th, 15289th, 18692nd and 19329th samples, thus the probability of missing detection is about 0.0901 %. These 17 cycle slips are all smaller than 5 cycles.

9.4.3 Repair Performance

The same data has been used to analyze and evaluate the performance of sequence-sum algorithm.

The repair result of raw data is showed in Fig. 9.5. Cycle slip is detected in the 17115th sample, and the estimated value of cycle slip is −2 cycles.

The repair result of data with cycle slips is showed in Fig. 9.6. There are 132 samples with non-zero estimated error. Three of them are false detected, seventeen of them are missing detected, and the rest of them are caused by the repair algorithm. These 112 estimated errors are all smaller than 3 cycles.

The repair performance is limited by the standard deviation of fourth order differential. In this case, the standard variance is about 1 cycle, it's reasonable that cycle slip within 3 cycles is difficult to repair.

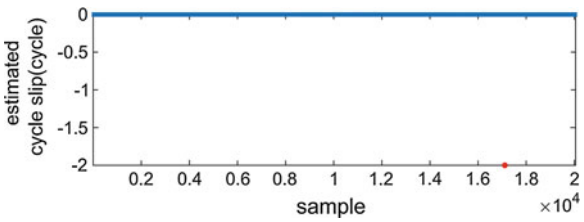

Fig. 9.5 Repair result of GPS PRN 1 raw data. The *blue dot* represents the sample with zero cycle slip, and the *red dot* represents the sample with non-zero cycle slip

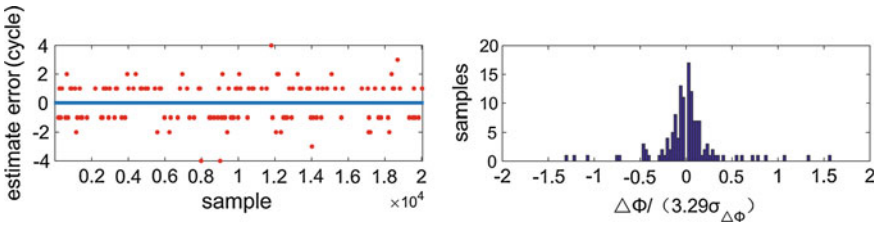

Fig. 9.6 *Left* Same as Fig. 9.5 but the repair result of GPS PRN 1 data with manually added cycle slips. *Right* The bounding distribution of estimated error

The sum of absolute values of these 132 estimated errors is 165 cycles. Considering that cycle slips are added every 60 s, the mean value of estimated errors is about 0.494 cycles per second, which is smaller than the cycle slip threshold of IFree filter.

The estimated error $\Delta\Phi$ and the corresponding variance of cycle slip estimated error $\sigma^2_{\Delta\Phi}$ are used to evaluate the repair accuracy. The result plotted in Fig. 9.6 shows that there are 6 times in which cases $\Delta\Phi$ is larger than 3.29 $\sigma_{\Delta\Phi}$. Thus, the bounding probability is about 99.97 %.

9.4.4 Dynamic Test

Carrier measurements were collected in a car moving at speed between 80 and 100 km/h on the Beijing-Xinjiang Expressway.

The dynamic performance has been analyzed and evaluated using 1257 carrier phase samples of BeiDou PRN 9. According to the repair result in Fig. 9.7, cycle slip is detected in the 1054th sample of raw data, and the estimated value of cycle slip is −23 cycles. According to the repair result in Fig. 9.8, there are 19 samples with non-zero estimated error. Two of them are false detected, three of them are missing detected, and the rest of them are all smaller than 7 cycles. The mean value of estimated errors is 3.34 cycles per second. There is no $\Delta\Phi$ larger than 3.29 $\sigma_{\Delta\Phi}$.

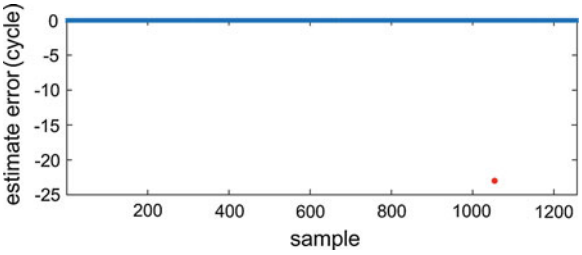

Fig. 9.7 Same as Fig. 9.5 but the repair result of BeiDou PRN 9 raw data

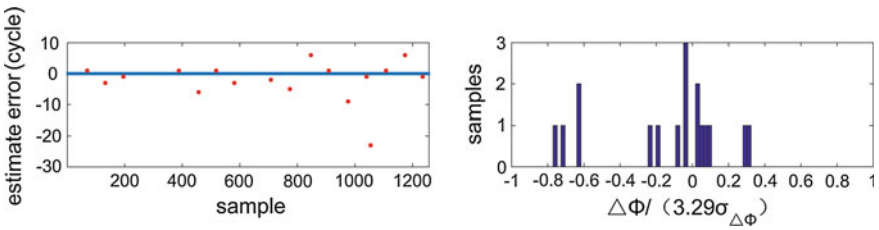

Fig. 9.8 Same as Fig. 9.6 but the repair result of BeiDou PRN 9 data with manually added cycle slips

There are two reasons why the mean value of estimated errors is larger than the cycle slip threshold of SFS filter. According to the fact that the standard deviation of the fourth order differential of BeiDou satellite carrier is about twice that of GPS satellite carrier, the first reason is the clock stability of BeiDou satellite is worse than that of GPS satellite. The second reason is that the clock stability of UR370 is not good enough for aviation.

9.5 Conclusion

This paper analyzes the requirement of cycle slip detection and repair for SBAS airborne receiver and describes a real-time cycle slip detection and repair method in detail, which combines chi-square detection algorithm and sequence-sum repair algorithm based on the statistical property of carrier fourth order differential. The cycle slip estimated error formula is given for integrity calculation.

Data collected by receiver UR370 has been used to evaluate the performance of the method. The result shows that cycle slip can be correctly detected and repaired, and that the cycle slip estimated error can bound the estimated error with the probability more than 99.9 %. The proposed method can be used in both the current SF SBAS and the coming DFMC SBAS.

Cycle slip repair accuracy is closely related to the statistical property of fourth order differential, which is affected by the stability of satellite clock and receiver clock, the state of motion and the environment. In order to improve the repair accuracy, SBAS airborne receiver should have a highly stabile inner clock, and selects navigation satellites with highly stabile clock onboard.

Acknowledgments The work is supported by National 973 Project China (Grant No. 2010CB731805).

References

1. Hwang PY, McGraw GA, Bader JR (1999) Enhanced differential GPS carrier-smoothed code processing using dual-frequency measurements. Navigation 46(2):127–137
2. Konno H, Pullen S, Rife J, Enge P (2006) Evaluation of two types of dual-frequency differential GPS techniques under anomalous ionosphere conditions. In: Proceedings of the ION national technical meeting, pp 18–20
3. Walter T, Blanch J, Enge P (2010) Vertical protection level equations for dual frequency SBAS. In: Proceedings of the 23rd international technical meeting of the satellite division of the institute of navigation, Portland, OR, pp 2031–2041
4. Zhao L, Li L, Liu Y, Li N (2014) Cycle slip detection and repair with triple frequency combination method. In: Position, location and navigation symposium-plans 2014, 2014 IEEE/ION, pp 846–854 (IEEE)

Chapter 10
Study on Space-Based All Source Navigation Technology

Ying Wang, Yansong Meng, Zhe Su and Xiaoxia Tao

Abstract All source navigation technology is the method using any available information for navigation and positioning. While the full source of space-based navigation used satellite navigation signal to obtain the position and time reference to generate the navigation signal, and then broadcast through the microwave downlink. It is a new scheme and the cost is relative low. In the paper, the payload carrying platform, signal receiving, building and maintain of clock, RF signal generation and broadcast and other aspects are analysed and discussed on this full source of space-based navigation.

Keywords All source navigation · Backup · Enhance

10.1 Introduction

A complete global navigation satellite system needs to maintain the normal operation of more than 24 satellites, so the life limit of satellite makes the need to continuously add and update satellites, which makes the cost of system construction and operation very high. The reason that navigation satellites can be used for navigation is that the navigation load on these satellites provides high precision of spatial and temporal information, and the information can be transmitted to the ground through the navigation signal. Therefore, under the existing technical conditions, it is important to evaluate the feasibility and develop the method using general satellites for backup navigation. This system can be called as all source of space-based navigation system (SB-ASNS). The satellite as a carrier of all source space-based navigation system, must has the payload to establish and maintain space-time datum. By configuring the GNSS receiver, the payload acquires high accuracy retrieval of spatial and temporal information. After establishment of high precision space-time datum, the standard-

Y. Wang (✉) · Y. Meng · Z. Su · X. Tao
China Academy of Space Technology (Xi'an), Xi'an 710100, China
e-mail: eaglesoars@126.com

J. Sun et al. (eds.), *China Satellite Navigation Conference (CSNC) 2015 Proceedings: Volume II*, Lecture Notes in Electrical Engineering 341,
DOI 10.1007/978-3-662-46635-3_10

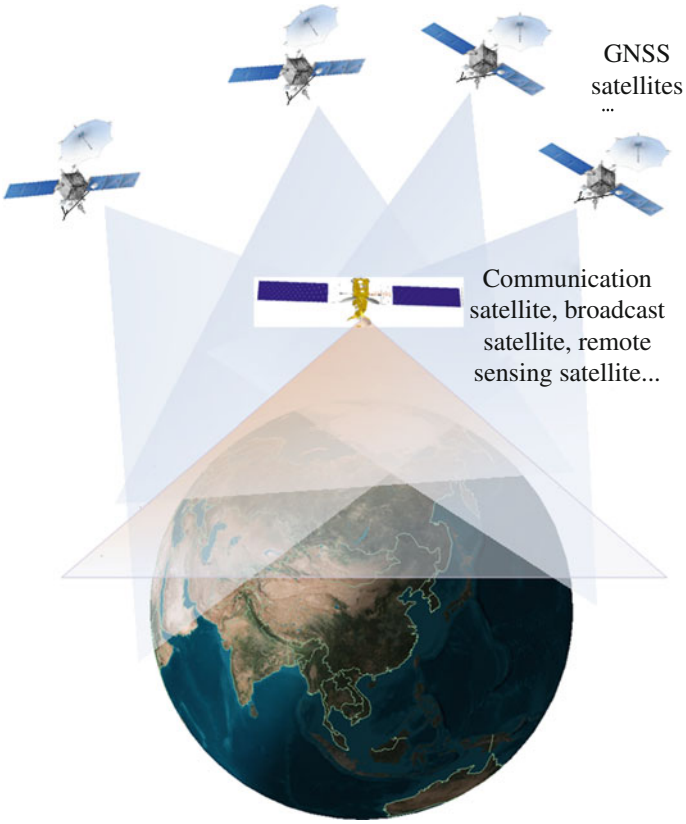

Fig. 10.1 Navigation diagram

ized navigation signal is generated broadcasted using the RF channel in company with the communication signal, the digital signal or radar signal. Then the realization of space-based PNT system backup and enhanced ability can improve the survival ability of combats, as shown in Fig. 10.1.

The research on the all source of space-based navigation system was carried out earlier in the world. Rabinowitz et al. analyzed receiver autonomous integrity monitoring (RAIM, Receiver Autonomous Integrity Monitoring) algorithm under the condition of the Globalstar system enhanced GPS [1]. The error model of GPS under the Iridium enhancement and related performance analysis were proposed in [2]. The RAIM algorithm based on least squares under enhanced GPS system is researched and the pseudo range observation equations, simulation and analysis were carried out in [3]. Using Iridium satellites or Globalstar to enhance GPS for realization of space-based PNT system backup and enhanced ability is a space-based navigation realization way of full source navigation.

This paper discussed the architecture of space-based full source navigation system, described the task and the characteristics of each part. After that, the payload was analyzed and discussed, and puts forward some applications, finally the performance influence was discussed.

10.2 Space-Based Navigation System Architecture

Its main characteristic lies in the space segment load working for:

1. Receiving any other satellite navigation system available signal, location, time calculation, combined with the star itself frequency source, establish and maintain a space-time datum.
2. The establishment of a unified, standardized message, ranging code signal according to the time and space coordinates, the formation of the baseband or intermediate frequency modulation signal.
3. Reasonably combining with the original signals are broadcast using the RF channel and bandwidth.

This payload's goal is turning any broadcast signal in satellites into a spatial temporal reference, the reference is not only to provide to their own, but also through the signal to broadcast to the ground and aerial users.

Space-based navigation system load can be divided into two parts; signal receiving system and transmitting system. Signal receiving system onboard Omni-directional antenna to receive satellite navigation systems such as GPS and Galileo systems, BDS civilian public signal, multiple vector systems satellite tracking, and where and when the solution processing, receive location, time (with time scales). By calibrating the local clock to get timing reference signal, except for distribution to satellite use, the generated data, location code, the carrier of the message, attached to the existing communications, remote sensing and other signals to transmit on. Overall structure is shown in Fig. 10.2.

For space transmission, signal spectrum can be located in the L band, S band, C band or higher or lower band. The signal receiving antenna is larger if the signal spectrum is lower than the L band, and the attenuation is higher if the signal spectrum is lower than the C band. The ionosphere has more effect on the signals those spectrums lower than the L band and less effect on the signals those spectrums higher than the C band. Because of frequency difference, the same satellite condition, when signals reach the ground, the variation range of Doppler difference is larger, and the same band, the motion of satellite platform is different, Doppler is also different.

The receiver for the space-based system signal has the following characteristics:

1. According to the emission signal frequency and bandwidth, the receiver needs adjust the front end design, adapting to the combining with its surroundings or communication signal or radar signal, and has certain anti-interference ability;

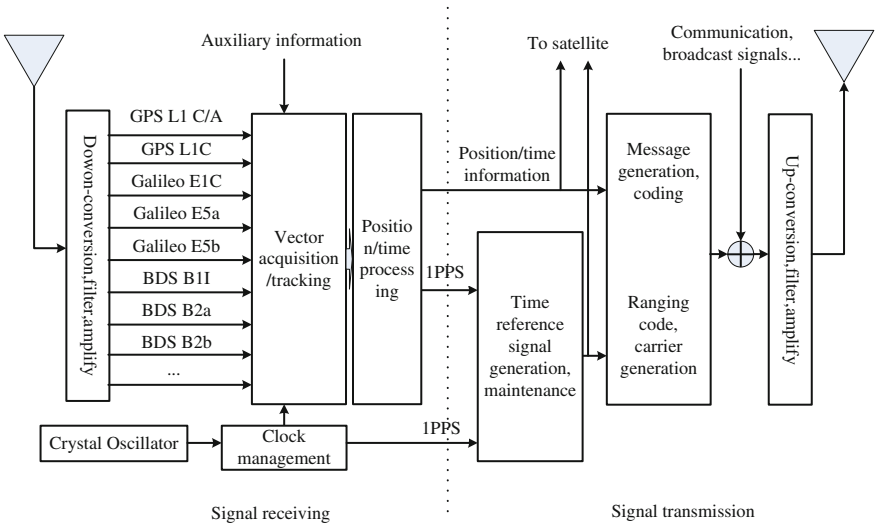

Fig. 10.2 Payload framework

2. Due to the limit of band and payload power, the signal after reaching ground may be very weak, that needs receiver have a certain ability to receive weak signal.

After the system architecture and the signal finally realized, GNSS receiver on the ground, under the condition of appropriate adjustment RF front end and the digital channel less changed, can receive the backup signal for positioning and timing. One solution is to increase the corresponding antenna, filter and frequency conversion unit in a common receiver that can use the original work on the system. Another option is to increase the processing channel in the receiver, and the original signal processing system can work in parallel.

10.3 Space Based Navigation System-Wide Load Design

10.3.1 Space Platform

According to the application, there are communication satellites, remote sensing satellites, direct broadcast satellites. All these satellites including other broadcasting signals to ground satellite and space vehicle, can be used as the platform of space-based all source navigation system.

Global beam used in the early stage of communication satellites, limited by communication capacity, but facilitate for global navigation, such as America maritime satellite communication (Marisat). Later communication satellites gradually

service the regional area by regional, spot beam, or multi beam. That is more favorable for military applications, such as the international maritime satellite-3 (Inmarsat-3). LEO satellite communication system realizes the multi star network by receiving ground signal and forwarding, can improve ground cellular communication technology. Generally, the satellite is smaller and more, such as the Globalstar system and America Iridium satellite system. The communication equipment of L, S or C band was equipment, more channels that can facilitate to use its idle channel to broadcast signal.

Direct broadcast satellite has the characteristics of large power, long service life, small user receiving antenna, system stability and so on, including live TV and sound broadcasting. The International Telecommunication Union ITU made the division regulations of frequency of UHF, Ku, Ka, V band for satellite TV service. At present, the application of Ku band is the most common, of which the third region of the 11.7–12.2 GHz band for the Asia Pacific countries to use [4]. Direct broadcast satellite transponders were also mainly use program upload and broadcast, its broadcast rate is relatively constant and the broadcast is continuous. Limited by the power and system, it requires by the larger antenna for receiving the signal and is difficult for omnidirectional receiving.

Remote sensing satellite mainly refers to the satellite for earth observation, generally refers to visible light, infrared, microwave remote sensing equipment for detecting terrestrial, marine, underground, atmosphere, gravity, geomagnetism, sea ice, temperature, wind field and so on. The satellite receiving signals from passive observation can only using the data transmission path for navigation and the path is generally high data rate transmission and high frequency. Synthetic aperture radar (SAR) load need emission microwave signal (usually a L band), can be used as a navigation signal sending path, and space-based SAR for area coverage, strip scanning, can achieve the purpose of the designated area backup and enhanced.

Astronomy satellite, the solar system science satellite observation data are need to be transmitted to the ground, theoretically can also be used as a carrying platform. But if the apogee distance and signal is weak, there are the higher requirements for antenna aperture and pointing.

From the analysis, satellite communication is the most suitable satellite platform. Some communication satellites and broadcast satellites, in order to maintain continuous coverage area of concern, are located in the earth synchronous orbit, so its orbit is higher, and is helpful to improve the navigation coverage. Space-based SAR imaging requires the Doppler information, generally the orbit is low to focus on regional imaging, and also can broadcast navigation information. These satellite payload is mainly used for communication, broadcast, remote sensing and other fields, the additional load must not affect the function and the performance of these applications, and must not substantially increase the satellite payload size, weight and power consumption, therefore the navigation loads must be miniaturization, light weight and low power consumption.

10.3.2 Signal Receiving

1. Receives the signal content

According to the 2014 September baseline, the world now broadcast and civil satellite navigation signal is transmitted with GPS L1 C/A code signal, L1C, L2C, E1C, L5 signals, E5 signals of Galileo system, BDS B1I, B1C, B2 signals. These civil signals can be as the receiving signal is received. The reference solution is shown in Table 10.1.

2. Receiver design on the satellite navigation

Distinguished from single frequency receiver designs, satellite receiver design that need to be considered at the beginning of multiple systems and multi-frequency integration problems, save the front-end burden of complexity of RF and digital processing. Examples are as follows:

The signals were received by antennas, then respectively filtered by the RF filter. The filter, 1568.259 and 1191.795 MHz as the center frequency, its bandwidth is larger than 20.46 MHz. The signals (including B1I), whose center frequency is 1575.42 MHz, were down conversion to 6.811, and 1561.098 MHz down conversion to −6.811 MHz. If it is real frequency, −6.811 MHz signal is falling in 6.811 MHz. The Galileo system E5 signal and BDS B2 signal are AltBOC(15,10) modulation, so frequency of the local oscillator can be set as the center frequency of 1191.795 MHz, then E5a and B2a center frequency is in the −15.345 MHz, E5b and B2b in 15.345 MHz. If real down conversion, E5a and B2a also fall in the 15.345 MHz. The highest frequency of the signal is located at 15.345 + 10.23 = 25.575 MHz. According to the Nyquist theorem, the sampling frequency must be more than two times of that, taking into account the sampling frequency to avoid as far as possible for the rational factor code rate and subcarrier rate, therefore the sampling frequency can be set as 53 MHz or higher reasonable values (Fig. 10.3).

Table 10.1 The received signal

GNSS	Signal	Center frequency/MHz	Receiver bandwidth/MHz	If center frequency/MHz
GPS	L1 C/A	1575.42	8.184	6.811
	L1C	1575.42	8.184	6.811
Galileo	E1C	1575.42	8.184	6.811
	E5a	1176.45	20.46	−15.345
	E5b	1207.14	20.46	15.345
BDS	B1I	1561.798	8.184	−6.811
	B1C	1575.42	8.184	6.811
	B2a	1176.45	20.46	−15.345
	B2b	1207.14	20.46	15.345

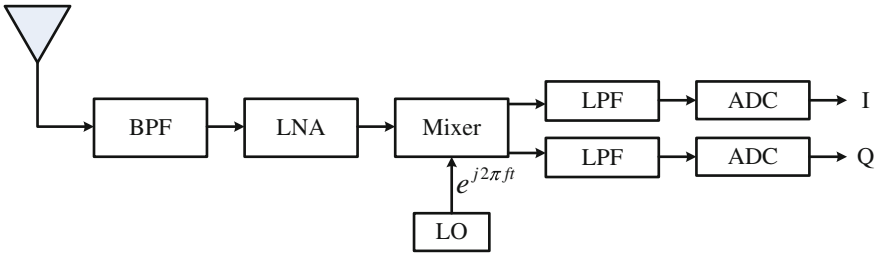

Fig. 10.3 Complex sampling architecture

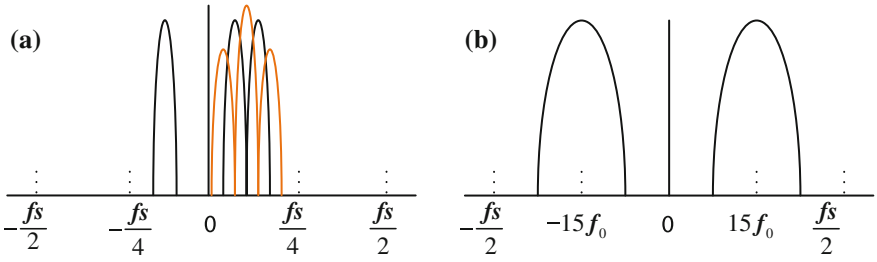

Fig. 10.4 The signal spectrum of complex sampling. **a** L1\B1, **b** E1\B2

In the complex sampling, signal spectrum pattern as shown in Fig. 10.4, where $f_0 = 1.023$ MHz.

By two-band signal distribution, we can see the main signal L1\B1 band falls on $[-f_s/4, f_s/4]$ in the digital domain. We can first use half-band FIR filters for filtering part of the signal and extraction. Respectively, using complex half band filter and extraction, in the lower half of the sampling rate at the same time, the L1 \B1 band signals can be distinguished from other.

3. The received signal amplitude

Satellite navigation signals, when it reaches the Earth's surface, a typical power level is −125 to −130 dB m. According to the different orbit, receiving GNSS broadcast side lobe signals, the payload established temporal and spatial reference [5].

The EIRP of antenna side lobe signals is at least 14 dB lower than the main lobe [6]. According to the calculation [5], a better case on LEO, GEO, HEO, the signal carrier to noise ratio C/N0 is about 43.0, 29.8 and 27.4 dB-Hz, lower than to the ground (51.4 dB-Hz) at least 7 dB. So using the weak signal for location, satellite receiver need to extend the integration time, large pieces correlator or special algorithm of high-sensitivity receiver.

10.3.3 Precision Clock Maintenance Technology

The clock of non-navigation satellite is worse in terms of stability. Today, timing accuracy of navigation receiver is 20 ns that could meet most of the precision timing requirements. But, as the navigation backups and enhanced load, it needs to improve the accuracy for the standard as a timing source. In addition, after the satellite navigation signal lost, generally, timing precision of the receiver will be dramatically reduced, and we need to study higher-performance timekeeping systems.

There are several aspects to improve timing accuracy, one of which is to receive multiple satellite signals of the system using wide-band RF front-end, high ADC, high sample rate, long integration times and multiple correlation arm, better discriminator and correlation spacing, allowing better performance, correlation peak depiction more accurate and precise.

Based on the small size, low power consumption and cost considerations, atomic frequency standard is not as the load. Mainly considering temperature compensated crystal oscillator (TCXO) or constant temperature crystal oscillator (OCXO), so its frequency accuracy and stability determines timekeeping accuracy.

As the source of the navigation design, it needs to take advantage of multiple GNSS satellite information to overcome platform clock drift, temperature changes, the error of orbital parameters and other unfavorable factors. It needs to significantly improve the accuracy of time, then can be as good sources for navigation. As shown in Fig. 10.5, Kalman vector tracking architecture can be used.

The technology of clock setting up includes channel delay, delay test and calibration to ensure the stability and consistency of signal.

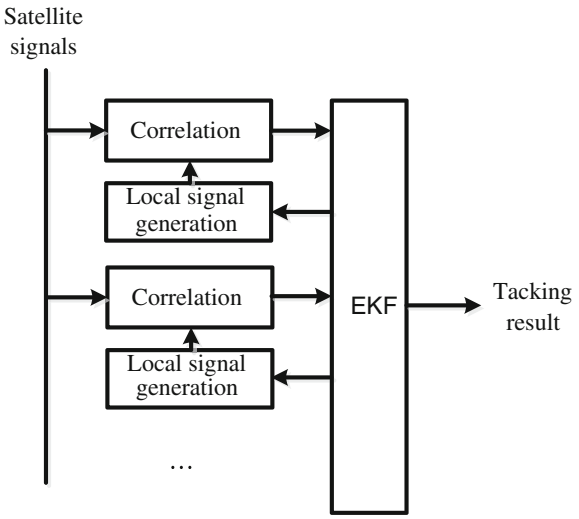

Fig. 10.5 Tracking architecture

10.3.4 Signal Design

Signal system design includes the center frequency, bandwidth, frequency, location code, bit rate, data rate, message encoding, and many other content. The factors taking into account include satellite platforms, RF channel atmospheric attenuation and delay, restriction, interference and difficulty of receiver. To complete backup and enhancement, improve accuracy, and reduce complexity remain the target of signal design.

If communications satellite is the main considerations carrying platform, taking into account the possible interference and other factors, navigation signals available bandwidth should be less than 20 MHz. The center frequency shall be designed according to the platform RF load, power and omnidirectional receiving restrictions. So L band and C band are the more suitable band. Ranging codes and data are as far as possible to maintain interoperability with existing signal receiving for reducing complexity. Because China's Beidou satellite navigation system released the B1I signal of ICD, according to the inheritance and compatibility of the system, the signal will be continued to broadcast, so we can use signal ranging code and message design modeled on the design of the all source navigation signal.

In C-band navigational signal design, link analysis, transmitting and receiving, transmitting positioning system, the Chinese regional navigation satellite system (CAPS, Chinese Area Positioning System) based on communications satellite will be a useful reference [7]. The study and research for Galileo satellite navigation system in C band 5010–5030 MHz; can also be used as a signal system design reference [8].

10.3.5 RF Signal Generation and Advertisement

The navigation payload on non-navigational satellite must be minimal impact on other critical loads; therefore we require use of miniaturization, low power signal generation techniques. At present, the development of ASIC technology makes a massive filter, frequency converter can be gradually replaced, there were several possible application scenarios and technologies.

1. Zero intermediate frequency up-conversion architecture

For zero intermediate frequency up-conversion architecture, on the digital side, baseband I and Q signals were generated, D/A converted in the DAC chip, and make use of the local oscillator signal for complex up-conversion, then direct RF signal is sent out. After that, the band-pass filtered output signal is coupled with communications, radar, using the back-end to transmit to high power amplifiers, filters, and antennas.

2. Direct RF generation

The biggest difference between direct RF generation system and zero intermediate frequency up-conversion architecture lies in the up-conversion in the digital domain. Digital clock frequency is usually not very high, so by means of multiple parallel processing we can decrease dramatically processing rates, then using polyphase filter and parallel-serial conversion, directly becoming RF signal output.

10.4 Performance Analysis

Space-based navigation performance depends mainly on the four aspects of the technology, the first is space loading time to obtain and maintain accuracy, the second is accuracy of signal generation and for the advertisements, the third is the impact of space environment on signal quality, the forth is ground receivers the processing power.

The time precision to obtain and maintain mainly depends on the GNSS signal quality, signal processing, and local clock stability. Number of visible and less visible time, poor satellite geometry layout, resulting in decreased accuracy and precision of surveying time. Signal processing will also introduce some errors. Long steady despite the calibration of the local clock, but the short stable are still affecting the signal processing.

Advertise the accuracy is affected by signal generation and signal generation and broadcast channels from undesirable factors, such as channel device performance itself is not ideal, poor amplitude-frequency characteristic and group delay characteristic. Channel properties influence is also reflected in the device over time, changes caused by changes in temperature and other aspects of aging. Under certain conditions, these effects may be conducted in the pretreatment of signal certain compensation.

Main effects of space environment on the signal are the ionosphere and troposphere attenuation, dispersion, and signal frequencies, data models, meteorological and solar activity, and so on.

At present, the GPS L1 C/A code signal timing accuracy can reach more than 20 ns. GNSS system multi-signal timing accuracy is expected to reach less than 10 ns. Considering the introduction of errors in each stage, eventually reaching the ranging accuracy of the ground 5 m, positioning accuracy is associated with other satellite signal conditions and other factors.

10.5 Conclusions

Space-based navigation technology achieved the full source-based positioning, navigation, and timing (Positioning, Navigation and Timing, PNT) backup and capacity by adding navigation load on the satellite platform loads. The present

proposed scheme and architecture clearly showed the implementation of ideas and related signal reception, regeneration and miniaturization, low power technology research and ideas. Navigation signal was broadcasted at higher frequency, the attenuation was larger, while the satellite power limited, ground application needs to improve the gain of GNSS weak signal reception. Besides, the reception of the signal of high orbit satellite also has the problem, further study is necessary to focus on this aspect.

References

1. Rabinowitz MA (2000) Differential carrier-phase navigation system combining GPS with low Earthorbit satellites for rapid resolution of integer cycle ambiguities. Stanford University, Stanford
2. Joerger M, Gratton L, Pervan B et al (2010) Analysis of iridium-augmented GPS for floating carrier phase positioning. Navigation 57(2):137–160
3. Tian S, Li G, Chang J, Lu J, Dai W (2013) Receiver autonomous integrity monitoring in iridium-augmented GPS. J PLA Univ Sci Technol (Natural Science Edition) 14(3):237–241
4. Zhu Y, Feng J, Cai X, Chen Z (2004) The latest development of international digital DBS service I. Radio TV Broadcast Eng (7)105–109
5. Braasch MS, Uijt de Haag M (2006) GNSS For LEO, GEO, HEO and Beyond
6. Dion A, Calmettes V, Boutillon E (2007) Reconfigurable GPS-galileo receiver for satellite based applications. In: ION GNSS 20th international technical meeting of the satellite division, Fort Worth, 25–28 Sept 2007
7. Ai G, Shi H, Wu H, Li Z, Guo J (2008) Principle of communication based on satellite positioning system. Sci China. Series G: Phys Mech Astron 38(12):1615–1633
8. Hein GW, Irsigler M, Avila-Rodriguez JA, Wallner S, Pany Th, Eissfeller B, Hartl Ph (2007) Envisioning a future GNSS system of systems, Part3: a role for C-band? Inside GNSS

Chapter 11
Carrier-Phase RAIM Algorithm Based on a Vector Autoregressive Model

Qianqian Zhang and Qingming Gui

Abstract A new CRAIM algorithm is designed for multiple faults detection and identification in RTK positioning using vector auto regression (VAR) model, and the corresponding protection level is given. Firstly, the RTK positioning process is introduced, and then we fit the double differenced carrier phase observations with VAR model. Based on the model, we predict the observations and obtain their prediction residuals which are used to detect and identify the potential faults in the observations. If a prediction residual of a certain observation is deviated from the normal range, we demonstrate that the corresponding observation is abnormal. Secondly, according to the accurate calculation of missed detection, a quantitative analysis method is designed for the reliability of the faults detection and identification algorithm. Thirdly, a new allocation method for integrity risk of CRAIM is designed. Then starting from the integrity risk, an algorithm for computing protection levels is given. Examples illustrate that the new algorithm can handle many types of faults, such as the faults caused by serious multipath, incorrect ambiguity resolution and the errors of atmospheric propagation. Besides, the probability of missed detection is investigated under the condition of different faults sizes and observational times. The results demonstrate that probability of missed detection satisfies the requirements of users. Finally, the availabilities for the new algorithm in different flight phase are analyzed by the computation of protection levels.

Keywords CRAIM · Vector autoregressive model · Outlier detection · RTK · Protection levels

Q. Zhang (✉)
Institute of Geospatial Information, Information Engineering University,
No. 62, Kexue Road, Zhengzhou 450001 China
e-mail: zhangqianqian0216@163.com

Q. Gui
Institute of Science, Information Engineering University,
No. 62, Kexue Road, Zhengzhou 450001 China
e-mail: guiqingming@126.com

J. Sun et al. (eds.), *China Satellite Navigation Conference (CSNC) 2015 Proceedings: Volume II*, Lecture Notes in Electrical Engineering 341,
DOI 10.1007/978-3-662-46635-3_11

11.1 Introduction

Carrier-phase RAIM has a wide range of applications, such as aircraft landing, precision approach and various high precision applications [1–4]. Compared to the traditional RAIM algorithm based on code pseudo-ranges, carrier-phase RAIM faces with more difficult problems. In the carrier phase positioning algorithms, double differenced observations are frequently used and correlations among the errors of these observations are strong. It is necessary for us to handle the correlations correctly when we design a robust and reliable positioning algorithm. A variety of faults will appear in the carrier phase positioning, such as satellite failures, multipath errors and cycle slips and so on. Therefore, carrier phase RAIM algorithms face with multiple types of faults. In addition, the carrier phase ambiguities are estimated together with the estimation of the position solution [5].

In recent years, carrier-phase RAIM has got a certain development. Firstly, [6] designed a carrier-phase RAIM for RTK positioning based on Kalman filter. In this method, the testing statistic for faults detection was constructed by the innovative series, but the testing statistic cannot identify faults and it cannot deals with the cases of multiple faults. A CRAIM algorithm, using a Gaussian sum filter, was described in detail by [7]. It pointed out that the actual carrier phase error did not exactly follow the Gaussian distribution, because the performance of the conventional CRAIM algorithm was not optimal. A Gaussian sum filter could deal with any non-Gaussian error distribution and accurately presented the posterior distributions of states. [8] discussed the application of CRAIM in airport surface movement, and the ambiguity resolution procedure was improved.

From the current development of CRAIM, some problems still remain to be solved. Firstly, the problem for multiple faults detection and identification is not solved properly, but the multiple faults occur frequently in RTK positioning, such as the fault patches caused by wrong estimation of ambiguity. Secondly, a quantitative method for evaluating the reliability of faults detection and identification is not given. According to the characteristics of CRAIM and in order to solve the existing problems above, a new carrier-phase RAIM algorithm is proposed in this paper; we detect and identify the multiple faults using time series prediction and the corresponding protection levels is also given.

11.2 Algorithms for Multiple Faults Detection and Identification Based on Vector Autoregressive Mode

11.2.1 Navigation Equation of RTK Position

The equations based on double differenced carrier phase observations are as follows:

$$\nabla\Delta\varphi_{im}^{jg}(t) = \nabla\Delta R_{im}^{jg}(t) + V_{im}^{jg}(t) - \lambda_1\nabla\Delta N_{im}^{jg} - I_{im}^{jg}(t) + \Delta(t) \tag{11.1}$$

where $\nabla\Delta\varphi_{im}^{jg}(t)$ is the double differenced carrier phase observable between reference station and satellite, m denotes the reference station, i denotes the rover station, j denotes the satellite that is visible by reference station and satellite commonly, g denotes reference satellite with a maximum elevation angle, $\nabla\Delta R_{im}^{jg}(t)$ is the double differenced geometric distance between reference station and satellite, $V_{im}^{jg}(t)$ denotes the troposphere residual, λ_1 is the wavelength of L1, $\nabla\Delta N_{im}^{jg}$ is the double differenced ambiguity, $I_{im}^{jg}(t)$ is the ionospheric residual, $\Delta(t)$ is measurement error.

In this paper, we implement the positioning algorithm by Kalman filter based on the navigation equation above. The method for ambiguity estimation that is proposed by Clyde C. Goad is used.

11.2.2 The Implementation Process for Kalman Filter

The double differenced carrier phase observable $\nabla\Delta\varphi_{im}^{jg}(t)$ is denoted as $L_k = (L_{1k}, \ldots, L_{hk})^T$, where h is the number of the observables at epoch k. Then we obtain the positioning solutions by the following Kalman filter [6, 9]. The measure equation and state equation are as follows:

$$L_k = A_k X_k + e_k \tag{11.2}$$

$$X_k = \Phi_{k-1|k} X_{k-1} + W_k \tag{11.3}$$

where A_k is the design matrix, X_k is the state vector, e_k is the measurement noise vector, $\Phi_{k-1|k}$ is the state transition matrix from epoch k–1 to k, W_k is the process noise. e_k and W_k are series of Gaussian white noise.

$$\Sigma_{e_k e_i} = \begin{cases} \Sigma_k, k = i \\ 0, k \neq i \end{cases}, \quad \Sigma_{W_k W_i} = \begin{cases} \Sigma_{W_k}, k = i \\ 0, k \neq i \end{cases}$$

Based on (11.2) and (11.3), we can obtain the various Kalman filter equations:

$$\overline{X}_k = \Phi_{k-1|k} X_{k-1} \tag{11.4}$$

$$\Sigma_{\overline{X}_k} = \Phi_{k-1|k}\Sigma_{\hat{X}_{k-1}}\Phi_{k-1|k}^T + \Sigma_{W_k} \tag{11.5}$$

$$K_k = \Sigma_{\overline{X}_k} A_k^T \left(A_k \Sigma_{\overline{X}_k} A_k^T + \Sigma_k\right)^{-1} \tag{11.6}$$

$$r_k = L_k - A_k \overline{X}_{k-1} \tag{11.7}$$

$$\hat{X}_k = \overline{X}_k + K_k r_k \tag{11.8}$$

$$\Sigma_{\hat{X}_k} = (I - K_k A_k)\Sigma_{\overline{X}_k} \tag{11.9}$$

where $\overline{X}_k$ predicted vector of state, $\Sigma_{\overline{X}_k}$ is the covariance matrix of $\overline{X}_k$, K_k is Kalman gain matrix, r_k is the innovation vector, $\hat{X}_k$ is the estimate of state vector at epoch k, $\Sigma_{\hat{X}_k}$ is the covariance matrix of $\hat{X}_k$.

In the conventional CRAIM algorithm, the statistics for faults detection are formed by the weighted square of the innovation vector. However, this method cannot identify faults and cannot handle multiple faults. Therefore, a new method for satellite faults detection and identification is proposed in this paper based on the technology of online prediction of time series.

11.2.3 The Theory of Faults Detection and Identification Based on Vector Autoregressive Model

Double differenced carrier phase observables have the spatial and temporal correlations, so it is improper for us to process them separately. Therefore, we fit this kind of observations using vector autoregressive model (VAR) [10]. Based on the model, we predict the observations and obtain their prediction residuals which are used to detect and identify the potential faults in the observations. If a prediction residual of a certain observation is deviated from the normal range, we demonstrate that the corresponding observation is abnormal.

It is assumed that $L_k = (L_k^1, \ldots, L_k^h)^T$ is a stationary time series with mean 0 and obeys the following VAR model:

$$L_k = \Phi_1 L_{k-1} + \cdots + \Phi_p L_{k-p} + \varepsilon_k \tag{11.10}$$

That is to say,

$$\Phi(B) L_k = \varepsilon_k \tag{11.11}$$

where $\Phi_1, \ldots, \Phi_p$ are the autoregressive coefficient matrixes and $\Phi(B) = I - \Phi_1 B - \cdots - \Phi_p B^p$ obeys the stationary conditions. $\varepsilon_k = (\varepsilon_k^1, \ldots, \varepsilon_k^h)^T$ obeys multivariate normal distribution, that is to say, $\varepsilon_k \sim N(0, \Sigma_\varepsilon)$. From model (11.10), it can be seen that we not only consider the autocorrelations among L_k and the precious p epochs in the time direction, but also consider the spatial correlations of $\{L_k^1, \ldots, L_k^h\}$.

Then we obtain the prediction of L_k based on the VAR model using the conditional expectation prediction method. According to the characteristics of the conditional expectation, we can obtain that

$$\begin{aligned}\widehat{L}_k(l) &= E(L_{k+l}|L_k, L_{k-1}, L_{k-2}\ldots) \\ &= \Phi_1\widehat{L}_k(l-1) + \Phi_2\widehat{L}_k(l-2) + \cdots + \Phi_{l-1}\widehat{L}_k(1) + \Phi_l L_k + \cdots + \Phi_p L_{k+l-p}\end{aligned} \tag{11.12}$$

where $\widehat{L}_k(l)$ is the l step prediction of L_{k+l}. From (11.12), It can be seen that we need to get the estimates of the parameters $\Phi_j, j = 1, 2, \ldots, p$, if we want to obtain the predicted value $\widehat{L}_k(l)$. In this paper, we can estimate the parameters by maximum likelihood method or obtain the estimates of the parameters by the ARX function in Matlab.

Based on the prediction $\widehat{L}_k(l)$, we can get the predicted residual of L_{k+l}.

$$e_{k+l} = L_{k+l} - \widehat{L}_k(l) \tag{11.13}$$

Then we analyze the distribution of the predicted residual for faults detection and identification. According to the assumption in model (11.12), $\Phi(B)$ satisfies the stationary conditions, so that we can give an equivalent form of model (11.12),

$$L_{k+l} = \Phi^{-1}(B)\varepsilon_k = \sum_{j=0}^{\infty} G_j \varepsilon_{k+l-j} \tag{11.14}$$

where $G_j, j = 0, 1, \ldots$ are Green functions. By (11.14), we can get another representation of the predictive value of L_{k+l},

$$\begin{aligned}\widehat{L}_k(l) &= E(L_{k+l}|L_k, L_{k-1}, L_{k-2}\ldots) \\ &= \sum_{j=0}^{\infty} G_j E(\varepsilon_{k+l-j}|L_k, L_{k-1}, L_{k-2}\ldots) \\ &= \sum_{j=l}^{\infty} G_j \varepsilon_{k+l-j}\end{aligned} \tag{11.15}$$

Connected (11.14) with (11.15), another representation of the predictive residual of L_{k+l} can be obtained as follows.

$$e_{k+l} = L_{k+l} - \widehat{L}_k(l) = G_0\varepsilon_{k+l} + G_1\varepsilon_{k+l-1} + \cdots + G_{l-1}\varepsilon_{k+1} \tag{11.16}$$

Since $\varepsilon_k \sim N(0, \Sigma_\varepsilon)$, it can be concluded that the predictive residual obeys normal distribution and the mean and variance are as follows:

$$E(e_{k+l}) = 0, Var(e_{k+l}) = \sum_{j=0}^{k-1} G_j \Sigma_\varepsilon G_j^T \tag{11.17}$$

Therefore, $e_{k+l} = L_{k+l} - \widehat{L}_k(l) \sim N_h(0, \sum_{j=0}^{k-1} G_j \Sigma_\varepsilon G_j^T)$. Further, according to the characteristics of multivariate normal distribution, each component $e_{k+l}^i, i = 1, \ldots, h$ of e_{k+l} obeys one dimensional normal distribution $N(0, \sigma_{ii}^2)$, where σ_{ii}^2 is the diagonal elements of $\sum_{j=0}^{k-1} G_j \Sigma_\varepsilon G_j^T$. Therefore, the confidence intervals of the predictive residuals of L_{t+l}^i are given as follows with $1 - \alpha$ confidence level,

$$\left(-z_{1-\alpha/2}\sigma_{ii}, \quad z_{1-\alpha/2}\sigma_{ii}\right) \tag{11.18}$$

where $z_{1-\alpha/2}$ is the quantile of normal distribution. If the predictive residual deviates from the confidence interval, we claim that the observation L_{t+l}^i contains outliers with the probability $1 - \alpha$, where α can be determined according to the false alarms of user requirements.

11.2.4 Quantitative Analysis of the Performance of Faults Detection and Identification Algorithm

Whatever the detection method is used, the phenomena of false alarm and missed detection always exist. In fact, the false alarm rate and the missed detection probability are the first and the second kinds of mistakes in hypothesis testing, respectively. How to quantitatively calculate the false alarm rate and the missed detection probability is a premise to decide whether this algorithm applicable. Currently, the existing methods often fixed the false alarm rate firstly, and then calculated the missed detection probability by numerical and statistical methods. The calculation method is not a quantitative, but this is a problem needed to be solved in the practical application. According to the definition of the missed detection probability, its calculation formula is as follows:

$$P_{MD,i} = P\{|\tau_i| < T_i | H_1\} = \int_{-T_i}^{T_i} \varphi_i(x)dx \tag{11.19}$$

where τ_i is the test statistics, T_i is the detection threshold, $\varphi_i(x)$ is the probability density function of normal distribution $N(\mu_i, \sigma_{ii}^2)$.

When the observation contains a fault but not be detected, we cannot know the magnitude μ_i of the fault, of course. Therefore, the missed detection cannot be obtained, which is needed for the calculation of missed detection probability. However, when a fault is detected, we can get the magnitude μ_i using the prediction

residual, so as to accurately calculate the missed detection probability. Although this missed detection probability cannot be used to calculate the protection levels, it can be used to evaluate the performance of the fault detection and identification algorithm.

When a fault is detected, the test statistic τ_i obeys the following distribution

$$\tau_i \sim N(L_{i,k+1} - \widehat{L}_{ik}(1), \sigma_{ii}^2) \tag{11.20}$$

Then connected (11.19) with (11.20), we can get the missed detection probability accurately.

11.3 The Method for Calculating Protection Levels

In this paper, we provide the method for computing the protection levels based on the basic idea of integrity risk. In civil aviation, there are two types of risks: the integrity risk and the continuity risk. The integrity risk is the probability of hazardously misleading information (PHMI) which is defined as any event where the position error is greater than the dynamically calculated protection level without any alarm for more than the required time to alert (TTA) and the continuity risk is defined as the probability of any interruption in approach service [11, 12]. The integrity risk is often divided into vertical component and horizontal component. In the fault free case, we can obtain the protection levels easily. While in the faulty case, due to the unknown value of the missed detection probability, we cannot obtain the exact values of the protection levels. In this paper, we let the missed detection probability equals to 10^{-3}.

11.3.1 Allocation of Integrity Risks

The total allowable integrity risk. $P_{HMI,\text{req}}$ requirement is allocated among three cases as illustrated in Fig. 11.1.

11.3.2 The Method for Computing Vertical Protection Levels

In order to obtain the vertical protection levels, we firstly investigate the formula of integrity risk,

$$P_{HMIv,req} = P\{(|x_v| > VPL) \cap (|\tau| < T)\} \tag{11.21}$$

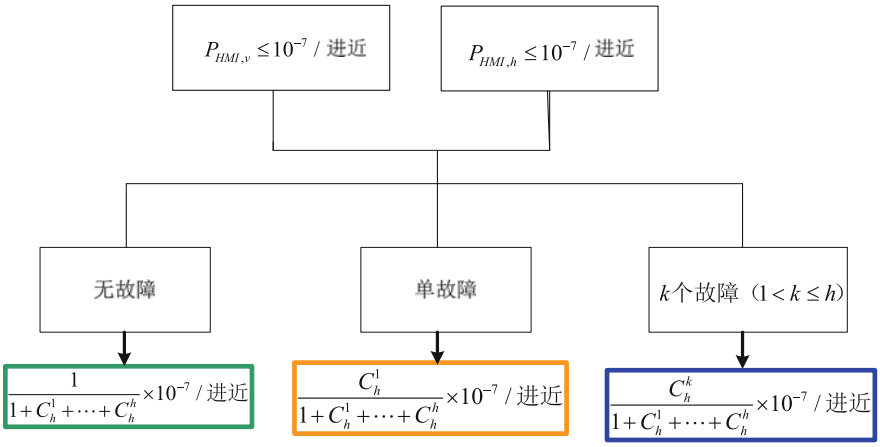

Fig. 11.1 Allocation of integrity risk for CRAIM

where $P_{HMIv,req}$ is the probability of the requirement of integrity risk, x_v is the vertical position errors, VPL is the unknown vertical protection level, τ is the test statistics, T is the testing threshold.

Due to the existence of the false alarm rate and the missed detection probability, even in the case of no alarms, there are two kinds of potential cases: observations containing faults and observations not containing faults. It is assumed that H_0 denotes the null hypothesis of the fault free case, H_1 denotes the alternative hypothesis of the faulty case, and

$$P\{H_0\} + P\{H_1\} = 1 \tag{11.22}$$

where $P\{H_0\}$, $P\{H_1\}$ are the prior probabilities of the two kinds of potential cases, respectively. Because the events $|x_v| > VPL$ and $|\tau| < T$ are independent, (11.21) can be written as the follows according to the statistical theories:

$$\begin{aligned} P_{HMIv,req} = {} & P\{|x_v| > VPL_0|H_0\}P\{|\tau| < T|H_0\}P(H_0) \\ & + P\{|x_v| > VPL_1|H_1\}P\{|\tau| < T|H_1\}P(H_1) \end{aligned} \tag{11.23}$$

Let

$$P_{HMIv,j} = P\{|x_v| > VPL_j|H_j\}P\{|\tau| < T|H_j\}P(H_j) \tag{11.24}$$

where $j = 0$ denotes the fault free case, $j = 1$ denotes the faulty case, $P_{HMIv,0} + P_{HMIv,1} \le P_{HMIv,req}$.

(1) According to the formula of the integrity risk in the fault free case,

$$P_{HMIv,0} = P\{|x_v| > VPL_0|H_0\}P\{|\tau| < T|H_0\}P(H_0) \tag{11.25}$$

we can obtain that

$$P\{|x_v| > VPL_0|H_0\} = \frac{P_{HMIv,0}}{P\{|\tau| < T|H_0\}P\{H_0\}} \tag{11.26}$$

where $P\{|\tau| < T|H_0\}$ is the probability of the testing statistics τ in the normal scopes under the fault free case. From an analysis, it can be obtained that

$$P\{|\tau| < T|H_0\} = 1 - P_{FA} \tag{11.27}$$

where P_{FA} is the false alarm. In order to compute VPL_0, we need to derivate the distribution of the vertical position error x_v under the null hypothesis. According to (11.1), we can obtain that

$$\begin{aligned} \Delta X_k &= X_k - \hat{X}_k = X_k - \overline{X}_k - K_k r_k \\ &= W_k - K_k r_k \end{aligned} \tag{11.28}$$

where W_k is white noise series and $r_k \sim N_h(0, A_k \Sigma_{\overline{X}_k} A_k^T + \Sigma_k)$ [9]. Therefore, it can be concluded that $\Delta X_k \sim N_4(0, \Sigma_{\hat{X}_k})$, and then $x_v \sim N(0, (\Sigma_{\hat{X}_k})_{(3,3)})$. Finally, the formula of VPL_0 can be obtained,

$$VPL_0 = \sqrt{(\Sigma_{\hat{X}_k})_{(3,3)}} \cdot K(1 - \frac{P_{HMIv,0}}{(1 - P_{FA})P(H_0)}) \tag{11.29}$$

where $K(\cdot)$ is the $1 - \frac{P_{HMIv,0}}{(1-P_{FA})P\{H_0\}}$ quantile of Gaussian distribution.

(2) In order to derivate the formula of the vertical protection level VPL_1, we analyze the integrity risk under the faulty case,

$$P_{HMIv,1} = P\{|x_v| > VPL_1|H_1\}P\{|\tau| < T|H_1\}P\{H_1\} \tag{11.30}$$

where $P\{|\tau| < T|H_1\}$ is the missed detection probability P_{MD}. Under the faulty case, the probability distribution of x_v is $x_v \sim N(\mu_i, (\Sigma_{\hat{X}_k})_{(3,3)})$, where μ_i is the unknown failure magnitudes of the ith satellite. In this paper, we find the μ_i according to the following formula

$$10^{-3} = \int_{-T_i}^{T_i} \varphi_i(x)dx \tag{11.31}$$

where T_i is the detection threshold, $\varphi_i(x)$ is the probability density function of $x_v \sim N(\mu_i, (\Sigma_{\hat{X}_k})_{(3,3)})$. Thus, the formula of VPL_1 can be obtained,

$$VPL_1 = \sqrt{(\Sigma_{\hat{X}_k})_{(3,3)}} \cdot K(1 - \frac{P_{HMIv,1}}{P_{MD}P\{H_1\}}) + \sum_{i=1}^{h} K_k(3,i) \times \mu_i \tag{11.32}$$

where K_k is Kalman gain matrix. Finally, the formula of vertical protection levels is $VPL = \max\{VPL_0, VPL_1\}$.

11.3.3 The Method for Computing Horizontal Protection Levels

In order to obtain the horizontal protection levels, we investigate the formula of the horizontal integrity risk,

$$P_{HMIh,j} = P\{||x_h|| > HPL_j|H_j\}P\{|\tau| < T|H_j\}P\{H_j\} \tag{11.33}$$

where $P_{HMIh,0} + P_{HMIh,1} \leq P_{HMIh}$, $x_h = (x_1, x_2)^T$ denotes the horizontal position errors in the east and north directions, $||\cdot||$ denotes a weighted norm, HPL_j is the unknown horizontal protection level.

(1) According to the formula of the integrity risk in the fault free case,

$$P_{HMIh,0} = P\{||x_h|| > HPL_0|H_0\}P\{|\tau| < T|H_0\}P\{H_0\} \tag{11.34}$$

In order to compute HPL_0, we need to derivate the distributions of the horizontal position error x_h and its norm $||x_h||$ under the fault free case. According to the formula of (11.28) and the characteristics of the multivariate normal distribution, we can obtain that

$$x_h \sim N_2(0, C\Sigma_{\hat{X}_k}C^T) \tag{11.35}$$

where $C = \begin{pmatrix} 1 & 0 & \cdots & 0 \\ 0 & 1 & \cdots & 0 \end{pmatrix}_{m\times 2}$. Considering the correlations between the east and the north position errors, the norm of the horizontal position errors is as follows,

$$||x_h||^2 = x_h^T C \Sigma_{\hat{X}_k} C^T x_h \tag{11.36}$$

From the formula of (11.35), it can be seen that the figure of norm above is an elliptic curve. In this paper, the errors in the direction of the error ellipse's semi-major axis are defined as the horizontal position errors. In this direction the horizontal position errors follow the normal distribution and the variance is as follows,

$$\sigma_H^2 = \frac{b_1^2 + b_2^2}{2} + \sqrt{(\frac{b_1^2 - b_2^2}{2})^2 + b_{12}^2} \tag{11.37}$$

where $b_1^2 = (\Sigma_{\hat{X}_k})_{(1,1)}, b_{12} = (\Sigma_{\hat{X}_k})_{(1,2)}, b_2^2 = (\Sigma_{\hat{X}_k})_{(2,2)}$. Thus, the formula for computing HPL_0 is

$$HPL_0 = \sigma_H \cdot K(1 - \frac{P_{HMIh,0}}{(1 - P_{FA}) \cdot P\{H_0\}}) \tag{11.38}$$

(2) In order to derivate the formula of the vertical protection level HPL_1, we analyze the integrity risk under the faulty case,

$$P_{HMIh,1} = P\{||x_h|| > HPL_1 | H_1\} P\{|\tau| < T | H_1\} P\{H_1\} \tag{11.39}$$

where $P\{|\tau| < T | H_1\}$ is the missed detection probability P_{MD}. Here, we find the failure magnitudes $\mu_{hor,i}$ according to the following formula

$$10^{-3} = \int_{-T_i}^{T_i} \varphi_{h,i}(x) dx \tag{11.40}$$

where $\varphi_{h,i}(x)$ is the probability density function of $N(\mu_{hor,i}, \sigma_H^2)$. Thus, the formula of HPL_1 can be obtained,

$$HPL_1 = \sigma_H \cdot K(1 - \frac{P_{HMIh,1}}{P_{MD} \cdot P\{H_1\}}) + b_h \tag{11.41}$$

where $b_h = \max\{\sum_{i=1}^{h} K_k(1,i) \times \mu_{hor,i}, \sum_{i=1}^{h} K_k(2,i) \times \mu_{hor,i}\}$. Finally, the formula of horizontal protection level is $HPL = \max\{HPL_0, HPL_1\}$.

11.4 The Implementation Process of the CRAIM Algorithm

The detailed flow chart is as follows (Fig. 11.2).

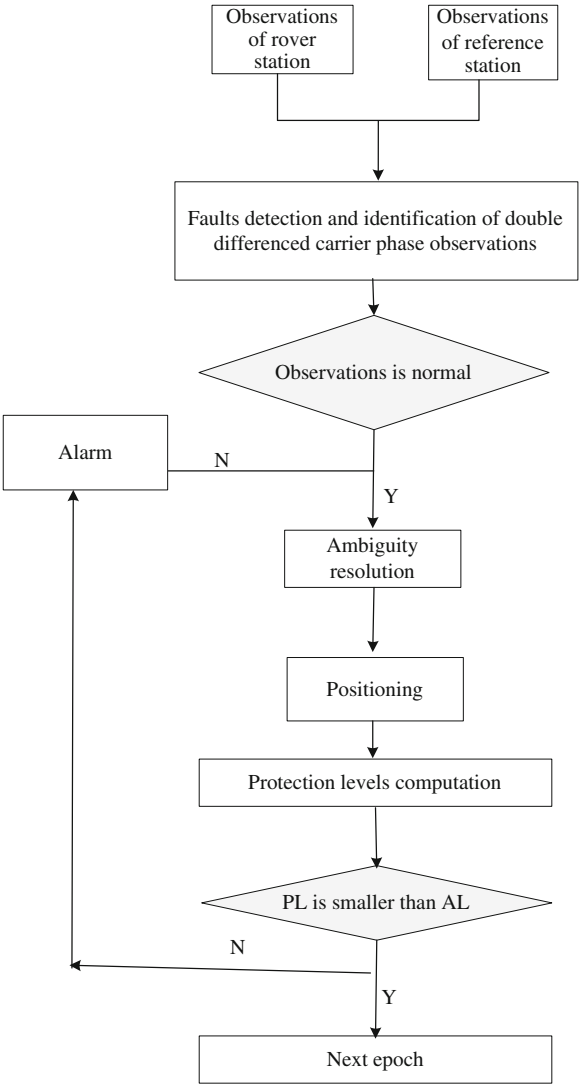

Fig. 11.2 The flow chart of the CRAIM algorithm

11.5 Examples and Analysis

In order to examine the correctness and the feasibility of the new algorithms in this paper, we design the following experimental schemes. The RTK positioning algorithm is implemented based on one reference station and one rover station under GPS. The length of baseline is 30.016 km. The observation time is 24 h and the sampling rate is 30 s.

11.5.1 Examine the Effectiveness of the Faults Detection and Identification

In order to examine the effectiveness of the faults detection and identification, two faults cases are considered. Firstly, faults occur in continuous epochs of a certain observation, which are caused by multipath errors or mistakes in ambiguity resolution. Secondly, faults occur in different satellites of a certain epoch, which are caused by atmospheric propagation errors. The probability of false alarm is $1 \times 10^{-9}/150$ s.

Scheme 1: add faults in the second double differenced carrier phase observation with the abnormal magnitudes equal to 70 cm at epoch 300 to epoch 305. The result is shown in Fig. 11.3.

Scheme 2: add faults in the first and the third double differenced carrier phase observation with the abnormal magnitudes equal to 60 and 55 cm at epoch 350 and epoch 1400, respectively. The results are shown in Figs. 11.4 and 11.5, respectively.

11.5.2 Investigate the Probabilities of Missed Detection Under Different Conditions

In order to investigate whether the probabilities of missed detection under different conditions satisfy the requirements or not, we examine the probabilities of missed detection with the variation of two different factors.

Scheme 3: Select one of the double differenced carrier phase observations randomly and add faults to the selected observation. The faulty biases are increased from 50 cm to 3 m with step length 5 cm. The purpose of this scheme is to examine

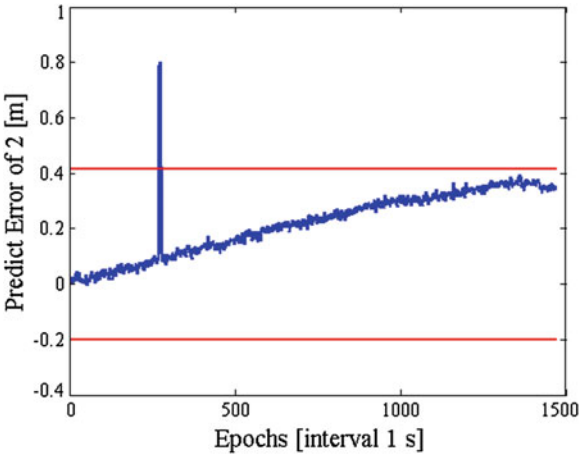

Fig. 11.3 Predicted errors of Scheme 1

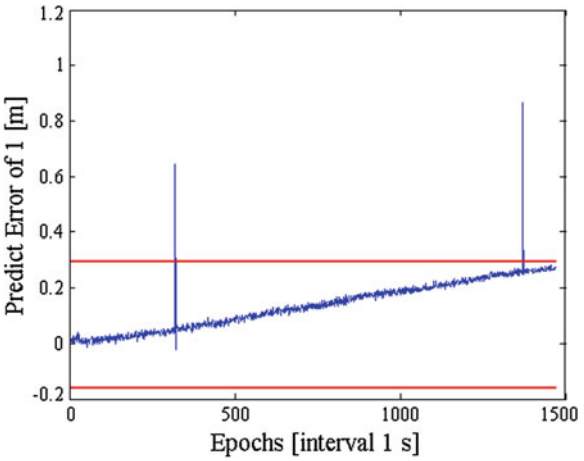

Fig. 11.4 Predicted errors of the first double differenced carrier phase observation of Scheme 2

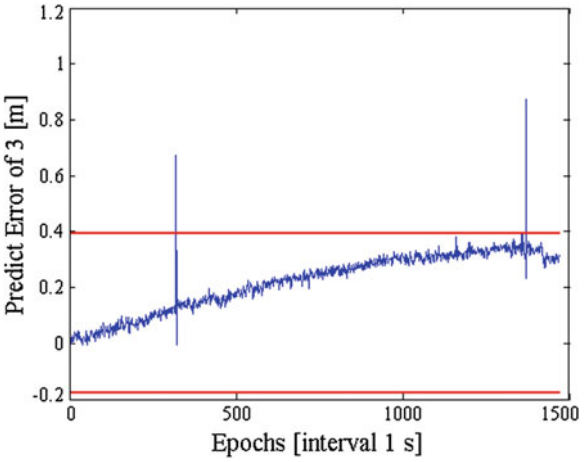

Fig. 11.5 Predicted errors of the third double differenced carrier phase observation of Scheme 2

the probabilities of missed detection with the variation of the faults biases. The results can be seen in Fig. 11.6.

From Fig. 11.6, it can be concluded that the probabilities of missed detection are decreased along with the increase of faults biases, and the maximum probability of missed detection is smaller than 10^{-3}. It is demonstrated that the algorithm in this paper can satisfy users' requirements.

Scheme 4: Select one of the double differenced carrier phase observations randomly and add faults with the abnormal magnitude equal to 50 cm at epochs with uniformly interval. The purpose of this scheme is to examine the probabilities of missed detection with the variation of observable epochs.

From Fig. 11.7, it can be seen that the probabilities of missed detection vary along with a certain tendency under different epochs, and the maximum probability

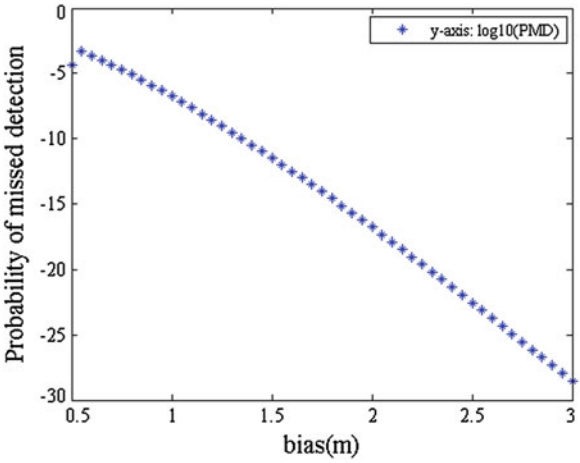

Fig. 11.6 The probabilities of missed detection under different faults biases

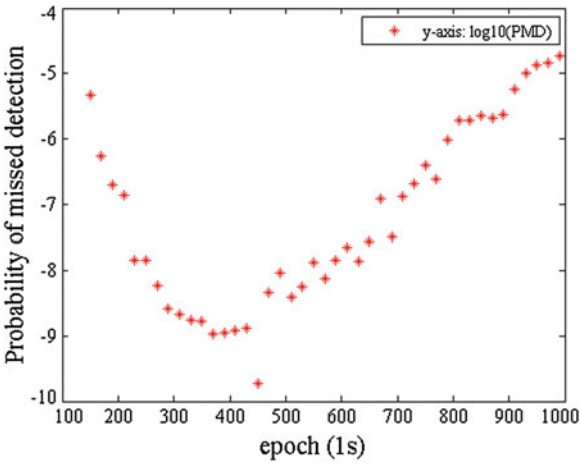

Fig. 11.7 The probabilities of missed detection under different epochs

of missed detection is also smaller than 10^{-3}. It is demonstrated that the algorithm in this paper can satisfy users' requirements.

11.5.3 The Computation of Protection Levels

In order to examine the availability of the CRAIM algorithm, experimental schemes are designed as follows. The computation results of the protection levels are shown in Figs. 11.8 and 11.9, respectively.

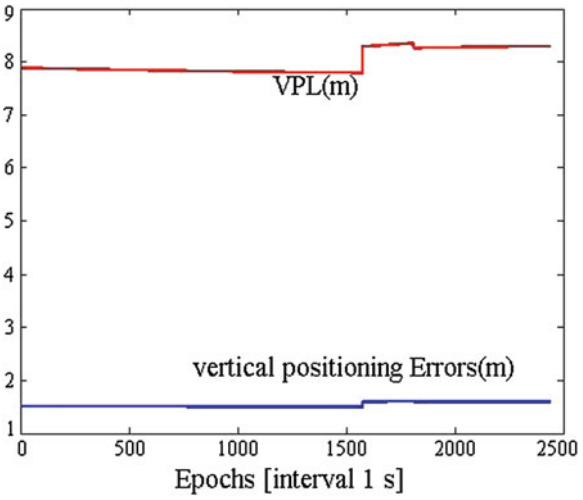

Fig. 11.8 Vertical protection levels

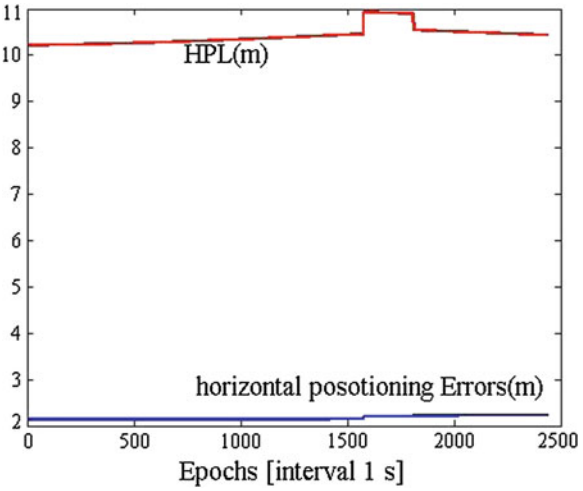

Fig. 11.9 Horizontal protection levels

It can be seen from Figs. 11.8 and 11.9 that the VPL and HPL can envelope the corresponding positioning errors well, and they can be used to the navigation of CAT-I.

11.6 Conclusions

(1) A faults detection and identification algorithm is designed using VAR model. Based on the model, we predict the observations and obtain their prediction residuals which are used to detect and identify the potential faults in the

observations. If a prediction residual of a certain observation is deviated from the normal range, we demonstrate that the corresponding observation is abnormal.

(2) According to the accurate calculation of missed detection, a quantitative method is proposed for the performance analysis of the faults detection and identification algorithm.

(3) Starting from the integrity risk, an algorithm for computing protection levels is given. A new allocation method for integrity risk of CRAIM is designed. On the one hand, we can evaluate the performance of the faults detection and identification algorithm by the protection levels. On the other hand, the positioning errors can be monitored by the protection levels. When the errors are abnormal, an alarm is given to users.

(4) Examples illustrate that the new algorithm can handle many types of faults, such as the faults caused by serious multipath, incorrect ambiguity resolution and the errors of atmospheric propagation.

(5) The probability of missed detection is investigated under the condition of different faults sizes and observational times. The results demonstrate that probability of missed detection satisfies the requirements of users. According to the analysis of protection levels, it is concluded that the algorithms in this paper can be used to the navigation of CAT-I.

Acknowledgments This research was supported jointly by National Science Foundation of China (No.41474009, No.41174005), State Key Laboratory of Geo-information Engineering (SKLGIE2014-Z-2-1) and Funded Project with youth of Annual Meeting of China's satellite navigation. Thanks for the help and support of the iGMAS analysis center of Information Engineering University, Zhengzhou, China.

References

1. Heo M (2004) Robust carrier phase DGPS navigation for shipboard landing of aircraft. Ph.D., llinois Institute of Technology, USA
2. Huang J (2007) A high-integrity carrier phase batch processor for differential satellite positioning. Ph.D., The Russ College of Engineering and Technology of Ohio University
3. Gratton L, Joerger M, Pervan B (2010) Carrier phase relative RAIM algorithms and protection level derivation. J Navig 63:215–231
4. Lee YC (2011) A position domain relative RAIM method. IEEE Trans Aerosp Electron Syst 47(1):85–97
5. Khanafseh S, Pervan B (2008) A new approach for calculating position domain integrity risk for cycle resolution in carrier phase navigation systems. In: Proceeding of the IEEE position, location, and navigation symposium (PLANS '2008), Monterey, CA, April 2008
6. Feng SJ, Ochieng W, Moore T, Hill C, Hide C (2009) Carrier phase-based integrity monitoring for high-accuracy positioning. GPS Solution 13:13–22
7. Yun H, Yun Y, Kee C (2011) Carrier phase-based RAIM algorithm using a Gaussian sum filter. J Navig 64:75–90

8. Schuster W, Bai J, Feng SJ, Ochieng W (2012) Integrity monitoring algorithms for airport surface movement. GPS Solution 16:65–75
9. Yang YX, Gao WG (2006) An optimal adaptive Kalman filter. J Geodesy 80:177–183
10. Shumway RH, Stoffer DS (2009) Time series analysis and its applications with R examples, 2nd edn. Springer, New York
11. Jiang YP, Wang JL (2014) A new approach to calculate the vertical protection level in A-RAIM. J Navig. doi:10.1017/S0373463314000204
12. GEAS (2008) GNSS evolutionary architecture study, GEAS Phase I—Panel Report, FAA

Chapter 12
A Beidou Based Multiple-GNSS Positioning Algorithm for Mission Critical Applications

Shaojun Feng, Shenghai Wang, Jianye Liu, Qinghua Zeng and Washington Ochieng

Abstract With the development of the Global Navigation Satellite Systems (GNSS), countries that own a GNSS have realised that critically national infrastructures using Position Navigation and Timing (PNT) services and a portion of the national economy associated with GNSS applications should not be over reliant on other countries. Recently, both China and Russia have made their systems mandatory for some applications. This paper addresses this issue and proposes a Beidou based multiple-GNSS positioning algorithm. It involves three stages: (1) Understanding of the quality of Beidou solutions. This was achieved by Receiver Autonomous Integrity Monitoring (RAIM) embedded in the Beidou positioning algorithm. (2) A real time validation and modelling algorithm for the measurements from the other constellations if Beidou solution is proved good in stage 1. The measurement residual errors relative to the Beidou position solution are assessed. (3) Introduction of measurements from the other constellations if there is not enough Beidou measurements. At this stage, the models derived in stage 2 are applied to the non-Beidou measurements. The tests were carried out using the Beidou and GPS data from a reference station. The signal blockage of Beidou and GPS constellation is simulated. The test results show that the proposed methods can benefit from the validated measurements from the GPS constellation. The performance can be significantly improved in terms of accuracy, continuity, integrity and availability in difficult environments. It can be extended for critical applications where any constellation is mandated.

Keywords Beidou · Multiple GNSS · Integrity · Continuity · Mission critical applications

S. Feng (✉) · W. Ochieng
Centre for Transport Studies, Department of Civil & Environmental Engineering, Imperial College London, London SW7 2AZ, UK
e-mail: s.feng@imperial.ac.uk

S. Wang · J. Liu · Q. Zeng
Navigation Research Centre, Nanjing University of Aeronautics and Astronautics, Nanjing, China

J. Sun et al. (eds.), *China Satellite Navigation Conference (CSNC) 2015 Proceedings: Volume II*, Lecture Notes in Electrical Engineering 341,
DOI 10.1007/978-3-662-46635-3_12

12.1 Introduction

With the modernization of the US Global Positioning System, the revitalization and modernization of the Russian GLONASS and the deployment of European Galileo and China's Beidou systems, it is expected that the full operation of multiple constellations is on the horizon. This will bring opportunities for user level positioning and integrity monitoring including more satellites, frequencies, message types, and better signal design and geometry. These will enable a multi-constellation receiver having the potential to support many more applications (e.g. urban rail operations, stand-alone precision aircraft operations and personal navigation services) than a single constellation receiver. Considerable research has been undertaken on positioning and integrity monitoring using multiple Global Navigation Satellite Systems (GNSS). However, due to the differences among the systems such as system time, spatial reference frame, signal quality and the performance of ephemeris, the best way to employ multiple constellations is still a challenge. For example the existing Solutions Separation method is a trade-off between two positioning solutions. It removes the negative impact of system time difference. However, it reaches a solution that is not as good as the better one of the two solutions from each individual constellation.

This paper addresses the technical issues of the existing methods and proposes a Beidou constellation based multiple-GNSS positioning and integrity monitoring algorithm. A Receiver Autonomous Integrity Monitoring (RAIM) is embedded in the positioning algorithm with the Beidou constellation. In order to benefit from the other constellations without compromising the trust on the Beidou constellation, a real time validation algorithm for the measurements from GPS constellations is developed using the solution from the Beidou constellation. The measurements from GPS constellation are pre-processed with conventional methods including correcting of satellite clock, the ionosphere effect and troposphere delay. The measurement residual errors relative to the position solution from the Beidou constellation are assessed. Upon pass the validation process, the measurements from other constellations are integrated to benefit from the feature of multiple constellations and generate a better solution.

The tests were carried out using the Beidou and GPS data from a reference station in China. Beidou was used as core constellation; while the errors in the GPS measurements are monitored and modelled. The test results show that the proposed methods can effectively identify potential issues and can benefit from the validated measurements from GPS. It can be used in critical applications where there are not enough Beidou measurements available.

12.2 Multi-Constellation Positioning and RAIM Algorithm

In single constellation, the positioning algorithm is usually based on least squares or filtering method. In any case, the measurements are pre-processed to mitigation various errors as much as possible by applying error models. It is generally assumed that the remaining un-modelled errors are acceptable. Therefore, the linearized form is:

$$\Delta\rho = H \cdot \Delta X + \epsilon \tag{12.1}$$

where $\Delta\rho$ is the difference between measured range (pre-processed) and expected range. $H = [\, G \quad (\mathbf{1}) \,]$ is the design matrix. G is the matrix consists of the direction vectors. ($\mathbf{1}$) is a vector with the same number of row as G with all its elements being one. $\Delta X = [\, \Delta x \quad \Delta y \quad \Delta z \quad \Delta t_r \,]$ is the positioning and receiver clock error. ϵ is the measurement error vector.

With two constellations, the number of navigation satellites is roughly doubled. This will provide better geometry, more redundancy and further enhance the positioning performance if two constellations could be used in combination. If more constellations are used in combination, even better positioning performances may be expected. The major issues in combining multiple constellations for positioning are differences in the system reference and signal quality. There are two types of approach in combining two or more constellations for positioning. One is combining in the position domain; the other one is in measurement (range) domain.

The approach of combining two constellations in position domain is to perform positioning independently in each constellation, with the ultimate possibility of determining the final solution as a weighted average of independent solutions [1]. In theory, the position domain method provides a capability to support RAIM. The algorithm called Optimally Weighted Average Solution (OWAS) method [2] provides a capability to provide integrity in the presence of multiple faults in a single constellation by comparing one constellation to another. The use of this method is subject to the RAIM availability within each constellation. Obviously, if there is not enough visible satellites (e.g. less than 4) in either constellation. The weighted average method does not work at all. Even with enough number of visible satellites (e.g. more than 4) in each constellation, the weighted average method is a trade-off between positioning solutions from two constellations.

In the measurement domain, there are three methods. The major difference is the way of handling the differences between constellations. The first compensates for differences between constellations by using correction to GPS time relative to other constellation (e.g. Beidou) time broadcast by the system [3]. The second method in the measurement domain is to take the differences (e.g. reference time) as unknowns to be estimated as part of the positioning solution [4]. The third method in the measurement domain is to employ single differences technique between pairs of measurements from two or more constellations. Each pair of measurement is selected from different constellation for example one from GPS and the other one

from Galileo [5]. In this case, the receiver clock bias and drift error are removed by the single difference. The inter-system time difference between any two constellations appears as a bias. In addition, a carefully selected pair can also mitigate correlated un-modelled errors such as tropospheric residual error.

In terms of RAIM, the measurements domain approach can fully exploit the redundancy provided by multiple constellations. Conventional Receiver Autonomous Integrity Monitoring (RAIM) assumes that only one failure occurs at a time. For the standard weighted least squares method [6, 7], the Sum of the Squared Errors (SSE) is used to construct a test statistic:

$$test\ statistic = \sqrt{SSE} \tag{12.2}$$

where $SSE = w^T w = \varepsilon^T S^2 \varepsilon = \varepsilon^T S \varepsilon$, $S = I - H \cdot (H^T \cdot W \cdot H)^{-1} \cdot H^T \cdot W$. The SSE has a chi-square distribution with $n - 4$ (n is the number of visible satellites) degrees of freedom (assuming that the measurement errors are independent and normally distribution with zero mean). Based on this assumption, a threshold can be derived for a given probability of false alert. This threshold is used to judge if there is any failure in the measurements

A protection level is an estimate of the up bound of positioning error. The Horizontal Protection Level (HPL) and Vertical Protection Level (VPL) are addressed as:

$$HPL = \max(Hslope(i)) * Pbias \tag{12.3}$$

$$VPL = \max(Vslope(i)) * Pbias \tag{12.4}$$

where $Hslope(i) = \sqrt{(A_{1i}^2 + A_{2i}^2)/S_{ii}}$, $Vslope(i) = A_{3i}/\sqrt{S_{ii}}$ is the sensitivity of the horizontal and vertical error to test statistics respectively. The *Pbias* is Minimum Detectable Bias (MDB) taking into account the threshold and probability of missed detection.

12.3 Beidou Based Multi Constellation Algorithms

Core constellation is the constellation mandated or its integrity is monitored by independent systems and known by users. Figure 12.1 shows the function diagram of the Beidou based method. Even though the integrity of signals from Beidou constellation may be monitored independently, the user level integrity monitoring is still necessary because it is difficult for an independent system to monitor the errors coming from the user local environments such as multipath, local interference and receiver related errors. Therefore, RAIM must be used in the core constellation positioning algorithm in order to provide a trust or quality indicator of the corresponding solutions. In general, the core constellation only can provide positioning solutions if there are enough satellites in view. However, it is not always the case

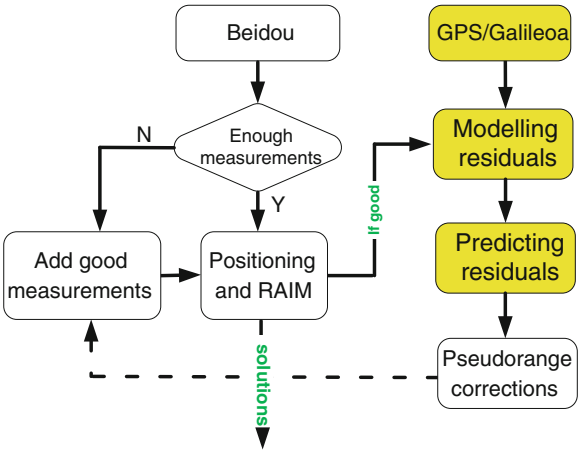

Fig. 12.1 The core constellation based method

where there are more than 4 satellites in view for example signal blockage. In order to provide continuous positioning solutions, measurements from other (non-core) constellations will be needed. In order to reach a good solution, only those measurements being validated can be used together with measurements from the core constellation. The positioning with the Beidou constellation can adopt the conventional least squares method or its variations. The corresponding RAIM is based on failure detection and the calculation of protection levels described in the previous section. Upon passing the RAIM tests, the positioning solution based on Beidou constellation is used to calculate the range residual errors for non-core constellations.

The error of range between a receiver and a satellite can be expressed as:

$$\rho^B - d^B_{geom} = ct - cT^B + d^B_{orb} + d^B_{ion} + d^B_{mp} + \varepsilon^B \tag{12.5}$$

$$\rho^G - d^G_{geom} = ct - cT^G + d^G_{orb} + d^G_{ion} + d^G_{trop} + d^G_{mp} + \varepsilon^G + ct_{sys} \tag{12.6}$$

where, the superscript B denotes Beidou constellation; G denotes GPS constellation, c is the speed of light, d is the range, t is the receiver clock offset, T is the satellite clock offset, ε is the measurement noise, t_{sys} is the system time difference between constellations, the subscript *orb* denotes orbit, *ion* denotes ionosphere, *trop* denotes troposphere, *mp* denotes multipath.

Figure 12.2 shows the geometry distance between a GPS satellite (k) and position of the user receiver. The true position where the pseudoranges are taken by a receiver is unknown. However, one of the estimates is the positioning solution from the Beidou constellation. Since the Beidou constellation may be monitored by an independent system and a RAIM algorithm is embedded, the estimate should be close to the true position. The position error d_E in Fig. 12.2 should be relatively small. As a result, the estimate of geometry distance $\hat{d}^G_{geom}$ should be close to the

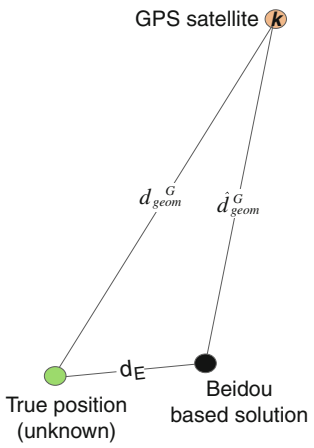

Fig. 12.2 Geometry distance

true geometry distance d^G_{geom}. Therefore, the estimated pseudorange residual from a GPS satellite can be expressed as:

$$r = \rho^G - \hat{d}^G_{geom} = ct - cT^G + d^G_{orb} + d^G_{ion} + d^G_{trop} + d^G_{mult} + \varepsilon^G + ct_{sys} \tag{12.7}$$

The residual is considered as the correction for GPS measurements. Given the fact that the positioning error (d_E in Fig. 12.2) is relatively small, most of the errors are highly correlated in spatial. These errors are also temporally correlated. The correction for measurement from a GPS satellite can be modelled as:

$$r(t) = \alpha_0 + a_1(t - t_0) + a_2(t - t_0)^2 \tag{12.8}$$

The coefficients a_0, a_1 and a_2 are determined when the Beidou solutions continuously passes integrity monitoring test since t_0. This model is then used in perdition mode when measurements from non-core constellation are needed. If the predicted correction (12.8) is applied to (12.6), the receiver clock and system clock difference error are included in the correction. The remaining errors are the multipath and noise. Therefore, the design matrix is written as

$$H = \begin{bmatrix} G^B & 1 \\ G^G & 0 \end{bmatrix} \tag{12.9}$$

where, matrix G consists of the direction vectors. (**1**) is a vector with the same number of row as G with all its element being one. (**0**) is a vector with the same number of row as G with all its element being zero.

The corresponding integrity monitoring needs to detect potential problems associated with the Beidou and GPS measurements. In addition, if the residual error models are not accurate, the un-modelled errors will appear in the test statistic. Therefore, the un-modelled error will not escape the detection.

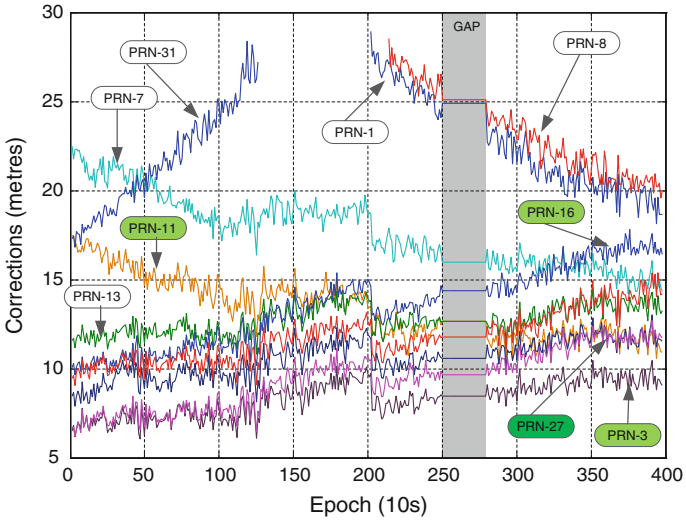

Fig. 12.3 Residuals of GPS measurements

12.4 Tests and Results

The data from a reference station in China which contain Beidou, GPS and GLONASS measurements were selected to verify the method proposed. Beidou was used as a core constellation, while GPS was used as a non-core constellation. Signal blockages were simulated for a period. Figure 12.3 shows the residuals of GPS measurements. During period when Beidou was not able to monitor its integrity, the GPS residuals were not monitored and modelled.

Two scenarios were tested. The first one was designed with four satellites in each constellation; while the second scenario was designed with three satellites in each constellation. For comparison purpose, six types of results are shown to demonstrate the performance of method proposed.

12.4.1 Results for the First Scenario

This scenario was designed to show the performance of the proposed method when each constellation has the capability to derive positioning solutions even during partial blockage period. Figure 12.4 shows the number of satellites during the test period. Figure 12.5 shows the sky plot during the signal partial blockage period. It can be seen that the geometry of both Beidou and GPS are poor. This also demonstrates that the positioning errors are relatively big during the same period as shown in Figs. 12.6 and 12.7.

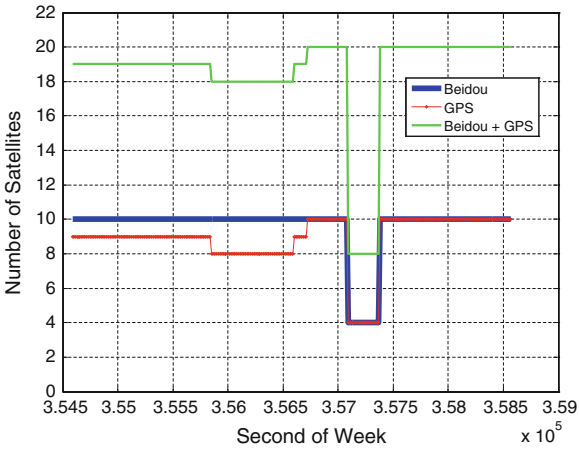

Fig. 12.4 Number of visible satellite

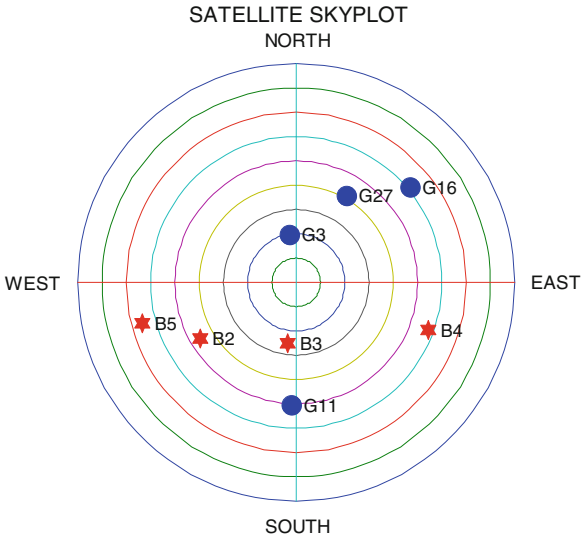

Fig. 12.5 Skyplot during blockage

In terms of integrity monitoring, Fig. 12.8 shows that even during the partial blockage period, the proposed algorithm still has the failure (or inconsistence of modelled GPS with Beidou) detection capability. Figure 12.9 shows the horizontal protection levels (HPL). The HPLs overbound the horizontal position error (in Fig. 12.8) all the time.

During the partial blockage period, the positioning accuracy was very poor. Neither Beidou nor GPS was able to performance integrity monitoring. The proposed method can improve the accuracy and be able to carry out integrity monitoring.

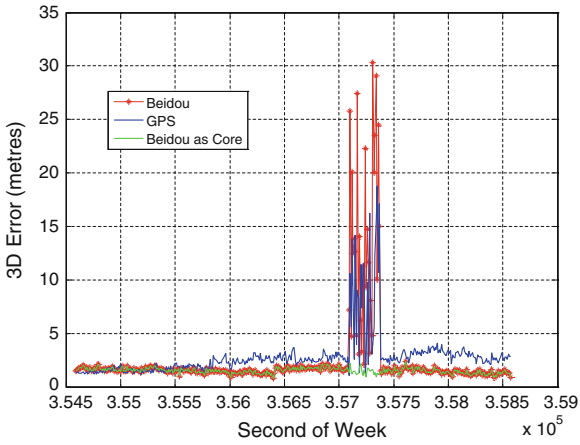

Fig. 12.6 3D positioning errors

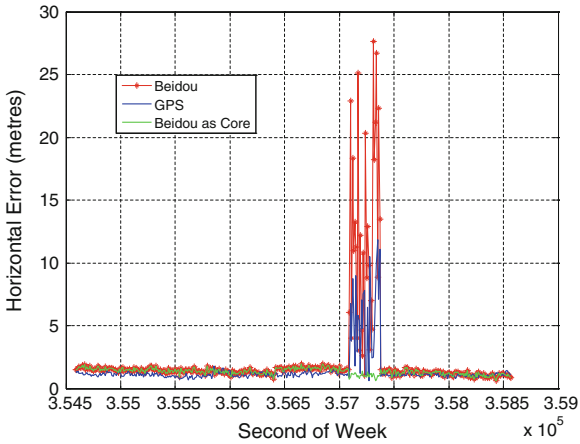

Fig. 12.7 Horizontal positioning errors

12.4.2 Results for the Second Scenario

This scenario was designed to show the performance of the proposed method when each constellation doesn't have the capability to derive positioning solutions during partial blockage period. Figure 12.10 shows the number of satellites during the test period. Figure 12.11 shows the sky plot during the signal partial blockage period. Figures 12.12 and 12.13 show the positioning error. During partial blockage period, the proposed method can still produce good solutions. In terms of integrity monitoring, Fig. 12.14 shows that the proposed algorithm still has the failure detection capability even during the partial blockage period. Figure 12.15 shows the horizontal protection levels (HPL). The HPLs overbound the horizontal position error (in Fig. 12.13) all the time.

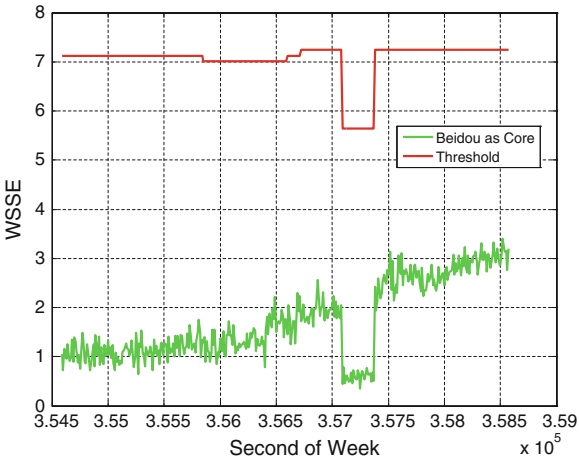

Fig. 12.8 Test statistics and thresholds

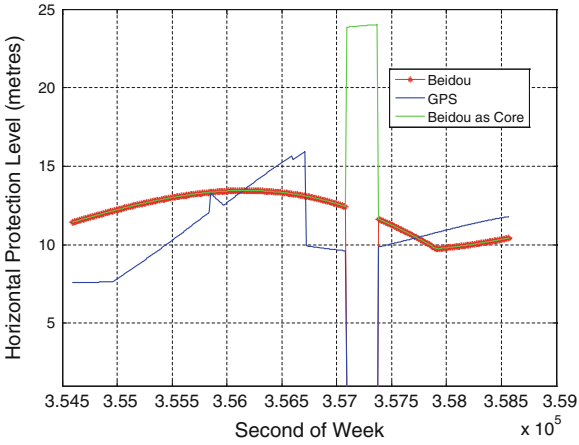

Fig. 12.9 Horizontal protection levels

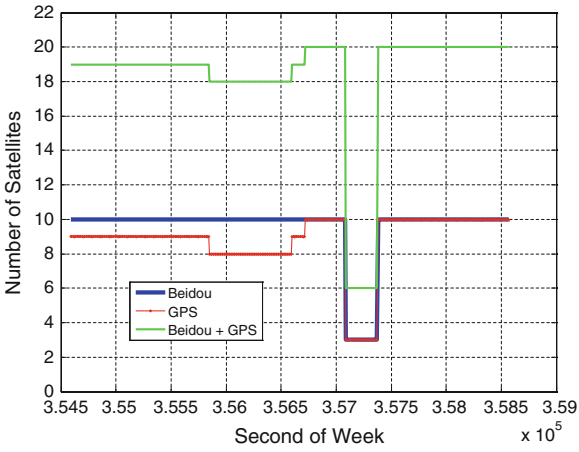

Fig. 12.10 Number of visible satellite

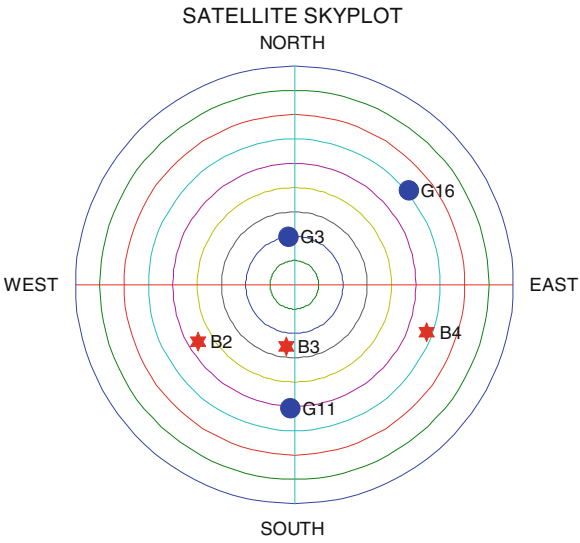

Fig. 12.11 Skyplot during blockage

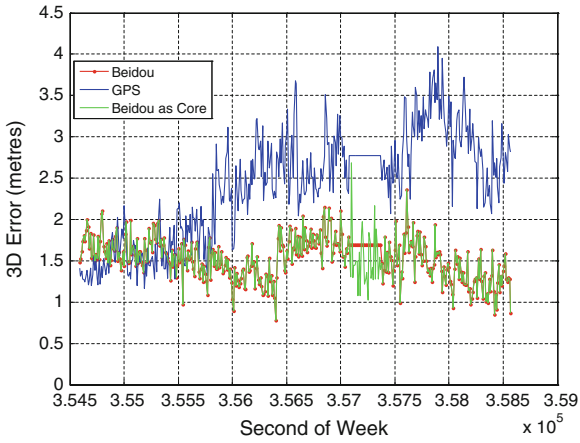

Fig. 12.12 3D positioning errors

During the partial blockage period, neither Beidou nor GPS was able to perform positioning and integrity monitoring. The proposed method can perform both positioning and integrity monitoring. What should be highlighted here is that the inconsistence of modelled GPS error with Beidou measurements is also taken into account. This prevents the unmonitored GPS measurements contaminating the overall solutions.

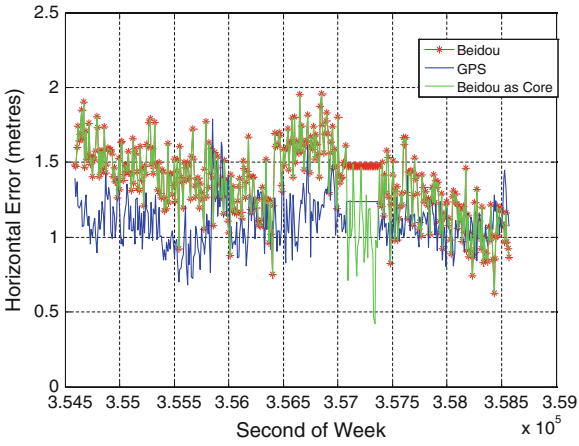

Fig. 12.13 Horizontal positioning errors

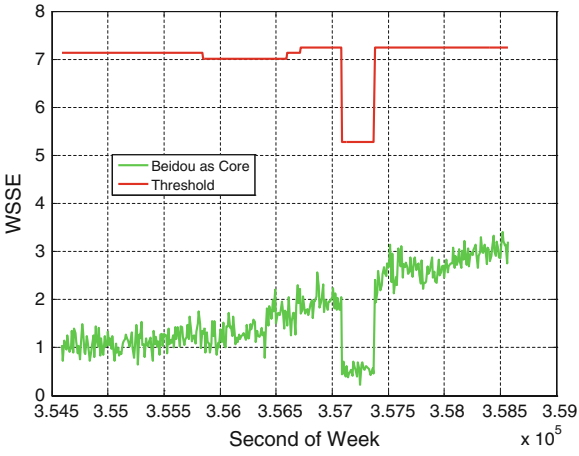

Fig. 12.14 Test statistics and thresholds

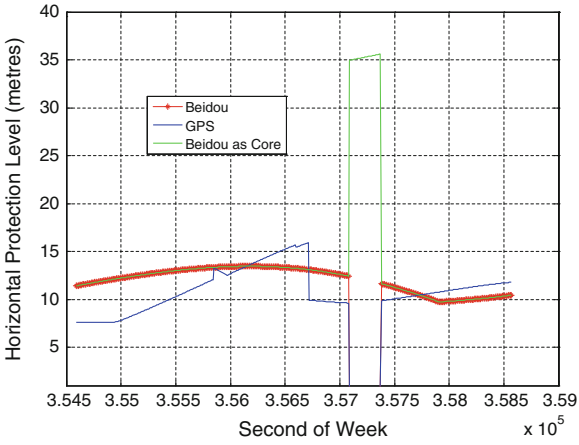

Fig. 12.15 Horizontal protection levels

12.5 Conclusions

Positioning solutions with a single constellation GNSS (e.g. GPS) have been widely used. The performance in terms of accuracy, continuity and integrity of these solutions is compromised in difficult environments such as city canyons. Multiple GNSS constellations provide more satellites, frequencies, message types, and better signal design and geometry. These will enable a multi-constellation receiver having the potential to support many more applications. There are also challenges including the best way to handle differences (e.g. system quality) and to maximum the benefits of multiple constellations. However, due to the interest of the owner of a GNSS, one constellation may be mandated. The mandated constellation is referred to as "core constellation". Its performance may be enhanced by independent systems.

The positioning solution is based on Beidou as core constellation together with RAIM when it has enough measurements. In the meantime, it models the residuals of all GPS measurements. In case there are a limited number of Beidou measurements, the GPS measurements are used together with the predicted correction using the residual model. Test results with real data have shown that the proposed method can achieve the best performance both with limited number and enough number of visible satellites. It has the potential to be used in applications where one constellation is mandated. It can achieve a better accuracy without losing continuity and integrity in relatively difficult environments. This paper takes Beidou and GPS constellations as an example to verify the Beidou based positioning and integrity monitoring method. The method can be extended to multiple constellations cases.

Acknowledgments This work was partially supported by the National Natural Science Foundation of China (NSFC: 61328301).

References

1. Lee YC (2006) New improved RAIM method based on the optimally weighted average solution (owas) under the assumption of a single fault. In: Proceedings of the institute of navigation national technical meeting (NTM), Monterey, CA, 18–20 Jan 2006
2. Lee YC et al (2005) GPS and Galileo with RAIM or WAAS for vertically guided approaches. In: Proceedings of the ION GNSS 2005, Long Beach, California, 13–16 Sept 2005
3. BeiDou-ICD, China Satellite Navigation Office, Dec 2013
4. Cai C, Gao Y (2009) A combined GPS/GLONASS navigation algorithm for use with limited satellite visibility. J Navig 62:671–685
5. Feng S, Milner C, Jokinen A, Ochieng W, Hide C, Moore T, Hill C, Ziebart M, Bahrami M, Groves P, Jiang Z (2011) A novel positioning and integrity monitoring algorithm for a multiple constellation receiver. In: Proceedings of the 24th international technical meeting of the satellite division of the institute of navigation (ION GNSS 2011), Portland, OR, Sept 2011, pp 2681–2688
6. Walter T, Enge P (1995) weighted RAIM for precision approach. In: Proceedings of the 8th international technical meeting of the satellite division of the institute of navigation (ION GPS 1995), Palm Springs, CA, Sept 1995, pp 1995–2004
7. Feng S, Ochieng WY, Walsh D Ioannides R (2006) A measurement domain receiver autonomous integrity monitoring algorithm. GPS Solutions 10(2):85–96

Chapter 13
A Novel RAIM Algorithm for Single-Frequency GNSS Receiver Based on Virtual Triple-Frequency Techniques

Leijin Han, Hu Lu, Yan Xie and Chen Chen

Abstract In GNSS era, how to effectively enhance the navigation signal integrity monitoring capacity by using multi-frequency information is becoming a hot topic and the mainstream of RAIM technique. Based on "virtual multi-frequency" ionosphere delay model, the paper proposed a novel virtual multi-frequency integrity monitoring algorithm for the single-frequency receiver, then presented a new prewhitening technique which was easily implemented in the receiver hardware when the measurement error covariance matrix was not diagonal. The simulation results showed that the "virtual multi-frequency" RAIM technique not only broke through the number limit of visible satellites of traditional RAIM algorithms, but also greatly enhanced the RAIM performance without changing the receiver hardware structure. And the researches of this paper may have a harmonious theoretical significance and practical value to the RAIM technique.

Keywords Virtual multi-frequency techniques · RAIM · Parity vector method · Global navigation satellite system (GNSS)

13.1 Introduction

The performance of the navigation satellite receiver is determined by users' location solving algorithm and integrity monitoring methods. The integrity monitoring technique is an indispensable part of the aircraft navigation system, meanwhile,

L. Han (✉) · H. Lu
Information and Navigation Institute, Air Force Engineering University, Xi'an 710077, China
e-mail: lei391@qq.com

Y. Xie
Mingde College, Northwestern Polytechnical University, Xi'an 710124, China

C. Chen
Troops 94778, PLA, Shanghai 200433, China

J. Sun et al. (eds.), *China Satellite Navigation Conference (CSNC) 2015 Proceedings: Volume II*, Lecture Notes in Electrical Engineering 341,
DOI 10.1007/978-3-662-46635-3_13

which is a measure metrics of capability for timely warning when the location and guidance information provided by satellite navigation terminal could not meet the requirements of flight activity. The new generation of global satellite navigation systems (GNSS) represented by BeiDou is developing to the globalization, multi-frequency signal, multi-system compatible interoperability direction [1–3]. As the appearance of novel technologies for improving receiver positioning performance, the location accuracy of terminal is becoming easy to meet the flight equipment, but the integrity monitoring technology of satellite navigation information for aerospace applications is developing relatively slowly. How to effectively improve the integrity monitoring capability of GNSS receiver to ensure the navigation information reliable is the main research background of this article.

The current receiver autonomous integrity monitoring algorithms (RAIM) was the "snapshot" methods mostly based on single-frequency signals, which included the least squares residuals method [4], parity vector method [5] and the pseudorange comparison method [6]. When five visible satellites were observed, this algorithms could detect the fault satellite, and it would identify the fault satellite when six visible satellites were observed. In addition, for the existing single-frequency "snapshot" RAIM algorithms, when the pseudorange deviation was small or slowly changing, the algorithms would have no ability to detecting and correcting errors [2, 3]. To solve these shortcomings currently, the main method was accumulating non-coherent integration of multi-epoch parity vector to improve the monitoring performance of the algorithm [7], but due to the accumulation of information from multiple epochs, the existing algorithm had a very long alarming time. It was difficult to meet the targets of aviation navigation systems, and this algorithm cannot work out the above problem in essential.

With the development of the global navigation satellite system (GNSS), the GNSS receiver will use multi-frequency signals to position and navigate in the future. Therefore, how to enhance the navigation signal integrity monitoring capacity by effectively using multi-frequency information is becoming a hot topic and the mainstream of RAIM development [8–10]. But the multi-frequency practical researches are relatively rare comparing to the single-frequency methods. New theories are urgently needed to develop. The multi-frequency RAIM algorithms given by conference [2, 3] were based on the algorithms of integrated navigation system, which performed integrity detection by using different frequencies in different systems. But the essence was still single-frequency integrity algorithm. The paper [9] fused redundant informations of different frequencies to the observation, proposing a multi-frequency RAIM method. However, the assumption that the noise of each frequency was independent did not comply with the real triple-frequency signals. Then the computational complexity of this algorithm is very large and difficult to accomplish in multi-frequency user receiver. Although the reference [10] giving a reasonable assumption for each frequency noise of the triple-frequency RAIM algorithm, but did not explain why triple-frequency algorithm could improve the system integrity, so the result of this paper needs to be further deepened.

Researches showed that different pseudorange of the same satellite was related to the ionosphere delay in the transmission [11]. However, this information had't been used in the existing receiver RAIM technologies [9, 10]. Therefore, this paper focused on: single-frequency GNSS receiver how to deduce the receiver "unused" frequency ionosphere delay by the ionosphere delay of known carrier frequency. Based on the "virtual" multi-frequency ionosphere delay model of single-frequency receiver, the paper proposed a novel virtual multi-frequency integrity monitoring technique for single-frequency receiver. Taking virtual triple-frequency for instance, the paper gave the detailed steps of the new algorithm. For the issues that measurement error covariance matrix is not diagonal, the paper propose a new method for pre-whitening which could easily implemented in a receiver. The results showed that the "virtual multi-frequency" RAIM method not only broke the traditional RAIM algorithms limit on the number of visible satellite, but also greatly enhanced the integrity performance of the receiver monitoring without changing the hardware structure of single-frequency receiver. The researches of this paper may have a harmonious theoretical significance and practical value to the RAIM technique.

The structure of this paper is as follows: the first section mainly introduced how to obtain and calculate the virtual triple-frequency ionosphere delay vector; the second section introduced virtual triple-frequency observation equations and the pre-whitening processing method, and this section also analysed the virtual triple-frequency RAIM fault detection and recognition algorithms; Finally the feasibility of the algorithm were verified by simulations.

13.2 Virtual Triple-Frequency Ionosphere Delay Model

GNSS dual-frequency receiver (assume L1 and L2 frequency) can directly determine the ionosphere delay by using dual-frequency measurements without any mathematical model [11]. If the pseudorange measurements on L1 and L2 carriers launched by the same satellite at the same time represent with ρ_1 and ρ_2, the pseudorange observation equations can be expressed as follows:

$$\rho_1 = r + \delta t_u - \delta t^{(s)} + I_1 + T + \varepsilon_{\rho_1} \tag{13.1}$$

$$\rho_2 = r + \delta t_u - \delta t^{(s)} + I_2 + T + \varepsilon_{\rho_2} \tag{13.2}$$

where r is the geometrical distance between satellite and receiver. δt_u and $\delta t^{(s)}$ are the receiver clock error and the satellite clock error. I_1 and I_2 are two frequencies ionosphere delay. Respectively, T is the tropospheric delay, and ε_{ρ_1} and ε_{ρ_2} are zero mean Gaussian measurement noise for the dual-frequency signals.

Due to the ionosphere delay for various frequency is different, ρ_1 and ρ_2 are also different. However, because of the difference between I_1 and I_2 is not obvious, the

difference between ρ_1 and ρ_2 is also not obvious. As is known that the ionosphere is a diffuse medium related to the electromagnetic wave frequency [11], and the geometric distance r, receiver clock error δt_u and satellite clock error $\delta t^{(s)}$ are public. If we don't consider the measurement noise, there are only the difference of ionospheric delay on right sides of the Eq. (13.1) and the Eq. (13.2).

Equation (13.1) minus Eq. (13.2):

$$\rho_1 - \rho_2 = I_1 - I_2 \tag{13.3}$$

With the relationship between the carrier frequency and the ionosphere delay [11], dual-frequency ionosphere delay can be represented as:

$$I_1 = 40.28\frac{N_e}{f_1^2} = \frac{\kappa}{f_1^2} \tag{13.4}$$

$$I_2 = 40.28\frac{N_e}{f_2^2} = \frac{\kappa}{f_2^2} \tag{13.5}$$

where, $\kappa = 40.28N_e$ is the ionosphere delay parameters. f_1 and f_2 are carrier frequencies. κ is defined as the ionosphere delay parameters. It can be obtained from the above equations:

$$I_1 \cdot f_1^2 = I_2 \cdot f_2^2 = \kappa \tag{13.6}$$

Brought the Eq. (13.6) into the Eq. (13.3):

$$\begin{aligned}\rho_1 - \rho_2 = I_1 - I_2 = I_1 - \frac{I_1 \cdot f_1^2}{f_2^2} = \frac{f_2^2 - f_1^2}{f_2^2} \cdot I_1 = I_1 - I_2 = \frac{I_2 \cdot f_2^2}{f_1^2} - I_2 \\ = \frac{f_2^2 - f_1^2}{f_1^2} \cdot I_2\end{aligned} \tag{13.7}$$

By Eq. (13.7) it can get:

$$I_1 = \frac{f_2^2}{f_2^2 - f_1^2}(\rho_1 - \rho_2) \tag{13.8}$$

$$I_2 = \frac{f_1^2}{f_2^2 - f_1^2}(\rho_1 - \rho_2) \tag{13.9}$$

So far, as long as getting L1 frequency ionosphere delay (see paper [11]), we can calculate L2 frequency ionosphere delay by Eqs. (13.8) and (13.9). This procedure is the core of the theory of virtual multi-frequency RAIM method.

In following, we will build a virtual multi-frequency RAIM ionosphere delay model.

For a single-frequency GNSS receiver (set to L1 frequency), the pseudorange measurements on L1 carrier launched by the same satellite represent with ρ_1. At the same time, assuming the receiver also can receive L2 and L5 frequencies pseudorange measurements represented by the ρ_2 and ρ_3, those can be get by:

$$\rho_1 = r + \delta t_u - \delta t^{(s)} + I_1 + T + \varepsilon_{\rho_1} \tag{13.10}$$

$$\rho_2 = r + \delta t_u - \delta t^{(s)} + I_2 + T + \varepsilon_{\rho_2} \tag{13.11}$$

$$\rho_3 = r + \delta t_u - \delta t^{(s)} + I_3 + T + \varepsilon_{\rho_3} \tag{13.12}$$

Refer to the Eq. (13.7), by Eqs. (13.10) and (13.12) it can get:

$$\begin{aligned}\rho_1 - \rho_3 = I_1 - I_3 = I_1 - \frac{I_1 \cdot f_1^2}{f_3^2} = \frac{f_3^2 - f_1^2}{f_3^2} \cdot I_1 = I_1 - I_3 = \frac{I_3 \cdot f_3^2}{f_1^2} - I_3 \\ = \frac{f_3^2 - f_1^2}{f_1^2} \cdot I_3\end{aligned} \tag{13.13}$$

By Eq. (13.13) it can get:

$$I_1 = \frac{f_3^2}{f_3^2 - f_1^2}(\rho_1 - \rho_3) \tag{13.14}$$

$$I_3 = \frac{f_1^2}{f_3^2 - f_1^2}(\rho_1 - \rho_3) \tag{13.15}$$

The single-frequency receiver can only receive L1 signal. After get the I_1 (see [11]) ionosphere delay, we can calculate the L2 frequency ionosphere delay I_2 by Eqs. (13.8), (13.9) and calculate the L5 ionosphere delay I_3 by Eqs. (13.14), (13.15).

Virtual triple-frequency signals are obtained by the above, the ionosphere delay models described as: $I = [\, I_1 \quad I_2 \quad I_3 \,]$.

13.3 Virtual Triple-Frequency RAIM Algorithm

13.3.1 Virtual Triple-Frequency Pseudorange Observation Model

The signals delay are different when various frequencies signal across the ionosphere. Here the paper introduce the ionosphere delay parameters (available from

the Eq. (13.6)). Assuming that the receiver can observe n visible satellites, then the virtual triple-frequency linear observation equations can be expressed:

$$\begin{bmatrix} y_1 \\ y_2 \\ y_3 \end{bmatrix} = \begin{bmatrix} H_{\mathrm{n}\times 4} & I_n \\ H_{\mathrm{n}\times 4} & c_1 I_n \\ H_{\mathrm{n}\times 4} & c_2 I_n \end{bmatrix} \cdot \begin{bmatrix} x_{TF} \\ f_1^{-2}\kappa_{\mathrm{n}\times 1} \end{bmatrix} + \begin{bmatrix} e_1 \\ e_2 \\ e_3 \end{bmatrix} \tag{13.16}$$

where y_1 is the N dimensional measurement vector for a traditional single-frequency RAIM algorithm (here set as L1 frequency). y_2 and y_3 are L2 and L5 signals which can get from Eqs. (13.7), (13.13) which are N dimensional measurement vector. $H_{\mathrm{n}\times 4}$ is single-frequency observation equation coefficient matrix, x_{TF} is 4 × 1 state vector represented the positioning deviation parameters and user clock bias deviation parameters; $\kappa_{\mathrm{n}\times 1}$ represents ionosphere delay parameters of n satellites (can be obtained from Eq. (13.6)); e_1, e_2 and e_3 are Gaussian noises vector with different covariance; $c_1 = f_1^2/f_2^2, c_2 = f_1^2/f_3^2$, f_1, f_2 and f_3 are the carrier frequencies for triple-frequency signals.

Briefly, Eq. (13.16) is depicted as:

$$y_{TF} = G_{TF} \cdot \tilde{x}_{TF} + e_{TF} \tag{13.17}$$

Further analysis shows that the measurement error vectors of the virtual triple-frequency observation Eq. (13.17) include the clock error, troposphere delay, multipath and receiver noise, etc. The user range error variance for (URE) is in follows:

$$\sigma_{URA}^2 = \sigma_{URA}^2 + \sigma_e^2 + \sigma_\varepsilon^2 \tag{13.18}$$

where σ_{URA}^2 is defined as the covariance of the user measure precision; σ_e^2 is the covariance of multipath and receiver noise; σ_ε^2 is the noise covariance of the clock error and tropospheric delay.

In traditional multi-frequency RAIM algorithm analysis, errors were independent of each other among different satellites. But in the virtual triple-frequency model, the calculating process using the same satellite clocks and ephemeris, therefore the clock error and tropospheric delay between the triple-frequency points of the same satellite is exactly the same (here again simplifies the complexity of the traditional multi-frequency RAIM algorithm). The multipath and receiver noise in different frequency of the same satellite should be independent of each other. But due to the other two frequency point information are completely virtual, we can identify multipath and receiver noise the same. As a results, the error covariance matrix of virtual triple-frequency observation equation can be defined as follows:

$$C_{TF} = E\left[e_{TF} e_{TF}^T\right] = \begin{bmatrix} \left(\sigma_e^2 + \sigma_\varepsilon^2\right) I_n & \sigma_\varepsilon^2 I_n & \sigma_\varepsilon^2 I_n \\ \sigma_\varepsilon^2 I_n & \left(\sigma_e^2 + \sigma_\varepsilon^2\right) I_n & \sigma_\varepsilon^2 I_n \\ \sigma_\varepsilon^2 I_n & \sigma_\varepsilon^2 I_n & \left(\sigma_e^2 + \sigma_\varepsilon^2\right) I_n \end{bmatrix}_{3n\times 3\mathrm{n}} \tag{13.19}$$

Due to C_{TF} is not a diagonal matrix, the originally parity vector method used for single-frequency signal cannot be used directly [11]. The observation equation needs pre-whiten processing to transform the $\tilde{e}_{TF}$ covariance matrix of the transformation to the diagonal matrix, which need to meet that diagonal elements are the same, namely each frequency noise are subject to the same distribution.

If C_{TF} is a symmetric matrix, then there will be an orthogonal array P, satisfying [11]:

$$P^{-1}C_{TF}P = P^{T}C_{TF}P = \lambda \tag{13.20}$$

The λ is the diagonal matrix whose diagonal elements are the eigenvalues of the C_{TF}. All the matrices of Eq. (13.20) are the 3n × 3n matrices.

$$P = \begin{bmatrix} -\frac{1}{\sqrt{2}}I_n & -\frac{1}{\sqrt{6}}I_n & \frac{1}{\sqrt{3}}I_n \\ \frac{1}{\sqrt{2}}I_n & -\frac{1}{\sqrt{6}}I_n & \frac{1}{\sqrt{3}}I_n \\ 0 & \frac{2}{\sqrt{6}}I_n & \frac{1}{\sqrt{3}}I_n \end{bmatrix}_{3n\times 3n} \tag{13.21}$$

$$\lambda = \begin{bmatrix} \sigma_e^2 I_n & 0 & 0 \\ 0 & \sigma_e^2 I_n & 0 \\ 0 & 0 & \left(\sigma_e^2 + 3\sigma_{\tilde{e}}^2\right)I_n \end{bmatrix}_{3n\times 3n} \tag{13.22}$$

Let's continue to transform the Eq. (13.22). Make the same covariance of the transformed noise vector so that it subject to the same normal distribution. The whitened virtual triple-frequency linearized observation equations is denoted as follows:

$$\tilde{y}_{TF} = \tilde{G}_{TF} \cdot \tilde{x}_{TF} + \tilde{e}_{TF} \tag{13.23}$$

where $\tilde{y}_{TF}$ is the 3n × 1 vector; $\tilde{G}_{TF}$ is a 3n × (n + 4) matrix; $\tilde{x}_{TF}$ is the (n + 4) × 1 vector; $\tilde{e}_{TF}$ is the 3n × 1 vector.

After the pre-whitening procedure, the measurement noise $\tilde{e}_{TF}$ will obey to the standard normal distribution. Therefore, it can use least squares residuals method [4], parity vector method [5] and pseudorange comparison method [6] and other traditional RAIM algorithm to the monitor integrity of receiver.

13.3.2 Fault Detection of Virtual Triple-Frequency RAIM Algorithm

There are 3n equations and (n + 4) unknown in virtual triple-frequency observation equation. Therefore the dimension of the generated parity space is (2n − 4).

The configured parity matrix is (2n − 4) × 3n matrix. The paper [5] pointed out that the parity space matrix must satisfy:

$$P_{TF}\tilde{G}_{TF} = 0 \tag{13.24}$$

$$P_{TF}P_{TF}^{T} = I_{2n-4} \tag{13.25}$$

For the $\tilde{G}_{TF}$ matrix is 3n × (n + 4) matrix, using QR decomposition method to solve parity matrix is rather complexed. The conference [10] gave a resolution.

$$P_{TF} = \begin{bmatrix} r_1 P_{(n-4)\times n} & r_2 P_{(n-4)\times n} & r_3 P_{(n-4)\times n} \\ d_1 I_n & d_2 I_n & d_3 I_n \end{bmatrix}_{(2n-4)\times 3n} \tag{13.26}$$

There: $P_{(n-4)\times n}$ is the single-frequency parity matrix. $r_1 = \frac{1}{\sqrt{1+\alpha^2+\beta^2}}, r_2 = \frac{\alpha}{\sqrt{1+\alpha^2+\beta^2}}, r_3 = \frac{\beta}{\sqrt{1+\alpha^2+\beta^2}}$, α and β are the following expressions: $\alpha = \frac{b(1+c_1-2c_2)}{a(1-c_1)}, \beta = \frac{a^2(c_1-1)^2+b^2(1+c_1-2c_2)^2}{ac(1-c_1)(1+c_1+c_2)}$. c_1 and c_2 have been given definitions in the observation equation. $d_1 = \frac{b(1+c_1-2c_2)}{\sqrt{a^2(c_1-1)^2+b^2(1+c_1-2c_2)^2}}, d_2 = \frac{a(c_1-1)}{\sqrt{a^2(c_1-1)^2+b^2(1+c_1-2c_2)^2}}$, $d_3 = 0$, After getting the virtual triple-frequency parity matrix P_{TF}, virtual triple-frequency parity vector can be represented as:

$$P_{TF} = P_{TF} \cdot \tilde{y}_{TF} = P_{TF} \cdot \tilde{e}_{TF} \tag{13.27}$$

The virtual triple-frequency parity vector P is (2n − 4) × 1 vector. The reference [5] pointed out that test statistics can be expressed by $SSE = P_{TF}^{T}P_{TF}$. Therefore, the SSE is $\chi^2(2n-4)$, where $\chi^2(v)$ represents the chi-square distribution with v degrees of freedom. According to the single-frequency parity vector method, it can determine the detection threshold T. SSE will be compared with a threshold T to judge whether the system is failed or not. In theory, as long as the number of visible satellites not less than 3 it could be used to identify the fault detection. Due to parity vector of the Eq. (13.26) is obtained by the QR decomposition, which limit the number of visible satellites cannot under five. Therefore as long as the number of satellites greater than four the receiver can be executed the RAIM algorithm in order to confirm the availability of current visible satellites before location.

13.3.3 Fault Detection of Virtual Triple-Frequency RAIM Algorithm

The virtual triple-frequency observation equations brought the spread of the ranging fault after the pre-whitening procedure. So we can't directly use the traditional identification methods to identify fault satellites. Equation (13.23) shows that the fault deviation spread as follows:

$$\tilde{e}_{TF} = W_{TF}^{T} \cdot (e+b) = \begin{bmatrix} -aI_n & -bI_n & cI_n \\ aI_n & -bI_n & cI_n \\ 0 & 2bI_n & cI_n \end{bmatrix}^{T}_{3n\times 3n} \cdot \begin{bmatrix} e_1+b_1 \\ e_2+b_2 \\ e_3+b_3 \end{bmatrix}_{3n\times 1} \tag{13.28}$$

where b_1 is the n dimensional column vector of L1 frequency fault offset. For the remaining two frequency data is virtual, we consider there is no fault deviation. That is, $b_2 = b_3 = 0_{n\times 1}$. In general, assuming that the failure occured on the first satellite, then:

$$W_{TF}^{T} \cdot b = \begin{bmatrix} -aI_n & -bI_n & cI_n \\ aI_n & -bI_n & cI_n \\ 0 & 2bI_n & cI_n \end{bmatrix}^{T}_{3n\times 3n} \cdot \begin{bmatrix} bias \\ 0_{(3n-1)\times 1} \end{bmatrix}_{3n\times 1} = \begin{bmatrix} (-a)\cdot bias \\ 0_{(n-1)\times 1} \\ (-b)\cdot bias \\ 0_{(n-1)\times 1} \\ c\cdot bias \\ 0_{(n-1)\times 1} \end{bmatrix}_{3n\times 1} \tag{13.29}$$

By formula (13.29), if the first satellite was failure, after pre-whitening process the deviation spread to the second and third frequency point in the satellite. So when identifying the fault, it can refer to the single-frequency parity vector method. Only detecting the three columns of virtual triple-frequency parity matrix at the same time, it can detect the fault by linear combine the three columns of the virtual triple-frequency parity matrix.

The virtual triple-frequency parity matrix is (2n − 4) × 3n matrix. The first n columns can identify the L1 frequency of satellite fault, and the remaining 2n columns can identify the satellite fault of L2 and L5 frequency points. According to the situations of the spread of the bias b, it can obtain the characteristic deviation vector that could recognize the satellite fault.

$$v_{1,i} = (-a)\cdot p_{1,i} - b\cdot p_{2,i} + c\cdot p_{3,i} \tag{13.30}$$

where $v_{1,i}$ is the (2n − 4) × 1 failure identification vector of the first frequency of ith satellite. $p_{1,i}$ is the ith column of virtual triple-frequency parity matrix. $p_{2,i}$ is the (n + i)th column of virtual triple-frequency parity matrix. $p_{3,i}$ is the (2n + i)th column of virtual triple-frequency parity matrix. For the virtual triple-frequency RAIM algorithm only consider the fault identification of single-frequency. Therefore, it can't consider for the fault identification of the other two frequency point.

Virtual triple-frequency parity vector p_{TF} can directly reflect the observation error information, which can be saw from Type (30) that observation error reflects on the three columns of the parity vector through the virtual triple-frequency parity matrix P_{TF}. The p_{TF} and the three columns of P_{TF} have inseparable relations, so we can identify the fault of the satellite by the geometric relationships between them.

Supposed that there were 4 visible satellites and a deviation bias on the first satellite. Ignoring the effects of observation noise, as is shown there is a bias in the type (29), the projection of the deviation can be expressed as follows:

$$\begin{bmatrix} p_{TF_1} \\ p_{TF_2} \\ p_{TF_3} \\ p_{TF_4} \end{bmatrix}_{4\times 1} = \begin{bmatrix} p_{1,1} & \cdots & p_{1,4} & p_{2,1} & \cdots & p_{2,4} & p_{3,1} & \cdots & p_{3,4} \end{bmatrix}_{4\times 12} \begin{bmatrix} (-a)\cdot bias \\ 0_{3\times 1} \\ (-b)\cdot bias \\ 0_{3\times 1} \\ c\cdot bias \\ 0_{3\times 1} \end{bmatrix}_{12\times 1}$$

$$= \begin{bmatrix} (-a)\cdot p_{1,1} & 0_{4\times 3} & (-b)\cdot p_{2,1} & 0_{4\times 3} & c\cdot p_{3,1} & 0_{4\times 3} \end{bmatrix}_{4\times 12} \cdot bias$$

$$= \begin{bmatrix} (-a)\cdot p_{TF_{1,1}} & 0_{1\times 3} & (-b)\cdot p_{TF_{1,5}} & 0_{1\times 3} & c\cdot p_{TF_{1,9}} & 0_{1\times 3} \\ (-a)\cdot p_{TF_{2,1}} & 0_{1\times 3} & (-b)\cdot p_{TF_{2,5}} & 0_{1\times 3} & c\cdot p_{TF_{2,9}} & 0_{1\times 3} \\ (-a)\cdot p_{TF_{3,1}} & 0_{1\times 3} & (-b)\cdot p_{TF_{3,5}} & 0_{1\times 3} & c\cdot p_{TF_{3,9}} & 0_{1\times 3} \\ (-a)\cdot p_{TF_{4,1}} & 0_{1\times 3} & (-b)\cdot p_{TF_{4,5}} & 0_{1\times 3} & c\cdot p_{TF_{4,9}} & 0_{1\times 3} \end{bmatrix}_{4\times 12} \cdot bias \tag{13.31}$$

where $P_{TF_{i,j}}$ is the ith row jth column elements of the virtual triple-frequency parity matrix. By type (30), the effect of the first satellite deviation caused by the parity vector will be located in the corresponding three columns on the parity matrix.

For the virtual triple-frequency RAIM algorithm, the rule of isolated failure satellite is—making the parity vector p_{TF} projection to the feature bias line $v_{1,i}$ then standardized treatment. The satellite which has the largest projection length is fault satellite.

If the equation $\frac{\left|p_{TF}^T \cdot v_{1,k}\right|}{\left|v_{1,k}\right|} = \max_{1\le i\le n}\left(\left|\frac{\left|p_{TF}^T \cdot v_{1,i}\right|}{\left|v_{1,i}\right|}\right|\right)$ is set up, we can identify that the fault satellite is the kth satellite which must be ruled out.

Due to virtual triple-frequency RAIM algorithm is fault identification algorithm based on single-frequency point, it doesn't need to consider which frequency point signal is wrong. The method simplifies the traditional multi-frequency RAIM recognition algorithm.

It brought the spread of the ranging fault due to pre-whitening process in the virtual triple-frequency observation equations. The previous sections have analyzed the fault diffusion in detail. When there is a fault satellite, triple-frequency parity vector as shown in type (27). $\tilde{e}_{TF}$ is 3n × 1 column. Because of the deviation diffusion after pre-whitening processing, it allows three elements of $\tilde{e}_{TF}$ to grow in deviation under the influence of the deviation bias and also lead to the modules of parity vector becomes larger. Reference [5] points out that test statistic *SSE* is virtually the modulus square of parity vector. The spread of the fault lead to *SSE* increases exponentially. Even if the pseudorange deviation is small, the *SSE* can also exceed the detection threshold T. So the virtual triple-frequency RAIM algorithm can still be executed when the pseudorange deviation is small; Secondly, the

extensive *SSE* makes the recognition rate and fault detection are better than single-frequency RAIM algorithm at each sampling instant, which can make up for the single-frequency RAIM algorithm of detecting low recognition rate.

13.4 Simulation Results

The simulation conditions:

Selecting the 24 satellites of GPS navigation system. Set the satellite elevation angle is 7.5°. Ionosphere parameters were calculated from the intermediate frequency of data which were received by the GNSS receiver (GNRF0302). Respectively, the frequency of the triple-frequency points as follows: $f_1 = 1575.42\,\text{MHz}$, $f_2 = 1227.60\,\text{MHz}$, $f_3 = 1176.45\,\text{MHz}$, Missing alarm rate set at 0.001. In general, assuming that the geographical position of user receiver is (116, 40, 500), trajectory is parallel to the equator orbit, the user is westward movement and the speed is 300 m/s. The trajectory as shown in Fig. (13.1).

The pseudorange error is shown in Table (13.1)

First of all, assumed that the geographical position of user receiver was (116, 40, 500). The data sampling time of receiver was 3600 s, sampling every 10 s at a time. The range error variance was set form −10 to 10 m. Step length was 1 m.

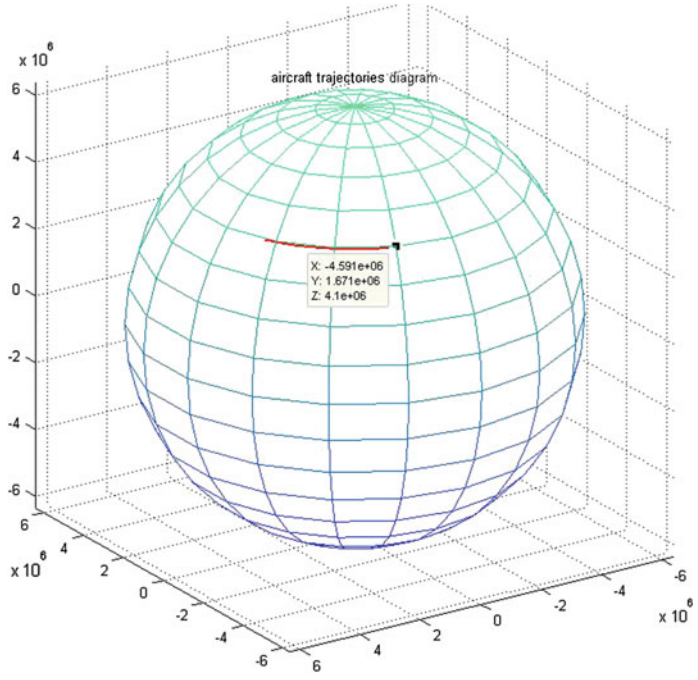

Fig. 13.1 Aircraft trajectories

Table 13.1 Pseudorange error table

Error sources	The standard deviation of error (m)
URA	1.0
Ionosphere delay	5.0
The troposphere delay	0.5
The clock error	2.0
Multipath and receiver noise	1.2

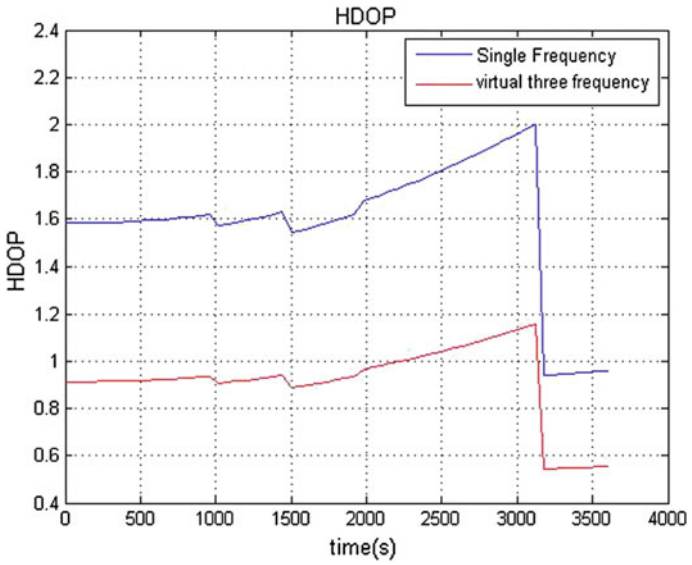

Fig. 13.2 HDOP comparison of two algorithms

Figure 13.2 is the HDOP comparison the single-frequency and virtual triple-frequency algorithm. Figure 13.2 shows that virtual triple-frequency HDOP value is smaller than single-frequency algorithm. This is because there are 3n virtual triple-frequency algorithm equations, equaling to 3n visible satellites to participate in the positioning solution.

In order to verify the performance of virtual triple-frequency RAIM algorithm in fault detection and identification, and analyze the performance compared with the traditional single-frequency RAIM algorithm and real triple-frequency RAIM algorithm, it set the first satellite the fault satellite and add 0–200 m bias to the satellite which deviation of step length is 1 m. Figure 13.3 shows the contrast figure of the fault detection results.

From the Fig. 13.3 can be seen that the satellite fault detection effect of two kinds of triple frequency RAIM algorithm is superior to single-frequency RAIM algorithm. When the deviation is greater than 40 m, the detection rate of single-frequency algorithm is gradually increasing, until to 100 % detection with the

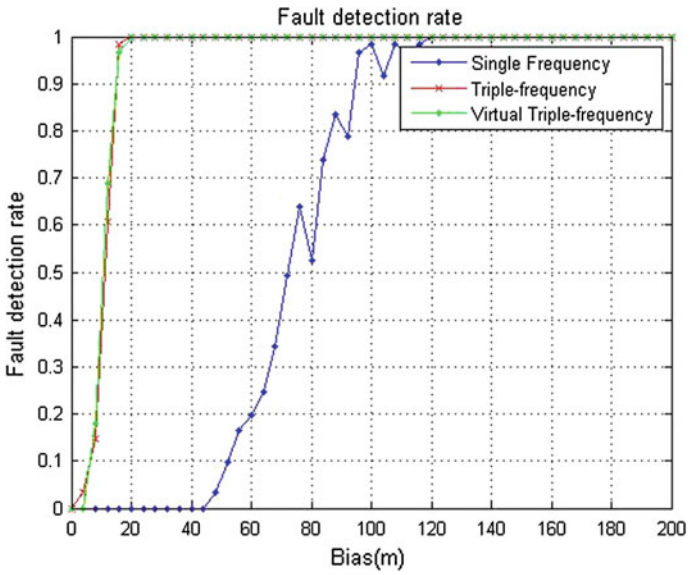

Fig. 13.3 Three contrast figure RAIM algorithm for fault detection

deviation of 120 m. When the deviation is less than 40 m, the detection rate is close to zero and the fault satellite can't been detected. However, for the triple-frequency and virtual triple-frequency RAIM algorithm, the detection rate can reach 50 % at the deviation of 10 m. Still deviation is higher than 17 m, it can detect the fault 100 %. In addition, the virtual triple-frequency RAIM algorithm of satellite fault detection results is similar with triple-frequency RAIM algorithm. The satellite fault detection performance of Virtual triple-frequency RAIM algorithm is the same as the real triple-frequency RAIM algorithm without any increase in frequency point information under the situation of excess.

The Fig. 13.4 shows three RAIM algorithm for identifying the fault satellite chart. It can be seen from the diagram, the single-frequency GPS RAIM algorithm for fault recognition effect is very poor. When the deviation increased to 200 m, the recognition rate was still less than 100 %. There is still a breakdown satellite at some point that can't be identified. There is no guarantee for the reliability of the receiver positioning results. When the deviation is small, recognition effect is not obvious, and when the deviation is less than 30 m, recognition rate is 0. While the other two RAIM algorithms have good effects. The recognition rate is 97 % at the deviation of up to 20 m, and it would reach 100 % when deviation is higher than 27 m. Identification performance of virtual triple-frequency RAIM algorithm and the real triple-frequency RAIM algorithm is better. But virtual triple-frequency RAIM algorithm doesn't need to be further identified which frequency point is wrong, so the calculation is more straightforward. Furthermore, the triple-frequency RAIM algorithm can not only identify the malfunctioned satellite, but also identify the wrong frequency of this satellite, so the alarm time is longer than virtual

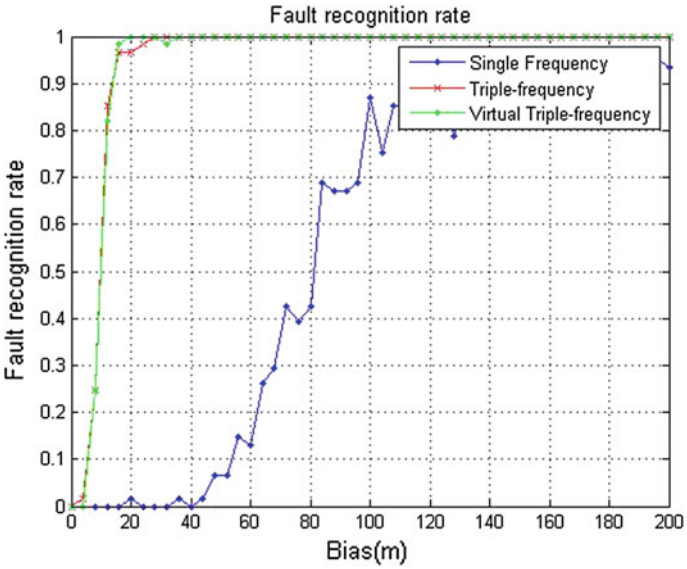

Fig. 13.4 The fault identification contrast figure of three kinds of RAIM algorithm

triple-frequency RAIM algorithm. In addition, in identifying the fault satellite, virtual triple-frequency RAIM algorithm only need to rule out the fault satellite, however the real triple-frequency RAIM algorithm at the moment need to further analysis the troubleshoot satellite or troubleshoot fault frequency in the satellite.

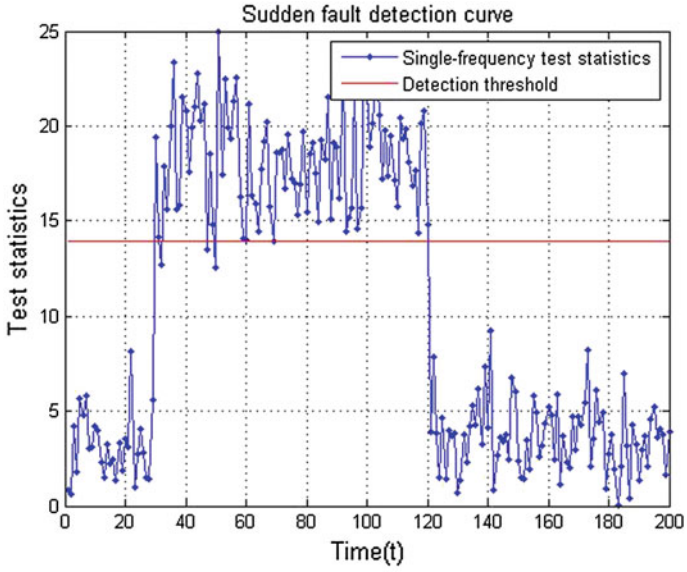

Fig. 13.5 Fault detection curve of a single-frequency unexpected accident (bias = 40 m)

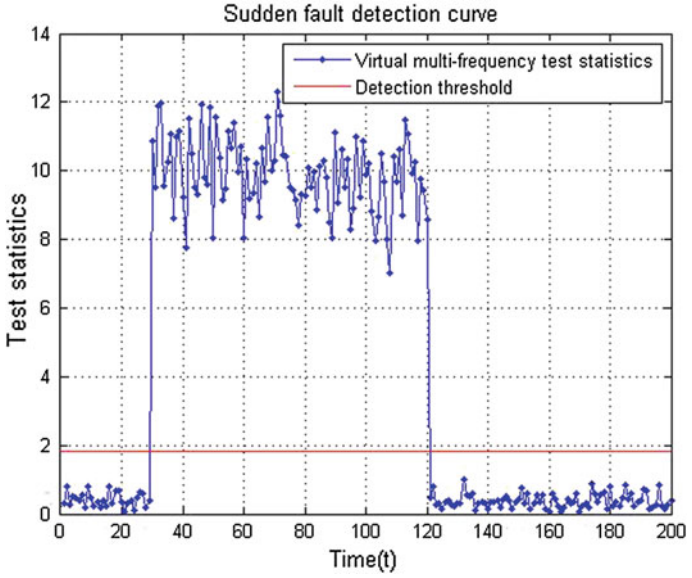

Fig. 13.6 Fault detection curve of a virtual triple-frequency unexpected accident (bias = 30 m)

Figure 13.5 shows the relationship between detection threshold and test statistics for the algorithm of single-frequency. When t = 30–120 s, the 40 m fault bias is applied to a satellite. As is shown in the figure that the statistics were smaller than the threshold at some points, and couldn't achieve 100 % to detect the fault.

Figure 13.6 shows the relationship graph between detection threshold and test statistics for the algorithm of Virtual triple-frequency. When t = 30–120 s, the 30 m fault bias is applied to a satellite. As is shown the statistics in a deviation is greater than detection threshold. In other times, the statistics are smaller than the threshold value.

13.5 Conclusion

Based on the theory of triple-frequency RAIM algorithm, without changing the hardware structure of single-frequency receiver, we generated the virtual triple-frequency ionosphere delay vector only using an ionosphere delay of single-frequency point I_1 through the analysis of satellite ionosphere delay between different frequency signals. Then virtual triple-frequency monitoring RAIM algorithm was given. The results showed that the "virtual multi-frequency" RAIM method not only beaked the traditional RAIM algorithms limit on the number of visible satellites, but also greatly enhanced the integrity performance of the receiver monitoring and positioning accuracy, which would have a promising theoretical

and practical value. At the same time, the research which may further promote the theory and technologies of navigation to maturity, the theoretical and practical values are very significant.

References

1. Hu L, Jie L (2010) Research on RAIM algorithm of beidou receiver. J Air Force Eng Univ 11(3):53–57
2. Lijun P, Kai J, Xiaojun D et al (2012) Receiver autonomous integrity monitoring parameter design and analysis for multi-constellation navigation. In: China satellite navigation conference (CSNC) 2012 proceedings. Springer Berlin Heidelberg, pp 15–27
3. Joerger M, Neale J, Pervan B et al (2010) Measurement error models and fault-detection algorithms for multi-constellation navigation systems. Position location and navigation symposium (PLANS), 2010 IEEE/ION. IEEE, pp 927–946
4. Parkinson B, Axelrad P (1988) Autonomous GPS integrity monitoring using the pseudorange residual. Navig J Inst Navig 35(2):255–274
5. Sturza M (1988–1989) Navigation system integrity monitoring using redundant measurements. Navig J Inst Navig 35(4):483–501
6. Lee Y (1986) Analysis of range and position comparison methods as a means to provide GPS integrity in the user receiver. ION AM 1986, Seattle, WA, USA
7. Hai S, Xinming H et al (2014) Research on the RAIM method based on non-coherent accumulation for tiny pseudo-range bias. J Astronaut 35(6):708–712
8. Xiaohao X, Chuansen Y, Ruihua L (2013) Review and prospect of GNSS receiver autonomous integrity monitoring. J Astronaut 34(3):451–463
9. Tsai Y, Chang F, Yang W (2004) Using multi-frequency for GPS positioning and receiver autonomous integrity monitoring. In: IEEE international conference on control applications, Taibei
10. Jing G, Mingquan L et al (2011) Research on RAIM algorithm for triple-frequency GNSS receiver. J Astronaut 32(8):1734–1739
11. Gang X (2011) Principles of GPS and receiver design. Publishing House of Electronics Industry, Beijing

Chapter 14
Evaluation Method Research on GNSS Signal-in-Space Continuity

Yang Tang and Rui Li

Abstract As a statistical measure of the frequencies of satellite navigation system performance loss, continuity is an important embodiment of satellite navigation system reliability evaluation. In fact, the continuity index is initially developed from the demand of civil aviation users and mainly focus on the service layer. The signal-in-space continuity concept is not clearly put forward in GPS SPS PS document until 2008, relevant standard system is not yet mature and there are few results of the study on GNSS signal-in-space continuity evaluation. So this paper first studies the relationship between signal-in-space continuity and service continuity through analyzing the development of continuity index. And further analyzes specific connotation of signal-in-space continuity from the basic concept, index system. Then this paper studies the evaluation method of signal-in-space continuity based on the principle of basic reliability, and takes GPS for example to statistic all the unscheduled outages happened from 1999 to 2013 and calculates the mean time between failure to evaluate GPS signal-in-space continuity. The result is consistent with the performance standard announced by the GPS SPS PS (2008), which verifies the rationality and validity of this method. The method of evaluating signal-in-space continuity proceeded in this paper is to provide theoretical reference for the test and evaluation of BDS performance.

Keywords GNSS · Signal-in-space · Continuity · Unscheduled outage

14.1 Introduction

The formation and development of Global Navigation Satellite System GNSS including GPS as well as China's BeiDou is promoting the rapid progress of its applications in various fields. Meanwhile, the requirements of users' application

Y. Tang (✉) · R. Li
School of Electronic and Information Engineering of Beihang University, Beijing, China
e-mail: heatun@163.com

J. Sun et al. (eds.), *China Satellite Navigation Conference (CSNC) 2015 Proceedings: Volume II*, Lecture Notes in Electrical Engineering 341,
DOI 10.1007/978-3-662-46635-3_14

also promote the research development of GNSS application performance. Incipiently, the integrity and continuity index were not taken into account. In essence, the application performance requirements of satellite navigation system in the civil aviation service led to the development of GNSS performance index, thus prompted the GNSS gradually to pay attention to integrity and continuity index. But originally the ICAO (International Civil Aviation Organization) focused on reliability of service, including integrity, continuity of service and availability. The signal-in-space continuity concept is not clearly put forward in GPS SPS PS (Global Positioning System Standard Positioning Service Performance Standard) document until 2008 and the related standard is not consummate. Also the research finding about signal-in-space continuity evaluation at home and abroad is very little.

Therefore, this article accounts for the essence of studying the signal-in-space continuity through analysing the development of continuity index, also analyzes the basic concept and standards of signal-in-space continuity and studies the evaluation method based on the principle of basic reliability. Then takes GPS for example, through measured data of nearly a decade to verify the correctness of the method. Mainly uses FAA (Federal Aviation Administration) failure report of every quarter to statistics mean time between failures, further analyzes GPS signal-in-space continuity, contrasting the result with GPS standard put forward by the GPS SPS PS to validate the effectiveness of the proposed method. Finally, this paper will provide theoretical references for the evaluation of BDS signal-in-space continuity.

14.2 Continuity Index Development Research

14.2.1 The Development of Continuity Index

Aviation demands for the performance of satellite navigation system has led to the development of GNSS performance index. As a system providing service to all customers within the airspace with continuous navigation service, the continuity often said of the satellite navigation system represents its ability of telling the user of system's normal and continuous work. But different users have different navigation performance requirements as well as definition of continuity, the concern level is also various.

At first, Aeronautical Telecommunications ANNEX 10 to the Convention on International Civil Aviation (Volume I) issued by ICAO illustrated the GNSS application performance requirements of civil aviation, including Accuracy, Integrity, Continuity of service and Availability. Also the performance standards for different phases of aircraft flight were presented. And the Continuity index was specifically referred as the Continuity of service, which is the capability of the system to perform its function without unscheduled interruptions during the intended operation.

But in the Appendix D of Aeronautical Telecommunications ANNEX 10 Volume I (2004), ICAO introduced aviation application performance for the main GNSS respectively at that time including GPS, GLONASS. Section 4.1 focused on the GPS and clearly pointed out that additional information about the GPS aviation application performance can be found in GPS SPS PS (2001) as well as the Interface Control Document (ICD)-GPS-200-c. This to some extent explains that the performance index of GNSS in the field of civil aviation is inseparable with the basic application service performance evaluation of concrete global satellite navigation system.

As for GPS, the US DoD (Department of Defense) successively presented four versions of the Standard Positioning Service Performance Standard document (US DoD, 1993, 1995, 2001, 2008) [2, 3]. Among them, the former 3 editions did not involve the concept of continuity, the latest version (2008) began to pay close attention to the continuity index and only provided the concepts and specific standards of signal-in-space (SIS) continuity. As a whole, the fourth edition of GPS SPS PS focused on SIS, which is also the obvious difference with the former 3 versions.

In a nutshell, the GNSS performance requirements in the aviation is more strict and comprehensive compared with other applications, so it almost leads GNSS performance development. For example, the GPS SPS PS released by U.S. DoD and FAA GPS measurement performance reports [4] mainly formulate the corresponding standards and analysis of the measured data based on the GNSS aviation applications performance requirements. Currently, GPS SPS PS documents basically dominate the satellite navigation system performance standards and the evaluation index system, which in fact becomes the GNSS performance evaluation standard.

14.2.2 The Analysis on Evolution of the Continuity of Service to SIS Continuity

Through the main official documents on the study of continuity index above, this paper argues that the reasons why GNSS focuses on SIS continuity mainly include the following two points:

A. Considering SIS performance is more direct and feasible for GNSS developers

According to the study of GNSS performance by ICAO, although it proposed the continuity of service standards for different typical civil aviation flight phase, it was in essence used as a starting point to derive GNSS signal-in-space performance requirements. Because for the developers or operation management departments of different satellite navigation systems including GPS as well as GLONASS, it is more direct to put forward the corresponding standards respectively according to

their own satellite navigation products to make their products meet the demand of the terminal application. After all, the continuity of service for GNSS terminal application involves many uncertain factors including aviation equipment as well as transmission environment, which can't be guaranteed by GNSS developers. However, they can ensure the concrete performance of the satellite from their own product and thus considering SIS is more direct.

B. SIS continuity determines continuity of service in part

GNSS service continuity requirements by ICAO focus on service interruption frequency. In fact, for GNSS, interruption caused by single satellite fault and limited DOP because of insufficient visible satellite both can lead to a service interruption. So this paper argues that the service continuity was mainly affected by SIS continuity and DOP availability. For example, GPS constellation design of redundancy guarantees the DOP availability to some extent, also the SIS continuity for single satellite ensures the interrupt probability triggered by a number of satellites' failure in the constellation is very small, thus ensure the service continuity of the whole system to meet specific application requirements. This is also the reason this paper argues why the GPS PS SPS (2008) did not mention the service continuity but SIS continuity and PDOP availability index were given.

Therefore, according to the above analysis and the latest research trends of the current GPS SPS PS, this paper mainly studies the GNSS SIS continuity.

14.3 GNSS SIS Continuity Evaluation Method Research

14.3.1 GNSS SIS Continuity

The GPS SPS PS (2008) pointed out that SIS continuity for a healthy SPS SIS is the probability that the SPS SIS will continue to be healthy without unscheduled interruption over a specified time interval. Also the document argued that the standard positioning service SIS continuity is directly related to the SIS reliability.

The SIS continuity for BeiDou system public service [3] refers to the probability of a public health service signal continuously work without occur unscheduled interrupt in the required period of time, which also means that SIS continuity is closely related to the unscheduled interrupt.

GPS SPS PS (2008) provided the performance standard of SPS SIS continuity, as shown in Table 14.1. Also, it points out that an interruption is defined as a period in which the SIS from a satellite does not comply with the standards defined in this SPS PS. Among which, unscheduled interruption mainly results from system malfunctions or maintenance occurring outside the scheduled period and will be announced to the Coast Guard and the FAA as soon as possible, it includes unscheduled failure interruption and unscheduled maintenance interruption.

Table 14.1 GPS SPS SIS continuity standards

SIS continuity standard	Conditions and constraints
Unscheduled Failure Interruptions: • ≥0.9998 probability over any hour of not losing the SPS SIS availability from a slot due to unscheduled interruption	• Calculated as an average over all slots in the 24-slot constellation, normalized annually • Given that the SPS SIS is available from the slot at the start of the hour
Unscheduled Maintenance Interruptions: • No performance specified	• A future version of this SPS PS may establish a standard

14.3.2 Evaluation Method Analysis Based on the Reliability Theory

Based on the connotation of SIS continuity for GPS and BDS, SIS continuity in essence reflects unscheduled interrupt frequency for every single satellite. To some extent, the probability of system continuous operation without continuity loss (or unscheduled interrupt) described by SIS continuity is equivalent to the probability of system reliable operation. Therefore, SIS continuity is another way to present the reliability of satellite navigation system, therefore this paper in turn analyzes SIS continuity evaluation method based on the principle of reliability.

From the elementary reliability theory, if one can assume a constant hazard rate (probability of failure) for a system over time, then the probability of reliable operation (no failure) of that system in any given hour is:

$$P(\text{No Failure/h}) = e^{-(1/MTBF)} \tag{14.1}$$

Given that the system was operating at the start of the hour and that no interruptions are planned during that hour. The MTBF is Mean Time Between Failure as the average failure time interval, in hours.

Continuity is essentially a certain reliability, thus specific assessment of corresponding continuity can be obtained depending on the type of fault reflected by MTBF. So on reference to the principle of reliability, SIS continuity can be characterized by Mean Time Between Unscheduled Outages (MTBUO):

$$P_{SIS\_Con} = e^{-(1/MTBUO)} \tag{14.2}$$

$$P_{SIS\_C\_risk} = 1 - e^{-(1/MTBUO)} \tag{14.3}$$

where, P_{SIS_Con} is for the SIS continuity probability, $P_{SIS\_C\_risk}$ is for SIS continuity risk probability.

In fact, this model characterizes unscheduled interruption frequency through MTBUO and further characterizes SIS continuity. The smaller the MTBUO is, the

more frequently the unscheduled interruption will occur, also the SIS continuity performance will be lower; Whereas the SIS continuity will be better.

14.4 The Verification by Statistics of Data

By the analysis above for SIS continuity evaluation model on the basis of reliability. The key for this method is to obtain MTBUO. However, to get MTBUO needs monitoring the long-term operational status of the GNSS. So this article uses the earliest actual operation GPS as analysis object and refers to corresponding standard in GPS SPS PS to verify the correctness and effectiveness of the proposed method.

14.4.1 Statistics of GPS MTBUO

As for GPS, MTBF for different types of fault provided by GPS SPS PS officially is just a rough value, can't reflect specific single satellite failure frequency. For the analysis of GPS SIS continuity, this paper statistics the actual mean time between unscheduled outages of each satellite for GPS. Mainly according to the GPS quarterly performance reports provided by FAA, this paper statistics all unscheduled interruption of per GPS satellite since 1999. But the basic fault reports mainly statistics satellite failure condition according to the satellite PRN number. For a specific single satellite, considering the status of changing satellites, this paper first statistics the corresponding SVN for each satellite PRN and the specific operation time since 1999. Part of the satellites did not occur unscheduled outages, and only one unscheduled interruption occurred for part of the satellites, as shown in Table 14.2.

Except for these satellites with no or just one unscheduled interruption, the distribution of MTBUO for other satellite is as follows in Fig. 14.1.

From the figure above, MTBUO approximately obeys the exponential distribution. On this basis, the paper statistics MTBUO for GPS satellites, with results shown as below in Fig. 14.2.

Table 14.2 GPS satellites of one unscheduled outage, 1999–2013

SVN	PRN	BLOCK	Unscheduled outage time
50	5	IIR-M	2009.9.5 22:28
67	6	IIF	2014.6.30 24:00
36	6	IIA	2006.6.29 11:05
17	17	IIR	2001.5.13 1:52
53	17	IIR-M	2007.9.15 12:50
18	18	IIR	2000.6.28 13:19
47	22	IIR	2006.1.8 19:31
60	23	IIR	2012.2.27 20:14

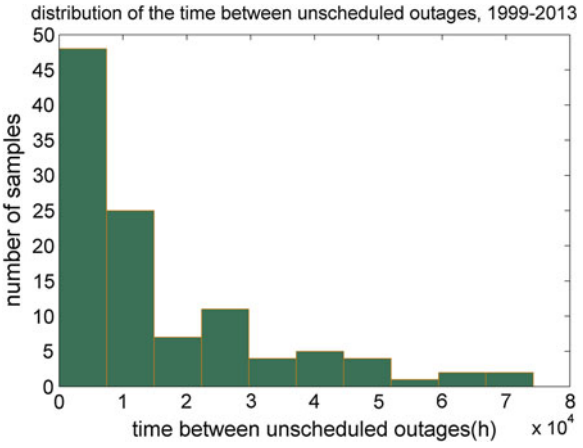

Fig. 14.1 Distribution of the time between unscheduled outages, 1999–2013

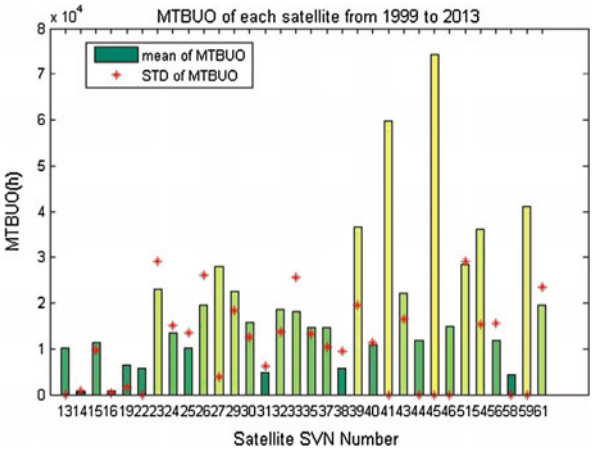

Fig. 14.2 MTBUO of GPS per satellite, 1999–2013

The figure shows that the MTBUO of BLOCK IIR\IIR-M satellite is bigger compared with the BLOCK II and IIA series. It is easy to understand, the SIS continuity is also improved with the launch and upgrade of GPS satellites. In addition to the SVN 41\45 satellites whose MTBUO is large (>50,000 h), the MTBUO for other satellites is of stationary distribution. On average, the mean MTBUO of BLOCK IIR\IIR-M satellites is 26590.85 h.

In addition, this paper statistics the GPS MTBUO of every year since 1999, shown as the following Fig. 14.3.

By above figure, the GPS MTBUO is basically at the trend of rising every year, which reflects that the system overall performance is in the continuous improvement.

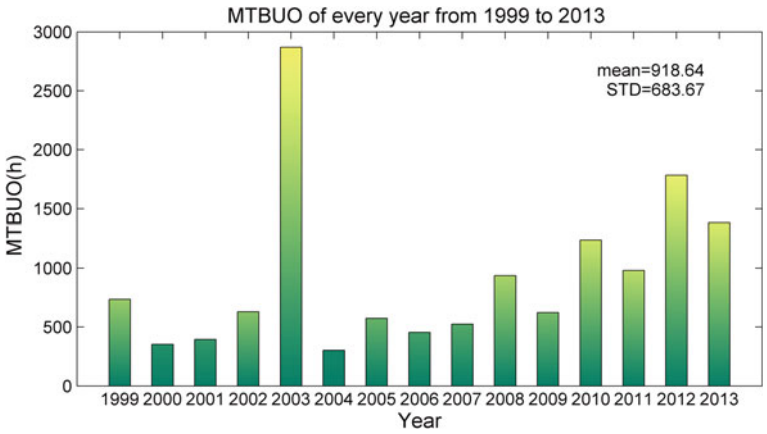

Fig. 14.3 MTBUO of every year for GPS, 1999–2013

14.4.2 SIS Continuity Analysis for Single Satellite

Based on the above evaluation model, this paper further researches GPS SIS continuity for each satellite using the measured average MTBUO, and the result is shown in Fig. 14.4.

As seen in Fig. 14.4, the probability of GPS satellite SIS continuity is not less than 0.9998/h except for the SVN 14 and SVN 16 which both belong to the retired

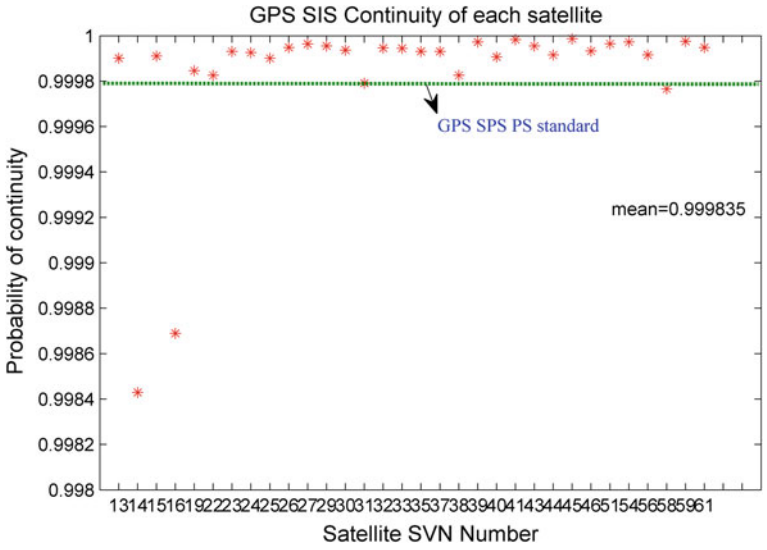

Fig. 14.4 SIS Continuity of GPS satellites, 1999–2013

BLOCK II. Therefore, the results comply with the SIS continuity standard given by GPS SPS PS (2008), which also proves the correctness and effectiveness of the evaluation method for GNSS SIS continuity discussed in this paper. And the average of SIS continuity for all the satellites in operation is 0.999938/h, far more than 0.9998/h.

In conclusion, the GNSS SIS continuity evaluation method based on the principle of reliability discussed in this paper is effective, expected to be applied to BDS SIS continuity analysis.

14.5 Conclusion

This article clarified the significance of the current study on GNSS SIS continuity through studying the evolution process of continuity index, further researched the definition and performance standards of GNSS SIS continuity. Then, studied SIS continuity evaluation model from the principle of reliability and analyzed GPS SIS continuity of each satellite according to the practical operation since 1999 based on the evaluation method. The results showed that the average GPS SIS continuity of each satellite is over 0.9999/h, consistent with the SIS continuity standards proposed by GPS SPS PS (2008), which verified the correctness and validity of this assessment method for GNSS SIS continuity expected to provide certain theoretical references for the evaluation and analysis of BDS SIS continuity.

Based on GNSS SIS continuity evaluation method research above which takes GPS as an example, this paper summarizes the following conclusions for BDS SIS continuity evaluation as a reference:

(1) The key of GNSS SIS continuity evaluation is to statistics all the unscheduled outages. For BDS, therefore, it is necessary to provide satellite failure reports periodically similar to GPS which is provided by FAA every quarter, listing all specific performance test of each satellite occured since launch to retirement.
(2) Improving GNSS SIS continuity is of great significance to promoting the reliability of the system. For BDS, the constellation layout is uneven and the redundancy is not so good as GPS. So in the case of DOP limited, to meet the demand of the service reliability of specific applications, improving the BDS SIS continuity is particularly important.

Acknowledgments The authors gratefully acknowledge the support of the National Basic Research Program of China (Grant No. 2010CB731805).

References

1. ICAO (1996) Aeronautical telecommunications ANNEX 10 to the convention on international civil aviation, 5th edn, vol I
2. U.S. Department of Defense (1993 and 1995) Global positioning system standard positioning service signal specification. Washington, DC
3. U.S. Department of Defense (2001 and 2008) Global positioning system standard positioning service performance standard. Washington, DC
4. Federal Aviation Administration (2013) Global positioning system (GPS) standard positioning service (SPS) performance analysis report. PAN#26–PAN#85
5. 中国卫星导航系统管理办公室. 北斗卫星导航系统公开服务性能规范 (2013)
6. Kovach K (1998) Continuity: the hardest GNSS requirement of All. In: Proceedings of ION-GPS-98, 2003–2019

Chapter 15
A New Method of Ionospheric Grid Correction Based on Improved Kriging

Qidong Zhang and Rui Li

Abstract Ionospheric delay is one of the main sources of GNSS positioning error. The single frequency user of WAAS calculates ionospheric delay corresponding to the satellite in sight as well as confidence bound with grid ionospheric correction. Currently, Kriging algorithm is adopted in WAAS to estimate GIVD and GIVE. However, only spatial correlation of samples is considered in conventional Kriging. And just IPP delays in current moment are applied in the algorithm. Since the limited IPP measurements information, the uncertainty of the estimated GIVD is high, that is the estimated GIVE is conservative. Under the condition of meeting the requirement of integrity, an accurate estimation of the uncertainty of GIVD to decrease the GIVE can increase the service availability of system. Therefore, this paper proposes an Improved Kriging algorithm which can provide more reasonable GIVE. The temporal and spatial correlations of IPP delays are considered, and IPP delays during update period are applied in the new algorithm. The simulation is made using ionospheric data collected from WAAS reference stations in this paper. Firstly, we analyze the estimation accuracy of the two Kriging algorithms. Then, we evaluate the estimation performances of the two Kriging algorithms. Finally, we use the two Kriging algorithms to correct user IPP delay with grid ionospheric correction. The results show that the two Kriging algorithms have basically the same ionospheric delay correction accuracy. And the GIVE provided by Improved Kriging is smaller. Consequently, the UIVE from Improved Kriging can bound the ionospheric delay correction error more tightly.

Keywords Ionospheric delay · Grid ionospheric correction · Kriging algorithm

Q. Zhang (✉) · R. Li
Beihang University, Beijing, China
e-mail: zqd10000@163.com

J. Sun et al. (eds.), *China Satellite Navigation Conference (CSNC) 2015 Proceedings: Volume II*, Lecture Notes in Electrical Engineering 341,
DOI 10.1007/978-3-662-46635-3_15

15.1 Introduction

Ionospheric delay is one of the main sources of Global Navigation Satellite System (GNSS) positioning error. It is an important factor of restricting the positioning accuracy of single-frequency user. The single-frequency user of Wide Area Augmentation System (WAAS) calculates ionospheric delays corresponding to the satellites in sight as well as confidence bounds with grid ionospheric correction. The basic principle of the grid ionospheric correction is that the ionosphere is equivalent to a fixed height of thin shell, and master station real-time collect ionospheric delay measurements from dual-frequency receivers of ground reference stations to estimate Grid Ionospheric Vertical Delay (GIVD) and Grid Ionospheric Vertical Delay Error (GIVE) and broadcast to user. According to the Ionospheric Pierce Point (IPP) location, user selects 3 or 4 grid points around the IPP to calculate the IPP ionospheric delay and confidence bound by bilinear interpolation.

Currently, Kriging algorithm is adopted in WAAS to estimate GIVD and GIVE. However, only spatial correlation of samples is considered in conventional Kriging. And just IPP delays in current moment are applied in the algorithm. Caused by the limited IPP measurements information used in the algorithm, the uncertainty of the estimated GIVD is high, that is the estimated GIVE is conservative. Under the condition of meeting the requirement of integrity, an accurate estimation of the uncertainty of GIVD to decrease the GIVE can increase the service availability of system. Therefore, this paper proposes an Improved Kriging algorithm which can estimate the uncertainty of GIVD more accurately.

The algorithm simulation is made using ionospheric data collected from WAAS reference stations in this paper. Firstly, we analyze the estimation accuracy of the two Kriging algorithms. Then, we evaluate the estimation performances of the two Kriging algorithms. Finally, we take Continuously Operational Reference Station (CORS) as user, and use the two Kriging algorithms to calculate user IPP delay and confidence bound with grid ionospheric correction, and compare the correction performances.

15.2 Ionospheric Delay Estimation

15.2.1 Kriging Algorithm

Kriging algorithm is a main research method in geostatistics, which is a Best Linear Unbiased Estimator (BLUE) based on the regionalized variable. There is need to estimate GIVD and GIVE of a number of fixed grid points in service area. Ionospheric vertical delay can be regarded as regionalized variable. Therefore Kriging algorithm is applicable to estimate ionospheric vertical delay.

15.2.1.1 Vertical Ionospheric Delay Model

Vertical ionospheric delay model can be expressed as the sum of the planar trend field and spatial random field [3]. Then the vertical ionospheric delay measurement is given by:

$$I_{meas}(x_k) = a_0 + a_1 x_k^{(north)} + a_2 x_k^{(east)} + r(x_k) + \varepsilon \tag{15.1}$$

where, the first three terms define the planar trend field, $r(x_k)$ is the spatial random field and ε is the measurement noise. After smoothing by carrier phase, the accuracy of vertical ionospheric delay measurement is close to the accuracy of carrier phase, so ε can be ignored.

15.2.1.2 Grid Ionospheric Vertical Delay Estimation

Assuming that there are n IPP measurements $I(x_1), I(x_2), \ldots, I(x_n)$ around the grid point x which is to be estimated, the ionospheric vertical delay estimation formula in x is:

$$\begin{aligned} GIVD = \hat{I}(x) &= \sum_{k=1}^{n} \lambda_k I(x_k) \ = \Lambda^T I \\ I = [I_1, I_2, \ldots, I_n]^T, &\quad \Lambda^T = [\lambda_1, \lambda_2, \ldots, \lambda_n] \end{aligned} \tag{15.2}$$

where, Λ is the Kriging coefficient to be estimated. According to the unbiased and minimum mean square error criterion, the estimation problem can be transformed into the following problem which is to seek optimal value:

$$\begin{cases} \text{Min } (\hat{\sigma}^2 = \Lambda^T C(\mathbf{h})\Lambda - 2\Lambda^T C(\mathbf{h_0}) + C(0)) \\ \text{s.t.} \quad G^T \Lambda = X \end{cases} \tag{15.3}$$

where, $\hat{\sigma}^2$ is the Kriging estimation variance, C is the covariance of $r(x_k)$, $\mathbf{h}$ is the distance matrix whose elements are distances among IPPs, $\mathbf{h_0}$ is the distance vector whose elements are distances between grid point x and IPPs. The definitions of G and X are the following:

$$G^T = \begin{bmatrix} 1 & 1 & \ldots & 1 \\ Lat_1 & Lat_2 & \ldots & Lat_n \\ Long_1 & Long_2 & \ldots & Long_n \end{bmatrix}, X = \begin{bmatrix} 1 \\ Lat \\ Long \end{bmatrix}$$

We can obtain the Kriging coefficient Λ using Lagrange Multiplier Method:

$$\begin{aligned} \Lambda &= (W - HG^T W)C(\mathbf{h_0}) + HX \\ H &= WG(G^T WG)^{-1}, W = C^{-1}(\mathbf{h}) \end{aligned} \tag{15.4}$$

We analyze the spatial correlation of $r(x_k)$ in vertical ionospheric delay model under nominal ionospheric condition using experimental variogram which is a tool used in geostatistics, and obtain the following exponential variogram model:

$$\gamma(h) = c\left(1 - e^{-\frac{h}{a}}\right) + v, \gamma(0) = 0 \tag{15.5}$$

The parameters are: $c = 0.9\,\mathrm{m}^2$, $a = 8000\,\mathrm{km}, v = 0.1\,\mathrm{m}^2$. We can further obtain the covariance function of $r(x_k)$ as follow:

$$C(h) = c + v - \gamma(h) = ce^{-\frac{h}{a}}, C(0) = c + v \tag{15.6}$$

From equations above, we can obtain the GIVD of the grid point.

15.2.1.3 Grid Ionospheric Vertical Delay Error Estimation

Affected by solar activities, the characteristics of ionosphere become irregular. It should be taken into account when estimating GIVE. According to the level of ionospheric irregularity, we can drive the GIVE at each IGP from an inflated value of the formal estimation error [4]. Ionospheric irregularity of IPP undersampled will not be considered in this paper. The GIVE can be obtained as follow:

$$GIVE = \kappa_{99.9\,\%}\sigma_{GIVE},\ \sigma^2_{GIVE} = R^2_{irreg}\hat{\sigma}^2_{IGP} \tag{15.7}$$

where, $\kappa_{99.9\,\%}$ is the quantile of 99.9 % confidence interval for the standard normal distribution, R^2_{irreg} is the inflation factor which is a function of chi-square statistics of IPP measurements. It indicates the level of ionospheric irregularity. The inflation factor can be obtained as follow:

$$R^2_{irreg} = \alpha_n I^T_{meas}(W - WG(G^T WG)^{-1}G^T W)I_{meas} \tag{15.8}$$

$$P = \frac{2}{\pi}\int_{\phi=0}^{\frac{\pi}{2}} \left(K^2\frac{\alpha_n}{\sin^2(\phi)} + 1\right)^{-\frac{n-3}{2}} d\phi \tag{15.9}$$

where, α_n is a function of n which is possible to compute a table off-line from Eq. (15.9). In Eq. (15.9), P which is set to 2.25×10^{-8} is the Probability of

Hazardously Misleading Information from ionospheric error and K which is 5.592 is the quantile corresponding to the P. A more thorough derivation can be found in the work of Blanch [1].

15.2.2 Improved Kriging Algorithm

Only spatial correlation of samples is considered in conventional Kriging which we have introduced above, and just IPP delays in current time are applied to estimate GIVD and GIVE. Since the limited IPP measurements information, uncertainty of the estimated GIVD is high, that is the estimated GIVE is conservative. Under the condition of meeting the requirement of integrity, an accurate estimation of the uncertainty of GIVD can increase the service availability of system.

IPP delay measurements during grid point information update period are applied to the new algorithm in this paper. Since extending the time dimension of IPP delays, the vertical ionospheric delay model in Eq. (15.1) is changed to:

$$I_{meas}(x_k, t) = a_0 + a_1 x_k^{(north)} + a_2 x_k^{(east)} + a_3 \Delta t + r(x_k, t) \tag{15.10}$$

where, $\Delta t = t_0 - t$, t is the observation time of IPPs which are used in the new algorithm, and t_0 is the reference time, that is the current update time. Measurement noise has been ignored. Noting the effect of Earth's rotation during update period, we need to convert the position of IPP during update period to the position of IPP in coordinate system of current update time. Then, G and X have changed to:

$$G^T = \begin{bmatrix} 1 & 1 & \ldots & 1 \\ Lat_1 & Lat_2 & \ldots & Lat_n \\ Long_1 & Long_2 & \ldots & Long_n \\ \Delta t_1 & \Delta t_2 & \ldots & \Delta t_n \end{bmatrix}, X = \begin{bmatrix} 1 \\ Lat \\ Long \\ 0 \end{bmatrix}$$

In addition, $r(x_k, t)$ is the temporal and spatial random field. We analyze the temporal and spatial correlation of $r(x_k, t)$ under nominal ionospheric condition using experimental variogram, and we use the following model to represent its covariance function:

$$C_{st}(h_s, h_t) = k_1 C_s(h_s) C_t(h_t) + k_2 C_s(h_s) + k_3 C_t(h_t) \tag{15.11}$$

or equivalently

$$\begin{aligned} \gamma_{st}(h_s, h_t) = {} & [k_2 + k_1 C_t(0)] \gamma_s(h_s) \\ & + [k_3 + k_1 C_s(0)] \gamma_t(h_t) - k_1 \gamma_s(h_s) \gamma_t(h_t) \end{aligned} \tag{15.12}$$

where, C_{st} is the space-time covariance function, C_t is the time covariance function, C_s is the space covariance function, γ_{st}, γ_t, γ_s are corresponding variogram respectively,and $C_{st}(0,0)$, $C_t(0)$, $C_s(0)$ are 'sills' corresponding to γ_{st}, γ_t, γ_s. We can obtain the model coefficients k_1, k_2, k_3 from the following equation, a more thorough derivation can be found in the work of Cesare et al. [2].

$$\begin{aligned} k_1 &= [C_s(0) + C_t(0) - C_{st}(0,0)]/C_s(0)C_t(0) \\ k_2 &= [C_{st}(0,0) - C_t(0)]/C_s(0) \\ k_3 &= [C_{st}(0,0) - C_s(0)]/C_t(0) \end{aligned} \tag{15.13}$$

We have obtained the space variogram model and covariance function in above. We use the same method to analyze the temporal correlation in this section and obtain the following exponential variogram model and covariance function:

$$\begin{aligned} \gamma_t(h_t) &= c_t\left(1 - e^{-\frac{h_t}{b}}\right) + v_t, \gamma_t(0) = 0 \\ C_t(h_t) &= c_t + v_t - \gamma_t(h_t) = c_t e^{-\frac{h_t}{b}}, C_t(0) = c_t + v_t \end{aligned} \tag{15.14}$$

The parameters are: $c_t = 0.9\,\mathrm{m}^2, b = 1800\,\mathrm{s}, v_t = 0.1\,\mathrm{m}^2$. For the $C_{st}(0,0)$, there is:

$$\lim_{h_s, h_t \to \infty} \gamma_{st}(h_s, h_t) = C_{st}(0,0) \tag{15.15}$$

It is easy to get $C_{st}(0,0)$ which is 1.5 m^2 using experimental variogram to estimate the convergence value when the space-time variogram tends to infinity. And we further obtain the model coefficients k_1, k_2, k_3 that all of them are 0.5. So far, we have obtained the space-time covariance function of $r(x_k, t)$, and apply it to the Improved Kriging algorithm.

In addition, the degree of freedom of vertical ionospheric delay model in Eq. (15.10) is 4, and the Eqs. (15.8), (15.9) shows that the α'_n belongs to Improved Kriging is equal to α_{n-1} belongs to conventional Kriging. The rest calculation procedure of Improved Kriging is the same as the conventional Kriging.

15.3 Algorithm Simulation and Results

The algorithm simulation is made using ionospheric measurement data collected from 26 WAAS reference station receivers and 8 CORS receivers in Fig. 15.1. The degree of elevation cut-off angle of the satellite as viewed from the receiver is set to 15. For conventional Kriging, the IPP selection parameters have the following values: $R_{\min} = 800\,\mathrm{km}$, $R_{\max} = 2000\,\mathrm{km}$, $\Delta R = 50\,\mathrm{km}$, $N_{\text{target}} = 30$ and $N_{\min} = 10$. That is we search for IPPs within a circular region centered upon the point to be estimated, whose radius is R which belongs to between $R_{\min}$ and $R_{\max}$. When the

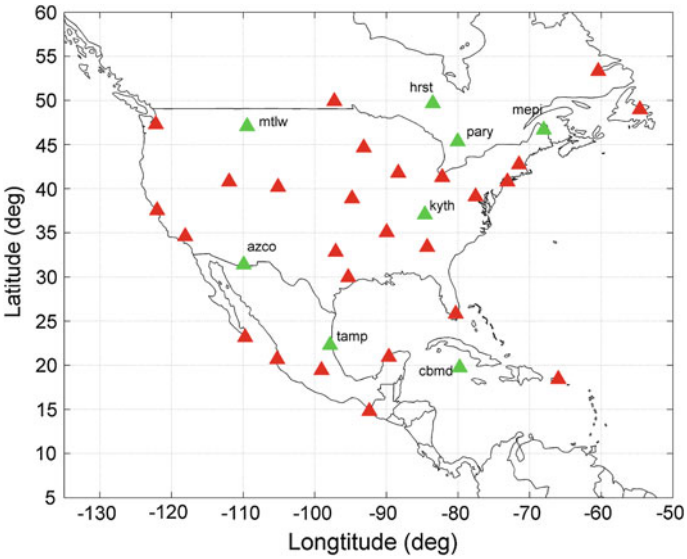

Fig. 15.1 26 WAAS reference station receivers and 8 CORS receivers (the *red triangles* represent WAAS receivers, the *green* represent CORS receivers)

number of IPPs is larger than or equal to N_{target}, we calculate the ionospheric delay and error. Otherwise, we expand the search radius by the step of ΔR until the condition above is met. When R is equal to $R_{\max}$, if the number of IPPs is larger than or equal to $N_{\min}$, we calculate the ionospheric delay and error. Otherwise, the algorithm is unavailable. Since the addition of IPP delay measurements during grid point information update period in Improved Kriging, the IPP selection parameters have changed to: $N_{\text{target}} = 200$, $N_{\min} = 50$, and others are unchanged.

15.3.1 Algorithm Estimation Accuracy Analysis

A productive way to analyze the estimation accuracy of algorithm is cross-validation. The specific procedures as follow: For each IPP measurement, we first leave it out temporarily and estimate the IPP delay with the remaining measurements, then put it back and repeat the above steps to estimate all IPP delays. We can obtain all of the estimation error of IPP delays.

We consider data from 3 days exhibiting different ionospheric conditions in 2014: a quiet day (16 January 2014), a day of moderate disturbance (10 February 2014) and a disturbed day (19 February 2014). The level of ionospheric disturbance is reflected by the two geomagnetic indices Dst and Kp. For 16 January 2014, 10 February 2014 and 19 February 2014, the Dst index dropped to 1.5, −17.6, and −92.6 nT, respectively, while the Kp index attained maxima of 1, 4, and 6.

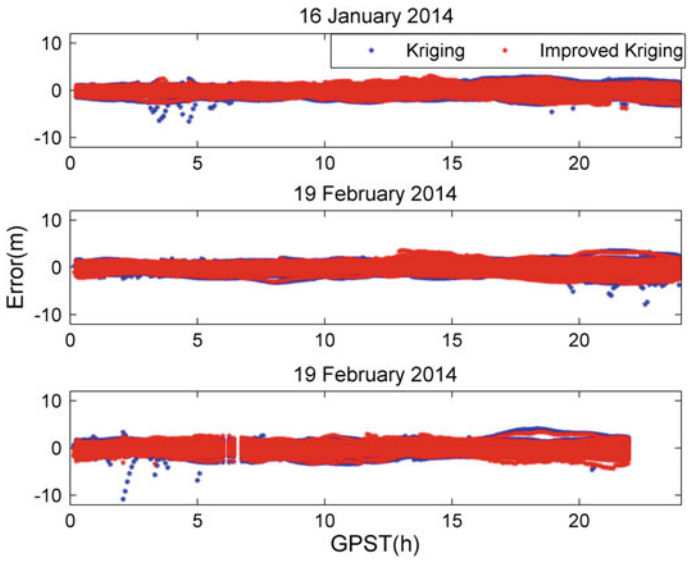

Fig. 15.2 Estimation error of IPP delays from conventional Kriging and Improved Kriging algorithms under different ionospheric conditions

Table 15.1 The maximum (x) and the root mean square (RMS) of the estimation error of IPP delays from Kriging and Improved Kriging algorithms under different ionospheric conditions

Date	Kriging		Improved Kriging	
	x (m)	RMS (m)	x (m)	RMS (m)
2014.1.16	6.572	0.634	3.782	0.602
2014.2.10	7.813	0.666	3.586	0.661
2014.2.19	10.811	0.709	4.308	0.704

Figure 15.2 displays the estimation error of IPP delays and Table 15.1 shows the statistical properties of them under different ionospheric conditions. The results indicate that the maximum of the estimation error of IPP delays from Improved Kriging is significantly less than the maximum from conventional Kriging. However, the root mean squares of IPP delays from the two Kriging are very close, that is the two Kriging algorithms have basically the same estimation accuracy overall.

15.3.2 Algorithm Estimation Performance Analysis

In order to evaluate the estimation performances of the two Kriging algorithms, the estimation standard deviations at the IGP provided by the two algorithms are compared. We take two time points of the GPS time in 10 February 2014, which are

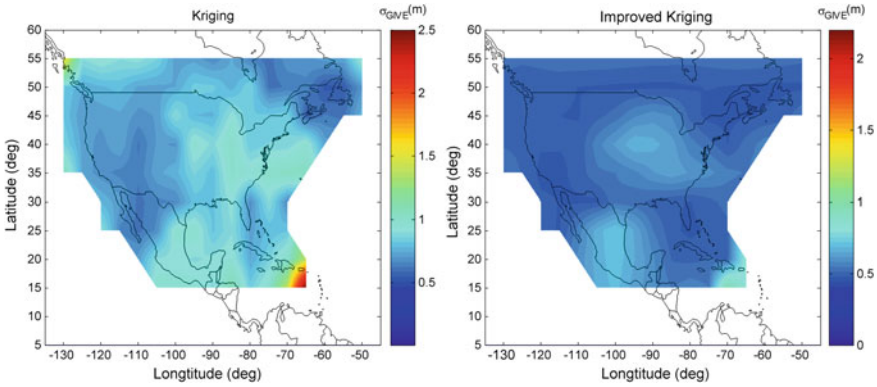

Fig. 15.3 Map of σ_{GIVE} provided by conventional Kriging and Improved Kriging at GPS time of 18,000 s in 10 February 2014

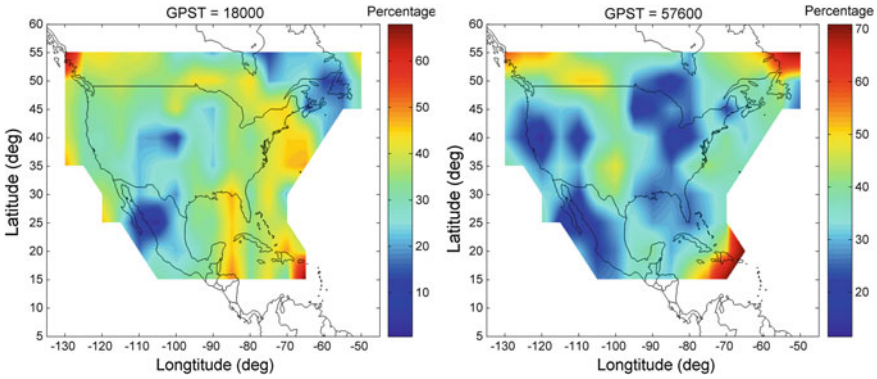

Fig. 15.4 Reduction in GIVE provided by Improved Kriging over the conventional Kriging at GPS time of 18,000 and 57,600 s in 10 February 2014

18,000 s at night and 57,600 s in the day to conduct the comparison [5]. In Fig. 15.3, the value between the IGPs is obtained by bilinear interpolation. Figure 15.4 shows the map of the percentage of reduction in GIVE provided by Improved Kriging over the conventional Kriging. The results indicate that almost all of the values of σ_{GIVE} provided by Improved Kriging are less than the values of σ_{GIVE} provided by conventional Kriging in the selected service area, and the percentage of reduction in GIVE provided by Improved Kriging over the conventional Kriging is more than 20 % in most areas under different time of 1 day.

15.3.3 User Grid Correction Analysis

We take 8 CORS receivers as users in Fig. 15.1 and use the two Kriging algorithms to calculate user IPP delay and confidence bound with grid ionospheric correction. The data sets which are used in Sect. 15.3.1 are used.

Figure 15.5 shows the results that we use two the Kriging algorithms to correct user IPP delay with grid ionospheric correction when KYTH and AZCO stations continuously track the GPS PRN 4 and PRN 8, respectively. The reduction in UIVE in Table 15.2 is the mean reduction percentage of the UIVEs from the location of all user IPPs in the whole day, which are from Improved Kriging over the conventional Kriging.

Figure 15.5 and Table 15.2 indicate that UIVEs from two Kriging can bound the ionospheric delay correction error with the probability of 99.9 % under different ionospheric conditions, and the RMSs of the correction errors are very close, that is the two Kriging algorithms have basically the same estimation accuracy overall. Moreover, UIVE from Improved Kriging can bound the user IPP delay correction error more tightly and the mean reduction percentage of the UIVE from Improved Kriging over the conventional Kriging is more than 30 % under different ionospheric conditions.

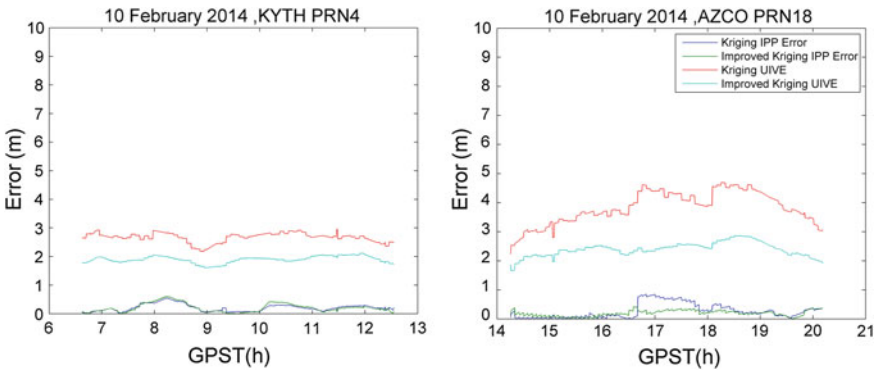

Fig. 15.5 Results of user ionospheric delay correction error and error bound from two Kriging algorithms

Table 15.2 The correction performance of the two Kriging algorithms

Date	Kriging		Improved Kriging		Reduction in UIVE (%)
	Error RMS (m)	UIVE bounding (%)	Error RMS (m)	UIVE bounding (%)	
2014.1.16	0.4748	100	0.5041	99.9945	30.85
2014.2.10	0.4894	100	0.5157	99.9293	32.98
2014.2.19	0.5211	99.9843	0.5256	99.9215	32.89

15.4 Conclusion

To solve the problem which the estimated GIVE provided by conventional Kriging is conservative, this paper proposes an Improved Kriging algorithm which can estimate the uncertainty of GIVD more accurately and obtain reasonable GIVE based on the conventional Kriging algorithm. Firstly, we analyze the estimation accuracy of the two Kriging algorithms. Then, we evaluate the estimation performances of the two Kriging algorithms. Finally, we use the two Kriging algorithms to calculate user IPP delay and confidence bound with grid ionospheric correction.

The results indicate that the Improved Kriging algorithm has basically the same estimation accuracy with conventional Kriging under different ionospheric conditions. Moreover, UIVEs from the two algorithms can bound the user ionospheric delay correction error with the probability of 99.9 %, and UIVE from Improved Kriging can bound the user IPP delay correction error more tightly and the mean reduction percentage of the UIVE from Improved Kriging over the conventional Kriging is more than 30 %. Therefore the Improved Kriging proposed in this paper can provide tighter ionospheric delay estimation error bound, and provide smaller protection level, and increase the service availability of system, and is important for engineering application of grid ionospheric correction.

Acknowledgments The work is supported by National 973 Project China (Grant No. 2010 CB731805).

References

1. Blanch J (2003) Using Kriging to bound satellite ranging errors due to the ionosphere. Stanford University, Stanford
2. Cesare LD, Myers DE, Posa D (2001) Estimating and modeling space-time correction structures. Stat Probab Lett 51(1):9–14
3. Sparks L, Blanch J, Pandya N (2011) Estimating ionospheric delay using Kriging: 1. Methodology. Radio science, RS0D21. doi:10.1029/2011RS004667
4. Sparks L, Blanch J, Pandya N (2011) Estimating ionospheric delay using Kriging: 2. Impact on satellite-based augmentation system availability. Radio science, RS0D22. doi:10.1029/2011RS004781
5. Wang S, Zhu B (2013) A new method to make ionospheric delay corrections in SBAS for GPS and compass dual constellations. In: Proceedings of ION GNSS+ 2013, Nashville, TN, 16–20 Sept 2013, pp 865–874

Chapter 16
A RAIM Method of Pseudo-range Residual Based on Positioning Result of Proportion of Visible Satellites

Jie Wu, Ao Peng and Jianghong Shi

Abstract The conventional receiver autonomous integrity monitoring (RAIM) algorithm of pseudo-range residual causes large residual error without a relatively accurate priori receiver position, which may lead to fault detection and identification. Therefore, measurements with gross errors may be used in positioning instead of high quality ones, especially when there are more than one measurement being distorted by gross errors. Meanwhile, the accuracy of the positioning result will be seriously deteriorated. In order to solve this problem, a new robust RAIM algorithm with positioning result based on the proportion of visible satellites is proposed in this paper. Using the proportion of visible satellites, the new algorithm produces a coarse position by the least squares method to calculate the pseudo-range residual. Accordingly, a robust approach to evaluate the accuracy of the coarse position based on the least median square (LMedS) is also proposed to make sure the position can meet the requirements of the following fault detection. In addition, the threshold mentioned in the new algorithm is derived theoretically. Finally, the performance of the new algorithm is good in simulations and real-data-tests, compared with conventional approaches. Results show that under the complicated scenarios the new algorithm can provide a considerable reduction of the probability of miss detection (7.89 % in this test), and improve the positioning accuracy remarkably.

Keywords RAIM · Priori receiver position · Pseudo-range residual · Fault detection and fault identification · Robust · LMedS · Proportion of visible satellites

J. Wu · A. Peng · J. Shi (✉)
Department of Communication Engineering, Xiamen University, Xiamen 361005, China
e-mail: shijh@xmu.edu.cn

J. Wu
e-mail: 371771085@qq.com

J. Sun et al. (eds.), *China Satellite Navigation Conference (CSNC) 2015 Proceedings: Volume II*, Lecture Notes in Electrical Engineering 341,
DOI 10.1007/978-3-662-46635-3_16

16.1 Introduction

Receiver Autonomous Integrity Monitoring (RAIM) is the ability to detect and identify the failures in GNSS by using measurements from receiver which needs more than 4 visible satellites to detect failures and more than 5 to identify failures. As far as we are concerned, the relative study of integrity is seldom in China.

Among the RAIM method, the "Snapshot" algorithm is most wildly used for it can realize the fault detection and identification only by the measurements of current scenarios. The typical "snapshot" algorithms are "comparison method" proposed by Lee [1], "Least Squares Residual Algorithm" proposed by Parkinson [2], and "parity Algorithm" proposed by Sturza [3]. Brown (1992) proved the equivalence of these methods [4]. These methods used receiver priori position to calculate pseudo-range residuals and detected fault based on those residuals. But the performance of conventional methods are not well enough, when there are multiple or large errors in the observation scenarios. With the development of various navigation systems, there is a sharp increase in the number of visible satellites. Accordingly, the probability of multiply gross measurements will increase. However, the conventional RAIM methods are difficult to meet the demands of the navigation system.

This paper firstly takes the Least Squares Residual Algorithm as an example to point out the drawbacks of conventional methods. In the conditional way, fault detection and fault identification may happen without the accurate receiver priori position information. Secondly, a robust RAIM algorithm with positioning result based on proportion of visible satellites is proposed, aiming at solving the problem. Finally, the performance of the proposed algorithm is evaluated by real-data-tests, compared with conventional approaches. Results show that under the complicated scenarios proposed algorithm can provide an obvious reduction of the probability of false exclusion and miss detection, and positioning accuracy is also remarkable improved.

16.2 Description of Least Squares Residual Algorithm

Measurement model of the conventional least squares pseudo-range residuals algorithm is given by [2]:

$$Z = HX + V \tag{16.1}$$

where "Z" represents the pseudo-range residuals, $Z = \rho - R - \delta_{t0}$

$$H = \begin{bmatrix} \frac{x_{S1} - x}{R_1} & \frac{y_{S1} - y}{R_1} & \frac{z_{S1} - z}{R_1} & -1 \\ \frac{x_{S2} - x}{R_2} & \frac{y_{S2} - y}{R_2} & \frac{z_{S2} - z}{R_2} & -1 \\ \vdots & \vdots & \vdots & \vdots \\ \frac{x_{SN} - x}{R_n} & \frac{y_{SN} - y}{R_n} & \frac{z_{SN} - z}{R_n} & -1 \end{bmatrix} \quad R_i = \sqrt{(\mathrm{x}_{si} - x)^2 + (\mathrm{y}_{si} - y)^2 + (\mathrm{z}_{si} - z)^2}$$

$\mathrm{X}_{Si} = (x_{si}, y_{si}, z_{si})$ represent satellite position, $\mathrm{X}_p = (x, y, z)^T$ represent receiver position. $\mathrm{X} = (\mathrm{dx}, \mathrm{dy}, \mathrm{dz}, \delta_t)$ is user's position and time bias. $V \in R^{\mathrm{n}\times 1}$ is noise vector, $V \sim N(0, \sigma^2)$. If there is error in measurements, $V + \delta$ is used [2].

And the least squares solution vector x is:

$$\hat{\mathrm{X}} = (\mathrm{H}^T\mathrm{H})^{-1}H^T \cdot Z \tag{16.2}$$

So pseudo-range residual:

$$Z_{\mathrm{w}} = Z - H\hat{\mathrm{X}} = [\mathrm{I} - H(\mathrm{H}^T\mathrm{H})^{-1}\mathrm{H}^T] \cdot Z = S_W \cdot Z \tag{16.3}$$

where the mapping matrix: $S_W = [\mathrm{I} - H(\mathrm{H}^T\mathrm{H})^{-1}\mathrm{H}^T]$.

Definition of pseudo-range residual sum of squares of each component is: $\mathrm{F} = Z_{\mathrm{w}}^T Z_w$. Whose mean value is zero, variance is σ^2. So F/σ^2 obeys the centralized chi-square (χ^2) distribution probability function. The degree of freedom of distribution probability function is $\mathrm{n} - 4$ [5].

And the test statistics for fault detection can be made as:

$$\gamma = \sqrt{F/(\mathrm{n} - 4)} \tag{16.4}$$

Fault detection conducted by comparing $\gamma = \sqrt{F/(\mathrm{n} - 4)}$ with the threshold, the fault happened when $\gamma > T_D$. After fault detection, the test statistics can be made as:

$$\mathrm{d}(\mathrm{i}) = Z_w(\mathrm{i})/\left(\sigma \cdot \sqrt{\mathrm{S}_w(\mathrm{i},\mathrm{i})}\right) \tag{16.5}$$

And then do the following assumptions [6]:

Not fault assumptions H_0: $E(\mathrm{d}) = 0$; then $\mathrm{d} \sim \mathrm{N}(0, 1)$
Faulty assumptions H_1: $E(\mathrm{d}) \neq 0$; then $\mathrm{d} \sim \mathrm{N}(\delta_i, 1)$

Using the maximum likelihood method to exclude fault of observations, and repeat fault detection and identification, until the statistical tests is less than the detection threshold [7]. The flow-process diagram can be seen as fellows.

16.3 Mathematic Model of Conventional RAIM's Problem

16.3.1 Problem in Conventional Methods

Figure 16.1 shows that the conventional RAIM method changes the pre-positioning pseudo-range residuals to post-positioning pseudo-range residuals by adjusting the bias of receiver position and offset of clock between satellite and receiver step by step. And in every step, the positioning result of last step will be used as priori receiver position to calculate pseudo-range residuals in this step.

$$Z_{\mathrm{w}} = Z - H\overset{\wedge}{\mathrm{X}} = \rho - R_p - \delta_{t0} + V_p \tag{16.6}$$

But the bias of receiver's priori position will pollute the whole pseudo-range residuals. (Figure 16.2 shows that an error of measurement is absorbed by all the pseudo-range residuals.) If the conventional method is used in the scene with great bias of priori position, then measurements with gross errors may be used in positioning while measurements with high quality being excluded [8].

A static mode test by single-frequency receiver has been conducted in the scene with multiple gross errors. Results show that in consecutive 840 s the false rejection rate is up to 17.5 %, and the probability of miss detection is 7.89 %. Table 16.1 is a group of measured data. In which, measurement of satellite 37, 38, 39, 40, 41 contains gross errors. It can be seen from Table 16.1 that conventional method excluded the satellites 5, 15, 30, 29, 10, 6, 34 improperly, while kept the satellites 38, 41 with gross error.

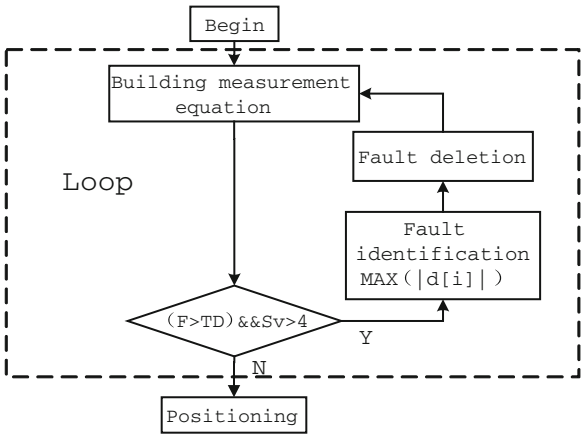

Fig. 16.1 Flow-process diagram of conventional approaches

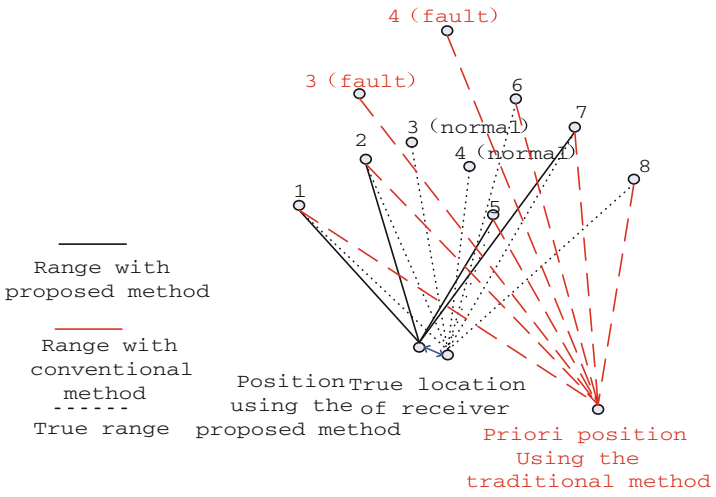

Fig. 16.2 The influence of priori position to range

Table 16.1 Measured data of fault elimination

Satellites number	Iterations	Z_W (m) 1	Z_W (m) 2	Z_W (m) 3	–	Z_W (m) 11	Fault satellites (Yes/no)
5		36645.3	−22765.1	−4755.5	–	Delete	No
15		113109.5	66675.3	25096.6	–	Delete	No
30		78802.1	86504.6	67284.8	–	Delete	No
29		82191.2	25993.8	15731.0	–	Delete	No
10		98030.8	100831.2	77222.9	–	Delete	No
6		180279.5	165527.4	97765.5	–	Delete	No
34		−253567.6	Delete	Delete	–	Delete	No
26		−21899.5	13635.5	−16013.1	–	4.5	No
2		16069.3	35729.1	16985.8	–	4.3	No
35		80937.5	56030.8	18315.5	–	−7.5	No
38		−34767.9	−34174.1	−16490.4	–	−11.7	Yes
41		38261.0	34.4	−573.3	–	11.5	Yes
40		−155826.3	−197063.1	Delete	–	Delete	Yes
37		123713.9	18060.3	−45988.4	–	Delete	Yes
39		−80475.5	−123499.4	−205411.9	–	Delete	Yes

16.3.2 Mathematic Model

It can be analysed theoretically that when the observation scene contains gross error, according to conventional methods, the measurement with gross error will be used to calculate receiver priori position. It can directly deteriorate the accuracy of

priori position. Thus, the estimate ranges between satellite and receiver will be all contaminated (Fig. 16.2). Further, pseudo-range residuals will also be polluted.

The receiver position (with the bias ε^T) can be express as:

$$\mathrm{X}_{p\varepsilon}^{T} = (\mathrm{x} + \varepsilon_x,\ \mathrm{y} + \varepsilon_y,\ \mathrm{z} + \varepsilon_z) = \mathrm{X}_{p}^{T} + \varepsilon^{T} \tag{16.7}$$

So,

$$R_{\varepsilon i} = \sqrt{(x_{Si} - x - \varepsilon_x)^2 + (y_{Si} - y - \varepsilon_y)^2 + (z_{Si} - z - \varepsilon_z)^2} \tag{16.8}$$

$$\begin{aligned} Z_{\mathrm{w}\varepsilon} &= \rho - R_{\varepsilon} - \delta_{t\varepsilon} + V_p \\ &= \rho - \delta_t + V_p - \sqrt{(x_{Si} - x - \varepsilon_x)^2 + (y_{Si} - y - \varepsilon_y)^2 + (z_{Si} - z - \varepsilon_z)^2} \end{aligned} \tag{16.9}$$

Taking one of measurements substituted into formula (16.9) to get the quadratic coefficient of Taylor:

$$\frac{\partial^2 z_i}{\partial \varepsilon_x^2} = \frac{(x_{si} - x - \varepsilon_x)^2 - (\rho - \delta_{t\varepsilon} - z_i)^2}{(\rho - \delta_{t\varepsilon} - z_i)^3} \tag{16.10}$$

Since the pseudo-range measurement is much greater than position bias, therefore, quadratic term can be ignored. So, only reserve the first items in Taylor expansion:

$$Z_i \approx \frac{\partial z_i}{\partial \varepsilon_x} \cdot \varepsilon_x + \frac{\partial z_i}{\partial \varepsilon_y} \cdot \varepsilon_y + \frac{\partial z_i}{\partial \varepsilon_z} \cdot \varepsilon_z \tag{16.11}$$

where, $\dfrac{\partial z_i}{\partial \varepsilon_x} = \dfrac{x_{si} - x - \varepsilon_x}{\rho - \delta_{t\varepsilon} - z_i + v_{pi}}$, $\dfrac{\partial z_i}{\partial \varepsilon_y} = \dfrac{y_{si} - y - \varepsilon_y}{\rho - \delta_{t\varepsilon} - z_i + v_{pi}}$, $\dfrac{\partial z_i}{\partial \varepsilon_z} = \dfrac{z_{si} - z - \varepsilon_z}{\rho - \delta_{t\varepsilon} - z_i + v_{pi}}$

Calculating the partial derivatives ε_x can obtain that:

$$\frac{\partial z_i}{\partial \varepsilon_x}(\rho - \delta_{t\varepsilon} - z_i + v_{pi}) - z_i \frac{\partial z_i}{\partial \varepsilon_x} \approx x_{si} - x - \varepsilon_x - \varepsilon_x \tag{16.12}$$

Then, it can be obtained that: $\partial z_i / \partial \varepsilon_x \approx \varepsilon_x / z_i$. Similarly $\partial z_i / \partial \varepsilon_y \approx \varepsilon_y / z_i$, $\partial z_i / \partial \varepsilon_z \approx \varepsilon_z / z_i$. Substituting it into Eq. (16.14) so $z_i \cdot z_i \approx \varepsilon_x \cdot \varepsilon_x + \varepsilon_y \cdot \varepsilon_y + \varepsilon_z \cdot \varepsilon_z$ it can be written as: $\sqrt{z_i \cdot z_i} \approx \sqrt{\varepsilon_x \cdot \varepsilon_x + \varepsilon_y \cdot \varepsilon_y + \varepsilon_z \cdot \varepsilon_z} = \sqrt{\varepsilon_x \cdot \varepsilon_x + \varepsilon_y \cdot \varepsilon_y + \varepsilon_z \cdot \varepsilon_z} + \mathrm{v}_i$. Where v_i present noise. Matrix form can be written as:

$$\sqrt{Z_{\mathrm{w}\varepsilon} \cdot Z_{\mathrm{w}\varepsilon}^{T}} = \sqrt{\varepsilon^T \varepsilon} + V \tag{16.13}$$

It can be known from Eq. (16.13) that an approximately proportional relationship between position bias and root-mean-square (rms) of pseudo-range residuals.

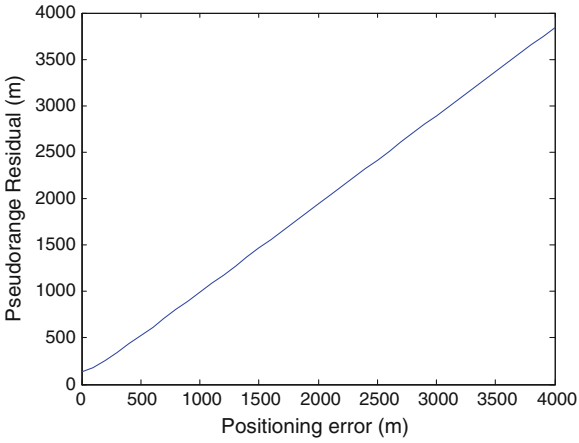

Fig. 16.3 Positioning error—pseudo-range residual

This paper calculated pseudo-range residuals by setting bias of receiver priori position manually under a continuously 800 s scene, result is shown in Fig. 16.3, and the ordinate takes the data from the average rms residual in 800 s. It can be seen that when the position bias is within 4000 m, the position bias and rms of pseudo-range residuals basically meet the linear relationship of formula (16.13).

It can be obtained from the analysis above that the bias of receiver priori position directly reflects pseudo-range residuals. So, if the pseudo-range residuals calculated with the current receiver position, the value of the pseudo-range residuals can be used to estimate the accuracy of receiver position.

16.4 The Method Based on Positioning Result of a Proportion of Visible Satellites

16.4.1 Description of the Method

Based on the analysis above, it can be seen that the key problem of the conventional least squares pseudo-range residuals method is that large error of receiver priori position information may lead to failure of fault detection and identification.

Given the problem above, a new RAIM algorithm based on the positioning results of proportion of visible satellite (without gross measurements) is proposed, firstly, this new method randomly selected a combination of small-scale visible satellites to calculate a coarse position, then using least median square (LMedS) method [9] to estimated the precision of the coarse position results (according to Eq. (16.13)) until the precision reach the demands of subsequent pseudo-range residuals computation, next calculated pseudo-range residuals with this coarse result. Finally, conducted fault detection, identification and exclusion with the calculated pseudo-range residuals.

The core algorithm's advantage of this new method is that, compared to conventional methods, this method used a receiver position with certain guarantee of accuracy to calculate the pseudo-range residual, thus ensured the accuracy of each satellite's pseudo-range residuals in the event of fault detection and identification. So the new method avoided the problem which occurred in conventional methods.

16.4.2 Procedure of the Method

16.4.2.1 Estimate the Accuracy of Coarse Positioning Result

It can be seen from Eq. (16.13) that $\sqrt{Z_{w\varepsilon} \cdot Z_{w\varepsilon}} = \sqrt{\varepsilon^T \varepsilon} + V$. The mathematical model shows the pseudo-range residuals directly reflect the accuracy of receiver position. Therefore, this proposed method can judge the value of pseudo-range residuals to estimate the accuracy of receiver position with the specific least median square (LMedS) method [9].

The specific process of the estimation will be described as follows.

First, a combination of four or five visible satellites should be generated, then solving the least squares solution by using the selected combination.

$$\tilde{X}_\varepsilon = (\tilde{H}_p^T \tilde{H}_p)^{-1} \tilde{H}_p^T \cdot Z \tag{16.14}$$

where $\tilde{X}_\varepsilon : (\tilde{x}_\varepsilon, \tilde{y}_\varepsilon, \tilde{z}_\varepsilon)$ represent the receiver position based on the selected combination and $\tilde{H}_p$ is design matrix of the selected combination.

And then calculate the PDOP value as follows.

$$PDOP = \sqrt{\mathrm{tr}\{(\tilde{H}_p^T \cdot \tilde{H}_p)^{-1}\}} \tag{16.15}$$

Pseudo-range residuals of all the visible satellites can be calculated by the Eq. (16.12): $\tilde{Z} = \rho - \tilde{R}_\varepsilon - \delta_{t0} + \tilde{V}$. The median of rms of all the visible satellites' pseudo-range residuals is made to be the test statistics $\tilde{r}$.

$$\tilde{r} = median\left(\sqrt{\tilde{Z} \cdot \tilde{Z}^T}\right) \tag{16.16}$$

And then do the following assumptions:

Not fault assumptions H_0: $E(\tilde{r}) = \bar{\varepsilon}_{ls}$, thus $r_i \sim N(\bar{\varepsilon}_{ls}, \sigma^2)$

Faulty assumptions H_1: $E(\tilde{r}) \neq \bar{\varepsilon}_{ls}$, thus $r_i \sim N(\bar{\varepsilon}_{ls} + \delta_i, \sigma^2)$

where $\bar{\varepsilon}_{ls}$ represents mean deviation of receiver position: $\sqrt{\varepsilon^T \varepsilon}$.

The detection threshold is sat by Neyman-Pearson criterion, namely: given false alarm rate, to keep the smallest miss alarm rate.

$$T_{ls} = \bar{\varepsilon}_{ls} + \mathrm{T}_{\sigma} \tag{16.17}$$

where T_{σ} represents the allowable biggest bias in a given alarm rate, so T_{σ} determined by the false alarm rate. And the value of $\bar{\varepsilon}_{ls}$ need to consider the positioning accuracy that least squares algorithm itself can achieve as well as the influence of pseudo-range measurement's errors.

The accuracy of least squares positioning were studied in Ref. [10], noting that elimination of atmospheric effects, the mean accuracy of horizontal positioning is about 20 m, the mean positioning accuracy of elevation is around 40 m [10], therefore, the overall accuracy ε_{ls} is about 45 m.

But the ionospheric delay and tropospheric delay is the main error sources of a good pseudo-range measurement, Ref. [11] pointed out that the value of ionospheric delay in 50–150 m, tropospheric delay value in 2.3–20 m, using the mathematical models can eliminate about 70 % of the ionospheric delay, and 90–95 % of the tropospheric delay [11], therefore, the remaining of ionospheric and tropospheric delay $\varepsilon_{i\&t}$ in 17–47 m.

PDOP value is defined by [12]: $PDOP = \sqrt{\varepsilon_x^2 + \varepsilon_y^2 + \varepsilon_z^2}/\varepsilon_{\rho r}$. So, the positioning accuracy which affected by the errors of pseudo-range measurement as follow:

$$D_p \approx \varepsilon_{i\&t} \cdot PDOP \tag{16.18}$$

Taking all this into consideration, a single point positioning accuracy of least squares method can be expressed as:

$$\bar{\varepsilon}_{ls} \approx \varepsilon_{ls} + D_p = \varepsilon_{ls} + \varepsilon_{i\&t} \cdot PDOP \tag{16.19}$$

The corresponding T_{σ} can be calculated by following formula.

$$P_r\left(\frac{\tilde{\mathrm{r}} - \bar{\varepsilon}_{ls}}{\sigma} > \mathrm{T}_{\sigma}\right) = 2\int_{\mathrm{T}_d}^{\infty} f_{N(0,1)}(\mathrm{x})\,\mathrm{dx} = P_{FA} \tag{16.20}$$

Figure 16.4 and Table 16.2 show the relationship between T_{σ} and false alarm rate P_{FA}.

Therefore, the specific threshold can be set as:

$$T_{ls} = \bar{\varepsilon}_{ls} + \mathrm{T}_{\sigma} = \varepsilon_{ls} + \varepsilon_{i\&t} \cdot PDOP + \mathrm{T}_{\sigma} \cdot \sigma \tag{16.21}$$

In addition, the study of PDOP factors show that when PDOP < 6, the linear equations of user's navigation and positioning system is benign. Namely, position

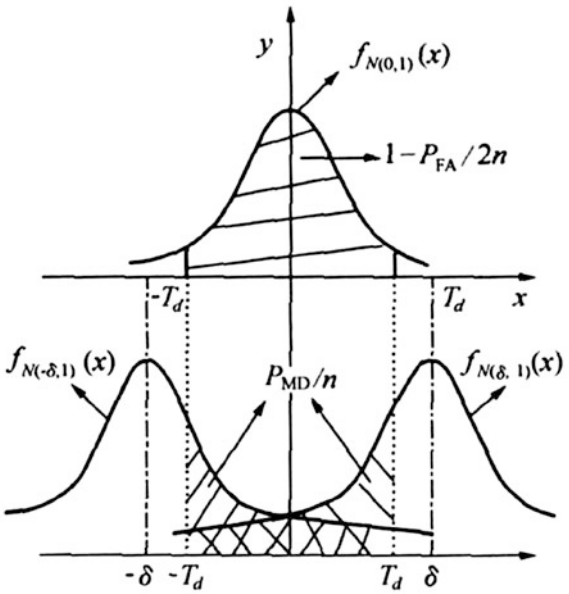

Fig. 16.4 Relationship between T_σ and P_{FA}

Table 16.2 The relationship between T_σ and P_{FA}

Visible satellite number (n)	T_σ 10–3	T_σ 10–5	T_σ 10–7	
6	3.765	4.790	5.644	–
7	3.803	4.821	5.670	–
8	3.836	4.848	5.693	–
9	3.865	4.871	5.713	–
–	–	–	–	–

error and measurement error satisfies the linear relationship [13]. Therefore, in order to guarantee the availability of positioning result, this method only uses the positioning result whose PDOP < 6.

16.4.2.2 Fault Detection and Exclusion

When the accuracy of the receiver position based on the proportion of visible satellite reach the demands of following fault detection, it will be used in pseudo-range residual calculation. And then compare the calculated pseudo-range residuals with the judgment threshold, if the pseudo-range residuals greater than the threshold it should be excluded, otherwise, it should participate in the final least-squares

positioning equation. Test statistic $\mathrm{r}_i = \sqrt{Z_{\mathrm{w}i}^2}$ constructed according to the mathematical model. And then do the following assumptions:

No fault assumptions, H_0: $E(\mathrm{r}_i) = \varepsilon_{pi}$ then $\mathrm{r}_i \sim \mathrm{N}(\varepsilon_{pi}, \sigma^2)$

Faulty assumptions, H_1: $E(\mathrm{r}_i) \neq \varepsilon_{pi}$ then $\mathrm{r}_i \sim \mathrm{N}(\varepsilon_{pi} + \delta_i, \sigma^2)$

In which ε_{pi} represents the average error of small-scale positioning result $\sqrt{\varepsilon^T \varepsilon}$, and mathematical model (16.18) shows that it is proportional relationship between the error of positioning result and pseudo-range residuals, therefore, this paper take the square root of sum of the squares of pseudo-range residuals which is less than the threshold T_{ls} to estimate the mean of the test statistic ε_{pi}. Then,

$\varepsilon_{pi} = \sqrt{\sum_{i=1}^{n} Z(\mathrm{i})^2 / n}$. And the threshold can be set:

$$T_d = \sqrt{\sum_{i=1}^{n} Z(\mathrm{i})^2 / n} + \mathrm{T}_\sigma \cdot \sigma \tag{16.22}$$

16.5 Performance

16.5.1 Comparison of Fault Detection

Table 16.3 is the result of fault detection of conventional method and proposed method under same false alarm rate.

16.5.2 Comparison of Positioning Accuracy

As can be seen above, the conventional method can't work well in complicated scenario while the proposed method can keep integrity availability all the time, and it can get a more effectively faults detection and higher positioning accuracy (Fig. 16.5 and Table 16.4).

Table 16.3 The comparison of fault detect

	Fault detection rate (%)	Miss detection rate
Conventional method	92.11	7.89 %
Proposed method	100.00	0

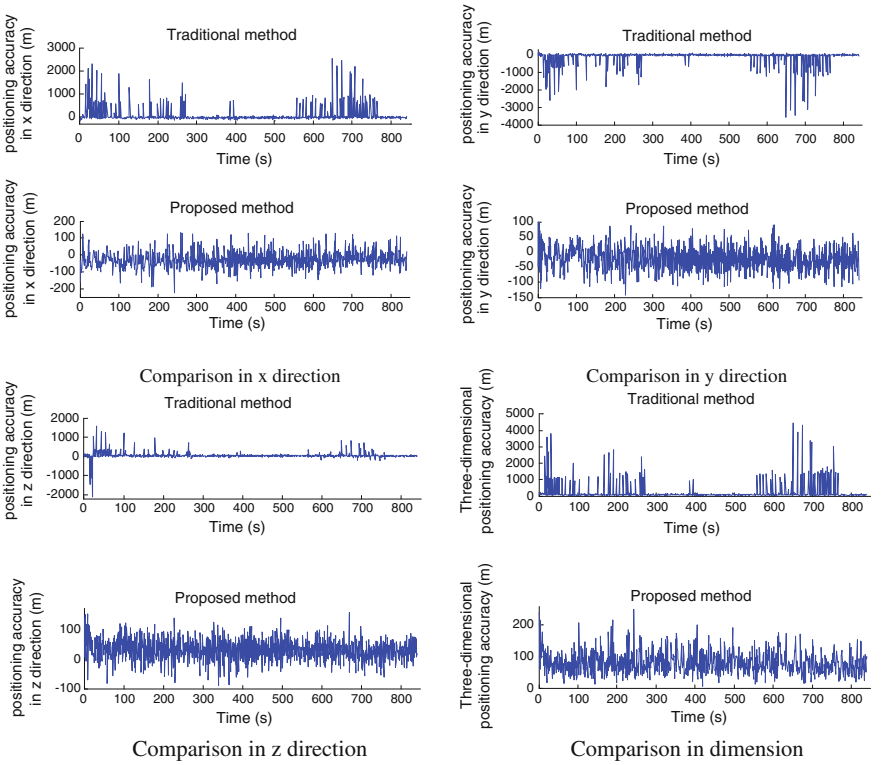

Fig. 16.5 The comparison of positioning accuracy

Table 16.4 The comparison of positioning accuracy

Positioning accuracy	Conventional method (m)			Proposed method (m)		
	Mean	Max deviation	>200 (%)	Mean	Max deviation	>200
x direction	134.04	2526.23	10.48	46.61	131.14	0.11 %
y direction	149.15	3558.63	10.48	33.99	120.69	0
z direction	76.47	2097.39	6.55	39.15	154.42	0
Dimension	230.22	4439.73	10.95	80.44	250.19	0.71 %

16.6 Conclusions

This paper firstly analyzed the conventional RAIM methods and then proposed a new method to overcome the drawbacks existing in these methods. Finally, the experimental results show that the proposed method, compared to conventional pseudo-range residual method, has a lower miss detection rate given the same false

alarm rate. Meanwhile, the adaptive detection threshold can enhance RAIM's presence availability and improve the positioning accuracy.

Acknowledgments This work was supported by the Xiamen Satellite Navigation R&D Test Base, funding number 3502Z20121010.

References

1. Lee YC (1986) Analysis of range and position comparison methods as a means to provide GPS integrity in the user receiver. In: Proceedings of the ION 42nd annual meeting
2. Parkinson BW, Axelrad P (1988) Autonomous GPS integrity monitoring using the pseudo-range residual. Navig J Inst Navig 35(2):255–274
3. Sturza MA (1988) Navigation system integrity monitoring using redundant measurements. Navigation 35(4):483–501
4. Brown RG (1992) A baseline GPS RAIM scheme and a note on the equivalence of three RAIM methods. J Inst Navig 39(3):301–316
5. Parkinson B, Spilker J, Axelrad P, Enge P (1996) Global positioning system: theory and applications. American Institute of Aeronautics and Astronautics, Washington
6. Yang C (2011) Research on receiver autonomous integrity monitoring theory in global navigation satellite system. In: Thesis for the degree of doctor of philosophy in Nanjing University of Aeronautics and Astronautics
7. Hawkins DM (1980) Identification of outliers. Chapman & Hall, London
8. Lu G (1991) Quality control for differential kinematic GPS positioning. In: M. Sc., Thesis, University of Calgary, Canada
9. Rousseeuw PJ, Leoy AM (2003) Robust regression and outlier detection. Wiley, New York
10. Cai C, Li Z, Zhang X (2002) Analysis of positioning accuracy of a single GPS receiver before and after removal of SA. J Geomat 27(3):24–25
11. Liu L, Ji Y, Sun X, Tan L (2013) The impact of ionosphere and troposphere to the positioning of single-frequency receiver. J Guilin Univ Electron Technol 33(3):196–199
12. Elliott D. Kaplan, Understanding GPS Principles and Applications. Artech House, Inc, 2002
13. Shuai P, Qu G (2006) Condition of satellite navigation positioning equation. J Spacecraft TT&C Technol 25(1):1–5

Chapter 17
Zenith Tropospheric Delay Modeling Method for Sparse Reference Station Network Considering Height Difference

Yang Yang, Guorong Yu, Shuguo Pan, Wang Gao and Weirong Chen

Abstract A new method of zenith tropospheric delay modeling (HTIM) for sparse reference station network is put forward in this paper. The zenith tropospheric hydrostatic delay (ZHD) is calculated by the UNB3m model. In addition, the zenith tropospheric wet delay (ZWD) with high precision is estimated by conventional precise point positioning (PPP) using ionosphere-free combination. Considering the relationship between height factor and zenith tropospheric delay (ZTD) in UNB3m model, the zenith tropospheric delay is divided into two parts, the height weakly correlated and the height strongly correlated. The new method of zenith tropospheric delay modeling is established using the two parts of the zenith tropospheric delay. Based on the results of regional modeling, the zenith tropospheric delay of rover station is augmented. The new method is compared with conventional modeling methods. The results show that the new zenith tropospheric delay modeling method is superior to other methods in the undulated region only using four reference stations, RMS is 0.020 m and the absolute deviation is nearly within 0.03 m. It also shows that the RMS is 0.008 m and the rate of absolute deviation within 0.01 m reaches 75.95 % in the sparse reference station network. In the new method, the interpolation precision is not limited by the number of reference stations and three reference stations also can be used to get the interpolation results with high reliability. The results show that the new zenith tropospheric delay modeling method is superior to conventional methods, especially for the undulated region in a sparse reference station network.

Keywords Sparse reference station · Zenith tropospheric delay · Height difference · PPP

Y. Yang (✉) · G. Yu · W. Gao · W. Chen
School of Transportation, Southeast University, Sipailou 2#,
Nanjing 210096, Jiangsu, China
e-mail: johnny2014@sina.com

S. Pan
School of Instrument Science and Engineering, Southeast University, Nanjing, China

J. Sun et al. (eds.), *China Satellite Navigation Conference (CSNC) 2015 Proceedings: Volume II*, Lecture Notes in Electrical Engineering 341,
DOI 10.1007/978-3-662-46635-3_17

17.1 Introduction

Using the GNSS (Global Navigation Satellite System) observations, post-processed satellite ephemeris and satellite clock offset with high precision, precise point position (PPP) technology can get the positioning solution [1, 2]. Although the precision of satellite orbits and the satellite clock offset are high, it still costs PPP users at least 30 min to converge the positioning results within 10 cm [3, 4]. Because of the restriction of environmental factors, such as atmospheric delay, the promotion and application of PPP technology are greatly limited.

Through researches, domestic and foreign researchers indicate that the convergence speed of PPP can be significantly improved with the prior information of atmospheric delay [3, 5]. The real-time atmospheric delay with high precision of reference stations can be calculated with the known exact coordinates and the successive observations. PPP users in the region can get the prior information of atmospheric delay to greatly shorten the initialization time and improve the precision of positioning by interpolation modeling of the prior information [6].

More researches of conventional interpolation models are studied in network real time kinematic (NRTK), such as Linear Interpolation Model (LIM) [7], Linear Combination Model (LCM) [8] and considering Height Linear Interpolation Model (HLIM), etc. These models are put forward in connection with the double difference error correction in NRTK on the whole.

Chen compared the differences between conventional PPP methods and improved PPP method which is based the enhancement of continuously operating reference stations (CORS) network. The results showed that the improved PPP method is equivalent to conventional methods in precision, while the convergence time is shortened by 30 % [9]. But the precision of interpolation is limited by the number of reference stations and the distances between reference stations and the rover station. Li puts forward a method to enhance the PPP with the contribution of regional CORS network [5, 10], which is gradually developed into the popular PPP-RTK technology [11] nowadays. He also proposed the Modified Linear Combination Model (MLCM) [5] to interpolate the tropospheric delay. Based on the analysis of the relationship between the height factor and the zenith troposphere delay of different stations, Zhang presented six spatial regression models. The results showed that the H1QX1 model and H1QM3 model are superior to other models. Besides, interpolation precision is 10 mm in the flat region and 20 mm in the undulated region [12]. But his methods are still based on regional CORS and had certain requirements on the number of reference stations and spatial distances. The methods mentioned above are might not suitable for the remote areas which are augmented by a sparse reference station network.

In this paper, a new method of zenith tropospheric delay modeling for sparse reference station network is put forward based on the research of the relation between height difference and zenith tropospheric delay. According to the relation between height factor and zenith tropospheric hydrostatic delay, zenith tropospheric wet delay in the UNB3m model [13], the zenith tropospheric delay of reference

station is divided into two parts, the height weakly correlated and the height strongly correlated. The new method of zenith tropospheric delay modeling is established using the two parts of the zenith tropospheric delay. Based on the results of regional modeling, the zenith tropospheric delay of rover station is augmented. In sparse reference station region, the applicability and feasibility of the new method are analyzed by experiments.

17.2 Relation Between Height and ZTD

For a certain region, the troposphere in height direction is vertically mixed and the troposphere of horizontal direction is unevenly distributed, which is due to the meteorological characteristics of the troposphere. The 24 h observations of 513 stations of the US CORS on August 8th of 2013 are used to calculate the daily average ZTD by PPP using ionosphere-free combination. The ZTD of different stations are all based on the results after the convergence of ambiguity. The distribution of stations is shown in Fig. 17.1. The relation between height and ZTD of different stations is calculated in Fig. 17.2. It is obvious that ZTD has strong correlation with height. So, the impact of height must be considered when the regional tropospheric delay is modeled by interpolation.

When the ZTD is calculated by PPP using ionosphere-free combination, the ZHD is calculated by UNB3m model and the ZWD is obtained by parameter estimation. The UNB3m model is defined as follows:

$$ZHD(H) = \frac{10^{-6} K_1 R}{g_m} P_0 \left(1 - \frac{\beta H}{T_0}\right)^{\frac{g}{R\beta}} \tag{17.1}$$

$$ZWD(H) = \frac{10^{-6}(T_m K_2 + K_3) R}{g_m - \beta R} \frac{e_0}{T_0} \left(1 - \frac{\beta H}{T_0}\right)^{\frac{(\lambda+1)g}{R\beta} - 1} \tag{17.2}$$

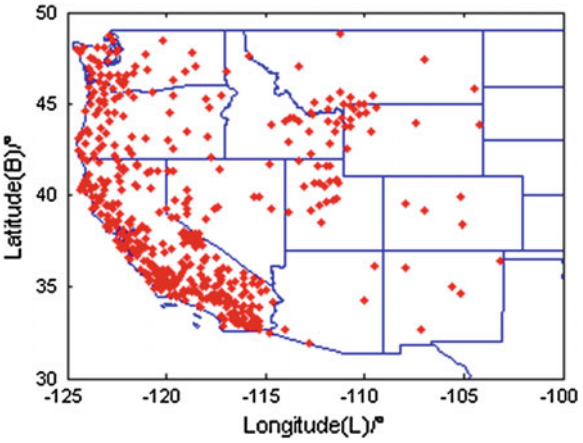

Fig. 17.1 The distribution of US CORS stations (Date: August 8th of 2013)

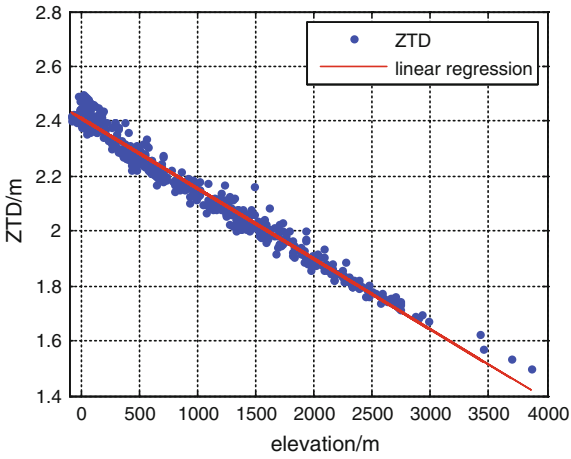

Fig. 17.2 Linear regression between height and ZTD

where H (m) is the height of the station; g_m (m/s^2) is the acceleration of gravity of station; T_m (K) is the temperature around station; P_0 (mbar), T_0 (K), e_0 (mbar), β (K/m), λ (mbar/m) are respectively the atmospheric pressure, temperature, vapor pressure, temperature change rate, vapor pressure change rate at sea level, which are interpolated by meteorological parameters grid using the latitude (ϕ) of the station; $T_m = T_0[1 - \beta R/(g_m(\lambda + 1))]$; $K_1 = 77.60$ k mbar^{-1}; $K_2 = 16.6$ k mbar^{-1}; $K_3 = 377{,}600$ k mbar^{-1}; $g = 9.80665$ m/s^2; $R = 287.054$ J kg^{-1} K^{-1}.

Besides, $g_m = 9.784(1 - 2.66 \times 10^{-3} \cos(2\phi) - 2.8 \times 10^{-7} H)$, the height and latitude of station have a little effect on the value of the acceleration of gravity. So, the acceleration of gravity of station is approximately equal to 9.784. It is also obvious that the ZWD and ZHD have strong correlation with height in the UNB3m model.

17.3 The ZTD Modeling Method Considering Height Difference

17.3.1 Tropospheric Delay Separation of Reference Stations

Based on the dual-frequency observations and the precise coordinates of regional reference stations, the zenith tropospheric wet delay of reference station (ZWD_r) is calculated by parameter estimation with the PPP filter using ionosphere-free combination. The zenith tropospheric hydrostatic delay (ZHD_r) is calculated by the UNB3m model before the parameter estimation. r is the number of reference stations.

Considering the relationship between height factor and zenith tropospheric delay (ZHD and ZWD) in UNB3m model, the zenith tropospheric delay is divided into

two parts, the height weakly correlated ($ZHDD_r$ and $ZWDD_r$) and the height strongly correlated ($ZHDH_r$ and $ZWDH_r$). For zenith tropospheric hydrostatic delay, the two parts are calculated as follows:

$$\begin{aligned} ZHDD_r &= ZHD(H=0) \\ ZHDH_r &= ZHD(H=h) - ZHDD_r = ZHD_r - ZHDD_r \end{aligned} \tag{17.3}$$

In a similar way, the zenith tropospheric wet delay is separated as follows:

$$\begin{aligned} ZWDD_r &= ZWD_r \cdot ZWD(H=0)/ZWD(H=h) \\ ZWDH_r &= ZWD_r - ZWDD_r \end{aligned} \tag{17.4}$$

The height weakly correlated zenith tropospheric delay $ZTDD_r$ and the height strongly correlated zenith tropospheric delay $ZTDH_r$ are calculated as follows:

$$\begin{aligned} ZTDD_r &= ZHDD_r + ZWDD_r \\ ZTDH_r &= ZTDH_r + ZWDH_r \end{aligned} \tag{17.5}$$

17.3.2 The ZTD Modeling Method Considering Height Difference

According to the positional relationship between rover station and reference stations, height weakly correlated zenith tropospheric delay and the height strongly correlated zenith tropospheric delay are modeled separately.

17.3.2.1 The Height-Strongly Correlated ZTD Modeling Method

Suppose that $ZTDD_r = a_1 + a_2 x_r + a_3 y_r$, where $a_i (i = 1, 2, 3)$ are interpolation coefficients; x_r, y_r are the plane coordinates of stations; n is the number of reference stations. When interpolating, a local coordinate system is set up which is centered by the rover station. So, x_r and y_r are the values of the local coordinate system. Besides, x_r and y_r of rover station are both equal to 0. Thus:

$$ZTDH_u = a_1 \tag{17.6}$$

The interpolation coefficients satisfy the following formula:

$$[\, a_1 \quad a_2 \quad a_3 \,]^T = (A^T A)^{-1} A^T V \tag{17.7}$$

where,

$$A = \begin{bmatrix} 1 & x_1 & y_1 \\ \vdots & \vdots & \vdots \\ 1 & x_n & y_n \end{bmatrix}, \quad V = \begin{bmatrix} ZTDD_1 \\ \vdots \\ ZTDD_n \end{bmatrix} \tag{17.8}$$

17.3.2.2 The Height Weakly Correlated ZTD Modeling Method

Suppose that $ZTDH_u = b_1 ZTDH_1 + b_2 ZTDH_2 \cdots + b_n ZTDH_n$, where $b_i (i = 1, 2, \ldots, n)$ is interpolation coefficients, which satisfy the formulas that $\sum_{i=1}^{n} b_i = 1$, $\sum_{i=1}^{n} b_i h_i = 0$, $\sum_{i=1}^{n} b_i^2 =$ min. h_i are the height of reference stations. When interpolating, a local coordinate system is set up which is centered by the rover station. So, h_i are the values in the local coordinate system. Besides, the interpolation coefficients satisfy the following formula:

$$[b_1 \quad b_2 \quad \cdots \quad b_n]^T = N(NN)^{-1} B^T W, \; N = B^T B \tag{17.9}$$

$$B = \begin{bmatrix} h_1 & h_2 & \cdots & h_n \\ 1 & 1 & \cdots & 1 \end{bmatrix}, \quad W = \begin{bmatrix} 0 \\ 1 \end{bmatrix} \tag{17.10}$$

Through the interpolation model of height strongly correlated and height weakly correlated ZTD which are extracted from reference stations, the height strongly correlated ZTD ($ZTDH_u$) and height weakly correlated ZTD ($ZTDD_u$) of rover station can be obtained. The zenith tropospheric delay of rover station (ZTD_u) can be gained via combining the two parts together.

$$ZTD_u = ZTDH_u + ZTDD_u \tag{17.11}$$

17.4 Experiment Results and Analyses

17.4.1 Interpolation Modeling in Undulated Region

The area of 34°–36° north latitude and 119°–121° west longitude of the US CORS is selected as the experimental area aiming at the area where there is a bigger height difference. As is shown in the Fig. 17.3, five stations are chosen, among which, the middle one is used as a rover station (triangle), and the others as reference stations (circle). The maximum value of the height of the reference stations is 1526.119 m, minimum 284.566 m. And the height of the rover station is 1709.067 m, mean distance between the rover and reference stations 66.06 km. Data used in the experiment are the observations of 24 h on August 8th of 2013, with a sampling rate of 15 s.

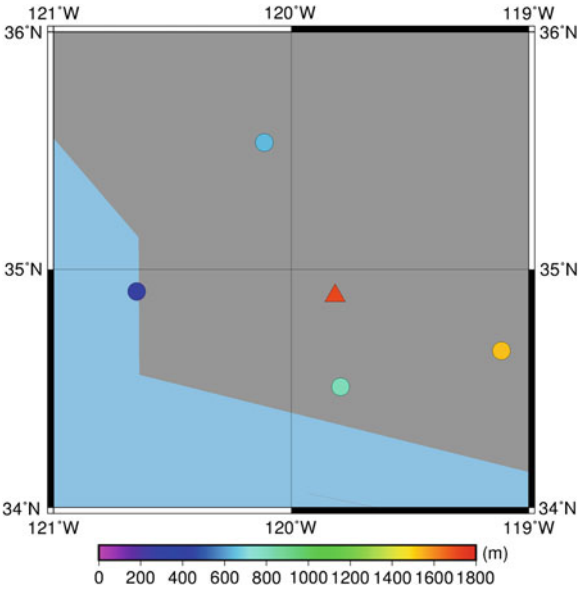

Fig. 17.3 The distribution of stations

2000 epochs of ZTD values are real-time regional modeled, which are based on the convergence of ambiguity in the PPP solutions of stations. The ZTD value of the rover station via PPP is as the true value. At the same time, the HTIM method proposed in this paper is compared with HLIM and MLCM methods. The result is shown in Fig. 17.4. The absolute deviation and root mean square error (RMS) of 2000 epochs are counted in Table 17.1.

As the table shows, aiming at the area which is undulated, when there are fewer reference stations, the method of HTIM is better than the other two methods in that the interpolation accuracy is higher with the absolute deviation within 0.03 m

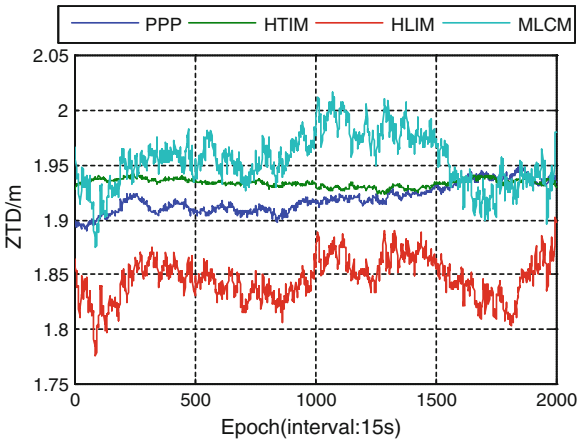

Fig. 17.4 The ZTD interpolated by different models and the true value

Table 17.1 Absolute deviation and RMS of different models

Absolute deviation	HTIM	HLIM	MLCM
<0.03 m	91.40 %	0.40 %	31.70 %
<0.02 m	56.75 %	0.00 %	21.75 %
<0.01 m	39.45 %	0.00 %	12.45 %
RMS/m	0.020	0.076	0.046

basically above 90 %, and within 0.01 m reaching 40 % nearly, and in that the mean square error is obviously smaller. Also, while interpolating using the HTIM, there is less fluctuation. Thus, evidently, under the circumstance where the height difference is bigger, only a few reference stations are needed to conduct regional interpolation that could generate higher precision compared with conventional methods.

17.4.2 Interpolation Modeling with Sparse Reference Stations

The area of 40°–45° north latitude and 118°–125° west longitude of the US CORS is selected as the experimental area aiming at the large area with sparse reference stations. As is shown in the Fig. 17.5, five stations are chosen, among which, the middle one is used as a rover station (triangle), and the others as reference stations (circle). The maximum value of the height of the reference stations is 1584.542 m, minimum 27.092 m. And the height of the rover station is 1390.816 m, mean distance between the rover and reference stations 233.79 km. Data used in the experiment are the observations of 24 h on August 8th of 2013, with a sampling rate of 15 s.

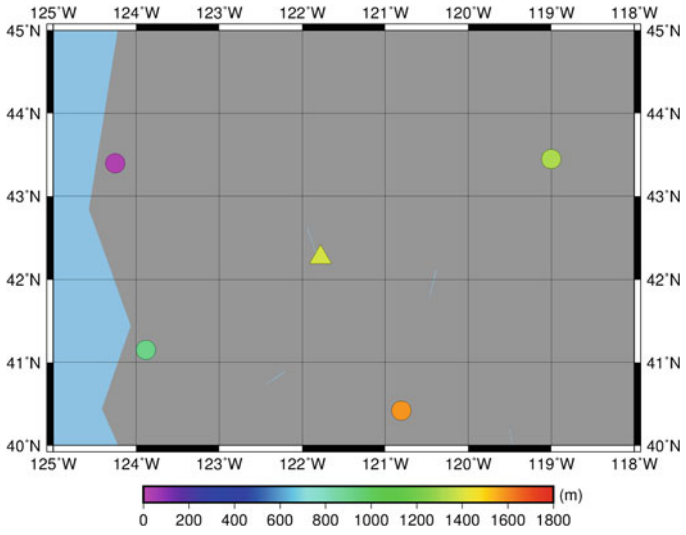

Fig. 17.5 The distribution of stations

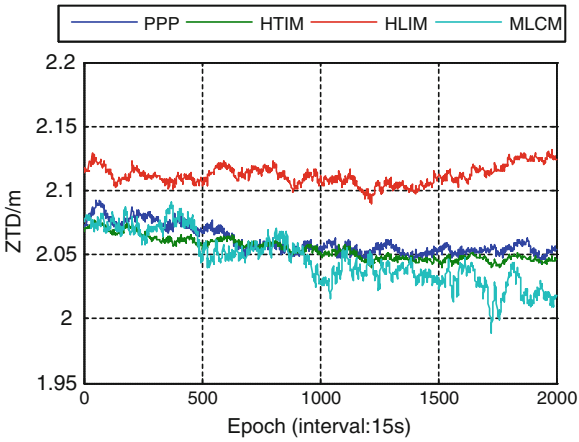

Fig. 17.6 The ZTD interpolated by different models and the true value

Table 17.2 Absolute deviation and RMS of different models

Absolute deviation	HTIM	HLIM	MLCM
<0.03 m	100.00 %	1.25 %	87.95 %
<0.02 m	99.95 %	0.00 %	68.30 %
<0.01 m	75.95 %	0.00 %	35.30 %
RMS/m	0.008	0.053	0.020

The analytical methods are same as which used in Sect. 17.4.1. The result is shown in Fig. 17.6. The absolute deviation and root mean square error (RMS) of 2000 epochs are counted in Table 17.2.

As the table shows, aiming at the large area with sparse reference stations, the method of HTIM is better than the other two methods in that the interpolation accuracy is higher with the absolute deviation is totally within 0.03 m, and within 0.01 m reaching 75.95 %, and in that the mean square error is obviously smaller. Thus, evidently, under the circumstance where reference stations are spare, only a few reference stations are needed to conduct regional interpolation that could generate higher precision compared with conventional methods.

17.4.3 Interpolation Modeling with Different Number of Reference Stations

The number of reference stations has an impact on the interpolation accuracy. The area of 34°–36° north latitude and 118°–121° west longitude of the US CORS is selected as the experimental area to analysis the impact of the number of reference stations on the interpolation precision of HTIM model. As is shown in the Fig. 17.7, eight stations are chosen, among which, the middle one is used as a rover station

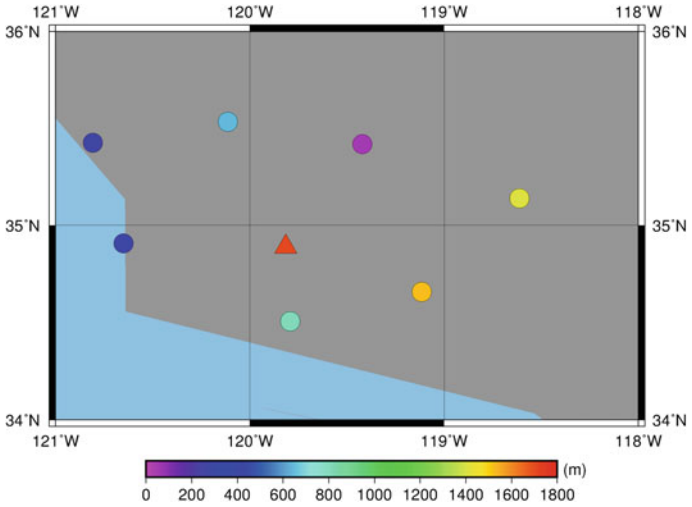

Fig. 17.7 The distribution of stations

(triangle), and the others as reference stations (circle). The maximum value of the height of the reference stations is 1526.119 m, minimum 56.588 m. And the height of the rover station is 1709.067 m, mean distance between the rover and reference stations 79.25 km. Data used in the experiment are the observations of 24 h on August 8th of 2013, with a sampling rate of 15 s.

The analytical methods are same as which used in Sect. 17.4.1. The result is shown in Fig. 17.8. The absolute deviation and root mean square error (RMS) of 2000 epochs are counted in Table 17.3.

As the table shows, with the increase of the number of reference stations, the interpolation accuracy of the HTIM model is improved, especially in absolute

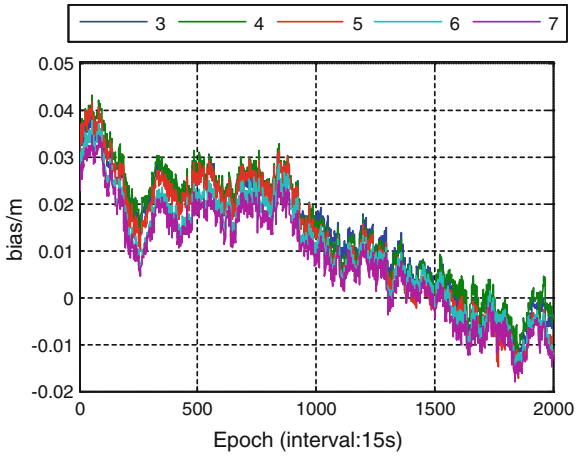

Fig. 17.8 The ZTD interpolated by different models and the true value

Table 17.3 Absolute deviation and RMS of different models

Absolute deviation	Number of reference stations				
	3	4	5	6	7
<0.03 m	93.85 %	91.40 %	93.25 %	95.40 %	97.00 %
<0.02 m	58.80 %	56.75 %	62.25 %	75.35 %	85.95 %
<0.01 m	34.60 %	39.45 %	38.65 %	43.60 %	45.50 %
RMS/m	0.019	0.020	0.018	0.016	0.014

deviation. It is three reference stations that the HTIM model can perform the interpolation model by. And the interpolation accuracy of HTIM model using three reference stations has reached the need of zenith tropospheric delay modeling, with absolute deviation within 0.03 m basically above 93.85 % and the RMS value within 0.020 m. It is should pointed out that the accuracy of true value is within several millimeters. So, it is accepted that the RMS of three reference stations is superior to the result of four reference stations. Besides, the absolute deviation within 0.01 m of four reference stations is far more than the percentage of three stations, although the other two indicators of absolute deviation of three reference stations are slightly better than four stations.

17.5 Concluding Remarks

Based on the analysis of the relationship between zenith tropospheric delay and the height of station, the new method of zenith tropospheric delay modeling (HTIM) for sparse reference station network is put forward. According to the relation between height factor and zenith tropospheric hydrostatic delay, zenith tropospheric wet delay in the UNB3m model, the zenith tropospheric delay of reference station is divided into two parts, the height weakly correlated and the height strongly correlated. The new method of zenith tropospheric delay modeling is established using the two parts of the zenith tropospheric delay. Based on the results of regional modeling, the zenith tropospheric delay of rover station is obtained. Through experiment and analysis, the method shows fair results and the conclusions are as follows:

1. In the certain region, there is a strong correlation between the height and the zenith tropospheric delay that the higher height is, and the smaller the zenith tropospheric delay is.
2. In the undulated area, only using four reference stations, the method of HTIM is better than the other two methods (HLIM and MLCM) in that the interpolation accuracy is higher with the absolute deviation within 0.03 m basically above 90 %, and within 0.01 m reaching 40 % nearly, and in that the RMS reaches 0.020 m.

3. In the large area with four sparse reference stations, the method of HTIM is better than the other two methods (HLIM and MLCM) in that the interpolation accuracy is higher with the absolute deviation is totally within 0.03 m, and within 0.01 m reaching 75.95 %, and in that the RMS is only 0.008 m.
4. The HTIM modeling method is basically unlimited by the number of reference stations. Using three reference stations, the RMS of interpolation is guaranteed to be less than 0.02 m and the absolute deviation is basically within 0.03 m.

In the paper, the zenith tropospheric delay of reference stations is not completely separated. The region for the experiment is in the US CORS, and the result in the other area has not been studied. So, there are further analysis and researches.

Acknowledgments This work is supported by the Key Projects in the National Science & Technology Pillar Program during the Twelfth Five-year Plan Period (No. 2012BAJ23B01). The authors are very grateful to the anonymous reviewers for their constructive comments and suggestions.

References

1. Liu J, Ye S (2002) GPS precise point positioning using undifferenced phase observation. Geomatics Inf Sci Wuhan Univ 27(3):234–239
2. Wu X, Li Z (2002) Precise point positioning. Wtusm Bull Sci Technol 6:016
3. Bisnath S, Gao Y (2008) Current state of precise point positioning and future prospects and limitations: observing our changing earth. Springer, Berlin Heidelberg, pp 615–623
4. Li L, Long S, Li H et al (2014) Precise point positioning based on reference stations augmentation information. Acta Geodaetica et Cartogaphica Sinica 43(5):481–485
5. Li X, Zhang X, Ge M (2011) Regional reference network augmented precise point positioning for instantaneous ambiguity resolution. J Geodesy 85(3):151–158
6. Li H, Chen J, Wang J et al (2010) Network based real-time precise point positioning. Adv Space Res 46(9):1218–1224
7. Wanninger L (1995) Improved ambiguity resolution by regional differential modelling of the ionosphere. In: Proceedings of ION GPS-95, pp 55–62
8. Han S, Rizos C (1998) Instantaneous ambiguity resolution for medium-range GPS kinematic positioning using multiple reference stations: advances in positioning and reference frames. Springer, Berlin Heidelberg, pp 283–288
9. Chen W, Gao C, Cao X, Pan S (2013) Improved PPP resolution considering regional CORS based tropospheric information. J Southeast Univ (Natural Science Edition), 43 sup(II):370–374
10. Geng J, Teferle FN, Meng X et al (2011) Towards PPP-RTK: ambiguity resolution in real-time precise point positioning. Adv Space Res 47(10):1664–1673
11. Wübbena G, Schmitz M, Bagge A (2005) PPP-RTK: precise point positioning using state-space representation in RTK networks. In: Proceedings of ION GNSS, vol 5, pp 13–16
12. Zhang X, Zhu F, Li P, Zhai G (2013) Zenith troposphere delay interpolation model for regional CORS network augmented PPP. Geomatics Inf Sci Wuhan Univ 6:012
13. Leandro R, Santos MC, Langley RB (2006) UNB neutral atmosphere models: development and performance. In: Proceedings of ION NTM, pp 564–573

Chapter 18
Performance Monitoring of BeiDou Navigation Satellite System Ionospheric Grid

Hui Zhang, Daliang Gong, Mo Wu, He Zhao and Long Bai

Abstract The correction principle, definition and usage of the ionospheric grid of BeiDou navigation satellite system (BDS) are introduced. Based on the BDS ionospheric grid information received by BDS receivers, and compared with ionosphere delay evaluated using double-frequency measurements, the correction performance of BDS ionospheric grid in different latitudes and in different periods is evaluated. In addition, the wide-area differential positioning results of BDS B1I in Beijing, Chengdu, and Sanya are analyzed. Real data analysis indicates that, the average correction accuracy of B1I using BDS ionospheric grid is 91.17 %, the average correction accuracy is 0.32 m, and the horizontal positioning accuracy of B1I differential positioning is 4.54 m (95 confidence level), the height positioning accuracy is 5.32 m (95 % confidence level).

Keywords BeiDou navigation satellite system · Ionospheric grid · Navigation-receivers · Performance analysis

18.1 Introduction

The ionospheric delay is one of the maximum error sources in Global Satellite Navigation System (GNSS) measurements [1]. In order to reduce the impact of ionospheric delay, and improve the accuracy of satellite navigation and positioning services, the ionospheric grid correction method is adopted in most satellite-based augmentation systems (SBASs) such as the wide-area augmentation system (WAAS) [2]. The real-time, large-scale, accurate ionospheric correction information is broadcast to the user in the service area.

The integrated design of basic navigation services and augmentation services is one of the characteristics of Chinese BeiDou satellite navigation system (BDS), and

H. Zhang (✉) · D. Gong · M. Wu · H. Zhao · L. Bai
Beijing Satellite Navigation Center, Beijing 100094, China
e-mail: andyzhang518@aliyun.com

J. Sun et al. (eds.), *China Satellite Navigation Conference (CSNC) 2015 Proceedings: Volume II*, Lecture Notes in Electrical Engineering 341,
DOI 10.1007/978-3-662-46635-3_18

avoids the duplication of satellite navigation system. To meet the needs of different users, the BDS provides both basic navigation messages and wide-area differential and integrity message at the same time. Therefore, BDS single frequency user can enjoy free high-precision differential services without relying on any other system, and obtain high-precision positioning and timing performance.

First of all, the correction principle, related definitions and usage of BDS ionospheric grid are introduced. Subsequently, the coverage of BDS ionospheric grid is analyzed. What's more, based on the BDS ionospheric grid information received by BDS receiver (located in Beijing, Chengdu and Sanya, China), compared with the ionospheric delay calculated from BDS receivers B1I and B2I dual-frequency pseudorange data as a benchmark, the correction performance of BDS ionospheric grid is evaluated. In addition, the BDS grid ionospheric correction rate, correction accuracy and B1I differential positioning accuracy are analysed. Last but not least, the conclusion of BDS ionospheric grid application performance is given. The results show that, the average correction rate of BDS grid ionospheric is 91.17 %, the average correction accuracy is 0.32 m, and the horizontal positioning accuracy of B1I differential positioning is 4.54 m (95 % confidence level), and the height positioning accuracy is 5.32 m (95 % confidence level).

18.2 BDS Ionospheric Grid Model

18.2.1 Principle of BDS Ionospheric Grid Corrections

The ionospheric grid correction model is based on a provision of artificial spherical grid [3]. BDS current ionospheric grid is described as a shell at height of 375 km above the Earth surface, and covers 70–145°E and 7.5–55°N latitude. This area is divided into 320 ionospheric grid points (IGPs) of longitude 5° × latitude 2.5°. Several monitoring stations and a processing center are distributed in service area. Each monitoring station is equipped with dual-frequency receivers to collect signals of all visible satellites, and the ionospheric delays at ionospheric pierce points (IPPs) are calculated and transmitted to the processing station via the communication links. Based on these real-time data, the vertical ionospheric delay and estimation error at each grid point are calculated in the processing station, and broadcast to the service area in the D2 navigation message by five geostationary earth orbit (GEO) satellites. Using the satellite signals and ionospheric grid information received, and according to the algorithm recommended by BDS Signal In Space Interface Control Document (BDS-SIS-ICD-2.0, [4]), the ionospheric delay of the satellite ranging signals can be calculated.

18.2.2 Definition of BDS Ionospheric Grid

The information about each BDS ionospheric grid point (Ion) consists of the vertical delay at grid point ($d\tau$) and its error index (Grid point Ionospheric Vertical delay Error Index, GIVEI) [4].

BDS ionospheric grid has 320 IGPs, and the ionospheric grid information is broadcast in D2 navigation message by the GEO satellite. IGPs numbered 1–160 IGP is a group, IGPs numbered 161–320 is a another group, one of the two groups is updated every 3 min, the updating cycle time of entire grid is 6 min.

BDS ionosphere grid is the superimposition of two grid of longitude 5° × latitude 5°. The definition of ionospheric grid point (IGP) numbers ≤160 is listed in Table 18.1.

When IGP ≤ 160, the corresponding longitudes and latitudes are:

$$L = 70 + INT((IGP - 1)/10) \times 5 \tag{18.1}$$

$$B = 5 + (IGP - INT((IGP - 1)/10) \times 10) \times 5 \tag{18.2}$$

where $INT(*)$ refers to round down.

The definition of IGP numbers 161–320 is shown in Table 18.2.

When IGP > 160, the corresponding longitudes and latitudes are:

$$L = 70 + INT((IGP - 161)/10) \times 5 \tag{18.3}$$

$$B = 2.5 + (IGP - 160 - INT((IGP - 161)/10) \times 10) \times 5 \tag{18.4}$$

where $INT(*)$ refers to round down.

$d\tau_i$ is the vertical ionosphere delay on B1I signal at the ith grid point, expressed in distance with a scale factor of 0.125 and with unit of meters. The effective range

Table 18.1 IGP number (a)

N-Lat.	E-Log.															
	70	75	80	85	90	95	100	105	110	115	120	125	130	135	140	145
55	10	20	30	40	50	60	70	80	90	100	110	120	130	140	150	160
50	9	19	29	39	49	59	69	79	89	99	109	119	129	139	149	159
45	8	18	28	38	48	58	68	78	88	98	108	118	128	138	148	158
40	7	17	27	37	47	57	67	77	87	97	107	117	127	137	147	157
35	6	16	26	36	46	56	66	76	86	96	106	116	126	136	146	156
30	5	15	25	35	45	55	65	75	85	95	105	115	125	135	145	155
25	4	14	24	34	44	54	64	74	84	94	104	114	124	134	144	154
20	3	13	23	33	43	53	63	73	83	93	103	113	123	133	143	153
15	2	12	22	32	42	52	62	72	82	92	102	112	122	132	142	152
10	1	11	21	31	41	51	61	71	81	91	101	111	121	131	141	151

Table 18.2 IGP number (b)

N-Lat.	E-Log.															
	70	75	80	85	90	95	100	105	110	115	120	125	130	135	140	145
52.5	170	180	190	200	210	220	230	240	250	260	270	280	290	300	310	320
47.5	169	179	189	199	209	219	229	239	249	259	269	279	289	299	309	319
42.5	168	178	188	198	208	218	228	238	248	258	268	278	288	298	308	318
37.5	167	177	187	197	207	217	227	237	247	257	267	277	287	297	307	317
32.5	166	176	186	196	206	216	226	236	246	256	266	276	286	296	306	316
27.5	165	175	185	195	205	215	225	235	245	255	265	275	285	295	305	315
22.5	164	174	184	194	204	214	224	234	244	254	264	274	284	294	304	314
17.5	163	173	183	193	203	213	223	233	243	253	263	273	283	293	303	313
12.5	162	172	182	192	202	212	222	232	242	252	262	272	282	292	302	312
7.5	161	171	181	191	201	211	221	231	241	251	261	271	281	291	301	311

Table 18.3 GIVEI definitions

GIVEI	GIVE (m, 99.9 %)
0	0.3
1	0.6
2	0.9
3	1.2
4	1.5
5	1.8
6	2.1
7	2.4
8	2.7
9	3.0
10	3.6
11	4.5
12	6.0
13	9.0
14	15.0
15	45.0

of $d\tau_i$ is 0–63.625 m. When $d\tau_i = 63.750$ m, it means that this IGP is not monitored; When $d\tau_i = 63.875$ m, the vertical ionosphere delay is not available.

The grid ionosphere vertical error (GIVE) describes the delay correction accuracy at ionosphere grid points and is indicated with GIVEI.

See Table 18.3 for the relationship between GIVEI and GIVE.

18.2.3 Usage of BDS Ionospheric Grid [4]

The user can select effective data of the grid points adjacent to or nearby the observed intersection point with $d\tau_i$ and GIVEI to design the model and compute the delay correction for ionospheric pierce point (IPP) by interpolation. The Bilinear interpolation is recommended in *BDS-SIS-ICD*-2.0. The guiding fitting algorithm is given as follows:

Figure 18.1 illustrates the user IPP and its surrounding grid points. Where IPP represented with geographic latitudes and longitudes as (ϕ_p, λ_p), is the geographic

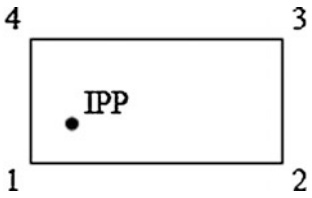

Fig. 18.1 Schematic: users IPP and grid point

location where the line-of-sight between the user and the satellite intersects with the ionospheric layer. The positions of the four surrounding grid points are represented with $(\phi_i, \lambda_i, i = 1{-}4)$ and the vertical ionospheric delays on the grid points are represented with $VTEC_i(i = 1{-}4)$ respectively. And $\omega_i(i = 1{-}4)$ shows the distance weight between IPP and the four grid points. As long as there are at least grid points surrounding the user IPP are available and effective, the IPP ionospheric delay can be calculated from the vertical ionospheric delay of the effective grid points.

$$Ionodelay_p = \frac{\sum_{i=1}^{4} \omega_i \cdot VTEC_i}{\sum_{i=1}^{4} \omega_i} \tag{18.5}$$

where $x_p = \frac{\lambda_p - \lambda_1}{\lambda_2 - \lambda_1}, y_p = \frac{\phi_p - \phi_1}{\phi_4 - \phi_1}$,

$$\omega_1 = \left(1 - x_p\right) \cdot \left(1 - y_p\right) \tag{18.6}$$

$$\omega_2 = x_p \cdot \left(1 - y_p\right) \tag{18.7}$$

$$\omega_3 = x_p \cdot y_p \tag{18.8}$$

$$\omega_1 = \left(1 - x_p\right) \cdot y_p \tag{18.9}$$

If any grid point of this observation epoch is marked as ineffective, its weight is zero.

For B2I users need to multiply a factor $k(f)$ because of the vertical ionospheric delays on the grid points broadcast in the navigation message are based on B1I signal.

$$k(f) = \frac{f_1^2}{f_2^2} = \left(\frac{1561.098}{1207.140}\right)^2 \tag{18.10}$$

where, f_1 refers to the nominal carrier frequency of B1I, f_2 refers to the nominal carrier frequency of B2I, and the unit is MHz.

18.3 Evaluation of BDS Ionospheric Grid Application Performance

18.3.1 Analysis of BDS Ionospheric Grid Availability

Based on the ionospheric grid information received by a BDS receiver on September 3, 2014, 24 h a day (without special declaration, the time system adopted in this paper is BDS Time, BDT), the availability of BDS ionospheric grid is analyzed. And, the results are shown in Fig. 18.2.

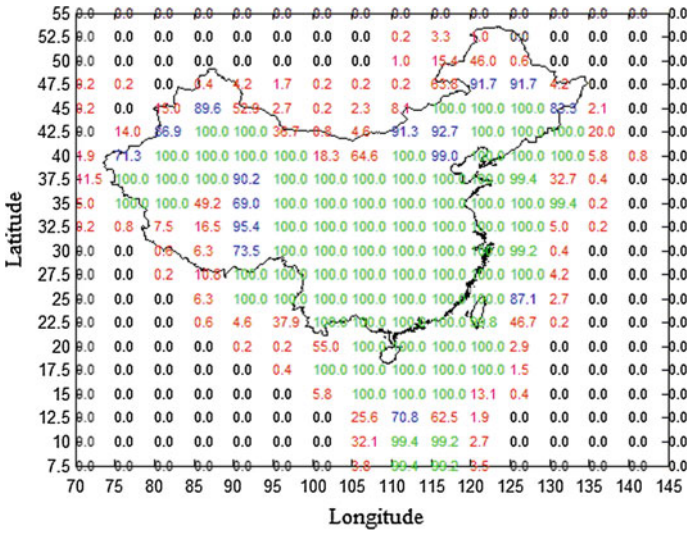

Fig. 18.2 Availability of BDS ionospheric grid (September 3, 2014)

The results show that the total number of IGPs whose availability is better than 99 % (shown in green numbers) is 86. The BDS ionospheric grid points in most region of Chinese mainland and coastal have a good availability. Due to the influence of the satellite constellation and regional distribution of stations, the distribution of IGPs whose availability is more than 99 %, is similar to the shape of Chinese territory after translated to the southeast.

The GIVE is analyzed, and the results are shown in Fig. 18.3.

In Fig. 18.3, the number at the IGP means the mean value of its GIVEI when it's available, less than 3.00 in green, greater than 3.00 and less 8.00 in blue, unlabelled represents unavailable. As can be seen from Fig. 18.3, the GIVE of IGPs in mid-latitude is less than low-latitude. Statistics, the mean of GIVEI of the IGPs whose availability >99 % is 3.76, i.e. GIVE is less than 1.5 m.

18.3.2 Analysis of BDS Grid Ionospheric Correction Accuracy

The distribution of ionospheric electron density is related to latitude [5]. The application performance of the ionospheric grid of wide-area precise real-time positioning system is analyzed in [6], and the result reveals that ionospheric correction accuracy is related to latitude. Figure 18.4 also shows GIVE of BDS is related to latitude. Therefore, to evaluate the correction accuracy of BDS

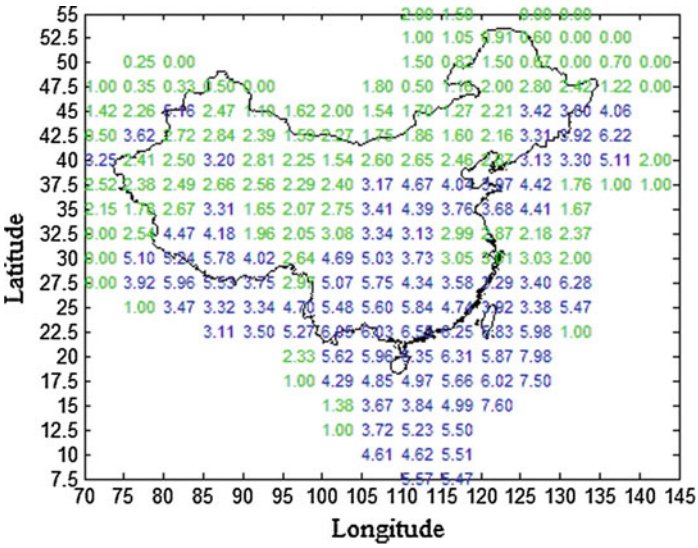

Fig. 18.3 GIVEI of available ionospheric grid (September 3, 2014)

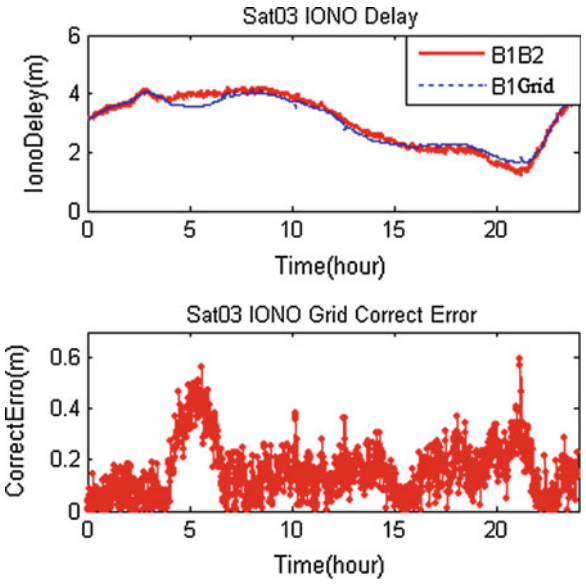

Fig. 18.4 Ionospheric delay correction of B1 based on BDS ionospheric grid (Beijing, Sat03)

ionospheric grid, the real measurements from BDS receivers located in Beijing, Chengdu, Sanya, whose latitudes are different are selected. The data was collected on September 3, 2014.

Considering impact of Time Correction of Group Delay (T_{GD}) of satellite signal, the accurate ionosphere delay can be calculated from BDS receiver B1I and B2I dual-frequency pseudorange measurements, the relevant algorithms refer to [7]. Compared with the ionospheric delay calculated from BDS receivers B1I and B2I dual-frequency pseudorange data as a benchmark, the correction accuracy of BDS ionospheric grid is evaluated in this section. The ionosphere delay involved is based on B1 frequency, sampling interval is 1 min, and the elevation mask angle of 15°. Owing to the limitation of space and BDS constellation structure, the ionosphere correction timing diagrams of 3 satellites is given, satellite No. 3 (GEO, always visible, IPP position is almost fixed), satellite No. 6 (IGSO, arc of observation is long, IPP is moving over time), satellite No. 11 (MEO, arc of observation is short, IPP is moving over time). The result is shown in Figs. 18.4, 18.5, 18.6, 18.7, 18.8, 18.9, 18.10, 18.11 and 18.12.

Conclusions of Figs. 18.4, 18.5, 18.6, 18.7, 18.8, 18.9, 18.10, 18.11 and 18.12:

1. The correction performance of BDS ionospheric grid changes relatively stable throughout a day.
2. When 13:00–14:00 (Local time), the electron density is largest, the ionospheric grid correction accuracy is slightly worse.
3. As the elevation is lower during the satellite immigration, the ionospheric grid correction accuracy is lower.

To evaluate the BDS grid ionospheric correction accuracy, two indicators, the average correction rate and the average correction accuracy of all IPP of three stations is analyzed. The definition of the average correction rate and the average correction accuracy is as follows:

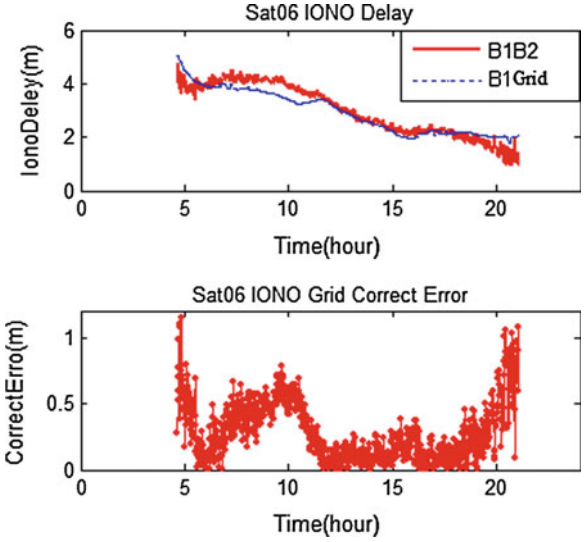

Fig. 18.5 Ionospheric delay correction of B1 based on BDS ionospheric grid (Beijing, Sat06)

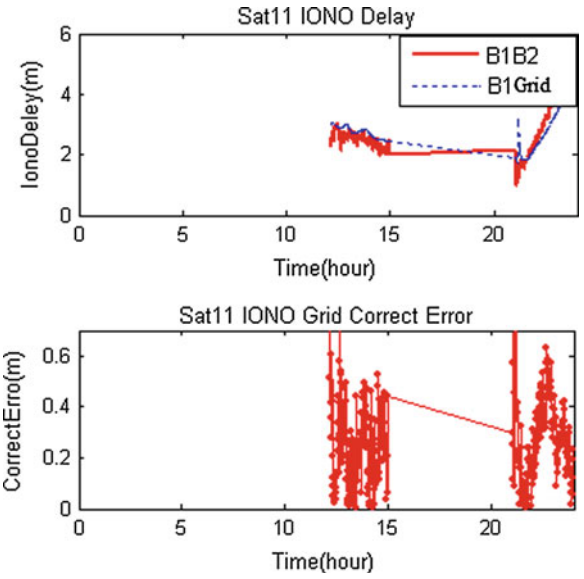

Fig. 18.6 Ionospheric delay correction of B1 based on BDS ionospheric grid (Beijing, Sat11)

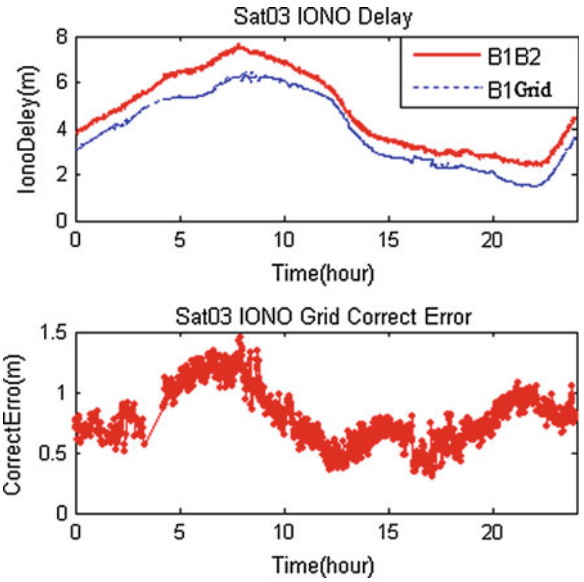

Fig. 18.7 Ionospheric delay correction of B1 based on BDS ionospheric grid (Chengdu, Sat03)

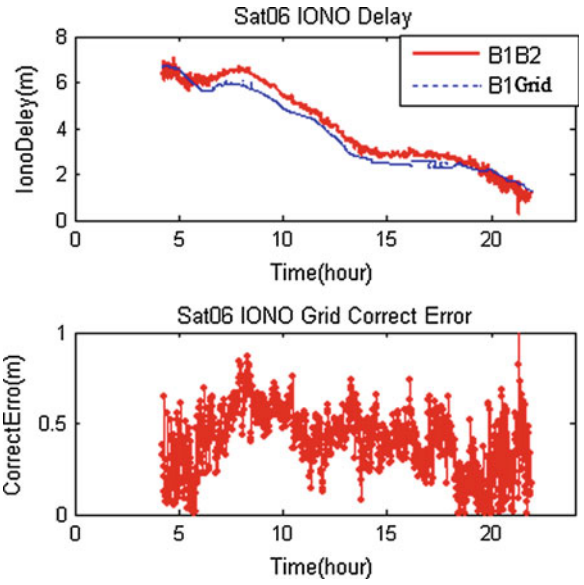

Fig. 18.8 Ionospheric delay correction of B1 based on BDS ionospheric grid (Chengdu, Sat06)

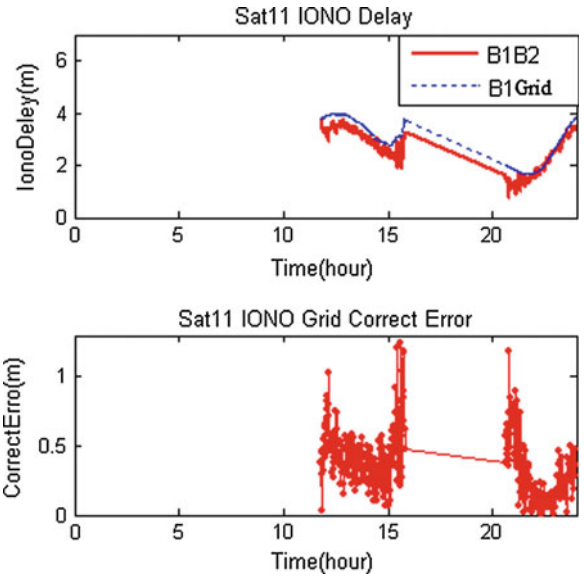

Fig. 18.9 Ionospheric delay correction of B1 based on BDS ionospheric grid (Chengdu, Sat11)

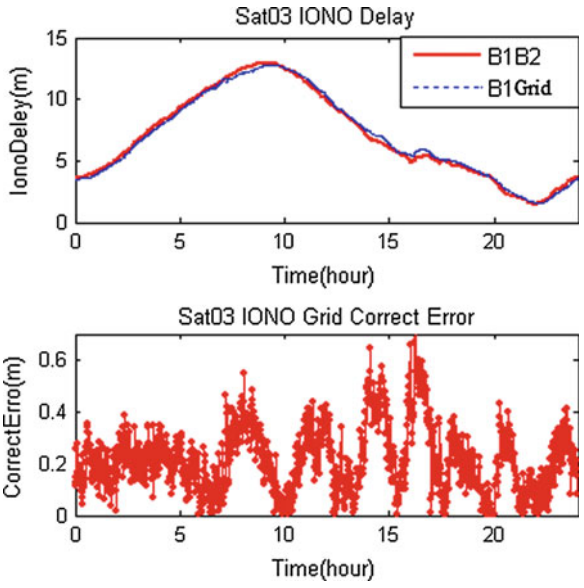

Fig. 18.10 Ionospheric delay correction of B1 based on BDS ionospheric grid (Sanya, Sat03)

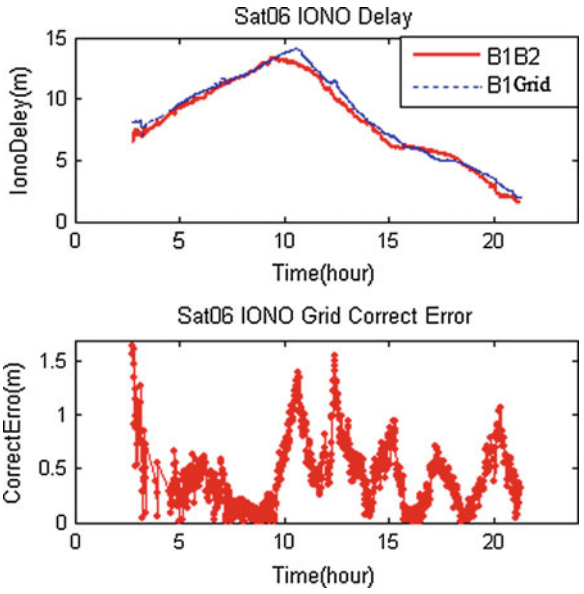

Fig. 18.11 Ionospheric delay correction of B1 based on BDS ionospheric grid (Sanya, Sat06)

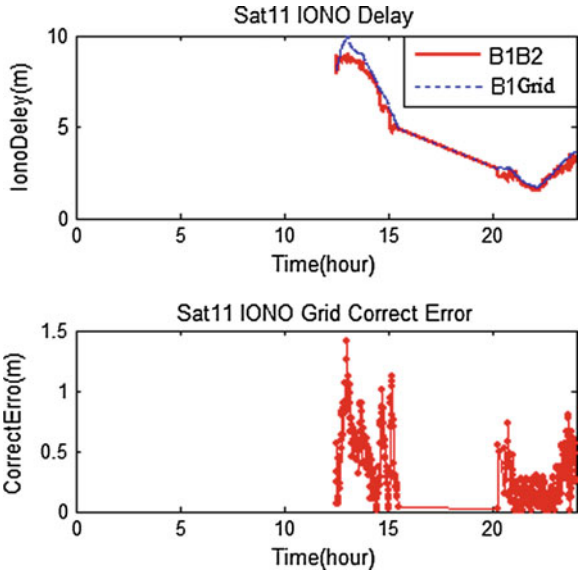

Fig. 18.12 Ionospheric delay correction of B1 based on BDS ionospheric grid (Sanya, Sat11)

$$CorrectRatio = \frac{\sum_{i=1}^{n}\left(1 - \frac{|GridIon_k - Vtec_k|}{Vtec_k}\right)}{n} \tag{18.11}$$

$$CorrectError = \frac{\sum_{i=1}^{n}|GridIon_k - Vtec_k|}{n} \tag{18.12}$$

where, $GridIon_k$ is BDS ionospheric grid information, $Vtec_k$ is the ionosphere delay of the IPP calculated using dual-frequency pseudorange measurements, n is the total number of observations.

The Statistical results of ionospheric grid correction of the receivers located in Beijing, Chengdu, Sanya are shown in Table 18.4.

Table 18.4 shows that, the average correction of BDS ionospheric grid was 91.17 %, the average correction accuracy is 0.32 m.

Table 18.4 Statistics: correction accuracy of BDS ionospheric grid

Stations	Average correction rate (%)	Average correction accuracy (m)
Beijing	92.00	0.21
Chengdu	88.87	0.40
Sanya	92.65	0.36
Mean	**91.17**	**0.32**

18.3.3 Analysis of BDS B1 Differential Positioning Accuracy

To evaluate the positioning performance after using BDS ionospheric grid information to correct the ionosphere delay, the B1I differential positioning accuracy of three monitoring points is analyzed. The results are shown in Figs. 18.13, 18.14, 18.15 and Table 18.5.

The statistical results show that: using BDS ionospheric grid to correct ionosphere delay, in B1I differential positioning mode, the horizontal positioning accuracy is 4.54 m (95 confidence level), the elevation positioning accuracy is 5.32 m (95 % confidence level).

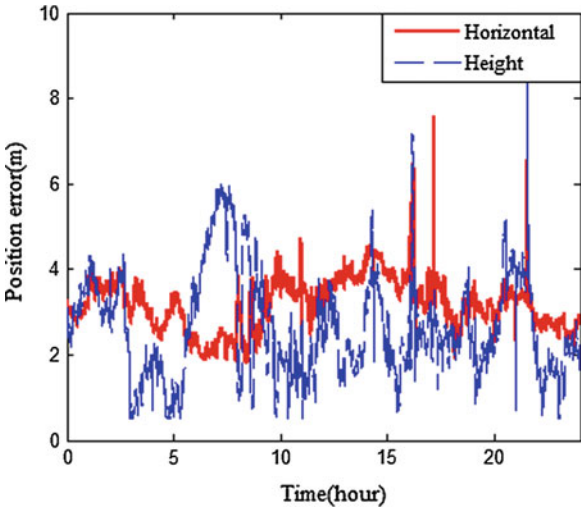

Fig. 18.13 Results of B1I wide-area differential positioning, in Beijing

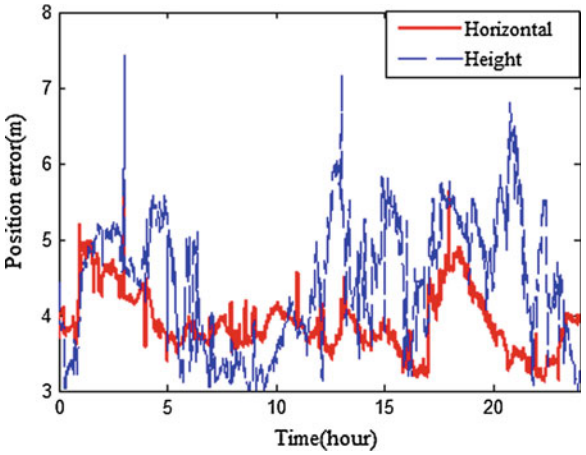

Fig. 18.14 Results of B1I wide-area differential positioning, in Chengdu

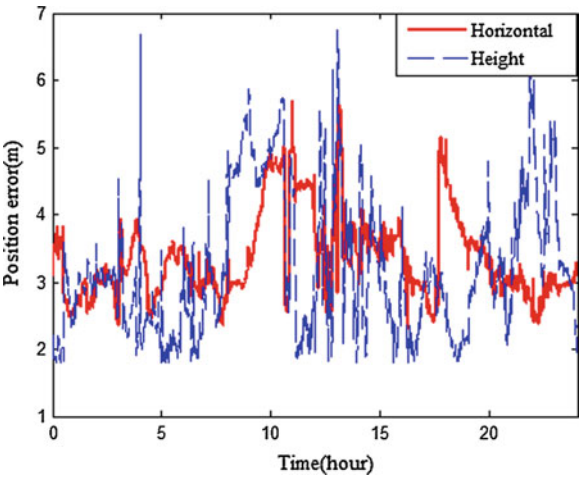

Fig. 18.15 Results of B1I wide-area differential positioning, in Sanya

Table 18.5 Statistics: accuracy of BDS BI wide area differential positioning

Stations	Horizontal (m, 95 % confidence level)	Height (m, 95 % confidence level)
Beijing	4.19	5.07
Chengdu	4.71	5.63
Sanya	4.73	5.25
Mean	**4.54**	**5.32**

18.4 Conclusions

Based on real measurements from BDS receivers located in Beijing, Chengdu, Sanya, the application performance of BDS ionospheric grid is evaluated. To summarize, the following conclusions:

1. In BDS service area, the BDS IGPs in most region of Chinese mainland and coastal have a good availability.
2. The correction performance of BDS ionospheric grid at mid-latitude is better than low latitude.
3. The average correction accuracy of B1I using BDS ionospheric grid is 91.17 %, the average correction accuracy is 0.32 m.
4. In B1I differential positioning mode, the horizontal positioning accuracy is 4.54 m (95 confidence level), the height positioning accuracy is 5.32 m (95 % confidence level).

References

1. Xie G (2013) Principles of GNSS: GPS, GLONASS and Galileo. Publishing House of Electronics Industry, Beijing
2. FAA (1994) Specification for wide-area augment at ion (WAAS)
3. Zhang X, Liu R, Yang Z (2012) A study on the grid ionospheric delay algorithm in Beidou. Aerosp Control 30(1):15–19
4. CSNO (2013) Beidou navigation satellite system signal in space interface control document, open service signal (Version 2.0)
5. Wu X, Han C, Ping J (2013) Monitoring and analysis of regional ionosphere with GEO satellite observations. Acta Geodaet Cartogr Sin 42(1):13–18
6. Feng W, Chen X, Wu X, Ye X (2011) Influence of space latitude on differential ionospheric grid system. J Geodesy Geodyn 30(4):135–138
7. Yu M, Guo J, Guo J (2004) Ionospheric delay values from Klobuchar model and dual frequency measurements: comparison and analysis. Bull Surv Mapp (6):5–8

Chapter 19
Analysis and Improvement to Ionosphere Grads Integrity Monitoring Algorithm in Ground Based Augmentation System

Zhaodong Xing, Jingbo Zhao, Zhenhua Wang and Chunyang Zhi

Abstract Ground Based Augmentation System (GBAS) can strongly support aircraft's precise approach and landing, and integrity monitoring is not only the difficulty of the system realization but also the key point to safeguard the flight. The ionosphere grads is the uppermost element that influence the GBAS integrity. Several algorithms are used together to achieve the ionosphere grads monitoring and ensure the ionosphere grads in an acceptable limit, ultimately guarantee GBAS integrity. In this paper, the theory basis of the ionosphere grads monitoring algorithm is analyzed firstly, then an improved algorithm is proposed, which can increase ionosphere grads monitoring sensitivity effectively. The comparable experimental analysis of present and improved algorithm is given; the results show that multi-monitoring algorithm can monitor ionosphere grads from different aspects, while the improved algorithm can increase monitoring effect apparently.

Keywords GBAS · Integrity · Ionosphere grads monitoring

19.1 Introduction

Although satellite navigation systems have been extensively used in flight navigation, it still can not satisfy the integrity requirements for aircraft precision approach and landing. ICAO requires that CAT I integrity risk must go down to 10^{-7}/approach with the warning time not more than 6 s and the continuity up to 1–4 × 10^{-6}/15 s, CAT III (blind landing) integrity risk must go down to 10^{-9}/approach with the warning time not more than 2 s [1]. Thus, it is required to

Z. Xing (✉) · J. Zhao · Z. Wang · C. Zhi
The 54th Research Institute of CETC, Shijiazhuang, China
e-mail: xzd1231@126.com

Z. Xing · J. Zhao · Z. Wang · C. Zhi
Satellite Navigation Technology and Equipment Engineering Technology Research Center of Hebei Province, Shijiazhuang, China

J. Sun et al. (eds.), *China Satellite Navigation Conference (CSNC) 2015 Proceedings: Volume II*, Lecture Notes in Electrical Engineering 341,
DOI 10.1007/978-3-662-46635-3_19

take a series of integrity monitoring measures in GBAS to improve the integrity level of the navigation system when the continuity and availability is ensured, thereby to satisfy the integrity requirements for precision approach and landing.

As one of important factors that affect GBAS integrity and precision, the differential correction residual of ionosphere is caused by different paths of signal going through the ionosphere to arrive at the aircraft and at the Ground-Reference Station (GRS). In case of an ionosphere storm, the spatial correction residual of ionosphere will build up high enough to affect the system integrity. As per the results of a research based on statistical data, an ionosphere storm can be expressed with a model that consists of four parameters, i.e., slope, width, speed and maximum delay. Computation shows that the vertical positioning error resulting from ionosphere grads will exceed 19 m in the worst case. It is an effective solution to introduce real-time monitoring of ionosphere grads into the assurance of positioning accuracy and integrity.

19.2 Ionosphere Grads Integrity Monitoring Principle

Using empirical data, ionosphere storm may be simplified as a linear model for research. The ionospheric effect to GBAS is shown in Fig. 19.1 [2]. Since navigation signal takes different paths to reach the aircraft and the GBAS separately, the differential correction for the ground station varies from that actually needed by the aircraft.

Delay of code phase and lead of carrier phase will occur when navigation signal goes through the ionosphere, as expressed by Eq. (19.1). Therefore, it is practical to use the change rate of $\rho 1 - \varphi 1$ among the observed quantities for monitoring the magnitude of ionosphere grads or use the carrier-phase change rate that excludes satellite clock error because of high-precision carrier phase and its constant

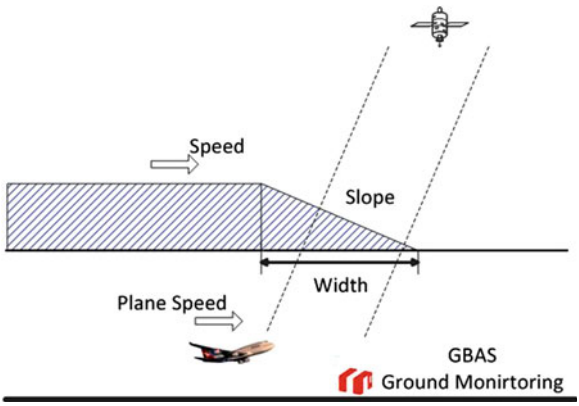

Fig. 19.1 Ionosphere storm model

ambiguity of a full cycle. When the monitored quantity exceeds a threshold, the current satellite observation quantity will be considered unavailable, thereby to assure the integrity.

$$\begin{aligned} \rho_1 &= R + C + i_1 + n_{\rho 1} \\ \varphi_1 &= R + C - i_1 + N_1 + n_{\varphi 1} \end{aligned} \tag{19.1}$$

where, ρ1 and φ1 represent the navigation signal code and the carrier observed quantity respectively; R represents the real distance between the reference receiver antenna and satellite; C represents the sum of satellite clock error, ephemeris error and tropospheric error as the common component error in ρ_1 and φ_1; i_1 represents the ionospheric delay, N_1 represents the full-cycle ambiguity; $n_{\rho 1}$ and $n_{\varphi 1}$ represent the sum of receiver noise and multipath error in the code and carrier observed quantities respectively.

19.3 Ionosphere Grads Monitoring Algorithm for GBAS

The GBAS integrity monitoring platform consists of several receivers and a information processing system (IPS), as shown in Fig. 19.2. The GBAS integrity monitoring process involves separate modular algorithms for ionospheric monitoring, including carrier-smoothed code inno, code-carrier divergence, carrier acceleration-ramp-step (Acc-Ramp-Step) [3]. The evaluation logics for ionosphere grads integrity monitoring are as follows: the individual channel will be unavailable for a while if a single monitoring value is labeled with an integrity token (i.e., exceeded the threshold); the satellite observation quantities will be all unavailable if two or more monitoring values for the same satellite are labeled with integrity tokens.

The carrier-smoothed code inno (*Inno*) is monitored for detecting pulse and step error in original pseudo-range measurement.

$$Inno_{m,n}(t) = \rho_{m,n}(t) - \left[\rho_{s,m,n}(t-1) + \phi_{m,n}(t) - \phi_{m,n}(t-1)\right] \tag{19.2}$$

where, $\rho_{s,m,n}(t-1)$ represents the observed quantity of smoothed code.

If three successive *Inno* values exceed the threshold, then an integrity token will come up and the corresponding channel will be excluded by the subsequent comprehensive actuating logic. If only a single *Inno* value exceeds the threshold, then the pseudo-range original value at that moment will be skipped in the smoothing process and only the measured value of carrier phase will be used in the carrier smoothed code.

The carrier Acc-Ramp-Step monitoring algorithm assumes that quick change like pulse, step or acceleration occurs in carrier phase measurement, which would bring about pseudo-range correction error or carrier phase correction error.

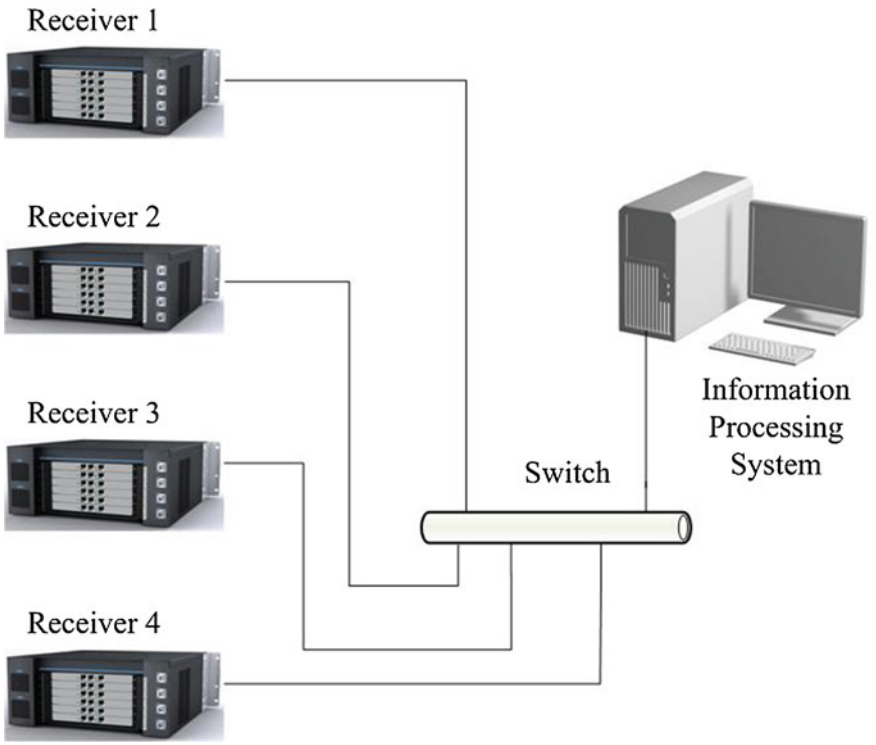

Fig. 19.2 GBAS integrity monitoring platform

The specific processing method is to calculate the carrier phase at the nearest ten successive known points next to Point k, e.g., k−9 through k.

$$\phi^*_{m,n}(t) = \phi_{c,m,n}(t) - \frac{1}{N_m}\sum_{j\in S_m(t)}\phi_{c,m,j}(t) \tag{19.3}$$

where, S_m represents the satellites tracked by the receiver and N_m represents the number of satellites tracked by the receiver.

The equation is fitted using the method of least squares based on the calculation results at the ten known points:

$$\phi^*_{m,n} = \phi^*_{0,m,n} + \frac{d\phi^*_{m,n}}{dt}\Delta t + \frac{d^2\phi^*_{m,n}}{dt^2}\frac{\Delta t^2}{2} \tag{19.4}$$

With the quadratic term, the linear term and the constant term acquired from the fitted equation, the acceleration, ramp and step are defined as follows:

$$Acc_{m,n} = \frac{d^2\phi^*_{m,n}}{dt^2} \tag{19.5}$$

$$Ramp_{m,n} = \frac{d\phi^*_{m,n}}{dt} \tag{19.6}$$

$$Step_{m,n}(t) = \phi^*_{mean,m,n}(t) - \phi^*_{pred,m,n}(t) \tag{19.7}$$

where, $\phi^*_{mean,m,n}$ represents the measured value at epoch t and $\phi^*_{pred,m,n}$ represents the predicted value calculated from the fitting curve (19.4).

In case of any monitoring value beyond the threshold, exclude the channel to which the maximum monitoring value that exceeds the threshold correspond and recalculate the Acc-Ramp-Step. If the maximum value is present in different channels, MQM simply reserves the calculation result and highlights the logic rather than excluding all the failed channels and consequently disabling the channel availability. However, the above evaluation does not mean these channels have passed the detection; in contrast, the comprehensive logics will make a comprehensive decision to the failure token with other integrity monitoring algorithms. The failure probability happened simultaneously with multiple channels is very low; therefore, such an evaluation logic will not be used more than twice.

Using GMA model, the code-carrier divergence monitoring (Dvgc) estimates the degree of separation between the code observed quantity and the carrier observed quantity.

$$Dvgc(k) = \frac{\tau - T}{\tau} Dvgc(k-1) + dz(k) \tag{19.8}$$

where, τ_d represents a time constant, T_S represents the updating interval at which observed quantity in the GBAS is reported and Z represents the difference between the code observed quantity and the carrier observed quantity, which is expressed as follows.

$$\begin{aligned} Z(k) &= \rho(k) - \phi(k) \\ &= 2I(k) - N + n \end{aligned} \tag{19.9}$$

where, I represents the ionospheric error, N represents the full-cycle ambiguity and n represents error like receiver noise.

When the $Dvgc$ value exceeds the predetermined monitoring threshold, an integrity token will come up.

19.4 Combinatorial Monitoring Value Algorithm and Performance Analysis

19.4.1 Combinatorial Monitoring Value Algorithm

The actual distribution of integrity monitoring values is non-Gaussian, not in favor of data analysis and threshold determination. In practice, the distribution model of monitoring values is converted into Gaussian distribution with Gaussian expansion method. Thus, the monitoring value X_i can be expressed as Gaussian distribution subject to mean value μ_i and mean square error σ_i.

$$\mathrm{X}_i \; - \; \mathrm{N}(\mu_i, \sigma_i) \tag{19.10}$$

The monitoring performance will be upgraded by monitoring a new monitoring quantity Y, which is established by combining a number of monitoring values.

$$Y = \sum_{i=1}^{k} \left(\frac{X_i - \mu_i}{\sigma_i} \right)^2 \tag{19.11}$$

Y appears χ^2 distribution with K degrees of freedom, where K represents the mean value and 2K represents the variance.

X_i may be considered as the actual distribution of monitoring values in the ionosphere grads monitoring module. The threshold in integrity monitoring practice is usually set to $\mu_i \pm 6\sigma_i$ [3], then the warning probability of a single channel for integrity monitoring is 1.97×10^{-9}.

For the Y distribution that appears χ^2 distribution, pick up a combination of three mutually uncorrelated monitoring quantities, then the degree of freedom is 3 and we obtain:

$$P(\chi_3^2 > 43.45) = 1.97 \times 10^{-9} \tag{19.12}$$

Conclusively, taking 43.45 as the threshold of Y distribution will provide the same continuity as taking $\mathrm{Y_i} = 6^2 + 6^2 + 6^2 = 108 > 43.45$ as the threshold of Gaussian distribution. The following section will analyze how the improved algorithm to upgrade the performance.

19.4.2 Performance Analysis of Combinatorial Algorithm

Paper 4 consider three possible scenarios in which the threshold is exceeded by one, two and three monitoring values of X_i separately [4].

Scenario 1 Assuming that all X_i values exceed the threshold, an integrity token comes up and $X_i \leq \mu_i - 6\sigma_i$ or $X_i \leq \mu_i - 6\sigma_i$, then

$$Y_i \geq 6^2 + 6^2 + 6^2 = 108 > 43.45 \tag{19.13}$$

Scenario 2 Assuming that two X_i values exceed the threshold, an integrity token comes into being, $X_i \geq \mu_i + 6\sigma_i$ or $X_i \leq \mu_i - 6\sigma_i$ (i = 1 and 2 respectively) and $X_i \leq \mu_i + 6\sigma_i$ or $X_i \geq \mu_i - 6\sigma_i$ (i = 3), then

$$Y_i \geq 6^2 + 6^2 + 0 = 72 > 43.45 \tag{19.14}$$

Scenario 3 Assuming that one Xi value exceeds the threshold, an integrity token comes up, $X_i \geq \mu_i + 6\sigma_i$ or $X_i \leq \mu_i - 6\sigma_i$ (i = 1) and $X_i \geq \mu_i + 6\sigma_i$ or $X_i \leq \mu_i - 6\sigma_i$ (i = 2 and 3 respectively), then

$$Y_i \geq 6^2 + 0 + 0 = 36 < 43.45 \tag{19.15}$$

Conclusively, the combinatorial monitoring value will surely exceed the threshold and an integrity token will come up if two or three separate monitoring values exceed the threshold. The combinatorial monitoring value will not necessarily exceed the threshold if only one separate monitoring value exceeds the threshold. As a matter of fact, as per the original algorithm, a single monitoring quantity X_i exceeding the threshold suggests to exclude an individual channel that is in trouble, and multiple monitoring quantities simultaneously exceeding the threshold suggest unavailability of the satellite due to excessive ionosphere grads. Since the threshold 43.45 for the combinatorial monitoring value is obviously smaller than the threshold magnitude for multiple monitoring quantities (108, 72), the process to exclude faulty satellite by means of ionosphere grads monitoring with a combinatorial monitoring value will be significantly accelerated without influence to the continuity.

19.4.3 Combination Mode of Monitoring Values

For Y to surely appear χ^2 distribution, the monitoring values must be enveloped by Gaussian distribution and uncorrelated mutually. As per theoretical analyses and experiments, *Dvgc* is suitable for monitoring the ionosphere grads with an insignificant and constant deviation, *Inno* is suitable for monitoring short-time or instant fluctuation of ionosphere and *Acc-Ramp-Step* is suitable for monitoring the ionosphere in short-time fluctuation or of a constant ramp within a certain range or of a changing acceleration. These three monitoring quantities are strongly uncorrelated. Assuming that they are uncorrelated mutually, then it is possible to develop new

monitoring quantities on the basis of *Inno*, *Ramp* and *Step*, i.e., to exclude the unavailable satellite resulting from short-term change of ionosphere grads and to monitor the ionosphere grads having a constant deviation with *Dvgc*, *Acc* and *Ramp*.

19.5 Experiment and Tests

The data collected in SJZ ZhengDing International Airport with the integrity monitoring platform provided by CETC54 for 3 successive months are taken as test data. The monitoring platform consists of 4 receivers dedicated for integrity monitoring and necessary integrity processing software. The monitoring threshold can be figured out after the inflation factor is determined with inflated Gaussian factor algorithm. Taking the threshold computation for code-carrier separation as example, firstly process the standard deviation with inflated Gaussian algorithm [5, 6]. As shown in Fig. 19.3, the dot represents the actual distribution, the dash represents standard Gaussian distribution and the solid represents the inflated Gaussian distribution which envelopes the tail of the actual distribution. The computation results showed that the thresholds were 0.0703, 0.0344, 0.022, 0.0143, 0.0097, 0.0074, 0.0055 and 0.005 at the angles ranging from 0–15, 15–25, 25–35, 35–45, 55–65, 65–75 and 75–90 respectively. The computation processes for the thresholds of the other monitoring quantities are similar to the above example.

As shown in Figs. 19.4, 19.5, 19.6 and 19.7, the horizontal coordinates represent the time after the satellite is visible and the longitudinal coordinates represent the monitoring values. In the regular tests on a large data size, the test results based on *Dvgc/Inno/Acc* and combinatorial monitoring value were both within the limit of

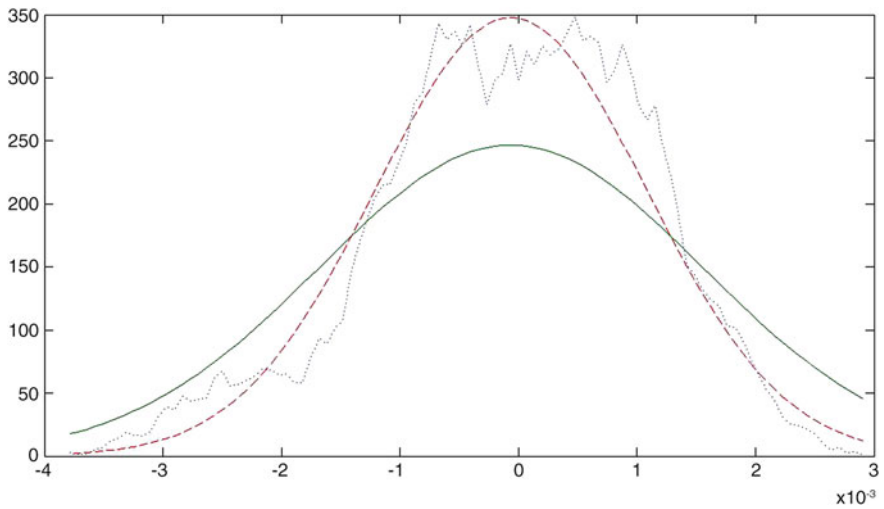

Fig. 19.3 Inflated Gaussian distribution of Dvgc

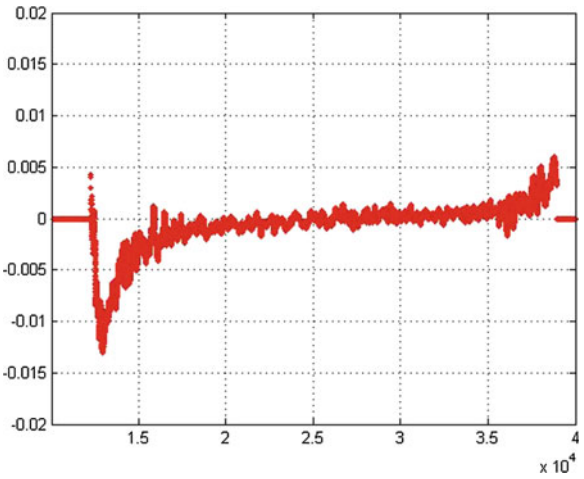

Fig. 19.4 Dvgc test results

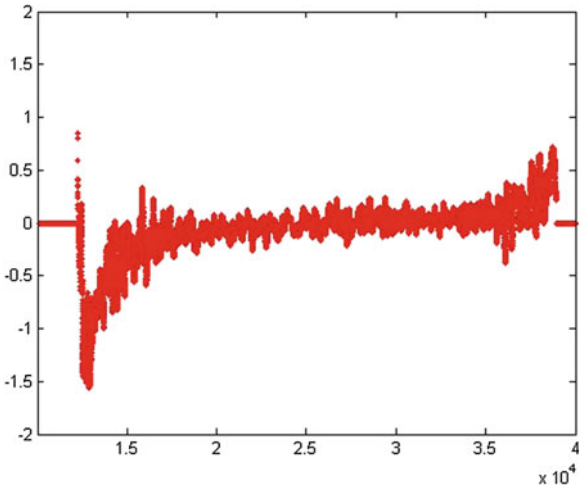

Fig. 19.5 Inno test results

the threshold. The monitoring mode based on combinatorial monitoring value never gave a false alarm with no impact to the system continuity.

So far, the theoretical effects achieved from the combination of multiple monitoring values have been analyzed and validated. In practical tests, the effects were inconsistent due to the influence resulting from the combination mode of monitoring values, the specific failure of ionosphere grads, satellite elevation and test data. Here, the test results are shown after a 0.005 m/s failure of ionosphere grads derived from the ionospheric failure model was introduced when the satellite elevation was 50°. The test results show that *Acc-Ramp-Step* and *Inno* had no value exceeded their thresholds though they gave minor response to the tests due to the ionosphere grads having an insignificant and constant deviation. After a fault

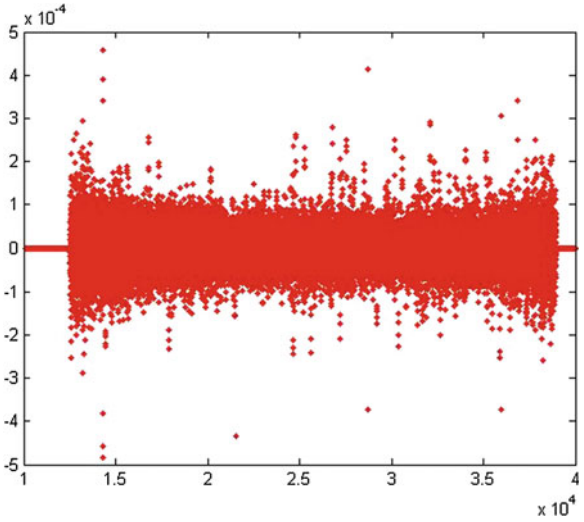

Fig. 19.6 Acc test results

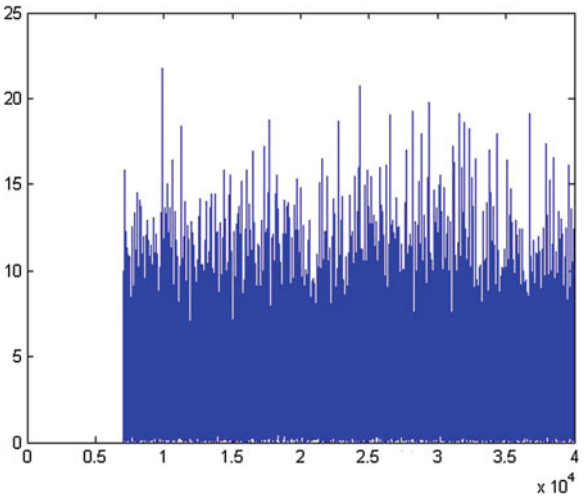

Fig. 19.7 Improved algorithm test results

was introduced, an integrity token came up about 200 s after *Dvgc* exceeded the threshold and about 150 s after the combinatorial monitoring value of *Dvgc*, *Acc* and *Ramp* exceeded the threshold.

19.6 Conclusion

GBAS integrity monitoring is of important significance for precision approach and landing of aircraft, in which ionosphere grads monitoring is an important component. This paper describes the principle of ionosphere grads monitoring in GBAS

and the GBAS integrity monitoring module involved in ionospheric monitoring. Moreover, the monitoring algorithm based on combinatorial monitoring values and the combination mode are proposed. As per our theoretical analyses and actual tests, combinatorial monitoring values may upgrade the algorithm performance in ionosphere grads monitoring while the original system continuity is maintained. However, further consideration must be made to the correlation among monitoring quantities and the optimum combination mode in the combinatorial monitoring quantity algorithm. And more theoretical analyses and actual tests are required for different cases such as the combination mode of monitoring quantities, specific failure of ionosphere grads, satellite elevation and test data.

Acknowledgments This paper received both software and hardware supports from the project team who were working on the subproject "GNSS Multibeam Monitoring Receive System for Airport" (2011BAH24B04) of "the Demonstration Project of Integrated Application of Air Traffic Control Technologies by Air Traffic Controller in Collaboration with Civil Aviation Authority in China", which is funded by the MOST as per the National Key Technology Support Program of the 12th China National Five-Year Plan. Here, the author would like to express the great appreciation.

References

1. Braff R et al (1997) Description of the FAA's local area augmentation system (LAAS). NAVIGATION: J Inst Navig 44(4):411–423
2. Luo M, Pullen S, Datta BS, Zhang G, Walter T, Enge P (2005) LAAS Study of slow-moving ionosphere anomalies and their potential impacts. In: Proceedings of ION GNSS 2005, Long Beach, CA, 13–16 Sept, pp 2337–2349
3. Xie G et al (2001) Integrity design and updated test results for the stanford LAAS integrity monitor testbed. In: ION 57th Annual meeting/CIGTF 20th biennial guidance test symposium, The Institute of Navigation, Albuquerque, NM, 06, 11, pp 681–693
4. Xie G (2004) Optimal on airport monitoring of the integrity of GPS-based landing systems. In: PhD Stanford University, pp 143–151
5. Lee J (2005) GPS-based aircraft landing system with enhanced performance beyond accuracy. In: PhD dissertation, Aeronautics and Astronautics, Stanford University
6. Pervan B, Pullen S, Sayin I (2009) Sigma estimation, inflation, and monitoring in the LAAS ground system. In: Proceedings of ION GPS, Salt Lake City, UT, 19–22, 2000–2009, pp 1234–1244

Chapter 20
Calibration Method of the IGSO Satellites Ascending Node Longitude

Quan-jun Li, Da-li Wang, Yong Yuan and Ni Kang

Abstract As the ascending node longitude of IGSO satellites should be maintained in a relatively large range with long control period and high precision, it is necessary to predict the long-term variation of the ascending node longitude accurately in order to obtain the accurate ascending node longitude and drift rate. A calibration model is established by using several orbit measurement results, the drift rate and drift acceleration of the ascending node longitude is calibrated by using the least squares method, and the ascending node longitude of long-term forecast is calculated according to the calibration results. The practical results show that the forecasting accuracy of the method is quite similar with that of orbit prediction. This method can accurately calculate the drift rate of the satellites ascending node longitude and avoid the orbit prediction error due to the effect of measurement data.

Keywords IGSO satellite (Inclined geo synchronous orbit) · Ascending node longitude · Drift rate · Drift acceleration

20.1 Introduction

As a vital part of the second generation navigation constellation, IGSO satellite has an orbit altitude of 35,786 km and orbital inclination of 55°. Because of the influence of tesseral harmonic terms J_{22} in non-spherical gravitational potential, IGSO satellite orbit period will be changed, which will cause the change of ascending node longitude [1–4]. And regular orbit maintenance is therefore required. The orbit maintenance of IGSO satellite features a wide maintenance range, a long control cycle and a high control precision. For these characteristics,

Q. Li (✉)
State Key Laboratory of Astronautic Dynamics, Xi'an, China
e-mail: lqj1983@163.com

D. Wang · Y. Yuan · N. Kang
Xi'an Satellite Control Center, Xi'an, China

J. Sun et al. (eds.), *China Satellite Navigation Conference (CSNC) 2015 Proceedings: Volume II*, Lecture Notes in Electrical Engineering 341,
DOI 10.1007/978-3-662-46635-3_20

long-term prediction of accurate ascending node longitude is needed so as to acquire the precise ascending node longitude and its drift rate before and after orbit maintenance. The traditional approach is that based on the track measurement and determination result, the ascending node longitude is calculated using numerical method, and the last orbit determination calculation result shall prevail. This method cannot effectively calibrate the ascending node longitude, drift rate and drift rate acceleration by multiple measurements. Drift rate and drift rate acceleration is crucial factors to make IGSO orbit maintenance strategies, which directly affects the accuracy and period of IGSO orbit maintenance [5, 6].

20.2 Analysis of IGSO Satellite's Orbit Perturbation

IGSO satellite's orbit perturbation includes perturbation induced by the earth's shape, luni-solar perturbation and solar radiation pressure perturbation, of which the first two are the main factors for the change of ascending node longitude.

20.2.1 Perturbation Induced by the Earth's Shape

J_2 in perturbation induced by the earth's shape would cause the change of Ω and ω. Its analytical solution [7] is:

$$\dot{\Omega}_{J_2} = \frac{3}{2}\frac{nJ_2}{(1-e^2)^2}\left(\frac{R_e}{a}\right)^2 \cos i \tag{20.1}$$

$$\dot{\omega}_{J_2} = \frac{3}{2}\frac{J_2}{p^2}R_e^2 n\left(2 - \frac{5}{2}\sin^2 i\right) \tag{20.2}$$

$$\dot{\lambda}_{J_2} = \dot{\omega}_{J_2} + \dot{M}_{J_2} = \frac{3}{2}\frac{J_2}{p^2}R_e^2 n\left[\left(2 - \frac{5}{2}\sin^2 i\right) + \left(1 - \frac{3}{2}\sin^2 i\right)\sqrt{1-e^2}\right] \tag{20.3}$$

Among them, e is the orbital eccentricity, a is the orbital radius, n is the orbital angular velocity, i is the orbital inclination, R_e is the radius of the earth.

The earth's gravitational field J_{22} item will have significant long-periodic influence on A, and eventually lead to nonlinear changes of satellite phase:

$$\frac{da}{dt} = \frac{3R_e^2 J_{22}}{a} n(1+\cos i)^2 \sin 2(\lambda_C - \lambda_{22}) \tag{20.4}$$

Among them, λ_C is the nominal ascending node longitude.

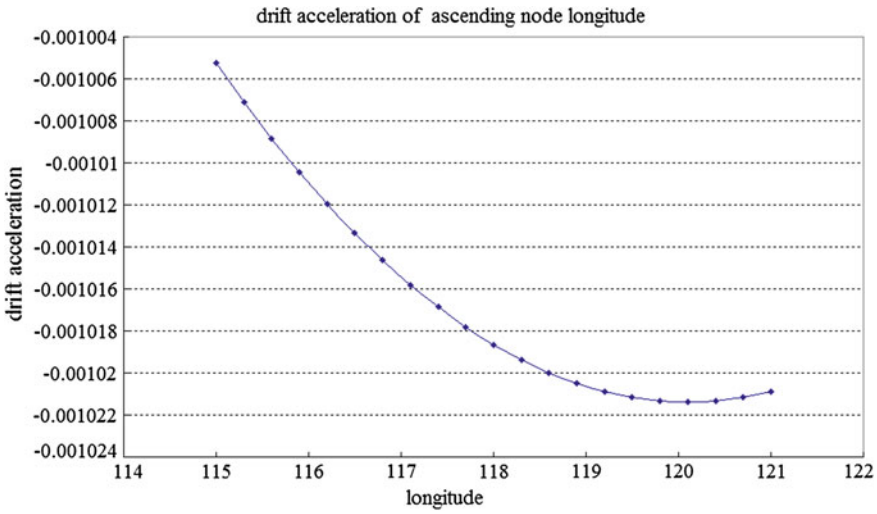

Fig. 20.1 Drift acceleration near 118°

The corresponding second-order change item of ascending node's geographical longitude (drift acceleration) is:

$$\ddot{\lambda}_{J_{22}} = -18\pi^2 J_{22} \frac{R_e^2}{a^2}(1+\cos i)^2 \sin 2(\lambda_C - \lambda_{22}) \tag{20.5}$$

By applying analytical solutions, drift acceleration in different longitude can be solved. In terms of those IGSO satellites whose ascending node longitude is near 118° and 95°. If it is necessary to maintain ascending node longitude within a range of 5°, the theoretical value of their drift acceleration is shown in Figs. 20.1 and 20.2.

20.2.2 Luni-solar Perturbation

The luni-solar perturbation will cause long-term drift for Ω, ω. Its analytical solution [7] is:

$$\dot{\Omega}_{sun} = -\frac{3}{4}\beta_{es} a^3 (1 - \frac{3}{2}\sin^2 i_s)(1 + \frac{3}{2}e^2)(1-e^2)^{-\frac{1}{2}} n \cos i \tag{20.6}$$

$$\dot{\omega}_{sun} = \frac{3}{4}\beta_{es} a^3 (1 - \frac{3}{2}\sin^2 i_s)[(2 - \frac{5}{2}\sin^2 i) + \frac{1}{2}e^2](1-e^2)^{-\frac{1}{2}} n \tag{20.7}$$

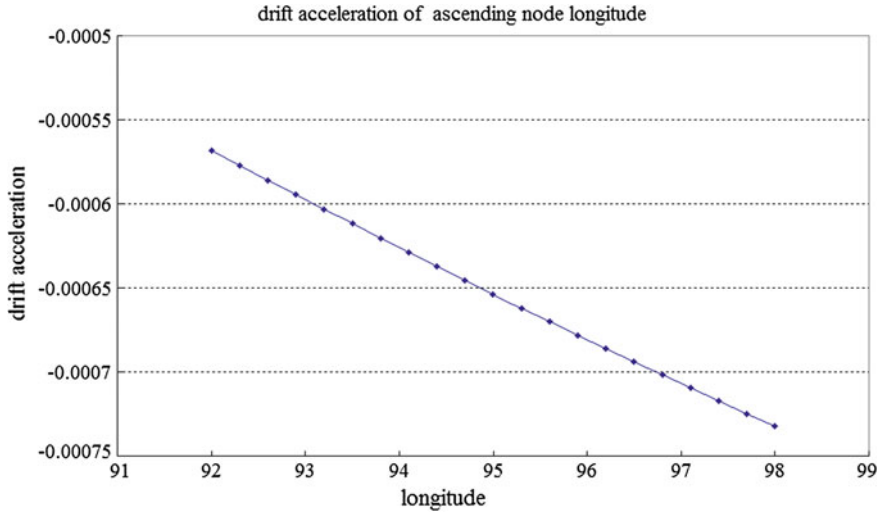

Fig. 20.2 Drift acceleration near 95°

$$\dot{\Omega}_{moon} = -\frac{3}{4}\beta_{em}a^3(1-\frac{3}{2}\sin^2 i_m)(1+\frac{3}{2}e^2)(1-e^2)^{-\frac{1}{2}}n\cos i \tag{20.8}$$

$$\dot{\omega}_{moon} = \frac{3}{4}\beta_{em}a^3(1-\frac{3}{2}\sin^2 i_m)[(2-\frac{5}{2}\sin^2 i)+\frac{1}{2}e^2](1-e^2)^{-\frac{1}{2}}n \tag{20.9}$$

Among them: $\beta_{es} = \mu_s/r_{es}^3\mu$, $\beta_{es} = \mu_m/r_{em}^3\mu$, μ_s is the constant of the sun's gravitational field, μ_m is the constant of the moon's gravitational field, r_{es} is the distance from the earth to the sun, r_{em} is the distance from the earth to the moon, i_s is the angle between ecliptic and equator, i_m is the angle between the equator and moon's path.

Therefore, the drift motion of ascending node longitude of IGSO satellite can be described as:

$$\lambda_G = \lambda_{G0} + \dot{\lambda}_G(t-t_0) + \frac{1}{2}\ddot{\lambda}_G(t-t_0)^2 \tag{20.10}$$

Among them: $\dot{\lambda}_G = \dot{\Omega}_{J_2} + \dot{\Omega}_{sun} + \dot{\Omega}_{moon} + \dot{\lambda}_{J_2} + \Delta n$, $\ddot{\lambda}_G = \ddot{\lambda}_{J_{22}}$, Δn is the change rate of ascending node longitude caused by orbital semi major axis. By solving the long-term changes of Ω, the theoretical value of $\dot{\Omega}$ is $-0.0101°$/day.

20.3 Calibration Model of the IGSO Satellites Ascending Node Longitude

Because of the long control period of IGSO satellites (more than 160 days), as required by satellite management, track measurement should be launched every two weeks during the period of two times control. By applying each measuring result of ascending node longitude, the following method is a long term forecast for the ascending node longitude.

If t_i refers to each measuring time $(i = 1, 2, \ldots, N)$, $\lambda(t_i)(i = 1, 2, \ldots, N)$ refers to the ascending node longitude to be calculated, $\dot{\lambda}(t_i)(i = 1, 2, \ldots, N)$ refers to the drift rate of ascending node longitude, and $\ddot{\lambda}(t)$ refers to the drift acceleration ascending node longitude, then the nth ascending node longitude can be presented as:

$$\begin{cases} \lambda(t_1) = \lambda(t_1) \\ \lambda(t_2) = \lambda(t_1) + \dot{\lambda}(t_1) \cdot (t_2 - t_1) + \int_{t_1}^{t_2} dt \int_{t_1}^{t} \ddot{\lambda}(t) dt \\ \vdots \\ \lambda(t_{n-1}) = \lambda(t_{n-2}) + \dot{\lambda}(t_{n-2}) \cdot (t_{n-1} - t_{n-2}) + \int_{t_{n-2}}^{t_{n-1}} dt \int_{t_{n-2}}^{t} \ddot{\lambda}(t) dt \\ \lambda(t_n) = \lambda(t_{n-1}) + \dot{\lambda}(t_{n-1}) \cdot (t_n - t_{n-1}) + \int_{t_{n-1}}^{t_n} dt \int_{t_{n-1}}^{t} \ddot{\lambda}(t) dt \end{cases} \tag{20.11}$$

Among them $n \in (1, N)$.

By summating the right and left sides of the above equation, the calculation equation of nth ascending node longitude can be showed as follows:

$$\begin{aligned} \lambda(t_n) &= \lambda(t_1) + \sum_{i=1}^{n-1} \dot{\lambda}(t_i) \cdot (t_{i+1} - t_i) + \sum_{i=1}^{n-1} \int_{t_i}^{t_{i+1}} dt \int_{t_i}^{t} \ddot{\lambda}(t) dt \\ &= \lambda(t_1) + \dot{\lambda}(t_1)(t_n - t_1) + t_n \sum_{i=2}^{n-1} \int_{t_{i-1}}^{t_i} \ddot{\lambda}(t) dt - \sum_{i=2}^{n-1} t_i \int_{t_{i-1}}^{t_i} \ddot{\lambda}(t) dt + \sum_{i=1}^{n-1} \int_{t_i}^{t_{i+1}} dt \int_{t_i}^{t} \ddot{\lambda}(t) dt \end{aligned} \tag{20.12}$$

Because the range of IGSO ascending node longitude keeps within 5°, according to the results of the theory, the ascending node longitude changes approximately as a linear drift acceleration. For convenient calculation, the drift acceleration of ascending node longitude can be simplified as the linear relationship in which the ascending node longitude is variables, namely,

$$\ddot{\lambda}(t) = k\lambda(t) + b \tag{20.13}$$

When $t \in (t_{i-1}, t_i)$, $\lambda(t)$ can be approximated by linear change, then

$$\lambda(t) = \lambda(t_{i-1}) + \frac{\lambda(t_i) - \lambda(t_{i-1})}{t_i - t_{i-1}}(t - t_{i-1}) \tag{20.14}$$

When synthesize the Eqs. (20.13) and (20.14). Equation (20.14) can be reduced to:

$$\begin{aligned}\lambda(t_n) = \lambda(t_1) + \dot{\lambda}(t_1)(t_n - t_1) + b[t_n(t_{n-1} - t_1) - \sum_{i=2}^{n-1} t_i(t_i - t_{i-1}) + \frac{1}{2}\sum_{i=1}^{n-1}(t_{i+1} - t_i)^2] \\ + k[t_n \sum_{i=2}^{n-1}\frac{1}{2}(\lambda(t_i) + \lambda(t_{i-1}))(t_i - t_{i-1}) - \sum_{i=2}^{n-1}\frac{1}{2}t_i(\lambda(t_i) + \lambda(t_{i-1}))(t_i - t_{i-1}) \\ + \sum_{i=1}^{n-1}\frac{1}{6}(\lambda(t_{i+1}) + 2\lambda(t_i))(t_{i+1} - t_i)^2]\end{aligned} \tag{20.15}$$

The Eq. (20.15) can be simplified as:

$$\lambda(t_n) = \lambda(t_1) + \dot{\lambda}(t_1)(t_n - t_1) + B_n b + A_n k \tag{20.16}$$

Among them: $B_n = t_n(t_{n-1} - t_1) - \sum_{i=2}^{n-1} t_i(t_i - t_{i-1}) + \frac{1}{2}\sum_{i=1}^{n-1}(t_{i+1} - t_i)^2$

$$\begin{aligned}A_n = t_n \sum_{i=2}^{n-1}\frac{1}{2}(\lambda(t_i) + \lambda(t_{i-1}))(t_i - t_{i-1}) - \sum_{i=2}^{n-1}\frac{1}{2}t_i(\lambda(t_i) + \lambda(t_{i-1}))(t_i - t_{i-1}) \\ + \sum_{i=1}^{n-1}\frac{1}{6}(\lambda(t_{i+1}) + 2\lambda(t_i))(t_{i+1} - t_i)^2\end{aligned}$$

According to the several measuring results of ascending node longitude, $\lambda(t_1), \dot{\lambda}(t_1), b, k$ in Eq. (20.16) can be solved by applying least squares solution theoretically.

20.4 Simulating Calculation Result of Calibration Model

By using the ascending node longitude which is calculated by IGSO extrapolation ephemeris as observation data, and the values of k and b within 118 ± 3° calculated by the above the mechanical model, the calculation results are shown in Table 20.1, of which the theoretical value is the result of analytical solutions of the results of linear fitting results.

From solving the results showed that the k value is not stable within different longitude, it shows that k is sensitive to data error. In the model, the k value impact on the ascending node longitude is less than 0.1° in 200 days. Therefore, it can get

Table 20.1 k and b simulation and theoretical calculation results in calibration model

Ascending node	k		b	
	Simulation	Theoretical	Simulation	Theoretical
115–121	−0.0000548	−0.00000258	−0.0010392	−0.001007
115–120	−0.0000443	−0.00000314	−0.0010768	−0.0010084
115–119.5	−0.0000398	−0.00000351	−0.0010942	−0.0010091
115–119.3	−0.0000357	−0.00000369	−0.0011044	−0.0010089
115–118.7	−0.0000199	−0.00000406	−0.0011138	−0.0010097
115–118.4	−0.0000058	−0.00000424	−0.0011095	−0.0010096
115–118	0.0000140	−0.00000443	−0.0010905	−0.0010107
115–117.5	0.0000522	−0.00000479	−0.0010465	−0.0010107
115–117.3	0.0000585	−0.00000498	−0.0010084	−0.0010119

Table 20.2 The value of b solved by the fixed k

Scope of longitude	115–121	115.7–120.3	116.2–119.8	116.7–119.3	117.1–118.9
b	−0.00113952	−0.00114002	−0.00113672	−0.00112952	−0.00112072

the average value (0.00000394) of k theoretical calculation results as a fixed value to solute b in the model of the theoretical calculation, the results are shown in Table 20.2.

As can be seen from the Table 20.2, b value is relatively stable, the average of b is 0.0011333.

20.5 Calibration Model Validation Results

Using actual measurement results as the observation data, the ascending node longitude drift acceleration of three IGSO satellites fixed 118° has been calibrated, the results such as Table 20.3.

In the calculation results, the average value of b is −0.001131678. The results agree with the theoretical calculation.

Table 20.3 The value of b calculated by measured data

Name	Time	Date	b
IGSO-1	2011-2 to 2011-5	6	−0.001166588
	2011-6 to 2011-9	9	−0.001153685
IGSO-2	2011-3 to 2011-8	10	−0.001116778
	2011-8 to 2011-11	9	−0.001101323
IGSO-3	2011-4 to 2011-7	8	−0.001203821
	2011-7 to 2011-11	10	−0.001047872

Table 20.4 IGSO-1 satellite data validation results from February 2011 to May 2011

Date	The measured ascending node longitude (°)	The predicted ascending node longitude on 30 May (°)		The measured ascending node longitude on 30 May (°)
		The model prediction	Orbit prediction	
2011-2-22	115.648	×	117.378	117.824
2011-3-21	117.383	×	117.884	
2011-4-1	117.829	117.978	117.843	
2011-4-20	118.239	117.871	117.826	
2011-5-18	118.129	117.827	117.824	

The ascending node longitude of IGSO satellites fixed 118° has been forecasted by this model, and k is −0.00000394, b is −0.0011333. On the premise of at least three measurements between two controls, the forecasting method can be calculated. In order to verify the correctness of this method, the model forecast results, orbit prediction results and measured results are compared. Detailed comparison method is: during the two controls starting with the third measurement, the ascending node longitude has been predicted by model and orbit after each measurement, and the prediction results have been compared with the last measured results. The calculation results show in the following Tables 20.4, 20.5 and 20.6:

From the tables we can see that, the model precision of prediction is quite similar with the orbit prediction precision, and the forecast accuracy improves with increasing the times of measurement. Using this model, the ascending node longitude can be calculated by the measurement data when the IGSO satellites pass the ascending node, the measurement data can be increased not through the entire arc

Table 20.5 IGSO-2 satellite data validation results from March 2011 to August 2011

Date	The measured ascending node longitude (°)	The predicted ascending node longitude on 9 August (°)		The measured ascending node longitude on 9 August (°)
		The model prediction	Orbit prediction	
2011-3-10	115.739	×	115.859	115.89
2011-3-21	116.597	×	115.967	
2011-4-6	117.637	115.71	115.839	
2011-4-18	118.217	115.722	115.849	
2011-5-17	118.987	115.788	115.808	
2011-5-31	119.05	115.845	115.788	
2011-6-19	118.75	115.877	115.797	
2011-7-12	117.84	115.897	115.802	
2011-7-25	117.074	115.912	115.80	

Table 20.6 IGSO-3 satellite data validation results from April 2011 to July 2011

Date	The measured ascending node longitude (°)	The predicted ascending node longitude on 5 July (°)		The measured ascending node longitude on 5 July(°)
		The model prediction	Orbit prediction	
2011-4-17	117.752	×	117.7	117.487
2011-4-28	118.167	×	×	
2011-5-9	118.455	117.733	117.495	
2011-5-24	118.592	117.682	117.486	
2011-6-7	118.481	117.646	117.495	
2011-6-21	118.136	117.615	117.483	

orbit measurement, and the prediction accuracy has been improved. The ascending node longitude drift rate can be directly calculated by the model, and single orbit measurement error can be avoided.

20.6 Conclusion

In this essay, a calibration model is established by using several orbit measurement results, the drift rate and drift acceleration of the ascending node longitude is calibrated by using the least squares method, and the ascending node longitude of long-term forecast is calculated according to the calibration results. The practical results show that the forecasting accuracy of the method is quite similar with that of orbit prediction. The ascending node longitude can be calculated by the measurement data when the IGSO satellites pass the ascending node, the measurement data can be increased not through the entire arc orbit measurement. This method can accurately calculate the drift rate and the drift acceleration of the ascending node longitude, witch can be applied to the IGSO satellite orbit maintenance strategy.

References

1. Chu H, Zhang N, Gu X (2005) Constellation optimum design of satellite positioning system based on MEO and GEO satellites. Chin Space Sci Technol 2:52–58
2. Yang Y, Fan L, Dong X (2008) IGSO constellation analysis and its optimal design. Netw Inf Technol 27(11):53–55
3. Xiang J, Zhang Y (2007) Study on configuration optimization and coordination control strategy for the regional coverage satellite constellation. Flight Dyn 25(3):87–91
4. Mao Y, Song X, Jia X (2009) The evolvement of satellite orbit and constellation configuration. Sci Surv Mapp 34(1):119–121

5. Li H, Li J, Jiao W (2010) Analyzing perturbation motion and studying configuration maintenance strategy for compass-M navigation constellation. J Astronaut 31(7):1756–1761
6. Zhu M, Hu S (2009) Location evolution and keeping of IGSO cross node. Chin Space Sci Technol 29(1):41–44, 51
7. Liu L (2000) Orbit theory of spacecraft. National Defend Industry Press

Chapter 21
Ionosphere Integrity Monitoring Based on the Combined System of GPS and BDS

Chuanhua Zhao, Jinzhong Bei, Shan Pan and Hongying Zhang

Abstract The ionosphere delay is one of the main error sources affecting the positioning and its changes are very complicate. Integrity is the ability which the system sending out warning signals to users when navigation system has any failure or error exceeding can't be applied for navigation and positioning service. As far as the user safety is considered, the integrity of the navigation system weights more than its precision. The ionosphere integrity monitoring is indispensable in order to guarantee the reliability and availability of the user positioning. With the increase of the number of the BDS satellites gradually, the BDS is more and more approaching perfection. The combined system data of GPS and BDS of the Hebei CORS were used to conduct ionosphere integrity monitoring in this paper. So the stable of ionosphere were discussed. The results showed that the ionosphere delay calculated by these data was stable and these data were available.

Keywords Ionosphere delay · Reliability · Integrity monitoring · BDS

21.1 Introduction

Integrity is the ability which system sending out warnings to users when the navigation system has any failure or error overrunning, and it can't be used for navigation and positioning. The integrity information of the system is required no matter when

C. Zhao (✉)
Shandong Agricultural University, Taian 271018, China
e-mail: zhaochuanhua2007@126.com

J. Bei
China Academy of Surveying and Mapping, Beijing 100830, China

S. Pan
Shandong Lutai Coal CO.LTD, Jining 272350, China

H. Zhang
Jiang Su Food & Pharmaceutical Science College, Huaian 223003, China

J. Sun et al. (eds.), *China Satellite Navigation Conference (CSNC) 2015 Proceedings: Volume II*, Lecture Notes in Electrical Engineering 341,
DOI 10.1007/978-3-662-46635-3_21

and where, it is a kind of measure of the credible degree with the information providing to users. It including the ability which the system provides timely and effective warning information to users, and it is an important parameter which guarantee the safety of users [1].

The ionosphere delay is one of the main error sources of the RTK positioning, and whose change is the most complex. So it's the most difficult to model accurately. And, in some cases, some of the ionosphere high-order residuals will still remain in the short baseline which is composed by virtual reference station and mobile users. It makes affect on the ambiguity solution and coordinate calculation. In some cases it make the flow sides cannot be initialized. Therefore, in order to guarantee the reliability and availability of the position of mobile users, it is necessary to induct integrity monitoring with ionosphere [2].

Extensive researches have been conducted on the ionosphere integrity monitoring by many overseas and domestic scholars. The most significant researches are made by Chen X and Zhou Dongwei. Two linear indicators with ionosphere residual integrity monitoring (IRIM) and ionosphere residual interpolation uncertainty (IRIU) were proposed by Chen X in 2003. The data of Japan and Germany network were made to analysis. The results showed that the two indicators can estimate ionosphere residual error well [3]. The ionosphere integrity monitoring indicator based on the double-difference was proposed by Zhou Dongwei in 2007. The CORS network data of Sichuan province were used to induct ionosphere integrity monitoring, the results achieved good effect.

The data of combined system with GPS and BDS in Hebei province was inducted to ionosphere integrity monitor in this paper. Some useful conclusions are obtained.

21.2 Algorithm Processing

In order to monitor the ionosphere integrity, it needs to calculate ionosphere delay of combined system. Because the two coordinate systems are different, so transformation of space-time system is needed to be inducted firstly.

21.2.1 Transformation of Space-Time System

1. Transformation of coordinate system

(1) Transformation of coordinate system between WGS84 and CGCS2000

WGS84 coordinate system is used to GPS, but CGCS2000 is used to BDS. In order to implement the transformation between two different coordinate systems, the usual approach is to build a model and to determine the transformation parameters. [4–6] literatures introduce the commonly used coordinate transformation model named Bursa model.

The Bursa model of coordinate transformation as follows.

$$\begin{bmatrix} X \\ Y \\ Z \end{bmatrix} = \begin{bmatrix} dX_0 \\ dY_0 \\ dZ_0 \end{bmatrix} + (1 + dm) \begin{bmatrix} 1 & \beta_Z & -\beta_Y \\ -\beta_Z & 1 & \beta_X \\ \beta_Y & -\beta_X & 1 \end{bmatrix} \begin{bmatrix} U \\ V \\ W \end{bmatrix} \tag{21.1}$$

where dX_0, dY_0, dZ_0 are translation parameters, β_X, β_Y, β_Z are spinning parameters, dm is scale factor.

When the numbers of ground points more than there, the optimal transformation parameters can be got using the least squares.

2. Transformation of time system

(1) GPST

In order to meet the need of precision positioning and navigation, the time system is established at the beginning of the system designing named GPST. GPST belongs to the atomic time, its scale is the same to atomic time, but there origin is different. So there is a constant between the GPST and the IAT in any second, their relation as follows:

$$IAT - GPST = 19(s) \tag{21.2}$$

(2) BDT

BDT is the time reference standard of the BDS, which is a kind of atomic time, composed and kept by many sets of high precision atomic clocks. It is the basic unit of seconds and its scale is the same to IAT. Its origin is the same to UTC at the moment of 0 o'clock in January of 2006. The difference between BDT and UTC is less than 100 ns [7].

(3) Transformation between BDT and GPST

The relationship between BDT and GPST is defined as follows:

$$BDT - GPST = 14(s) \tag{21.3}$$

After the transformation of space-time system ionosphere integrity monitoring can be inducted.

Ionosphere integrity monitoring includes four parts: calculation of double-difference ionosphere delay, establishment of interpolation model, calculation of IRIM; calculation of IRIU.

21.2.2 Calculation of Double-Difference Ionosphere Delay

The algorithm of ionosphere delay with combined system is from the ordinary single system. The basic idea is to integrate the observations of two satellite systems into the same observation equation. Then own equation is established according to

the algorithm of the single system to calculate the ionosphere delay [8]. Now the ionosphere delay model of GPS and BDS combined system is introduced as fellows.

$$\Delta\nabla I_G=\left(\frac{f_{2G}^2}{f_{1G}^2-f_{2G}^2}\right)[(\lambda_{1G}\Delta\nabla\varphi_{1G}-\lambda_{2G}\Delta\nabla\varphi_{2G})+(\lambda_{1G}\Delta\nabla N_{1G}-\lambda_{2G}\Delta\nabla N_{2G})] \tag{21.4}$$

$$\Delta\nabla I_B=\left(\frac{f_{2B}^2}{f_{1B}^2-f_{2B}^2}\right)[(\lambda_{1B}\Delta\nabla\varphi_{1B}-\lambda_{2B}\Delta\nabla\varphi_{2B})+(\lambda_{1B}\Delta\nabla N_{1B}-\lambda_{2B}\Delta\nabla N_{2B})] \tag{21.5}$$

where the subscript G, B representing GPS and BDS respectively; 1 and 2 representing two frequencies respectively.

21.2.3 Establishing Ionosphere Area Interpolation Model

Various interpolation models including Linear Combination Model, Low-order Surface Model, Linear Interpolation Model, Distance Based Linear Interpolation Model and Least-Square Collocation Model. These models have no significant difference in the interpolation error of spatial correlation according to the study of Dai in 2001 [9]. But low-order surface model has very good approximation and fitting within the scope of the ionosphere delay spatial correlation [10], so the weighted low-order surface model method is used in the calculation of double-difference ionosphere delay interpolation in this paper.

Mathematical model as follows:

$$\Delta\nabla I_{i,n}=\alpha_1\Delta X_{i,n}+\alpha_2\Delta Y_{i,n}+\alpha_3 \tag{21.6}$$

When the reference station numbers (given n) more than 3, the interpolation coefficient vector can be obtained by least squares solution

$$\begin{bmatrix}\alpha_1\\ \alpha_2\\ \alpha_3\end{bmatrix}=\left(A^TPA\right)^{-1}A^TPL,\ A=\begin{bmatrix}\Delta X_{1,n} & \Delta Y_{1,n} & 1\\ \Delta X_{2,n} & \Delta Y_{2,n} & 1\\ \vdots & \vdots & \vdots\\ \Delta X_{n-1,n} & \Delta Y_{n-1,n} & 1\end{bmatrix},\ L=\begin{bmatrix}\Delta\nabla I_{1,n}\\ \Delta\nabla I_{2,n}\\ \vdots\\ \Delta\nabla I_{n-1,n}\end{bmatrix},$$
$$P=diag\left(d_{u,1}^{-1},\ldots,d_{u,n}^{-1}\right) \tag{21.7}$$

where d are the distance between rover stations and every reference station. The double-difference ionosphere delay between rover station and the main reference station can be represented as follows:

$$\Delta\nabla I_{u,n} = B \cdot \begin{bmatrix} \alpha_1 \\ \alpha_2 \\ \alpha_3 \end{bmatrix} \tag{21.8}$$

where, $B = [\,\Delta X_{u,n} \quad \Delta Y_{u,n} \quad 1\,]$ ΔX and ΔY is the coordinate difference in the same coordinate system respectively.

21.2.4 Ionosphere Residual Integrity Monitoring

Chen X put forward two non-difference ionosphere linear indicators in 2003, IRIM and IRIU. Japan and Germany's network data were used in the experimental analysis, the results showed that the indicator can better estimate ionosphere interpolation error and ionosphere residual error of rover stations (Chen X 2003) [7].

The calculation process of IRIM is following. After calculating the double-difference ionosphere delay of baselines by type (21.5), (21.6), named calculation. Then some several baselines (at least two) are selected to interpolate another baseline. The ionosphere delay of interpolating baselines can be got, named estimator. Then the difference between calculation and estimator can be calculated. The weighted RMS (weighted method using high angle weighted method) of all satellites in each epoch is calculated, and then the weighted RMS is cumulated (cumulative interval takes an hour) to get IRIM. The weighted method as follows:

$$P(z) = \cos^2(z) \tag{21.9}$$

where, z is the satellites' zenith angle of reference station.

21.2.5 Ionosphere Residual Interpolation Uncertainty

Although IRIM can reflect the overall situation of ionosphere, but the ionosphere delay interpolation uncertainty of every epoch still need to consider for some users. Interpolation uncertainty can reflect the reliability of the positioning. IRIU is used for this purpose.

The calculation process of interpolation standard deviation as follows.

Firstly, interpolation coefficient α is calculated.

$$\alpha = \begin{bmatrix} \alpha_1 \\ \alpha_2 \\ \alpha_3 \end{bmatrix} = \left(A^T PA\right)^{-1} A^T PL \tag{21.10}$$

Secondly, the unit weighted error of α is calculated.

$$\delta_0^2 = \frac{V^T PV}{n-3} \tag{21.11}$$

$$V = \begin{bmatrix} \Delta\nabla V_{1,n} \\ \Delta\nabla V_{2,n} \\ \vdots \\ \Delta\nabla V_{n-1,n} \end{bmatrix},\ P = diag\left(d_{u,1}^{-1}, \ldots, d_{u,n}^{-1}\right)$$

where, n is the number of reference stations, d are the distance between rover station and reference stations.
Thirdly, the covariance matrix of α is calculated.

$$Q = \delta_0^2 \cdot \left(A^T PA\right)^{-1} \tag{21.12}$$

Forth, the variance of $\Delta\nabla I_{u,n}$ is calculated.

$$\delta_{\nabla\Delta I}^2 = BQB^T \tag{21.13}$$

The standard deviation can be got after. The ionosphere interpolation uncertainty can be tested through the comparison between the double-difference ionosphere delay (absolute value) and its standard deviation. The interpolation standard deviation can be used for ionosphere interpolation uncertainty. IRIU is obtained after the interpolation standard deviation through weighting average.

21.3 Example Analyses

21.3.1 Calculation of Ionosphere Delay

The data of GPS and BDS with Hebei CORS network is used for experimental analysis in this paper. Data sampling interval is 30 s. Here SZ station is used for reference station, NP station is used for rover station. The double-difference ionosphere delay of SZ-MC, SZ-LC, SZ-LX and SZ-NP is calculated. The ionosphere delay is shown in Fig. 21.1.

From Fig. 21.1 we can see that most of the delay value within 0.5 m. Overall the ionosphere delay between 4 o'clock and 9 o'clock is bigger compared to other time. The main reason is that Hebei locates in east eight time zone, GPST from 4 o'clock

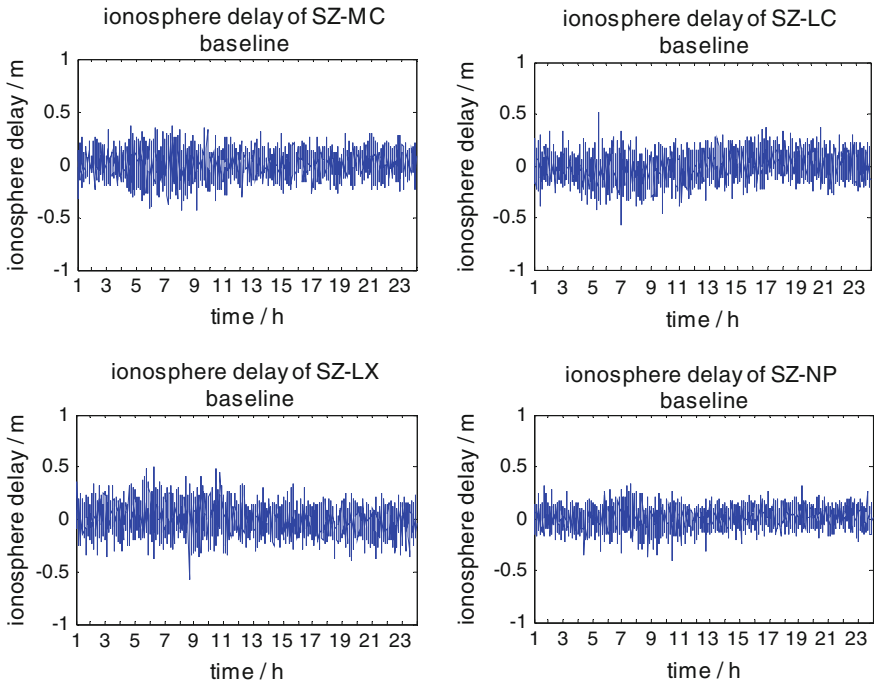

Fig. 21.1 The ionosphere delay of four baselines

to 9 o'clock corresponding to from 12 to 17 of local time, at this time the sun radiation is more violent, and ionosphere activity is more severe, so the ionosphere delay is larger. When GPST from 18 o'clock to 3 o'clock corresponding to from 2 to 11 of local time, the section is mainly night and morning, the sun radiation is weak, and layer is stable, so the ionosphere delay is smaller.

21.3.2 Ionosphere Area Interpolation Model

The ionosphere delay estimator of the baseline from rover station to reference station (SZ-NP baseline in this paper) can be calculated using weighted low-order surface model. Thus the interpolation residual is calculated through estimator and calculator. The interpolation residual is shown in Fig. 21.2.

From Fig. 21.2 we can see that interpolation residual achieves cm-level precision. By the statistics the maximum of interpolation residual is 0.052 m; the mean is 0.000072 m, the standard deviation is 0.016 m. The interpolation residual within 4 cm accounts for 99.9 %, within 5 cm accounts for 99.5 %. So the precision of interpolation residual is high.

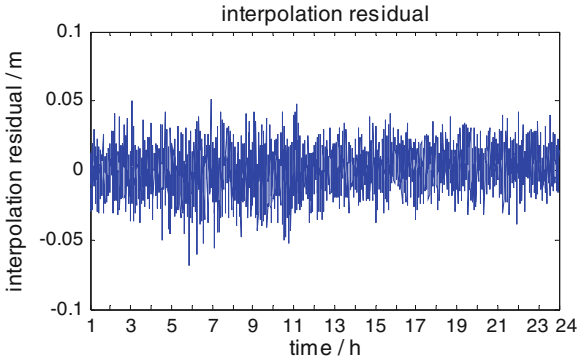

Fig. 21.2 Interpolation residual

21.3.3 Calculation of IRIM

Form Fig. 21.3 we can see that the overall change trend of IRIM is gentle. The trend of IRIM is the similar to the change trend of ionosphere delay. The maximum of IRIM appears at GPST 6 o'clock. The reason is that GPST 6 o'clock corresponding to 14 o'clock of local time, then solar activity is violent, and radiation is stronger so the ionosphere delay is bigger, lending to bigger IRIM. The ionosphere residual of GPST from 6 to 10 is bigger, IRIM also reflect this very well. The change trend of IRIM and ionosphere delay has the very good consistency. It fully illustrates that IRIM has the effectiveness to monitor the ionosphere residual.

21.3.4 Calculation of IRIU

Figures 21.4 and 21.5 is IRIU of 8 o'clock and 15 o'clock respectively. Two figures reflect the distribution of ionosphere delay residual in space intuitively. Compared

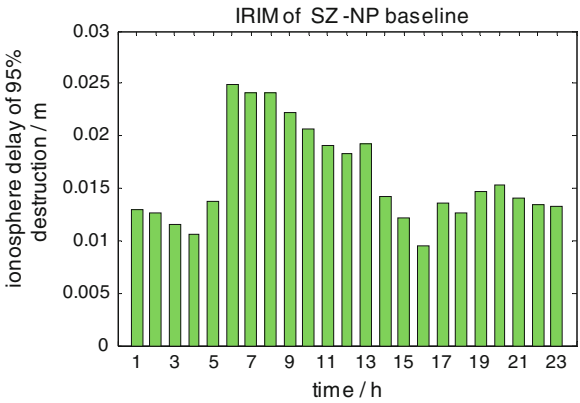

Fig. 21.3 The IRIM of SZ-NP baseline

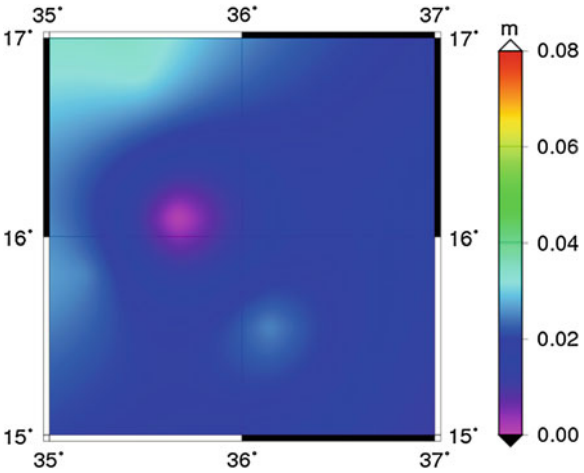

Fig. 21.4 The whole network IRIU of 8:00 o'clock

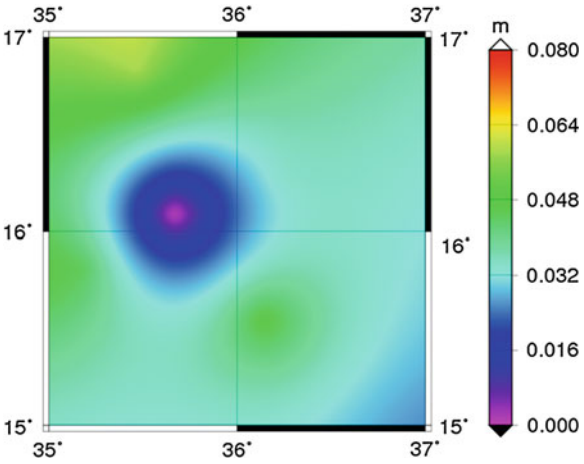

Fig. 21.5 The whole network IRIU of 15:00 o'clock

to Fig. 21.4, the IRIU of Fig. 21.5 is larger relatively, because the ionosphere residual of 15 o'clock is larger than 8 o'clock. Its interpolation accuracy is smaller lending to bigger uncertain. But overall, the ionosphere is state. Illustrating ionosphere activity above measurement area is stable, the ionosphere delay is smaller, and numerical indicator is reliable. The data of GPS and BDS is available.

21.4 Conclusions

Through the calculation and analysis of ionosphere delay with four baselines, the conclusion can be obtained that most delay within 0.5 m. The IRIM can monitor the ionosphere residuals effectively and IRIU reflects the distribution of ionosphere

residual range in space area with a moment. Two indicators can reflect the ionosphere delay and interpolation residual. The ionosphere delay calculated by the data of GPS and BDS combined system is smaller. The ionosphere above area is stable in this time period, and instructing the data are available. Monitoring the ionosphere of active time and active region will be the focus of the next researches.

Acknowledgments This study is funded by the National Natural Science Funds of China (No: 41401111), Natural Science Foundation of Shandong, China (No: 2014ZRB019RU) and the Scientific Research of the Forest Public Welfare Industry (No: 20140403010801).

References

1. Bei J (2010) GNSS integrity monitoring method, technology and application. Wuhan University, Wuhan pp 18–19
2. Zhou D (2007) Investigation into quality control and integrity monitoring For VRS technique. Southwest Jiao tong University, Sichuan (2007)
3. Chen X, Landau H, Vollath U (2003) New tools for network RTK integrity monitoring. In: Proceedings of ION GPS/GNSS, Protland, OR, pp 1355–1360
4. Jiao W (2003) Researches on the realization of satellite navigation coordinate reference system. Shanghai Astronomical Observatory Chinese Academy of Sciences, Shanghai
5. Liu Y, Zheng R, Cao L (2005) Analysis of errors in conversion methods of two seven-parameter coordinate systems in positioning with GPS. China Harbour Eng 3:24–27
6. Chen JY (2003) Necessity and feasibility for a geocentric 3D coordinate system employed in China. Acta Geodetica et Cartographica Sinica 11:283–288
7. Chen H, Chen X (2011) Applications of time service for Beidou satellite navigation system. Navig Lect 6:54–55
8. Wei Z (2008) Research and realization of GPS/BD-2 integrated positioning algorithm based on DSP. Wuhan University of Technology, Wuhan
9. Qiu L, Chen Y, Duan Y (2010) Research on ionosphere delay modeling technology based on GPS RTK network. J Geodesy Geodyn 2(30):57–58
10. Dingfa H, Letao Z, Chenggang L (2009) The theory of GPS augmentation reference station network. Science Press, Beijing

Chapter 22
Localizability Analysis of Cooperative Positioning with Range Measurement

Yaning Liu, Guangxia Li, Jing Lv, Jiang Chang and Shiwei Tian

Abstract This paper analyses the user localizability with range measurement from the observability perspective. Positioning is an estimation problem in essence. An unavoidable issue to be addressed in estimation problem is the observability analyzing. Observability in positioning issue and Localizability are analyzing of whether the state of users can be uniquely and accurately decided. From this view, they are coincident. In order to solve the position of users in challenged environment, such as forests and indoor, we put forward the concept of Cooperative Positioning. This paper analyses the localizability of Cooperative Positioning system through observability theory, and we use the rank of observability matrix to judge whether the system is observable or not. For the first time, we can analyze the localizability of users in theory, and we get a necessary condition of localizability. Simulation results indicate that it's feasible to use the observability theory in Cooperative Positioning systems. The conclusion of this paper is useful for the guidance of developing and constructing the positioning system.

Keywords Cooperative positioning · Range measurement · Observability · Observability matrix · Localizability

22.1 Introduction

Out of regard for the security of information, more and more countries are constructing their own navigation systems. Nowadays, America is experiment their GPS III navigation satellites, and the positioning precision will be about 0.6 m. The GLONASS of Russia has been joined with the more modernized member, GLONASS-K navigation satellite. GALILEO will be global navigation system in about 2020. But the development of Chinese Beidou navigation system is stronger

Y. Liu (✉) · G. Li · J. Lv · J. Chang · S. Tian
College of Communications Engineering, PLAUST, Nanjing, China
e-mail: liuyaninghope@163.com

J. Sun et al. (eds.), *China Satellite Navigation Conference (CSNC) 2015 Proceedings: Volume II*, Lecture Notes in Electrical Engineering 341,
DOI 10.1007/978-3-662-46635-3_22

and powerful, and will have built a global navigation system composed of five geo-synchronous earth orbit satellites and thirty non-geosynchronous earth orbit satellites in about 2020. With the help of these systems, we will get a very good positioning performance in outdoor environment. But in some challenged environment like indoor and forests, due to the absence of visible satellite, single user can't be positioned by themselves.

To solve this problem, researchers put forward many methods to improve the ability of satellite navigation system. Cooperative Positioning reduces the dependent of foundation establishment and become one of the most potential methods. The concept of cooperative positioning was first proposed by Japanese scholar Ryo Kurazume for acquiring real-time positioning information of mobile robots [1]. After that, Cooperative Positioning is widely used in robot positioning, wireless network positioning and other fields. In satellites positioning, cooperative technique hasn't been widely researched, it's mainly concentrate in the research of theoretic positioning precision and positioning algorithm [2]. Additionally, the localizability of agents in cooperative positioning has been researched in some degree [3]. Actually, precision and availability are the key factors of any position and navigation systems. Except for the analysis of theoretic positioning precision, the method of description the availability is also important. This paper uses observability theory to analyse the localizability of users in Cooperative Positioning.

The concept of controllability and observability were put forward by Kalman to analysis the control system in 1960s [4]. In control theory, input and output are external variables of the systems, the system state is internal variables, so there exist a question that whether internal variables can be influenced by the input or whether they can be reflected by the output, and this is the question of controllability and observability. Localizability analyse is to analysis whether the state of users can be uniquely and precisely decided. Based on the above description, observability theory can be used to analysis Localizability. And rank of observability matrix reflects whether the state can be observed. If the rank of observability matrix is full, then the states of system can be fully observed, and vice versa.

The pseudorange equations between users and satellites or users themselves are nonlinear equations. There are three methods to solve this nonlinear problem: the first one is to analysis the local weak observability of the system directly [5]; the second one, the method of analysis the observability matrix of the linear system can be used through linearize the nonlinear system [6]; the third one, it can use the simulation result of filter algorithm to analysis, as [7].

In this paper, observability analyse is used to analysis the localizability of users in Cooperative Positioning system. The main innovations of this paper are that, considered the specific scenario of Cooperative Positioning, we suppose that users cooperate through sharing the information of measuring distance. And for the first time, we theoretically prove that Cooperative Positioning can improve the localizability of users. The last but not the least, simulation results validate that cooperative positioning can improve users' localizability and the correctness of using observability in localizability analysis of cooperative positioning.

The rest of this paper is organized as follows. Section 22.2 reviews the theory of Cooperative Positioning and observability. Section 22.3 builds up the model of Cooperative Positioning and users' state transition equations and measurement equations. For the specific scenario of Cooperative Positioning, Sect. 22.4 analyzes the observability of these different scenarios. Simulation results exist in Sect. 22.5. Section 22.6 concluded this paper.

22.2 Background Knowledge

22.2.1 Cooperative Positioning Principle

The cooperative between users is mainly through communication and range measurement for the purpose of getting relative position information and clock bias between users. Through measuring distance between users and putting these equations into positioning equations, it can not only improve positioning precise but also enable some users who can't be positioned by themselves positioned.

22.2.1.1 Cooperative with Communication

In point to point (P2P) network, users can communicate with it's neighbourhood without foundation establishment like communication base station, it makes cooperative convenient and cheaper. In GNSS only Cooperative Positioning, using the aided information related to GNSS system, such as visible satellites and navigation information, we can get the signal Doppler frequency shift, SNR and code delay, so it can reduce the positioning time.

22.2.1.2 Cooperative with Range Measurement

The method of range measurement is mainly as: Received Signal Strength (RSS), Time of Flight (TOF), Doppler (DP), Angle of Arrived (AOA) and Time Difference of Arrived (TDOA). The last three methods require users to be in a state of motion, with multi-antenna and time synchronization respectively, the cost is too high. So we use RSS and TOF to measure range in general.

Compared the cooperative method of communication and range measurement, it finds that through communication, users exchange information of satellites signal, so it makes users capture satellites easily and quickly and reduce positioning time. While through range measurement, it gets the equation of range between users, and it will improve the localizability of the system.

22.2.2 Observability Theory

Observability analysis is a method to analyse whether the state of users can be decided by the observations. Observability analysis can be divided into local observability analysis and whole observability analysis. The local observability analysis is to analyse whether the state of users can be observable in a period of time, while the whole observability analysis is in the whole time.

Based on the whole observability matrix, [8] puts forward the necessity and sufficiency of Piecewise of Constant System (PWCS). But as [9] demonstrated, this method can't be directly used into nonlinear dynamic system. [10] puts forward a new method, that is using Fisher Information Matrix (FIM) to analyse Simultaneous Localization and Mapping (SLAM) system.

22.3 Observability Model

To analyse the observability of nonlinear systems, the state transition equations and measurement equations of system should be built. Through discreting the equations of continuous system, we can use observability theory to analyse the discreted equations.

22.3.1 The State Model

For Cooperative Positioning system, the model of position, velocity and timing (PVT) is considered. The state of user can be defined as,

$$\mathbf{x}_u = \left(x_A, y_A, z_A, b_1, \dot{x}_A, \dot{y}_A, \dot{z}_A, \dot{b}_1\right)^T \tag{22.1}$$

where (x_A, y_A, z_A, b_1) represents users' position and clock bias $\left(\dot{x}_A, \dot{y}_A, \dot{z}_A, \dot{b}_1\right)$ represents users' velocity of x, y, z axis and rate of clock bias change. Without considering the error of range measurement, the state transition equation of the system can be built as,

$$\dot{\mathbf{x}}_u(t) = \mathbf{A}_u \mathbf{x}_u(t) \tag{22.2}$$

where $\mathbf{A}_u = \begin{bmatrix} 0_{4\times4} & \mathbf{I}_{4\times4} \\ 0_{4\times4} & 0_{4\times4} \end{bmatrix}$. And the state of satellite can be defined as $\mathbf{x}_s = (x_1, y_1, z_1, \dot{x}_1, \dot{y}_1, \dot{z}_1)^T$, the position and velocity of satellite are known. So the

state transition equation is $\dot{\mathbf{x}}_s(t) = \mathbf{A}_s\mathbf{x}_s(t)$, with $\mathbf{A}_s = \begin{bmatrix} 0_{3\times3} & \mathbf{I}_{3\times3} \\ 0_{3\times3} & 0_{3\times3} \end{bmatrix}$. Discreted the state transition equation of users and satellites respectively,

$$\mathbf{x}_u(t_{k+1}) = \mathbf{B}_u\mathbf{x}_u(t_k),\ \mathbf{x}_s(t_{k+1}) = \mathbf{B}_s\mathbf{x}_s(t_k) \tag{22.3}$$

where $\mathbf{B}_u = \begin{bmatrix} \mathbf{I}_{4\times4} & T\mathbf{I}_{4\times4} \\ 0_{4\times4} & \mathbf{I}_{4\times4} \end{bmatrix}, \mathbf{B}_s = \begin{bmatrix} \mathbf{I}_{3\times3} & T\mathbf{I}_{3\times3} \\ 0_{3\times3} & \mathbf{I}_{3\times3} \end{bmatrix}$
For analysis convenience, we combine the state of users and satellites and define state $\mathbf{x} = \left[\mathbf{x}_u^T, \mathbf{x}_s^T\right]^T$, so the discreted state transition equation is $\mathbf{x}(t_{k+1}) = \mathbf{Z}\mathbf{x}(t_k)$, where $\mathbf{Z} = diag[\mathbf{B}_u, \mathbf{B}_s]$.

22.3.2 The Observation Model

The range measurement equations can be described as $\left\|\mathbf{x}_i - \mathbf{x}_j\right\| + b_{ij}c = t_{ij}$, where $\mathbf{x}_i$ represent user's position and $\mathbf{x}_j$ may be satellite's or user's, b_{ij} and t_{ij} is the clock bias and range difference between i and j respectively, constant c represents the speed of light.

So the observation matrix of system can be described as

$$\mathbf{H} = \left(h_{a,i,j}\ 0_{1\times4}\ h_{b,i,j}\ 0_{1\times3}\right) \tag{22.4}$$

$$\begin{aligned} h_{a,i,j} &= \left(\frac{x_i - x_j}{\left\|\mathbf{x}_i - \mathbf{x}_j\right\|}\frac{y_i - y_j}{\left\|\mathbf{x}_i - \mathbf{x}_j\right\|}\frac{z_i - z_j}{\left\|\mathbf{x}_i - \mathbf{x}_j\right\|}\mathrm{c}\right) \\ h_{b,i,j} &= \left(-\frac{x_i - x_j}{\left\|\mathbf{x}_i - \mathbf{x}_j\right\|} - \frac{y_i - y_j}{\left\|\mathbf{x}_i - \mathbf{x}_j\right\|} - \frac{z_i - z_j}{\left\|\mathbf{x}_i - \mathbf{x}_j\right\|}\right) \end{aligned} \tag{22.5}$$

22.4 Solution of Cooperative Positioning

In order to analyse the necessity condition of user's localizability in cooperative positioning, this paper puts forward the theory of observability analysis. The scenarios are listed in Table 22.1, the states of satellites are known, including their

Table 22.1 Different scenarios of cooperative positioning

Scenarios	Number of users	Number of satellites
1	1	1
2	2	1
3	1	2
4	2	2
5	m	n

position and velocity in all three axes. The state of users' are unknown and the model of our scenarios are PVT model.

Algorithm of user's observability analysis in Cooperative Positioning

0: The vector of satellites vectors are known, and hypothesize that users are making uniform linear motion.
1: Analyse the state variable of system and get the variable number x.
2: List the state transition equations and observation equations.
3: Calculate the observability matrix.
4: Analyse the rank of observability matrix n
If $n \geq x$
Then the system is observable
else added one more observation time slot
and continued step 4.
5: For multiple time slots, if $n < x$ is always true, then this system is $x-n$ rank deficient and isn't observable.

Scenario 1: For the scenario of one user and one satellite, the state of user is unobservable. When the observation time slot reaches to 7, the rank of this system is 13, and deficient by 1.

Analysis: The variable of system state can be defined as $\mathbf{x} = \left[\mathbf{x}_A^T, \mathbf{x}_1^T\right]^T$, so this system has 14 states. If the rank of observation matrix can reach to 14, then the system is observable. As the state transition matrix is $\mathbf{Z}_{A,1} = diag[\mathbf{B}_{uA}, \mathbf{B}_{s1}]$, so the observation matrix can be described as $\mathbf{H}_{A,1} = \begin{pmatrix} h_{a,1,1}\, 0_{1\times 4} & h_{b,1,1}\, 0_{1\times 3} \\ 0_{6\times 8} & \mathbf{I}_{6\times 6} \end{pmatrix}$. As we know, the state of satellite is prior known, that is to say, they are observable. So the l steps observation matrix can be listed as follows,

$$\mathbf{O}(t_0, t_l) \begin{bmatrix} h_{a,1,1} & 0_{1\times 4} & h_{b,1,1} & 0_{1\times 3} \\ h_{a,1,1} & Th_{a,1,1} & h_{b,1,1} & Th_{b,1,1} \\ h_{a,1,1} & 2Th_{a,1,1} & h_{b,1,1} & 2Th_{b,1,1} \\ \cdots & \cdots & \cdots & \cdots \\ h_{a,1,1} & lTh_{a,1,1} & h_{b,1,1} & lTh_{b,1,1} \\ & 0_{6\times 8} & & \mathbf{I}_{6\times 6} \end{bmatrix} \tag{22.6}$$

From this matrix we know, for the observation matrix $\mathbf{O}_{(l+7)\times 14}$, when the observation time slot is added by one then the rank of this matrix is added by one before l reaches to 7. But when the time slot is 7, the first six columns of the observation matrix is linearly dependent, as the equation shows $\sum_{i=1}^{6} \alpha_i \mathbf{O}_i = 0$, where $\mathbf{O}_i$ represent the ith column of the observation matrix,

$$\begin{aligned}\alpha_1 &= \frac{-y_A(t_0)+y_s(t_0)}{\dot{x}_A(t_0)}, \alpha_2 = \frac{x_A(t_0)-x_s(t_0)}{\dot{x}_A(t_0)} \\ \alpha_3 &= 0, \alpha_4 = \frac{-\dot{y}_A(t_0)}{\dot{x}_A(t_0)}, \alpha_5 = 1, \alpha_6 = 0\end{aligned} \tag{22.7}$$

So with the increasing of the time slot, the matrix is always one rank deficient, and user's state is unobservable in this scenario.

Scenario 2: In the system consisted of two users and one satellite, when the time slot is 5, the state of these two users can be observable.

Analysis: In this scenario, the observation matrix can be described as $\mathbf{O}(t_0, t_l) \in \mathbf{R}^{(9+3l)\times 22}$, when the time slot is added by one, the rank of matrix is added by 3. When l is reached to 5, $\mathbf{O}(t_0, t_5) \in \mathbf{R}^{24\times 22}$. Considered that the columns of this matrix are independent, so the rank of the observation matrix is 22. The rank of this matrix is full, so in this scenario, the users' states are observable.

$$\mathbf{O}(t_0, t_l) = \begin{bmatrix} h_{a,A,1}\, 0_{1\times 4} & 0_{1\times 8} & h_{b,A,1}\, 0_{1\times 3} \\ 0_{1\times 8} & h_{a,B,1}\, 0_{1\times 4} & h_{b,B,1}\, 0_{1\times 3} \\ h_{c,A,B}\, 0_{1\times 4} & h_{d,A,B}\, 0_{1\times 4} & 0_{1\times 6} \\ \cdots\cdots & \cdots\cdots & \cdots\cdots \\ h_{a,A,1}\, Tlh_{a,A,1} & 0_{1\times 8} & h_{b,A,1}\, Tlh_{b,A,1} \\ 0_{1\times 8} & h_{a,B,1}\, Tlh_{a,B,1} & h_{b,B,1}\, Tlh_{b,B,1} \\ h_{c,A,B}\, Tlh_{c,A,B} & h_{d,A,B}\, Tlh_{d,A,B} & 0_{1\times 6} \\ 0_{6\times 16} & & \mathbf{I}_{6\times 6} \end{bmatrix} \tag{22.8}$$

Scenario 3: Considering the scenario of one user and two satellites, when the observation time slot is reached to 3, the system is observable.

Analysis: In this scenario, the observability matrix can be described as,

$$\mathbf{O}(t_0, t_l) = \begin{pmatrix} h_{a,1,1}\, 0_{1\times 4} & h_{b,1,1}\, 0_{1\times 3} & 0_{1\times 6} \\ h_{a,1,2}\, 0_{1\times 4} & 0_{1\times 6} & h_{b,1,2}\, 0_{1\times 3} \\ \cdots\cdots & \cdots\cdots & \cdots\cdots \\ h_{a,1,1}\, Tlh_{a,1,1} & h_{b,1,1}\, Tlh_{b,1,1} & 0_{1\times 6} \\ h_{a,1,2}\, Tlh_{a,1,2} & 0_{1\times 6} & h_{b,1,2}\, Tlh_{b,1,2} \\ 0_{12\times 8} & & \mathbf{I}_{12\times 12} \end{pmatrix} \tag{22.9}$$

$\mathbf{O}(t_0, t_l) \in \mathbf{R}^{(14+2l)\times 20}$, so with the increase of observation time slot, the rows of this matrix is added by two once a time. Considering that the rows are independent, so the rank of matrix is added by two. When the observation time slot is reached to 3, the rank of the observation matrix is 20, so this scenario is observable.

Scenario 4: Considering the scenario of two satellites and two users, the state variables of this system is 28. When the observation time slot is reached to 3, the system is observable.

Analysis: In this scenario, the measuring matrix and observability matrix can be described as,

$$\mathbf{H}_{A,B,1,2} = \begin{pmatrix} h_{a,A,1}\,0_{1\times4} & 0_{1\times8} & h_{b,A,1}\,0_{1\times3} & 0_{1\times6} \\ h_{a,A,2}\,0_{1\times4} & 0_{1\times8} & 0_{1\times6} & h_{b,A,2}\,0_{1\times3} \\ 0_{1\times8} & h_{a,B,1}\,0_{1\times4} & h_{b,B,1}\,0_{1\times3} & 0_{1\times6} \\ 0_{1\times8} & h_{a,B,1}\,0_{1\times4} & 0_{1\times6} & h_{b,B,2}\,0_{1\times3} \\ h_{c,A,B}\,0_{1\times4} & h_{d,A,B}\,0_{1\times4} & 0_{1\times6} & 0_{1\times6} \\ 0_{12\times16} & & & \mathbf{I}_{12\times12} \end{pmatrix} \tag{22.10}$$

Considering $\mathbf{O}(t_0, t_l) \in \mathbf{R}^{(17+5l)\times28}$, columns of this matrix are independent, so when the time slot is added by one, the rank of the matrix is added by 5. When the time slot is increased to 3, the rows of this system is 32. Considering that the columns of this matrix is also independent, so the rank of observability matrix is 28, and this scenario is observable.

Scenario 5: Taking the general system consisted of m users and n satellites into considering, when the observation time slot x satisfied the requirement

$$x \geq \frac{17m - m^2 - 2mn}{m^2 - m + 2mn} \tag{22.11}$$

then the states of users are observable.
Analysis: The state can be described as

$$\mathbf{x} = \left[\mathbf{x}_A^T, \mathbf{x}_B^T, \ldots, \mathbf{x}_m^T, \mathbf{x}_1^T, \mathbf{x}_2^T, \ldots, \mathbf{x}_n^T\right]^T \tag{22.12}$$

so the state transition matrix is

$$\mathbf{Z}_{A,B,\ldots,m,1,2,\ldots n} = diag[\mathbf{B}_{uA}, \mathbf{B}_{uB}, \ldots, \mathbf{B}_{um}, \mathbf{B}_{s1}, \mathbf{B}_{s2}, \ldots, \mathbf{B}_{sn}] \tag{22.13}$$

The number of the variables is $8m + 6n$, and the observability matrix is

$$\mathbf{O}(t_0, t_l) = \begin{pmatrix} h_{a,A,1}\,0_{1\times4} & 0_{1\times8(m-1)} & \cdots & h_{b,A,1}\,0_{1\times3} & \cdots & 0_{1\times6(n-1)} \\ h_{c,A,B}\,0_{1\times4} & h_{d,A,B}\,0_{1\times4} & 0_{1\times8(m-2)} & & 0_{1\times6n} & \\ \cdots & & \cdots & & \cdots & \\ h_{a,A,1}\,Tlh_{a,A,1} & 0_{1\times8(m-1)} & \cdots & h_{b,A,1}\,Tlh_{b,A,1} & \cdots & 0_{1\times6(n-1)} \\ h_{c,A,B}\,Tlh_{c,A,B} & h_{d,A,B}\,Tlh_{d,A,B} & 0_{1\times8(m-2)} & & 0_{1\times6n} & \\ \cdots & & \cdots & & \cdots & \\ 0_{6n\times8m} & & & & \mathbf{I}_{6n\times6n} & \end{pmatrix} \tag{22.14}$$

From the observability matrix we known, as the observation time slot is added by one, the rank of the matrix is added by $\frac{m(m-1)}{2} + mn$. As for time slot x, if this

Table 22.2 The result of observability analysis of cooperative positioning

Scenario	Observability	Time slot l
1	No	7
2	Yes	5
3	Yes	3
4	Yes	3
5	Yes	$x \geq \frac{17m - m^2 - 2mn}{m^2 - m + 2mn}$

scenario is observable, then x should satisfy the requirement $\left(\frac{m(m-1)}{2} + mn\right)(x+1) + 6n \geq 8m + 6n$. That is to say,

$$x \geq \frac{17m - m^2 - 2mn}{m^2 - m + 2mn} (m \geq 1, n \geq 1, mn \neq 1) \tag{22.15}$$

Notification: For the multi-users and multi-satellites system, we must have a stable time source, that is to say, the amount of satellites is at least one. When n = 1, time slot of the observable system is $x \geq \frac{15-m}{m+1}$, in this situation, as for m = 7, we know that x ≥ 1. That is to say, for the system of seven users and one satellite, just one time measurement can make the system observable on the assumption that users can measure distance between each other.

Table 22.2 concludes the result of observability analysis of different Cooperative Positioning scenario.

22.5 Simulation Results

We use the method of Extended Kalman Filter (EKF) to simulate the localizability of users in scenario 4. In our simulation, the error of pseudorange and measurement are thought to be Gauss white noise with covariance of 5 and 0.2 respectively. The initial state of users and satellites are prior known. The number of Monte Carol trails is 500, and we do 5 times of iteration in every time slot.

Figures 22.1 and 22.2 are user A's positioning error and velocity respectively. As for Fig. 22.1, we know that the positioning precision of vertical direction is higher than horizontal direction. That is because when user is moving, the state change in vertical direction is smaller than horizontal direction. And for 500 times Monte Carol trails, the percent of positioning error is less than 10 m is about 70 %, that is to say, the simulation result is stable. From Fig. 22.2, we can conclude that the velocity of three directions can be stable after about 15 s. The simulation results validate the correction of theory deduction.

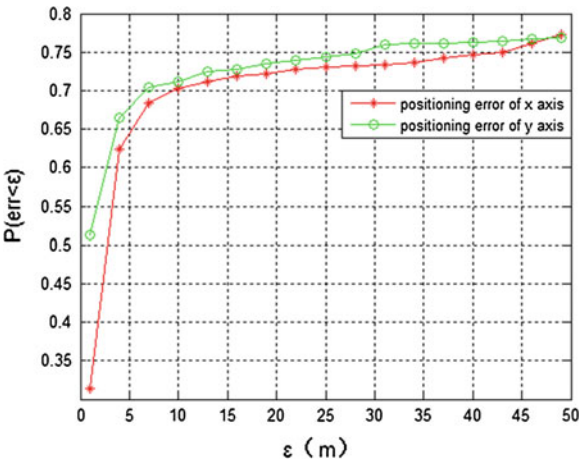

Fig. 22.1 The positioning error of user A

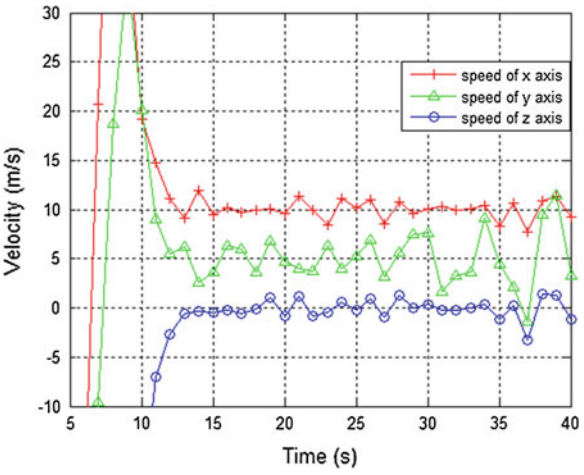

Fig. 22.2 The velocity of user A in x, y and z direction

22.6 Conclusions

This paper analysis the users' localizability of Cooperative Positioning system based on range measurement with observability theory. For some specific scenarios, the necessity condition has been analyzed. Simulation results validate the correctness of theory deduction. For future work, we would use observability theory to analyze the degree of localizability and the influence of pseudorenge and measurement errors.

References

1. Kurazume R, Hirose S, Nagata S, Sashida N (1996). Study on cooperative positioning system (basic principle and measurement experiment). In: Robotics and Automation, 1996. Proceedings., 1996 IEEE International Conference on, vol. 2, pp 1421–1426. IEEE
2. Penna F, Caceres MA, Wymeersch H (2010) Cramér-Rao Bound for Hybrid GNSS-Terrestrial Cooperative Positioning. IEEE Commun Lett 14(11):1005–1007
3. Tian S, Dai W, Chang J, Li G (2013) On the Agent Localizability of Hybrid GNSS-Terrestrial Cooperative Positioning. In: China Satellite Navigation Conference (CSNC) 2013 Proceedings. Springer, Berlin Heidelberg, pp 567–575
4. Kalman RE (1960) On the general theory of control systems. In: Proceedings of the 1st IFAC, Butterworth, London
5. Robert H, Arthur JK (1977) Nonlinear control and observability. IEEE Trans Autom Control 22(5):728
6. Chen Z (1991) Local observability and its application to multiple measurement estimation. IEEE Trans Industr Electron 38:491–496
7. Ham FM, Brown RG (1983) Observability, eigenvalues and Kalman Filterin. IEEE Trans Aerosp Electron Syst AES–19:269–273
8. Goshen-Meskin D, Bar-Itzhack I (1983) Observability analysis of piecewise constant systems–part I: theory. IEEE Trans Aerosp and Electron Systvol 19(2):269–273
9. Kassas Z, Humphreys T (2012) Observability analysis of opportunistic navigation with pseudorange measurements. In: Proceedings of AIAA guidance, navigation, and control conference
10. Perera L Nettleton E (2009) On the nonlinear observability and the information form of the SLAM problem. In: Proceedings of IEEE international conference on intelligent robots and systems

Chapter 23
Code-Carrier Divergence Monitoring for BeiDou Ground-Based Augmentation System

Lin Zhao, Weixin Yang, Liang Li and Fuxin Yang

Abstract Carrier-Smoothed-Code (CSC) can effectively suppress the multipath effect and receive noise in the code based differential positioning, which is widely adopted by the Ground Based Augmentation System (GBAS). Since the BeiDou Navigation Satellite System (BDS) code measurement suffers from the severer measurement noise, the CSC is necessary for the BDS based GBAS. However, the accuracy of smoothing pseudorange can be degraded significantly by the ionospheric delay error, which caused by the Code-Carrier Divergence (CCD) effect. The theoretical analysis shows that the CCD will greatly affect the precision of the smoothed pseudorange, thus, ionospheric delay error has to be considered for the services related to the safety-of-life (SoL). Based on the traditional CCD monitoring techniques, this paper proposed a new two first-order linear time invariant filter sequentially to improve the CCD performance. Meanwhile, sigma-inflation method is used to obtain the CCD detection threshold considering the impact from the non-ideal distribution of the constructed statistic. The real-world experiment result has shown that the proposed method can suppress the measurement noise more effectively when compared with the traditional first-order linear monitoring method with satisfying the predefined false alarm requirement, which make the proposed method more adaptable to the small bias from CCD.

Keywords CSC · GBAS · BDS · Ionospheric delay error · CCD · Sigma-inflation

L. Zhao · W. Yang (✉) · L. Li (✉) · F. Yang
Harbin Engineering University, Harbin, China
e-mail: heuyang@163.com

L. Li
e-mail: liliang@hrbeu.edu.cn

J. Sun et al. (eds.), *China Satellite Navigation Conference (CSNC) 2015 Proceedings: Volume II*, Lecture Notes in Electrical Engineering 341,
DOI 10.1007/978-3-662-46635-3_23

23.1 Introduction

Carrier-Smoothed-Code (CSC) can effectively suppress the multipath error and receive noise in the code based differential positioning, which is widely adopted by the Ground Based Augmentation System (GBAS) to improve the accuracy and reliability of differential positioning [1]. However, the existence of the Code-Carrier Divergence (CCD) effect will introduce double ionosphere delay to the smoothed pseudorange [2]; and that the using of CSC is based on the assumption that the ionosphere fluctuations are very small [3], so when the ionosphere has a quick and large change, the precision of the smoothed pseudorange will be greatly diverged, then lead to unacceptable position error.

In order to reduce the impact of ionospheric delay error on the smoothed pseudorange, many researchers have been working on the problem. Park et al. [4] designed an optimal Hatch filter with an adaptive smoothing window width. But the deriving of the smoothing window width requires the priori statistical knowledge of ionospheric delay and receiver noise, which is hardly to be acquired in real-world applications. Hwang and Mc Graw [5] proposed an Ionosphere-free filter (IFS) method which combines the dual-frequency measurement algorithm. Although the IFS can effectively solve the impact of ionosphere delay on the smoothed pseudorange, but IFS will introduce larger pseudo-random noise, resulting in a loss of position precision, besides, the method is not available to the single frequency receiver. Thus, it is difficult to directly deal with the ionospheric delay error in CSC. The Federal Aviation Administration (FAA)'s Local Area Augmentation System (LAAS) uses a geometric moving averaging (GMA) method to estimate and monitor the CCD [6], confirming whether or not the ionosphere has abnormal fluctuations based on the monitor result. FAA recommend a first-order Linear Time Invariant (LTI) low-pass filter for GMA to suppress the high frequency noise, but the monitoring performance is limited by the response time and detection efficiency. This paper proposed a new two first-order LTI filter sequentially to improve the CCD monitoring performance.

This paper is organized as follows: First, analyzing the impact of the ionospheric delay error on CSC based on Hatch filter. Second, introducing the traditional and proposed CCD monitor method. Third, designing the CCD threshold based on the sigma-inflation method. The test results show the CCD monitor method proposed in this paper is available.

23.2 Carrier Smoothed Code

23.2.1 Hatch Filter

In the process of pseudorange-based differential positioning, CSC can effectively suppress the multipath error and receiver noise in the pseudorange measurements.

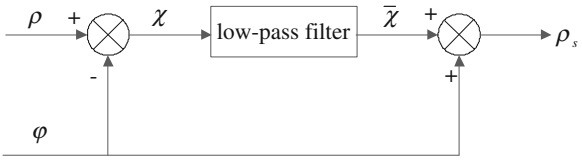

Fig. 23.1 Hatch filter

Hatch filter is a typical CSC method which is widely used in the GBAS [7], the structure of which is shown in Fig. 23.1.

In Fig. 23.1, ρ is the measured code pseudorange; φ is the measured carrier phase measurement; ρ_s is the smoothed pseudorange; and the transfer function of the low-pass filter can be modeled as:

$$G(s) = 1/(\tau s + 1) \tag{23.1}$$

where τ is filter smoothing time constants. According to the definition of the bandwidth of control system [8], the bandwidth of the filter is $\omega_b = 1/\tau$. It passes signals with a frequency lower than ω_b and attenuates signals with frequencies higher than ω_b. So in order to suppress the high frequency signal and get a better smoothed results, we should set a big τ value.

According to Fig. 23.1, the smoothed pseudorange can be modeled as:

$$\rho_{s,k} = \frac{1}{L}\rho_k + \frac{L-1}{L}\left(\rho_{s,k-1} + \varphi_k - \varphi_{k-1}\right) \tag{23.2}$$

where $L = \tau/T_s$, T_s is the output interval of the raw measurements. The subscript k indicates the kth epoch. The initial value of the filter is the pseudorange at the initial time, namely $\rho_{s,1} = \rho_1$.

23.2.2 The Error Analysis in the Process of CSC

The BeiDou code and carrier phase measurement can be modeled as:

$$\rho = r + \delta t_s + I + T + \delta t_u + \varepsilon_\rho \tag{23.3}$$

$$\varphi = r + \delta t_s - I + T - \lambda N + \delta t_u + \varepsilon_\varphi \tag{23.4}$$

where r is true range from a satellite to a receiver. δt_s is satellite clock bias. I is ionosphere delay. T is tropospheric delay. δt_u is user clock bias. λ is carrier wavelength. N is integer ambiguity. ε_ρ is represents other code phase measurement errors. ε_φ is represents other carrier phase measurement errors.

Define the smoothed code pseudorange error e [9] as:

$$e_k = \rho_{s,k} - r_k - T_k - I_k - \delta t_{u,k} \tag{23.5}$$

Substituting Eq. (23.2) into Eq. (23.5), we can obtain:

$$e_k = \frac{L-1}{L} e_{k-1} + \frac{L-1}{L}(\rho_{k-1} - \rho_k) + \frac{L-1}{L}(\varphi_k - \varphi_{k-1}) + (\varepsilon_{\rho,k} - \frac{L-1}{L}\varepsilon_{\rho,k-1}) \tag{23.6}$$

If the output interval of the raw measurements is small, the tropospheric delay change between adjacent epochs will very small, it can be neglect; the multipath error and user clock bias in carrier phase measurement is much smaller than their in code phase measurement, so they can be neglect too. According to Eqs. (23.3) and (23.4), then we can obtain the dynamic equation of the smoothed code pseudorange error as (for convenience of writing, the subscript ρ is omitted):

$$e_k = \frac{L-1}{L} e_{k-1} - 2\frac{L-1}{L}(I_k - I_{k-1}) + \frac{1}{L}\varepsilon_k \tag{23.7}$$

On the premise of equal interval sampling, let $I_k - I_{k-1} = \dot{I}T_s$, $\dot{I}$ is the ionosphere gradients, then (23.7) can be rewritten as:

$$e_k = \frac{L-1}{L} e_{k-1} - 2T_s\frac{L-1}{L}\dot{I} + \frac{1}{L}\varepsilon_k \tag{23.8}$$

So the accumulative error e up to the kth epoch can be obtained by:

$$e_k = -2\dot{I}T_s \sum_{i=0}^{k-1}\left(\frac{L-1}{L}\right)^{i+1} + \frac{1}{L}\sum_{i=0}^{k-1}\left(\frac{L-1}{L}\right)^{i}\varepsilon_{k-i} \tag{23.9}$$

Note that $0 < (L-1)/L < 1$, then Eq. (23.9) can be expressed as:

$$e_k = -2\dot{I}T_s \sum_{i=0}^{k-1}\left(\frac{L-1}{L}\right)^{i+1} + \frac{1}{L}\sum_{i=0}^{k-1}\left(\frac{L-1}{L}\right)^{i}\varepsilon_{k-i} \tag{23.10}$$

Equation (23.10) shows that the steady error is determined by ionospheric delay error, multipath error and filter smoothing time constant. So when the ionosphere has a quick and large change or the multipath effect becomes serious, the accumulated error will probably be much larger. Equation (23.10) also shows that the smoothed error contains double effects of ionosphere delay, this is because CSC is the a combination of code phase measurement and carrier phase measurement, however, the ionosphere affects satellite signal propagation by delaying code phase measurement while advancing carrier phase measurement, that is Code-Carrier Divergence.

Obviously, in order to achieve a smeller accumulative error e, the value of L should be small, namely τ should be small; but in order to get a better effect of suppress the high frequency noise, we need a big value of τ. Therefore, the value of the filter smoothing time constants τ should be moderate.

23.2.3 Smoothed Pseudorange Differential Positioning Simulation Analysis

The pseudorange differential positioning test of selecting different filter smoothing time constants has carried on. The test data is a set of zero-base line data received in Curtin University, the output interval of the raw measurements is 30 s, the length of the data is 24 h, the total numbers of the epoch are 2880.

When smoothing time constant for CSC is 20 s, comparing with the non-smoothed pseudorange differential positioning, the positioning precision in three dimensions of the smoothed pseudorange differential positioning are improved 70.4, 72.6 and 64.2 %, respectively, it is clear: when choosing suitable time constant, the use of CSC can great improve the pseudorange differential positioning precision. Figures 23.2, 23.3 and 23.4 show that the positioning results become very smooth when using CSC in the pseudorange differential positioning, considering the test data is a set of zero-base line data, smooth positioning result means the receiver noise is well suppressed. Figures 23.2, 23.3 and 23.4 also show that under the condition of the same sampling time, the effect of different filter smoothing time constant on the positioning result is different, as discussed, too big or too small of the filter smoothing time constant will degrade the positioning precision. In the GPS system, the range of the smooth weight $L(\tau/T_s)$ is 20–100 [3].

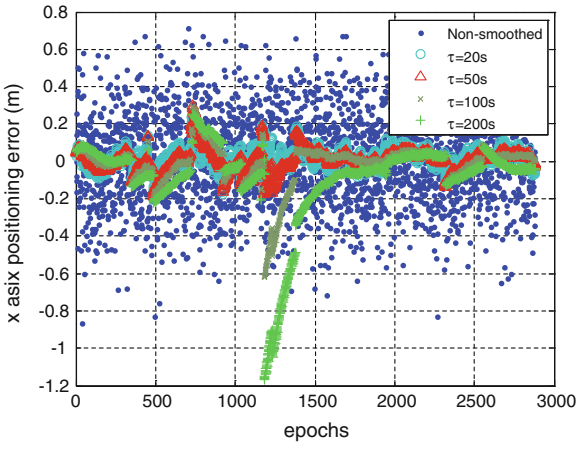

Fig. 23.2 The x axis position error with different time constants

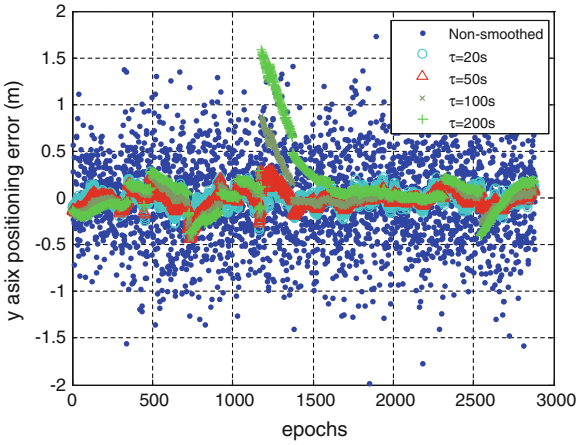

Fig. 23.3 The y axis position error with different time constants

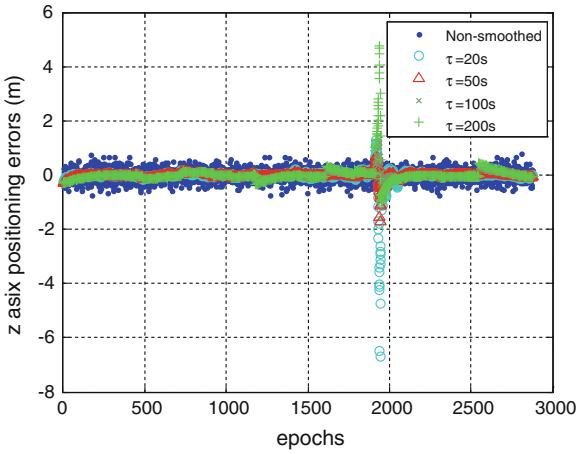

Fig. 23.4 The z axis position error with different time constants

23.3 CCD Algorithm Analysis

In the ideal situation, for the same satellite, the increments of code phase measurement are equal to the increments of carrier phase measurement between adjacent epochs at the same frequency. But, because of ionosphere and multipath interference, the code phase measurement will deviate from carrier phase measurement, then the increments will not equal, this is the reason of the smoothed code pseudorange error. If we can eliminate or virtually eliminate the influence of multipath on code phase measurement by some technological means, then we can think of the CCD is caused by the ionosphere on the propagation path, then we can detect the ionosphere anomaly by monitor CCD.

The implementation of CCD monitor through estimate the CCD value, comparing the estimate value with the CCD threshold value, according to the result of

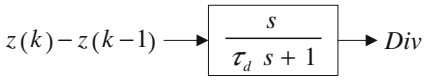

Fig. 23.5 Typical CCD estimator model (model 1)

the comparison to determine if there is a ionosphere anomaly and adjust the weighting factors of CSC, to ensure the accuracy of the smoothed pseudorange, and then ensure the accuracy of differential positioning.

The typical CCD estimator is a first-order LTI, it is a low-pass filter, and the structure of the filter is shown in Fig. 23.5:

The CCD estimates *Div* can be expressed as:

$$Div(k) = \frac{\tau_d - T}{\tau_d} Div(k-1) + \frac{1}{\tau_d}(z(k) - z(k-1)) \tag{23.11}$$

where τ_d is the time constant, T is the output interval of the raw measurements, and z is defined as the raw code-minus-carrier measurement. According to Eqs. (23.3) and (23.4),

$$z(k) = \rho(k) - \varphi(k) = 2I(k) + \varepsilon_\rho(k) - \varepsilon_\varphi(k) - \lambda N \tag{23.12}$$

Suppose there is no cycle slip in carrier phase measurement, then Eq. (23.12) can be rewritten as:

$$z(k) - z(k-1) = 2\dot{I}(k) + \Delta\varepsilon_\rho(k) - \Delta\varepsilon_\varphi(k) \tag{23.13}$$

In the usual situation the value of $\Delta\varepsilon_\rho$ is hundred times as many as $\Delta\varepsilon_\varphi$, so we can neglect $\Delta\varepsilon_\varphi$, then Eq. (23.13) can be rewritten as:

$$z(k) - z(k-1) = 2\dot{I}(k) + \Delta\varepsilon_\rho(k) \tag{23.14}$$

Multipath error $\Delta\varepsilon_\rho$ is high frequency noise, it can be virtually eliminated after through the low pass filter, so the CCD estimates reflect the change of ionosphere.

In order to obtain better effect of removing high frequency noise, this paper use two first order filter LTI in series to compute the CCD estimator value, the filter illustrated in Fig. 23.6 [1]:

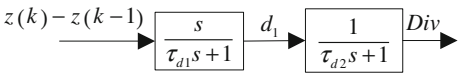

Fig. 23.6 Divergence estimator model 2 (model 2)

CCD estimates can be modeled as:

$$\begin{aligned} d_1(k) &= \frac{\tau_{d1} - T}{\tau_{d1}} d_1(k-1) + \frac{1}{\tau_{d1}}(z(k) - z(k-1)) \\ Div(k) &= \frac{\tau_{d2} - T}{\tau_{d2}} Div(k-1) + \frac{T}{\tau_{d2}} d_1(k) \end{aligned} \tag{23.15}$$

In order to test the performance of the two models in suppressing the high frequency noise, this paper conduct a test. During the test, the time constant of model 1 is set at 200 s, and the time constants of model 2 are set at 30 s, namely $\tau_{d1} = \tau_{d2} = 30$ s, the output interval of the raw measurements (T) is 1 s, the input data of the two models are the same, which is a white Gaussian noise ($\mu = 0$, $\sigma = 0.5$), Fig. 23.7 illustrates the test results. Figure 23.7 shows the performance of the model 2 is superior (lower output noise) to model 1, even when the latter has a much longer filter time constant (200 s), and that the standard deviation and amplitude of the output of model 2 compared to the model 1 was reduced by 40.8, 63.8 %, respectively. So this paper uses model 2 to estimate CCD values.

23.4 Design CCD Threshold and Simulation

In this paper, we assume that the Probability Density Function (PDF) of the CCD estimates is Gaussian, we typically calculate the threshold from traditional sigma-inflation method, using Gaussian distribution that overbounds the two tails of the apparent distribution. In this test, the test data is a set of a static data which received in Beijing University of Civil Engineering and Architecture, the output interval of the raw measurements is 1 s. During the test, the time constants $\tau_{d1} = \tau_{d2} = 30$ s. The steps of getting the threshold are as follow [10]:

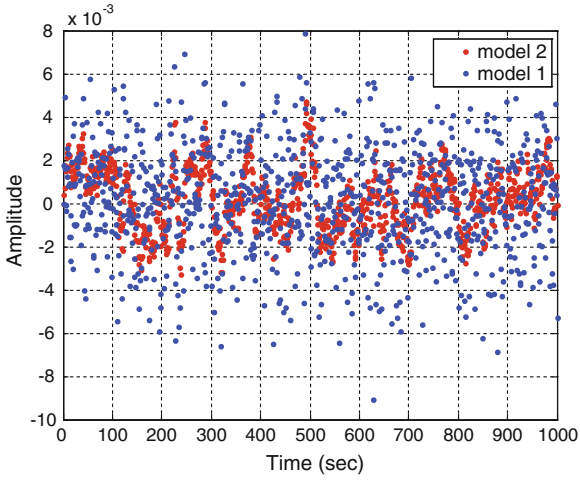

Fig. 23.7 Filter response to Gaussian noise

(1) Taking all of the raw measurements of all of the satellites as a whole, getting rid of the measurements of satellites which elevation are lower than 10°, calculating the CCD estimates *Div* through the divergence estimator model 2, then divide them into eight bins according to the elevation, each bin contains 10°, the results are shown in Fig. 23.8.

(2) Calculating the mean μ_e and the standard deviation σ_e of *Div* in each bin, getting the mean and the standard deviation at other elevations through high-order polynomial fitting, the results are shown in Fig. 23.9.

(3) Calculating the normalized value Div_{N} of *Div*, $Div_N = (Div - \mu_e)/\sigma_e^2$, counting the numbers of every Div_{N}, recording the numbers as ND, the results are shown in Figs. 23.10 and 23.11

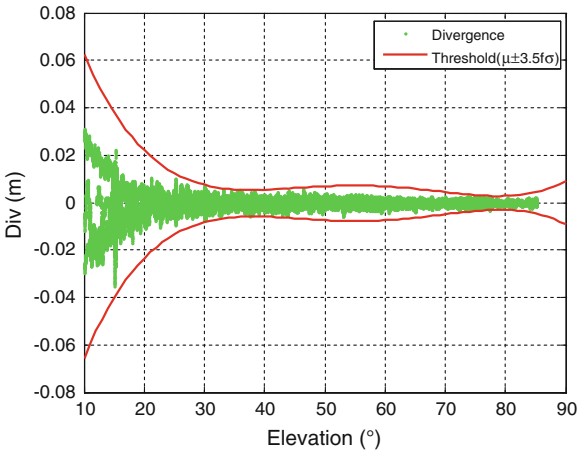

Fig. 23.8 Code carrier divergence and its threshold

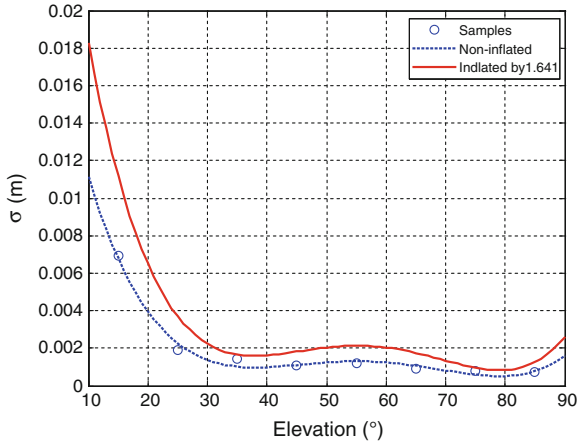

Fig. 23.9 Divergence standard deviation and its threshold

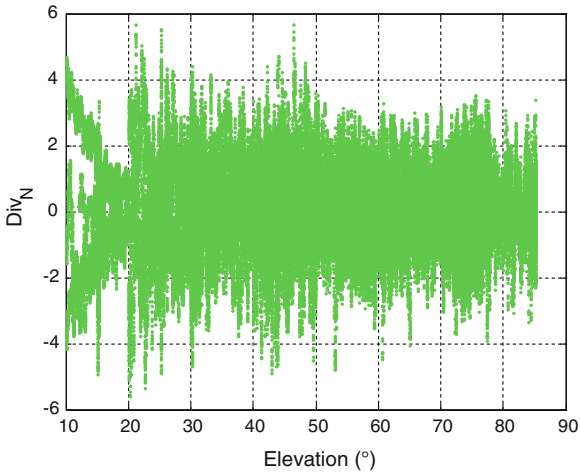

Fig. 23.10 Normalized divergence

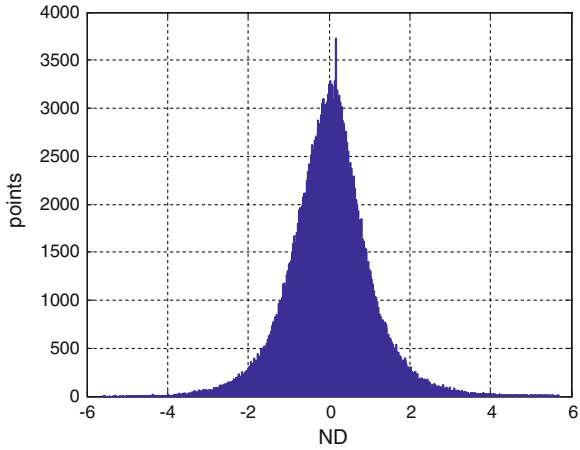

Fig. 23.11 Histogram of normalized divergence

(4) Calculating the PDF of Div_N, inflating σ_e, getting the minimum inflation factor f, the Gaussian distribution with its mean 0 and standard deviation $f\sigma_e$ should overbounds the tails of Div_N's distribution, the results are shown in Fig. 23.12.

(5) To ensure low Constant False Alarm Rate (CFAR), noting we assume the PDF of the CCD estimates are Gaussian in this paper, the threshold is modeled as:

$$Th_e = \mu_e \pm 3.5 f \sigma_e \tag{23.16}$$

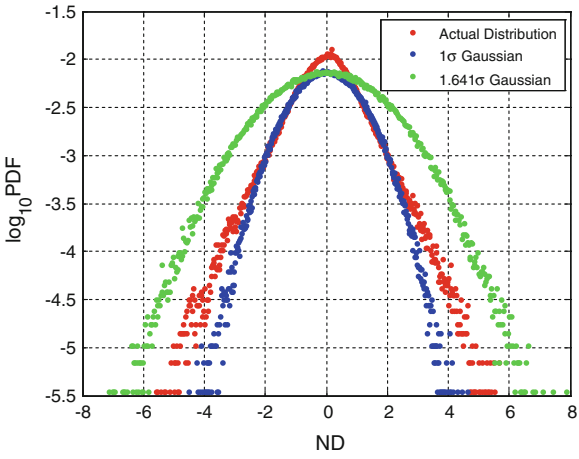

Fig. 23.12 PDF of normalized divergence

The threshold is shown as the inflation red curve in Figs. 23.8 and 23.9. Since $Div \sim \mathrm{N}\left(\mu_e, f^2\sigma_e^2\right)$, according to the threshold achieved from Eq. (23.16), the CFAR can be computed as:

$$P(|Div - \mu_e| > 3.5f\sigma_e) = 2 - 2\Phi(3.5) = 4 \times 10^{-4} \tag{23.17}$$

Figure 23.8 shows in the zenith angle the means and standard deviations of the CCD estimates are smaller, where the means and standard deviations in the low elevation are larger, this situation corresponds to the ionosphere delay when the ionosphere has no abnormal fluctuations, so we can say, the test data is received under the conditional that the ionosphere has no abnormal fluctuations, so the proposed CCD monitor in this paper mainly reflect the CFAR performance in the no fault-free condition.

If the CCD estimate exceeds the threshold, we can say that the ionosphere has abnormal fluctuations, in order to ensure the accuracy of the smoothed pseudorange, the user should adjust the smoothed filter time constant.

23.5 Conclusions

This paper analyzes the effect of ionosphere delay for Carrier smoothed code on the BDS differential positioning, which shows that the CCD will greatly affect the precision of the smoothed pseudorange. Based on the ionospheric error propagation analysis, this paper proposes a new CCD monitor algorithm based on two-order linear filter, based on which the test statistic and the corresponding detection threshold for CCD is constructed. The test results show the outputs of the CCD monitoring algorithm is consistent with the change of the actual ionosphere delay,

which proves the feasibility of the proposed method. Furthermore, in order to compensate the non-ideality of the constructed test statistic, this paper uses the traditional sigma-inflation method to design the CCD thresholds, the thresholds reflect the CFAR performance in the no fault-free condition.

Acknowledgments This research was jointly funded by China Natural Science Foundation (No. 61304235, 61273081), the Fundamental Research Funds for Central Universities (No. HEUCFD1431), and the support from transponding satellite system project.

References

1. Simili DV, Pervan B (2006) Code-carrier divergence monitoring for the GPS local area augmentation system. In: IEEE
2. Zhao L, Li L, Sun M (2010) Novel adaptive Hatch filter to mitigate the effects of ionosphere and multipath on LAAS. J Syst Eng Electron Technol 21(6):1046–1053
3. Xie G (2009) Principles of GPS and receiver design. Publishing House of Electronics Industry, Beijing
4. Park B, Sohna K, Kee C (2008) Optimal Hatch filter with an adaptive smoothing window width. J Inst Navig 61(3):435–454
5. Hwang PY, Mc Graw G (1999) Enhanced differential GPS carrier smoothed code processing using dual frequency measurements. J Inst Navig 46(2):127–137
6. U.S. FAA (2002) Specification: performance type one local area augmentation system ground facility. Washington, D.C., FAA-E-2937A, 17 April 2002
7. Zhao L, Ding J, Ma X (2011) The principle and application of satellite navigation. Northwestern Polytechnical University Press, Xi'an
8. Hu S (2010) Automatic control theory. Science Press, Beijing
9. Zhao L, Li L (2009) An adaptive Hatch filter to minimize the effects of ionosphere and multipath for GPS single point positioning. In: 2009 Proceedings of the IEEE international conference on mechatronics and automation, Changchun
10. Xie G (2004) Optimal on-airport monitoring of the integrity of GPS-based landing systems. PhD dissertation, Stanford University

Chapter 24
Threshold Determination for Integrity Monitoring in Local Area Augmentation System

Shuai Xiong

Abstract In local area augmentation system, the quality monitoring of measurement data is necessary for system integrity monitoring. The way of quality monitoring is comparing the observations collected with corresponding thresholds, and then decides if a failure is happening. Proper valued thresholds are usually the key to achieving the desired performance of the integrity monitoring. This paper proposed a Gaussian overbounding method to determine thresholds. The requirement of false alarm probability of the system is considered, and the threshold is calculated from a Gaussian distribution that overbounds the two tails of the probability density distribution of the observation data. Comparing to the threshold determination methods depending on engineering experience or threshold models, this method satisfies the requirement of false alarm probability of the system; moreover, it accords with the real characteristic of the system due to the thresholds are calculated using own observation data of the system.

Keywords Local area augmentation system · Integrity monitoring · Threshold · False alarm probability

24.1 Introduction

The local area augmentation system is a system developed to support precision approach and landing operations and other navigation and surveillance applications within a local area including and surrounding an airport. It is a ground-based augmentation satellite navigation system, and consists of ground subsystem and airborne subsystem. The ground subsystem uses several (usually 3 or 4) reference receivers whose locations are precisely known to collect valid ranging signals and navigation data of all satellites in view, then the differential corrections are calculated and

S. Xiong (✉)
Xi'an Research Institute of Navigation Technology, Xi'an, China
e-mail: xiongs@mail.ustc.edu.cn

J. Sun et al. (eds.), *China Satellite Navigation Conference (CSNC) 2015 Proceedings: Volume II*, Lecture Notes in Electrical Engineering 341,
DOI 10.1007/978-3-662-46635-3_24

broadcasted. The airborne subsystem that gets the differential corrections shall gains much better navigation service by using some differential augmentation methods.

Precision approach requires great high positioning accuracy and integrity. The P_{HMI} requirement of CAT II and CAT III is 2×10^{-9}/approach, where P_{HMI} is the probability of Hazardously Misleading Information (HMI) [1]. It means only 2 events that the system should not be used for navigation and the airborne subsystem doesn't get a warning are allowed in a billion approaches. The rigorous integrity requirement determines that, before the ground subsystem sends augmentation information to the airborne subsystem, the integrity monitoring is absolutely necessary to avoid sending misleading information.

The faults of ground devices and space satellite signals are the main causes of misleading information in local area augmentation system, and corresponding quality monitoring including SQM (signal quality monitoring), DQM (data quality monitoring) and MQM (measurement quality monitoring) is executed to detect these faults [1]. In local area augmentation system, the way of quality monitoring is comparing the observations collected with corresponding thresholds, and then decides if a failure is happening.

24.2 Conventional Threshold Determination Methods

Thresholds which are too hardly will make normal observations fail the quality monitoring and reduce the continuity of the system, otherwise, too soft thresholds will make anomalous observations pass the quality monitoring and increase the false alarm probability. Proper valued thresholds are usually the key to achieving the desired performance of the integrity monitoring. For integrity monitoring in local area augmentation system, a requirement of thresholds is: make the probability that normal observations fail the quality monitoring smaller than a specified probability value (corresponding to the requirement of false alarm probability of the system) to satisfy the system's continuity requirement.

There are two main conventional approaches of thresholds determination. The first method determines the thresholds for various observations depending on engineering experience. This method doesn't satisfy the requirement of false alarm probability of the system since it is lack of theory bases. This method is not applicable to all satellite navigation system (especially the BDS) since most engineering experience is based on GPS satellites and GPS receivers. The second method determines the thresholds based on threshold models of various observations [2]. The actual application conditions (location of the reference stations, performance of the reference receivers, environment condition, the satellite navigation system and so on) of the threshold model are probably different from the conditions of building the threshold model, therefore, determining the thresholds according to threshold models is not always accurate for specified local area augmentation system. In addition, the application field of the threshold model method is limited since not every kind of observation has a corresponding threshold model.

Usually, in a specified local area augmentation system, it is hard to make sure that the threshold determination methods is completely applicable even though the method depending on engineering experience and the method based on threshold models are used together.

24.3 Threshold Determination

Due to the disadvantages of the conventional threshold determination methods mentioned above, this paper researched the threshold determination for integrity monitoring in local area augmentation system and proposed a Gaussian overbounding threshold determination method. The requirement of false alarm probability of the system is considered, and the threshold is calculated from a Gaussian distribution (Gaussian distributions are used since avionics assume that measurement errors are Gaussian [3]) that overbounds the two tails of the probability density distribution of the observation data. The threshold determination method consists of the following steps (Fig. 24.1):

Step 1. Calculate the Multiplier
Assume the false alarm probability of the local area augmentation system is p, for a Gaussian distribution $X \sim N(\mu, \sigma^2)$, make the threshold $T = \mu \pm a \cdot \sigma$, where a is the multiplier which determines the false alarm probability p, and

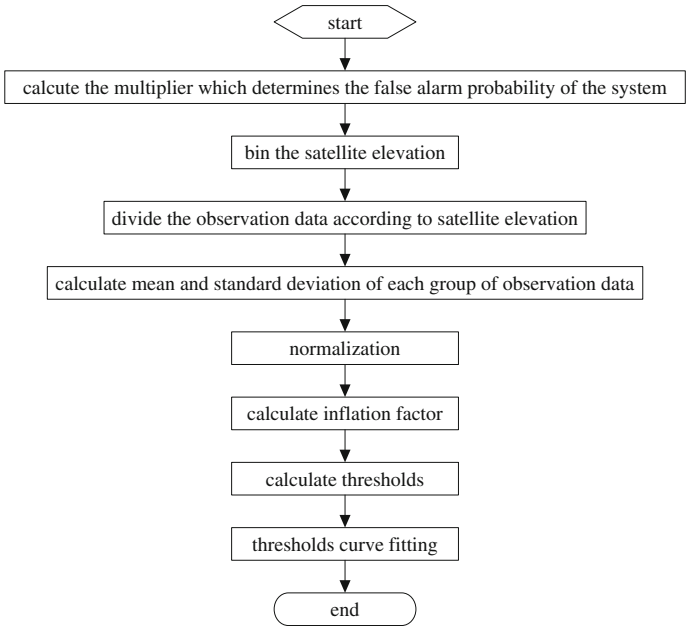

Fig. 24.1 Steps of threshold determination

$a > 0$. The probability that the distribution X exceeds the threshold T is $P(|X - \mu| > a \cdot \sigma) = P(|S| > a) = p$, where S is the standard normal distribution $S \sim N(0, 1)$. The multiplier a can be calculated by $a = Q^{-1}(p/2)$, where function $Q(s) = P(S > s)$ and Q^{-1} is the inverse function of Q.

Step 2. Bin the Satellite Elevation
Most observations of integrity monitoring in local area augmentation system are satellite elevation angle dependent. Measurement errors tend to grow at low elevation angles because multipath is more severe and the obliquity factors for the ionosphere and the troposphere are larger. Thus, test statistics for low elevation satellites have greater variability [4]. Therefore, when determining thresholds, it is necessary to bin the satellite elevation. The satellite elevation value varies from 0° to 90°. There are $M = 90/L$ elevation bins of L (usually L is 5 or 10) degrees each, $(0, L], (L, 2L], (2L, 3L], \ldots, (90 - L, 90]$.

Step 3. Divide the Observation Data
Divide the observation data into groups according to satellite elevation. Make the observation data belong to the same satellite elevation bin a group, and there will be M groups of observation data, $D_1, D_2, D_3, \ldots, D_M$.

Step 4. Calculate Mean and Standard Deviation
For the M groups of observation data, $D_1, D_2, D_3, \ldots, D_M$, calculate mean $\mu_1, \mu_2, \mu_3, \ldots, \mu_M$ and standard deviation $\sigma_1, \sigma_2, \sigma_3, \ldots, \sigma_M$.

Step 5. Normalization
For the M groups of observation data $D_i (i = 1, 2 \ldots M)$, subtract μ_i from each data point, and divide the result by its standard deviation σ_i, then we get M groups of normalized observation data $Dn_1, Dn_2, Dn_3, \ldots, Dn_M$.

Step 6. Calculate Inflation Factor [5]
For each group normalized observation data $Dn_i (i = 1, 2 \ldots M)$ whose probability density distribution is $Yn_i (i = 1, 2 \ldots M)$, a zero-mean Gaussian distribution $Gn_i \sim N(0, f_i^2)$ with an inflated standard deviation f_i is used to overbound the tails of Yn_i, in other words, at the two tails, the desired Gaussian distribution has a larger probability than the discretized, apparent data distribution Yn_i. The standard deviation inflation factor f_i should be minimized during the overbounding process in order to protect integrity.

Step 7. Calculate Thresholds
For the M elevation bins, the thresholds are $T_i = \mu_i \pm a \cdot f_i \cdot \sigma_i (i = 1, 2 \ldots M)$, where a is the multiplier calculated by step 1, μ_i and σ_i are the mean and standard deviation calculated by step 4, and f_i is the Inflation factor calculated by step 6. It is obviously that the probability density distribution Y_i of D_i is overbounded by Gaussian distribution $G_i \sim N(\mu_i, (f_i \cdot \sigma_i)^2)$. The probability that D_i exceeds its threshold T_i is $P_i(|D_i - \mu_i| > a \cdot f_i \cdot \sigma_i)$. Since $P_i(|D_i - \mu_i| > a \cdot f_i \cdot \sigma_i) < P_i(|G_i - \mu_i| > a \cdot f_i \cdot \sigma_i)$ and $P_i(|G_i - \mu_i| > a \cdot f_i \cdot \sigma_i) = P_i(|S| > a) = 2Q(a) = p$, where S and Q have the same meaning as in step 1, so we have $P_i(|D_i - \mu_i| > a \cdot f_i \cdot \sigma_i) < p$. It means the probability that D_i exceeds its

threshold T_i is smaller than the false alarm probability p, in other words, the requirement of false alarm probability of the system is satisfied.

Step 8. Threshold Curve Fitting
With the thresholds $T_i(i = 1, 2...M)$ of the M elevation bins, we can get a threshold curve by curve fitting. For actual quality monitoring, when we want to get the threshold value of a specified satellite elevation, we can use the value of the threshold curve of the same elevation.

24.4 Threshold Determination Instance

In order to verify the threshold determination method proposed above, an instance of threshold determination of the carrier phase acceleration monitoring in a local area augmentation system based on BDS and BD receivers is given here. Carrier acceleration monitoring a kind of measurement quality monitoring, it calculates the carrier phase acceleration value from the carrier phase measurement, then compares it with corresponding threshold to determine whether the carrier phase measurement is normal.

1. Calculate the multiplier

Assume the requirement of false alarm probability of the local area augmentation system is $p = 1 \times 10^{-9}$, the corresponding multiplier a is $a = Q^{-1}(p/2) = Q^{-1}(1 \times 10^{-9}/2) \approx 6.1095$.

2. Bin the satellite elevation

Make 10° a bin, then we get 9 bins of satellite elevation which are $(0, 10]$, $(10, 20]$, $(20, 30]$, $(30, 40]$, $(40, 50]$, $(50, 60]$, $(60, 70]$, $(70, 80]$ and $(80, 90]$.

3. Divide the observation data

Divide the carrier phase acceleration data into 9 groups $Acc_i(i = 1, 2...9)$ as Fig. 24.2.

4. Calculate mean and standard deviation

For each group $Acc_i(i = 1, 2...9)$, calculate its mean $\mu_i(i = 1, 2...9)$ and standard deviation $\sigma_i(i = 1, 2...9)$, the result is shown in Table 24.1.

5. Normalization

For $Acc_i(i = 1, 2...9)$, subtract μ_i from each data point, and divide the result by its standard deviation σ_i, the result is normalized data $Accn_i(i = 1, 2...9)$ as shown in Fig. 24.3.

6. Calculate inflation factor

For $Accn_i(i = 1, 2...9)$, calculate the inflation factor $f_i(i = 1, 2...9)$. Take $Accn_3$ as a example, the result is shown in Fig. 24.4, $f_3 = 1.365$.

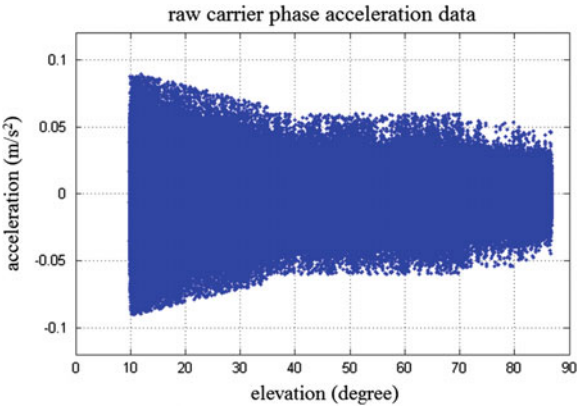

Fig. 24.2 Raw carrier phase acceleration data

Table 24.1 Mean and standard deviation

Elevation (degree)	Data	μ (m/s^2)	σ (m/s^2)
(0, 10]	Acc_1	–	–
(10, 20]	Acc_2	−3.1917e-04	0.0212
(20, 30]	Acc_3	−2.9717e-04	0.0155
(30, 40]	Acc_4	−2.8823-04	0.0129
(40, 50]	Acc_5	−2.5429e-04	0.0107
(50, 60]	Acc_6	−2.7007e-04	0.0108
(60, 70]	Acc_7	−2.3773e-04	0.0109
(70, 80]	Acc_8	−3.2659 e-04	0.0107
(80, 90]	Acc_9	−3.8491e-04	0.0106

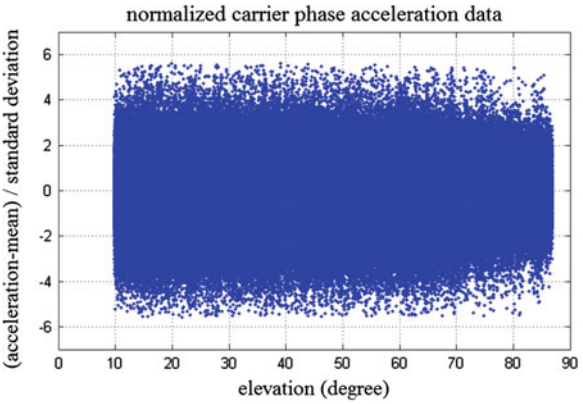

Fig. 24.3 Normalized carrier phase acceleration data

Table 24.2 shows the inflation factor $f_i(i = 1, 2...9)$ of each elevation bin.

7. Calculate thresholds

For each elevation bin, calculate thresholds $T_i = \mu_i \pm a \cdot f_i \cdot \sigma_i (i = 1, 2...9)$, the result shows in Table 24.3.

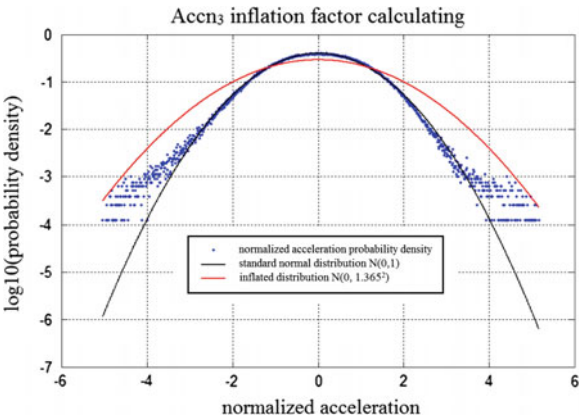

Fig. 24.4 $Accn_3$ inflation factor calculating

Table 24.2 Inflation factor of each elevation bin

Elevation (degree)	Data	Inflation factor f_i
(0, 10]	Acc_1	–
(10, 20]	Acc_2	1.236
(20, 30]	Acc_3	1.365
(30, 40]	Acc_4	1.535
(40, 50]	Acc_5	1.561
(50, 60]	Acc_6	1.616
(60, 70]	Acc_7	1.606
(70, 80]	Acc_8	1.543
(80, 90]	Acc_9	1.568

Table 24.3 Thresholds of each elevation bin

Elevation (degree)	Threshold (m/s^2)	
	$\mu_i + a \cdot f_i$	$\mu_i - a \cdot f_i$
(0, 10]	–	–
(10, 20]	0.1598	−0.1604
(20, 30]	0.1290	−0.1296
(30, 40]	0.1208	−0.1214
(40, 50]	0.1018	−0.1023
(50, 60]	0.1059	−0.1065
(60, 70]	0.1066	−0.1071
(70, 80]	0.1003	−0.1009
(80, 90]	0.1015	−0.1022

8. Threshold curve fitting

The result of threshold curve fitting with the thresholds calculated above is shown in Fig. 24.5.

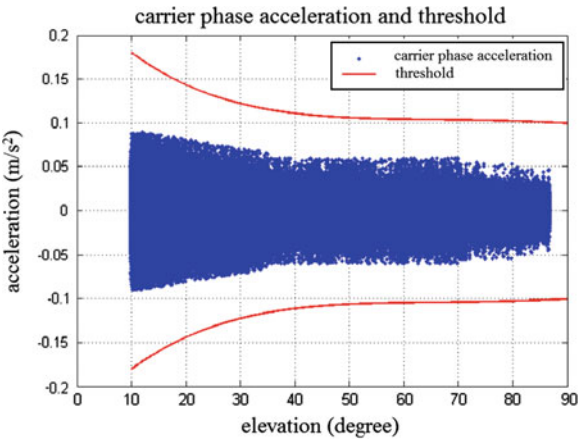

Fig. 24.5 Threshold curve of carrier phase acceleration

24.5 Conclusions

This paper proposed a Gaussian overbounding method to determine thresholds. The requirement of false alarm probability of the system is considered, and the threshold is calculated from a Gaussian distribution that overbounds the two tails of the probability density distribution of the observation data. Comparing to the threshold determination methods depending on engineering experience or threshold models, this method satisfies the requirement of false alarm probability of the system; moreover, it accords with the real characteristic of the system due to the thresholds are calculated using own observation data of the system. This method has been well utilized in a local area augmentation system based on BDS and BD receivers. Threshold determination method that satisfies the continuity and other requirements of the system will be the focus of future work.

References

1. Xie G (2004) Optimal on-airport monitoring of the integrity of GPS-based landing system. Stanford university
2. Minimum Aviation System Performance Standards for Local Area Augmentation System (LAAS). Washington, D.C., RTCA SC-159, WG-4A, DO-245, 28 Sept 1998
3. Minimum Operational Performance Standards for GPS/Local Area Augmentation System Airborne Equipment. Washington, D.C., RTCA SC-159, WG-2, DO-229C, 28 Nov 2001
4. Misra P, Enge P (2001) Global positioning system: signals, measurements, and performance. Ganga-Jamuna Press, Lincoln
5. Shively C, Braff R (2000) An overbound concept for pseudorange error form the LAAS ground facility. In: ION Annual Meeting, San Diego, CA, 26–28 June 2000

Chapter 25
Multi-constellation Receiver Autonomous Integrity Monitoring with BDS/GPS/Galileo

Yuan Sun, Yanbo Zhu and Rui Xue

Abstract The existing Receiver Autonomous Integrity Monitoring (RAIM) algorithms for multiple faults have problems to determine the number of faults with high efficiency. To solve the problem, a multi-constellation RAIM method for multiple faults is proposed in this paper. By establishing the distribution of likelihood probability under different fault modes, the faults with unknown number of faults can be identified. The simulations with BDS/GPS/Galileo show that our approach can effectively identify fault satellites in both the single-fault scenario and the multi-faults scenario.

Keywords BDS · Multi-constellation · RAIM

25.1 Introduction

Receiver Autonomous Integrity Monitoring (RAIM) which is embedded in navigation receiver as an algorithm of integrity monitoring can accurately detect and identify the fault from the satellite observations in real time. It has been a mandatory function for navigation receiver. However, the current RAIM algorithm with GPS alone can only meet the requirements for en-route and non-precision approach with the constraint of visible GPS satellites. With combined BDS, GPS and Galileo multi-constellation, the increased number of visible satellites will provide more

Y. Sun (✉) · R. Xue
School of Electronic and Information Engineering, Beihang University, Beijing, China
e-mail: sunyuan@ee.buaa.edu.cn

R. Xue
e-mail: xuerui@buaa.edu.cn

Y. Zhu
Aviation Data Communication Corporation, Beijing, China
e-mail: zyb@adcc.com.cn

J. Sun et al. (eds.), *China Satellite Navigation Conference (CSNC) 2015 Proceedings: Volume II*, Lecture Notes in Electrical Engineering 341,
DOI 10.1007/978-3-662-46635-3_25

redundant measurements for RAIM which is expected to support the precision approach [1].

For multi-constellation navigation, the probability of multiple faults can no longer be neglected so that the RAIM algorithm based on single fault hypothesis is not applicable [2]. The RAIM algorithm for multiple faults with unknown number of faults has been extensively studied in recent years. The processing scheme of existing RAIM algorithms for multiple faults could be classified into two categories: the "Top Down" approach and the "Bottom up" approach. The "Top Down" approach is an extension of single fault RAIM method, which iteratively executes the RAIM algorithm under the assumption of specific number of faults [3, 4]. As the "Top Down" approach is designed for specific number of faults, it performs poorly when the actual number of faults is not consistent with the assumption [5, 6]. To solve the problem with unknown number of faults, the "Bottom up" approach is proposed by testing the goodness-of-fit for each minimal sample set. However, the threshold for the goodness-of-fit test appeals to empirical evidence and lacks of logical support [7, 8].

The unknown number of faults is the main limiting factor of RAIM multiple faults. To solve the problem, a multi-constellation RAIM method for multiple faults is proposed in this paper. By introducing the fault mode matrix, the number of contaminated measurements and the corresponding ranging sources can be expressed. Then, the fault bias under each fault mode hypothesis can be estimated using the criterion of maximum likelihood estimation. For the modes with different number of faults, the statistical distribution of the likelihood probability is deduced to realize fault mode identification. The simulations with BDS/GPS/Galileo demonstrate the effectiveness of multi-constellation RAIM for multiple faults proposed in this paper over the existing "Bottom Up" approach in the probability of correct identification. Moreover, our approach has a good compatibility for both the single-fault scenario and multi-fault scenario.

The remainder of this paper is organized as follows. Section 25.2 is the description and analysis of existing RAIM method for multiple faults. Section 25.3 is the proposed multi-constellation RAIM approach for multiple faults. Section 25.4 is the experiments to demonstrate the performance of our approach. Finally the conclusions are shown in Sect. 25.5.

25.2 The Existing RAIM Method for Multiple Faults

RAIM method is based on the consistency check using the residuals of the satellite pseudoranges [9]. The processing scheme of existing RAIM method for multiple faults could be classified into two categories: the "Top Down" approach and the "Bottom up" approach [7].

25.2.1 "Top Down" Approach

The "Top Down" approach uses all available measurements to obtain the least-squares positioning solution. The fault identification of "Top Down" approach is designed for specific number of faults. It iteratively conducts the fault detection and identification process to finish the identification for all faults.

The processing scheme of the "Top Down" approach is as follows,

(1) Calculate the overall residuals based on the full-set positioning solution.
(2) Apply consistency check to detect whether fault occurred.
(3) Identify and eliminate the fault satellite measurement based on the assumption of specific number of faults.
(4) Repeat the above process until no fault is detected.

As the "Top Down" approach is designed for specific number of faults, the performance of "Top Down" approach will decrease significantly when the actual number of faults is not equal to the assumed number.

25.2.2 "Bottom Up" Approach

To solve the problem of unknown number of faults, the "Bottom Up" approach uses only subset of the measurements to obtain the least-squares solution.

The processing scheme of the "Bottom Up" approach is as follows,

(1) Test the goodness-of-fit for each minimal sample set to determine a reference positioning reference.
(2) Calculate the residuals of remaining measurements.
(3) Compare the residuals to the threshold. If the residual falls outside the threshold, the corresponding measurement will be identified as fault.

The "Bottom Up" approach involves two threshold settings in the goodness-of-fit test and fault identification process. The threshold settings are empirical with the recommended value 2.5σ [9, 10].

Besides, the "Bottom Up" approach needs to calculate the least-square solutions of all the minimal sample set. It is time-consuming, thus is limited in practical application.

25.3 Multi-constellation RAIM for Multiple Faults

By introducing the fault mode matrix, the fault bias under each fault mode can be estimated with maximum likelihood estimation. On this basis, the method to determine the number of faults is proposed to improve the reliability of RAIM for multiple faults.

25.3.1 Fault Mode

Using BDS/GPS/Galileo multi-constellation as an example, the normalized measurement equation is described by an over-determined linear system [11].

$$z_w = \boldsymbol{H}_w \boldsymbol{x} + \boldsymbol{\varepsilon}_w + \boldsymbol{b}_w \tag{25.1}$$

where $z_w = \boldsymbol{W}^{1/2} z$, z is a vector of pseudorange measurement residuals, $\boldsymbol{W} = \boldsymbol{\Sigma}^{-1}$, $\boldsymbol{\Sigma}$ is the diagonal covariance matrix of measurement noise, $\boldsymbol{H}_w = \boldsymbol{W}^{1/2}\boldsymbol{H}$,

$$\boldsymbol{H} = \begin{bmatrix} [\boldsymbol{H}_{BD} & \boldsymbol{0} & \boldsymbol{0}] \\ [\boldsymbol{H}_{GPS} & \boldsymbol{0} & \boldsymbol{0}] \\ [\boldsymbol{H}_{GAL} & \boldsymbol{0} & \boldsymbol{1}] \end{bmatrix} \tag{25.2}$$

where $\boldsymbol{H}_{BD}, \boldsymbol{H}_{GPS}, \boldsymbol{H}_{GAL}$ is the observation matrix of single-constellation navigation corresponding to BDS, GPS and Galileo separately. $\boldsymbol{x}$ is the state vector to be estimated, $\boldsymbol{\varepsilon}_w$ is the normalized measurement noise as,

$$\varepsilon_w \sim N(0, 1) \tag{25.3}$$

$\boldsymbol{b}_w$ is the normalized vector of fault bias.

In this paper, fault mode matrix $\boldsymbol{T}$ is introduced to indicate the number of faults and the corresponding fault satellite. $\boldsymbol{T}$ is a $n \times m$ matrix of zeros and ones where n is the number of visible satellites and m is the number of faults. Each column of matrix $\boldsymbol{T}$ has single non-zero element to indicate the measurement fault. Each row of $\boldsymbol{T}$ has no more than one non-zero element. Then the non-zero fault bias $\boldsymbol{f}$ can be extracted from fault bias $\boldsymbol{b}_w$,

$$\boldsymbol{b}_w = \boldsymbol{T} \cdot \boldsymbol{f} \tag{25.4}$$

where $\boldsymbol{f}$ is a $m \times 1$ vector of non-zero fault bias.

25.3.2 Maximum Likelihood Estimation

To eliminate the correlation between the elements of pseudorange residuals, matrix $\boldsymbol{H}_w$ is decomposed so that the state space is transformed to the parity space.

$$\boldsymbol{H}_w = [\boldsymbol{U}_1 \quad \boldsymbol{U}_2] \begin{bmatrix} \boldsymbol{R}_1 \\ \boldsymbol{0} \end{bmatrix} \tag{25.5}$$

where $\boldsymbol{U}_1 \in \boldsymbol{R}^{n \times 6}$ and $\boldsymbol{U}_2 \in \boldsymbol{R}^{n \times (n-6)}$ constitute the unitary matrix $\boldsymbol{U} \in \boldsymbol{R}^{n \times n}$, $\boldsymbol{R}_1 \in \boldsymbol{R}^{6 \times 6}$ is the first six row of $\boldsymbol{R} \in \boldsymbol{R}^{n \times 6}$.

The parity vector $\boldsymbol{p}$ in $(n-6)$ dimensional parity space is,

$$\boldsymbol{p} = \boldsymbol{U}_2^T \boldsymbol{z}_w \tag{25.6}$$

The parity vector follows the distribution of jointly normal distribution with the mean of $\boldsymbol{U}_2^T \boldsymbol{T}\boldsymbol{f}$ and the covariance of $\boldsymbol{I}_{n-6}$,

$$p(\boldsymbol{p}|\boldsymbol{T}, \boldsymbol{f}) = \frac{1}{(2\pi)^{(n-6)/2}} \exp(-\boldsymbol{J}/2) \tag{25.7}$$

where $\boldsymbol{J} = (\boldsymbol{p} - \boldsymbol{U}_2^T \boldsymbol{T}\boldsymbol{f})^T (\boldsymbol{p} - \boldsymbol{U}_2^T \boldsymbol{T}\boldsymbol{f})$ can be expanded as,

$$\boldsymbol{J} = \boldsymbol{z}_w^T \boldsymbol{S}_w \boldsymbol{z}_w + \boldsymbol{z}_w^T \boldsymbol{S}_w \boldsymbol{T}\boldsymbol{f} + (\boldsymbol{T}\boldsymbol{f})^T \boldsymbol{S}_w \boldsymbol{z}_w - (\boldsymbol{T}\boldsymbol{f})^T \boldsymbol{S}_w (\boldsymbol{T}\boldsymbol{f}) \tag{25.8}$$

where $\boldsymbol{S}_w = \boldsymbol{U}_2 \boldsymbol{U}_2^T$ is a symmetric idempotent matrix. To calculate the maximum value of $p(\boldsymbol{p}|\boldsymbol{T}, \boldsymbol{f})$, the derivative of vector $\boldsymbol{f}$ is,

$$\frac{\partial \boldsymbol{J}}{\partial \boldsymbol{f}} = 2\boldsymbol{T}^T \boldsymbol{S}_w \boldsymbol{z}_w - 2\boldsymbol{T}^T \boldsymbol{S}_w \boldsymbol{T}\boldsymbol{f} = 0 \tag{25.9}$$

Then the estimated $\hat{\boldsymbol{f}}$ with maximum likelihood estimation is,

$$\hat{\boldsymbol{f}} = (\boldsymbol{T}^T \boldsymbol{S}_w \boldsymbol{T})^{-1} \boldsymbol{T}^T \boldsymbol{S}_w \boldsymbol{z}_w \tag{25.10}$$

Substitute Eq. (25.10) to Eq. (25.7), the likelihood probability is determined as,

$$p(\boldsymbol{p}|\boldsymbol{T}, \hat{\boldsymbol{f}}) = (\boldsymbol{S}_w \boldsymbol{z}_w)^T \boldsymbol{T} (\boldsymbol{T}^T \boldsymbol{S}_w \boldsymbol{T})^{-1} \boldsymbol{T} (\boldsymbol{S}_w \boldsymbol{z}_w) \boldsymbol{p} \tag{25.11}$$

In the process of receiver autonomous integrity monitoring, not all the fault modes is taken into account. Only the fault modes which may cause the integrity risk exceeding the requirements need to be considered. For RAIM with BDS/GPS/Galileo, we just consider three simultaneous faults at most [12].

For modes with the same number of faults, the one maximizing the likelihood probability is most likely to happen under the specific number of faults. By comparing the likelihood function, we can get the probable fault mode $\boldsymbol{T}_1$, $\boldsymbol{T}_2$, $\boldsymbol{T}_3$ corresponding to the single fault, two faults and three faults separately.

25.3.3 Fault Mode Identification

For modes $\boldsymbol{T}_1$, $\boldsymbol{T}_2$, $\boldsymbol{T}_3$ with different number of faults, we cannot directly compare the likelihood function. Instead, the statistical distribution of the likelihood probability under different number of faults is derived to assist fault mode identification.

Without loss of generality, we assume $\boldsymbol{T}_\alpha$ is a $n \times \alpha$ matrix and $\boldsymbol{T}_\beta$ is a $n \times \beta$ matrix, $\alpha > \beta$. In addition, β columns of $\boldsymbol{T}_\alpha$ are the same with that of $\boldsymbol{T}_\beta$ where n is the number of visible satellites, α and β are the number of faults corresponding to mode $\boldsymbol{T}_\alpha$ and $\boldsymbol{T}_\beta$. Then the difference between the likelihood probability under mode $\boldsymbol{T}_\alpha$ and $\boldsymbol{T}_\beta$ is,

$$p(\boldsymbol{p}|\boldsymbol{T}_\alpha,\hat{\boldsymbol{f}}_\alpha) - p(\boldsymbol{p}|\boldsymbol{T}_\beta,\hat{\boldsymbol{f}}_\beta) = \boldsymbol{z}_w^T \boldsymbol{M} \boldsymbol{z}_w \tag{25.12}$$

where $\boldsymbol{M} \triangleq \boldsymbol{S}_w^T \boldsymbol{T}_\alpha (\boldsymbol{T}_\alpha^T \boldsymbol{S}_w \boldsymbol{T}_\alpha)^{-1} \boldsymbol{T}_\alpha^T \boldsymbol{S}_w - \boldsymbol{S}_w^T \boldsymbol{T}_\beta (\boldsymbol{T}_\beta^T \boldsymbol{S}_w \boldsymbol{T}_\beta)^{-1} \boldsymbol{T}_\beta^T \boldsymbol{S}_w$

It can be proved that $\boldsymbol{M}$ has properties as follows,

1. $\boldsymbol{M}$ is symmetric.
2. $\boldsymbol{M}$ is idempotent
3. *rank* ($\boldsymbol{M}$) = α–β

Then matrix $\boldsymbol{M}$ can be decomposed as,

$$\boldsymbol{M} = [\,\boldsymbol{V}_1 \quad \boldsymbol{V}_2\,] \begin{bmatrix} \boldsymbol{I}_{\alpha-\beta} & \boldsymbol{0} \\ \boldsymbol{0} & \boldsymbol{0} \end{bmatrix} \begin{bmatrix} \boldsymbol{V}_1^T \\ \boldsymbol{V}_2^T \end{bmatrix} = \boldsymbol{V}\boldsymbol{V}_1^T \tag{25.13}$$

where $\boldsymbol{V}_1$ and $\boldsymbol{V}_2$ are unitary matrix. Define $\boldsymbol{r} = \boldsymbol{V}_1^T \boldsymbol{z}_w$, the elements of vector $\boldsymbol{r}$ are independent of each other following the nominal distribution. The difference between the likelihood probabilities under mode $\boldsymbol{T}_\alpha$ and $\boldsymbol{T}_\beta$ can be expressed as,

$$p(\boldsymbol{p}|\boldsymbol{T}_\alpha, \hat{\boldsymbol{f}}_\alpha) - p(\boldsymbol{p}|\boldsymbol{T}_\beta, \hat{\boldsymbol{f}}_\beta) = \boldsymbol{r}^T \boldsymbol{r} \tag{25.14}$$

According to the definition of chi-square distribution, if $\boldsymbol{T}_\beta$ involves all the faults, then $\boldsymbol{r}^T\boldsymbol{r}$ follows the central chi-square distribution with α–β freedom. If $\boldsymbol{T}_\beta$ does not involve all the faults while $\boldsymbol{T}_\alpha$ involves other faults, then $\boldsymbol{r}^T\boldsymbol{r}$ follows the non-central chi-square distribution with α–β degrees of freedom.

By establishing the statistics using the difference between the likelihood probabilities, the number of faults can be determined. As an example, $\boldsymbol{T}_1$ and $\boldsymbol{T}_2$ are used in the following discussion.

The column vector of $\boldsymbol{T}_2$ which is different from the column of $\boldsymbol{T}_1$ is extracted as $\boldsymbol{l}_1 \sim \boldsymbol{l}_k$ (k = 1 or k = 2).

Use mode matrix $\boldsymbol{A}_i$ to calculate the statistics where $\boldsymbol{A}_i$ is,

$$\boldsymbol{A_i} = [\boldsymbol{T_1}, \boldsymbol{l_i}], \boldsymbol{i} = \boldsymbol{1} \sim \boldsymbol{k} \tag{25.15}$$

Establish statistics δ_{12} to determine the number of faults between $\boldsymbol{T}_1$ and $\boldsymbol{T}_2$,

$$\delta_{12} = \max_i (p(\boldsymbol{p}|\boldsymbol{A}_i, \hat{\boldsymbol{f}}(\boldsymbol{A}_i)) - p(\boldsymbol{p}|\boldsymbol{T}_1, \hat{\boldsymbol{f}}(\boldsymbol{T}_1))) \tag{25.16}$$

The threshold for comparison is determined by central chi-square distribution with 1degree of freedom,

$$D = Q^{-1}(p_f|1) \tag{25.17}$$

where p_f is the probability when the nominal measurement is mistakenly identified as fault, $Q^{-1}(p_f|1)$ is the inverse function of $Q(\chi^2|1)$ which has the following relation,

$$Q(\chi^2|1) = 1 - P(\chi^2|1) \tag{25.18}$$

where $P(\chi^2|1)$ is the cumulative chi-square distribution with 1 degree of freedom.

If $\delta_{12} < D$, output $\boldsymbol{T}_1$. Otherwise, output $\boldsymbol{T}_2$.

25.3.4 Algorithm Process

The processing scheme of our approach is as follows:

Step 1 Calculate the likelihood probability: Calculate the likelihood probabilities under the fault mode corresponding to the single fault, two faults and three faults, respectively.

Step 2 Comparisons among the modes with the same number of faults: Obtain the probable fault modes with the maximum value of likelihood probability under single fault, two faults and three faults, respectively. The probable fault modes are denoted as $\boldsymbol{T}_1$, $\boldsymbol{T}_2$, $\boldsymbol{T}_3$.

Step 3 Comparisons among the modes with different number of faults:
Establish statistics δ_{12} with $\boldsymbol{T}_1$ and $\boldsymbol{T}_2$

If $\delta_{12} < D$
  Establish statistics δ_{13} with $\boldsymbol{T}_1$ and $\boldsymbol{T}_3$
  If $\delta_{13} < D$
    Output $\boldsymbol{T}_1$
  Else
    Output $\boldsymbol{T}_3$
  End If
Else
  Establish statistics δ_{23} with $\boldsymbol{T}_2$ and $\boldsymbol{T}_3$
  If $\delta_{23} < D$
    Output $\boldsymbol{T}_2$
  Else
    Output $\boldsymbol{T}_3$
  End If
End If

25.4 Performance Evaluation

To evaluate the performance of our approach, the simulations under single-fault scenario, two-faults scenario and three-faults scenario are performed which compare the performance of our approach with that of "Bottom Up" approach.

In the simulations, the nominal GPS constellation with 24 satellites, the nominal Galileo constellation with 27 satellites and the BDS regional constellation with 14 satellites are used. The fault bias is randomly added to the observed satellite pseudorange. The probability of correct identification and the minimal identifiable bias is calculated and compared. It is defined as correct identification when all the fault satellites are identified and no normal satellite is in the results. The minimal identifiable bias is the minimal bias magnitude such that 90 % probability of correct identification can be achieved. Figures 25.1, 25.2 and 25.3 are the performance comparisons of our approach and the "Bottom Up" approach under single-fault scenario, two-faults scenario and three-faults scenario separately.

As shown in Fig. 25.1, the intersection of the dashed line with horizontal axis is the minimal identifiable bias. The experimental result shows that the minimal

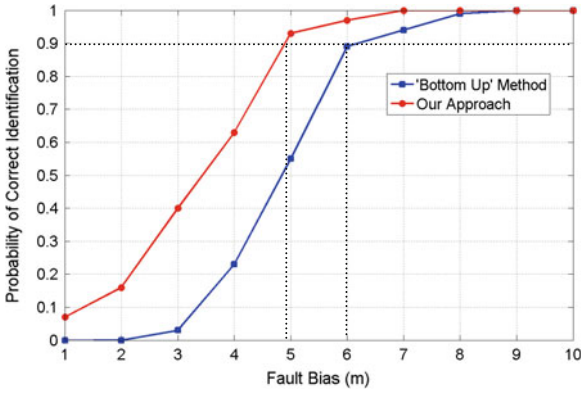

Fig. 25.1 The probability of correct identification in the presence of single fault

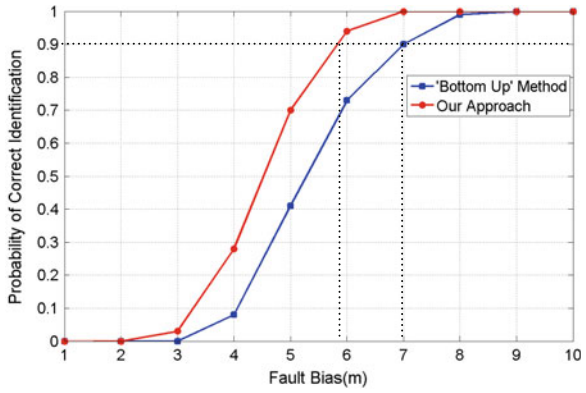

Fig. 25.2 The probability of correct identification in the presence of two faults

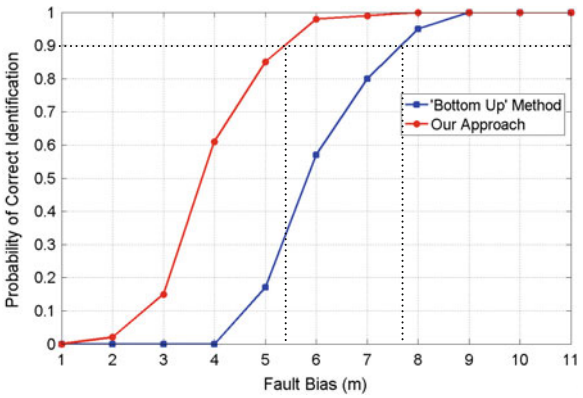

Fig. 25.3 The probability of correct identification in the presence of three faults

identifiable bias of our approach is 20 % smaller than that of "Bottom Up" approach in the presence of single fault.

To simulate the two-faults scenario, two equal-sized biases are randomly added to two different satellite pseudoranges separately. As shown in Fig. 25.2, the minimal identifiable bias is 7 m for the "Bottom Up" approach while the minimal identifiable bias of our approach is less than 6 m. Under the scenario with three faults, the minimal identifiable bias of our approach is improved by more than 25 % when compared with the "Bottom Up" approach.

In conclusion, the multi-constellation RAIM for multiple faults proposed in this paper can effectively identify fault satellites with unknown number of faults. Compared with the "Bottom Up" approach, our approach has a higher probability of correct identification to achieve smaller minimal identifiable bias.

25.5 Conclusions

The existing RAIM algorithms for multiple faults have problems to determine the number of faults with high efficiency. To solve the problem, a multi-constellation RAIM method for multiple faults is proposed in this paper. By introducing the fault mode matrix, the number of fault measurements and the corresponding ranging sources can be expressed. Then, the fault bias under each fault mode hypothesis can be estimated using the maximum likelihood estimation. For the modes with different number of faults, the statistical distribution of the likelihood probability is deduced to realize fault mode identification.

The simulations show that our approach can effectively identify fault satellites in both single-fault scenario and multi-faults scenario.

Acknowledgments The research is supported by the National Basic Research Program of China (973 Program) (No. 2011CB707004), National Natural Science Foundation of China (No. 61179054) and Beijing Municipal Natural Science Foundation (Grant No. 4154078).

References

1. Ochieng WY, Sheridan KF, Sauer K et al (2002) An assessment of the RAIM performance of a combined Galileo/GPS navigation system using the marginally detectable errors (MDE) algorithm. GPS Solutions 5(3):42–51
2. Hewitson S, Wang J (2006) GNSS receiver autonomous integrity monitoring (RAIM) for multiple outliers. Eur J Navig 4(4):47–57
3. Lee YC (2004) Performance of receiver autonomous integrity monitoring (RAIM) in the presence of simultaneous multiple satellite faults. In: ION 60th annual meeting, Dayton, June 2004
4. Ober PB, Harriman D (2006) On the use of multi constellation RAIM for aircraft approaches. In: Proceedings of the 19th international technical meeting of the satellite division of the institute of navigation (ION GNSS 2006), Fort Worth, Sept 2006, pp 2587–2596
5. Yoo CS, Lee SJ (2000) Study on two-failure GPS RAIM problem. In: Proceedings of the 15th Korea automatic control conference, 2000
6. Ni J, Zhu Y (2007) Guo W (2007) An improved RAIM scheme for processing multiple outliers in GNSS. IEEE Computer Society, USA, pp 840–845
7. Jiang Z, Groves P (2012) GNSS NLOS and multipath error mitigation using advanced multi constellation consistency checking with height aiding. In: Proceedings of the 25th international technical meeting of the satellite division of the institute of navigation (ION GNSS 2012), Nashville, Sept 2012, pp 79–88
8. Schroth G, Rippl M, Ene A, Blanch J, Belabbas B, Walter T, Enge P, Meurer M (2008) Enhancements of the range consensus algorithm (RANCO). In: Proceedings of the 21st international technical meeting of the satellite division of the institute of navigation (ION GNSS 2008), Savannah, Sept 2008, pp 93–103
9. Sturza M (1988) Navigation system integrity monitoring using redundant measurements. J Inst Navig 35(4):69–87
10. Groves P, Jiang Z (2013) Height aiding, C/N 0 weighting and consistency checking for GNSS NLOS and multipath mitigation in urban areas. J Navig 66(5):653–669
11. Milner CD, Ochieng WY (2011) Weighted RAIM for APV: the ideal protection level. The Journal of Navigation 64:61–73
12. Joerger M, Chan F, Langel S, Pervan B (2012) RAIM detector and estimator design to minimize the integrity risk. In: Proceedings of the 25th international technical meeting of the satellite division of the institute of navigation (ION GNSS 2012), Nashville, Sept 2012, pp 2785–2807

Chapter 26
The Service Performance Evaluation of Different Satellite Based Augmentation Systems

Yuechen Wang, Biao Jin and Shanshan Chen

Abstract For the sake of improving the accuracy, integrity, continuity and availability for civil aviation, etc., the satellite based augmentation system (SBAS) is widely used. Recently, the concept of dual-frequency augmentation signal is proposed. In order to analyze the service performance of SBAS and discuss the necessity of the dual-frequency SBAS (DFSBAS) signal, WAAS, EGNOS and MSAS are selected to analyze. They are evaluated in message type, accuracy and integrity of single-in-space (SIS), accuracy of position, integrity and availability of system and so on. The results show that in the service area, all systems can meet the requirement of non precision approach (NPA); in a part of area can satisfy the approach procedure with vertical I (APV-1). Finally, the simulation shows that dual-frequency SBAS signals will decrease the ranging error and improve the redundancy of system, improve the SBAS service to satisfy the requirement of. precision approach (PA).

Keywords SBAS · Service performance · Integrity · Availability

26.1 Introduction

In order to improve the position accuracy, integrity, availability and continuity of satellite navigation system, satellite based augmentation system (SBAS) is widely used [1]. With the help of ground monitor stations, SBAS determines and forecasts satellite orbit, clock and ionosphere delay. Then GEO satellite is used to broadcast augmentation message to users in a certain service area, mainly includes long-term and fast corrections, grid point ionosphere vertical delay, user difference range error (UDRE), grid ionosphere vertical error (GIVE) and so on. User uses the GPS and

Y. Wang (✉) · B. Jin · S. Chen
Space Star Technology Co. Ltd., Beijing 100086, China
e-mail: wangyuechenpavel@126.com

J. Sun et al. (eds.), *China Satellite Navigation Conference (CSNC) 2015 Proceedings: Volume II*, Lecture Notes in Electrical Engineering 341,
DOI 10.1007/978-3-662-46635-3_26

SBAS message to position and benefits from the improvement of service performance [1, 2].

Now, only a single signal (L1) is used to broadcast pseudorange augmentation message in all SBAS, and dual-frequency (DF) SBAS signals (L1+L5) have been proposed [3]. For the purpose of analyzing the service performance of SBAS and discussing the necessity of DF signals, the WAAS, EGNOS and MSAS data are selected, combined with the broadcast, precise ephemeris and observation of IGS, the analysis of message type and time interval, signal-in-space (SIS) accuracy and integrity, position accuracy, integrity and availability of system are achieved to evaluate different systems.

26.2 Comparison and Analysis of SBAS Service Performance

26.2.1 Comparison of Message

The message broadcasted by WAAS, EGNOS and MSAS all followed the rules of RTCA DO229, in which 64 types message are defined [2], as the Table 26.1 shows.

Decoding the downloaded message, there are these conclusions:

1. All SBASs broadcast message type (MT) 0,1,2 ~ 4,6,7,9 ~ 10,17 ~ 18,24 ~ 26, what's more, WAAS, MSAS uses MT28 and EGNOS uses MT27, their contents are different but all present the variety of UDRE in different areas, which called $\delta UDRE$;
2. The accuracy of fast correction is 0.125 m, the orbit long-term correction's accuracy is 0.125 m, as well as the clock long-term correction's is 2^{-31} s, which effects the corrected SIS error's accuracy directly;
3. In WAAS and MSAS, the MT2 ~ 4 update every 6 s, if there is blank during 6 s, MT63 will be broadcasted, while the MT2 ~ 4 update 4–6 s in EGNOS and no blank or MT63 exist.

Table 26.1 Message types of SBAS

MT	Content	MT	Content
0	Can't use	17	GEO Almanacs
1	PRN MASK	18	Ionospheric Grid Point Masks
2–5	Fast correction and UDRE	24	Mixed Fast/Long Term Corrections
6	Integrity (UDRE)	25	Long Term Satellite Error Corrections
7	Degradation of fast correction	26	Ionospheric delay correction
8	RMS of errors	27	service message
9	GEO navigation message	28	Clock-ephemeris covariance matrix
10	Degradation factor	62	Internal test
12	Time parameter	63	Null

Note Other types are all reserved for future

26.2.2 Comparison of Service Performance

The SBAS data, IGS ephemeris and observation are processed, then statistics results can be got. WAAS and EGNOS data is downloaded from FTP, from 2014.6.29 to 2014.8.2, MSAS data is received by receiver in Beijing, from 2014.12.1 to 2014.12.10. The processing time interval is 30 s. 22 IGS stations are stated in Europe and North America, each 11 stations, in addition, 5 Asia stations are used together. The station's position information is shown in Table 26.2.

26.2.2.1 The SIS Accuracy and Integrity Analysis

The SIS error (SISE) mainly includes the broadcast ephemeris and satellite clock error. SBAS broadcasts the long-term and fast corrections to correct the SISE. Comparing the corrected SISE with the error between broadcast and precise ephemeris, the correcting performance can be evaluated. The long-term correction is in the MT24 and 25 and the error can be corrected by (26.1). What's more, with the help of MT2 ~ 4 and Eq. (26.2), the error on pseudorange can be calculated and the integrity performance of SIS can be evaluated by comparing the satellite residual error for the worst user location (SREW) with the UDRE bound.

$$\begin{cases} \delta\Delta t_{SV} = \delta a_{f0} + \delta a_{f1}(t - t_0) + \delta a_{fG0} \\ \begin{bmatrix} \delta x \\ \delta y \\ \delta z \end{bmatrix} = \begin{bmatrix} \delta x \\ \delta y \\ \delta z \end{bmatrix} + \begin{bmatrix} \delta \dot{x} \\ \delta \dot{y} \\ \delta \dot{z} \end{bmatrix} (t - t_0) \end{cases} \tag{26.1}$$

$$\begin{cases} PR_{corrected}(t) = PR_{measured}(t) + PRC(t_{of}) + RRC(t_{of}) \cdot (t - t_{of}) \\ RRC(t_{of}) = \dfrac{PRC_{current} - PRC_{previous}}{t_{current} - t_{previous}} \end{cases} \tag{26.2}$$

Results are shown in the figures below. Because limitation of paper, Figs. 26.1 and 26.2 are only show the PRN15 as example and others are almost the same: Fig. 26.1 presents the SISE with and without long-term corrections, Fig. 26.2 shows the SREW before and after using fast corrections, as well as the UDRE bound. Then Fig. 26.3 shows integrity bound probability of all satellites. The following conclusions can be got from all figures:

1. The performance of SIS correction of all SBASs are almost the same, the corrected error on each orient is nearly 2 m and on pseudorange is nearly 4 m;
2. The long-term correction of SBAS can make little help on the improvement of SISE because its update interval is tens of seconds and correction's accuracy decreases by the extrapolation, so it must be used with the fast correction, what's more, limited by the location of stations, the corrections are bad when satellites get in and out the observation area;

Table 26.2 The position of IGS stations

	Europe	Latitude	Longitude	America	Latitude	Longitude	Asia	Latitude	Longitude
1	AJAC	41.56°N	8.46°E	ALGO	45.58°N	101.56°W	AIRA	31.22°N	130.19°W
2	BOGI	52.29°N	21.02°E	AMC2	38.48°N	75.29°W	BJFS	39.61°N	115.89°W
3	BRUX	50.48°N	4.22°E	BARH	44.24°N	111.47°W	CHAN	43.7°N	125.27°W
4	BUCU	44.28°N	26.08°E	BCOV	50.33°N	126.51°W	DAEJ	36.24°N	127.22°W
5	BZRG	46.30°N	11.20°E	BRMU	32.22°N	115.18°W	GMSD	30.33°N	131.01°W
6	EBRE	40.49°N	0.30°E	CRO1	17.45°N	115.25°W	MIZU	39.08°N	141.08°W
7	HERT	50.52°N	0.20°E	DRAO	49.19°N	60.23°W			
8	HOFN	64.16°N	154.49°W	GODE	39.01°N	103.10°W			
9	HUEG	47.50°N	7.36°E	GOLD	35.26°N	63.07°W			
10	MADR	40.26°N	175.45°W	HER2	29.04°N	11.04°W			
11	NYA1	78.56°N	11.52°E	NANO	49.18°N	55.55°W			

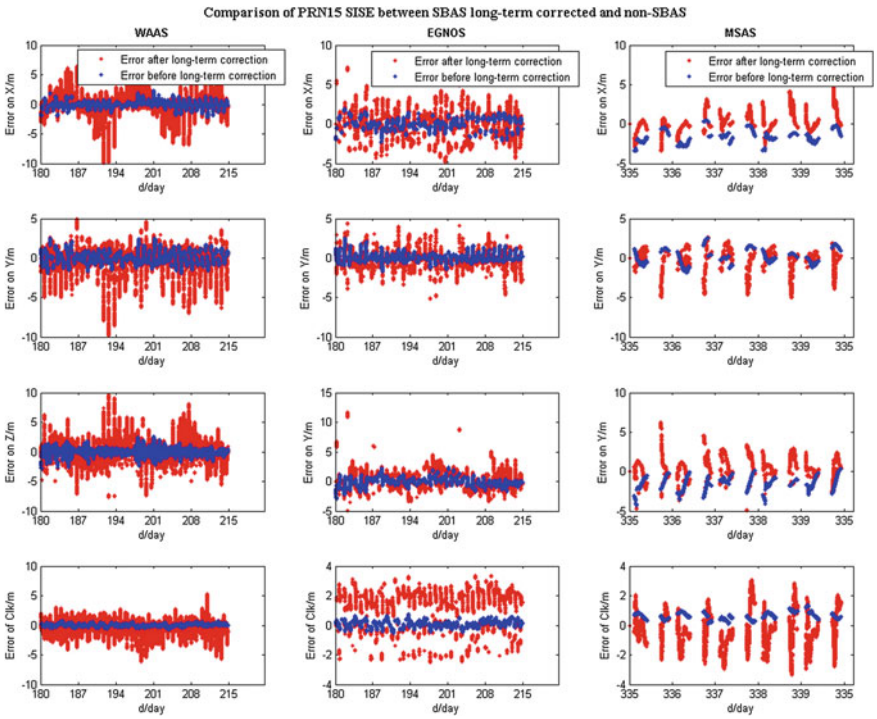

Fig. 26.1 The comparison of SISE between SBAS long-term corrected and non-SBAS

3. The fast correction of SBAS can decrease the SISE on pseudorange effectively, although there is also the bad effect when satellites get in and out the observation area;
4. According to the bound between UDRE and corrected SREW, WAAS, EGNOS and MSAS all can't reach 100 %, the performance of WAAS is better because it can bound at the probability of 98–100 % and only one satellite is less than 90 %, but in EGNOS and MSAS, there are some satellites' bound probability is less than 50 %, the location and number of stations may lead to this result.

26.2.2.2 The Analysis of Position Accuracy

The augmentation message of SBAS can decrease the SISE and ionosphere delay. With the help of weighted least square (WLS) position algorithm in RTCA DO229, the weight matrix is as (26.3) shown [2]. $\sigma^2_{i,flt}$ is the variance corresponding to the broadcasted UDRE; $\sigma^2_{i,UIRE}$ is the variance of the residual of the corrected ionosphere delay, c is the speed of light, T_{iono} is the correction of ionosphere, F_{pp} is the

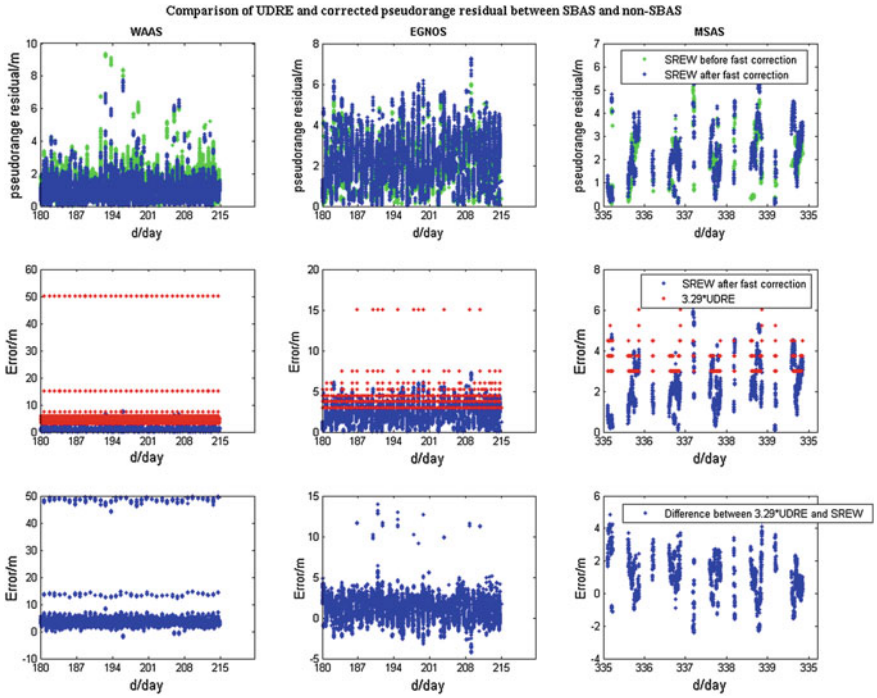

Fig. 26.2 The comparison of UDRE and fast corrected SREW between SBAS and non-SBAS

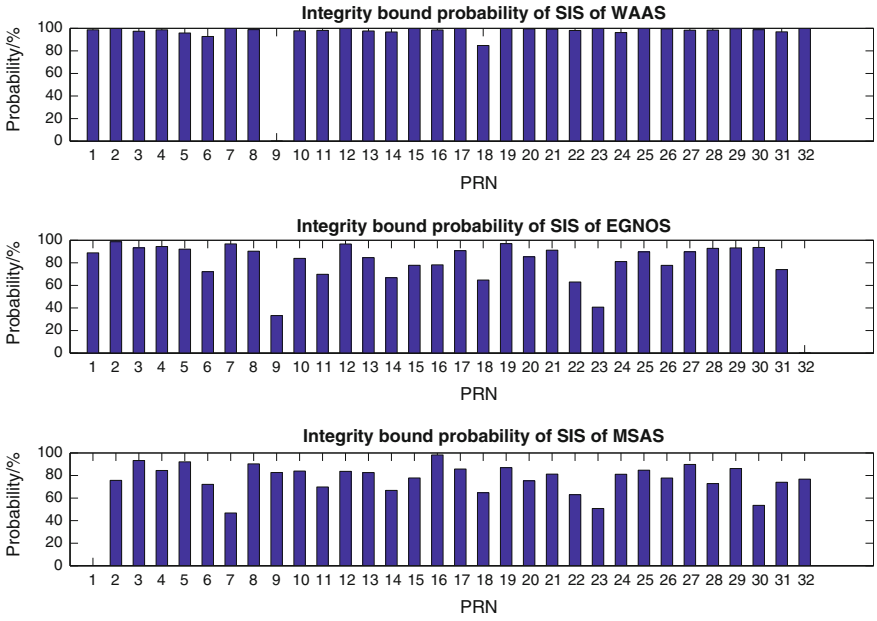

Fig. 26.3 The integrity bound probability of SBAS

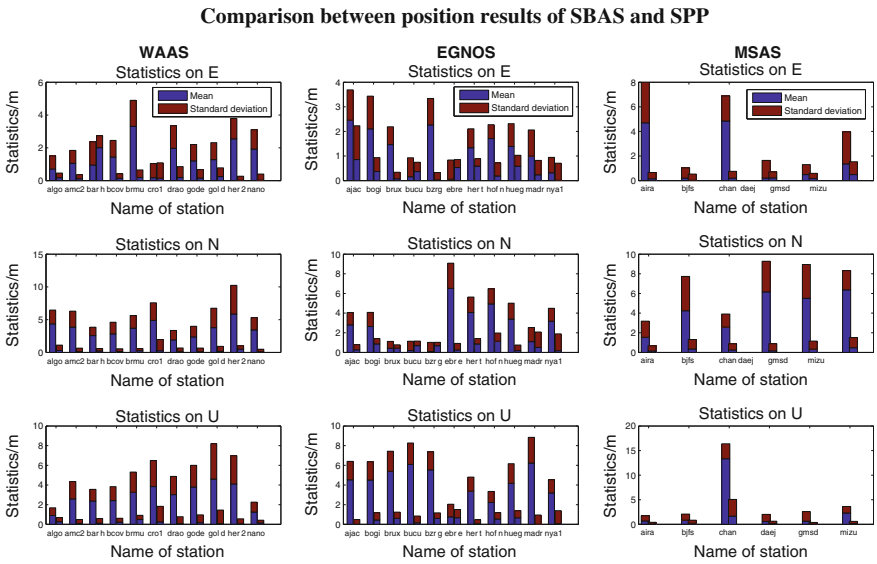

Fig. 26.4 The comparison of position error between SBAS and SPP

factor, ϕ_m is the latitude of geomagnetism; $\sigma^2_{i,air}$ is the variance of noise of receiver and multiple-path; $\sigma^2_{i,tropo}$ is the variance of the residual of troposphere.

Position results with SBAS and without SBAS are compared in Fig. 26.4. For each station the left bar is the position error's mean and standard deviation without SBAS, while the right one is results augmented by SBAS. It can be concluded that:

1. The position accuracy of all systems are almost the same: about 1–2 m in the each of the ENU orient, because of the influence of fast and long-term corrections' accuracy, the augmented position's accuracy is limited;
2. Comparing with the single point position (SPP), the error of ENU are all decrease from 5–10 to 1–2 m with the help of SBAS, what's more, the improvement of U orient is more outstanding;
3. The position accuracy of centre users is obvious, while the system performance on the edge of service area is limited and even can't be used, this also relates to the stations because they can't supply corrections of all visible satellites for edge users.

$$
\begin{aligned}
W &= \begin{bmatrix} w_1 & 0 & \cdots & 0 \\ 0 & w_2 & \cdots & 0 \\ \vdots & \vdots & \ddots & \vdots \\ 0 & 0 & \cdots & w_N \end{bmatrix}, w_i = \frac{1}{\sigma_i^2} \\
\sigma_i^2 &= \sigma_{i,flt}^2 + \sigma_{i,UIRE}^2 + \sigma_{i,air}^2 + \sigma_{i,trop}^2 \\
\sigma_{i,UIRE}^2 &= \mathrm{MAX}\left\{ (cT_{iono}/5)^2, (F_{pp}\tau_{vert})^2 \right\}, \tau_{vert} = \begin{cases} 9 & 0 \le |\phi_m| \le 20 \\ 4.5 & 20 < |\phi_m| \le 55 \\ 6 & |\phi_m| > 55 \end{cases} \\
\sigma_{i,tropo}^2 &= \left(0.12 \times 1.001 \Big/ \sqrt{0.002001 + \sin^2(El_i)} \right)^2
\end{aligned}
\tag{26.3}
$$

26.2.2.3 The Analysis of System's Integrity and Availability

The horizontal/vertical position error (HPE/VPE) can be calculated by the results of SBAS position. By the rotation of coordinate, the error's covariance matrix can be got. According to civil aviation's requirements for different flight phase, the horizontal/vertical protection level (HPL/VPL) can be calculated. Comparing the HPL/VPL, horizontal/vertical alert limit (HAL/VAL), HPE/VPE and the requirement of position accuracy [4]:

- When HPL/VPL>HAL/VAL, the integrity requirement cannot be satisfied, there is integrity risk and the alert must be sent
- When HPE/VPE<HPL/VPL<HAL/VPL, as well as the position error meet the position accuracy's requirement, system is available
- When HPL/VPL<HPE/VPE<HAL/VPL, there is mislead information (MI) and system can't alert to users, so the application of navigation may lead to risk
- When HPL/VPL<HAL/VAL<HPE/VPE, there is hazard mislead information (HMI) and system still can't alert, the application of navigation may lead to hazard risk

According to different requirements shown in Table 26.3, the integrity and availability are evaluated.

As the limitation of paper, one station is selected as example for each system and other stations' results are almost the same. From the Figs. 26.5, 26.6 and 26.7, it can be seen that:

1. In the statistic period, all systems' service at monitor station can meet NPA: the integrity risk is 0 and the availability is 100 %;
2. In the statistic period, the APV-I can't be satisfied at all stations: the availability is mostly above 99 % and there is 90 % or less on the edge of service area, but there is neither MI nor HMI;

Table 26.3 The requirement of different flight phase

	Horizontal/vertical position accuracy	HPL/VPL	Integrity risk	Alert time (s)	Availability
Non Precision Approach (NPA)	220 m/none	556 m/none	10^{-7}/h	10	0.99–0.99999
Approach Procedure with Vertical I (APV-1)	16 m/20 m	40 m/50 m	8×10^{-6}/15 s	10	0.99–0.99999
Approach Procedure with Vertical II (APV-II)	16 m/8 m	40 m/20 m		6	0.99–0.99999
Category I (CAT-1)	16 m/4 m	40 m/10 m		6	0.99–0.99999

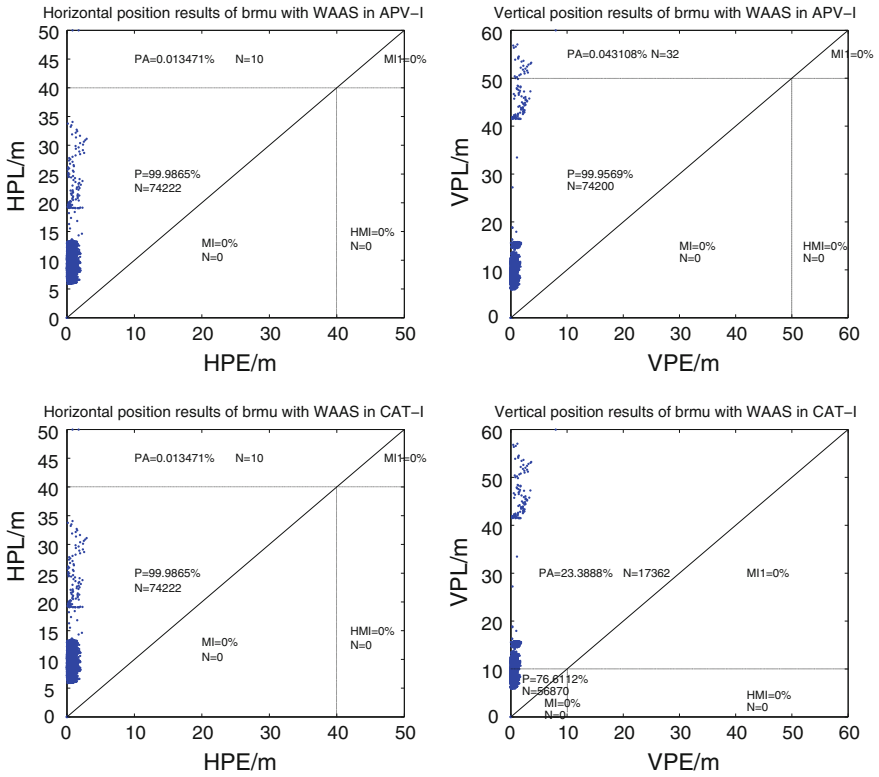

Fig. 26.5 The station brmu's availability of WAAS in different navigation phase

3. In the statistic period, the availability of CAT-I is about 60–80 % and can't satisfy the requirement;
4. The mainly factor limits service performance is VPL, although SBAS improves position accuracy in vertical effectively, it still can't satisfy the demand of precision approach (PA).

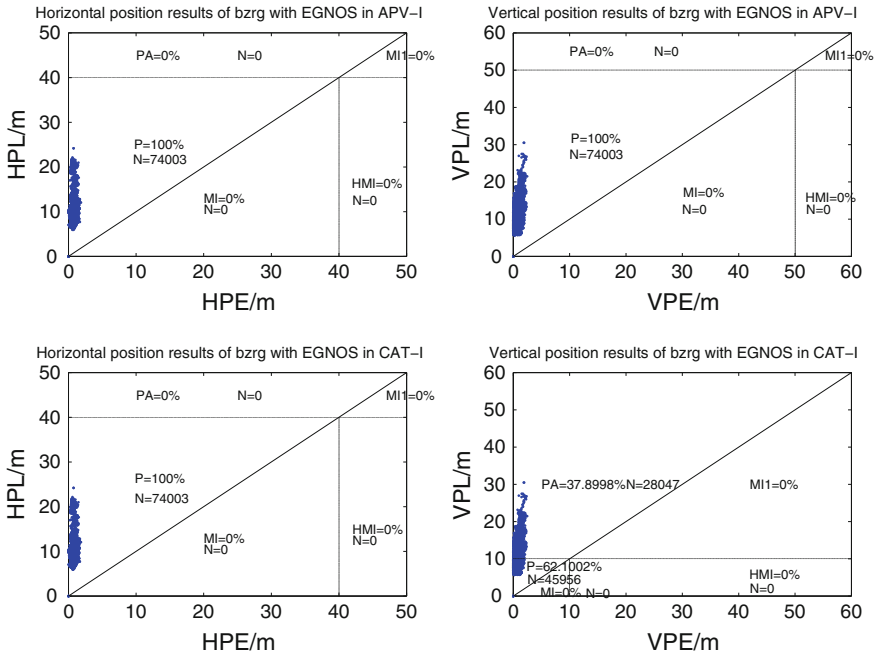

Fig. 26.6 The station bzrg's availability of EGNOS in different navigation phase

26.3 The Analysis of Dual-Frequency SBAS Performance

From the results and analysis above, the SBAS improves the position accuracy, integrity, availability of single-frequency pseudorange. Because the stations are built in local area, the position accuracy of edge users are limited and system can't meet the requirement of PA. So the dual-frequency SBAS (DFSBAS) is necessary for recent SBAS. In order to verify the performance of DFSBAS, GPS is used to simulate and analyze.

In the simulation, the broadcast ephemeris can be got from the combination of precise ephemeris and orbit, satellite clock errors, which are Gauss-Markov process, $\sigma_{eph} = 2m, \sigma_{clk} = 2m$. The ionosphere and troposphere delays are simulated by models, other noise are set as Gaussian white noise. 20 Stations in Europe are selected and station clock errors are Gauss-Markov process the same, the observation can be simulated as receivers really operate. The satellites' precise orbits and clock errors can be determined by WLS, then corrections and integrity parameters can be calculated by corresponding algorithm [5, 6], note that the integrity parameter is different from UDRE because the application of DF signals, it can be called DF range error (DFRE). As the DF signals can eliminate the ionosphere delay, the element of WLS weight matrix changes:

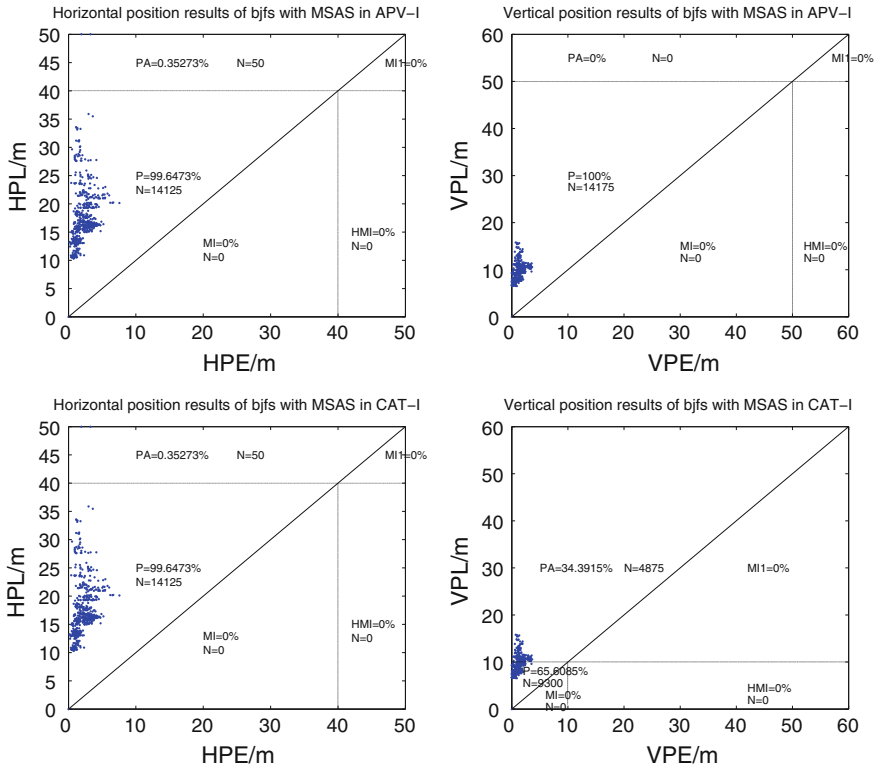

Fig. 26.7 The station bjfs' availability of MSAS in different navigation phase

$$\sigma_i^2 = \sigma_{i,flt}^2 + \sigma_{i,air}^2 + \sigma_{i,trop}^2 \tag{26.4}$$

With the elimination of ionosphere delay, the ranging noise is magnified, which leads to the increase of$\sigma_{i,air}^2$, as:

$$\sigma_{i,air}^2 = (f_1^2/(f_1^2 - f_5^2))^2 \sigma_{i,airL1}^2 + (f_5^2/(f_1^2 - f_5^2))^2 \sigma_{i,airL5}^2 + \sigma_{L1L5}^2 \tag{26.5}$$

The σ_{L1L5}^2 is the delay of receiver on DF signals and $\sigma_{L1L5} = 0.2m$ [7]. In addition, $\sigma_{i,flt}^2$ is the simulated DFRE and other errors are the same as (26.3) shown.

In the condition above, the interval is set 30 s and one day's simulation results are shown in Fig. 26.8. The station 'bzrg' is selected to show the performance in APV-II and CAT-I with the help of DFSBAS.

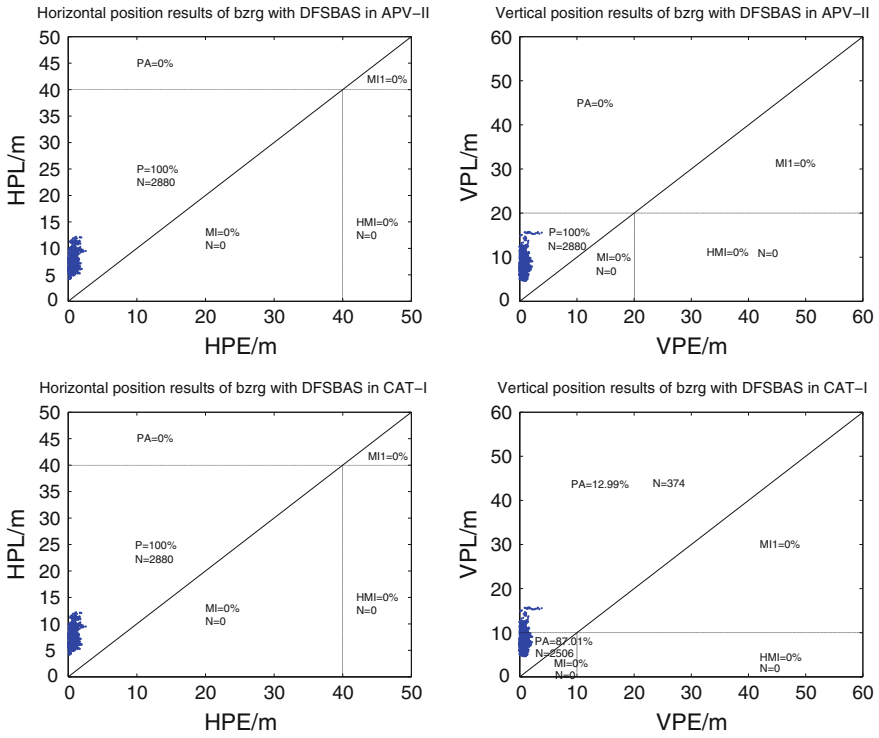

Fig. 26.8 The station bzrg' availability of DFSBAS in different navigation phase

The conclusion can be got that the DFSBAS can decrease the position errors and protection levels (PLs), especially in vertical. Comparing with the result of EGNOS in Fig. 26.6, the station bzrg can satisfy the requirement of AVP-II at 100 % and CAT-I above 85 %. What's more, if the corrections' accuracy can be improved, the performance maybe better.

26.4 Conclusion

By all statistics and analysis, the accuracy, integrity and availability are compared among different SBASs. It can be seen that:

Firstly, the SBAS have nearly the same service performance in service area. They improve the position accuracy from 5–10 to 1–2 m and satisfy the integrity as well as availability's requirement of NPA.

In addition, SBAS cannot fully meet PA's demand in their service area, because of the limitation of the station's location, number and the accuracy of corrections, the SIS corrected accuracy and integrity are a little poor.

Finally, the simulation of DFSBAS shows that it can decrease the errors and PLs, fully meet the APV-II, if more research can be hold, such as the improvement of correction accuracy, the satisfaction of CAT-I shouldn't be a difficulty.

References

1. Kaplan ED, Hegarty CJ (2010) Understanding GPS: Principles and Applications, 2nd edn. (trans: Kou Yan-hong). Beijing, Publishing House of Electronics Industry, vol 3, pp 256–258
2. Radio Technical Commission for Aeronautics (2006) Minimum operational performance standards for global position system/wide area augmentation system airborne equipment, RTCA, Do 229D, 13 Dec 2006
3. Schempp T, Peck S (2010) Incremental benefits of dual frequency signals for wide area augmentation system. Position Location and Navigation Symposium, Indian Wells, May 2010, pp 645–653
4. WADGPS Laboratory (Stanford University), WAAS precision approach metrics. accuracy, integrity, continuity and availability, http://waas.stanford.edu/metrics.html. Accessed Oct 1997
5. Shao B, Liu J, Zhao R, Huang Z, Li R (2011) A user differential range error calculating algorithm based on analytic method. Chin J Aeronaut 24: 762–767
6. Wang Y, Li R (2013) The analysis of character of user range accuracy (URA). China Satellite Navigation Conference (CSNC), pp 267–277
7. Roturier B, Chatre E, Ventura Traveset J (2001) The SBAS integrity concept standardised by ICAO: application to EGNOS. GNSS'2001, New York, 2001

Chapter 27
An Analysis of the QZSS Signal Based on the Data of IGS

Xin Nie, Fu Zheng, Yidong Lou, Jinjun Zheng and Zuhong Li

Abstract Based on the measured data of IGS, the characteristics of QZSS signal, namely, carrier to noise ratio, noise and multipath characteristics, inter-frequency bias, were studied in this paper. At the same time, the results were compared with those of other satellite navigation systems, such as GPS and Galileo, to analyze the reason for the differences. Methods and results provided in this paper have important reference values for the study and construction of satellite navigation systems.

Keywords QZSS · Signal · IGS

27.1 Introduction

The Quasi-Zenith Satellite System (QZSS) is the first component of a Japanese regional satellite navigation system which provides positioning, navigation and timing services to users. The QZSS signals have been designed to maximize the interoperability with GPS, as well as compatibility with other global navigation satellite systems. The QZSS is preliminarily designed to augment GNSS visibility in urban environments. Totally six signals are broadcasted by QZSS, that is, L1 C/A, L1C, L2C, L5, L1-SAIF, LEX. L1 C/A, L1C, L2C, L5 are completely compatible and interoperable with existing and future modernized GPS signals. L1-SAIF and LEX are augmentation signals, which are compatible and interoperable with GPS-SBAS and Galileo E6, respectively.

Based on the measured data of IGS, the signal characteristics of QZSS satellites, namely, carrier to noise ratio, noise and multipath characteristics and inter-frequency

X. Nie (✉) · J. Zheng · Z. Li
China Academy of Space Technology, Beijing, China
e-mail: nxbuaa@126.com

F. Zheng · Y. Lou
Wuhan University, Wuhan, China

J. Sun et al. (eds.), *China Satellite Navigation Conference (CSNC) 2015 Proceedings: Volume II*, Lecture Notes in Electrical Engineering 341,
DOI 10.1007/978-3-662-46635-3_27

bias are studied. At the same time, the results are compared to those of other navigation systems, such as GPS and Galileo to analyze the reason for the differences. In the Sect. 27.2, the main performance indicators, the carrier to noise ratio, noise and multipath characteristics and inter-frequency bias (IFB) are described. In Sect. 27.3, the data processing method is introduced. The results are presented and discussed in Sect. 27.4. Section 27.5 gives the conclusion.

27.2 Signal Characteristic

This paper focuses on the characteristics of QZSS signal arriving at the receiver. The following indicators of signal characteristics were analyzed.

Carrier to Noise Ratio Carrier to noise ratio reflects the relative relationship between signal and noise. Carrier to noise ratio affects the acquisition and tracking of satellites signal, and has importance influence on the positioning results.

Noise and Multipath Characteristics Noise and multipath signals can cause distortion of the correlation function between the received signal and the reference signal that the receiver generates locally, resulting in pseudo-range and carrier measurement errors. Noise and multipath characteristics are related to the surrounding of the monitoring stations, the type of receivers, antennas and satellites, as well as the elevation and azimuth of the arriving signal. The characteristics of noise and multipath are relatively complex.

Inter-frequency Bias At least signals of three different frequencies are broadcasted by current navigation system, e.g. GPS, Beidou, Galileo and QZSS. Two ionosphere-free (IF) combination can be used to eliminate the geometric distance, the main error ionosphere and troposphere, the residual error reflects the bias of pseudo-range and carrier phase between different carrier frequency (inter-frequency bias, IFB). The inter-frequency bias between the third frequency and the other two frequency signal has important implications on the precise estimation of satellite clock error, ionosphere error modeling and effective usage of the third frequency signal.

27.3 Data Processing Methodology

27.3.1 Carrier to Noise Ratio

Taking into account the fact that carrier to noise ratio is affected by the type of receivers and associated antennas, two or three types of receivers were selected. The carrier to noise ratio of QZSS L1 C/A, L1C, L1-SAIF, L2C, L5, LEX were

compared with other GNSS systems. The relationship between the carrier to noise ratio and the elevation was studied.

27.3.2 Noise and Multipath Characteristics

The noise and multipath characteristics can be computed as follows,

$$M(P_i, L_j, L_k) = P_i - L_j + (L_j - L_k) \cdot \frac{\lambda_i^2 + \lambda_j^2}{\lambda_i^2 - \lambda_k^2} + N + b \tag{27.1}$$

where P_i is pseudo-range observations of the ith frequency, L_i is carrier phase observations of the ith frequency, λ_i is the carrier wavelength, N is the ambiguity of carrier phase observations, and b is the delay caused by satellite and receiver hardware. When cycle slip does not occur, N can be treated as a constant, and eliminated by removing the mean value of the data. The hardware delay of satellites and receivers is relatively stable, and b can also be eliminated by removing the mean value.

In this paper, two or three types of receivers were selected. The noise and multipath characteristics of QZSS signals in different frequency were calculated using Eq. (27.1). The RMS value of noise and multipath characteristics were compared, and the relationship between the noise and multipath characteristic and elevation was investigated.

The absolute value of noise and multipath characteristics is hard to be obtained. In this paper, relative values of noise and multipath characteristics of different receivers and antennas are compared.

27.3.3 Inter-frequency Bias

At least signals of three different frequencies are broadcasted by current navigation system, e.g. GPS, Beidou, Galileo and QZSS. Two ionosphere-free (IF) combination can be used to eliminate the geometric distance, the main error ionosphere and troposphere, the residual error reflects the bias of pseudo-range and carrier phase between different carrier frequency (inter-frequency bias, IFB). The inter-frequency bias analysis requires a combination of three frequency observations. Two different ionosphere-free observations are used to eliminate the geometric distance, the main error of ionosphere and troposphere. The residual error reflects the bias of pseudo-range and carrier phase between different carrier frequency. The inter-frequency bias I can be computed as,

Table 27.1 Types of receivers and antennas

Station	Receivers	Antennas
GMSD	TRIMBLE R9	TRM59800.00
SIN1	TRIMBLE R9	LEIAR25.R3
CHOF	JAVAD TRE_G3TH	TRM57971.00
UNX2	JAVAD TRE_G3TH	LEIAR25.R3

$$I = f_1^2/\left(f_1^2 - f_2^2\right) \cdot L_1 - f_2^2/\left(f_1^2 - f_2^2\right) \cdot L_2 - f_1^2/\left(f_1^2 - f_5^2\right) \cdot L_1 + f_5^2/\left(f_1^2 - f_5^2\right) \cdot L_5 + N \tag{27.2}$$

For GPS and QZSS, the processing coefficients are given by

$$I = 0.285L_1 - 1.546L_2 + 1.261L_5 + N \tag{27.3}$$

$$I = 2.546L_1 - 13.801L_2 + 11.255L_5 + N \tag{27.4}$$

When the cycle slip does not happen, the ambiguity can be treated as a constant. The inter-frequency bias of different systems were calculated and compared. The impact of solar angle on the inter-frequency bias was also investigated.

27.3.4 Types of Receivers and Antennas

Different types of antenna and receiver are used in monitoring stations, which introduces difference of 2–3 dB to the measurement results [3]. The following table shows the type of antenna and receiver used in variety of monitoring station (Table 27.1).

27.4 Results and Analysis

27.4.1 Carrier to Noise Ratio

27.4.1.1 Comparison Between QZSS and GPS

The carrier to noise ratio of L1 C/A, L2C, L5 transmitted by QZSS with GPS BLOCK IIF satellites are shown in Fig. 27.1. The monitoring station is UNX2. From Fig. 27.1, we can see that the carrier to noise ratio of L5 signal is the largest. On the other hand, LEX signal has the smallest carrier to noise ratio. It can also be found that the C/N0 of QZSS signals (L1C, L2C, L5) is almost same with the C/N0 of corresponding GPS signals.

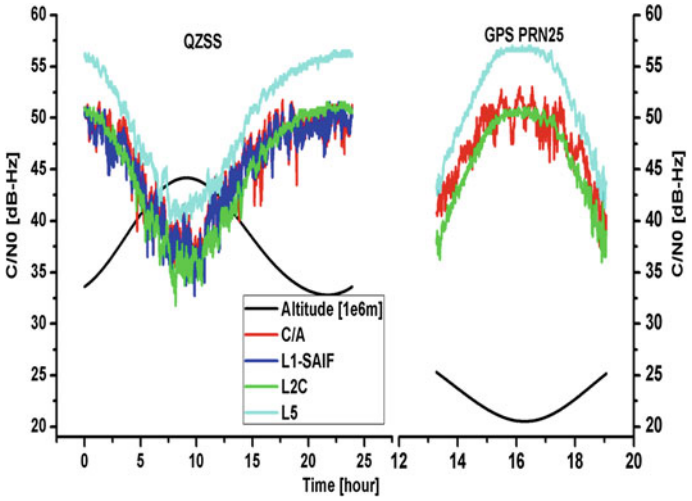

Fig. 27.1 C/N0 results of QZSS and GPS BLOCK IIF Satellites at station UNX2

Meanwhile, compared to the L1 and L2 signal, the energy of L5 signal is more concentrated in the high elevation angle direction. The C/N0 difference of L5 signal between the high elevation and the low elevation is larger than those of L1 and L2 signals, which due to the unique feeding network design of L5 signal [4].

27.4.1.2 Changes of C/N0 with the Elevation

Figure 27.2 shows the relationship between the carrier to noise ratio and elevation at station UNX2.

From the figure we can observe that the carrier-to-noise ratio was positively correlated with the elevation. When the elevation is 5°, the carrier to noise ratio is about 35 dBHz. The signal-to-noise ratio of L1 and L2 signals corresponding to the 90° elevation are about 50 dBHz. Meanwhile, the value of L5 signal was 55 dBHz. Throughout the observable range of elevation, the C/N0 dynamic range of L1 and L2 signal is 15 dB, and the C/N0 of L5 signal changes 20 dB.

At the same elevation, the difference of C/N0 between QZSS and GPS is about 2 dB. The difference is due to the orbital altitude. The orbital altitude of GPS is 20,200 km, and QZSS satellites fly at a highly elliptical orbit with height of 36,000 km [1].

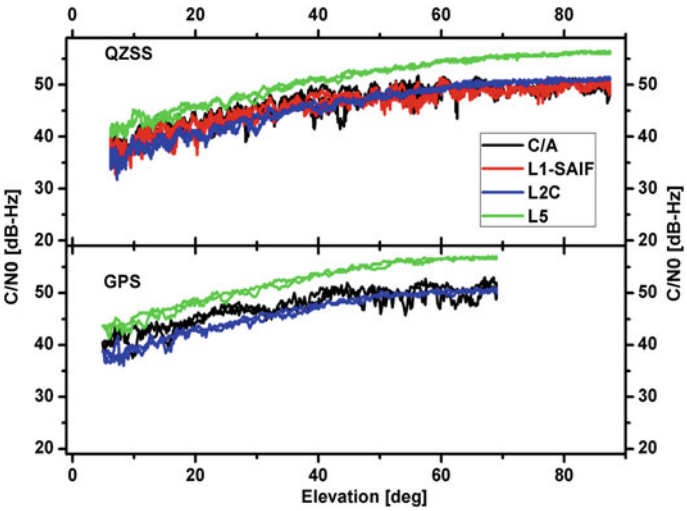

Fig. 27.2 Carrier to noise ratio of GPS BLOCK IIF and QZSS signal at station UNX2 QZSS

27.4.2 Noise and Multipath Characteristics

Figures 27.3 and 27.4 gives the noise and multipath characteristic of GPS and QZSS signals at station SIN1 and UNX2. From the curve, we can find the following phenomena.

Firstly, corresponding signal component of QZSS and GPS shows similar noise and multipath characteristics. The trend can be observed at different stations. The noise and multipath characteristic is mainly determined by the signal system (code rate, modulation, etc.). Since the signal systems of QZSS and GPS in L1, L2 and L5 are the same, noise and multipath characteristics show similar change trend.

Secondly, the observations of noise and multipath characteristics are related to the type of receivers.

In this section, the noise and multipath characteristics of L5 signal were calculated using the formula (27.5) and (27.6) respectively in order to assess the variation of hardware delays in L5 frequency. Equation (27.5) uses the L1 and L5 carrier phase observations to calculate ionosphere-free observations, and (27.6) uses the L1 and L2 carrier phase observations.

$$M(P_5, L_5, L_1) = P_5 + 3.521L_5 - 4.521L_1 \tag{27.5}$$

$$M(P_5, L_2, L_1) = P_5 + 4.318L_2 - 5.318L_1 \tag{27.6}$$

Figure 27.5 shows the noise and multipath characteristics of L5 signal for GPS and QZSS system calculated using (27.5) and (27.6). For GPS, the time series of noise and multipath calculated by (27.5) and (27.6) shows significant difference.

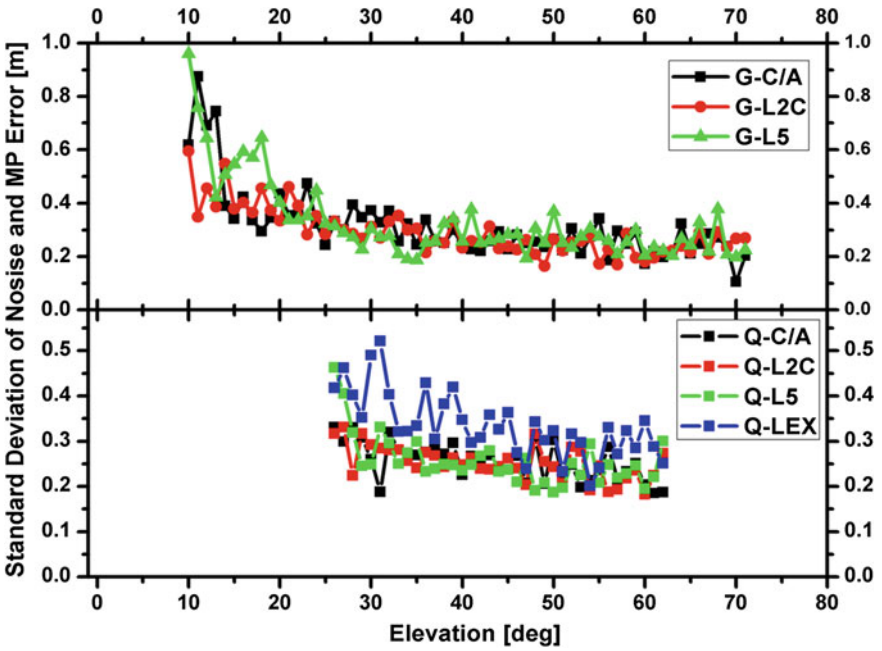

Fig. 27.3 Noise and multipath characteristics of GPS BLOCK IIF and QZSS signal at station SIN1

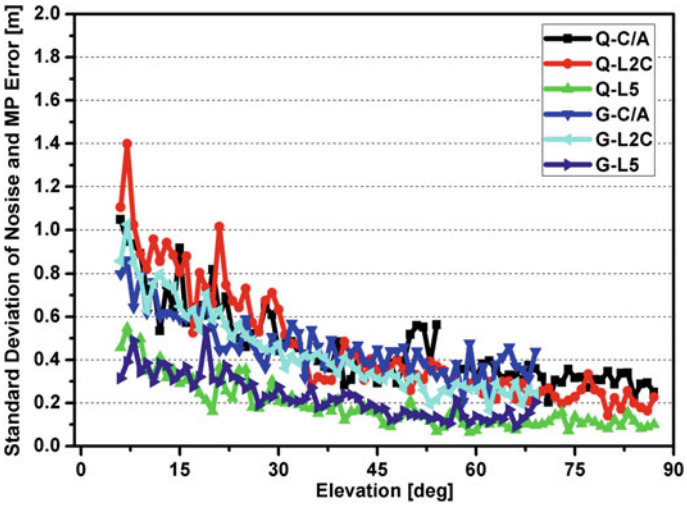

Fig. 27.4 Noise and multipath characteristics of GPS BLOCK IIF and QZSS signal at station UNX2

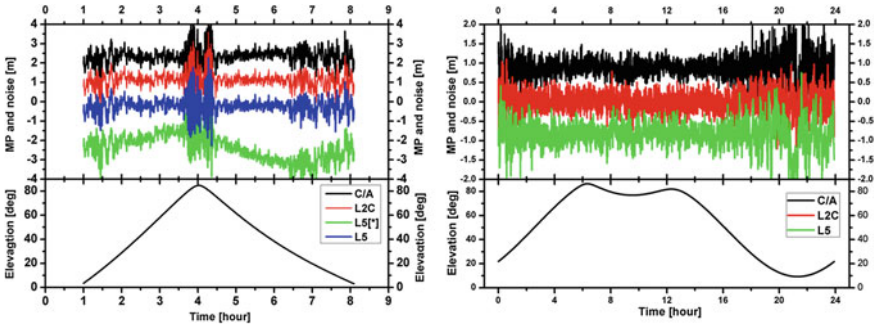

Fig. 27.5 Noise and multipath characteristics of GPS BLOCK IIF (*left*) and QZSS (*right*) signal calculated by two formulas

The reason is that the phase bias between the L5 signal and the other two frequencies (L1 and L2) is not constant in the time domain [5]. To get exact assessment of noise and multipath characteristics of L5 signal, the pseudo-range observation of L5 and carrier phase observation of L1 and L2 are suggested to be used. One the other side, the results of QZSS L5 signal are the same no matter which carrier phase observation is used.

27.4.3 Inter-frequency Bias

The IFB statistics of QZSS, Galileo and GPS signal were investigated in this section.

27.4.3.1 Carrier IFB Analysis of QZSS

Figure 27.6 shows the carrier IFB of QZSS J01 and Galileo E19 signals observed at two stations. It can be seen from the figure that the IFB of Galileo and QZSS signal is very stable in time domain and can be regarded as a constant.

The IFB of GPS BLOCK IIF satellites C01 is given in Fig. 27.7. The IFB embodies periodic variational regularity. The short term trend can be modeled and predicted by harmonic function [6].

27.4.3.2 Frequency Domain Analysis of QZSS IFB

In order to find out the impact of solar angle on the IFB and corresponding period, the time series of IFB were transformed to the frequency domain. The time series of

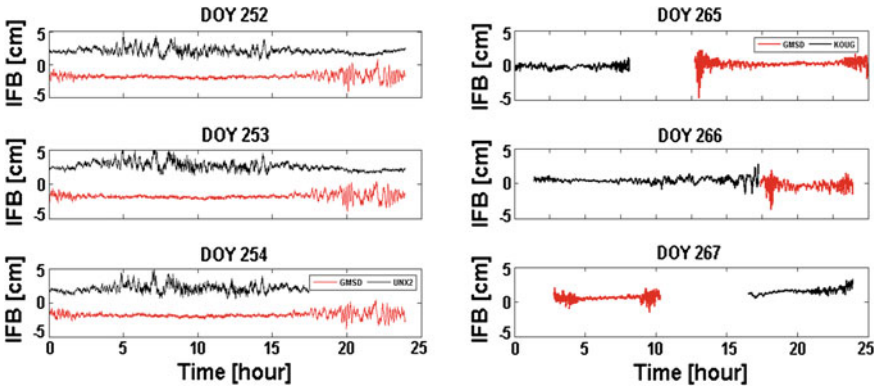

Fig. 27.6 The IFB time series of QZSS J01 (*left*) and QZSS E19 (*right*) at station GMSD and UNX2. For the Galileo E19 satellites, the E1, E5a and E5b signals were utilized to calculate the IFB

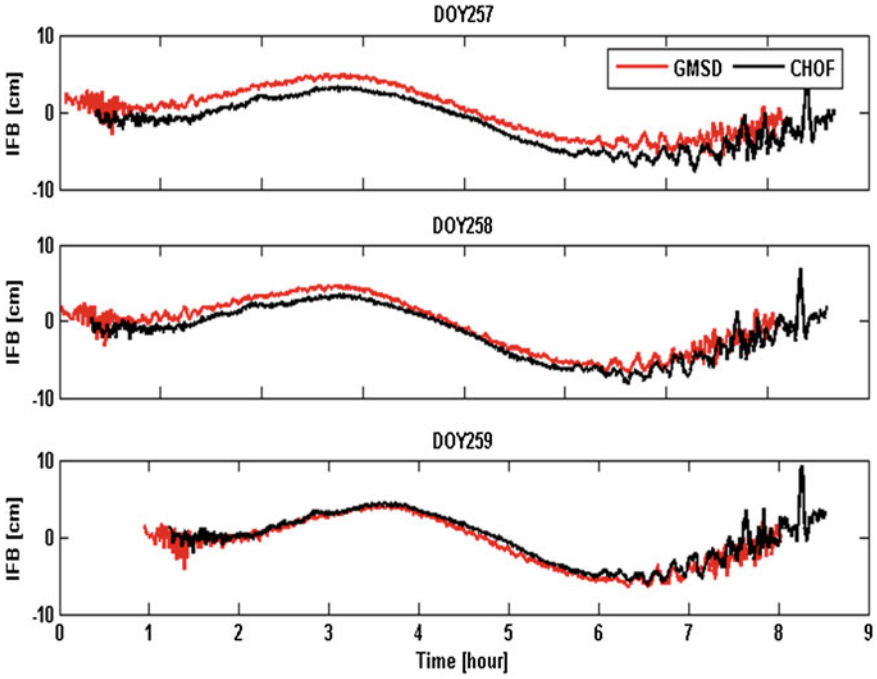

Fig. 27.7 The IFB time series of GPS G01 at station GMSD and CHOF. The observed data at station GMSD and CHOF were used

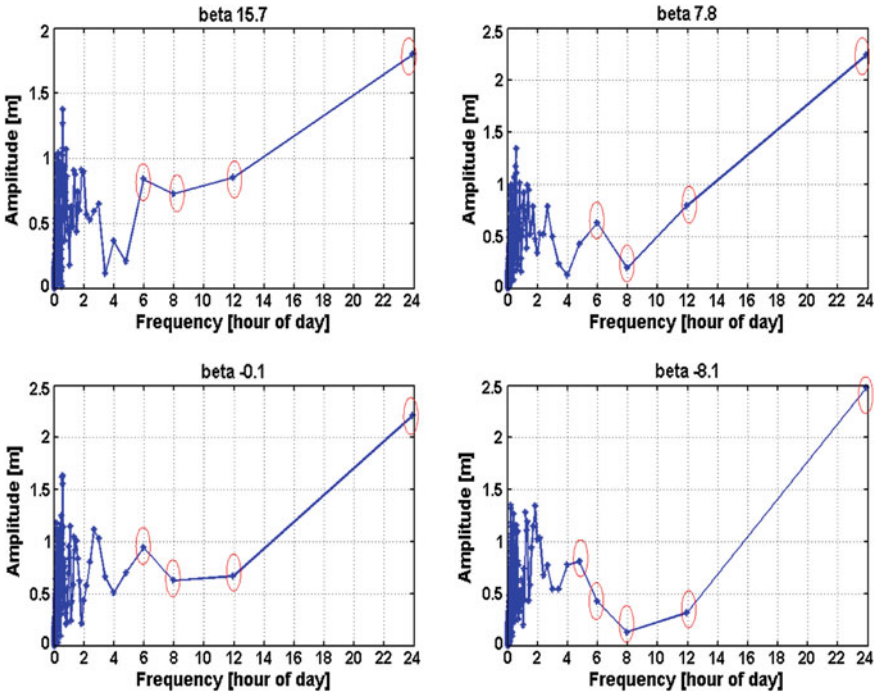

Fig. 27.8 Frequency domain analysis of IFB. From the *top left* corner to *lower right* corner, the solar angle is 15.7°, 7.8°, −0.1° and −8.7°, respectively

IFB corresponding to different solar angle were analyzed. From the curves of frequency domain analysis in Fig. 27.8, it can be seen that the IFB reflects a certain cycle characteristics and the changing period is 24, 12, 8, 6 h. The cause of this phenomenon may be due to the dynamic attitude control mode of satellites [1].

27.5 Conclusion

Based on the measured data of IGS, the signal characteristics of QZSS satellites, namely, carrier to noise ratio, noise and multipath characteristics and inter-frequency bias were studied. At the same time, the results were compared to those of other navigation systems, such as GPS and Galileo, to analyze the reason of the difference.

The carrier to noise ratio of L5 signal is the largest. On the other hand, LEX signal has the smallest carrier to noise. It can also be found that the C/N0 of QZSS signals (L1C, L2C, L5) is almost same with the C/N0 of corresponding GPS signals. Meanwhile, compared to the L1 and L2 signal, the energy of L5 signal is more concentrated in the high elevation angle direction. Corresponding signal

component of QZSS and GPS shows similar noise and multipath characteristics. The IFB of Galileo and QZSS signal is very stable in time domain and can be regarded as a constant, but the IFB of GPS embodies periodic variational regularity. From the frequency domain analysis, it can be seen that the IFB of QZSS reflects a certain cycle characteristics and the changing period is 24, 12, 8, 6 h, in which the 24-h period is the most remarkable.

Research methods and results given in this paper have importance reference values for the study and construction of satellite navigation systems.

References

1. Inaba N et al (2009) Design concept of quasi zenith satellite system. Acta Astronautica, Oct 2009
2. Wu F et al (2004) Performance evaluation of GPS augmentation using quasi-zenith satellite system. IEEE Trans Aero Electr 40(4):1249–1261
3. Montenbruck O et al (2011) Characterization of GPS/GIOVE sensor stations in the CONGO network. GPS Solut 15:193–205
4. Rho H, et al (2008) Evaluation of the new WAAS L5 signal. In: ION GNSS 2008
5. Montenbruck O et al (2010) Three's the challenge: a close look at GPS SVN62 triple-frequency signal combinations finds carrier-phase variations on the new L5, Aug 2010
6. Hauschild A et al (2012) Characterization of compass M-1 signals. GPS Solut 16:117–126

Chapter 28
Research on GPS Receiver Autonomous Integrity Monitoring Based on Auxiliary Particle Filter

Ershen Wang, Tao Pang, Pingping Qu and Yongming Yang

Abstract Utilizing the great advantages of the particle filter in processing nonlinear system with non-Gaussian noise, a new approach combining auxiliary particle filter (PF) with log-likelihood ratio (LLR) method is proposed for GPS receiver autonomous integrity monitoring (RAIM). Processing respectively all the measurements and partial measurements by particle filter algorithm, the fault satellite can be detected through establishing test statistics based on the log-likelihood ratio method. A theoretical analysis is implemented on the probability distribution of the log-likelihood ratio test statistic, and the detection threshold can be set according to the probability of false alarm. The satellite fault can be detected by comparing the system each epoch cumulative log-likelihood ratio with the detection threshold and can be isolated by the maximum likelihood criterion. Validated by the measured real data from GPS receiver are deliberately contaminated with the bias and ramp terms error, the results show that the proposed auxiliary PF accurately estimated the state of GPS receiver in the case of non-Gaussian measurement noise, successfully detected and isolated the faulty satellite by establishing log-likelihood ratio statistic for consistency test, verified the feasibility and effectiveness of applying the auxiliary PF in the GPS receiver autonomous integrity monitoring.

Keywords Global positioning system (GPS) · Receiver autonomous integrity monitoring (RAIM) · Auxiliary particle filter · Fault detection

E. Wang (✉)
School of Electronic and Information Engineering, Beihang University, Beijing, China
e-mail: wes2016@sau.edu.cn

E. Wang · T. Pang · P. Qu · Y. Yang
School of Electronic and Information Engineering, Shenyang Aerospace University, Shenyang, China

J. Sun et al. (eds.), *China Satellite Navigation Conference (CSNC) 2015 Proceedings: Volume II*, Lecture Notes in Electrical Engineering 341,
DOI 10.1007/978-3-662-46635-3_28

28.1 Introduction

With the development of the global navigation satellite system (GNSS) and the grows of user performance requirements for GNSS service, for safety-critical applications of global navigation satellite system (GNSS), such as aircraft and missile navigation systems, it is important to be able to detect and exclude faults that could cause risks to the accuracy and integrity, so that the navigation system can operate continuously without any degradation in performance. Because it needs a long time for satellite fault monitoring to alarm through the satellite navigation system itself, usually within 15 min to a few hours, that can't meet the demand of aircraft navigation. As a result, to monitor the satellite fault rapidly in the user segment, namely the receiver autonomous integrity monitoring (RAIM) has been researched a lot [1–3].

Currently, RAIM algorithms include two categories: one is to the snapshots algorithm using the current amount of pseudorange measurement, the other is the RAIM algorithm based on Kalman filter method. The snapshots algorithm does not need external supporting equipment, and it has the advantage of implement easily, and it has been widely used at present. This kind of algorithm mainly has parity space method, the sum of least squares of the error (SSE) method, and the largest interval method, etc. [4]. In recent years, fault diagnostic method based on Kalman filter has been widely used in nonlinear system fault diagnosis. And Kalman filter algorithm uses historical measurement to improve the performance of estimate. Moreover, this algorithm requires that the measurement noise obeys Gaussian distribution. However, in the actual measurement the noise is very difficult to strictly obey Gaussian distribution, the performance of the algorithm will downgrade much [5]. Because GNSS measurement error does not follow Gaussian distribution perfectly [6], the Kalman filter approach has to use an inaccurate error model that may cause performance degradation. Particle filter algorithm can better be suitable to any non-linear, non-Gaussian systems. And the algorithm has no any restrictions to the system process noise and measurement noise. The optimal state estimation can be easily gotten [7]. Therefore, compared to Kalman filter, the particle filter algorithm is more suitable for non-linear, non-Gaussian system fault detection, navigation and positioning applications [8, 9]. But basic particle filter algorithm exists the degeneracy phenomenon and alleviating the sample impoverishment problem [10].

This article describes the basic principles of particle filter algorithm for fault detection and establishes a model of receiver autonomous integrity monitoring. The likelihood function is established by cumulative state estimate, thus verify the feasibility and effectiveness of applying particle filter algorithm in the GPS receiver autonomous integrity monitoring.

28.2 Auxiliary Particle Filter for GPS RAIM

28.2.1 Basic Principle of Auxiliary Particle Filter for GPS RAIM

This paper used LLR method under particle filter to detect and isolate satellite fault, namely, through PF for generating the state estimates, calculating the LLR at each epoch, calculating the LLR among the window time to get the cumulative LLR, checking the consistency, then detected and isolated the satellite fault.

The system state equation can be expressed using a linear function:

$$X_k = F_{k-1}X_{k-1} + w_{k-1}$$

where, $X_k = [r_x, r_y, r_z, \Delta\delta]^T$, $\Delta\delta$ is the error of receiver time with respect to satellite time, F is the transfer matrix, which is characteristic matrix in the stationary state, w is the process noise.

The measurement equation can be expressed:

$$\rho^i(\mathrm{k}) = \mathrm{R}^i(\mathrm{k}) + \mathrm{c}\Delta\delta^i + T^i(\mathrm{k}) + \mathrm{E}^i(\mathrm{k}) + \varepsilon^i(\mathrm{k})$$

where, ρ^i is the pseudorange between receiver $(\mathrm{r}_x, \mathrm{r}_y, \mathrm{r}_z)$ and satellite $i(\mathrm{s}_x, \mathrm{s}_y, \mathrm{s}_z)$, c stands for light speed, $\Delta\delta$ is the time compensation, $T^i(\mathrm{k})$ is the troposphere error, $E^i(\mathrm{k})$ is the ephemeris error, $\varepsilon^i(\mathrm{k})$ is the code observation noise. And,

$$R^i = \sqrt{(\mathrm{r}_x - \mathrm{s}_x^i)^2 + (\mathrm{r}_x - \mathrm{s}_y^i)^2 + (\mathrm{r}_x - \mathrm{s}_z^i)^2}$$

It stands for the distance between the satellite i and the receiver.

The measurement selected as: coordinates of satellite $i(\mathrm{s}_x, \mathrm{s}_y, \mathrm{s}_z)$, pseudorange ρ^i, the compensation $\Delta\delta$ at each epoch, they all can be extracted from the measured data from the GPS receiver [11].

Assuming the current satellite number used for position, velocity and time (PVT) solution is $s = 6$, and one of them exists satellite fault. In order to detect and isolate satellite fault, we need $Q = s + 1$ PFs, one as the MAIN PF, remaining as auxiliary PFs. The MAIN PF calculates all satellites measurements to get system state estimation. Other s auxiliary PFs calculate the removal of the satellite measurements state estimation in turn for consistency check.

28.2.2 Test Statistics Establishment

The LLR test in this case is defined as comparison between probability density function (PDF) resulted by each auxiliary PF and the main PF as follows:

$$s^q(y) = \ln \frac{p^q(y)}{p^A(y)}$$

The cumulative LLR for the observations from y_j to y_k can be expressed as:

$$S_j^k(q) = \sum_{i=j}^{k} \ln \frac{p^q(y_i|Y_{i-1})}{p^A(y_i|Y_{i-1})}$$

Because the system state estimation is approximated as normalized weights in PF, so $p^q(y_i|Y_{i-1})$ and $p^A(y_i|Y_{i-1})$ can be expressed as:

$$p^q(y_i|Y_{i-1}) \approx \frac{1}{N} \sum_{m=1}^{N} \tilde{w}_i^q(m)$$

$$p^A(y_i|Y_{i-1}) \approx \frac{1}{N} \sum_{m=1}^{N} \tilde{w}_i^A(m)$$

Therefore, calculating the MAIN PF and auxiliary PFs normalized weights in every epoch, which is easy to do for PF algorithm. Accumulating LLR can be gotten for consistency test, thus the system detects whether there is a fault satellite.

Calculating each time accumulated LLR function and judging whether the system exist the fault according to the characteristic of the accumulated LLR function. The characteristic is that under normal circumstances the function curve is smooth with time. When the data fluctuates, it will produce a negative drift before the change and after the change produces a positive drift [12, 13].

Decision function for fault detection (FD) defined as the following equation:

$$\beta_k = \max_{k-U+1 \le j \le k} \max_{1 \le d \le D} S_j^k(d) > \tau$$

where U is a window size of the most recent past observations and τ is a threshold. The minimal window size $U_{\min}$ will depend on the level of disturbance W_k and measurement noise V_k in the system model and the fault size (i.e. the amplitude of the parameter change) to be detected. A high level of disturbance and noise and a small fault size to be detected will require a large window size W. The threshold $\tau > 0$ should be chosen large enough to avoid false alarm subject to minimizing the time delay for fault detection. The threshold will, again, depend on the level of disturbance W_k and noise V_k in the system. Since the use of sliding window is to avoid the linearly growing computation in the maximization of LLRs $S_j^k(q)$ over the time before the onset of a fault, in practice, the window size can be chosen large enough subject to the computational requirement. Then, for a given system the threshold can be determined through the required false alarm probability of the real system. Below we give the theoretical basis for calculating likelihood ratio test detection threshold.

28.2.3 Decision Threshold Computation

Simple null hypothesis $H_0 : \theta = \theta_0$ to alternative hypothesis $H_1 : \theta \neq \theta_0$, the likelihood ratio test statistic is:

$$\lambda(\mathrm{X}) = \frac{\prod_{i=1}^{n} p(X_i; \hat{\theta})}{\prod_{i=1}^{n} p(X_i; \theta_0)}$$

When the null hypothesis is established, the log likelihood ratio statistic $2 \ln \lambda(\mathrm{X})$ converges to $\chi^2(\mathrm{k})$ with n increasing. It can be seen that the log likelihood ratio test statistic $s^q(y)$ obey the chi-square distribution and cumulative log likelihood ratio test statistic $S_j^k(q)$ also obey the chi-square distribution.

When the GPS monitoring system is working properly and no pseudorange failure, then faulty alarm is false alarm. For given P_{FA} (probability of false alarm) as follow:

$$P_{FA} = (1 - P(\chi^2|r))(\tau|n-4)$$

The probability formula derivation:

$$P_r(\lambda(\mathrm{X}) < \tau^2) = \int_0^{\tau^2} f\chi^2_{(n-4)}(x)dx = 1 - P_{FA}$$

For given probability of false alarm, the detection threshold $\tau \sim \chi^2_{1-P_{FA}}(\mathrm{n}-4)$ can be determined by above the mentioned formula. If the decision function exceeds the threshold, that is $\beta_k > \tau$, it means that the fault has been occurred and alarm will be issued. When there is a satellite failure, comparing the test statistic with the detection threshold τ, it is undetected when $\beta_k < \tau$.

For missed detection probability P_{MD}, $P_{MD} = P(\tau/(n-4), \lambda)$

Should meet the following probability formula,

$$P_r(\lambda(\mathrm{X}) < \tau^2) = \int_0^{\tau^2} f\chi^2_{(n-4,\lambda)}(x)dx = P_{MD}$$

If the decision function exceeds the threshold τ, that is $\beta_k > \tau$. It means that a fault has been occurred and alarm will be issued. The fault isolation is then achieved by determining the index g of the faulty subset of measurements which is given by:

$$g = \arg \max_{1 \le d \le D} S_{t_a}^{k} \ (k > t_a)$$

where, g is the fault satellite number, t_a is alarm time.

28.3 Simulation Test and Results Analysis

The experimental raw measurement data are obtained by GPS receiver N220 (positioning accuracy is 2.5 m (1δ)), the measurement data including the satellite receiver position information and pseudorange parameters. The static measurement data set is 418 s. During the period of this experiment, there are 6 satellites used for PVT solution, the number of the satellite is 3, 15, 18, 19, 21, 26 respectively, and the corresponding pseudorange parameters can be expressed as $Y = (y_1, y_2, y_3, y_4, y_5, y_6)$. At the same time, the RCB-4H receiver from the u-blox monitors that the satellite is working normally. In the experiment, the number of particle is N = 100, the calculated decision function of window length is selected as 30, the experimental data measurement noise obeys Gaussian kernel Laplace distribution [6].

To demonstrate fault detection and isolation (FDI) performance, errors are intentionally inserted into the nominal GPS data measured. To illustrate FDI performance of the proposed method, two fault types are considered, i.e., bias error and ramp error. In the simulation, the pseudorange measurements of satellite 19 are contaminated, without loss of generality, by adding constant bias errors or time-varying ramp errors at time instant k = 200. Figures 28.1 and 28.2 show the results of applying the proposed FDI when the artificial failure occurred in the bias error form.

In Fig. 28.1a, bias errors are applied at epoch 200 with four different error magnitudes which are 100,150, 200 and 250 m. Figure 28.1b shows that the decision function is kept around 7 prior to the occurrence of a fault, but jumps over 10 significantly after the onset of the fault. Using the value of decision function and threshold τ set to 10, results show that the bias error larger than 150 m can be explicitly detected. Figure 28.1b also shows that the maximum of decision function curve 150 m max, 200 m max, 250 m max are all over the value of detection thresholds, achieves the purpose of fault detection. On the other hand, fault occurrence with another bias error less than 100 m is hardly detected because Fig. 28.1b shows the 100 m max below the threshold to distinguish the fault from the ordinary case cannot be obtained.

Accordingly, in Fig. 28.2, FI is conducted by checking each cumulative LLR when a fault is detected. By plotting cumulative LLR for each auxiliary PFs, the auxiliary PF that is free from the pseudorange contamination of bias error is determined numerically. Figure 28.2a shows the bias error of 100 m cannot be isolated, while Fig. 28.2b shows the bias error of 150 m can be isolated at 269 epoch, Fig. 28.2c shows the bias error of 200 m can be isolated at 228 epoch, Fig. 28.2d shows the bias error of 250 m can be isolated at 212 epoch.

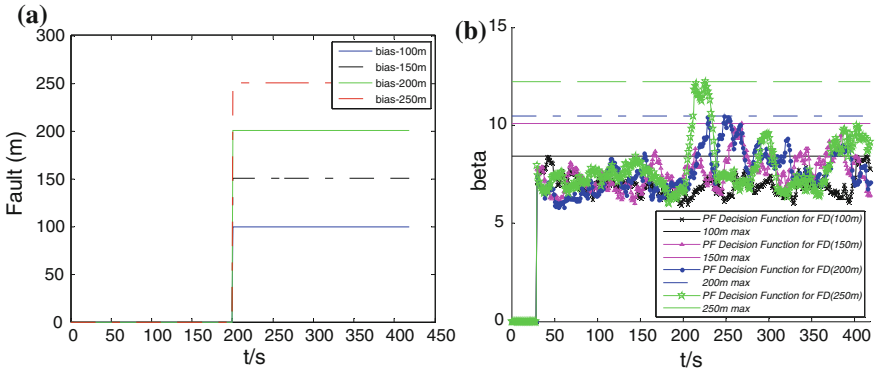

Fig. 28.1 **a** Applied error signal having bias fault. **b** Decision function for FD

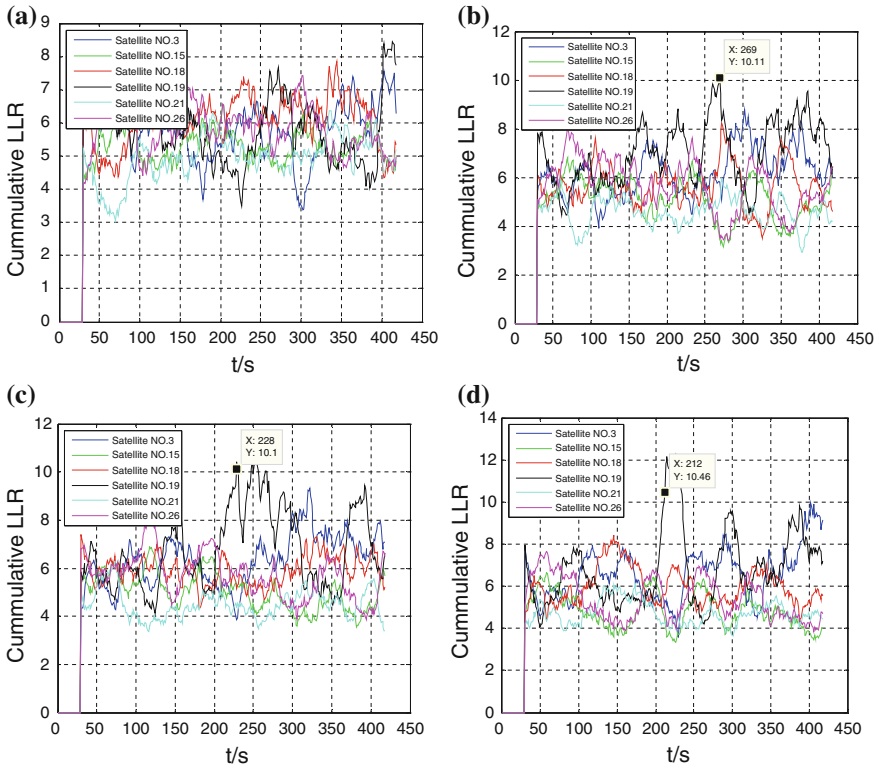

Fig. 28.2 **a** 100 m bias case. **b** 150 m bias case. **c** 200 m bias case. **d** 250 m bias case

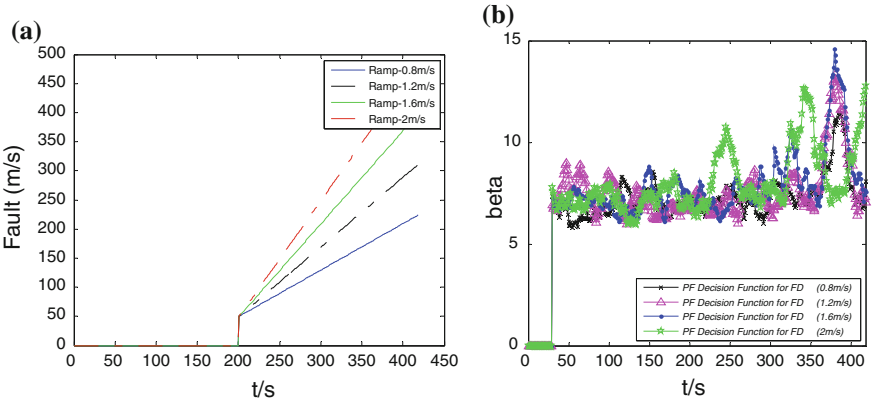

Fig. 28.3 **a** Applied error signal having ramp fault. **b** Decision function for FD

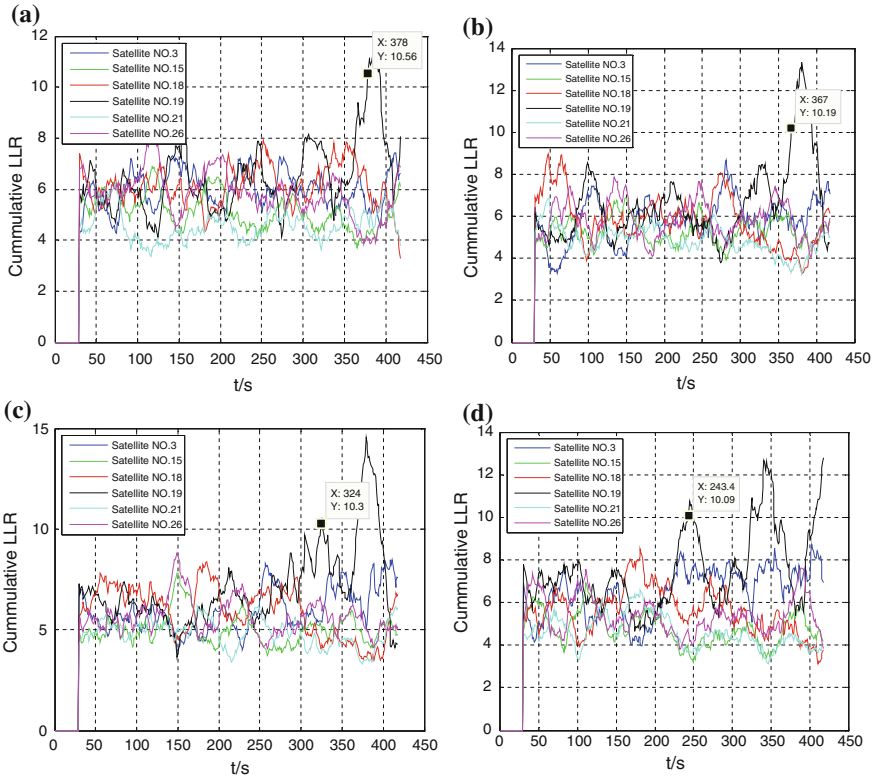

Fig. 28.4 **a** 0.8 m/s gradient fault. **b** 1.2 m/s gradient fault. **c** 1.6 m/s gradient fault. **d** 2 m/s gradient fault

Above results showed that the proposed FDI method provides limited performance on FI in the bias error case. Figures 28.3 and 28.4 show the results of the proposed FDI when the failure occurs in the ramp error form.

Similar to the bias error case illustrated in Fig. 28.3a, ramp errors start at 200 epoch with four different gradient values, 0.8, 1.2, 1.6 and 2 m/s, respectively. As seen in Fig. 28.3b, the decision function grows significantly according to the fault occurrence, and thus anomalies are detected by setting the threshold of decision function to 10. Meanwhile, 2 m/s ramp error changes faster than 1.6 m/s ramp error and the rate of decision function for 1.6, 1.2 and 0.8 m/s ramp errors slow increase in turn.

Accordingly, in Fig. 28.4, FI is conducted by checking each cumulative LLR graph when a fault is detected. By plotting cumulative LLR for each auxiliary PFs, the auxiliary PF that is free from the pseudorange contamination of ramp error is determined numerically. Figure 28.4a shows the 0.8 m/s gradient ramp error can be isolated at 378 epoch, Fig. 28.4b shows the 1.2 m/s gradient ramp error can be isolated at 367 epoch, and Fig. 28.4c shows the 1.6 m/s gradient ramp error can be isolated at 324 epoch and Fig. 28.4d shows the 2 m/s gradient ramp error can be isolated at 243 epoch.

28.4 Conclusions

This paper proposes a new FDI method in GPS integrity monitoring by using the particle filter and likelihood ratio test of the main and auxiliary particle filter structure. The proposed method makes it possible to detect ramp fault in partial measurements, such as the pseudorange that comes from the GPS satellite measurement. The likelihood function is established. Furthermore, the LLR test is used in fault detection, which compares the consistency of the measurement between the main PF and auxiliary PFs. The evaluation of FDI is conducted through simulation using the real GPS measurement data collected from the receiver. The measured data from GPS are deliberately contaminated with two different error types, the bias and ramp terms. Based on the simulation result, the proposed approach successfully demonstrated that it can detect the GPS measurement fault under non-Gaussian measurement noise environment, particularly in showing its performance when error is gradually increasing. The auxiliary PFs algorithm can improves the accuracy of state estimation. The results demonstrated that the auxiliary PFs algorithm is feasible and effective for GPS receiver autonomous integrity monitoring (RAIM).

Acknowledgments This study is funded by the National Basic Research Program of China (973 Program) (2010CB731805), the National Natural Science Foundation of China (61101161), and the Joint Funds of the Natural Science Foundation of Liaoning Province (2013024003).

References

1. Xu XH, Yang CS (2013) Review and prospect of GNSS receiver autonomous integrity monitoring. J Acta Aeronautica et Astronautica Sinica 34(3):451–463 (in Chinese)
2. Yun Y, Kim D (2007) Integrity monitoring algorithms using filtering approaches for higher navigation performance: consideration of the non-gaussian GNSS measurements. In: Proceedings of ION GNSS 20th international technical meeting of the satellite division, Fort Worth, TX, pp 3070–3071
3. Ishak M, Mohd A, Mahamod I (2009) Availability, reliability and accuracy of GPS signal in Bandar Baru Bangi for the determination of vehicle position and speed. In: Proceeding of the 2009 international conference on space science and communication, Port Dickson, Negeri Sembilan, Malaysia, pp 224–229
4. Sun GL, Sun MH, Chen JP (2006) A study on time and set combined method for receiver integrity autonomous monitoring. J Acta Aeronautica et Astronautica Sinica 27(6):1171–1175 (in Chinese)
5. Mathieu J, Boris P (2011) Integrity risk of Kalman filter-based RAIM. In: Proceedings of the 24th international technical meeting of the satellite division of the Institute of Navigation, ION, USA, pp 3856–3867
6. Sayim B, Pervan S, Pullen P (2002) Experimental and theoretical results on the LAAS sigma overbound. In: Proceedings of the ION GPS, Portland, Oregon, pp 29–38
7. Gordon NJ, Salmond DJ et al (1993) Novel approach to nonlinear/non-Gaussian Bayesian state estimation. IEEE Proc F Radar Signal Process 140(2):107–113
8. Vaswani N (2004) Bound on errors in particle filtering with incorrect model assumptions and its implication for change detection. In: Proceedings of IEEE international conference on acoustics, speech and signal processing, Montreal, Quebec, Canada, vol II, pp 729–732
9. Fredrik G (2002) Particle filters for positioning, navigation, and tracking. IEEE Trans Signal Process 50(2):425–437
10. Arulampalam M, Maskell S, Gordon N et al (2002) A tutorial on particle filters for online nonlinear/non-Gaussian Bayesian tracking. J IEEE Trans Signal Process 50(2):174–188
11. Kaplan E, Hegarty C (2006) Understanding GPS: principles and application, 2nd edn. Artech House, Norwood, pp 258–263
12. Li P, Kadirkamanathan V (2001) Particle filtering based likelihood ratio approach to fault diagnosis in nonlinear stochastic systems. J IEEE Trans Syst Man Cybern C 31(3):337–343
13. Rosihan A, Sebum C et al (2007) Particle filtering approach to fault detection and isolation for GPS integrity monitoring. In: Proceedings of ION GNSS 19th international technical meeting of the satellite division, Fort Worth, TX, pp 873–881

Chapter 29
Ranging Bias of COMPASS Satellite Signals

Jiancheng Liu, Jianjun Fan, Xiaochao Feng and Huaisheng Sang

Abstract Quantitative evaluation of signal quality of navigation satellites in orbit is one of the difficulties in satellite navigation signal quality monitoring research, so a quantitative evaluation method based on theoretic ranging bias is proposed. Based on Vernier sampling principle and a large diameter parabolic antenna is used for in-orbit satellite signal collection, and a clear waveform of code epoch is achieved after data processing. Based on the clear waveform, it's starting point is estimated, and leading signal and delay signal are produced, then the E-L discriminator curve is got, finally zero crossing bias is achieved, which is the ranging bias of the signal. A large diameter parabolic antenna is used for COMPASS satellite tracking, and signal collection and data processing is made, then theoretic ranging bias of I channel at B1 band of several COMPASS satellites are obtained, so the estimation method is verified.

Keywords Signal quality monitoring · Quantitative evaluation · Discriminator · Ranging bias · COMPASS

29.1 Introduction

The failure of in-orbit satellite navigation signal transmission channel will cause the signal waveform distortion, and for a healthy satellite in orbit there is a slight distortion of the signal waveform, but the signal waveform distortion will affect the receiver signal acquisition and tracking, thus reduce ranging accuracy [1–3], so quantitative monitoring of small signal distortion that may occur is needed and the assessment indicators should be directly related to the ranging performance.

In [4], estimation method of leading and lag parameters are studied on the basis of a clear pulse waveform, and the leading and lag parameters of GPS satellites in orbit

J. Liu (✉) · J. Fan · X. Feng · H. Sang
Beijing Satellite Navigation Center, Beijing 100094, China
e-mail: ljc-mymail@163.com

J. Sun et al. (eds.), *China Satellite Navigation Conference (CSNC) 2015 Proceedings: Volume II*, Lecture Notes in Electrical Engineering 341,
DOI 10.1007/978-3-662-46635-3_29

are obtain, then TMB models of different parameters and real measured waveforms are compared, but did not make a quantitative assessment methods. In [5], for real measured waveforms, several parameters as peak arrival time, rise time, fall time, stability transcend time and peak ratios are defined, and quantitative assessment of GPS signal pulse waveform is realized, but not directly related to the ranging performance. In [6, 7], for differential user receivers applied in augmentation system, the relative ranging deviation is proposed to assess the ranging performance of differential receivers, but not directly assess the satellites broadcast signals.

This paper presents a estimation method of ranging bias caused by satellite signal distortion on the basis of clear signal waveform, and the ranging bias of I channel at B1 band for COMPASS satellites. Firstly, based on Vernier sampling theory and the cumulative averaging, clear waveform of one code epoch is achieved after data processing, and the starting point of the clear waveform is estimated, so its leading signal and delay signal are produced, then the E-L discriminator curve is got, finally zero crossing bias is achieved, which is the ranging bias of the distorted signal.

29.2 Acquisition Method of Clear Satellite Signal Waveform

In order to make the received satellite signals involve the characteristics as possible when satellite broadcast it, some measures are adopted:

(1) Large-diameter parabolic antenna is used for received signal amplification and signal selection in space to reduce the impact of multipath and interference.
(2) Band-pass filter is used for frequency selection, and the filter bandwidth is match to satellite transmit signal bandwidth in order to reduce noise.
(3) Signal collection is done when Doppler radial velocity is zero in order to reduce the Impact of the radial motion on pulse width.
(4) Cumulative averaging is done by several code epochs to further reduce noise.

For high code rate but common data collection instrument, a process of data collection and data processing based on Vernier sampling is adopted. n sets of periodic data can combine one set, so the data rate increase n times. According to Vernier sampling principle, sampling rate of collecting device is calculated as:

$$f_s = \frac{n \cdot M - 1}{n \cdot T_r} \tag{29.1}$$

where $M = \lfloor T_r \cdot f_{\max} \rfloor$ is sampling points of one code epoch, and T_r is code epoch.

Data processing process is following:

(1) Eliminates the initial phase and frequency

In order to eliminate the initial phase and frequency of the data, adjusting frequency and initial phase, Reverse phase modulation processing is done by the collected

data, and check the real part and imaginary part of the resulting data whether show pulse shape, and pulse width is multiple pulse width which is determined by PRN code rate. Adjusting frequency and initial phase until satisfy that condition, and the real part is in-phase data.

(2) Discard non-integer code epoch part of the collected data

The collected data is down-sampled according to the code rate, and valued as 1 to −1 according to its symbol. PRN code sequence is generated according to the generator polynomial and initial state, and Check the position of PN sequence in collected data, then discard non-integer code epoch part of the collected data.

(3) Multiple epochs collected data accumulating

For multiple epoch collected data accumulating, information code of the collected data for accumulating must be the same. According to the relationship between the polarity of the data sequence and the polarity of the PN sequence the information code (maybe secondary code is included) is determined on M points cycle. The collected data with same information code accumulates on $n \cdot M - 1$ points cycle, then two new data sets are formed as $S_{21}(k)$ and $S_{22}(k)$. $S_{21}(k)$ is formed when information code is 1, and $S_{22}(k)$ is formed when information code is −1. The data length of the two data sets is both $n \cdot M - 1$, but with opposite sign.

(4) Data combination

According to Vernier sampling principle, $S_{21}(k)$ and $S_{22}(k)$ are changed as $S_{31}(k)$ and $S_{32}(k)$ after combination, and The data length is not changed but data sampling interval reduce n times, i.e.

$$T_{sd} = \frac{T_r}{n \cdot M - 1} \tag{29.2}$$

where T_r is code epoch.

After data processing, a clear signal waveform of one code epoch is got, which provides the basis for evaluation of the ranging performance of the signal, at the same time can view the details of any one chip.

29.3 Ranging Bias Estimation Method

To produce discriminator curve, the location of the first sampling point of local PN code in code epoch must be consistent with the first sampling point of received signal, but the first sampling point of the received signal is not real starting point of the pulse waveform, so the starting position of $S_{31}(k)$ and $S_{32}(k)$ should be determined, that is to estimate the distance between the first sampling data and the real zero cross point of the first pulse. Processing method of $S_{31}(k)$ and $S_{32}(k)$ is

same, and the mean of their ranging bias can be treated as the ranging bias of the received signal. The following take $S_{31}(k)$ as an example to illustrate the processing method.

29.3.1 Starting Position Estimation of the Pulse Waveform

Because the module of distance between first data point and different rising edges is equal, estimation method of distance between first data point and starting point of code epoch is proposed, including 4 steps:

(1) Firstly, all zero crossing positions of one code epoch are determined roughly according to the sign change of sampling data.
(2) Linear fitting is done when rough zero crossing positions are taken as the center to get exact zero crossing positions.
(3) Calculation the distance between different rising edges and the first data point, and modulus of chip width, then calculation the distance between the first data point of different rising edges and starting point of code epoch.
(4) The mean of the distance for different rising edges is the starting position estimation of the collected data.

29.3.2 Ranging Bias Estimation

DLL (Delay Lock Loop) of navigation receiver tracks the zero crossing point of discriminator curve as possible, which makes code tracking error near to zero. For normal signal, if the DLL reaches to steady-state, the code tracking bias is zero when discriminator output is zeros. But for distorted signal, the discriminator curve changes, and its zero crossing deviates from where code tracking bias is zero. The bias is just the ranging bias caused by the distorted signal, i.e.

$$\Delta R = \arg_{\hat{\tau}_0 - \tau_0}\{D_s = 0\} \tag{29.3}$$

where D_s is the discriminator output.

In order to obtain the ranging bias, the process includes:

(1) According to the waveform starting position, generation of local leading signal and the local delay signal.
(2) Respectively correlation with received signal, and the difference is the discriminator output.
(3) Linear fitting of the discriminator output to get precise zero crossing point position.
(4) Calculate the range between zero crossing point and center of discriminator output, which is the ranging bias.

29.4 Ranging Bias of COMPASS Signals at B1 Band

In the paper a large diameter parabolic antenna is adopted to receive COMPASS satellite signals at B1 band. The data is collected in intermediate frequency by Agilent E4445A with function of vector signal analysis. Its maximum analysis bandwidth is 80 MHz, let n = 20, and the sample rate is calculated as 102.25908 MHz. The collection length is 0.5 s. The data storage data type is mat, and the file size is about 400 MB.

29.4.1 Processing of Collected Data

The processing process of collected COMPASS satellite signals includes eliminates the initial phase and frequency, discard non-integer code epoch part of the collected data, Multiple period collected data accumulating, data combination, starting position estimation of the pulse waveform, generation of local leading signal and local delay signal,discriminator output, linear fitting and so on.

The following is an example as No. 1 of COMPASS satellites to describe processing results of collected data.

(1) Clear signal waveform for one code epoch

Read collected data of COMPASS No. 1 satellite signal at B1 band. Let initial phase is 2.0208 rad, residual frequency is 0.25 Hz, and after elimination of initial phase and residual frequency, Discard the previous data on 135 samples and 511 yards chip to form a new data set. For the new data set of 10 code epochs, The collected data with same information code averages, then two new data sets are formed as $S_{21}(k)$ and $S_{22}(k)$. $S_{21}(k)$ is formed when information code is 1, The front part of the data sequence shown in Fig. 29.1. As can been seen, accumulating and combination processing can get the clear signal waveform.

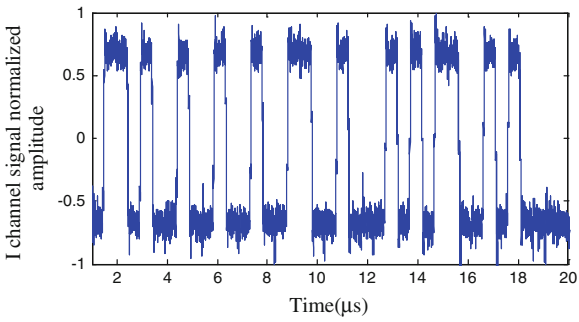

Fig. 29.1 Signal waveform segment

(2) TMA lag parameters estimation results

As can been seen in Fig. 29.1, for COMPASS No. 1 satellite, there is a positive pulse between second zero-crossing point and third zero-crossing point, and there is a negative pulse between first zero-crossing point and second zero-crossing point. Theoretically the pulse width are a multiple of chip width. After rough determining a zero crossing point, linear fit to obtain precise zero-cross point, then the positive pulse width bias and the negative pulse width bias are statistical determined. The positive pulse width bias of COMPASS No. 1 satellite is shown in Fig. 29.2, its mean is 2.0329 ns, approximately 2.0 ns, that is the falling edge of a positive pulse lags 2.0 ns. The negative pulse width bias of COMPASS No. 1 satellite is shown in Fig. 29.3, its mean is −1.9593 ns, approximately 2.0 ns. Because the falling edge of a positive pulse lags 2.0 ns, the negative pulse width should be reduced 2 ns, which is consistent with the results in Fig. 29.3.

According to TMA model, lag or leading of falling edge of chips is a model of digital circuit fault, so I channel signal at B1 Band of COMPASS No. 1 satellite lags 2.0 ns for digital circuit fault, which cause 1.0 ns in ranging bias.

According to [4], the TMA parameter of GPS satellites ranges from 0.2 to 4.5 ns, and the TMA parameter of COMPASS No. 1 satellite is in the range.

As can been seen in Fig. 29.1, for COMPASS No. 1 satellite, adjacent rising edge width is the distance between second zero-crossing point and fourth zero-crossing

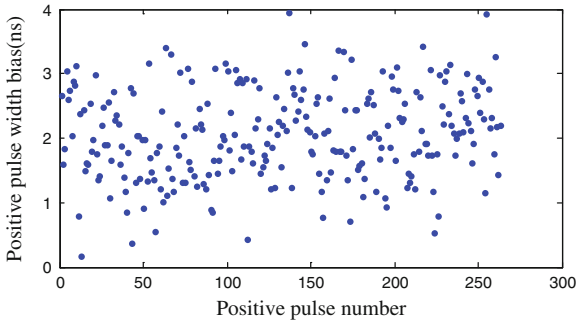

Fig. 29.2 Positive pulse width bias

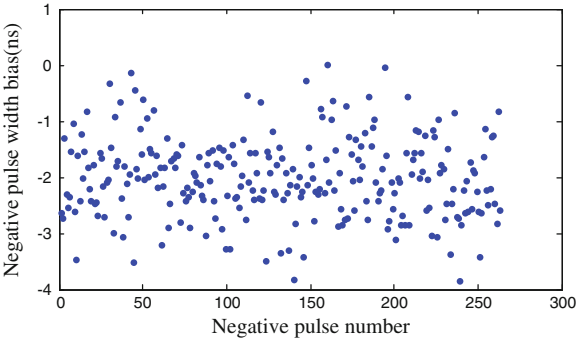

Fig. 29.3 Negative pulse width bias

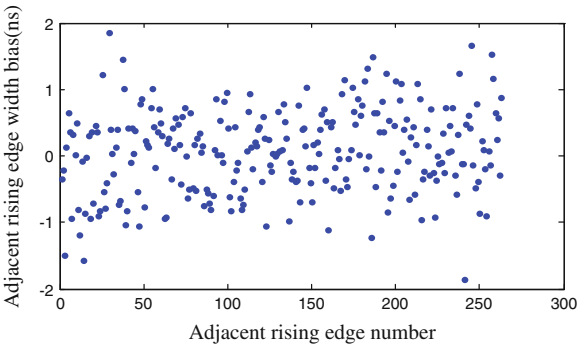

Fig. 29.4 Adjacent rising edge width bias

point, and adjacent falling edge width is the distance between first zero-crossing point and third zero-crossing point. Theoretically the width is a multiple of chip width. adjacent rising edge width bias and adjacent falling edge width bias are show in Figs. 29.4 and 29.5 respectively. As can been seen, the adjacent rising edge width bias and the adjacent falling edge width bias are both in the vicinity zeros. Statistical processing can obtain the mean respectively 0.0735 and 0.0566 ns, which can be approximated as 0, and the results are consistent with theory.

(3) Ranging bias estimation results

For data set $S_{21}(k)$, the starting position is 1.0665 ns. Let $T_d = 0.5T_c$, generation of local leading signal and the local delay signal, Respectively correlation with received signal, so the discriminator output is the difference of them, which is shown in Fig. 29.6. As can been seen, When the discriminator output error is zero, code tracking error is not zero. After linear fitting In the vicinity of zero-crossing point of the discriminator output, the ranging bias is 4.4175 ns.

For same parameters, the ranging bias of data set $S_{22}(k)$ is 4.4259 ns, then the mean of them is 4.4217 ns, so the ranging bias of I channel signal at B1 Band of COMPASS No. 1 satellite is 4.4217 ns.

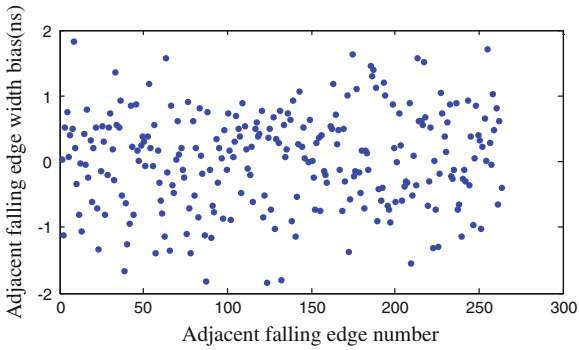

Fig. 29.5 Adjacent falling edge width bias

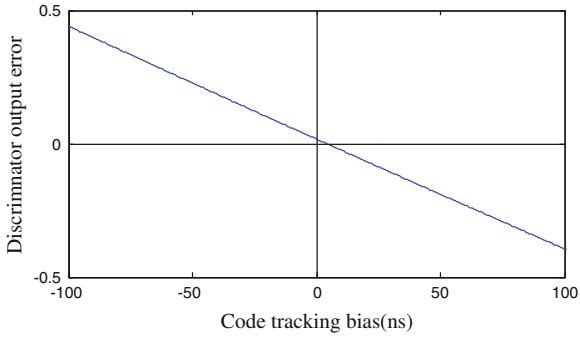

Fig. 29.6 Discriminator curve

29.4.2 Effect of Different Segments of Collecting Data on Ranging Bias Estimation

For above 10 PN code cycles of 20M − 1 length data, duration is about 0.2 s. Because total data duration is 0.5 s, Here for the second half of the collected data is processed. Select the initial phase is 2.0008 rad, residual frequency is 0.25 Hz. Other parameters is the same. According to $S_{21}(k)$ and $S_{22}(k)$, the estimated ranging bias are 4.4551 and 4.4022 ns, averaged for 4.4286 ns, which is approximately consistent with the results of the first half of the data. This indicates that ranging bias estimates for different data segment is consistent.

29.4.3 Ranging Bias Comparison of Multiple Satellites

Data collecting and data processing of I channel at B1 band of multiple COMPASS satellites have done, and the ranging bias of the tiny distorted signal are obtained in Table 29.1. As can be seen:

Table 29.1 Ranging bias of I channel at B1 band of COMPASS satellites

Correlator spacing	Satellite no.						
	No. 1	No. 2	No. 3	No. 4	No. 6	No. 7	No. 9
0.1Tc	4.3	3.1	4.6	3.6	3.2	3.3	3.6
0.2Tc	5.2	4.2	5.6	4.2	4.0	4.2	4.6
0.3Tc	5.5	5.2	5.8	4.0	4.6	4.9	5.4
0.4Tc	4.8	4.6	5.1	3.2	3.8	4.1	4.8
0.5Tc	4.4	4.2	4.7	2.8	3.4	3.7	4.6
0.6Tc	4.6	4.5	5.0	3.1	3.7	4.0	4.9
0.7Tc	5.1	5.1	5.6	3.8	4.3	4.6	5.5
0.8Tc	5.5	4.9	6.0	4.4	4.5	4.6	5.5
0.9Tc	5.7	4.9	6.2	4.8	4.6	4.8	5.6

(1) there is lag ranging bias for I channel at B1 band of COMPASS satellites
(2) There are different ranging bias for different satellites. When correlator spacing is 0.5Tc, the maximum lag bias is 4.7 ns, and the minimum lag bias 2.8 ns, so there is a difference of 1.9 ns.
(3) Different correlator spacing for same satellite, there are also different ranging bias. When correlator spacing is from 0.1Tc to 0.9Tc, Ranging bias of No. 9 satellite changes maximum. The minimum ranging bias is 3.6 ns, the maximum ranging bias is 5.6 ns, and there is a difference of 2.0 ns.

29.5 Conclusion

Quantitative evaluation of signal quality of navigation satellites in orbit is studied in the paper. A estimation method of ranging bias is proposed. After collecting and data processing of I channel at B1 band of multiple COMPASS satellites, the ranging bias of the tiny distorted signal are obtained. Data analysis showed that, there is lag ranging bias for I channel at B1 band of COMPASS satellites, There are different ranging bias of different satellites. Because ranging bias of different satellites will cause positioning errors, In the case of a known ranging bias, they can be compensated when positioning. Further study is comparing positioning error before and after compensation using known coordinates of the receiver to test the ranging bias.

References

1. Lu X, Zhou H (2010) Study on analysis method of GNSS space signal quality. SCIENTIA SINICA Phys Mech Astron 40(5):528–533
2. Liu J, Sang H, Xu Y, Feng X (2013) Effect of GNSS waveform distortions on SNR. Telecommun Eng 53(1):P28–P32
3. Phelts RE (2001) Multicorrelator techniques for robust mitigation of threats to GPS signal quality. PhD thesis, Stanford University, California, June 2001
4. Mitelman AM (2004) Signal quality monitoring for GPS augmentation systems. PhD thesis, Stanford University, California, Dec 2004
5. Phelts RE, Walter T, Enge P (2009) Characterizing nominal analog signal deformation on GNSS signals. In: Proceedings of the ION GNSS, Savannah, ION GNSS, GA, pp 1343–1350, Sept 2009
6. Wong G, Phelts RE, Walter T, Enge P (2011) Alternative characterization of analog signal deformation for GNSS-GPS satellite. In: Proceedings of the 2011 ITM of ION, San Diego, Jan 2011
7. Wong G, Phelts RE, Walter T, Enge P (2011) Bounding errors caused by nominal GNSS signal deformations. In: Proceedings of the ION GNSS, Manassas, ION GNSS, VA, pp 2657–2664, Sept 2011

Chapter 30
Research on the Dynamic Configuration of Air-Based Pseudolite Network

Da-peng Li, Ping-ke Deng, Bing Liu, Yi Qu, Ling-chuan Zeng and Ting Liu

Abstract To realize the adaptive adjustment of the air-based pseudo-lite (PL) navigation augmentation network, a dynamic configuration method for the air-based PL network deployment is proposed. By surveying and defining the indicators describing the performance of navigation augmentation network, based on the basic needs of navigation enhancement task, an objective function is designed for the optimization deployment of the air-based PLs. Using particle swarm optimization algorithm (PSO) for the fine search of the objective function of the air-based PL optimization deployment in multi-dimension, the dynamic optimal deployment is obtained. The simulation results show that, the proposed method could keep the navigation performance optimum, in the case of navigation enhancement service region changing or the local PL being interfered.

Keywords Air-based pseudo-lite · Navigation enhancement · Dynamic configuration of network · Particle swarm optimization algorithm

30.1 Introduction

From the GPS initial development (1970s) up to now, the application of pseudo-lite (PL) unceasingly changes with the development of satellite navigation. Early, the PL is mainly used to test the ground receiver devices, and now could be used instead of navigation satellite constellation in the environment, such as indoor, underground, where the satellite navigation signal is impeded. As an important supplement of navigation satellite constellation and enhance resource, PL could provide navigation enhancement service in the field where the availability is decreasing due to the disturbance of the signal.

This work was supported by National Natural Science Foundation of China (91438207).

D. Li (✉) · P. Deng · B. Liu · Y. Qu · L. Zeng · T. Liu
Academy of Opto-Electronics, Chinese Academy of Sciences, Takustr, Beijing, China
e-mail: lidapeng@aoe.ac.cn

J. Sun et al. (eds.), *China Satellite Navigation Conference (CSNC) 2015 Proceedings: Volume II*, Lecture Notes in Electrical Engineering 341,
DOI 10.1007/978-3-662-46635-3_30

According to the location of deployment, PL can be divided into two categories, which are air-based and ground-based. Compared with the ground-based, air-based PL is more widely used in military navigation enhancement, because of its flexibility, fast deployment, and wide covering range. The typical system are the GPX PL navigation augmentation system and the South Korea military air-based navigation backup system. In the application of the air-based PL navigation augmentation system, one of the most important problems need to be solved are the configuration of PL network. The good configuration could minimize geometric dilution of precision, and effectively improve the user positioning accuracy [1, 2].

At present, the relevant research on PL network configuration are mostly those using genetic algorithm optimization method [3, 4], which calculates the optimal PL network deployment in the aim of the navigation enhancement performance optimization, or the empirical method [5–8]. Usually those kinds of researches are assuming the PLs are no longer mobile when arrived at the deployment location. Because the PL constellation geometry does not change, so it can be called static network configuration. However, for some users, the active domain may exceed the enhancement service areas of navigation, or by external interference, a PL becomes unavailable, or even a PL failure completely. The situation above will make the PL navigation augmentation system cannot meet the needs of users, or even failure, resulting in enormous waste.

In order to meet the user demand, the PL network is necessary to dynamically change according to the user's location and the enhancement service quality (GDOP value, availability etc.). When the PL constellation geometry adaptively adjusts for the user demand, the best navigation enhancement service is available, so it can be called dynamic network configuration.

The design of PL network dynamic configuration needs to consider many aspects of the enhancement demand. In this paper, firstly, the indicators for the PL network performance evaluation are summarizes and definitions. Secondly, an objective function of optimization is designed considering the factors, such as PL geometry, the availability and the user migration. Thirdly, the particle swarm optimization method is used to search for the optimum PL network deployment. Finally, the validity of the method is verified through the simulation experiment.

30.2 Indicators of PL Network Performance Evaluation

The accuracy of PL positioning system is closely related to the spatial geometry. The positioning error equations can be expressed as

$$R - P = G_u \cdot X_u \tag{30.1}$$

where R is the true geometry distance between user and the i-th PL($1 \le i \le n$). $P = (\rho_1, \rho_2, \ldots, \rho_n)$ is the pseudo-range between user and the i-th PL.

$$G_u = \begin{bmatrix} -HE_{11} & -HE_{12} & -HE_{13} & 1 \\ -HE_{21} & -HE_{22} & -HE_{23} & 1 \\ \vdots & \vdots & \vdots & \vdots \\ -HE_{n1} & -HE_{n2} & -HE_{n3} & 1 \end{bmatrix} \tag{30.2}$$

$(HE_{i1}, HE_{i2}, HE_{i3})$ is the direction cosine between user and the i-th PL. $X_u = [\delta_x \delta_y \delta_z \delta_{ut}]$, where $(\delta_x \ \delta_y \ \delta_z)$ is position error, δ_{ut} is the ranging error caused by clock difference.

The user position correction can be obtain by least squares

$$X_u = [G_u^T G_u]^{-1} G_u^T [R - P] \tag{30.3}$$

The variance of the correction error is $\mathrm{cov}(\delta X_u) = [G_u^T G_u]^{-1} \mathrm{cov}[\delta(R - P)]$ $[(G_u^T G_u)^{-1} G_u^T]$. Assuming the distance error of each PL is identical and independent with mean zero and variance δ^2, thus

$$\mathrm{cov}(\delta X_u) = [G_u^T G_u]^{-1} \delta^2$$

where

$$[G_u^T G_u]^{-1} = \begin{bmatrix} q_{11} & q_{12} & q_{13} & q_{14} \\ q_{21} & q_{22} & q_{23} & q_{24} \\ q_{31} & q_{32} & q_{33} & q_{34} \\ q_{41} & q_{42} & q_{43} & q_{44} \end{bmatrix}$$

Then the position error of geometric error coefficient PDOP can be expressed

$$PDOP = \sqrt{q_{11} + q_{22} + q_{33}} \tag{30.4}$$

Generally speaking, the performance indicators of PL network mainly consider the GDOP value and availability of navigation enhancement service region, which are the fundamental basis for the augmentation effect evaluation.

The mean value of GDOP is used to describe the magnifying degree of distance error between PL and user, which reflects the positioning performance of whole navigation enhancement service area. It is defined as

$$\overline{GDOP} = \frac{\sum_{i=1}^{n} GDOP_i}{n} \tag{30.5}$$

where i = 1,…, n, n is the number of effective sampling points of GDOP distributed uniformly within the service area. The effective means the GDOP value is solvable, because within certain service area, the GDOP value cannot be obtained for invalid cosine of direction angle.

Considering the visible PL number for user has a great influence on navigation performance, we define the maximum visibility indicator

$$MaxVisible_i = \begin{cases} 1, \ if \ visible \ PL \ number = PL \ number \\ 0, \ if \ visible \ PL \ number < PL \ number \end{cases} \tag{30.6}$$

The calculation way is that when the number of visible PL obtained from the i-th sampling points in the service area is equal to the total number of PL, let $MaxVisible_i = 1$, else let $MaxVisible_i = 0$.

This indicator is used to judge if the sampling points in the navigation enhancement area can completely receive all the PL signals. It implies the contribution of PL network to the availability of the augmentation region.

30.3 Air-Based PL Network Dynamic Configuration

30.3.1 The Optimization Objective Function Design for Dynamic Configuration

Navigation augmentation system usually faces a lot of demands. In this paper we focus on two points: 1. the navigation augmentation service area migration; 2. individual PL is not available to some local area. On this premise, in the aim of maintaining navigation enhancement performance, improving availability, weakening the interference or the destructive influence, an objective function is designed fully coordinating PL resources meanwhile meeting the needs of the navigation enhancement task.

The definition of the objective function for PL dynamic configuration performance optimization shown in formula (30.7).

$$E(PS_i) = w_1 E_1 + w_2 E_2 + \cdots + w_M E_M \tag{30.7}$$

where $w_1, w_2, \ldots, w_M$ is the weight of indicators of navigation augmentation performance, which is used to control the adjustment of PL constellation optimization criterion. E_i is the i-th indicator.

Considering the mean values of GDOP and the visible PL number as the indicators to structure the objective function as following:

$$\begin{aligned} E(PS_i) &= w_1 \overline{GDOP}(PS_i) + w_2[Available(PS_i) - n] \\ Available &= \sum_{i=1}^{n} MaxVisible_i \\ w_1 + w_2 &= 1 \end{aligned} \tag{30.8}$$

where $\overline{GDOP}$ is the average value of GDOP sampling from the enhancement service area, see Eq. (30.5). Indicator Available is the sum of maximum visibility indicator from sampling points in the service area, see Eq. (30.6). Weight w_2 should be set to a large value to punish the behavior of reducing the average GDOP of the search algorithm, which could result in lower availability. We set w_2 to 0.9 experimentally, and call it penalty factor. The w_1 is set to 0.1.

30.3.2 Search for the Optimal Network Configuration Based on PSO

To search for the optimal network of PL, a kind of configuration strategy is regarded as a particle, the specific steps of search is as follows:

Step 1 In a given deployment space, m particles $PS_i, i = 1, 2, \ldots, m$ is initialized randomly. Namely m groups of PL position sequences: $(L_1^1, L_2^1, \ldots, L_N^1)$, $(L_1^2, L_2^2, \ldots, L_N^2), \ldots, (L_1^m, L_2^m, \ldots, L_N^m)$ are randomly generated, where N denotes the number of PLs, $L_j^i = (x_j^i, y_j^i, z_j^i)$, i = 1, 2,…, m, j = 1, 2,…, N. At the same time, m groups of particle moving velocity sequences: $(V_1^1, V_2^1, \ldots, V_N^1)$, $(V_1^2, V_2^2, \ldots, V_N^2), \ldots, (V_1^m, V_2^m, \ldots, V_N^m)$, are randomly generated. The coordinates $pbest^i$ of each of the particles is set to its current position.

Step 2 Particle performance depends on the fitness determined by the objective function. Each particle has a fitness is determined by the value of the objective function. According to Eqs. (30.8), each particle's fitness value $E(PS_i)$ is calculated. At the same time, the corresponding individual extreme is calculated according to the objective function $E(pbest^i)$, i = 1, 2,…, m. Maximum individual extreme, which corresponds to the particle's current position, is regarded as gbest.

Step 3 For each particle, its fitness value and individual extremum $E(pbest^i)$ are compared, if better, then the current individual extremum and $pbest^i$ are updated.

Step 4 For each particle, its fitness value and global extreme value Es (gbest) are compared, if better, then the current global extremum and gbest are updated.

Step 5 Each particle according to the fitness value to update the coordinate sequence of the PL deployment. In the update process, particles according to Eqs. (30.9) and (30.10), update their position and flight speed, uses the inertia decreasing weight (Linearly Decreasing Weight, LDW) strategy to improve the performance of PSO algorithm.

$$V_i = \omega \times V_i + c_1 \times rand() \times (pbest_i - L_i) + c_2 \times rand() \times (gbest - L_i) \tag{30.9}$$

$$L_i = L_i + V_i \tag{30.10}$$

where the first part in (30.9), called the memory term, represents the influence of the magnitude and direction of the last speed. Second part called self-cognition item, is a vector pointing from the particle current position to the individual best position, which represents the particle movement is coming from its experience. The third part called the group cognition item, is a vector pointing from the current best point to the population best point, which reflects the collaboration and knowledge sharing between particles. rand() is a random number uniformly distributed between 0 and 1. c1 and c2 are learning factors (generally equal to 2), representing the weights of the statistical acceleration term of each particle. ω is non negative, known as the inertia factor, which is introduced to improve the performance of PSO algorithm. When the algorithm to explore larger regions in the beginning, the approximate position of the optimal particles is quickly obtained. With the ω decreases gradually, the particle velocity slows down, and the fine local search could be achieved.
Let $\omega = \omega(k)$, $\omega(k)$ obtained by Eq. (30.11)

$$\omega(k) = \frac{(\omega_{ini} - \omega_{end})(T_{\max} - k)}{T_{\max}} + \omega_{end} \tag{30.11}$$

where T_{max} is the maximum generation. Set T_{max} = 1000, $\omega_{ini} = 0.9$, $\omega_{end} = 0.4$. ω decreases with the number of iterations from 0.9 to 0.4 with the linear coefficient $(\omega_{ini} - \omega_{end})/T_{max}$ = 1/2000.

Step 6 Stop iteration update when reach the criterion which generally selected the maximum number of iterations of T_{max} or (and) the best position of particle swarm to meet a predetermined minimum adaptive threshold according to the specific problems. At the same time, the optimal solution is outputted. A set of location of the global extreme point is the optimal air-based PL network deployment plan. Otherwise, go to Step 2, and continue the iteration.

30.3.3 Air-Based PL Mobile Control

After obtaining the optimal PL network deployment through optimization algorithm, the air-based PL need to move toward a destination location. At this time, a reasonable flight path should be planned considering the vehicle characteristics (duration, the flexibility, the scope of activities etc.), moving cost and risks. Due to space limitation, we does not focus on how to control the air-based PL moving to the optimal target location. The mobile control strategy is available in the references of path planning or wireless sensor network.

30.4 Simulations

Based on simulations, Refs. [7, 8] find out the basic rule of air-based PL network configuration, a set of strategy of PL deployment are provided by experimental results, these kind of methods are called empirical method. In this paper, we use the method of Refs. [7, 8] to do the comparison experiment. Assuming the navigation enhancement service region is located at (25º–27º, 110º–112º), set five 20 km high air-based PL locate at (25º, 110º), (27º, 110º), (25º, 112º), (27º, 112º), (26º, 111º) respectively.

30.4.1 Comparison for PLs Static Network Configuration

Under the constraint of PL's latitude and longitude changing within the range of [105º, 117º] × [20º, 32º] and locating at 20 km high, by minimizing the objective function using PSO, the optimal deployment of PLs is obtained, where the PL's latitude and longitude is: (113.09º, 25.97º), (111.46º, 25.48º), (110.42º, 25.68º), (111.08º, 26.58º), (108.91º, 25.97º) respectively, altitude is 20 km. The comparison results are shown in Fig. 30.1, in which the asterisk corresponds to the PL network laid by empirical method, the circle corresponds to the result obtained by the proposed method.

Further analysis of performance improvement are following figures. The first row is availability map of PL network. More deep the region color is, more the number of visible stars is. The rectangle is the service area of PL navigation augmentation.

The number of visible star in the rectangle reached 5 for both methods. However, comparing with the proposed method, the area of availability of the empirical method will be more at the cost of increasing the GDOP value, which will be explained in the subsequent section.

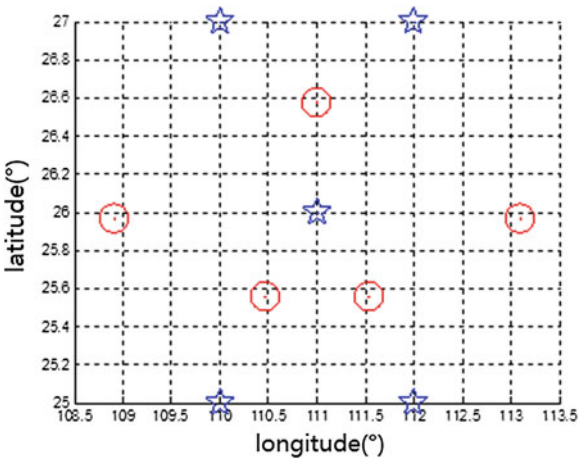

Fig. 30.1 The comparison results of the empirical method and the proposed one

The second row in Fig. 30.2 is the 3D GDOP value of PL network, and there are 3 valleys in the result of the proposed method. While only one valley is obtained by the empirical method, which could only ensure the GDOP value of the center region lower. The third row in Fig. 30.2 is the distribution of GDOP values. Most of the GDOP value is available between 3 and 4 by the proposed method. The result of the empirical method is more decentralized, and most concentrated between 8 and 9. Therefore, the proposed method met the requirement of availability, at the same time, reduced the GDOP value of service area as much as possible.

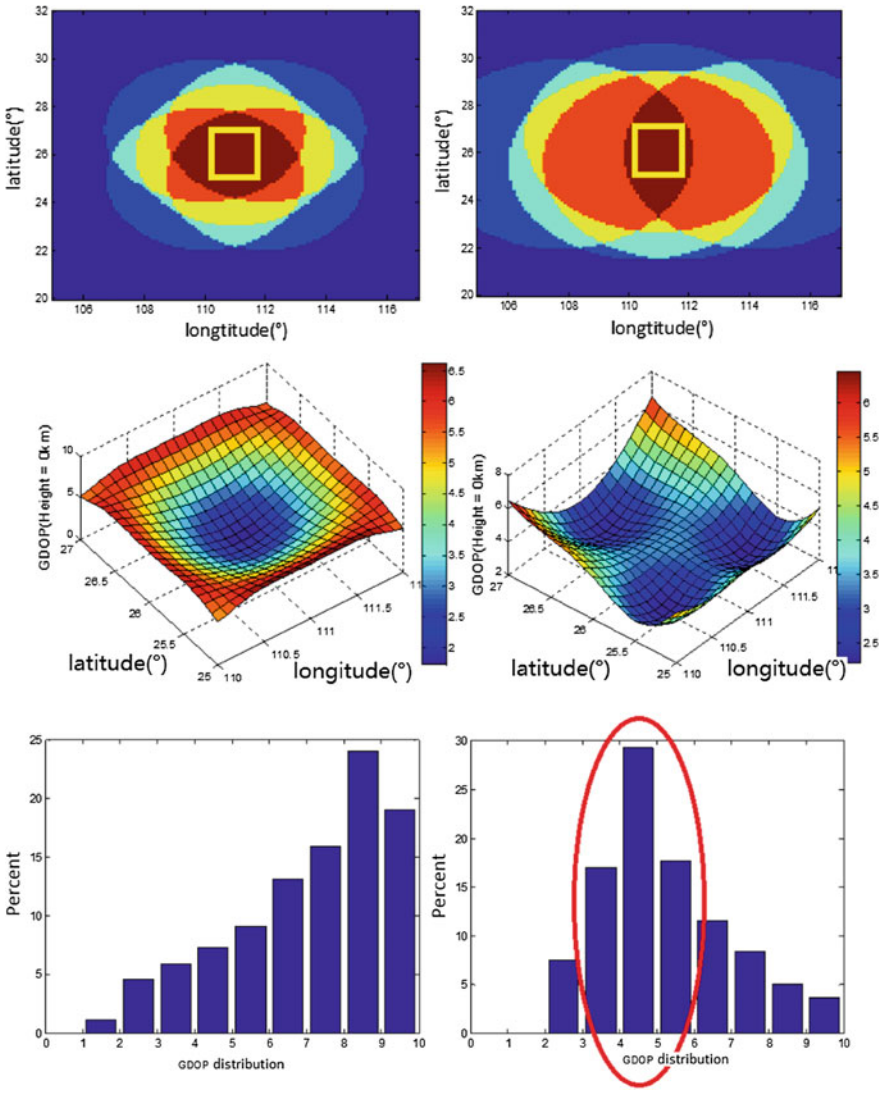

Fig. 30.2 Performance analysis

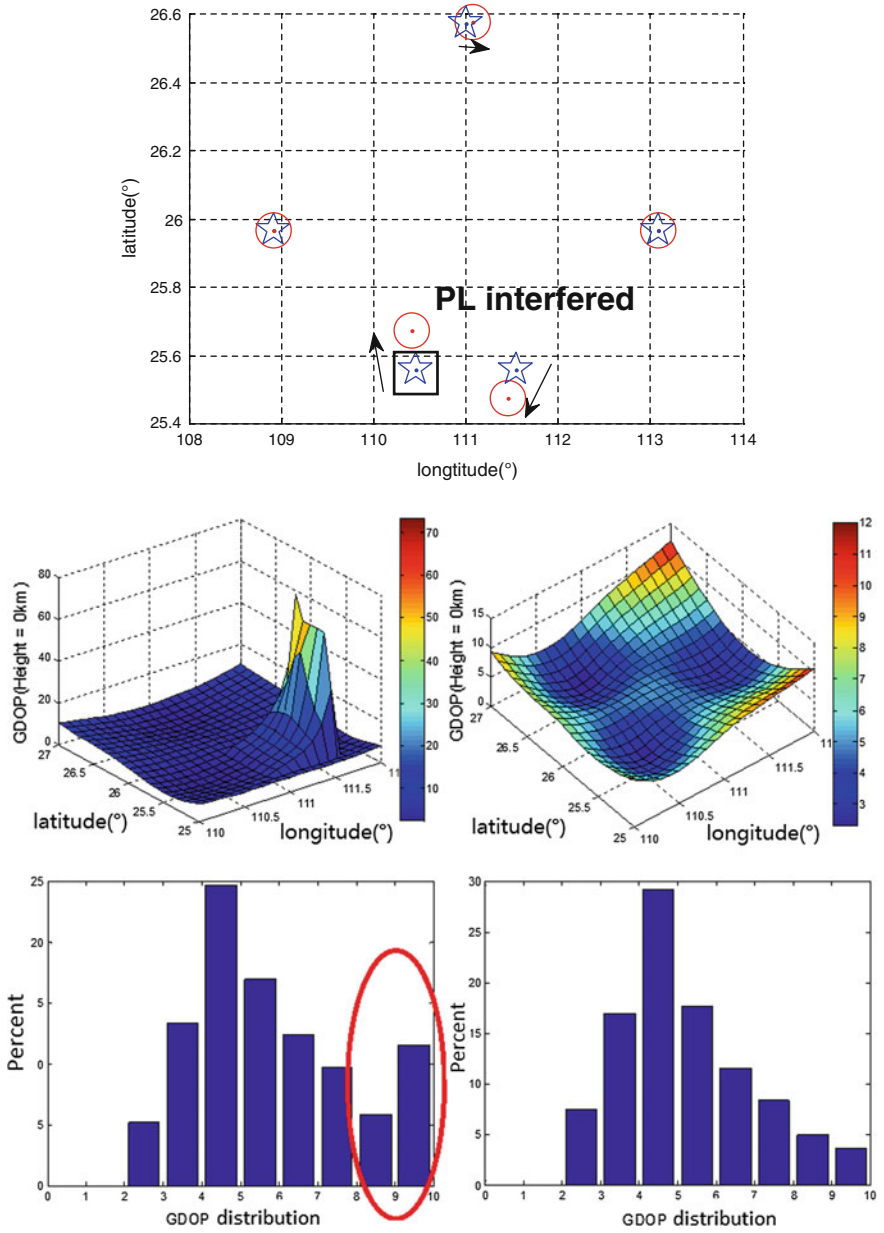

Fig. 30.3 The effect of anti-interference

Additionally, the proposed method could tackle the migration of navigation augmentation service area when the service area move toward north and east 1° respectively. This is the effect of introducing the punishment factor in the design of objective function. Because the result of the service area moving is the same as that not moving, the figures of result are ignored.

30.4.2 PL Dynamic Adjustment of Interference Suppression

The following simulation of local area appear disturbance situation, assume in (110.42°, 25.68°, 20 km) space based pseudo satellite for the service area [111°, 111.6°] * [25.2°, 25.8°]. By the pseudo satellite interference Fig. 30.3 shown in black box. At this point, the entire service area distribution of GDOP value will appear discontinuous, as Fig. 30.3 shown in second row on the left side.

A PL dynamic configuration is obtained by the proposed method, obtaining. There are 3 mobile PLs in the figure shown by the arrow. At this time, and enhance the GDOP value of the recovered nearly original form, such as on the right side of figure second shown on line, effectively eliminate the service area GDOP interference value caused by the deterioration of the influence of distribution. In this paper, the dynamic network method PL, in disturbed environments through local adjust the position, effect of the greatest possible interference suppression, realize empty base PL augmented dynamic optimal network deployment.

30.5 Conclusion

With the development of navigation augmentation, the technology of air-based PL network configuration is more and more attention-getting, and the corresponding methods have been proposed by some scholars. However, most current literatures focus on the static deployment of the PL network, which overlook the dynamic demands of the network configuration. In the face of complicated enhancement environment and the user needs, in order to make the PL navigation augmentation system to be practical, it is necessary to carry out research on the technology of PL network dynamic configuration. In this paper, a PL network dynamic optimal deployment method is proposed through the design of dynamic network optimization objective function, and the search algorithm is based on particle swarm optimization. With the deep research, the optimum mobile strategy of PL to the target destination will be considered, which could achieve a reasonable route planning of the PL meanwhile maintaining the service performance of the navigation augmentation system.

References

1. Zhang C, He C (2012) Pseudolite positioning network based on honeycomb distribution. Radio Eng 42(10):P9–P11
2. Luo M, Qian L, Wang J (2012) The research on positioning accuracy based on pseudolite system. Fire Control Command Control 37(7):P196–P199
3. Shi H, Yu F (2013) Wide area cellular network layout optimization of air-borne pseudo based on genetic algorithm. Ordnance Indus Autom 32(9):P68–P72
4. Yang L, Zhou J, Chen J (2008) The study of optimization of formation flying navigation augmentation platforms based on genetic algorithm. GNSS World China P9–P13
5. Yang Y, Gao S, Yang H (2013) Designing on geometric configuration schemes of pseudolite in near space. Syst Eng Electron 35
6. Yue Q, Qiu Z, Jia Y (2012) Impact of TDI CCD camera dynamic imaging on geometric quality by mathematic simulation. Sci Surveying Mapp 37(3):P21–P22
7. Meng J, Sun F (2008) Plans of augmenting regional satellite navigation using PLs. J Geomatics Sci Technol 25(3):213–215
8. Meng J, Sun F (2007) The research on the plans of PL-only positioning system. Hydrographic Surveying Charting 27(1):12–16

Part III
Satellite Navigation Models and Methods

Chapter 31
An Improved GNSS Global Ionospheric Model

Dun Liu, Xiao Yu, Liang Chen and Weimin Zhen

Abstract GNSS ionospheric correction models for single frequency user are realized through the combination of the information of long term variation from available background ionospheric model and the real-time information from GNSS measurements. Method of ionospheric model driven by GNSS data and models for the driven factor are cores for the GNSS ionospheric model. A factor of Equivalent Irradiation (*ER*) is introduced for ionospheric model driven method, and a new model of the factor for prediction is put forward based on its temporal and spatial variations, including a linear term and a periodic term. Analysis shows that the relative accuracy of more than 70 % could be achieved for GNSS ionospheric model based on the new driven factor model, better than that of GALILEO realization which based on a three-coefficient factor model. The driven factor model in GALILEO is a specific realization of the new model when a simplification is used.

Keywords GNSS · Ionosphere · Date-driven · ER factor

31.1 Introduction

Ionosphere is one of the most important error sources in GNSS positioning. The error can be compensated by ionospheric correction methods, generally developed based on ionospheric models. Ionospheric models usually used include IRI, NeQuick, and BENT etc.

In development of GNSS ionospheric correction method, technology of ionospheric model updating driven by GNSS measurements should be developed and models for the driving factor also should be established [1–6]. BENT model is chosen in GPS and parameters of the driving factor are chosen according to the day of year and averaged solar radiation flux of the past 5 days [7]. NeQuick model in

D. Liu (✉) · X. Yu · L. Chen · W. Zhen
No. 22nd Research Institute, CETC, Qingdao 266107, China
e-mail: dun.l@163.com

J. Sun et al. (eds.), *China Satellite Navigation Conference (CSNC) 2015 Proceedings: Volume II*, Lecture Notes in Electrical Engineering 341,
DOI 10.1007/978-3-662-46635-3_31

Galileo is updated with a three-coefficient Az model for driving factor. The three coefficients are broadcasted to users in ephemeris [1–4].

Method has been studied to ingest GNSS Data in experimental ionospheric model in previous work [8]. Here the modeling of driving factor and its use in GNSS single frequency correction model is detailed in this paper.

31.2 Method of Data Driving for Ionospheric Model and Its Realization

As the ionosphere varies periodically with the solar radiation, an Equivalent Irradiation (*ER*) factor is introduced to drive the ionospheric model. *ER* could be derived from TEC measurements. Based on variation with factors such as local time, season, solar activity and locations, a model of the *ER* could be constructed. Coefficients of the *ER* model could be used as the possible ephemeris parameters for GNSS broadcasting.

NeQuick, developed by ICTP Italy and the University of Graz Austria, is used in the work [2–4]. The global ionospheric map (GIM) from JPL (Jet Propulsion Laboratory) and GPS dual-frequency measurement from IGS are also used to for *ER* modeling [9].

31.2.1 Method of Data Driving in NeQuick Model

Procedure for *ER* estimation with GIM is constructed first. For each grid in GIM, TEC value $TEC_{NeQuick}$ can be estimated from NeQuick model with a certain *ER* value as input. By adjusting the *ER* value continuously, a series of $TEC_{NeQuick}$ can be achieved. Making the GIM TEC values at the grid as the reality, an optimal *ER* value fulfilling the following equation could be found and denoted as *OptER*.

$$OptER = \underset{ER_{\min} \le ERi < ER_{\max}}{\arg\min} \sum_{ti=1}^{12} \left[TEC_{NeQuick}(ERi, ti, lati, loni) - TEC_{GIM}(ti, lati, loni) \right]^2 \tag{31.1}$$

where TEC_{GIM} is the grid TEC from GIM, *ti* is the epoch time of GIM TEC, *lati* and *loni* are respectively latitude and longitude of the grid point.

Figure 31.1 shows the typical residual error variation of $TEC_{NeQuick}$ series with *ER*s. In this example, the grid location is 45°N, 0°E and the time is DOY (day of year) 150 of 2006. The error of $TEC_{NeQuick}$ is defined as below.

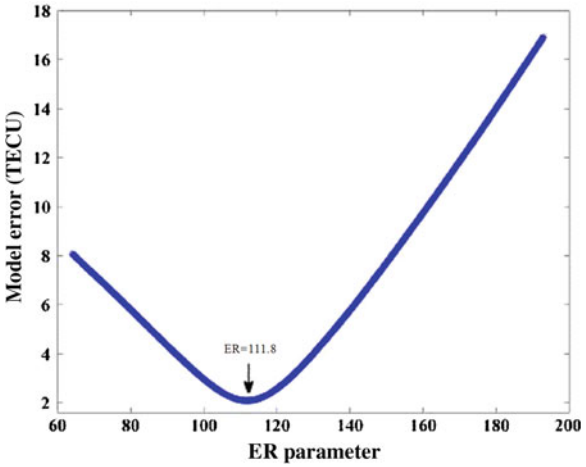

Fig. 31.1 Variation of estimated TEC with *ER* for NeQuick model

$$\sigma(ERi) = \sqrt{\frac{\sum_{ti=1}^{12} [TEC_{NeQuick}(ERi, ti) - TEC_{GIM}(ti)]^2}{12 - 1}}. \tag{31.2}$$

It can be seen that the error of TEC estimation is a parabola opening upwards which means an optimal *ER* minimizing the error could always be reached. More examples also sustain this statement. So an *ER* database can be constructed for the modeling with GIM data.

31.2.2 Spatial and Temporal Variation of Driving Factor ER

31.2.2.1 Variation of *ER* in Different Coordinates Frames

Variation of *ER* with latitudes in different coordinate frames is analyzed firstly, as the ionosphere varies most significantly with latitudes. Figure 31.2 shows a typical variation of *ER* with geophysical latitude, magnetic latitude and modified dip latitude (*MODIP*) (day of 30th May, 2006).

It can be seen that *ER* varies dramatically with geophysical latitude and magnetic latitude but mild with modified dip latitude. *ER* variation of a shape of "*W*" with *MODIP* is also evident. This trend will be much clear in the following part. So the *MODIP* is selected for ER modeling in the following work.

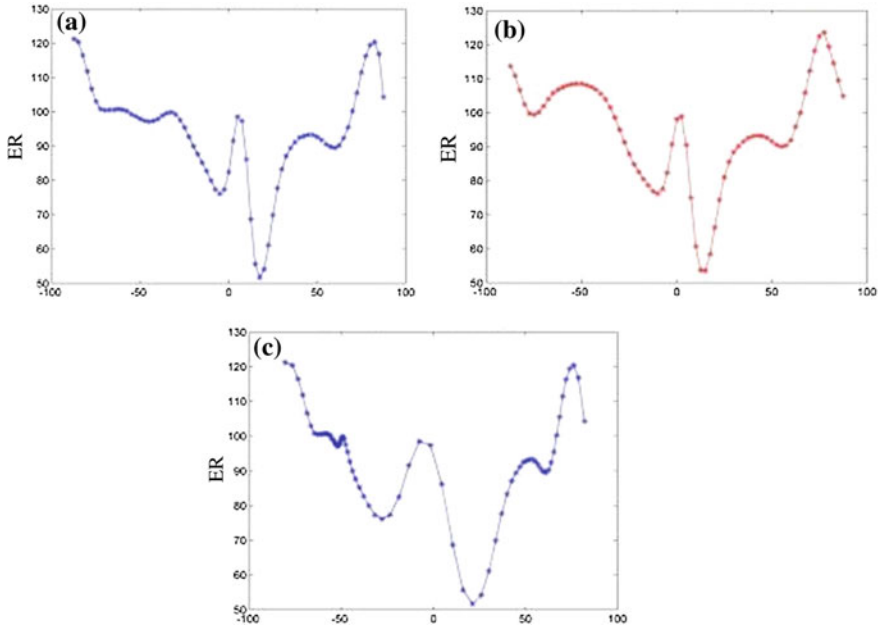

Fig. 31.2 ER factor variation with geographic latitude (**a**), geomagnetic latitude (**b**), and modified dip latitude (**c**)

31.2.2.2 Variation of *ER* with Time and *MODIP*

In order to get temporal and spatial variation of *ER* more clearly, variations of *ER* with *MODIP* on different longitudes in a day for different solar activities and different seasons are also analyzed.

Figure 31.3 shows the typical variation of *ER* with *MODIP* of all longitudes for days in different seasons of 1 year (respective 03/15, 06/15, 09/15, 12/15, 2003). The shape of "*W*" can be easily identified in *ER* variation with *MODIP*. Also a slant could be seen in the "W" shape, which is from south to north in spring and winter, and vice versa in summer and autumn. This means that *ER* varies with *MODIP* periodically, indicating by the shape of "W". At the same time, a linear variation with time also exists, as the trend of inclination shows.

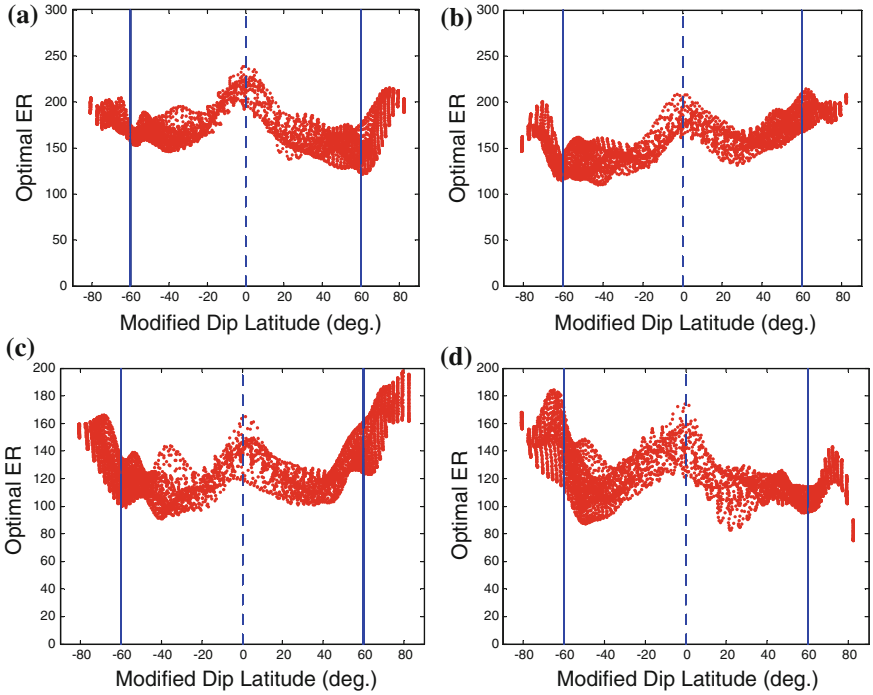

Fig. 31.3 Variation of *ER* with *MODIP* in different seasons 2003, **a** for 15th March, **b** for 15th June, **c** for 15th September and **d** for 15th October

31.2.3 Modeling of ER

Base on *ER* spatial and temporal variations, the following model is constructed:

$$ER = a_0 + a_1 \cdot MODIP + a_2 \cdot MODIP^2 + a_3 \cdot MODIP \cdot \cos\left(a_4 \cdot MODIP + a_5\right) \tag{31.3}$$

where, parameters $[a_0, a_1, a_2]$ is used to depict the *ER* linear variation, while $[a_3, a_4, a_5]$ is used to depict the amplitude, period and phase of the periodical variation respectively.

$$\tan\left(MODIP\right) = I/\cos\left(\phi\right) \tag{31.4}$$

where, I is true magnetic dip, and ϕ geographic latitude.

31.3 Test of ER Model with GNSS Data

The following procedures are made to analysis the feasibility of the *ER* model for NeQuick updating with GNSS data.

(1) A network of 12 IGS stations around the world is selected from the same station list as that used in NeQuick assessment in Refs. [2–4].
(2) Vertical TEC is estimated with the GNSS measurements for each station. Then the optimal *ER* denoted as ER_R is estimated with the method in Sect. 31.2.1.
(3) *MODIP* of each IGS station is acquired according to its latitude, longitude and the times of measurements.
(4) Coefficients of *ER* model is estimated in a least square sense with the ER_R values and *MODIP*s of all 12 IGS stations with the following equation.

$$Y = AX + V \tag{31.5}$$

where, Y is ER_R values of each IGS station, A is the matrix about the *MODIP* of each IGS station, X is coefficients of $[a_0, a_1, a_2, a_3, a_4, a_5]$ to be estimated, V is residual matrix. With the estimated coefficients, *ER* variation with *MODIPs* could be calculated with the *ER* model.
(5) Repeat the steps from 1 to 4 for continuous days and make comparison of the results from two adjacent days to analyze the predictability of *ER* model.

Figure 31.4 shows the typical result of the analysis. In the figure red star and blue rectangle are the ER_R values for IGS stations on the day of 21st and 22nd June 2012 respectively. The red curve and blue curve are the variation of *ER* with *MODIP* for the day of 21st and 22nd June 2012 respectively. The abscissa is in latitude to show the even distribution of the IGS sites.

It could be seen that *ER* estimated with GNSS measurements shows the periodical term (shape of "*W*") and linear term (inclination) of *ER* clearly. Good

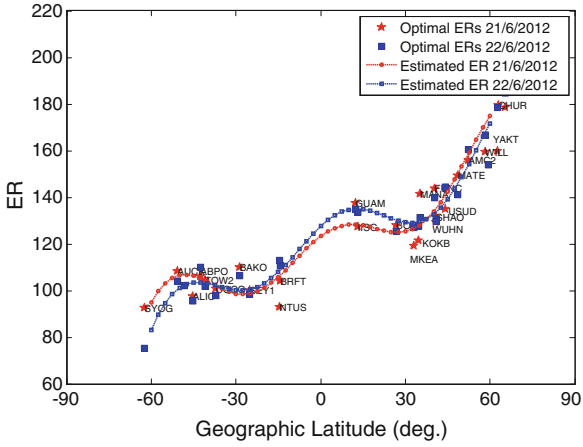

Fig. 31.4 *ER* variation on two adjacent days (*red* for 21st June 2012, and *blue* for 22nd June 2012)

consistency could also be seen for these two adjacent days. This is of great significance as the *ER* variation of the following day could be inferred with measurements of current day, meaning the predictability of *ER*.

31.4 Effectiveness Analysis of *ER* Model

31.4.1 Accuracy Analysis of NeQuick Based on ER Model

The following work is done to analyze the accuracy of NeQuick with *ER* model.

(1) The optimal *ER*s (denoted as ER_R) are estimated from GPS measurements from IGS stations for a day. Then the *ER* model is constructed and coefficients C_{ER} estimated. Here, the same network of 12 stations as that in Sect. 31.3 is used.
(2) IGS stations other than the 12 IGS stations around the world are chosen for test. The *ER* for the next day could be estimated with the C_{ER} coefficients and *MODIP* and time for each station. This forecasted *ER* is denoted as ER_F.
(3) The forecasted ER_F together with the position of each IGS station and the time of next day is input to NeQuick model to estimate TEC for this next day.
(4) TEC measurements from test stations on this next day are compared with the TECs estimated with the NeQuick to study the accuracy of the NeQuick model driven by *ER*s estimated from our model.

Figure 31.5 shows the cumulative probability distribution of relative error for the updated NeQuick model driven by *ER* model estimation for 2012, a high solar activity year, and 2008 a low solar activity year respectively. The accuracy of the updated NeQuick is respectively 77 % (1σ) and 76 % (1σ). More tests with data from 2002 to 2012 also have been done and show the same results.

The results show that the established model could be used to forecast *ER* for the next day, and the forecasted *ER* values could be used as the driving factor for

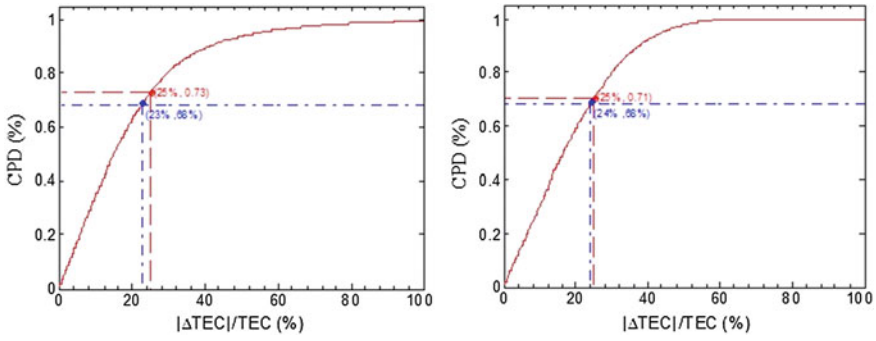

Fig. 31.5 Cumulative probability distribution of relative error for updated NeQuick model, *left* for 2012 and *right* for 2008

NeQuick model updating. The achieved accuracy of the updated NeQuick model is about 76 %, better than that for Galileo system [10].

31.4.2 Comparison of ER Model and Az Model in Galileo System

The Az model of Galileo system is as the following [1]

$$Az = a_0 + a_1 \cdot MODIP + a_2 \cdot MODIP^2 \tag{31.6}$$

Figure 31.6 shows the results of *ER* estimated and forecasted by Az model with 12 IGS stations (see Sect. 31.3), and Fig. 31.7 shows results with *ER* model. Red

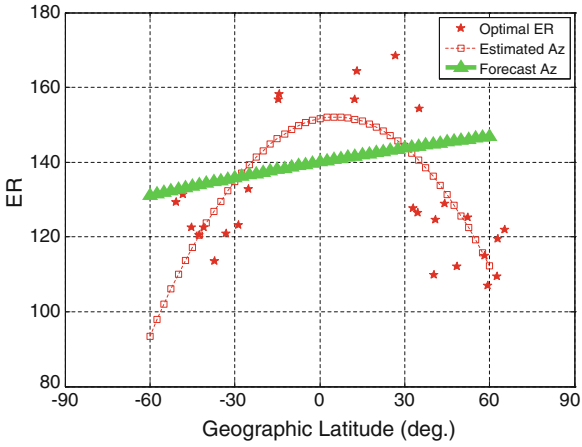

Fig. 31.6 Comparison of forecast Az with that estimated from measurements

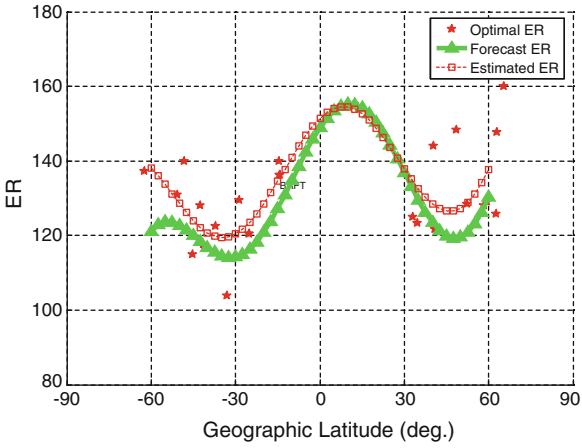

Fig. 31.7 Comparison of forecast *ER* with that estimated from measurements

stars is the ER_R estimated from the IGS stations measurements on 28th March 2012. Red line shows variation of the Az (Fig. 31.6) or ER (Fig. 31.7) estimated with ER_R and Az model or ER model respectively, while the blue line for the variation of the Az or ER forecasted with the data of previous day (2012/03/27) respectively.

It can be seen that, for the Az model, the deviation is significant between the Az estimated by intraday measurements (parabola) and that forecasted by previous day's measurements (almost a straight line). But for ER model, good consistency between estimated ER and forecasted ER is clear shown.

As Az model considers only the linear variation of the driving factor with $MODIP$, a possibility of false forecasting may exist when ER_Rs for two adjacent days vary differently. For ER model, a right forecasting could also be made as it describes the driving factor more exactly. Also can be seen that, the ER model could be simplified to Az model when $[a_3, a_4, a_5]$ is set to zero.

31.5 Conclusion

In this paper a parameter of Equivalent Irradiation (ER) is introduced and modeling the ER is studied to forecast this driving factor for NeQuick model updating. Two terms are included in ER model based on its spatial and temporal variation, one for the periodical variation and the other for linear variations with time, location etc.

ER model test with GNSS measurements from IGS stations also conducted. Results show that the ER could be forecast with the model, and the forecast ER could be used to updating experimental ionospheric models such as NeQuick to output more accuracy TEC estimation.

Analysis with IGS measurements shows that, the accuracy of the NeQuick model driven by ERs forecasted by the established model could be about 76 %, better than the accuracy of the Az model used in Galileo system to drive NeQuick model. The ER model also shows better feasibility for NeQuick driving factor forecast. Further analysis shows that the Az model used in Galileo system is actually a simplified form of the ER model.

Acknowledgments This work is sponsored by the International Technological Cooperation Projects (No. 2011DFA22270).

References

1. Arbesser-Rastburg B (2006) The Galileo single frequency ionospheric correction algorithm, ESWW3, Brussels, 15, Sept 2006
2. Nava B, Coïsson P, Amarnate GM, Azpilicueta F, Radicella SM (2005) A model assisted ionospheric electron density reconstruction method based on vertical TEC data ingestion. Ann Geoph 48(N.2):313–320

3. Miró Amarante G, Radicella SM, Nava B, Coïsson P (2003) Validation of a new method for ionospheric electron density reconstruction by means of vertical incidence data. In: Proceedings of 'atmospheric remote sensing using satellite navigation systems', special symposium of the URSI Joint Working Group, 2003, Matera (FG), Italy, pp 335–342
4. Nava B, Coïsson P, Miró Amarante G, Radicella SM (2003) A new model assisted method for ionosphere electron density reconstruction. In: Proceedings of 'atmospheric remote sensing using satellite navigation systems', special symposium of the URSI Joint Working Group, 2003, Matera (FG), Italy, pp 343–348
5. Bust GS, Coker C, Coco DS, Gaussiran II TL, Lauderdale T (2001) IRI data ingestion and ionospheric tomography. Adv Space Res 27(1), 157–165
6. Komjathy A, Langley RB, Bilitza D (1998) Ingesting GPS-derived TEC data into the international reference ionosphere for single frequency radar altimeter ionospheric delay correction. Adv Space Res 22(6):793–801
7. Klobuchar JA (1987) Ionospheric time-delay algorithm for single frequency GPS users. IEEE Trans Aerospace Electron Syst AES-23(3):325–331
8. Liu D, Yu X, Chen L, Ou M (2013) GNSS Data-based ingestion of ionospheric model and its application, CSNC 2013, Guangzhou
9. Schaer S (1999) Mapping and predicting the Earth's ionosphere using the global positioning system. Astronomisches Institut der Universitat Bern 1999
10. European Union (2010) European GNSS (GALILEO) OS SIS ICD, Issue 1.1, Sept 2010

Chapter 32
A New Method for Direct Calculation of Ionospheric Delay

Yadong Bao, Changjian Liu, Hongzhou Chai and Chen Liu

Abstract Existing methods for calculation of ionospheric delay was analyzed: observation error was amplified distinctly, and the information of geomagnetism and ionosphere was not utilized in triple-frequency combination method; Integral computation was no rigorous enough in traditional direction method, and the applicable area was limited. A new method to calculate the ionospheric delay was proposed in this paper: revising the direct calculation with the results in multi-frequency combination method. The information of geomagnetism and ionosphere was well used in the new method. Furthermore, the consistency was ensured same with triple-frequency combination method. A new thinking was proposed for calculation of ionospheric delay.

Keyword Ionospheric delay · High order · Triple-frequency combination method · Direct method

32.1 Introduction

With the development and perfection of multi-mode and multi-frequency Global Navigation Satellite Systems (GNSS), its level and characters have been improved infinitely, and higher precision demand in positioning is presented constantly. Current researches indicate that the ionospheric delay is one of the main error sources in navigation and positioning. The first-order propagation error has a meter level influence to GNSS positioning. And the second order has a centimeter level effect, even at zenith there still remains 0−2 cm [1, 9]. Therefore, the ionospheric delay should be taken sufficient consideration in precise positioning. Meanwhile, when the second order error estimated inaccurately, the bias would influence the precision estimation of VTEC, and then weaken the reliability of VTEC model.

Y. Bao (✉) · C. Liu · H. Chai · C. Liu
Institute of Geospatial Information, Information Engineering University, Zhengzhou, China
e-mail: 919668518@qq.com

J. Sun et al. (eds.), *China Satellite Navigation Conference (CSNC) 2015 Proceedings: Volume II*, Lecture Notes in Electrical Engineering 341,
DOI 10.1007/978-3-662-46635-3_32

Moreover, the second order error is taken seriously in the research and application of high-precision geodesy, such as crustal deformation monitoring, earthquake prediction, plate movement, etc. [3]. Researching the computing method of high order ionospheric delay is fundamental for improving positioning precision, refining ionospheric model, physical geography, etc.

There are two main methods to calculate high order ionospheric delay [8]. One is linear combination based on multi-frequency, and another is the direct method based on geomagnetic information. This paper will analyze the error magnification of observation in linear combination method, and then improve the direct method so as to present a new method for high order ionospheric delay calculation.

32.2 Method to Calculate Ionospheric Delay

According to Appleton-Hartree formula [5], the observation equation of carrier-phase with a view to second order ionospheric delay can be expressed by [1, 4, 6]

$$L_i = \rho + N_{Li} - I_{1Li} - I_{2Li} + v_{Li} \tag{32.1}$$

where i is the number of carrier-phase, L_i is the corresponding observed value, ρ is the geometric distance between the satellite and the receiver, N_{Li} is the ambiguity of L_i, I_{1Li} and I_{2Li} is the first and second order delay of ionosphere, and v_{Li} represents the noise. Because this paper mainly researches the ionospheric delay, when the ambiguity and noise is estimated correctly, Eq. 32.1 can be simplified as:

$$L_i = \rho - I_{1L1} - I_{2L1} \tag{32.2}$$

in which

$$\begin{aligned} I_{1L_i} &= \frac{40.308}{f_i^2} \int_s n_e ds \\ I_{2L_i} &= \frac{1.128 \times 10^{12}}{f_i^3} \int_s B \cos\theta n_e ds \end{aligned} \tag{32.3}$$

where f_i is the frequency, S is the ray-path from the satellite to the receiver, n_e is the electron density along the ray-path, B is the strength of geomagnetic field, and θ is the angle between the wave propagation direction and the geomagnetic field vector.

32.2.1 Combination of Triple-Frequency

According to the combination theory of multi-frequency observations [7], high order ionospheric delay can be calculated through the multi-frequency observations

linear combination. For triple-frequency observations, the combination can be expressed by:

$$\begin{aligned} I_{1L_i} &= \frac{40.308}{f_i^2}(\alpha_1 L_1 + \beta_1 L_2 + \gamma_1 L_3) \\ I_{2L_i} &= \frac{1.128 \times 10^{12}}{f_i^3}(\alpha_2 L_1 + \beta_2 L_2 + \gamma_2 L_3) \end{aligned} \tag{32.4}$$

where α_i, β_i and γ_i represents the combination coefficients. When the coefficient is estimated correctly, the ionospheric delay can be calculated from Eq. 32.4. The method from Eq. 32.4 can be achieved along with the triple-frequency signals launched by GPS and BDS, etc. Here the signal frequencies has been shown.

The combination coefficients for frequencies in Table 32.1 are shown in Table 32.2.

Different frequencies correspond to different combination coefficients in triple-frequency method as shown in Table 32.2. Assuming the accuracy of all the carrier observations as σ, the accuracy of ionospheric delay values based on each system can be calculated according to the theory of error propagation (Table 32.3). From Table 32.3, the sensitivity to observation errors is greatly increased in triple-frequency method. In the calculation of first order delay, magnification of errors can reach 84.9 at least and 142.1 at most for BDS (77.9 and 139.7 for GPS), in the second order can reach 49.5 at least and 106.9 at most for BDS (44.4 and 106.7 for GPS).

32.2.2 Direct Method

Direction vector of signal propagation can be gotten according to the outline coordinates of satellite and station. If $\bar{B}$ and n_e is known at the same time, the first

Table 32.1 Frequency in BDS and GPS (MHz)

System	f_1	f_2	f_3
BDS	1561.098	1207.14	1268.52
GPS	1575.42	1227.60	1176.45

Table 32.2 Combination coefficient in multifrequency BDS and GPS

System	$\alpha_1/\beta_1/\gamma_1(\times 10^{18})$	$\alpha_2/\beta_2/\gamma_2(\times 10^{17})$
BDS	1.038/2.999/–4.037	–0.306/–0.996/1.302
GPS	0.762/–3.708/2.946	–0.218/1.182/–0.964

Table 32.3 Precision of ionospheric delay (σ)

System	1st order			2nd order		
	f_1	f_2	f_3	f_1	f_2	f_3
BDS	84.9	142.1	128.6	49.5	106.9	92.2
GPS	77.9	128.3	139.7	44.4	93.9	106.7

order and second order delay can be calculated directly from Eq. 32.3. IGRF, WMM and some regional mode can describe the spatial distribution of the magnetic field vector for different scales, which provide valuable information to calculate the second order delay. In the exiting direct method, the integral operation is usually simplified by $\overline{B\cos\theta}$, and the simplified form can be expressed as:

$$\begin{aligned} I_{2L_i} &= \frac{1.128 \times 10^{12}}{f_i^3} \overline{B\cos\theta} \int_s n_e ds \\ &= \frac{1.128 \times 10^{12}}{f_i^3} \overline{B\cos\theta} \cdot STEC \end{aligned} \tag{32.5}$$

so that the key point becomes to define the value of $\overline{B\cos\theta}$. One way is to divide the ray-path into n parts, and choose the median value of different parts as $\overline{B\cos\theta}$. Electron density at different heights differs by more than 10 times, and the spatial distribution of the electron density is uneven, so that $\overline{B\cos\theta}$ is not strict [2]. The electron density profiles of the ionosphere are generated by the generalized Chapman profile formula:

$$n_e(h) = n_m \cdot \exp\left(\frac{1}{2}(1 - z - \exp(-z))\right) \tag{32.6}$$

where $z = (h - h_m)/H$, n_m is the maximum electron density, h_m is the peak height, H is the pressure scale height. At $B_0\cos\theta_0$ at the height $H_0 = h_\mathrm{m} - 20$ km can meet the value of $\overline{B\cos\theta}$. But this method can not be used at high latitudes and low latitudes, either the integral is no strict [8].

32.2.3 New Direct Calculation Method

As can be seen from the above: it is theoretically possible to calculate the amount of the ionospheric delay first order and second-order items via a linear combination. But this method magnified observation error greatly, and reduced the accuracy of ionospheric delay calculation. Meanwhile, the method does not consider changes in the geomagnetic field and electron density distribution of geophysical properties. Direct method takes these information into account, but there is a limited area of application and computing issues not strictly in the existing method. From Eq. 32.3 this paper proposes a new method to calculate each order ionospheric delay. Here is the process:

Step 1 calculate $n'_\varepsilon(h)$ (the approximate distribution function of electron density variation with height) using approximation of n_m, h_m and H.

Step 2 calculate $B\cos\theta\,(h)$ (change of $B\cos\theta$ with altitude) using the vector model of geomagnetic and coordinates of station and the satellite.

Step 3 calculate the approximate first order and second order delay I'_{1L} and I'_{2L} by substituting $n'_{\varepsilon}(h)$ and $B\cos\theta(h)$ into integral operation in Eq. 32.3.

Step 4 calculate STEC based on multi-frequency observations. There is usually $\frac{40.308}{f_i^2} STEC \neq I'_{1L_i}$, because of the approximate distribution function in Step 1. Then the correction coefficient can be expressed as $\omega = \frac{40.308}{f_i^2} STEC \Big/ I'_{1L_i}$.

Step 5 correct the distribution function of electron density as $n_e(h) = \omega n'_e(h)$, and repeat Step 2 and 3 to get the intent first order $I_{1\mathrm{L}}$ and second order $I_{2\mathrm{L}}$. The ionospheric delay could be calculated through the above process. The ω can be extracted outside the integration operation because the index of $n_{\varepsilon}(h)$ is constant 1. So that there is $I_{1L_i} = \omega I'_{1L_i} = \frac{40.308}{f_i^2} STEC$, and $I_{2L_i} = \omega I'_{2L_i}$. This shows that the method proposed in this paper can not only guarantee the consistency with multi-frequency combination method, but also make full use of the earth's magnetic field vector and the electron density distribution information, which unifies physical phenomena and numerical calculations.

32.3 Simulation and Analysis

Each order ionospheric delay of each time and each station can be calculated according to the new method proposed in this paper. Here, we take UTC = 04/11/00/2013 (mm/dd/hh/yy) into example, and calculate the ionospheric delay at a spatial resolution of 2.5° × 5° and direction of zenith. According to the spatial distribution of the electron density, the parameters in Eq. 32.6 is set as $n_{\mathrm{m}} = 10^{12}$ el/m^3, $h_{\mathrm{m}} = 400$ km, and $H = 350$ km. IGRF model is used to provide the geomagnetic information. The limit of integration ranges from 60 to 120 km for that the ionospheric electron distribution height is generally in the range of 60–2000 km. To reduce the amount of data calculation, this paper will use the GIMs VTEC values released by IGS to calculate corrections. Compared Eq. 32.3 with Eq. 32.4, it is clear that the result of different frequencies share a similar feature. There is a fixed constant of proportionality. To simplify the content, the paper just gives the results of f_2 in GPS.

Figure 32.1 shows the worldwide VTEC distribution. The peak area is near the equator in the Pacific Ocean which reaches 92TECu. Corresponding first order delay has a same distribution: approximately symmetrical about the equator, gradually decreases from the equator to the poles, maximum delay amount appears near the equator in the Pacific. Figure 32.2 shows the simulation results of second order delay.

For the second order delay, the northern hemisphere is mainly negative, and the southern hemisphere is mainly positive. The boundary coincides with the 0nT equipotential lines of geomagnetic vertical component. This phenomenon is mainly

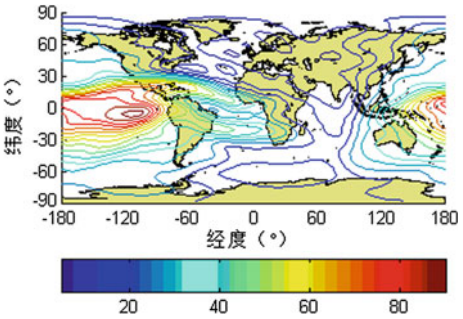

Fig. 32.1 Distribution of global VTEC (TECu)

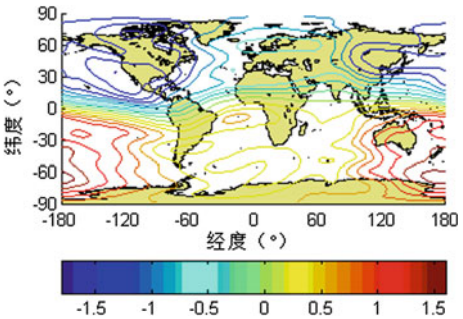

Fig. 32.2 2nd delay of GPS f_2 (cm)

Table 32.4 Results of statistics

Second order delay (cm)	$\lvert I_2\rvert < 0.5$	$\lvert I_2\rvert < 1.0$	$\lvert I_2\rvert < 1.5$	$\lvert I_2\rvert < 2.0$
Ratio	0.30	0.62	0.93	1.00

determined by the geomagnetic elements. Meanwhile, the maximum of second order appears near longitude 180°, which is similar to the maximum of VTEC values. Thus, the simulation results can simultaneously reflect the geomagnetic information and ionospheric distribution information. Here, we statistics the results of the second-order delay which is shown in Table 32.4. From Table 32.4, the second order delay at zenith are less than 2 cm. The result is consistent with the conclusion of [1], which demonstrates the effectiveness of this new method.

32.4 Conclusion

The weakness of tri-frequency combination method and general direct method to calculate ionospheric delay is analyzed, and a new direct method is proposed in this paper.

(1) The first order and second order delay can theoretically be calculated by the tri-frequency combination method. But the observation error is significantly

magnified, nor the geophysical information (magnetic field and ionosphere) is considered.

(2) There is calculation imprecise and restricted range in the general direct method.

(3) The new direct method proposed not only takes the effects of geomagnetic and ionospheric electron density into account, but also can ensure the consistency of the calculation results.

Acknowledgments The authors are grateful to IGS and IGGA for providing GIMs and IGRF2010 to download. Supported by National Natural Science Foundation of China: 41374041, 41274045.

References

1. Bassiri S, Hajj GA (1993) Higher-order ionospheric effects on the global positioning system observables and means of modeling them. Manuscripta Geodaetica 18(6):P280–P289
2. Brunner FK, Gu M (1991) An improved model for the dual frequency ionospheric correction of GPS observations Manuscripta Geodetics 16:205–214
3. Liu XF, Yuan YB, Huo XL et al (2010) Model analysis method (MAM) on the effect of the second-order ionospheric delay on GPS positioning solution Chin Sci Bull 55(12):162–1167
4. Hoque MM, Jakowski N, (2007) Higher order ionospheric effects in precise GNSS positioning. J Geod 81:P259–268
5. Papas CH (1965) Theory of electromagnetic wave propagation. McGraw-Hill, New York
6. Pireaux S, Defraigne P, Wauters L et al (2010) Higher-order ionospheric effects in GPS time and frequency transfer. GPS Solut 14:P267–27
7. 黄令勇, 宋力杰, 刘先东. 基于自适应聚类算法的 GPS 三频载波相位组合观测值优化选取. 大地测量与地球动力学, 2011, 31(4), P99–102
8. 李征航, 陈锴, 刘万科, 黄欢. 顾及f3项的电离层延迟模型. 武汉大学学报· 信息科学版, 2007, 32(2), P139–143
9. 张双成, 涂锐, 张勤, 黄观文. 电离层二阶项模型的构建及其变化规律分析研究. 测绘学报, 2011, 40(增刊), P105–110

Chapter 33
Precision Analysis of Wide-Area Ionospheric Correction Triangular Partition Method in Low Latitudes

Chao Xi, Chenglin Cai and Zhaochuan Wei

Abstract Ionospheric delay error is the main error source of the satellite navigation system, the current two common ionosphere error correction models—klobuchar and grid were initially put forward by the United States in order to improve its local GPS positioning precision and developed, which are currently two most commonly used and effective ionospheric error correction methods, but due to the characteristics of topography distribution in China: rooster-shape irregular distribution, and low latitudes occupy a larger proportion in the whole territory. There exists some limitations in the ionospheric delay error correction when its application to the beidou navigation system of China. Improving the positioning precision of the beidou navigation system needs further weaken the influence of various error sources, in order to solve the problem—ionosphere accurate correction of beidou navigation system in our country, wide-area ionosphere correction triangular partition method is proposed. Early according to the actual data of the China earthquake ionospheric monitoring network, The precision of the method is examined by eight reference stations of mid-latitude regions of our country, which has a better correction effect; Later using the observation data of China crustal observation net makes triangular partition method accuracy verification of low latitudes in China and makes comparison with grid mode, the results show that triangular partition method is not only improved obviously to the mid-latitude ionospheric error, but also is superior to grid model in low latitudes, which has important reference value to ionospheric delay error correction of beidou navigation system.

C. Xi (✉)
Aerors Inc, Xi'an 710000, China
e-mail: xichaofh@163.com

C. Cai · Z. Wei
Guangxi Key Laboratory of Precision Navigation Technology and Application,
Guilin University of Electronic Technology, Guilin 541004, China
e-mail: chengcailin@126.com

Z. Wei
e-mail: apple3143695@hotmail.com

J. Sun et al. (eds.), *China Satellite Navigation Conference (CSNC) 2015 Proceedings: Volume II*, Lecture Notes in Electrical Engineering 341,
DOI 10.1007/978-3-662-46635-3_33

Keywords Low latitudes · Total electron content (TEC) · Ionospheric correction · Triangular partition method · Model accuracy · Grid model

33.1 The Introduction

At present, the Beidou navigation industry has entered into a stage of rapid development, further improving the accuracy of the Beidou navigation and location services is the indispensable condition to accelerate China satellite navigation application specialization, industrialization and internationalization, ionospheric delay error is one of the main error sources affecting the satellite navigation system, the dual-frequency receiver users can weaken its impact through the way of dual-frequency combination; For single frequency receiver users, the current two relatively general and effective ionospheric error correction models klobuchar and grid can achieve correction accuracy at about 60 and 80 %, respectively [1–3], which largely weaken the influence of ionosphere delay error, but the two methods both have their own shortcomings, such as Klobuchar model accuracy is not high, difficult to meet the demand of high precision navigation applications; WASS grid mode is more appropriate to the ionospheric correction of the United States, which is geographical distribution of neat and located in the mid-latitudes [3], but due to the characteristics of topography distribution of China: rooster-shape irregular distribution, and low latitudes occupy a larger proportion in the whole territory. Adopting WAAS grid ionosphere correction model is hard to realize accurate correction, on the whole, in our country [4]. So researching on how to get a greater extent weaken of ionospheric delay error effect is a critical step to improve China's Beidou satellite navigation system position accuracy.

Aimed at this actual situation, through research and analysis, this paper proposes a new ionospheric delay error correction method, which has low demand on the regularity of the landscape, sparse distribution stations and wide-area ionosphere accurate correction, and which is called ionosphere correction triangular partition method, based on sparse triangular partition network of center radiation pattern. Respectively using the observational data of China seismic ionospheric monitoring network and China crustal movement observation network to make the model accuracy validation, the data analysis results show that even in low latitudes, triangular partition method is superior to grid model, not only in model accuracy but also complexity.

33.2 Triangular Partition Model

Wide area ionospheric delay error correction triangle partition method is this: Choosing one ionosphere monitoring station located in the mid-territory as the central station, combined with two outward radiation stations, forms a triangular geometry as

a triangular partition. And the coverage area of ionosphere monitoring stations is divided into several triangular partitions, According to the Vertical Total Electron Content (VTEC) obtained in three vertices (Stations) of the triangular area, in which the user IPP falls, calculate the VTEC at the IPP through the inverse distance power index weight method, then transform the VTEC into TEC of line-of-sight between the satellite and the ground receiver with slant factor.

Distance from the reference station to the sub-ionosphere puncture point:

$$d_i = \sqrt{(x_i - x_0)^2 + (y_i - y_0)^2 + (z_i - z_0)^2} \tag{33.1}$$

$$w_i = \frac{\frac{1}{d_i^k}}{\sum_{i=1}^{n} \frac{1}{d_i^k}} \tag{33.2}$$

where, w_i is the weight of the ionosphere reference station to the ionosphere puncture point. Weight: the k times power reciprocal of the distance, each ionosphere reference station makes different contribution to the prediction point, weight size varies with distance size.

The inverse distance weighted interpolation formula of VTEC in the ionosphere puncture point as shown below:

$$Z(x_0, y_0, z_0) = \begin{cases} \sum_{i=1}^{n} Z_i \times w_i & d_i \neq 0 \\ z_i & d_i = 0 \end{cases} \tag{33.3}$$

where, n = 3, and (x_i, y_i, z_i) is the earth rectangular coordinate of reference station, (x_0, y_0, z_0) is geodetic coordinate of test station, w_i is the weight value to test station from point of (x_i, y_i, z_i), Z_i is the vertical TEC observation value of the station (x_i, y_i, z_i), $Z(x_0, y_0, z_0)$ is test station's calculated vertical TEC value.

The VTEC of reference (base) stations in wide area differential system can be got in this way: choosing satellite pseudorange observation value at different azimuth Angle, of which the elevation angle is greater than a certain value (such as 40°), and do kalman filter, then through dual-frequency combination extract the VTEC of each puncture point at the same time, and then through interpolation to calculate the VTEC of the base station.

33.3 Model Precision Analysis in Low Latitudes

Early, the author used five monitoring stations in mid-latitude regions of China Seismo-Ionospheric Monitoring Network to set up triangular partition ionosphere model, which covered the entire network service area of the mid-latitude, and by using eight reference station data to evaluate correction precision of the method, the

results show that, for the inner regions of the triangular partition in mid-latitudes, this method can be revised to 90 % (DLHA 90, YANC 94, XNIN 88, JIXN 94, TAIN 92 and ZHNZ 95 %), which reflects the accuracy characteristics of the model; For triangular partition outside area within hundreds of kilometers, the method also can reach more than 80 % of the correction precision. The research results of mid-latitude mentioned in this paper later can be seen in "A New Wide Area Ionospheric Correction Method Based on Triangular Partition" of Geomatics and Information Science of Wuhan University (has been employed, to be published). Due to ionosphere is more active in low latitudes, verifying the triangular partition method in low latitudes can reflect more the stand or fall of this model and the superiority, so in the paper, we use part of the observation stations of crustal observation network of China and the ionosphere observation data to make the triangular partition method accuracy verification to southern China (in low latitudes). Due to the limitation of observation network station layout and quantity, we made model precision validation to the low latitudes in the southern with WUHN and LUZH two stations.

Choosing XIAA, SHAO, XIAM, WUHN, QION, XIAG and LUZH in China area, altogether seven stations to experiment, the geographical distribution of each station and triangle partition net work as shown in Fig. 33.1, based on triangular partition method proposed in this paper, taking ionospheric VTEC data of XIAA, SHAO and XIAM station to calculate its inner region WUHN station's VTEC value through distance power index weights of interpolation; and XIAA, QION, XIAG to calculate its inner region LUZH station. Experiment takes VTEC ionospheric data

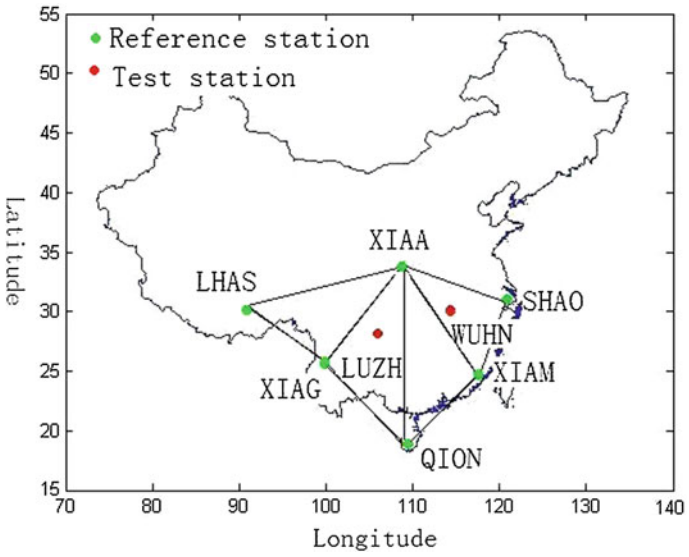

Fig. 33.1 The network test of triangular partition method in low latitudes of China

from 100 to 109 day of 2011, to make analysis, ionospheric data sampling interval is 15 min.

The data analysis length of model accuracy validation is 10 days, comparing the 10 days' calculated ionospheric VTEC value through triangular partition method with the observed data, Figs. 33.2 and 33.3 are respectively WUHN and LUZH stations' model calculating results. Statistics under different weight coefficient k value (1/2, 1, 2, 3, and 4) correction accuracy are more than 90 %, more than 80 % less than 90 %, more than 70 % less than 80 %, more than 60 % less than 70 % of the sample proportion in the total samples, as well as percentage on average and standard deviation, as shown in the following tables.

As can be seen from the statistics of Tables 33.1 and 33.2 that in southern China region model correction accuracy increases with the increase of weight coefficient k, when k = 3, using XIAA, SHAO and XIAM three stations can modify WUHN station the ionosphere accuracy to 88 %, and the use of XIAA, QION and XIAG three stations can modify LUZH's ionosphere accuracy to 93 %. Restricted by the stations number in southern China, as well as the layout of its distribution, currently only two stations verification, but as ionosphere is more active in the low latitudes, test in low latitudes can reflect more good or bad of triangular partition method, and the research results, to a great extent, illustrates the superiority of this model when applied to our country.

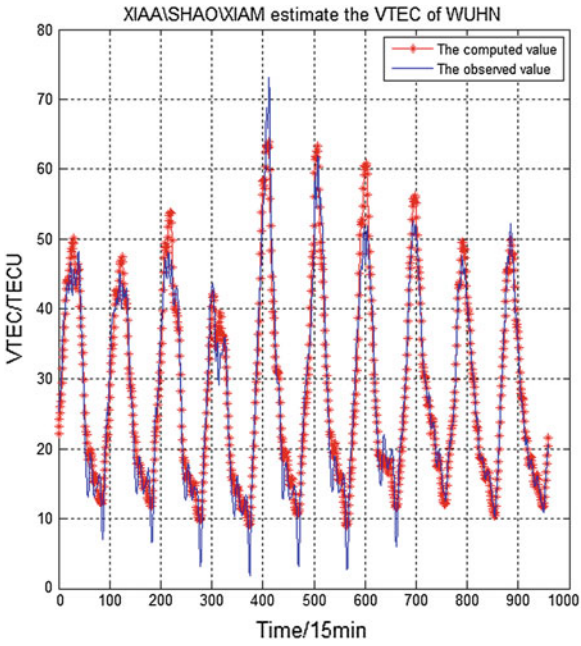

Fig. 33.2 The ionospheric VTEC model calculating results of WUHN station with weight coefficient k = 3

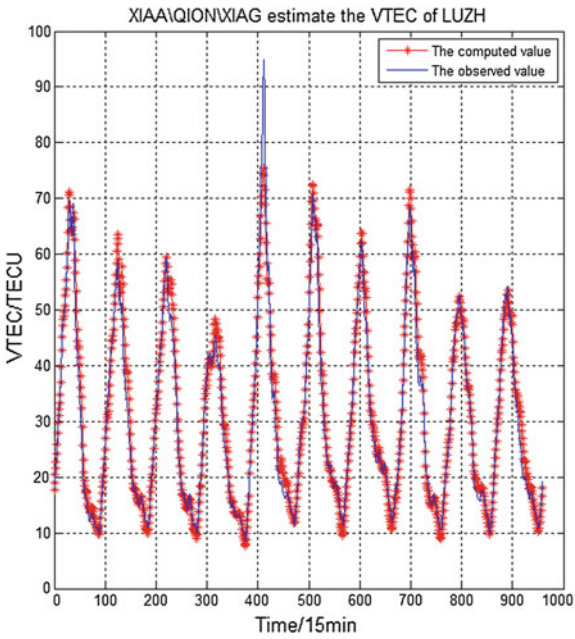

Fig. 33.3 The ionospheric VTEC model calculating results of LUZH station with weight coefficient k = 3

Table 33.1 The statistics of WUHN ionospheric model accuracy using XIAA, SHAO and XIAM (day 100–109 of year 2011)

Coefficient-k	100–90 %	90–80 %	80–70 %	70–60 %	Average percentage (%)	σ/TECU
k = 1/2	0.60	0.26	0.07	0.02	86.39	3.29
k = 1	0.62	0.25	0.06	0.02	86.85	3.18
k = 2	0.66	0.23	0.05	0.01	87.58	3.00
k = 3	0.67	0.22	0.04	0.01	88.09	2.88
k = 4	0.67	0.23	0.04	0.01	88.38	2.81

Table 33.2 The statistics of LUZH ionospheric model accuracy using XIAA, QION and XIAG (day 100–109 of year 2011)

Coefficient-k	100–90 %	90–80 %	80–70 %	70–60 %	Average percentage (%)	σ/TECU
k = 1/2	0.51	0.28	0.13	0.07	87.25	3.77
k = 1	0.59	0.25	0.12	0.03	89.37	3.43
k = 2	0.68	0.25	0.06	0.05	92.10	2.99
k = 3	0.74	0.23	0.03	0.00	93.14	2.80
k = 4	0.77	0.20	0.02	0.00	93.36	2.73

33.4 Comparison with the Grid Model

In order to make comparison between triangular partition method and grid model method, calculating the zenith directions ionospheric VTEC and ionospheric delay error correction accuracy of WUHN and LUZH two stations respectively by using the grid model method and triangular partition model method.

(1) Network layout of triangular partition and grid model (Fig. 33.4)
(2) Precision contrast analysis of the two models

The grid point data sources of Grid model: IGS data processing center CODE use the dual-frequency observation data of IGS tracking station distribution in global to calculate ionosphere TEC distribution around the world, and given in the form of daily IONEX file, starting from the everyday UTC time 0–24, a global ionospheric TEC figure can be got in every 2 h, a total of 13 pieces. The ionosphere TEC data of IGS is provided every 2 h on time, longitude direction every 5°, 2.5° latitude direction. For convenience of analysis, according to the partition of IGS website and the given grid ionosphere data, this article divided the ionosphere reference plane into the same grids. About the calculation method of grid model can reference [5, 6].

Benchmark data sources of triangular partition model: The ionosphere measured data of several stations in crustal movement observation network of China, the data interval is 15 min.

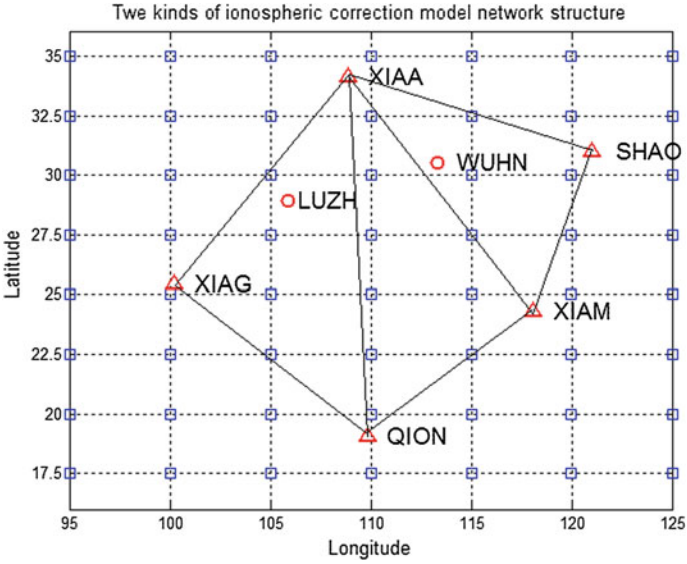

Fig. 33.4 Network test architecture of triangular partition method and grid model

Experiment also use the data in day 100–109 of 2011, a total of 10 days. Through the above two kinds of VTEC ionospheric data this paper compares and analyzes the mode precision validation of grid and the triangular partition, the data contrast sampling interval is 2 h. Figures 33.5 and 33.6 are the two models calculated results of WUHN and LUZH stations (Table 33.3).

Triangular partition method is proposed in order to solve the wide-area ionospheric correction accurately due to the characteristics of China's topography distribution, which is difficult to establish a wide-area of ionospheric grid model. Data analysis showed that triangular partition method can effectively solve the problem of the ionosphere modeling in irregular area.

Triangular partition model accuracy is significantly higher than the Klobuchar model, even if compared with the grid ionosphere model, wide-area ionospheric delay correction method of triangular partition has its significant advantages. It does not need to divide the ionosphere reference plane into a large number of grid cells, reducing the computational complexity. According to the distribution of ionospheric monitoring stations, the coverage area is divided into several triangular partitions; The service scope of a triangular partition is several times of a grid service scope, reducing switching frequency of regional service transition. Compared with the triangular partition method, the precision of the grid model are more closely linked with the distribution of the base stations. For users of triangular partition, the ionosphere calculating reference point is located at monitoring stations zenith, higher calculating precision; And for grid model the user's reference point is located in a virtual grid points, the basic value of which is also obtained by

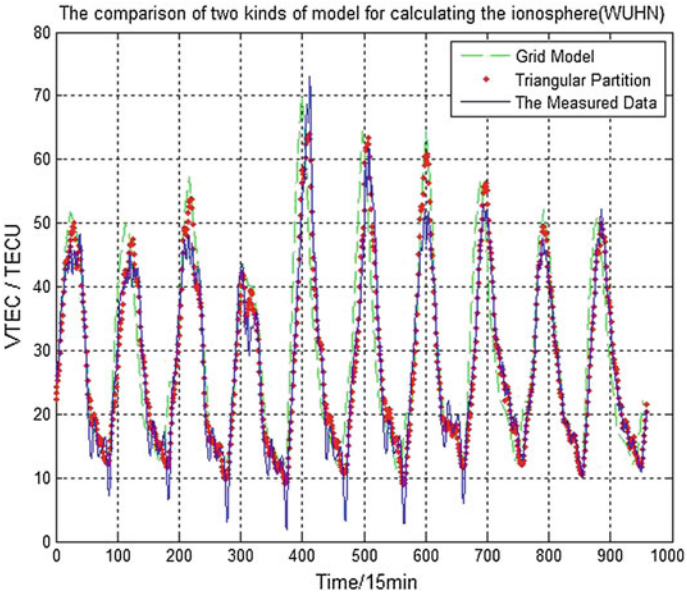

Fig. 33.5 Precision comparison of the two models in WUHN station

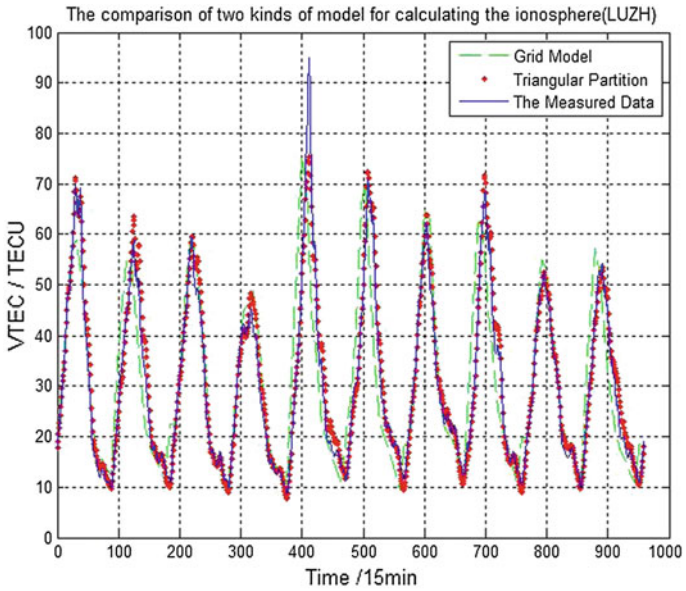

Fig. 33.6 Precision comparison of the two models in LUZH station

Table 33.3 The precision statistics of triangular partition and grid model

Percentage of correction	WUHN		LUZH	
	Grid mode	Triangular partition mode	Grid mode	Triangular partition mode
100–90 %	0.31	0.67	0.34	0.74
90–80 %	0.32	0.22	0.31	0.23
80–70 %	0.15	0.04	0.15	0.03
70–60 %	0.08	0.01	0.09	0.00
Average percentage of correction	75.78 %	88.09 %	80.12 %	93.14 %
Standard deviation	7.07	2.88	7.59	2.80

interpolation, but there is a strong correlation between the reference value and the number of puncture points in the four grids of its surroundings, because satellites are doing high-speed movement, and is affected by the distribution of the base stations, it is difficult to ensure that all grids have ionosphere puncture points at the same time, so it is difficult to ensure the accuracy of the grid nodes all the time.

33.5 Conclusion

A large number of examples analysis prove that: at the same time of guarantee the accuracy of model, the wide-area ionospheric correction triangular partition method can realize sparse network partition, reduce the load of navigation message, and is more simple and effective than grid model. Wide area differential system is a highly efficient, low cost differential positioning method. Because of that, many countries and regions research the new wide-area difference method and many WAAS are successively set up. Triangular partition method is not only improved obviously to the mid-latitude ionospheric error, but also is superior to grid model in low latitudes, which has important reference value to ionospheric delay error correction of beidou navigation system.

Acknowledgments This paper is supported by: The 863-plan Major Program (2012AA01A509); The National Natural Science Funds(61263028); The Guangxi Natural Science Fund (2012GXNSFDA053027) ; The Open Fund of Key Laboratory of Time & Frequency Primary Standards, CAS(Y000YR1S01); The Guangxi Wireless Broadband Key Laboratory Fund (GXKL0614107).

References

1. Kumar R, Munjal P (1997) Ionospheric modeling for WAAS. In: Proceedings of annual meeting institute of navigation, pp 431–439
2. Yang Z, Song SL, Xue JC et al (2012) Accuracy assessment of klobuchar model and NeQuick model in China. Geomat Inf Sci Wuhan Univ 37(6):704–708
3. Fan G, Wang W, Xi X et al (2010) Modeling of Ionosphere VTEC using generalized regression neural network. Acta Geodaetica Cartogr Sin 39(1):16–21
4. Li Q, Ning B-Q, Zhao B-Q et al (2012) Applications of the CMONOC based GNSS data in monitoring and investigation of ionospheric space weather. Chin J Geophys 55(7):2193–2202
5. Chao YC, Tsai YJ (1996) Generation of ionospheric correction and confidence estimates for WAAS. In: Institute of navigation, eds, proceeding of the ION annual technical meeting, Massachusetts, Cambridge, pp 139–146
6. Wang G, Wei Z (2000) A method and resulits of setting up grid ionospheric delay model. Bull Survey Mapp 9:1–2

Chapter 34
Analysis of Positioning Performance on Combined BDS/GPS/GLONASS

Xiaosan Man, Fuping Sun, Shuai Liu, Haifeng Li and He Ding

Abstract When single satellite navigation system be used for single point positioning, existing following problem: numbers of visible satellite are low and accuracy of positioning is low. This paper studies the model combination of BDS/GPS/GLONASS system of single point positioning, and a scheme of combined weighting is put forward. The characteristic of combined weight-method is that inside of system adopts elevation to determine weight-value, the inter-system adopts Helmert-Variance to determine weight-value. The experimental results show that the number of visible satellite of combination of BDS/GPS/GLONASS system are than any single-system, and the number of satellites are greatly increasing, and significantly improve user-satellite geometry, and greatly improve accuracy of positioning. Positioning performance of combined weighting is superior to the traditional weighting.

Keywords Single point position · Position of combined BDS/GPS/GLONASS · Combined weight · Accuracy

34.1 Introduction

As the modernization of GPS, the recovery of Russian GLONASS, the developing of Europe's Galileo as well as our country independent research and develop DeiDou satellite navigation system (BDS), which are gradually developing from regional satellite navigation system to the global satellite navigation system [1]. In the future, the air will become four system running at time, the number of satellites are greatly increasing, providing more stable, reliable and accurate services of navigation and positioning for global users.

X. Man (✉) · F. Sun · S. Liu · H. Li · H. Ding
College of Navigation and Aerospace Engineering, Information Engineering University, Zhengzhou 450001, China
e-mail: manxiaos@126.com

J. Sun et al. (eds.), *China Satellite Navigation Conference (CSNC) 2015 Proceedings: Volume II*, Lecture Notes in Electrical Engineering 341,
DOI 10.1007/978-3-662-46635-3_34

Owing to single-system existing problems of limited number of satellites, limited of positioning precision and lower reliability. Especially when the receiver is located in areas where are often less than four visible satellites, and lead to users can't make navigation and positioning such as in the urban-canyon environment. With improved of satellites navigation system and application unceasingly, the combination of Multi-system will increase number of available satellites, improve user-satellite geometry, which will greatly improve accuracy and reliability of the navigation and positioning. As a result, the combined Multi-system will necessarily be developed trend.

At present, a lot of literature about positioning performance of combination of two systems are analyzed, such as: GPS/GLONASS, GPS/Galileo, GPS/BDS [2–5], but combination of three-system is relatively less. Wu et al. [6] who investigate combined GPS/GLONASS/GALILEO positioning algorithm, and the result shows that combined system can improve positioning accuracy by simulation; He et al. [7] who investigate combined single point positioning of GPS/BDS/GLONASS, and the study shows that the weight-ratio between GPS, BDS and GLONASS was about 1:0.8:0.8.

This paper derived the combined BDS/GPS/GLONASS observation equations and mathematical model, and propose a set of combined weighting scheme. The combined BDS/GPS/GLONASS positioning performance are evaluated by positioning accuracy and GDOP value.

34.2 Mathematical Model

34.2.1 Observation Equations

The observation equations of the pseudorange for BDS, GPS and GLONASS can be expressed as:

$$P_B = \rho + c\left(\delta t_{r,B} - \delta t^s\right) + I_{ion} + T_{trop} + M_{multi} + \varepsilon_{p_B} \tag{34.1}$$

$$P_G = \rho + c\left(\delta t_{r,G} - \delta t^s\right) + I_{ion} + T_{trop} + M_{multi} + \varepsilon_{P_G} \tag{34.2}$$

$$P_R = \rho + c\left(\delta t_{r,R} - \delta t^s\right) + I_{ion} + T_{trop} + M_{multi} + \varepsilon_{P_R} \tag{34.3}$$

where B, G and R is respectively stand for BeiDou, GPS and GLONASS, P is the pseudorange measurement, ρ is the geometric range between satellite and receiver, $\delta t_{r,B}$, $\delta t_{r,G}$ and $\delta t_{r,R}$ is respectively receiver clock error of BDS, GPS and GLONASS in unit of seconds. c is the speed of light, I_{ion} and T_{trop} is respectively ionospheric delay and tropospheric delay, M_{multi} is multipath error in pseudorange, ε_p is receiver code noise in meters. Equations (34.1)–(34.3) can unify be expressed as:

$$P_{r,i}^{s} = \rho_r^s + c\left(\delta t_{r,i} - \delta t^s\right) + I_{ion} + T_{trop} + M_{multi} + \varepsilon_{P_{r,i}^s} \tag{34.4}$$

where r and s is respectively receivers and satellites, i is stand for satellite system (B for BeiDou, G for GPS, R for GLONASS).

The geometric range between satellite and receiver P can be expressed as:

$$\rho_r^s = \sqrt{(x^s - x_r)^2 + (y^s - y_r)^2 + (z^s - z_r)^2} \tag{34.5}$$

where (x^s, y^s, z^s) is known three-dimensional coordinate of satellites, (x_r, y_r, z_r) is unknown three-dimensional coordinate of receivers.

The one row in design matrix H can be expressed as:

$$\left[\frac{x^s - x_r}{\rho}, \frac{y^s - y_r}{\rho}, \frac{z^s - z_r}{\rho}, 1\right] \tag{34.6}$$

Let

$$\eta_{ij}(\cdot) = \frac{(\cdot)_{ij}^s - (\cdot)_r}{\rho_{ij}}$$

and the design matrix H can be expressed as:

$$H = \left[\eta_{ij}x_r, \eta_{ij}y_r, \eta_{ij}z_r, 1\right] \tag{34.7}$$

where i and j is stand for system and No. satellite.

34.2.2 Combined BDS/GPS/GLONASS Observation Equations

Owing to BDS, GPS and GLONASS system based on difference between coordinate system and time system. Therefore, when combined system is used to position, it is necessary to consider the unify of system of time-space.

The BDS adopts the China Geodetic Coordinate System 2000 (CGCS2000), GPS adopts the World Geodetic System 1984 (WGS 84) as reference coordinate system (ISGPS-200G 2012), and GLONASS uses PZ-90.02 as system reference frame (GLONASSICD 2008). The reference time for the BeiDou system is BeiDou Time (BDT) which is a continuous time without leap seconds. The start epoch of BDT was at 00:00:00 on 1st January 2006 UTC. The GPS system uses the GPS time (GPST) standard which is a continuous time without leap seconds. The start epoch of GPST was at 00:00:00 on 6st January 1986 UTC. GLONASS adopts GLONASS time (GLONASST) as reference time which is based on the National Time Scale of

Russian Federation, UTC (SU), with integer second corrections. The differences between the UTC and the local representations of UTC are illustrated in Fig. 34.1 [8].

As to the problem of unify of time system about combined BDS/GPS/GLONASS, which can be classified as two case:

(1) when each of the system clock error are estimated at the receiver at each epoch, therefor the estimated parameters are from four into six for combined system, the estimated states vector can thus be written as: $X = \left[x_r, y_r, z_r, \delta t_B, \delta t_G, \delta t_R\right]$, x_r, y_r, z_r is respectively three-dimensional coordinate of receivers, δt_B, δt_G, δt_R is receiver clock error of BDS, GPS and GLONASS. Hence, the design matrix H can be written as:

$$H = \begin{bmatrix} \eta_{B1}x_r & \eta_{B1}y_r & \eta_{B1}z_z & 1 & 0 & 0 \\ \vdots & \vdots & \vdots & \vdots & \vdots & \vdots \\ \eta_{Bl}x_r & \eta_{Bl}y_r & \eta_{Bl}z_r & 1 & 0 & 0 \\ \eta_{G1}x_r & \eta_{G1}y_r & \eta_{G1}z_r & 0 & 1 & 0 \\ \vdots & \vdots & \vdots & \vdots & \vdots & \vdots \\ \eta_{Gm}x_r & \eta_{Gm}y_r & \eta_{Gm}z_r & 0 & 1 & 0 \\ \eta_{R1}x_r & \eta_{R1}y_r & \eta_{R1}z_r & 0 & 0 & 1 \\ \vdots & \vdots & \vdots & \vdots & \vdots & \vdots \\ \eta_{Rn}x_r & \eta_{Rn}y_r & \eta_{Rn}z_r & 0 & 0 & 1 \end{bmatrix}$$

where l, m and n is respectively lth, mth and nth satellite of corresponding system.

(2) Each of time of system be unify to GPS time system, the estimated parameters are from four into six for combined system, the estimated states vector can thus be written as: $X = \left[x_r, y_r, z_r, \delta t_{r,G}, \Delta t_{B-G}, \Delta t_{R-G}\right]$, x_r, y_r, z_r is respectively three-dimensional coordinate of receivers, $\delta t_{r,G}$, Δt_{B-G}, Δt_{R-G} is respectively receiver clock error of GPS, clock-offset of between BDS and GPS, and clock-offset of between GLONASS and GPS. Hence, the design matrix H can be written as:

$$H = \begin{bmatrix} \eta_{G1}x_r & \eta_{G1}y_r & \eta_{G1}z_z & 1 & 0 & 0 \\ \vdots & \vdots & \vdots & \vdots & \vdots & \vdots \\ \eta_{Gm}x_r & \eta_{Gm}y_r & \eta_{Gm}z_r & 1 & 0 & 0 \\ \eta_{B1}x_r & \eta_{B1}y_r & \eta_{B1}z_r & 1 & 1 & 0 \\ \vdots & \vdots & \vdots & \vdots & \vdots & \vdots \\ \eta_{Bl}x_r & \eta_{Bl}y_r & \eta_{Bl}z_r & 1 & 1 & 0 \\ \eta_{R1}x_r & \eta_{R1}y_r & \eta_{R1}z_r & 1 & 0 & 1 \\ \vdots & \vdots & \vdots & \vdots & \vdots & \vdots \\ \eta_{Rn}x_r & \eta_{Rn}y_r & \eta_{Rn}z_r & 1 & 0 & 1 \end{bmatrix}$$

In this paper, the unified method of system time of combined BDS/GPS/GLONASS adopt second case. Supposed observed numbers of satellite for BDS,

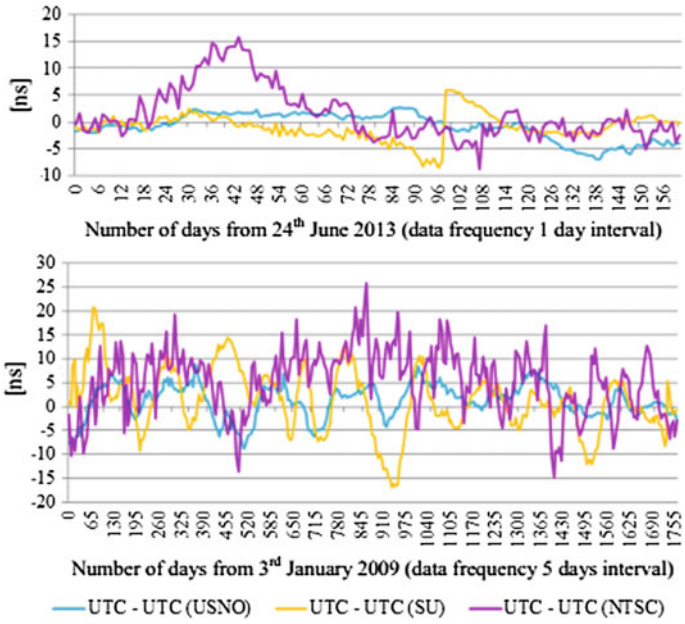

Fig. 34.1 The short term (*top*) and long term (*bottom*) difference between UTC and local representation of UTC

GPS and GLONASS are respectively l, m and n, the number of observation equations are $l + m + n$; unknown parameters are $X = [x_r, y_r, z_r, \delta t_{r,G}, \Delta t_{B-G}, \Delta t_{R-G}]$, then the degrees of freedom of equation are $(l + m + n - 6)$, BDS/GPS/GLONASS combined system linearized observation equation can be written as:

$$V = HX - l \tag{34.8}$$

where the weight-matrix is P, unknown parameters can be obtained through LS solution.

$$X = \left(H^T PH\right)^{-1} H^T Pl \tag{34.9}$$

34.3 Scheme of Determination to Weight

34.3.1 Elevation Weighting

Elevation angle of visible satellite can indirectly reflect the precision of observations, which can be used to determine weight-value of observations. In data processing, if the satellite elevation angle of observations is less than cut-off angle, this

observation will be deleted. The exponential elevation weighting function can be written as [9]:

$$P_{i,j} = \frac{\delta_0}{\sin E} \tag{34.10}$$

where i and j is respectively represented for No. system and No. satellite, E represents elevation.

34.3.2 Combined Weighting

When combined system are used to position, owing to inter-system existing difference, different systems have different URA (user range accuracy), and systematic error of satellites also are difference, but when single-system is used to position, without difference of inter-system. Therefore, when combined multi-system is used to position, we need to adopt a reasonably weight-method. This paper propose a combined weight-method, which adopts elevation angle to determine weight-value in the inside-system, and adopts Helmert-Variance to determine weight-value in the inter-system.

Due to observation of each system being independent, the combined BDS/GPS/GLONASS system is used to position, weight-matrix can be expressed as: P_B, P_G and P_R which are adopt elevation angle to determine weight-value. Based on literature [10] derived, Helmert variance can be expressed as:

$$\hat{\theta} = S^{-1} W_\theta \tag{34.11}$$

where S and W_θ can respectively be written as:

$$S = \begin{bmatrix} l - 2tr(N^{-1}N^B) + tr(N^{-1}N^B)^2 & tr(N^{-1}N^B N^{-1}N^G) & tr(N^{-1}N^B N^{-1}N^R) \\ tr(N^{-1}N^B N^{-1}N^G) & m - 2tr(N^{-1}N^G) + tr(N^{-1}N^G)^2 & tr(N^{-1}N^B N^{-1}N^R) \\ tr(N^{-1}N^B N^{-1}N^R) & tr(N^{-1}N^B N^{-1}N^R) & n - 2tr(N^{-1}N^R) + tr(N^{-1}N^R)^2 \end{bmatrix}$$

$$W_\theta = \begin{bmatrix} V_B P_B (V_B)^T & V_G P_G (V_G)^T & V_R P_R (V_R)^T \end{bmatrix}$$

where $\hat{\theta} = \left[\sigma_{0,B}^2, \sigma_{0,G}^2, \sigma_{0,R}^2\right]$ is the variance of unit weight for BDS, GPS and GLOANSS. The observation of each of system need to adopt $\hat{\theta}$ to determinate weight-value, unknown parameters are obtained through LS solution.

34.4 Experiment Analysis

Experimental data were collected by GPS/GLONASS/BDS three-system compatible receiver, which collected a set of eight-frequency data of three systems. The measurement interval is set to 1 s. First of all, the paper analyzes visible of satellites for an elevation angle of 15°. Secondly, in order to analyzes combined weight-method in the performance of combined positioning. Adopting following two solutions, (1) elevation weight-method; (2) the combined weight-method. Finally, in the following examples adopt combined weight-method. In order to analyze the performance of combined BDS/GPS/GLONASS positioning, following seven scheme were contrasted to analyze. (1) BDS; (2) GPS; (3) GLONASS (4) BDS+GPS; (5) BDS +GLONASS; (6) GPS+GLONASS; (7) BDS+GPS+GLONASS.

When the elevation cut-off angle is set to 15°, compared to between single-system and two-system, number of visible satellites of combined BDS/GPS/GLONASS system be obvious more at the same epoch (Fig. 34.2). In order to make sure number of satellites that are used to position, especially at the urban-canyon environment, provide the possible of continual positioning. Hence, in term of number of satellites, the combined BDS/GPS/GLONASS satellite navigation exceeds between single-system and combination of two-system.

Figures 34.3 and 34.4 show that the trends of results of combined weight-method keep with elevation weighting, which illustrate the correctness of combined weight-method. The STD and RMS value of two scheme in X, Y and Z, seen from Table 34.1, the accuracy of result of combined weight-method is higher than elevation weighting. Therefore, the combined weight-method exceed elevation weighting.

Figures 34.5, 34.6 and 34.7 are given positioning accuracy of various scheme in X, Y and Z. Table 34.2 shows the STD and RMS value of various scheme in X, Y and Z. Through Figs. 34.5, 34.6 and 34.7 and Table 34.2, it is easy to see positioning accuracy of scheme 7 which is better than other scheme. Positioning accuracy of scheme 3 is worst, which reach 20–30 m at times. By Fig. 34.4, we can

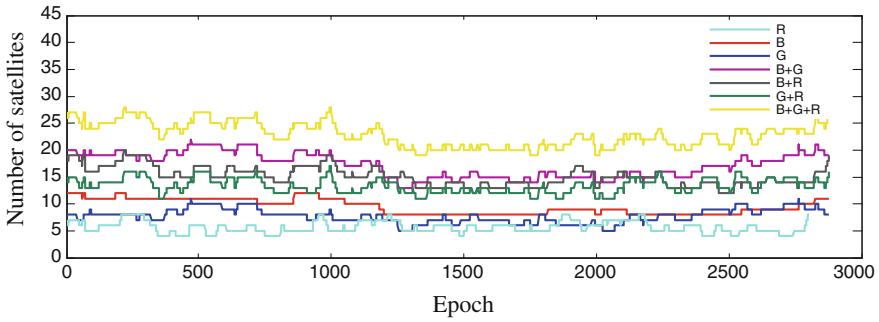

Fig. 34.2 Seven scheme satellite visibility at the epoch of observation with an elevation cut-off angle of 15° (B for BDS, G for GPS and R for GLONASS)

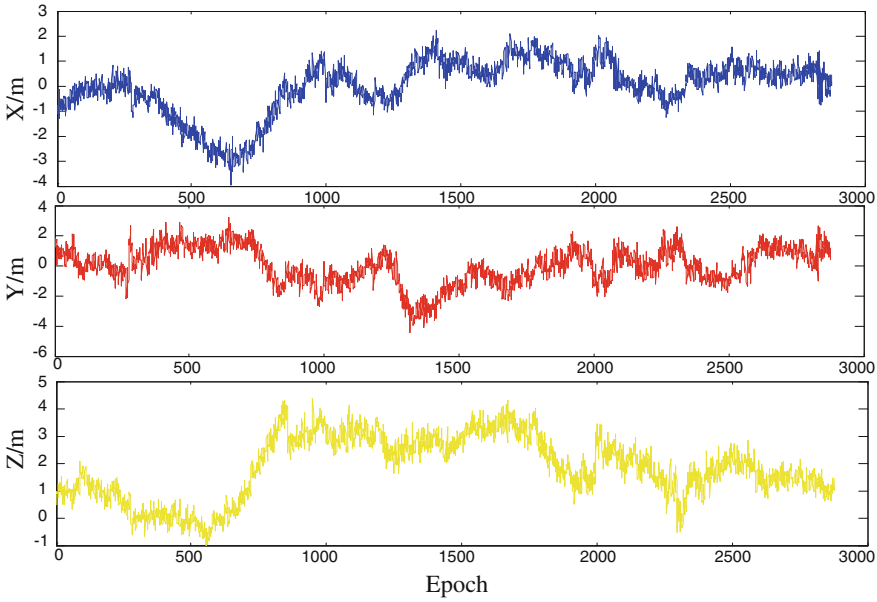

Fig. 34.3 Combined weight-method

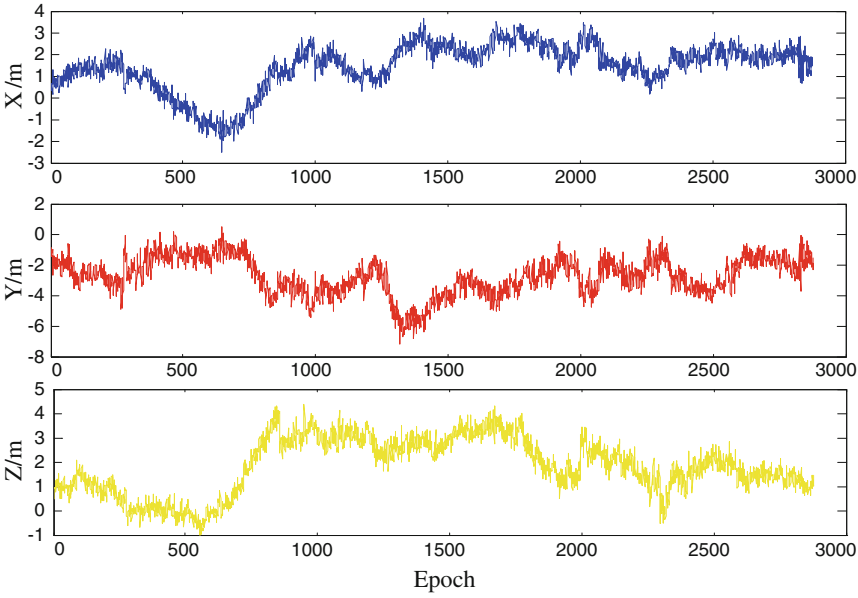

Fig. 34.4 Elevation weighting-method

Table 34.1 STDs and RMSs for combined weight and elevation weight in X, Y and Z

	STD			RMS		
	X/m	Y/m	Z/m	X/m	Y/m	Z/m
Combined weighting	0.7610	0.6686	1.6777	0.7618	0.6708	2.9441
Elevation weighting	0.8896	0.8321	1.8512	0.8791	0.8122	4.1509

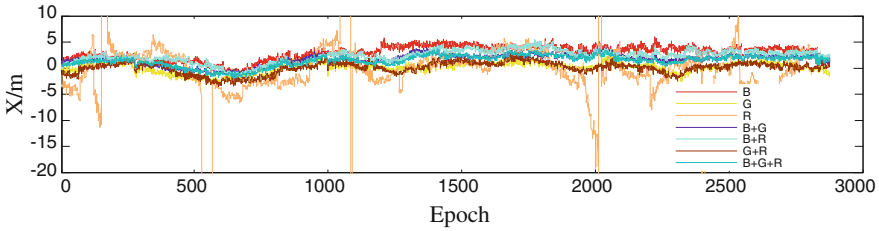

Fig. 34.5 Seven scheme positioning results in X

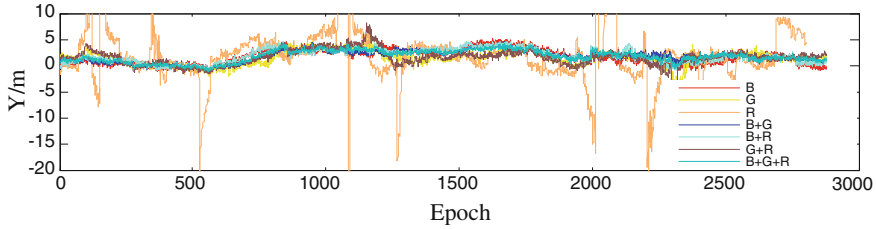

Fig. 34.6 Seven scheme positioning results in Y

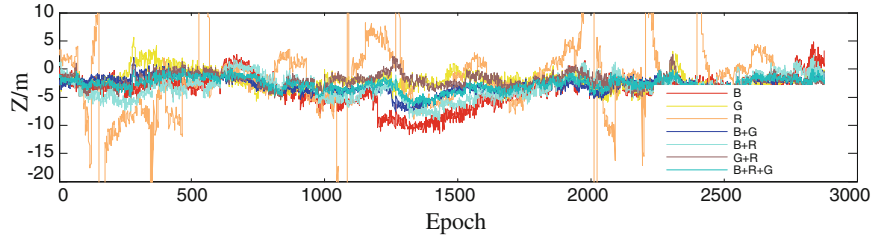

Fig. 34.7 Seven scheme positioning results in Z

see number of visible satellites that is only 4–5 at that periods, and Fig. 34.8 shows the GDOP value of scheme 3, and the GDOP value reach 10 or more in period which arise a large error in Figs. 34.5, 34.6 and 34.7. Therefore, the user-satellite geometry is relatively poor in this period.

Figure 34.8 shows GDOP value of seven scheme, we can clearly find GDOP value of scheme 7 that exceed other scheme, which GDOP value is less than 2. The

Table 34.2 STDs and RMSs of seven scheme in X, Y and Z

Scheme	X	Y	Z	X	Y	Z
	STD(m)			RMS(m)		
B	1.0677	1.2748	2.9411	1.0971	1.3884	5.6541
G	0.8182	0.8727	2.0618	0.9553	0.9021	2.0314
R	3.4117	2.8957	11.6980	3.6722	2.9238	12.8939
B+G	0.7614	0.6062	1.9318	0.8189	0.6882	2.4484
B+R	1.0419	1.1743	2.2681	1.0472	1.2474	5.7951
G+R	0.8622	0.9947	1.7361	0.8620	1.0684	2.1513
B+G+R	0.7610	0.6686	1.6777	0.7618	0.6708	2.9441

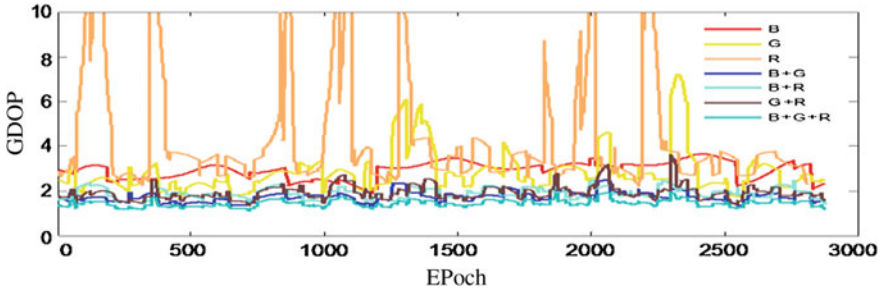

Fig. 34.8 GDOP of seven scheme

GDOP value of scheme 3 is worst, which reach 10 or more at same times. It is indirectly illustrated that positioning accuracy of combined three-system is better than single system or combined two-system.

34.5 Conclusions

In this paper, we investigate combined BDS/GPS/GLONASS positioning mathematical, and propose a kind of combined weight-method. On this basis, we analyze positioning performance of combined BDS/GPS/GLOANSS by compared to single system or combined two-system, and the following conclusions are obtained: (1) when combined BDS/GPS/GLONASS is used to position, number of visible satellites multiply increased, user-satellite geometry greatly improved, GDOP value is less than 2; (2) reasonable weight-value can improve accuracy of positioning at the combined system, and proposed combined weight-method in this paper is correct, which is better than traditional weight-method; (3) the positioning accuracy of combined BDS/GPS/GLONASS is better than single system or combined two-system.

References

1. Ning J, Yao Y (2013) The development review of GNSS. J Navig Position 1:3–8
2. Cai C, Dai W, Kuang C (2011) Accuracy assessment of combined single-frequency GPS/GLONASS single point positioning. J Geodesy Geodyn 3:85–89
3. Duan J, Shen Y (2011) GPS/GLONASS combined point positioning using variance component estimation. Bull Surv Mapp 4:4–6
4. Fan L, Zhong S, Ou J (2013) Precision analysis of standard point positioning by compass and GPS observation. In: The 4th China satellite navigation conference
5. Gao X, Ge M (1999) The data processing of GPS/GLONASS single point positioning. Bull Surv Mapp 4:8–9
6. Wu L, Sun Y (2009) Research on GPS/GLONASS/GALILEO multi-constellation integrated navigation system. Chin Space Sci Technol 3:23–28
7. He J, Yuan X (2014) Study on GPS/BDS/GLONASS combined single point positioning. Sci Surv Mapp 39:124–128
8. Rasika W (2013) Four-constellation GNSS reliability and the estimation of inter-system time-offsets for improved performance in challenging signal environments. University of Calgary
9. Lv J (2014) Research on GPS/BDS precision relative positioning technology. PLA Information Engineering University
10. Huang W (1992) Modern adjustment theory and application. The People's Liberation Army Press, Beijing

Chapter 35
A Real-Time Prediction Algorithm of BDS Satellite Clock Offset Considering Phase Jumps

Wenju Fu, Qin Zhang, Meng Ao, Guanwen Huang and Hairong Guo

Abstract On the basis of BDS satellite clock Offset phase jump models, the paper analyses characteristics of phase jumps of satellite clocks on orbit, and deduces detection methods of phase jumps, and then builds the prediction models of BDS satellite clock offsets considering corrections of starting point bias and periodic terms, and lastly obtains a real-time prediction algorithm of BDS satellite clock offsets considering phase jumps. For BDS satellite clock offsets with phase jumps, numerical examples show that the real-time prediction precision of new algorithm is superior to the traditional algorithm. Through analyzing BDS satellite clock real-time prediction precision of 322 days, it shows that the average prediction precisions of 24 and 6 h are 7.9 and 2.3 ns respectively.

Keywords BDS · Satellite clock · Clock offset prediction · Phase jump

35.1 Introduction

There have been many research results on prediction models of satellite clock offsets. In order to predict satellite clock offsets precisely, it usually selects different polynomial models for satellite clocks of different types [1]. Because the frequency drift of Rb clock has more significant than Cs clock, the former often adopts quadratic polynomial model to predict satellite clock offsets while the latter adopts linear

W. Fu (✉) · Q. Zhang · M. Ao · G. Huang
School of Geology Engineering and Geomatics, Chang'an University,
No.126, Yanta Road, Xi'an, China
e-mail: fuwenju2009@163.com

Q. Zhang
e-mail: zhangqinle@263.net.cn

H. Guo
Beijing Satellite Navigation Center, 100094 Beijing, China

J. Sun et al. (eds.), *China Satellite Navigation Conference (CSNC) 2015 Proceedings: Volume II*, Lecture Notes in Electrical Engineering 341,
DOI 10.1007/978-3-662-46635-3_35

model. In addition, selecting the order of the polynomial models automatically and considering periodic terms and the start point bias term can improve the prediction precision of satellite clock offsets furtherly [2–4].

However, during the long running process of the satellite clock, grosses and data interruptions as well as phase jumps often occur in the influence of satellite clock performance and space environments [5–9]. Especially in the real-time satellite clock offsets estimation, the change of the base clock will probably cause phase jumps of real-time satellite clock offsets. Because the traditional prediction model using moving windows can't resist abnormal clock jumps, a new real-time clock offset prediction algorithm considering phase jumps will have more advantages in order to get reliable results.

Now, BDS has provided continuous navigation positioning and timing services to china and surrounding areas. And BDS has 14 satellite clocks on orbit including 1–5 GEO satellite clocks, 6–10 IGSO satellite clocks and 11–14 MEO satellite clocks [10, 11]. Meanwhile, the analysis centres of the international GNSS Monitoring and Assessment System (iGMAS) also have provided BDS ultra-rapid orbit and clock products [12, 13]. In order to improve BDS real-time PPP precision, the real-time estimation and prediction of satellite clock offsets are necessary [14]. Therefore, the paper analyses BDS satellite clock Offset phase jump models, builds a real-time BDS satellite clock offset prediction algorithm considering phase jumps and assesses real-time prediction performance of BDS satellite clock offsets on orbit.

35.2 The Mathematic Model of Phase Jumps

When phase jumps happen, a constant offset is brought in the satellite clock offset sequence. However, the frequency and frequency drift sequence are not changed. Therefore, the mathematic model describing the satellite clock offset phase jumps can be expressed as:

$$y(t) = \begin{cases} a_0 + a_1 \cdot t + a_2 \cdot t^2 + \varepsilon & t < t_0 \\ a_0' + a_1 \cdot t + a_2 \cdot t^2 + \varepsilon & t \geq t_0 \end{cases} \tag{35.1}$$

where t is the time variable; $y(t)$ is the clock offset; t_0 denotes the moment of the phase jump; a_0 represents the phase before the phase jump and a_0' represents the phase after the phase jump; a_1 is the frequency; a_2 is frequency drift; ε is the clock offset noise.

From the above model, we can know that the clock offset sequence changes smoothly before or after the phase jump and its magnitude is greater than other time. When phase jumps happen, the fitting precision adopting polynomial model is poor. Therefore, in order to get the stable and reliable prediction clock offsets, a real-time prediction algorithm of BDS satellite clock offset considering phase jumps is meaningful.

35.3 The Prediction Model of BDS Satellite Clock Offset Considering Phase Jumps

Based on the mathematic model of phase jumps, through selecting the quadratic term parameter automatically by comparing the standard deviation of the fitting residuals, determining a few prominent periodic terms and start point bias corrections, choosing the weight function of observations according to the distance from the starting epoch to the prediction epoch, the new prediction model of BDS satellite clock offset can be obtained.

$$y(t) = \begin{cases} a_0 + \Delta a_0 + a_1 \cdot t + \beta \cdot 0.5 \cdot a_2^2 + \sum_{l=0}^{k} A_l \cdot \sin(\omega_l + \phi_l) + \varepsilon & t < t_0 \\ a_0' + \Delta a_0 + a_1 \cdot t + \beta \cdot 0.5 \cdot a_2^2 + \sum_{l=0}^{k} A_l \cdot \sin(\omega_l \cdot t + \phi_l) + \varepsilon & t \geq t_0 \end{cases} \tag{35.2}$$

where Δa_0 is the start point bias correction; β is 0 or 1 (When the standard deviation of the fitting residuals of the linear model is less than the quadratic polynomial model, β is 0; If not, β is 1); A_l, ω_l, $_l$ is the amplitude, angular velocity and phase of the periodic term respectively; Other parameters is the same as formula (35.1).

The above clock offset prediction model cannot confirm the moment phase jumps happen although it is no longer impacted by phase jumps. Therefore, on the basis of the prediction model of BDS satellite clock offsets considering phase jumps, building a real-time algorithm of BDS satellite offsets detecting phase jumps is very important.

35.4 The Real-Time Prediction Algorithm of BDS Satellite Clock Offset Considering Phase Jumps

Based on characteristics of BDS satellite clock phase jumps, the new algorithm uses the fitting precision to judge whether the phase jumps happen or not, and uses the data before and after the phase jump to position it, and then combines BDS satellite clock prediction model considering the phase jump, adopts the sequential least squares estimator to predict the real-time clock offsets lastly. The algorithm flow is shown as follow (Fig. 35.1).

Firstly, we use phase and frequency data to preprocess clock offset sequence through deleting invalid clock data and getting the clean satellite clock offset sequence. And then we fit the polynomial model, and deduct the periodic terms, and then calculate the fitting precision. If the fitting precision is less than the threshold (5.0 ns), we believe that the phase jump does not happen. However, if the fitting precision is greater than the threshold and the frequency sequence is stable, we also

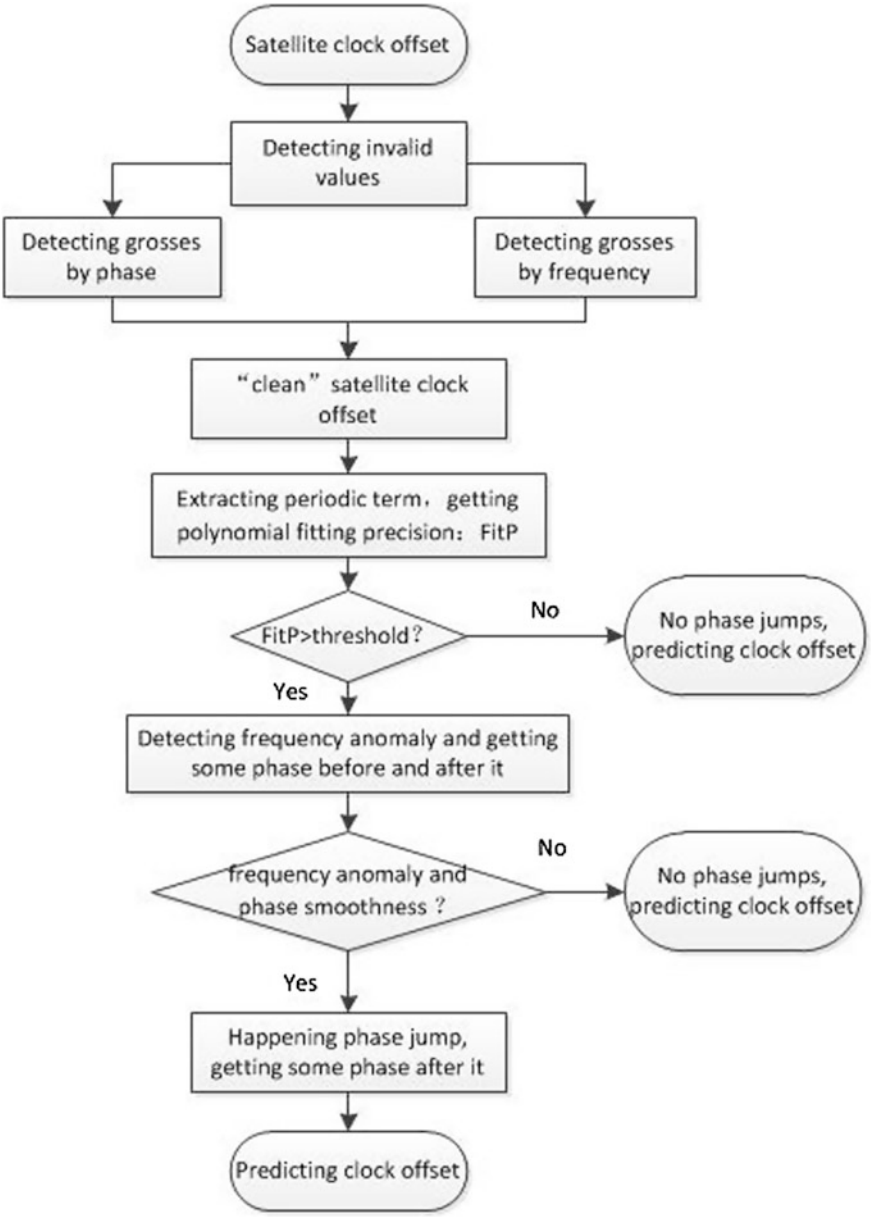

Fig. 35.1 BDS real-time satellite clock prediction algorithm considering phase skips

believe that the phase jump does not happen. In this case, we can predict clock offset directly. If the frequency sequence is not stable, we should position the time of frequency anomaly and use the follow-up data to predict clock offsets, which use moving windows to predict BDS satellite clock offsets continuously.

35.5 Numerical Examples

In order to analysis the feasibility and reliability of the real-time BDS satellite clock offset prediction model considering phase jumps, the experiment data choose BDS final clock offset products of Wuhan University, which totals 322 days lasting from February 13, 2013 to December 31, 2013, and then set moving windows and adopt the real-time satellite clock offset prediction algorithm to predict BDS satellite offsets. Given space limitations, for the clock offset sequence containing jumps, we choose BDS 05 satellite offset data whose phase jump is small in July 20, 2013 to verify BDS satellite offset prediction precision. At last, we evaluate 24 and 6-h real-time prediction precision of BDS 322 days' satellite clock offset sequence.

When BDS real-time satellite clock offsets contain phase jumps, the satellite clock offset sequence fitted by traditional clock offset prediction algorithm cannot describe the varying tendency at the moment of phase jumps. However, the results fitted by the clock offset prediction algorithm considering phase jumps coincide with the real clock offset sequence well. Figures 35.2 and 35.3 use the traditional and new algorithm to obtain BDS 05 satellite offset sequence in case of phase jumps in July 20, 2013 respectively, of which the black line denotes the original clock offset sequence and the red one is the fitting clock offset sequence. The 24-h fitting precision of the traditional algorithm is 19.0 ns while the 24-h fitting precision of the new algorithm is 0.8 ns, which shows that the latter is not affected by phase jumps. During the period of predicting the real-time clock offsets, because manual intervention is forbidden, an algorithm without the influence of phase jumps is very important.

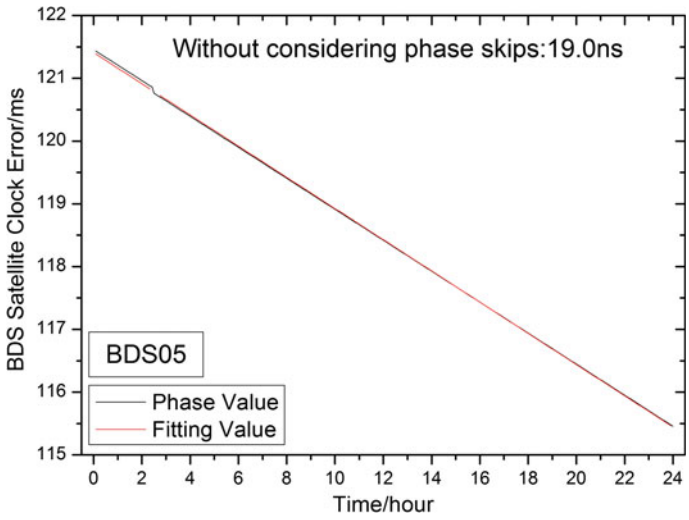

Fig. 35.2 The clock errors fitted by the traditional algorithm of BDS 05 with phase skips

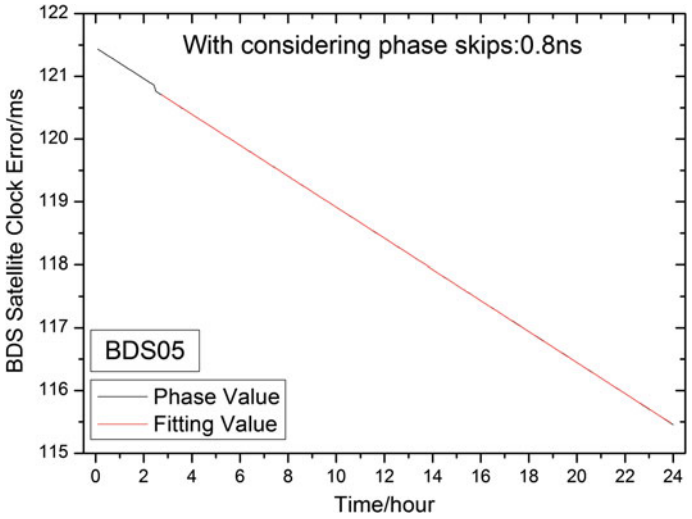

Fig. 35.3 The clock errors fitted by the new algorithm of BDS 05 with phase skips

After obtaining the fitting satellite clock offset prediction model, we use traditional and new algorithm to predict the clock offsets, whose residual sequence is shown as Fig. 35.4. In Fig. 35.4, the red line denotes prediction residuals of the traditional algorithm without considering phase jumps while the black line is prediction residuals of the new algorithm considering phase jumps. It shows that 24-h prediction precision of the new algorithm is 9.3 ns, which is superior to the traditional. The prediction precision of the traditional algorithm is 26.6 ns.

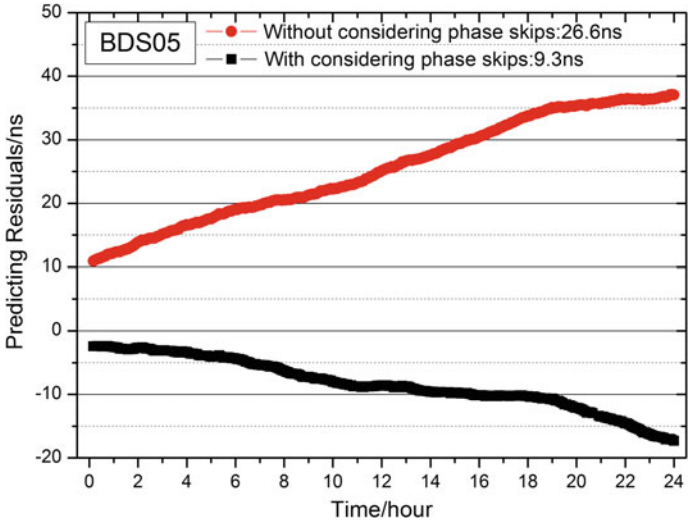

Fig. 35.4 The prediction residuals of BDS 05 with phase skips

In order to verify the stability of real-time BDS satellite clock offset prediction algorithm furtherly, and users are interested in 24 and 6-h satellite clock offset prediction precision because the prediction length and latency period of ultra-rapid clock offset products are 24 and 6 h respectively, the paper evaluates 24 and 6-h real-time prediction precision of 14 BDS satellite clocks, which totals 322 days lasting from February 13, 2013 to December 31, 2013 (Figs. 35.5 and 35.6).

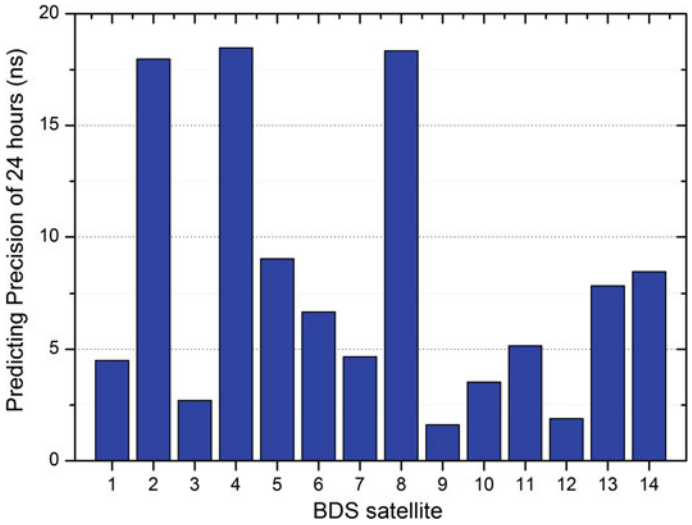

Fig. 35.5 The 24-h prediction precision of BDS satellite clocks

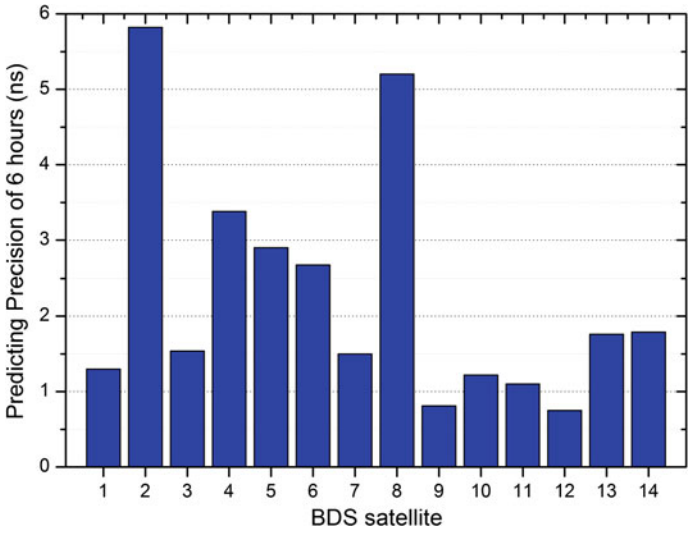

Fig. 35.6 The 6-h prediction precision of BDS satellite clocks

The above figure is the average prediction precision of 322 days, which shows that 24-h prediction precisions of most satellites are less than 10 ns except BDS 02, 04 and 08 while 6-h prediction precisions of all satellites are less than 3 ns. From the average prediction precision of BDS satellite constellation, we can see that 24-h average prediction precision is 7.9 ns and 6-h average prediction precision is 2.3 ns. Therefore, the new algorithm is suited to predict real-time clock offsets.

35.6 Conclusions and Suggestions

Based on mathematical models of phase jumps, the paper analysis the characteristics of phase jumps and then builds the model and algorithm of predicting real-time clock offset considering phase jumps. For BDS satellites on orbit, the new algorithm is better than the traditional satellite clock prediction algorithm when using the new algorithm to predict the clock offsets containing phase jumps. At last, the paper calculates 24 and 6-h prediction precision of BDS satellite clock offsets. Numerical examples show that 24-h prediction precisions of most satellite clocks are less than 10 ns while 6-h prediction precisions of all satellite clocks are less than 3 ns. Moreover, the average prediction precisions of 24 and 6 h are 7.9 and 2.3 ns respectively.

The real-time prediction algorithm of BDS satellite clock offsets considering phase jumps is much more suitable for high-rate BDS satellite clock offsets prediction in the real-time solution. And the short-time, high-precision, real-time, continuous and stable prediction clock offsets contribute to realize the high-precision real-time kinematic PPP. Although the algorithm is feasible and reliable to BDS satellite clock offsets prediction, it will be more meaningful if using it in the solution and prediction of BDS real-time satellite clock offsets, which is the next step of this research work.

Acknowledgments Thanks to BDS satellite clock offset products provided by the analysis center of Wuhan University. This study is supported by the funding of national natural science foundation of china (41104019, 41104022 and 41304033), open foundation of national key laboratory of aerospace dynamics (2013ADL-DW0103), open foundation of national key laboratory of geographic information engineering (SKLGIE2013-Z-2-1), the construction, operation and maintenance of analysis center from the second generation navigation major subject, (GFZX0301040308) and central university basic research funds (2014G1261051).

References

1. Jim R USNO Ultra-rapid clock predictions. http://igscb.jpl.nasa.gov/mail/igsmail/2000/msg00301.html
2. Huang GW, Zhang Q et al (2013) Real-time clock offset prediction with an improved GPS satellite clocks model. GPS Solution. doi:10.1007/s10291-013-0313-0
3. Huang GW, Zhang Q, Li HT et al (2013) Research on quality variation of GPS satellite clocks on-orbit using IGS clock products. Adv Space Res 51:978–987. doi:10.1016/j.asr.2012.09.041

4. Huang G (2012) Research on algorithms of precise clock offset and quality evaluation of GNSS satellite clock. Chang'an University
5. Guo H, Yang Y (2009) Analyses of main error sources on time-domian frequency stability for atomic clocks of navigation satellites. Geomatics Inf Sci Wuhan Univ 34(2):218–221
6. Guo H (2006) Study on the analysis theories and algorithms of the time and frequency characterization for atomic clocks of navigation satellites. Information Engineering University
7. Fu W, Huang G, Zhang Q, Yu H (2013) The analysis of the characterization for GLONASS and GPS on-board satellite clocks. Lecture notes in electronic engineering—China satellite navigation conference 2013 proceedings, March, Wuhan
8. Fu W (2014) Research on prediction and characteristics of GNSS satellite clock on orbit. Chang'an University
9. Niu F, Han C, Zhang Y et al (2009) Analysis and detection on atomic clock anomaly of navigation satellites. Geomatics Inf Sci Wuhan Univ 34(5):585–588
10. Yang YX, Li JL, Xu JY et al (2011) Contribution of the compass satellite navigation system to global PNT users. Chin Sci Bull 56:2813–2819. doi:10.1007/s11434-011-4627-4
11. Zhang S, W Li, Huang G (2010) New challenges and opportunities in GNSS. Geotech Invest Surv 8:49–53
12. Jiao WH, Ding Q, Li JW et al (2011) Monitoring and assessment of GNSS open services (in Chinese). Sci Sin Phys Mech Astron 41:521–527. doi:10.1360/132011-359
13. Su R, Zhang W, Xu A et al (2014) Research on evaluation for global GNSS positioning accuracy with precise analysis center products. CSNC
14. Ge Maorong, Chen Junping, Douša Jan, Gendt Gerd, Wickert Jens (2012) A computationally efficient approach for estimating high-rate satellite clock corrections in realtime. GPS Solutions 16:9–17. doi:10.1007/s10291-011-0206-z

Chapter 36
The Orbit and Clock Combination of iGMAS Analysis Centers and the Analysis of Their Precision

Kangkang Chen, Tianhe Xu, Guo Chen, Jiajing Li and Sumei Yu

Abstract Several analysis centers (AC) and a product integration and service center have been built by the international GNSS continuous Monitoring and Assessment System (iGMAS) currently. Product integration and service center (ISC) analyzes the quality of product provided by analysis centers, and then reprocesses to generate a combined product. The orbit and clock solutions are the vital products of ISC and important foundation data for satellite navigation and precise point positioning (PPP). First of all, this paper introduces the principles, methods and mathematical models of orbit and clock combination. Then, the precision of combined products and analysis centers' products with respect to the IGS final is compared and analyzed. Furthermore, the PPP tests are implemented to verify the accuracy and reliability of combined orbit and clock. The results show that the RMS of combined orbit and clock with respect to referenced solutions is better than the most analysis centers. The static PPP tests prove that the combined orbit/clock consistency is maintained at millimeter level. The standard deviation of single epoch PPP difference using combined orbit/clock is comparable to the best AC orbit/clock solutions.

Keywords iGMAS · Orbit combination · Clock combination · Robust estimation · Precise point positioning

K. Chen (✉) · J. Li · S. Yu
School of Geology Engineering and Geomatics, Chang'an University, Xi'an, Shanxi, China
e-mail: chenkkuser@126.com

T. Xu
State Key Laboratory of Geo-information Engineering, Xi'an, Shanxi, China

T. Xu
State Key Laboratory of Astronautic and Dynamics, Xi'an, Shanxi, China

T. Xu
Xian Research Institute of Surveying and Mapping, Xi'an, Shanxi, China

G. Chen
School of Geodesy and Geomatics, Wuhan University, Wuhan, Hubei, China

J. Sun et al. (eds.), *China Satellite Navigation Conference (CSNC) 2015 Proceedings: Volume II*, Lecture Notes in Electrical Engineering 341,
DOI 10.1007/978-3-662-46635-3_36

36.1 Introduction

Product integration and service center (ISC) is an important part of the international continuous monitoring and assessment system and is also the center of high-precision products reprocessing. Meanwhile it is the window of products distribution center. Currently, all iGMAS analysis centers have submitted the station coordinate, ERPs, satellite orbit and clock errors of GPS, GLONASS, BDS and Galileo to ISC. ISC analyzes the quality of all analysis centers' products on time, and provides the combination products and their precision assessment report at the same time.

The research on orbit and clock combination of analysis centers has a rich source nowadays. Gerhard Beutler and Jan Kouba proposed two schemes of a weighted averaging process of the earth-fixed satellite positions and the individual IGS orbit files as pseudo-observations in an orbit determination process [1]. Tim Springer found that there is significant difference between the orbit coordinate system of individual analysis centers, and gave an appropriate correction method [2]. Jan Kouba et al. introduced the methods of orbit and clock combination used by IGS in detail in the IGS 1994 technical report [3]. Tim Springer discussed the consistency and reliability of combined products, and proposed some measures to enhance the consistency of combined orbit and clock [4]. Jan Kouba introduced an improved approach of IGS station and satellite clock combination [5]. Yao Yibin studied the algorithm of using one-day-arcs to integrate n-day s-arc by the way of orbit overlaying in detail, which can improve the accuracy and continuity of orbit efficiently [6]. Feng Laiping et al. studied a method of combining orbit by robust M estimation and dynamic smoothing [7]. Jake Griffiths corrected the final orbit combining model of the IGS analysis centers [8]. In recent years, the GNSS data processing strategies and models have been significantly improved, especially the introduction of absolute antenna phase center correction, which greatly improved the quality of GNSS scale factor [9, 10]. On the basis of the previous studies, the algorithms of orbit and clock combination are optimized in this paper. The algorithms proposed in this paper are used by the iGMAS product integration and service center. Then the accuracy and reliability of combined products are analyzed and verified in detail.

36.2 The Method and Model of Orbit/Clock Combination

Usually, there is an obviously difference in the coordinate and time reference frame of AC' products. The abnormal values could be found in products of a single analysis center, especially the clock corrections. In order to obtain accurate and reliable combined products, the optimal data processing algorithms and robust estimation methods should be used in product combination. The consistency among integrated products should be taken into account in the orbit and clock combination, which is very important for those users who want to perform precise point

positioning. Therefore, the consistency correction parameters were introduced to the model of product combination. The systematic differences between different analysis centers' products were eliminated prior by unifying the reference frame of orbit and clock solutions. Finally, an appropriate robust estimation method was adopted to resist gross errors, and the combined solutions were obtained through weighted average calculation.

36.2.1 The Method and Model of Orbit Combination

Usually, the tracking station number and distribution of different ACs are not the same on the GNSS orbit determination. Meanwhile, the data processing software and strategies of analysis centers are also different. There is an obviously difference in the coordinate reference frame of AC orbits. Therefore, it is necessary to combine the satellite orbit submitted by analysis center and provide combined products. There are two general schemes of orbit combination. The first method consists of a weighted averaging process of the earth-fixed satellite positions as produced by the individual analysis centers. The advantage of this method is simple and flexible, and the algorithm is consistent with the clock combination. The disadvantage is the loss of the orbit kinetic information. The second method uses the individual AC orbit files as pseudo-observations in an orbit determination process. In addition to the initial conditions, different parameter sets may be estimated. The advantage of this method is that the kinetic information of orbit can be kept. The disadvantage is that the algorithm is more complex, and clock combination requires an additional set of algorithms. Both methods can achieve good results, the precision of baseline solution using combined orbit is comparable [1]. Currently, the precision of orbit has improved greatly. The high-precision combined orbit can be obtained by weighted average method. The Helmert transformation was adopted to establish the mathematical model of orbit combination in this paper.

The calculation model of Analysis Center final orbits is that satellite orbit, ground tracking station coordinates and ERPs are estimated at the same time using the original observation data. The Final procedures use a no-net rotation (or other removable) constraint, satisfied over the IGb08 core network. It is incumbent upon the ACs to ensure that their procedures are consistent with the expectations of the combinations. There are obvious system difference among analysis center' products, such as satellites orbit. In order to maintain the consistency between comprehensive of final product and ground station coordinates as well as ERP. The AC SINEX and ERP rotations were added to the combination model by T. Springer in early 2000 [8]. The mathematical model of Helmert transformation follows as:

$$\begin{aligned} X_i^{ac'} &= X_i^{ac} + TX^{ac} + D^{ac} \cdot X_i^{ac} + \tilde{R}Z^{ac} \cdot Y_i^{ac} - \tilde{R}Y^{ac} \cdot Z_i^{ac} \\ Y_i^{ac'} &= Y_i^{ac} + TY^{ac} + D^{ac} \cdot Y_i^{ac} - \tilde{R}Z^{ac} \cdot X_i^{ac} + \tilde{R}X^{ac} \cdot Z_i^{ac} \\ Z_i^{ac'} &= Z_i^{ac} + TZ^{ac} + D^{ac} \cdot Z_i^{ac} + \tilde{R}Y^{ac} \cdot X_i^{ac} - \tilde{R}X^{ac} \cdot Y_i^{ac} \end{aligned} \tag{36.1}$$

where $X_i^{ac'}$, $Y_i^{ac'}$, $Z_i^{ac'}$ are the orbit coordinates of AC satellite i after unifying the reference frame by Helmert transformation; X_i^{ac}, Y_i^{ac}, Z_i^{ac} are the original orbit coordinates of AC satellite i; TX^{ac}, TY^{ac}, TZ^{ac}, D^{ac} are the translation parameters and scale parameter of Helmert transformation; $\tilde{R}X^{ac}$, $\tilde{R}Y^{ac}$, $\tilde{R}Z^{ac}$ are the rotation parameters of Helmert transformation considering the consistency correction.

$$\begin{aligned} \tilde{R}X^{ac} &= RX^{ac} - RX_{snx}^{ac} \\ \tilde{R}Y^{ac} &= RY^{ac} - RY_{snx}^{ac} \\ \tilde{R}Z^{ac} &= RZ^{ac} - RZ_{snx}^{ac} \end{aligned} \tag{36.2}$$

where RX^{ac}, RY^{ac}, RZ^{ac} are the Helmert rotation parameters of AC orbits with respect to the first weighted orbit; RX_{snx}^{ac}, RY_{snx}^{ac}, RZ_{snx}^{ac} are the Helmert rotation parameters of AC station coordinates with respect to the combined station coordinates. The introduction of RX_{snx}^{ac}, RY_{snx}^{ac} and RZ_{snx}^{ac} was proposed by Jan Kouba to maintain consistency between the IGS SINEX and final orbit combinations. The approach is predicated upon the assumption that each set of AC Final orbits, ERPs, SINEX, and clocks are each internally self-consistent. Applying RX_{snx}^{ac}, RY_{snx}^{ac} and RZ_{snx}^{ac} ensures long-term consistency between the IGS terrestrial frame and the final orbits. RX_{erp}^{ac} and RY_{erp}^{ac} were introduced by T. Springer to approximate day-to-day variations in the AC orbits not captured by the AC weekly SINEX rotations [2, 8]. At that time, the IGS SINEX combinations were based on weekly integrations, and so the associated RX_{snx}^{ac}, RY_{snx}^{ac} and RZ_{snx}^{ac} were weekly averages. However, the SINEX combinations of iGMAS are based on daily integrations. There is no longer a need to include the ERP rotations in the combination model so that the final orbits are not unnecessarily harmed by the ERP rotations [8].

At the AC level, the ultra-rapid and rapid procedures transfer the terrestrial frame to the orbits by tightly fixing the a priori positions of the IGb08 reference frame stations. At the combination level, the main procedural difference between the rapid/ultra-rapid and final is that AC SINEX rotations are not applied for the iGMAS.

After unifying the reference frame and eliminating systematic difference of the AC orbits, the equivalent weight was calculated by robust least squares estimation, and the combined orbit was obtained through weighted average calculation. The AC initial weight was determined by posteriori variance of Helmert transformation parameters estimation. The computational formula follows as:

$$X_{com} = \frac{\sum_{i=1}^{n} \bar{P}_i \cdot X_i'}{\sum_{i=1}^{n} \bar{P}_i} \quad P_i^0 = \frac{\sigma_0^2}{\hat{\sigma}_i^2} \quad \hat{\sigma}_i^2 = \frac{V_i^T P V_i}{n_i - 7} \tag{36.3}$$

where X_i' is analysis center' orbit coordinate under the unified reference frame, n is the number of the ACs, $\hat{\sigma}_i^2$ is AC posteriori variance of Helmert transformation parameters estimation, P_i^0 is the ACs' initial weight, $\bar{P}_i$ is the equivalent weight obtained by robust least squares estimation iterative algorithm, X_{com} is the combined orbit.

The second generation BDS satellite constellation consists of GEO satellites, IGSO satellites and MEO satellites. The difference of orbit precision between GEO satellites and IGSO/MEO satellites is large. Therefore, the AC initial weight and combined orbit of GEO and IGSO/MEO satellites are calculated separately in this paper. The orbit precision of GEO and IGSO/MEO satellites is also evaluated separately.

36.2.2 The Method and Model of Clock Combination

In order to calculate the clock corrections, the time synchronization between satellite and tracking stations should be done prior. Then, an atomic clock (station/satellite) with good quality is selected as the reference clock. Finally, the clock corrections of satellites and stations can be calculated. The products of analysis centers are internal self-consistent. Orbit and clock combination is calculated separately, and they are both obtained by weighted average calculation. In order to maintain the consistency of combined orbit and clock, the following compatibility corrections are applied to AC clock solutions prior to maintain orbit/clock as well as SINEX/clock consistency [5].

$$\begin{aligned} \Delta clk_{sat} &= ((X_{ac} - X_{com}) \cdot X_{ac})/R_{sat}/c \\ \Delta clk_{sta} &= ((Y_{ac} - Y_{com} - DY) \cdot Y_{ac})/R_{sta}/c \end{aligned} \tag{36.4}$$

where Δclk_{sat} and Δclk_{sta} are the consistency corrections applied to AC station and satellite clock solutions respectively; X_{ac} and X_{com} are the orbit coordinates of analysis center and iGMAS, Y_{ac} and Y_{com} are station coordinates of analysis center and iGMAS, R_{sat} is the radius vector of satellite position in earth fixed coordinate system, R_{sta} is the radius vector of station position in earth fixed coordinate system, c is the speed of light, DY is geocenter motion. The consistency corrections of satellite clock removed the DY on the basis of IGS.

Since AC clock solutions, in general, refer to different reference clocks, significant inconsistency errors can be introduced, in particular in remote areas with solution gaps, or when satellites and/or stations are missing from AC clock solutions. The reference clock on different days of the same analysis center is not exactly the same. The time reference frame of analysis centers is indeterminate, and the clock corrections between day and day are not continuous. The clock combination accounts for these AC reference clock differences before the combination. It is important that the alignment of the combined clocks to a chosen reference time. Currently, broadcast clocks are used for this purpose, and the stable time reference frame of combined clock should be built. Linear transformation model was adopted to align the time reference frame to reference clock, which is consistent with the physical characteristics of the clock [3–5]. As the following showed:

$$clk'_{ac} = clk_{ac} + \Delta clk_{ac} + offset_{ac} + drift_{ac} \cdot t \tag{36.5}$$

where clk_{ac} is the AC initial clock corrections, Δclk_{ac} is the consistency corrections obtained by the Eq. (36.4), $offset_{ac}$ and $drift_{ac}$ are the linear transformation parameters when the AC clock unified to the reference clock, clk'_{ac} is the AC clock corrections aligned to the same time reference frame.

L1-norm estimation minimizes the sum of the absolute value of residuals, which only has the robustness but do not have minimum variance. A reliable initial is more important for robust estimation, but it not appropriate as a final solution [11]. In this paper, the robust least squares method is used to fit transformation parameters of the AC clock solutions time reference frame with respect to the broadcast clocks. The median was used to calculate the initial unit weight mean square error. The robust least squares estimation can remove harmful observations directly, and reduce the weight of low quality observation. The median method can ensure the reliability of initial unit weight mean square error, which will reduce the possibility of introducing pseudo observations [12–14]. The AC initial weight was determined by posteriori variance of linear transformation parameters estimation. The equivalent weight was calculated by robust least squares estimation, and clk'_{ac} is used to calculate the combined solutions through weighted average [14]. The equation is showed as following:

$$clk_{com} = \frac{\sum_{i=1}^{n} \bar{P}_i \cdot clk'_i}{\sum_{i=1}^{n} \bar{P}_i} \quad P_i^0 = \frac{\sigma_0^2}{\hat{\sigma}_i^2} \quad \hat{\sigma}_i^2 = \frac{V_i^T P V_i}{n_i - 2} \tag{36.6}$$

where clk'_i is the aligned AC clock calculated by the Eq. (36.5), n is the number of the analysis centers, $\hat{\sigma}_i^2$ is posteriori variance of liner transformation parameters estimation, P_i^0 is the ACs' initial weight, $\bar{P}_i$ is the equivalent weight obtained by robust least squares estimation iterative algorithm, clk_{com} is the weighted combined clock.

36.3 Calculation and Analysis

In order to compare and analyze the precision of orbit and clock, we calculated and analyzed the products during day of year 292–305 in 2014 (BDS week 0459–0460) submitted by iGMAS analysis centers.

36.3.1 The Calculation and Analysis of Orbit Combination

The combined orbits were calculated using six iGMAS analysis centers' final orbit products during BDS week 0459–0460. Then, the weighted root mean square errors

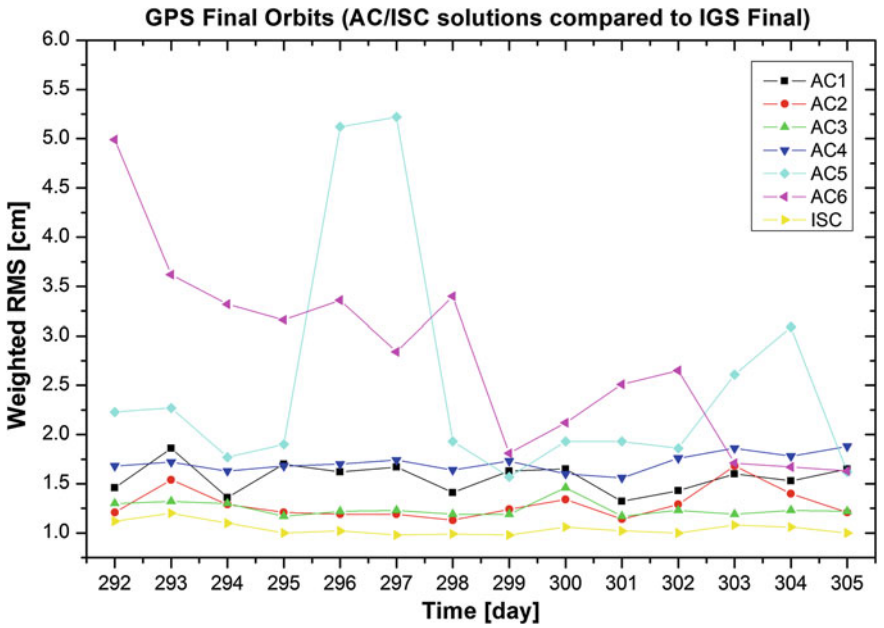

Fig. 36.1 WRMS of GPS satellite orbit with respect to the IGS final

(WRMS) of analysis center orbit with respect to the IGS final were computed. Figure 36.1 shows the WRMS of GPS satellite orbit with respect to the IGS final. Figure 36.2 shows the WRMS of GLONASS satellite orbit with respect to IGL final orbit. Figure 36.3 shows the WRMS of Galileo satellite orbit with respect to TUM final orbit. Figure 36.4 shows the WRMS of BDS MEO/IGSO satellite orbit with respect to GBM final orbit. Figure 36.5 shows the WRMS of BDS GEO satellite orbit with respect to GBM final orbit. Table 36.1 is the mean of WRMS of ACs and combined products with respect to the reference orbit during 2 weeks. ISC represents the combined orbit, AC1–AC6 refer to the six analysis centers.

From the results above, we can see that

(1) In the results of GPS satellite orbit with respect to the IGS final we can see that the WRMS of ISC and most analysis centers are less than 2 cm. The results of AC5 and AC6 are worse and unstable. The WRMS of ISC is better than analysis centers.
(2) The WRMS of GLONASS satellite orbit with respect to IGL final orbit: the WRMS of ISC, AC2 and AC3 are less than 3 cm; the WRMS of AC1, AC4 and AC6 are worse, which are less than 6 cm; the result of AC5 is worse in the first 2 days, the other days are all less than 6 cm. The WRMS of ISC has improved significantly than analysis centers.
(3) The WRMS of Galileo satellite orbit with respect to TUM final orbit: the WRMS of ISC and most analysis centers are less than 20 cm. The results of

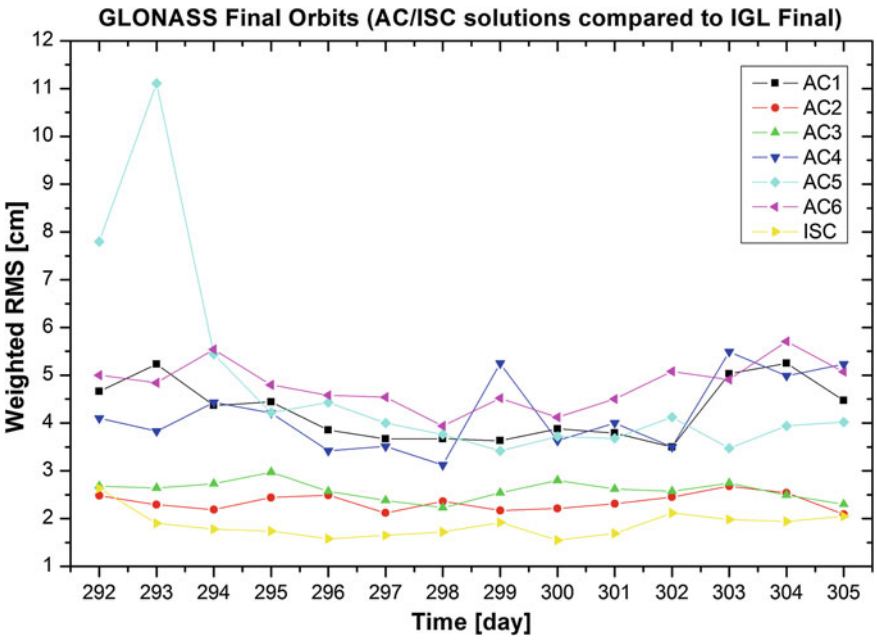

Fig. 36.2 WRMS of GLANASS satellite orbit with respect to IGL final orbit

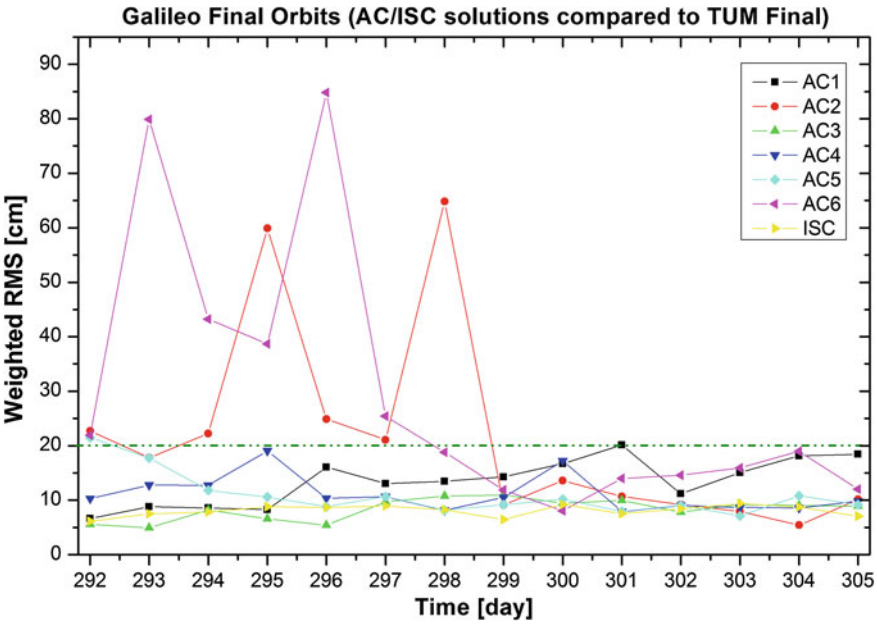

Fig. 36.3 WRMS of Galileo satellite orbit with respect to TUM final orbit

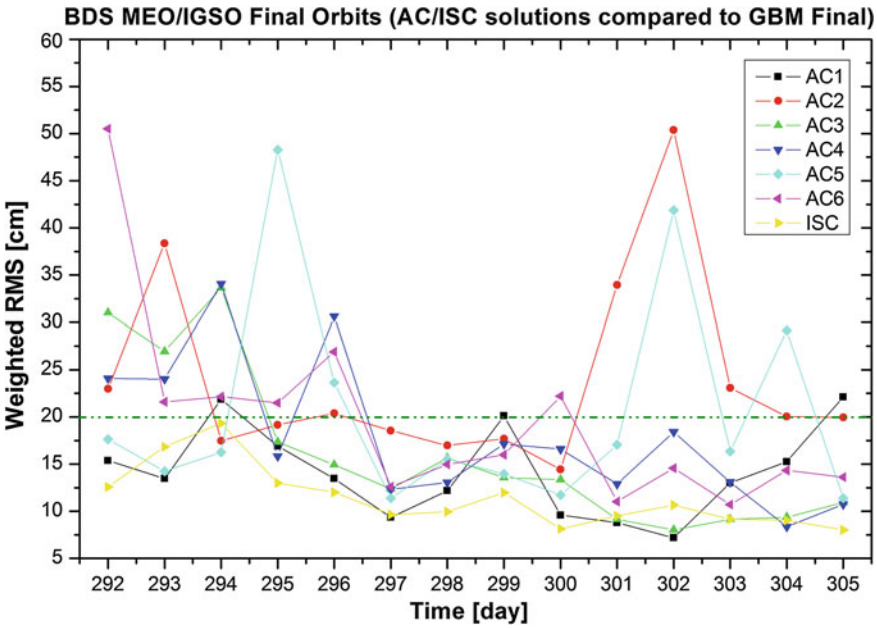

Fig. 36.4 WRMS of BDS MEO/IGSO satellite orbit with respect to GBM final orbit

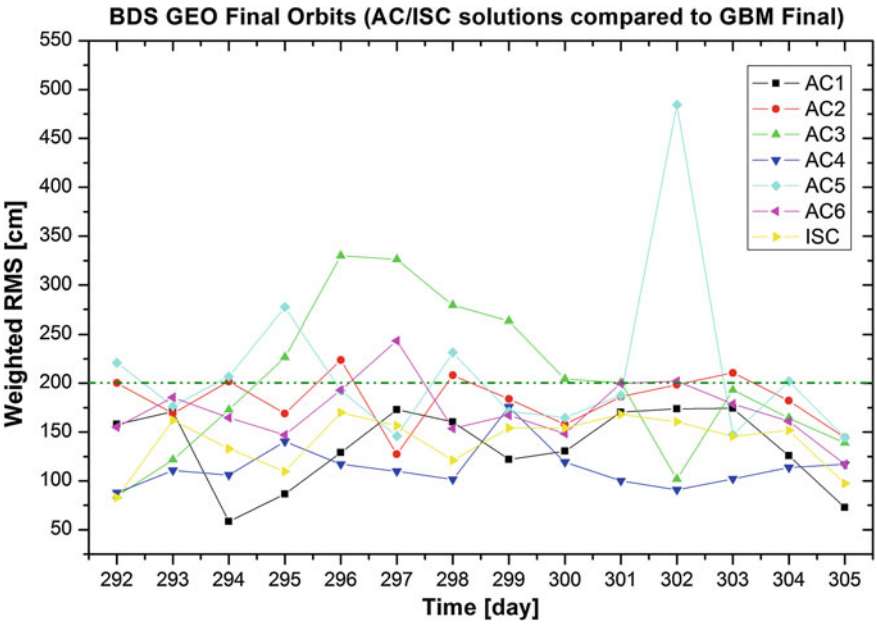

Fig. 36.5 WRMS of BDS GEO satellite orbit with respect to GBM final orbit

Table 36.1 The mean of WRMS ACs and combined orbits with respect to reference orbits during 2 weeks (unit: cm)

AC	System				
	GPS	GLONASS	Galileo	BDS(M/I)	BDS(G)
AC1	1.56	4.25	13.49	14.19	136.08
AC2	1.29	2.34	21.39	23.82	183.02
AC3	1.24	2.59	8.32	16.10	200.47
AC4	1.71	4.19	11.13	17.94	113.74
AC5	2.50	4.80	10.91	20.61	210.94
AC6	2.77	4.80	29.16	19.48	172.64
ISC	1.04	1.88	8.08	11.41	140.48

ISC and AC3 are the best, and the WRMS is less than 10 cm; the results of AC2 and AC6 are worse and unstable, the WRMS of the last week is less than 20 cm.

(4) The results of BDS MEO/ISGO satellite orbit with respect to GBM final orbit: the results of ISC and AC1 are better; the WRMS is less than 20 cm. The results of AC3, AC4 and AC6 last week are better than the first week. The results of AC2 and AC5 are unstable. The comparison results of BDS GEO satellite orbit with respect to GBM final orbit: the WRMS of ISC and most analysis centers are less than 200 cm. The result of AC4 is the best. The results of ISC and AC1 are comparable to AC4. The WRMS of AC5 and AC3 are worse and unstable.

(5) From the statistical results in Table 36.1: the GPS satellite orbit of the ACs and combined product are the best, the WRMS is about 2 cm; the GLONASS satellite orbit is a little worse than GPS, the WRMS is less than 5 cm; Galileo and BDS MEO/IGSO satellite orbits are worse than GPS and GLONASS orbit, the WRMS is about 20 cm; the WRMS of BDS GEO satellite orbit is the worst, the WRMS of most analysis centers are about 200 cm. The WRMS of GPS, GLONASS, Galileo and BDS MEO/IGSO satellite orbit of ISC are better than analysis centers. The WRMS of BDS GEO satellite orbit of ISC is better than the analysis centers except for AC4 and AC1.

36.3.2 The Calculation and Analysis of Clock Combination

The combined clock corrections were calculated using the same period final clock products submitted by iGMAS analysis centers. The RMS of ACs and combined GPS, GLONASS, Galileo and BDS satellite clock with respect to the appropriate reference solutions was computed respectively. There is no significant difference between the precision of BDS GEO and MEO/IGSO satellite clock. Therefore, the combination and accuracy assessment of all BDS satellite clock are calculated together.

The IGS, GFZ and TUM final clock was regard as an appropriate reference solution for GPS, GLONASS and Galileo satellite clock respectively. Currently, only the clock products provided by GFZ include BDS satellite clock corrections, which is a test product. The difference of clock solutions between iGMAS analysis centers and GFZ is very large. The PCO corrections of iGMAS analysis centers are different from GFZ. Therefore, there is no appropriate external reference solution for BDS satellite clock. We computed and analysed the RMS of ACs' BDS satellite clock with respect to combined clock. (ISC is the combined clock, AC1–AC6 refer to the six analysis centers' clock) (Figs. 36.6, 36.7, 36.8, 36.9 and Table 36.2).

From the results above, we can see that

(1) The results of GPS satellite clock with respect to IGS final clock: the result of AC6 is the worst, the RMS is larger than 1000 ps; the RMS of ISC and most analysis centers is less than 500 ps; the RMS of AC5 is less than 300 ps except for day of year 296 and 297. The result of ISC is significantly improved than analysis centers.
(2) The results of GLONASS satellite clock with respect to GFZ final clock: the RMS of ISC is less than 500 ps; the average RMS of AC5 is larger than 10,000 ps, which is the worst; the RMS of other ACs are less than 800 ps; the result of AC3 and AC6 is better than AC1 and AC2. The RMS of ISC is better than most analysis centers.
(3) The results of Galileo satellite clock with respect to TUM final clock: the result of AC6 and AC2 is worse and unstable, the last week is better than the

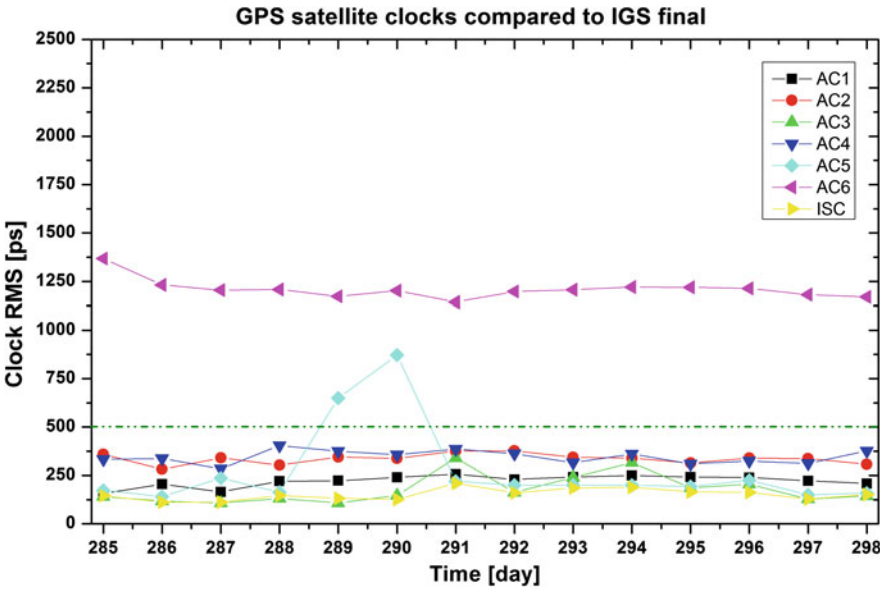

Fig. 36.6 RMS of GPS satellite clock with respect to IGS final clock

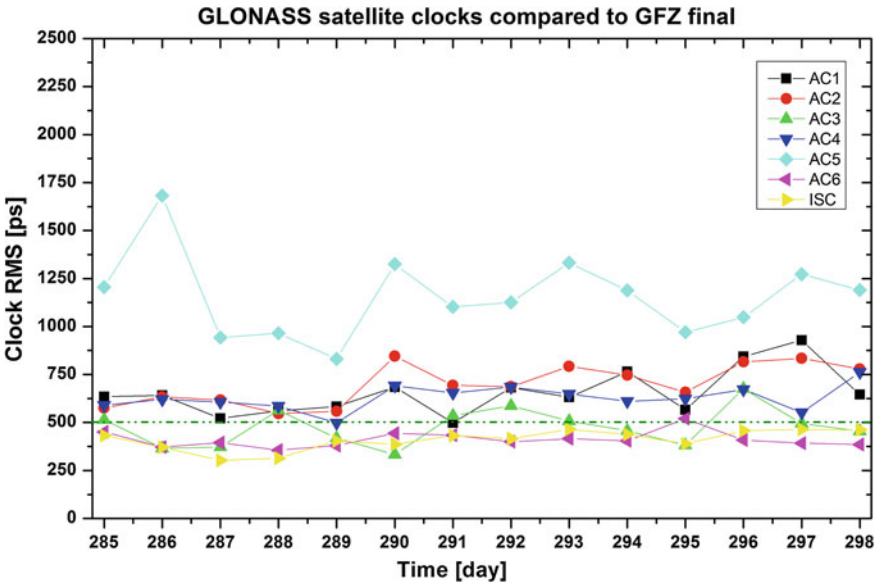

Fig. 36.7 RMS of GLONASS satellite clock with respect to GFZ final clock

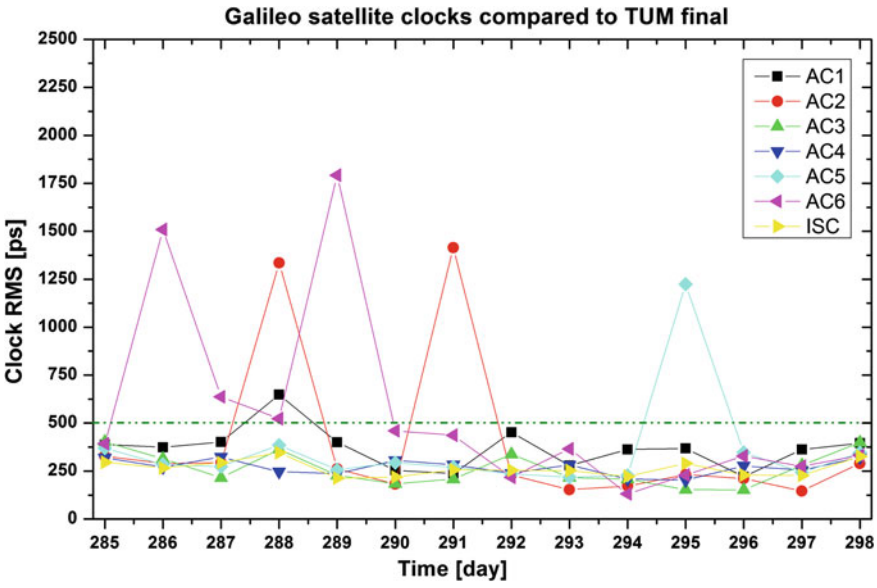

Fig. 36.8 RMS of Galileo satellite clock with respect to TUM final clock

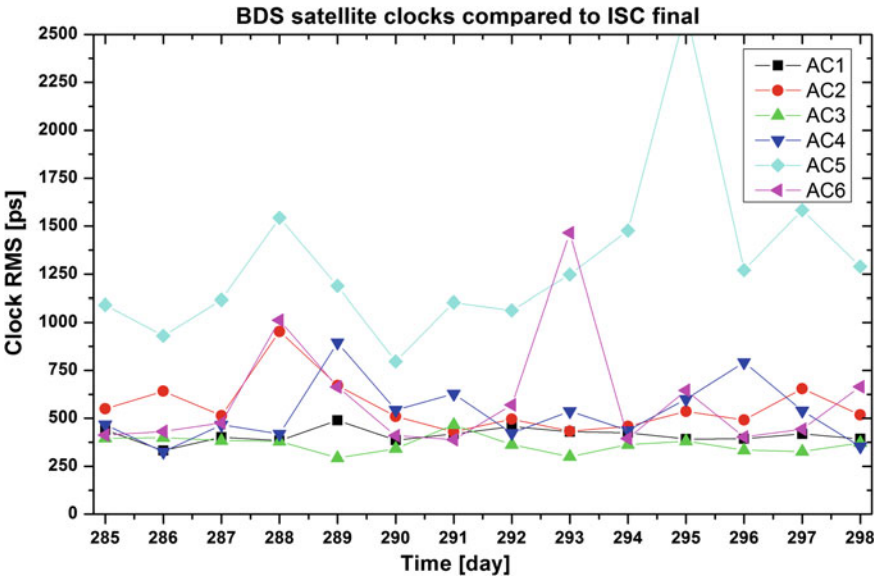

Fig. 36.9 RMS of BDS satellite clock with respect to final combined clock

Table 36.2 The average RMS of analysis center clock and combined clock with respect to reference solutions (unit: ps)

AC	System			
	GPS	GLONASS	Galileo	BDS
AC1	221	656	367	411
AC2	336	698	396	561
AC3	176	476	261	364
AC4	346	628	269	530
AC5	270	1156	355	1309
AC6	1210	411	546	599
ISC	152	409	263	/

first week; the RMS of AC5 is less than 400 ps except for day of year 302; the results of ISC, AC3 and AC4 are better, which are less than 400 ps.

(4) The results of BDS satellite clock with respect to final combined clock: the result of AC3 and AC1 are better, the RMS is less than 500 ps; the RMS of AC5 is worse, whose average RMS is larger than 1000 ps; the RMS of other ACs are all less than 1000 ps except for the result of AC6 in day of year 300.

(5) From the average RMS of analysis center clock and combined clock with respect to reference solutions in Table 36.2, what can be seen that the result of ISC and AC3 GPS satellite clock are better, the average RMS is less than 200 ps; the RMS of AC6 is the worst. The result of ISC and AC6 GLONASS satellite clock is the best, the mean RMS is less than 410 ps; the RMS of AC5 is the worst. The result of ISC, AC3 and AC4 Galileo satellite clock is better,

the average RMS is less than 300 ps, the RMS of AC6 is worse. The results of BDS satellite clock with respect to final combined clock, the RMS of AC3 is the best, the average RMS is 364 ps; the RMS of AC5 is worse. The result of ISC is stable and better than most analysis centers.

36.3.3 The Precise Point Positioning (PPP) Tests

Precise Point Positioning (PPP) is an effective method to evaluate the accuracy and reliability of orbit and clock corrections [5, 15]. In this paper, we select the same precise point positioning software and station observation data. The precise point positioning tests were implemented using the products BDS Week 0459–0460 (day of year 292–305 in 2014). The combined orbit and clock are obtained using independent orbit and clock of six iGMAS analysis centers. In the PPP tests, eight kinds of orbit and clock corrections were used respectively. The eight kinds of orbits and clock corrections are as follows: combined orbit and clock (ISC), IGS orbit and clock (IGS), orbit and clock of six iGMAS analysis centers (AC1, …, AC6). When solving the equation, the position parameters of single epoch (dynamic) PPP are calculated separately for each epoch. In the case of static, the position parameters are regarded as a constant.

The static PPP coordinate daily repeatability can verify the accuracy of orbit and clock effectively. The static PPP tests were respectively implemented using 9 IGS stations (AREQ, CONZ, CUSV, DRAO, MAG0, SUTV, TIDB, WSRT and ZAMB) observation data during day of year 292–305, which have good global distribution. The result of coordinate daily repeatability with different orbit and clock corrections is showed in Fig. 36.10 and Table 36.3.

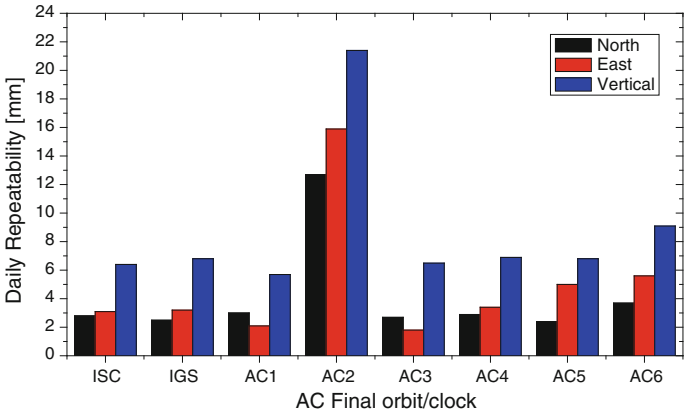

Fig. 36.10 Median daily repeatability (mm) of PPP with different orbits/clocks

Table 36.3 Median daily repeatability of PPP with different orbits/clocks (unit: mm)

Orbit/Clock	Period	North	East	Vertical
ISC	292–305	2.8	3.1	6.4
IGS	292–305	2.5	3.2	6.8
AC1	292–305	3.0	2.1	5.7
AC2	292–305	12.7	15.9	21.4
AC3	292–305	2.7	1.8	6.5
AC4	292–305	2.9	3.4	6.9
AC5	292–305	2.4	5.0	6.8
AC6	292–305	3.7	5.6	9.1

The result of single epoch PPP can reflect the precision and reliability of orbit and clock more clearly. Single epoch PPP tests were implemented using eight different orbit and clock products at day of year 292. Figures 36.11, 36.12 and 36.13 is respectively the SUTV station N, E, U component coordinate difference of single epoch PPP with respect to the IGS station coordinates solution. Table 36.4 is respectively the standard deviation of N, E, U component coordinate difference of single epoch PPP with different orbit/clock products.

From the results above, we can see that:

(1) In the results of static PPP tests we can see that the median of daily repeatability using different orbit/clock products is at millimeter level except for AC2. The result of AC1 and AC3 is the best, then the ISC and IGS. The median of daily coordinate components repeatability of ISC is better than most

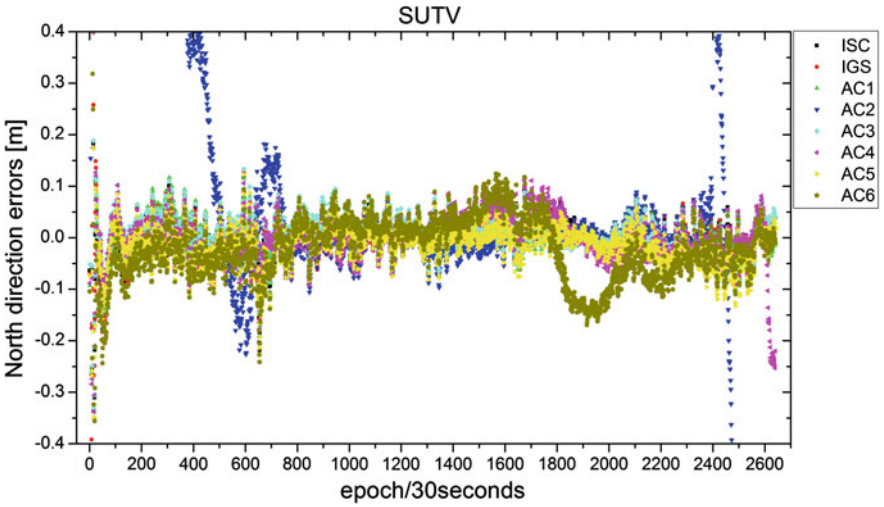

Fig. 36.11 The N component coordinate difference of single epoch PPP with respect to the IGS station coordinates solution

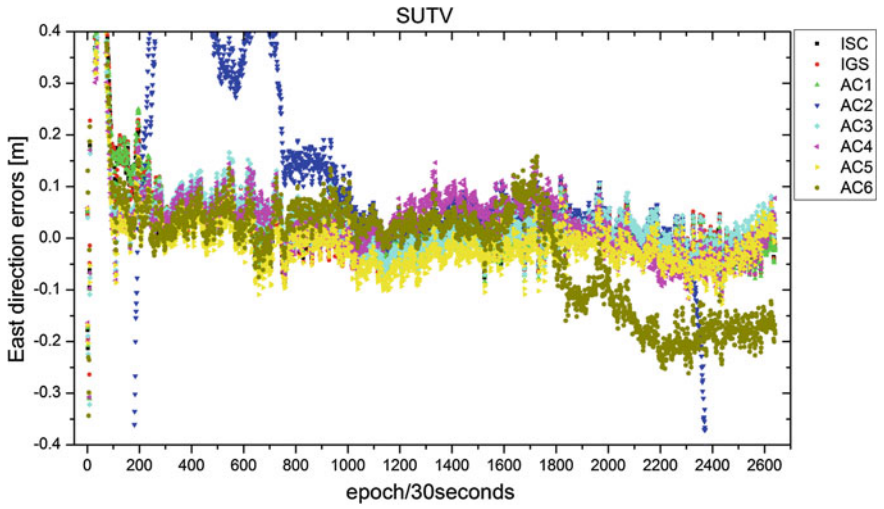

Fig. 36.12 The E component coordinate difference of single epoch PPP with respect to the IGS station coordinates solution

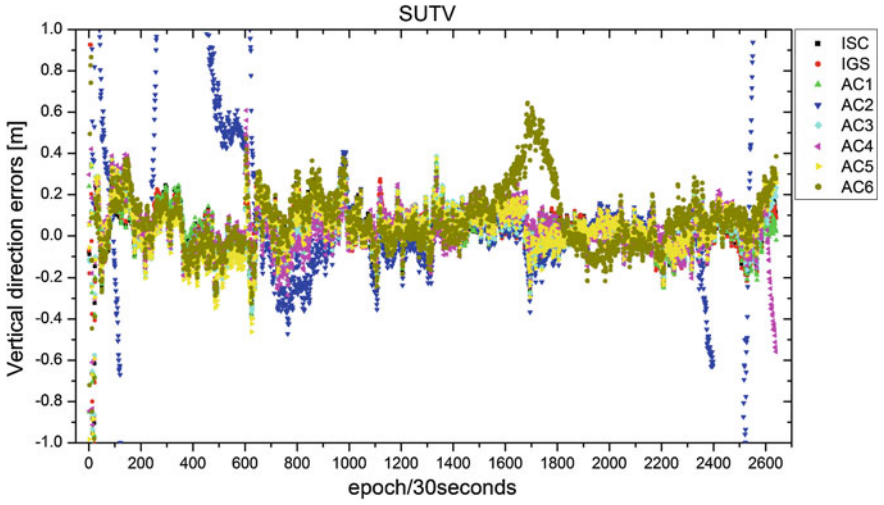

Fig. 36.13 The U component coordinate difference of single epoch PPP with respect to the IGS station coordinates solution

analysis centers, which proved that the precision and reliability of combined orbit/clock are very impressive.

(2) We can see that from the N, E, U component coordinate difference of single epoch PPP with different orbit/clock products in Figs. 36.11, 36.12 and 36.13 the difference of ISC, IGS and AC3 is smaller and more smooth. The difference of AC6 is larger than others. Meanwhile, the results of AC2 single epoch PPP is

Table 36.4 The standard deviation of each component coordinate difference of single epoch PPP (unit: m)

Orbit/Clock	North	East	Vertical
ISC	0.032	0.044	0.094
IGS	0.037	0.046	0.092
AC1	0.031	0.048	0.092
AC2	0.643	1.022	1.111
AC3	0.031	0.042	0.097
AC4	0.043	0.049	0.111
AC5	0.034	0.038	0.108
AC6	0.056	0.099	0.144

with poor speed of converging. It is supposed that there are some abnormal values in the satellite clock corrections. In addition to AC2, the results of single epoch PPP get convergence within 200 epochs. After convergence, the absolute value of N and E component coordinate difference is less than 10 cm, and the absolute value of V component coordinate difference is less than 20 cm.

(3) Table 36.4 is the standard deviation of the SUTV station N, E and V component coordinate difference of single epoch PPP with different orbit/clock products. We can see that the standard deviation of N component coordinate difference of AC1, AC3 and ISC are about 3 cm, which is smaller than others. The standard deviation of E component coordinate difference of AC5 and AC3 are within 4 cm, and the standard deviation of V component coordinate difference of IGS, AC1 and ISC are about 9 cm. The standard deviation of AC2 in N, E, V component coordinate difference is all larger, which is consistent with the difference sequence in Figs. 36.11, 36.12 and 36.13. The standard deviation of N, E, V component coordinate difference of ISC single epoch PPP is all better than the results of most ACs.

(4) The results of static PPP and single epoch PPP tests both proved that the combined orbit and clock have high precision and reliability. The precision of static and single epoch PPP tests using orbit and clock products provided by AC2 were both very poor, which didn't be found in the comparison with the reference solutions. The reason could be that the consistency of orbit and clock of AC2 is very poor or the clock data of some satellites is not complete and abnormal. From now on, we should check the data integrity and usability of the products submitted by ACs, and output the information of abnormal data and gross error identification in the product evaluation report.

36.4 Conclusions

Orbit and clock corrections are the important basic data of precise point positioning (PPP), which directly affects the accuracy of positioning. Combined orbit and clock are the main products provided by ISC. The accuracy and reliability of combined orbit/clock should be guaranteed. This paper introduced the models and methods of

orbit and clock combination using by ISC. The comparison with external reference solutions and PPP tests both proved that the precision and reliability of combined orbit and clock are impressive. Currently, the iGMAS analysis centers and ISC are in the experimental stage, which will face many new problems and challenges. Among them, the precision of iGMAS station related products, the consistency of combined products, the continuity of satellite and station clock corrections and the high-precision and stable spatial-temporal reference frame are all worth exploring and urgent to improve. The research of this paper provides guarantee for generating high-precision and reliable orbit and clock combination products.

Acknowledgments This work was supported by Natural Science Foundation of China (41174008) and the Open Foundation of State Key Laboratory of Geodesy and Earth's Dynamics (SKLGED2013-4-2-EZ) and State Key Laboratory of Astronautic and Dynamics (2014ADL-DW0101).

References

1. Beutler G, Kouba J, Springer TA (1995) Combining the orbits of the IGS analysis centers. Bull Geodesique 69:200–222
2. Springer TA, Beutler G (1993) Towards an official IGS orbit by combining the results of all IGS processing centers. In: Proceedings of the 1993 IGS workshop, March 24–26, Bern, Switzerland, pp 242–250
3. Kouba J, Mireault Y, Lahaye F (1995) 1994 IGS orbit/clock combination and evaluation, Appendix I of the analysis coordinator report. International GPS service for geodynamics (IGS) 1994 annual report, pp 70–94
4. Springer TA, Zumberge JF, Kouba J (1998) The IGS analysis products and consistency of the combined solutions. In: Proceedings of the IGS analysis center workshop, Darmstadt, Feb 9–11
5. Kouba J, Springer T (2001) New IGS station and satellite clock combination. GPS Solution 4 (4):31–36
6. Yao Y (2007) Theory and realization of GPS orbit integration. Geomatics Inf Sci Wuhan Univ 06:510–514
7. Feng L, Jia X et al (2010) A method of combining orbit by M estimation and dynamic smoothing. Scientia Sinica Phys, Mech & Astron, 603–607
8. Griffiths J (2012) A review of the IGS final orbit combination procedures, report from the analysis coordinator. http://acc.igs.org/
9. Ferland R, Piraszewski M (2009) The IGS-coordinates, earth rotation parameters and apparent geocenter. Geodesy 83:385–392
10. Altamimi Z, Collilieux X, Métivier L (2011) ITRF2008: an improved solution of the international terrestrial reference frame. J Geodesy 85(8):457–473
11. Qiu W (2003) Selecting weight iteration method with reliable initial values Geo Spat Inf Sci (8): 452–454
12. Zhou J, Huang Y, Yang Y, Ou J (1997) Robust least square method. Publishing House of Huazhong University of Science and Technology, Wu Han
13. Ou J (1996) An design of three-step robust solutions. Acta Geodaetica et Cartographica Sinica 8:173–179
14. Chen K, Xu T (2014) A new strategy on precise clock combination of IGS analysis centers. China Satellite Navigation Conference (CSNC) 2014 Proceedings, (2):255–268
15. Jan K, Pierre H (2001) Precise point positioning using IGS orbit and clock products. GPS Solution 5(2):12–28

Chapter 37
Regional Modeling of Atmosphere Delay in Network RTK Based on Multiple Reference Station and Precision Analysis

Bo Wu, Chengfa Gao, Shuguo Pan, Jiadong Deng and Wang Gao

Abstract Aiming to the disadvantages of traditional triangle network solution at present, this paper proposed a regional modeling method of atmosphere delay in network RTK based on utilizing redundant observation information of multiple reference station in regional GNSS network. The algorithm of ionosphere and troposphere delay corrections in network RTK is studied respectively. At last, the precisions of traditional triangulation linear interpolation model and regional model proposed by this paper are analyzed using measured data from American CORS. The results show that the precision of ionosphere delay correction interpolation model based on multiple reference station adopted by this paper is similar to that of traditional triangulation linear interpolation model. The precision of troposphere delay correction interpolation model concerning with elevation based on multiple reference station adopted by this paper is superior to the traditional triangulation linear interpolation model and is more stable. Especially for the satellites with low-elevation angles, its precision of interpolation model are much higher than those of traditional triangulation linear interpolation model.

Keywords Multiple reference station · Network RTK · Atmosphere delay · Regional model

37.1 Introduction

The technology of network real-time kinematic is also known as multi-reference stations real-time kinematic. It's a real-time positioning technology that calculating, broadcasting correction information of rover station, and making different error

B. Wu (✉) · C. Gao · J. Deng · W. Gao
School of Transportation, Southeast University, 2 Sipailou, 210096 Nanjing, China
e-mail: 632231333@qq.com

S. Pan
School of Instrument Science and Engineering, Southeast University, 2 Sipailou, 210096 Nanjing, China

J. Sun et al. (eds.), *China Satellite Navigation Conference (CSNC) 2015 Proceedings: Volume II*, Lecture Notes in Electrical Engineering 341,
DOI 10.1007/978-3-662-46635-3_37

corrections of the rover station user within the region based on precisely known coordinates of reference stations (three or more) built in the region [1]. It's a real-time high-precision positioning technology built and developed on GPS and conventional RTK [2]. And it has developed into a hot topic in urban GNSS application and been widely applied in land resource mapping and surveying industries nowadays [3–5].

At present, the system of network real-time kinematic is built on the basis of continuously operating reference system (CORS) [6]. Conventional RTK technology usually models regional atmosphere delay in triangular structure [7]. It uses triangle as basic resolution unit, chooses three reference stations which cover the rover station, and builds the model of atmosphere error correction in the triangle region [8]. The triangle resolution unit has simple structure, good reliability and precision of atmosphere delay correction. But some disadvantages remain [9]: 1. It doesn't make full use of observation information in regions with intense reference stations which is bad for the development of large-scale and long-baseline network RTK. 2. It limits the precision of available interpolation model, especially for the region with quite different height, because its resolution unit only has information of two baseline. 3. Its precision of atmosphere delay correction decreases sharply with the increase of distance for the rover station outside the network.

Therefore, this paper proposed a method of atmosphere delay correction regional modeling based on multi-reference stations in terms of the disadvantages of triangle resolution unit in conventional network RTK. It takes advantage of triangle resolution unit of reference stations and makes full use of redundant observation information of other reference stations at the same time, then chooses appropriate atmosphere delay correction model, analyses the precision compared with traditional triangle network linear interpolation model at last.

37.2 Atmospheric Delay Corrections Interpolation Model Based on Multiple Reference Stations in Network RTK

Currently in the network RTK atmospheric error corrections interpolation model, most adopt conventional interpolation model. There are linear interpolation model (LIM), a distance of linear interpolation model (DIM), a linear combination model (LCM) and the low-order surface model (LSM), etc. [10]. The conventional atmospheric error correction calculation model does not distinguish the ionosphere and troposphere delay error. Instead, all errors are taken into account to calculate comprehensive error. However, due to different factors between the various errors and the differences related features, only use a computational model of atmospheric error corrections and can't meet the accuracy and reliability of a variety of error corrections.

Therefore, the paper classifies the atmospheric error to model each other in the network RTK, thus further atmospheric error corrections is refined.

37.2.1 Ionosphere Delay Interpolation Model Based on Multiple Reference Stations

The ionosphere delay errors on each reference station network baseline can be calculated by dual-frequency carrier phase measurement. According to inter-carrier phase double difference observation equations, reference station ionosphere error double-difference corrections as Eq. (37.1) [11]:

$$\Delta\nabla I = \alpha[(\lambda_1\Delta\nabla\varphi_1 - \lambda_2\Delta\nabla\varphi_2) + (\lambda_1\Delta\nabla N_1 - \lambda_2\Delta\nabla N_2)] - \alpha(\Delta\nabla\varepsilon_1 - \Delta\nabla\varepsilon_2) \tag{37.1}$$

where $\Delta\nabla$ is the double-difference operator; $\Delta\nabla I$ is double-difference ionosphere error correction; $\lambda_i, f_i(i = 1, 2)$ are L1 and L2 carrier wavelength and frequency; $\varphi_i(i = 1, 2)$ are the carrier phase observations; $\varepsilon_i(i = 1, 2)$ are the effects of the carrier phase observations' noise and not-modelled error; α is equal to $f_2^2/(f_1^2 - f_2^2)$. For the baseline of 200 km or less, in the case of typical ionosphere conditions, random errors on the observed noise is not greater than 3 mm, and therefore can be ignored [12]. Simplified to Eq. (37.2):

$$\Delta\nabla I = \alpha[(\lambda_1\Delta\nabla\varphi_1 - \lambda_2\Delta\nabla\varphi_2) + (\lambda_1\Delta\nabla N_1 - \lambda_2\Delta\nabla N_2)] \tag{37.2}$$

During the time of ionosphere keeps calm in the area mid-latitudes, the accuracy of ionosphere linear interpolation model (LIM) is higher. So using linear interpolation (LIM) can well describe the spatial distribution of ionosphere characteristics within the time of ionosphere keeps calm. Therefore, the paper still uses the linear interpolation model (LIM) to calculate the double-differential ionosphere error corrections. Since the ionosphere delay error is not affected by the elevation factor, the interpolation model only considers the impact of plane coordinates factor. The error equation as Eq. (37.3):

$$V_I = A \cdot X \tag{37.3}$$

$$\begin{aligned} V &= \begin{bmatrix} \Delta\nabla I_{1,n} \\ \Delta\nabla_{2,n} \\ \vdots \\ \Delta\nabla_{n-2,n} \\ \Delta\nabla I_{n-1,n} \end{bmatrix}, \; A = \begin{bmatrix} a_1 & a_2 \end{bmatrix}, \\ X &= \begin{bmatrix} \Delta x_{1,n} & \Delta x_{2,n} & \cdots & \Delta x_{n-2,n} & \Delta x_{n-1,n} \\ \Delta y_{1,n} & \Delta y_{2,n} & \cdots & \Delta y_{n-2,n} & \Delta y_{n-1,n} \end{bmatrix} \end{aligned} \tag{37.4}$$

where $1, \cdots, n$ represent the number of reference stations; $1, 2, \cdots, n-1$ represent the auxiliary reference stations; n represents the master reference station;

a_1, a_2 are linear interpolation coefficients; Δx, Δy represent the difference of plane coordinate between the main reference station and the auxiliary reference stations.

According the features of LIM, the linear interpolation coefficients from Eq. (37.3), and the difference of plane coordinates between the rover station (m) and the master reference station, it can get the ionosphere error corrections of the rover station $\Delta\nabla I_{m,n}$, as Eq. (37.5):

$$\Delta\nabla I_{m,n} = a_1\Delta x_{m,n} + a_2\Delta y_{m,n} \tag{37.5}$$

37.2.2 Troposphere Delay Interpolation Model Based on Multiple Reference Stations

Compared with the ionosphere delay, Spatial distribution characteristics and related properties troposphere delays are significantly different. Troposphere delay error is affected not only by the horizontal direction, but also by the elevation direction. And the current interpolation model fits the estimated spatial error distribution through plane distribution of the reference stations network in the horizontal direction around rover station, constitutes a network interpolation plane. When the rover station in the horizontal direction is strongly constrained within a region constituted by the reference station, it may stay away from the surface in the area interpolation model in elevation direction. So troposphere delay corrections of the rover station must consider the impact of the elevation factor. The paper selects troposphere delay interpolation model considering the impact of height offset based on multiple reference stations.

According to the double difference carrier phase observation equation, and ionosphere transformation formula [13] $I_i = A/f_i^2$, double-difference troposphere error correction can be calculated between the reference station, as Eq. (37.6):

$$\Delta\nabla T = \frac{cf_1(\Delta\nabla\varphi_1 - \Delta\nabla N_1)}{f_1^2 - f_2^2} - \frac{cf_2(\Delta\nabla\varphi_2 - \Delta\nabla N_2)}{f_1^2 - f_2^2} - \Delta\nabla\rho \tag{37.6}$$

where $\Delta\nabla T$ is double-difference troposphere error correction; ρ is geometric distance between the satellite and the receiver.

Elevation factor h is added on troposphere delay linear interpolation model (LCM). The following interpolation model is established:

$$\Delta\nabla T_{i,n} = f(\Delta x_{i,n}, \Delta y_{i,n}, \Delta h_{i,n}) \tag{37.7}$$

The error equation as Eq. (37.8):

$$V_T = B \cdot X \tag{37.8}$$

where

$$V_T = \begin{bmatrix} \Delta\nabla T_{1,n} \\ \Delta\nabla T_{2,n} \\ \vdots \\ \Delta\nabla T_{n-2,n} \\ \Delta\nabla T_{n-1,n} \end{bmatrix}, \; B = [\, b_1 \quad b_2 \quad b_3 \quad b_4 \,], \qquad X = \begin{bmatrix} \Delta x_{1,n} & \Delta x_{2,n} & \cdots & \Delta x_{n-2,n} & \Delta x_{n-1,n} \\ \Delta y_{1,n} & \Delta y_{2,n} & \cdots & \Delta y_{n-2,n} & \Delta y_{n-1,n} \\ \Delta h_{1,n} & \Delta h_{2,n} & \cdots & \Delta h_{n-2,n} & \Delta h_{n-1,n} \\ 1 & 1 & \cdots & 1 & 1 \end{bmatrix} \tag{37.9}$$

b_1, b_2, b_3, b_4 are linear interpolation coefficients; Δh is the elevation difference between the auxiliary reference station and the master reference station.

It sets the interpolation coefficient satisfies the following constraints:

$$\begin{cases} \sum_{i=1}^{n} b_i = 1 \\ \sum_{i=1}^{n} b_i(\vec{X}_u - \vec{X}_i) = 0 \\ \sum_{i=1}^{n} b_i^2 = \min \end{cases} \tag{37.10}$$

where

$$\vec{X}_u - \vec{X}_i = (\Delta x_{mi}, \Delta y_{mi}, \Delta h_{mi}) \tag{37.11}$$

According to the linear interpolation coefficients from Eq. (37.8), and plane coordinate difference and elevation difference between the rover reference station and the master reference station. The troposphere delay correction $\Delta\nabla T_{m,n}$ is gained as Eq. (37.12):

$$\Delta\nabla T_{m,n} = b_1\Delta x_{m,n} + b_2\Delta y_{m,n} + b_3\Delta h_{m,n} + b_4 \tag{37.12}$$

37.3 Experiments

The GPS observation data from the American CORS network is used to test the effects of atmospheric interpolation model. The date is August 8, 2013. The length of time for observation data is 1 h 50 min. We select seven base stations, such as P322, P167, P349, P793, P060, P330, P345, which P322 is the central reference station, P167, P349, P793, P060 is auxiliary reference stations. They compose the solver unit of multiple reference stations. And we randomly select P322, P167,

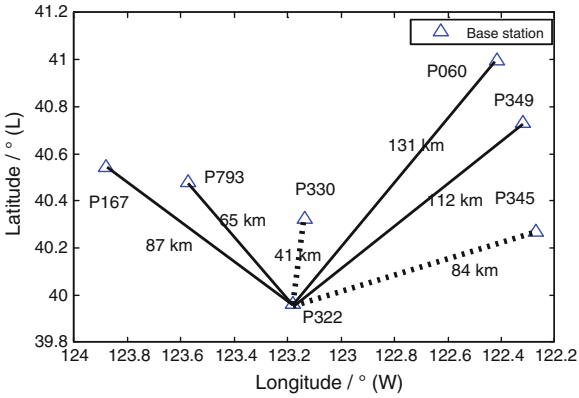

Fig. 37.1 Distribution of stations

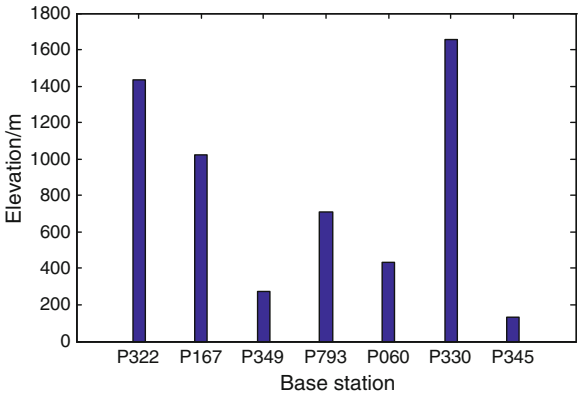

Fig. 37.2 Difference of height among stations

P349 as the solver unit of traditional triangular mesh. The average distance of baseline is about 90 km. P330 is the rover station within the network. P345 is the rover station outside the network. Figure 37.1 shows the distribution of stations. Figure 37.2 shows the difference of heights among stations.

We select the most representative two satellites from the observed data to test and analysis., which the satellite PRN 6 is selected as a high-elevation satellites (elevation angle decreases), the satellite PRN 14 is selected as a low-elevation angle satellite (elevation angle increases). Figure 37.3 shows the change of elevation about satellites.

Due to the effect of a traditional interpolation model is basically the same [14], we select the represent linear interpolation model (LIM) based on triangulation solver unit to compare with the method of MIM and MHM proposed in this paper. Then analysis of ionosphere delay and troposphere delay corrections interpolation result of the rover station. Figure 37.4 shows the variation of ionosphere biases for LIM and MIM. Figure 37.5 shows the variation of troposphere biases for LIM and MHM.

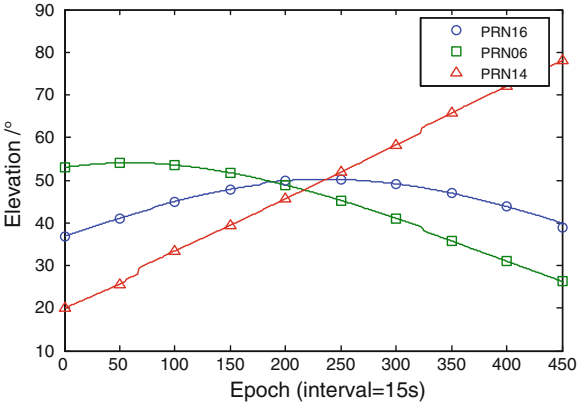

Fig. 37.3 The change of elevation about satellites

Figure 37.4 shows that for the ionosphere delay correction, when the rover station is within the network or outside the network, the model interpolation accuracy between the ionosphere delay interpolation model based on multiple reference stations and LIM based on triangulation solver unit is quite. Their ionosphere delay correction errors are about the same.

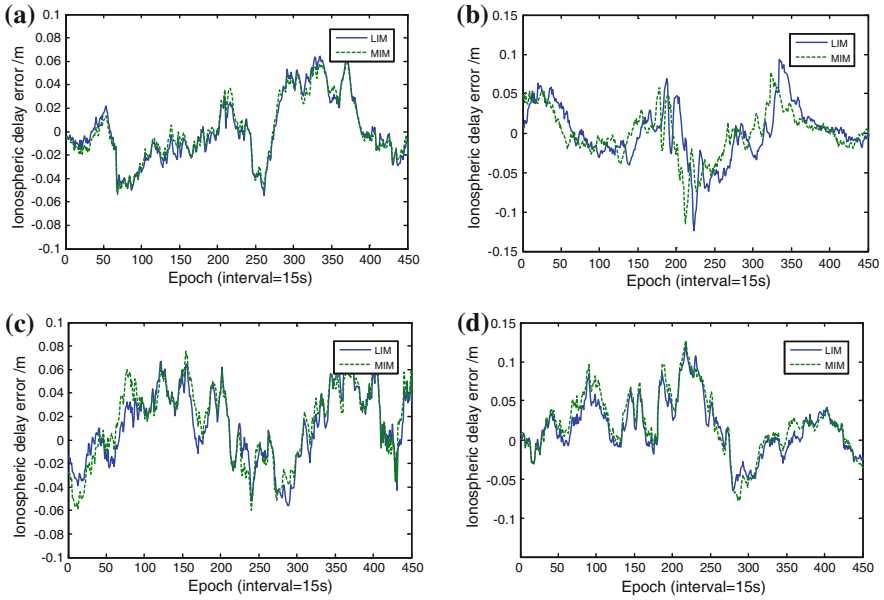

Fig. 37.4 The variation of ionosphere biases for LIM and MIM. **a** P330 (PRN 06). **b** P330 (PRN 14). **c** P335 (PRN 06). **d** P335 (PRN 14)

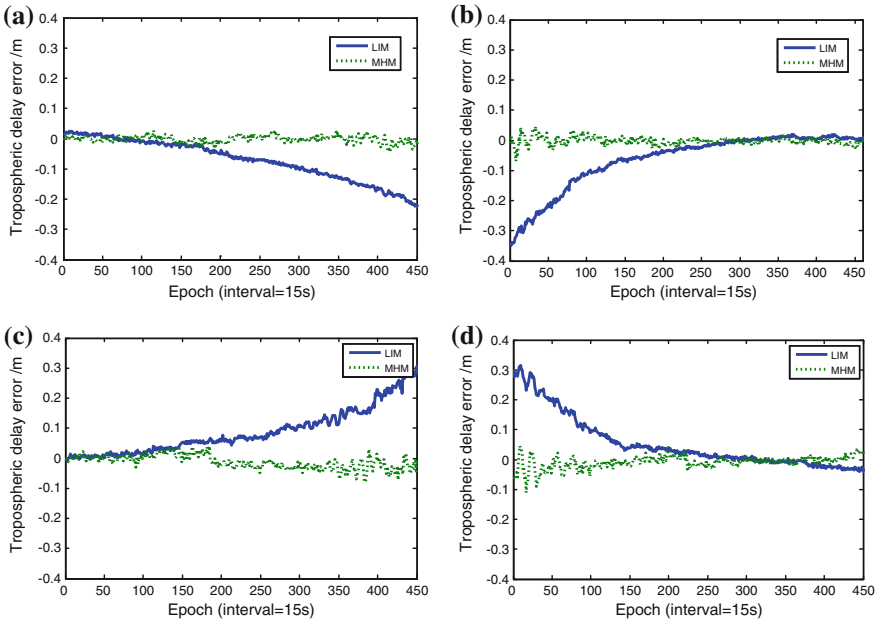

Fig. 37.5 The variation of troposphere biases for LIM and MHM. **a** P330 (PRN 06). **b** P330 (PRN 14). **c** P335 (PRN 06). **d** P335 (PRN 14)

Figure 37.5 shows that for the troposphere delay correction, with the decrease of satellite's elevation, the accuracy of the traditional triangulation interpolation model decreases. When the satellite's elevation increases, the accuracy of the traditional triangulation interpolation model increases also. However, when the satellite's elevation is low, the accuracy of traditional triangulation interpolation model is poor. The troposphere delay interpolation model based on multiple reference stations which the paper puts forward, its interpolation accuracy is higher and can keep stable, regardless of the satellite's elevation is high or low. Especially for low-elevation satellites. The Interpolation accuracy of the troposphere delay interpolation model based on multiple reference stations (MHM) is much higher than the traditional interpolation model (LIM) which is based on triangulation. Its interpolation accuracy is generally stable within 2.5 cm, has a high interpolation precision.

37.4 Conclusion

The paper proposed a regional modeling method of atmosphere delay in network RTK based on multiple reference stations. For the atmospheric error, we adopt classification modeling approach, obtain ionosphere and troposphere delay correction interpolation model. And its accuracy is analyzed. Main conclusions are as follows:

(1) The ionosphere delay interpolation model based on multiple reference stations (MIM), its model interpolation accuracy is quite to LIM which is based on triangulation solver unit.
(2) For the region of large undulating terrain, the troposphere delay interpolation model considering the impact of height offset based on multiple reference stations (MHM), its interpolation accuracy is generally stable within 2.5 cm, which is higher than the traditional triangulation interpolation model. Especially for low-elevation satellites, its effect is better than the traditional triangulation interpolation mode.

There are still following shortcomings: the paper sets up network manually for multiple reference stations. On the term of setting up network automatically, it should remain to be further studied.

Acknowledgments This work is supported by the Key Projects in the National Science & Technology Pillar Program during the Twelfth Five-year Plan Period (No. 2012BAJ23B01). The authors are very grateful to the anonymous reviewers for their constructive comments and suggestions.

References

1. He H, Li J, Yang Y et al (2013) Performance assessment of single-and dual-frequency BeiDou/GPS single-epoch kinematic positioning. GPS Solutions 1–11
2. Zhang F, Hao JM, Cong TW et al (2009) Algorithm searching of VRS and implementing based on the multiple reference station network. Surveying Mapp Technol 25(6):414–416
3. Gao CF, Hu WS (2011) Principles and applications of satellite navigation and positioning. China Communications Press, Beijing, pp 212–217
4. Hu G, Abbey DA, Castleden N et al (2005) An approach for instantaneous ambiguity resolution for medium-to long-range multiple reference station networks. GPS Solutions 9 (1):1–11
5. Jensen ABO, Cannon ME (2000) Performance of network RTK using fixed and float ambiguities. In: Proceedings of the 2000 national technical meeting of the institute of navigation, pp 797–805
6. Chen X, Han S, Rizos C et al (2000) Improving real time positioning efficiency using the Singapore integrated multiple reference station network (SIMRSN). In: Proceedings of the 13th international technical meeting of the satellite division of the institute of navigation (ION GPS 2000), pp 9–16
7. Yang RH, Niu RF, Wu WY et al (2008) Network RTK positioning technology and situation analysis. Gansu Sci Technol 24(10):33–35
8. Zou R, Liu H, Yao YC et al (2006) Application of Delaunay triangulated network to continuous operational reference system. Wtusm Bull Sci Technol 30(6):9–11
9. Yang XJ (2005) Virtual Reference Station (VRS) Technology Research and Differential Correction Information. Southwest Jiaotong University, Chengdu
10. Shen XF, Gao CF, Pan SG (2012) Algorithm for network RTK(VRS) based on star structure. Acta Geodaetica Cartogr Sin 41(1):33–40
11. Li CF, Huang DF, Yuan LG et al (2006) Ionosphere biases modeling technique for GPS multiple reference stations. J Southwest Jiaotong Univ 40(5):610–615

12. Wu BP (2003) GPS positioning principle and mathematical model about network RTK, China University of Geosciences
13. Li CG (2007) Generation and distribution technique of precise differential corrections for GPS/VRS network. Southwest Jiaotong Univ, Chengdu
14. He HB (2002) Precise kinematic GPS surveying and quality control. Institute of Surveying and Mapping, Information Engineering University, Zhengzhou

Chapter 38
Reliable RTK Positioning Method Based on Partial Wide-Lane Ambiguity Resolution from GPS/GLONASS/BDS Combination

Wang Gao, Chengfa Gao, Shuguo Pan, Yang Yang and Denghui Wang

Abstract Integration of multi-constellation GNSS creates a significant increase in the number of visible satellites, thus bring new opportunities for improving the accuracy and reliability of Real Time Kinematic (RTK) positioning. This paper proposes a reliable RTK positioning method based on partial wide-lane ambiguity resolution (AR) from GPS/GLONASS/BDS (G/R/C) combination. It takes advantage that wide-lane observation has much longer wavelength, and the multi-constellation combined wide-lane ambiguity-fixed observations are directly used to positioning calculation. In the paper, the G/R/C geometry-based wide-lane ambiguity resolution models are unified and combined. Then a partial ambiguity resolution (PAR) method is introduced to avoid the influence of extreme errors from low-elevation satellites. A set real G/R/C baseline data is used as typical example to reflect the benefits of the proposed method. Experiment results show that the multi-constellation combination can significantly improve the wide-lane AR effects, including the AR success rate, ratio and initialization speed. And the proposed PAR method can effectively avoid the negative influence of new-rising satellites. The positioning accuracy using the proposed method can still reach centimetre level.

Keywords GPS/GLONASS/BDS combination · Wide-lane · RTK (Real time kinematic) · Partial ambiguity resolution (PAR)

W. Gao (✉) · C. Gao · Y. Yang · D. Wang
School of Transportation, Southeast University, 2 Sipailou, Nanjing 210096, China
e-mail: gaowang_1990@126.com

S. Pan
School of Instrument Science and Engineering, Southeast University, 2 Sipailou, Nanjing 210096, China

J. Sun et al. (eds.), *China Satellite Navigation Conference (CSNC) 2015 Proceedings: Volume II*, Lecture Notes in Electrical Engineering 341,
DOI 10.1007/978-3-662-46635-3_38

38.1 Introduction

As a commonly used high-precision positioning technology, the real-time kinematic (RTK) has proven its efficient and reliable performance during the past a few years. However, both its availability and reliability deteriorate dramatically under some challenging conditions, for instance, the longer baselines than 15 km, deep open pit mines and urban canyon [1]. Especially for the single-system situation, in challenging observation conditions, not all available satellites are visible. In addition, affected by observation noises and atmospheric errors, the initialization often takes tens of seconds or even more depending on the number of tracked satellites, the baseline length and the observation environment [2, 3]. The fundamental reason is that the integer ambiguity cannot be resolved reliably. Integer ambiguity resolution (AR) is a prerequisite for precise RTK positioning [4–6]. The positioning accuracy can reach centimetre level if the ambiguities are correctly resolved. Otherwise the decimetre level even larger positioning bias will be introduced duo to the wrong ambiguities.

As the China's Navigation Satellite System (BDS) had provided regional service by the end of 2012, it has been one of the four global navigation satellite systems, together with the US system GPS, the Russian system GLONASS and the European system Galileo. Multi-constellation combination brings multiple satellites compared with single system, thus provides more redundant observation information. This contributes to the improvement of positioning stability [1, 7, 8]. Besides, multi-constellation combination will also contribute to AR, especially the geometry-based model, mainly for it can improve the ambiguity precision and thus improve the AR success rate [9, 10]. However for the systematic bias, for instance caused by atmospheric errors typically, the multi-constellation combination helps little. The existing commonly used RTK technology usually resolves the basic ambiguities, i.e. L1 (B1) or L2 (B2) ambiguities. The wavelengths of these basic carrier measurements are about from 18 to 25 cm. That is say, if the systematic bias reaches near half of the wavelength, the ambiguity can hardly be resolved correctly. Even if the ambiguity can be resolved correctly, it will take long time. That is the primary reason that the current RTK can just reach no more than 15 km. For the longer baseline, especially for the low-elevation satellites, atmospheric errors cannot be neglected, relatively to the wavelengths of basic carrier measurements.

In this contribution, in order to weaken the influence of atmospheric errors on AR, we proposed a reliable RTK positioning method. It takes advantage that wide-lane combination has much more longer wavelength, and the multi-constellation combined wide-lane ambiguity-fixed observations are directly used to positioning calculation. In the paper, firstly, the GPS/GLONASS/BDS combined geometry-based wide-lane AR model is introduced in Sect. 38.2. Then in Sect. 38.3, we introduce a partial ambiguity resolution (PAR) method to avoid the influence of extreme errors from low-elevation satellites. Lastly in Sect. 38.4, a typical example with real-data is given to reflect the benefits of the proposed method.

38.2 WL Ambiguity Resolution Model

38.2.1 Observation Model

Without loss of simplicity, the basic DD pseudorange and carrier observation equations can be expressed as below:

$$\Delta\nabla P_i = \Delta\nabla\rho + \Delta\nabla T + \Delta\nabla I_i + \Delta\nabla\varepsilon_{P_i} \tag{38.1}$$

$$\lambda_i \cdot \Delta\nabla\varphi_i = \Delta\nabla\rho + \Delta\nabla T - \Delta\nabla I_i + \lambda_i \cdot \Delta\nabla N_i + \Delta\nabla\varepsilon_{\phi_i} \tag{38.2}$$

where $\Delta\nabla(\cdot)$ is the double-difference operator; P and φ are pseudorange and carrier measurements respectively; λ is the wavelength; all the items with the subscript i represent the corresponding items in the ith frequency; ρ is the satellite-station distance; T is tropospheric delay; I is ionospheric delay; N is integer ambiguity; ϕ is the carrier observation by distance; ε_{P_i} and ε_{ϕ_i} are measurement noises of pseudorange and carrier respectively. Specifically for GLONASS, which adopt the Frequency Division Multiple Access (FDMA) model, $\lambda_i \cdot \Delta\nabla\varphi_i$ and $\lambda_i \cdot \Delta\nabla N_i$ can be further described as Eq. (38.3a, 38.3b):

$$\lambda_i \cdot \Delta\nabla\varphi_i = \lambda_{i,k}\nabla\varphi_{i,k} - \lambda_{i,r}\nabla\varphi_{i,r} \tag{38.3a}$$

$$\lambda_i \cdot \Delta\nabla N_i = \lambda_{i,k}\nabla N_{i,k} - \lambda_{i,r}\nabla N_{i,r} \tag{38.3b}$$

Based on the basic observation equations, the DD wide-lane measurement and corresponding observation equation can be expressed as Eqs. (38.4) and (38.5):

$$\Delta\nabla\phi_{wl} = \lambda_{wl} \cdot (\Delta\nabla\varphi_1 - \Delta\nabla\varphi_2) \tag{38.4}$$

$$\Delta\nabla\phi_{wl} = \Delta\nabla\rho + \Delta\nabla T - \Delta\nabla I_{wl} + \lambda_{wl} \cdot \Delta\nabla N_{wl} + \Delta\nabla\varepsilon_{\phi_{wl}} \tag{38.5}$$

Similarly to Eq. (38.3a, 38.3b), $\Delta\nabla\phi_{wl}$ and $\lambda_{wl} \cdot \Delta\nabla N_{wl}$ can also be further described as Eqs. (38.6) and (38.7):

$$\Delta\nabla\phi_{wl} = \lambda_{wl,k} \cdot \nabla\varphi_{wl,k} - \lambda_{wl,r} \cdot \nabla\varphi_{wl,r} \tag{38.6}$$

$$\lambda_{wl} \cdot \Delta\nabla N_{wl} = \lambda_{wl,k} \cdot \nabla N_{wl,k} - \lambda_{wl,r} \cdot \nabla N_{wl,r} \tag{38.7}$$

38.2.2 Wide-Lane Ambiguity Resolution with Geometry-Based Model

In geometry-based model, the unknown baseline vector parameters and wide-lane ambiguities are estimated together. The two pseudorange equations on f_1 and f_2, and

the wide-lane carrier equations are all used. The matrix form of calculating equation is as Eq. (38.8):

$$\begin{bmatrix} A^G & B^G & & \\ A^R & & B^R & \\ A^C & & & B^C \end{bmatrix} \begin{bmatrix} \mathrm{d}X \\ \Delta\nabla N_{wl}^G \\ \Delta\nabla N_{wl}^R \\ \Delta\nabla N_{wl}^C \end{bmatrix} = \begin{bmatrix} \Delta\nabla L^G \\ \Delta\nabla L^R \\ \Delta\nabla L^C \end{bmatrix} \tag{38.8}$$

where the superscript 'G', 'R', 'C' represent GPS, GLONASS, and BDS respectively; A is coefficient matrix of baseline vector parameters; B is coefficient matrix of DD ambiguities; $\mathrm{d}X$ represents the baseline vector parameters; $\Delta\nabla L$ is DD constant term matrix after linearization. From Eq. (38.8) we can calculate and get the float wide-lane ambiguity $\Delta\nabla\hat{N}_{wl}$ and its variance-covariance matrix (vc-matrix) $Q_{\hat{N}_{wl}}$. In order to make the DD ambiguity of GLONASS able to be calculated, we separate the DD ambiguity from Eq. (38.7) and rewrite it as (38.9) :

$$\lambda_{wl} \cdot \Delta\nabla N_{wl} = \lambda_{wl,k} \cdot [(\nabla N_{wl,k} - \nabla N_{wl,r}) + (1 - \frac{\lambda_{wl,r}}{\lambda_{wl,k}}) \cdot \nabla N_{wl,r}] \tag{38.9}$$

where $\nabla N_{wl,k} - \nabla N_{wl,r}$ is the DD wide-lane ambiguity which will be searched and fixed. From Eq. (38.9) we know, in order to separate DD wide-lane ambiguity of GLONASS, we need at first to know the station-single-difference wide-lane ambiguity of the reference satellite. It can be calculated using the Melbourne-Wübbena combination [11, 12], as Eq. (38.10).

$$\nabla N_{wl,r} = \nabla\varphi_{wl,r} - \frac{1}{\lambda_{wl,r}} \cdot \frac{f_{1,r} \cdot \nabla P_{1,r} + f_{2,r} \cdot \nabla P_{2,r}}{f_{1,r} + f_{2,r}} \tag{38.10}$$

The calculation of $\nabla N_{wl,r}$ is mainly affected by the measurement noises, especially the pseudorange noise. This problem can be solved through averaging method. In fact, the influence coefficient of the $\nabla N_{wl,r}$ on $\nabla N_{wl,k} - \nabla N_{wl,r}$ is $(1 - \lambda_{wl,r}/\lambda_{wl,k})$. And $\lambda_{wl,r}/\lambda_{wl,k}$ is a value near to one, so the bias of $\nabla N_{wl,r}$ will just has very small effect on $\nabla N_{wl,k} - \nabla N_{wl,r}$. It can be calculated that even if $\nabla N_{wl,r}$ has a ten-cycle bias, the influence on $\nabla N_{wl,k} - \nabla N_{wl,r}$ will be smaller than 0.05 cycle. After being processed by Eqs. (38.9) and (38.10), the DD wide-lane ambiguities of GLONASS can be search to integers like GPS or BDS.

38.3 Partial Ambiguity Resolution Method

From the method described in Sect. 38.2, we can get the float wide-lane DD ambiguities of all the three systems and the corresponding vc-matrix. We know that affected by atmospheric delays, measurement noises and multipath effects, the

measurements of low-elevation satellites generally have the much lower accuracy. If we fix all the ambiguities simultaneously, the low-elevation ones may influence the search system and make the search result unable to pass the acceptance test. So we can divide the ambiguities into two parts, of which the one is easy to be fixed, and of course the other one is not or maybe not to be fixed. As shown in Eq. (38.11), we suppose that $\hat{N}_a$, $Q_{\hat{N}_a}$ and $\hat{N}_b$, $Q_{\hat{N}_b}$ are the ambiguities and vc-matrix of the two parts respectively, as in Eq. (38.11).

$$\begin{bmatrix} \hat{N}_a \\ \hat{N}_b \end{bmatrix} \quad \begin{bmatrix} Q_{\hat{N}_a} & Q_{\hat{N}_a\hat{N}_b} \\ Q_{\hat{N}_b\hat{N}_a} & Q_{\hat{N}_b} \end{bmatrix} \tag{38.11}$$

If we can fix $\hat{N}_a$ reliably and the number of ambiguities in $\hat{N}_a$ is enough, we can directly use the fixed ambiguities to positioning calculation. Of course we can also use the fixed ambiguities to improve the accuracies of the remaining ambiguities and their vc-matrix, which can be referred from [13, 14]. In this paper we mainly consider the former, that is to say we directly use the selected fixed ambiguities to positioning calculation. However, the important thing is how to determine the subset. In this paper we get the subset by the following steps:

(1) Sort the elevations of all satellites as an ascend order, and we can get the new elevation set like Eq. (38.12)

$$E = \{e_1, e_2, \ldots, e_n \mid e_1 < e_2 < \cdots < e_n\} \tag{38.12}$$

where e_i represent the elevation in ith order.

(2) Set the cut-off elevation e_c at e_1, and we can get the subset $\hat{N}_a(e_1)$ and $Q_{\hat{N}_a}(e_1)$. Then the LAMBDA method [15] is applied into the ambiguity search process. If the search results meet the following three conditions, the fixed ambiguities can be considered to pass the acceptance test and be used into the flowing positioning calculation.

   (a) The bootstrapping AR success rate P_s, calculated according to Eq. (38.13) from the decorrelated vc-matrix [16] is larger than the set threshold, P_0;

$$P_s = \prod_{j=i}^{n} \left(2\Phi(\frac{1}{2\sigma_{\hat{z}_{j|J}}}) - 1 \right) \tag{38.13}$$

   where $\Phi(x) = \int_{-\infty}^{x} \frac{1}{\sqrt{2\pi}} \exp\{-\frac{1}{2}v^2\} dv$ and $\sigma_{\hat{z}_{j|J}}$ $(j = i, \ldots, n,\ J = \{j+1, \ldots, n\})$ denote the conditional standard deviations of the decorrelated ambiguities.

   (b) The ratio of the second minimum quadratic form of integer ambiguities residuals and the minimum one [17], which is shown in Eq. (38.14), is larger than the set threshold, t_0;

$$ratio = \frac{\| \hat{N}_a - \breve{N}_{a2} \|_{Q_{\hat{N}_a}}}{\| \hat{N}_a - \breve{N}_{a1} \|_{Q_{\hat{N}_a}}} \tag{38.14}$$

where $\breve{N}_{a1}$ and $\breve{N}_{a2}$ are the ambiguity candidates with the minimum and second minimum quadratic form respectively; $\| \cdot \|_{Q_{\hat{N}_a}} = (\cdot)^{\mathrm{T}} Q_{\hat{N}_a}^{-1} (\cdot)$.

(c) The number of ambiguities in the subset is larger than the set minimum threshold n_0 and the cut-off elevation is smaller than the set maximum threshold e_{c0}. The two conditions are set to ensure the selected satellites are still enough to get reliable positioning results, since too few or too

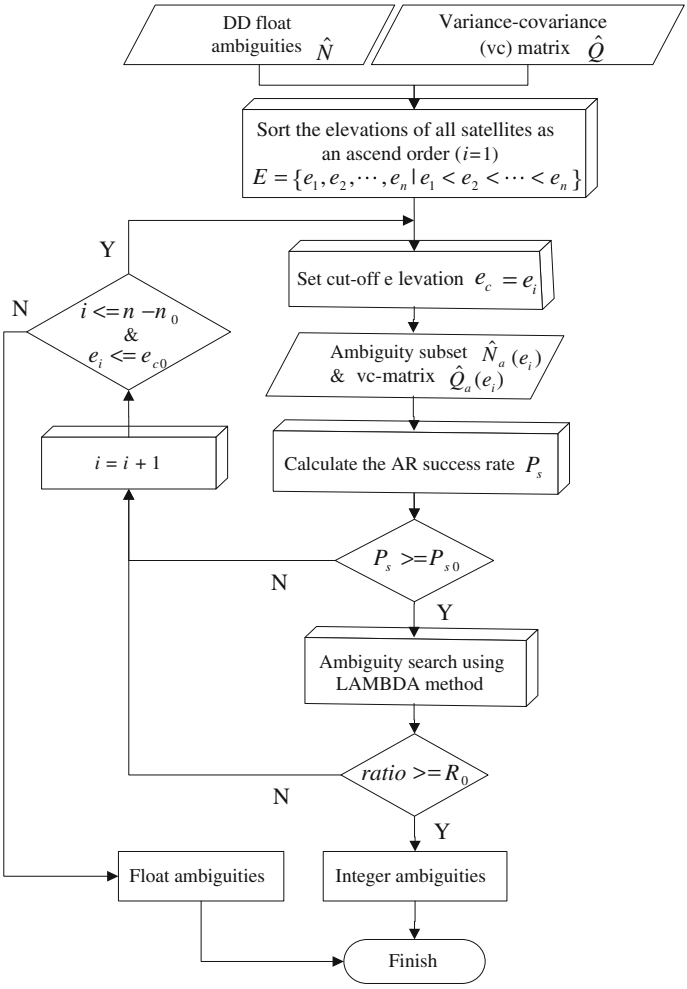

Fig. 38.1 The flowchart of ambiguity subset selection method in PAR model

high cut-off-elevation satellites are not adverse to the positioning stability, especially for the vertical direction.

(3) If the conditions in Step (2) cannot be met, the cut-off elevation will be set at e_2. Then the Step (2) will be repeated. Of course if cut-off elevation at e_2 is still unable to pass the acceptance test, the procedure will be continued with larger cut-off elevation. But if it runs into and meets the condition (c), the circulation will be stopped and the current epoch keeps the ambiguities float.
The procedure of the ambiguity subset selection method in PAR can also be expressed in Fig. 38.1. In the experiments of Sect. (38.4), P_0 is set at 0.999; t at 3.0; n_0 at 10 and e_{c0} at 35°.

38.4 Experiments

A 19.7-km baseline GNSS data is used to test the effects of the proposed RTK positioning method. The data contains observations from GPS, GLONASS and BDS systems. For lack of space, we just list and analyze the results from a selected typical period in detail. However, the method should be suitable for any other periods.

Figure 38.2 shows the residuals of DD wide-lane ambiguity-fixed carrier observations from three low-elevation satellites. The residuals mainly compose by two parts: ones are random items caused by the noises of carrier measurements, and the other ones are systematic items caused by atmospheric errors, i.e. tropospheric and ionospheric errors. We can see the residuals reach a considerable magnitude even larger than ten centimeters. Although the ionospheric errors in wide-lane observations are not equivalent to those in L1 or L2 observations, the absolute magnitude not differ significantly. For instance in GPS, the ionospheric error in the wide-lane observation is −1.283 times and −0.779 times from that in L1 or L2 observation. The similar results can also be obtained in GLONASS and BDS. So it can be seen the atmospheric errors will affect a lot to the L1 or L2 ambiguity resolution, where the corresponding wavelengths just range about from 19 to 25 cm.

Figure 38.3 shows the number of DD ambiguities to be fixed in several situations, including the three single-system situations of GPS, GLONASS and BDS, full ambiguity resolution (FAR) and PAR situations of G/R/C combination. We can see the G/R/C combined model almost triple the ambiguities in the single-system. And except the epochs where new satellite around, the number ambiguities in PAR model is almost the same with that in FAR model. This implies that the PAR model uses almost the same observation information with FAR. Figure 38.4 shows the success rates at the initial twenty epochs of AR in the five situations. As we can see, the G/R/C combined AR model dramatically improves the success rate, since the multi-constellation combination provides more redundant observation information. And this is the main contribution what multi-constellation combination takes to AR.

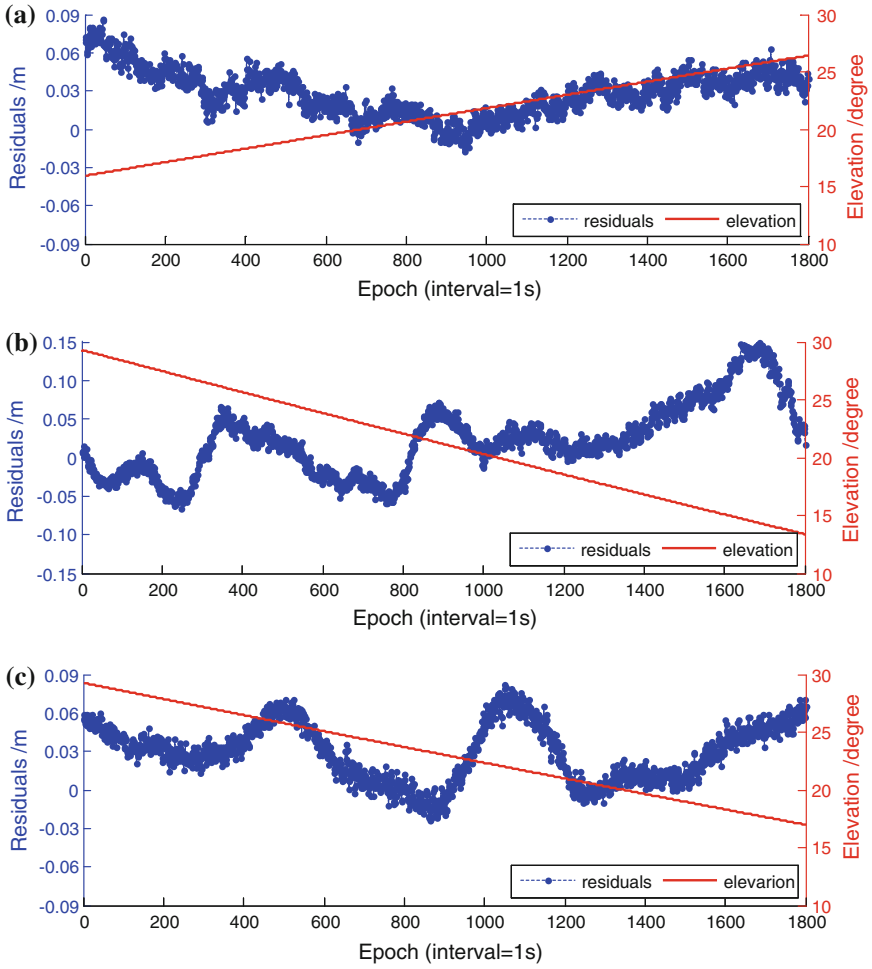

Fig. 38.2 Residuals of DD wide-lane ambiguity-fixed carrier observations from three low-elevation satellites. **a** G29. **b** R02. **c** C14

Figures 38.5 and 38.6 show the AR ratio values of G/R/C combined model and single-system model respectively. From Fig. 38.5 we can see, although in most time the single-system can get good ratio values larger than three, there are still some time where the ratio values are smaller than the threshold, for instance in the initial seventy epochs of GPS and the epochs around the time when the new satellite arises. Figure 38.6 show the FAR and PAR results both with G/R/C combined model, in which we can see at the initial phase, the ratio values are much larger than that of any single-system. When there has the new rising satellite, the FAR model suffers from the poor ambiguity precision and large ambiguity bias of low-elevation satellite, so the ratio drops suddenly. Nevertheless, the PAR model can avoid this

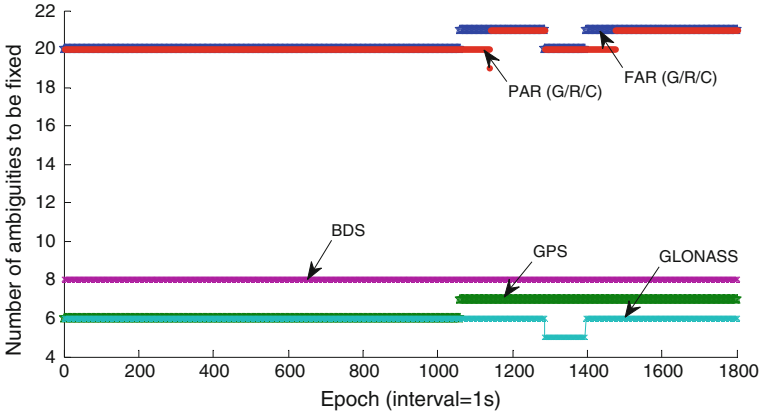

Fig. 38.3 Number of ambiguities to be fixed in the five situations

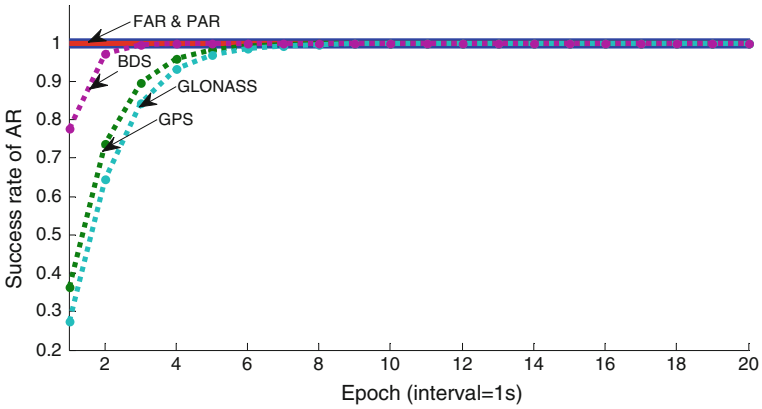

Fig. 38.4 Success rate of AR in the five situations

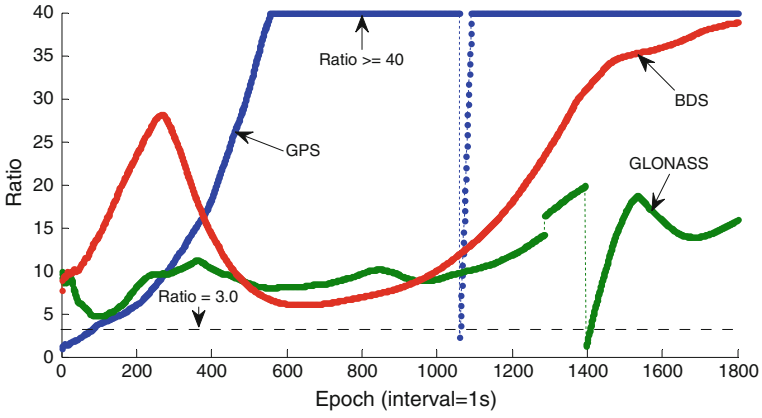

Fig. 38.5 Ratio in single-system AR

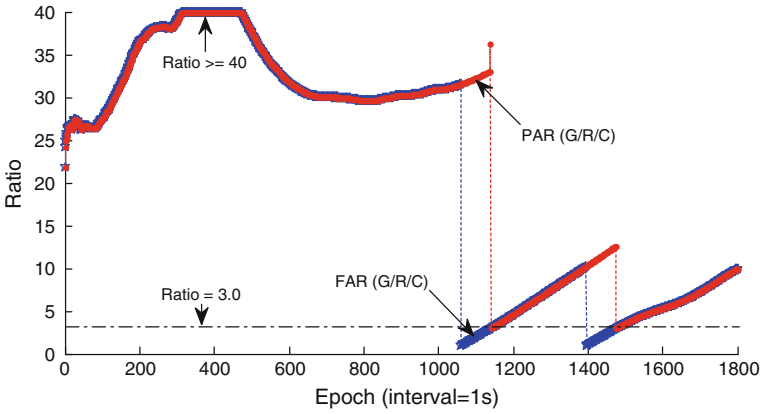

Fig. 38.6 Ratio in FAR and PAR model with G/R/C combination

problem. The reason is that the new rising satellite is removed adaptively according to the PAR criterions, and thus not involved in the ambiguity search and fixing. In the later epochs, as the elevation increases and the ambiguity precision improve, the 'new rising' ambiguity will be adopted in the ambiguity fixing. Although the ratio also drops a lot, it still meets the criterions, thus still ensure the AR reliability.

After fixing the wide-lane ambiguities by the PAR method, the fixed integer wide-lane ambiguities can be backtracked into the model like Eq. (38.8), and the positioning results can be calculated. The positioning biases of north, east and up (N/E/U in Fig. 38.7) directions are shown in Fig. 38.7. We can see the positioning biases of three directions are all within ±10 cm, especially the north and east, almost within ±5 cm. Affected by the residual atmospheric errors, the positioning results reflect some systematic biases especially in the up direction. However this may be already enough for many practical positioning applications.

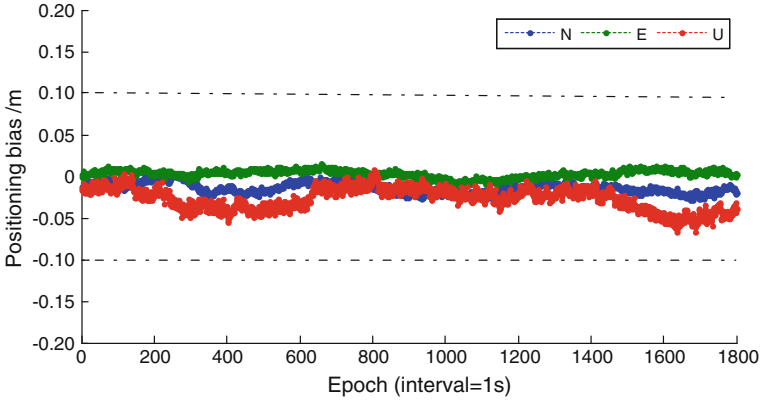

Fig. 38.7 Positioning bias of the G/R/C combined PAR model

38.5 Conclusion

The paper proposes a reliable RTK positioning method based on partial wide-lane ambiguity resolution from GPS/GLONASS/BDS Combination. The unified G/R/C geometry-based wide-lane AR model and the PAR method are introduced in detail. Real G/R/C baseline data is also calculated as typical example to reflect the benefits of the proposed method. Main conclusions are as follows:

(1) The method takes advantage that wide-lane observation has much longer wavelength and ambiguity easy to be fixed. So the wide-lane AR suffers much less from the atmospheric errors compared with the AR of basic observation, i.e. L1(B1) or L2(B2).
(2) Combined with the single-system based AR model, multi-constellation combination can significantly improve the wide-lane AR effects, including the AR success rate, ratio and initialization speed, as multi-constellation combination provides more redundant observation information.
(3) The proposed PAR method can effectively avoid the negative influence of new rising satellites, as it removes the new rising satellite(s) adaptively according to the PAR criterions thus ensure the AR stability. At the same time the PAR model uses almost the same satellites except removed new rising satellite(s). So the fixed ambiguities are enough to directly used in positioning calculation.
(4) The positioning accuracy with G/R/C combined ambiguity-fixed wide-lane observations can still reach centimetre level.

Acknowledgments This work is supported by the Key Projects in the National Science & Technology Pillar Program during the Twelfth Five-year Plan Period (No. 2012BAJ23B01). The authors are very grateful to the anonymous reviewers for their constructive comments and suggestions.

References

1. He H, Li J, Yang Y et al (2013) Performance assessment of single-and dual-frequency BeiDou/GPS single-epoch kinematic positioning. GPS Solutions 2013:1–11
2. Odijk D, Traugott J, Sachs G et al (2001) Two approaches to precise kinematic GPS positioning with miniaturized L1 receivers. In: Proceedings of the 20th international technical meeting of the satellite division of the institute of navigation (ION GNSS 2007), pp 827–838
3. Takasu T, Yasuda A (2008) Evaluation of RTK-GPS performance with low-cost single-frequency GPS receivers. In: Proceedings of international symposium on GPS/GNSS, pp 852–861
4. Li J, Yang Y, Xu J et al (2013) GNSS multi-carrier fast partial ambiguity resolution strategy tested with real BDS/GPS dual-and triple-frequency observations. GPS Solutions. http://link.springer.com/article/10.1007/s10291-013-0360-6
5. Deng C, Tang W, Liu J et al (2013) Reliable single-epoch ambiguity resolution for short baselines using combined GPS/BeiDou system. GPS Solutions. http://link.springer.com/article/10.1007/s10291-013-0337-5

6. Parkins A (2011) Increasing GNSS RTK availability with a new single-epoch batch partial ambiguity resolution algorithm. GPS Solutions 15(4):391–402
7. Yang YX, Li JL, Xu JY et al (2011) Contribution of the compass satellite navigation system to global PNT users. Chin Sci Bull 56(26):2813–2819
8. Li J, Yang Y, Xu J et al (2013) Performance analysis of single-epoch dual-frequency RTK by BeiDou navigation satellite system. In: China satellite navigation conference (CSNC) 2013 proceedings. Springer Berlin Heidelberg, pp 133–143
9. Teunissen PJG, Odolinski R, Odijk D (2014) Instantaneous BeiDou+GPS RTK positioning with high cut-off elevation angles. J Geodesy 88(4):335–350
10. Dai L (2000) Dual-frequency GPS/GLONASS real-time ambiguity resolution for medium-range kinematic positioning. In: 13th international technical meeting of the satellite division of the US institute of navigation, Salt Lake City, Utah, pp 19–22
11. Melbourne WG (1985) The case for ranging in GPS-based geodetic systems. In: Proceedings of 1st international symposium on precise positioning with GPS, Rockville, Maryland, pp 373–386
12. Wübbena G (1985) Software developments for geodetic positioning with GPS using TI-4100 code and carrier measurements. In: Proceedings of the first international symposium on precise positioning with the global positioning system, 15–19 April 1985, Rockville, Maryland, USA, pp 403–412
13. Teunissen PJG, Joosten P, Tiberius C (1999) Geometry-free ambiguity success rates in case of partial fixing. In: Proceedings of ION-NTM, pp 25–27
14. Li B, Shen Y, Feng Y et al (2014) GNSS ambiguity resolution with controllable failure rate for long baseline network RTK. J Geodesy 88(2):99–112
15. Teunissen PJG (1995) The least-squares ambiguity decorrelation adjustment: a method for fast GPS integer ambiguity estimation. J Geodesy 70(1–2):65–82
16. Teunissen PJG (1998) Success probability of integer GPS ambiguity rounding and bootstrapping. J Geodesy 72(10):606–612
17. Verhagen S, Teunissen PJG (2013) The ratio test for future GNSS ambiguity resolution. GPS Solutions 17(4):535–548

Chapter 39
Optimal Kalman Filtering in the Presence of Time-Correlated Process Noise

Zebo Zhou, Yunlong Wu and Hua Chai

Abstract Kalman filtering (KF), in previous works, assumes that system noises are white Gaussian noises (WGN) and are uncorrelated with each other. This assumption, however, is not reasonable in real-world navigation applications. This paper dedicates to develop an optimal Kaman filtering navigation algorithm in the time-correlated contained dynamic system. Efforts are made on its stochastic model establishment and the corresponding recursive formulae derivations. First, as a popular sort of time-correlated noise-whitening method, the principle of state augmentation based KF (SAKF) is reviewed and presented. Alternative method second moment information based KF (SMIKF) which directly compensates the variances through stochastic model is proposed and developed. To precisely establish the stochastic model of time-correlated process noise, a refined SMIKF (RSMIKF) is further rigorously proposed and derived from continuous-time dynamic model. We also investigate the numerical computation burden for these developed methods compared with conventional KF (CKF). Finally, a simulation experiment is carried out to illustrate the performances of our proposed algorithm. The accuracies of CKF and our proposed methods are all computed and analyzed for comparison purpose. The results show that the proposed RSMIKF algorithm adapts to the time-correlated process noise very well and obtains the accurate and reliable solutions compared with other methods as expected.

Keywords Time-correlated noise · Kalman filtering · Dynamic model · Autoregressive model · Stochastic model

Z. Zhou (✉)
School of Aeronautics & Astronautics, University of Electronic Science and Technology of China, Chengdu 611731, People's Republic of China
e-mail: klinsmann.zhou@gmail.com

Y. Wu (✉)
Key Laboratory of Earthquake Geodesy, Institute of Seismology, China Earthquake Administration, Wuhan 430071, People's Republic of China

H. Chai
Institute of Geodesy and Geophysics, Chinese Academy of Sciences, Wuhan 430077, People's Republic of China

J. Sun et al. (eds.), *China Satellite Navigation Conference (CSNC) 2015 Proceedings: Volume II*, Lecture Notes in Electrical Engineering 341,
DOI 10.1007/978-3-662-46635-3_39

39.1 Introduction

The Kalman filtering (KF), as an efficient time-domain sequential estimation method has been well-developed and extensively applied in various navigation fields [1]. It operates recursively on streams of noisy input data to produce a statistically optimal estimate of the underlying system state [2]. To obtain the highly precise solution, it is important not only formulating the correct function model, i.e. dynamic model and observation model, but also identifying a stochastic model that can accurately describe the noise characteristics [3, 4]. In conventional Kalman filtering (CKF), both process noise and observation noise are usually assumed to be white Gaussian noise (WGN). However, for real applications in a time-variant environment, the dynamic system inevitably contains time-correlated noise thus compromise the filtering accuracy [5]. An easy way to weaken the time-correlated noise is to increase the sampling interval [6], whereas it is not suitable for requirements of modern navigation.

In the past few decades, many efforts have been made on processing the time-correlated noise existing in the navigation applications. These literatures on this topic usually compensate the noise into functional model where the time-correlated noises are treated as the outputs driven by white noise [7–9]. These methods, however, are difficult to be implemented due to its fixed dimension [10]. Recently, many researches focus on the modeling the time-correlated noise by using auto-regressive (AR), autoregressive and moving average (ARMA) and Markov process theories etc. [11–13]. Thus state expansion becomes popular to deal with the time-correlated noise in the real navigation systems i.e., the inertial navigation system (INS) [14–16]. These can be referred as to state augmentation based KF (SAKF) methods. In essence, it is a noise-whitening method which treats the noise as a new component of the state vector. Actually, compensating noise influence through stochastic model in KF where the corresponding statistic variances are inflated, also provides reliable and accurate navigation solutions [17–22]. These approaches can essentially reduce or even withdraw influence of the inaccurate prior knowledge and adjust the contributions of dynamic model to final KF solution. However, time-correlation is absent for KF derivations in these literatures. For this reason, it would be attractive and promising for further extending the stochastic model compensation approaches in KF to the colored noise contained dynamic system. It is referred as to the second moment information based KF (SMIKF) in this paper.

Furthermore, for dealing with continuous time-correlated process noise, existing methods discretize it separating from the continuous-time differential state equation. However, this kind of methods is not rigorous from the point of view of the stochastic process theory since the discrete-time stochastic model of noise is accumulated through state transition. Therefore it needs to be rigorously established by discretizing the continuous-time noise along with the state transition differential equation.

By emphasizing the stochastic model construction and the corresponding filtering formulae derivations, we develop an optimal Kaman filtering algorithm for

navigation computation in presence of the time-correlated process noise. The reminder of paper is organized as follows. A briefly review on conventional Kalman filtering (CKF) with continuous-time dynamic model is introduced in Sect. 39.2. In Sect. 39.3, SAKF method is presented for dealing with time-correlated process noises. The SMIKF and the corresponding refined SMIKF (RSMIKF) methods are proposed and developed by compensating time-correlation influence through stochastic model of process noise in Sect. 39.4. The computation burden is presented and analyzed in Sect. 39.5. In Sect. 39.6, a simulation is implemented to illustrate the concept of our proposed method. The concluding remarks are given in Sect. 39.7.

39.2 A Brief Review on CKF with Continuous-Time Dynamic Model

This section briefs overall system model establishment of CKF. Generally, the system consists of the continuous-time dynamic model and the discrete-time observation model.

39.2.1 Continuous-Time Dynamic Model and Its Discrete Form

The state space representation of differential equation at epoch t is expressed as

$$\dot{\boldsymbol{x}}(t) = \boldsymbol{A}\boldsymbol{x}(t) + \boldsymbol{G}\boldsymbol{\omega}(t) \tag{39.1}$$

where $\boldsymbol{x}$ is the state vector with the dimension $m \times 1$; $\boldsymbol{A}$ is a constant $m \times m$ matrix; $\boldsymbol{G}$ is a $m \times m$ matrix. $\boldsymbol{\omega}$ is the m-dimensional dynamic driving noise with Gaussian distribution and $\mathrm{E}\left(\boldsymbol{\omega}(t)\boldsymbol{\omega}(\tau)^T\right) = \boldsymbol{Q}(t)\delta(t-\tau)$, where $\mathrm{E}(\bullet)$ is the expectation operator; $\boldsymbol{Q}$ and δ denote the variance of process noise and the Dirac function respectively. The discrete-time form of Eq. (39.1) at epoch t_k is written as

$$\boldsymbol{x}_k = \boldsymbol{\Phi}_{k,k-1}\boldsymbol{x}_{k-1} + \boldsymbol{w}_k \tag{39.2}$$

where $\boldsymbol{\Phi}_{k,k-1} = e^{\boldsymbol{A}(t_k - t_{k-1})}$ is the transition matrix which transforms the state of epoch t_{k-1} into t_k; $\boldsymbol{w}_k$ is a Gaussian discrete-time stochastic process with statistics of

$$\boldsymbol{w}_k = \int_{t_{k-1}}^{t_k} \boldsymbol{\Phi}_{k,i}\boldsymbol{G}\boldsymbol{\omega}(t_i)dt_i \tag{39.3}$$

It is easy to prove $\mathrm{E}(\boldsymbol{w}_k) = 0_{m\times 1}$ and the variance of $\boldsymbol{w}_k$

$$\boldsymbol{Q}_{\boldsymbol{w}_k} = \mathrm{E}\left(\boldsymbol{w}_k(\boldsymbol{w}_k)^T\right) = \int_{t_{k-1}}^{t_k} \boldsymbol{\Phi}_{k,i}\boldsymbol{G}\boldsymbol{\omega}(t_i)\,\boldsymbol{\omega}(t_i)^T\boldsymbol{G}^T\boldsymbol{\Phi}_{k,i}^T dt_i \tag{39.4}$$

39.2.2 CKF Formulae

The measurements are usually discrete rather than continuous outputs in most navigation systems. Therefore, we herein directly present the linear(ized) discrete-time observation model at epoch t_k,

$$\boldsymbol{l}_k = \boldsymbol{H}_k\boldsymbol{x}_k + \boldsymbol{\varepsilon}_k \tag{39.5}$$

where $\boldsymbol{l}$ is the measurement vector with dimension $n \times 1$; $\boldsymbol{H}$ is a $n \times m$ design matrix; $\boldsymbol{\varepsilon}$ is normally distributed noise with $\mathrm{E}(\boldsymbol{\varepsilon}_k) = 0_{n\times 1}$ and $\mathrm{E}\left(\boldsymbol{\varepsilon}_k\left(\boldsymbol{\varepsilon}_j\right)^T\right) = \delta(k-j)\boldsymbol{Q}_{\boldsymbol{\varepsilon}_k}$. According to Eqs. (39.1) and (39.5), the recursive formulae of CKF can be calculated by following Eqs. (39.6)–(39.12)

$$\hat{\boldsymbol{x}}_k = \bar{\boldsymbol{x}}_k + \boldsymbol{Q}_{\bar{\boldsymbol{x}}_k\bar{\boldsymbol{l}}_k}\boldsymbol{Q}_{\bar{\boldsymbol{l}}_k}^{-1}\left(\boldsymbol{l}_k - \bar{\boldsymbol{l}}_k\right) \tag{39.6}$$

$$\boldsymbol{Q}_{\hat{\boldsymbol{x}}_k} = \left(\boldsymbol{I} - \boldsymbol{Q}_{\bar{\boldsymbol{x}}_k\bar{\boldsymbol{l}}_k}\boldsymbol{Q}_{\bar{\boldsymbol{l}}_k}^{-1}\boldsymbol{H}_k\right)\boldsymbol{Q}_{\bar{\boldsymbol{x}}_k} \tag{39.7}$$

where the predicted state vector and its variance are

$$\bar{\boldsymbol{x}}_k = \boldsymbol{\Phi}_{k,k-1}\hat{\boldsymbol{x}}_{k-1} \tag{39.8}$$

$$\boldsymbol{Q}_{\bar{\boldsymbol{x}}_k} = \boldsymbol{\Phi}_{k,k-1}\boldsymbol{Q}_{\hat{\boldsymbol{x}}_{k-1}}\boldsymbol{\Phi}_{k,k-1}^T + \boldsymbol{Q}_{\boldsymbol{w}_k} \tag{39.9}$$

the predicted measurement vector and its variance are

$$\bar{\boldsymbol{l}}_k = \boldsymbol{H}_k\bar{\boldsymbol{x}}_k \tag{39.10}$$

$$\boldsymbol{Q}_{\bar{\boldsymbol{l}}_k} = \boldsymbol{H}_k\boldsymbol{Q}_{\bar{\boldsymbol{x}}_k}\boldsymbol{H}_k^T + \boldsymbol{Q}_{\boldsymbol{\varepsilon}_k} \tag{39.11}$$

the covariance matrix of $\bar{\boldsymbol{x}}_k$ and $\bar{\boldsymbol{l}}_k$ is easily derived by

$$\boldsymbol{Q}_{\bar{\boldsymbol{x}}_k\bar{\boldsymbol{l}}_k} = \boldsymbol{Q}_{\bar{\boldsymbol{x}}_k}\boldsymbol{H}_k^T \tag{39.12}$$

Letting gain matrix $\boldsymbol{K}_k = \boldsymbol{Q}_{\tilde{\boldsymbol{x}}_k\bar{\boldsymbol{l}}}\boldsymbol{Q}_{\bar{\boldsymbol{l}}_k}^{-1}$, the estimate error of CKF is

$$\tilde{\boldsymbol{x}}_k = \boldsymbol{x}_k - \hat{\boldsymbol{x}}_k = (\boldsymbol{I} - \boldsymbol{K}_k\boldsymbol{H}_k)\left(\boldsymbol{\Phi}_{k,k-1}\tilde{\boldsymbol{x}}_{k-1} + \boldsymbol{w}_k\right) - \boldsymbol{K}_k\boldsymbol{\varepsilon}_k \tag{39.13}$$

39.3 State Augmentation Based Kalman Filtering

As a straight and effective method to deal with time-correlated noise, whitening noise is the most popular way for KF computation in dynamic systems. It essentially either treats the process noise as the unknown parameters to be estimated together with state vector. It can be viewed as a state augmentation of original system model. Therefore we name it as the state augmented Kalman filtering (SAKF). In this section, we will present the SAKF method to deal with the process noise. Since the noise accompanying with whole dynamic progress, a continuous time-correlated noise model is employed here for further derivations. Herein for simplicity, assuming the noises mentioned above as a first-order Markov process, we have following noise model,

$$\dot{\boldsymbol{\omega}}(t) = -\alpha\boldsymbol{\omega}(t) + \boldsymbol{\eta}(t), \quad \boldsymbol{\eta}(t) \sim \mathrm{N}\left(0_{m\times 1}, \boldsymbol{Q}_{\boldsymbol{\eta}}\right) \tag{39.14}$$

where α is the correlation coefficients of process noise; η is the corresponding WGN of system. By discretizing Eq. (39.14), it arrives at

$$\boldsymbol{w}_k = (1-\alpha)\boldsymbol{w}_{k-1} + \boldsymbol{\eta}_k \tag{39.15}$$

It should be noticed that different from $\boldsymbol{\eta}(t)$, $\boldsymbol{\eta}_k$ contains the influences by transition matrix, e.g. for a constant velocity (CV) dynamic model, $\boldsymbol{Q}_{\boldsymbol{\eta}_k} = \begin{pmatrix} \frac{1}{3}\Delta t_k^3 & \frac{1}{2}\Delta t_k^2 \\ \frac{1}{2}\Delta t_k^2 & \Delta t_k \end{pmatrix} \otimes \boldsymbol{Q}_{\boldsymbol{\eta}}$. Combining Eqs. (39.15) with (39.2), the augmented state equation can be expressed by,

$$\boldsymbol{x}_k^a = \boldsymbol{\Phi}_{k,k-1}^a\boldsymbol{x}_{k-1}^a + \boldsymbol{w}_k \tag{39.16}$$

where $\boldsymbol{x}^a = \begin{pmatrix}\boldsymbol{x}^{\mathrm{T}} & \boldsymbol{w}^{\mathrm{T}}\end{pmatrix}^{\mathrm{T}}$, $\boldsymbol{\Phi}_{k,k-1}^a = \begin{pmatrix} \boldsymbol{\Phi}_{k,k-1} & \boldsymbol{I} \\ 0_{m\times m} & (1-\alpha)\boldsymbol{I}_{m\times m} \end{pmatrix}$, and $\boldsymbol{w}_k^a = \begin{pmatrix} 0_{m\times 1} \\ \boldsymbol{\eta}_k \end{pmatrix}$.

Let $\boldsymbol{H}_k^a = \begin{pmatrix}\boldsymbol{H}_k & 0_{n\times m}\end{pmatrix}$ and accordingly, the observation model is rewritten as,

$$\boldsymbol{l}_k = \boldsymbol{H}_k^a\boldsymbol{x}_k^a + \boldsymbol{\varepsilon}_k \tag{39.17}$$

Then we obtain the solution by implementing CKF equations with (39.6)–(39.12).

39.4 The Second Moment Information Based Kalman Filtering

For the AKF discussed in Sect. 39.3, it is not always convenient to reformulate system model for noise whitening, especially for these high-order correlated noises. Moreover, due to the state augmentation, the parameters to be estimated are double-times increased thus dramatically weakened the filtering model strength. Therefore, it is not suitable for real-time navigation fields where the observation is usually insufficient. In this section, we investigate the second moment information based Kalman filtering (SMIKF) method to deal with time-correlated process noise. Moreover, a refined SMIKF (RSMIKF) which propagates variance of process noise into the KF formulae is rigorously developed.

39.4.1 SMIKF

Let's start with the definition of predicted state error

$$\tilde{\boldsymbol{x}}_{k,k-1} = \boldsymbol{x}_k - \bar{\boldsymbol{x}}_k = \boldsymbol{\Phi}_{k,k-1}\tilde{\boldsymbol{x}}_{k-1} + \boldsymbol{w}_k \tag{39.18}$$

and the variance of $\bar{\boldsymbol{x}}_k$ is derived based on the error propagation law

$$\boldsymbol{Q}_{\bar{\boldsymbol{x}}_k} = \boldsymbol{\Phi}_{k,k-1}\boldsymbol{Q}_{\hat{\boldsymbol{x}}_{k-1}}\boldsymbol{\Phi}_{k,k-1}^{\mathrm{T}} - \boldsymbol{Q}_{\boldsymbol{w}_k\hat{\boldsymbol{x}}_{k-1}}\boldsymbol{\Phi}_{k,k-1}^{\mathrm{T}} - \boldsymbol{\Phi}_{k,k-1}\boldsymbol{Q}_{\hat{\boldsymbol{x}}_{k-1}\boldsymbol{w}_k} + \boldsymbol{Q}_{\boldsymbol{w}_k} \tag{39.19}$$

where $\boldsymbol{Q}_{\boldsymbol{w}_k}$ and $\boldsymbol{Q}_{\hat{\boldsymbol{x}}_{k-1}\boldsymbol{w}_k}$ are calculated by Eqs. (39.20) and (39.21)

$$\boldsymbol{Q}_{\boldsymbol{w}_k} = (1-\alpha)^2\boldsymbol{Q}_{\boldsymbol{w}_{k-1}} + \boldsymbol{Q}_{\boldsymbol{\eta}_k} \tag{39.20}$$

$$\boldsymbol{Q}_{\hat{\boldsymbol{x}}_{k-1}\boldsymbol{w}_k} = -(\boldsymbol{I} - \boldsymbol{K}_{k-1}\boldsymbol{H}_{k-1})\boldsymbol{Q}_{\boldsymbol{w}_{k-1}\boldsymbol{w}_k} \tag{39.21}$$

Noticed that $\boldsymbol{Q}_{\hat{\boldsymbol{x}}_{k-1}\boldsymbol{w}_k}$ in Eq. (39.21) can be obtained if the covariance $\boldsymbol{Q}_{\boldsymbol{w}_{k-1}\boldsymbol{w}_k}$ is extracted from Eq. (39.15) beforehand with

$$\boldsymbol{Q}_{\boldsymbol{w}_k\boldsymbol{w}_{k-1}} = (1-\alpha)\boldsymbol{Q}_{\boldsymbol{w}_{k-1}} \tag{39.22}$$

Replacing Eqs. (39.9) by (39.19), finally the KF formulae for the colored process noise contained system can be conducted followed by the progress of CKF implementations.

39.4.2 RSMIKF

As mentioned in Sect. 39.4.1, SMIKF uses the discrete-time stochastic model in Eq. (39.15) which is directly discretized from Eq. (39.14). Evidently, the discretization step is an approximation, and apparently does not involve any information from Eq. (39.1). Whereas, in fact, the rigorous discretization should be implemented by considering both Eqs. (39.1) and (39.14) to precisely establish the stochastic model in KF. It will be illustrated to be very essential and important in the simulation part.

Let us start with the exact solution of Eq. (39.14)

$$\boldsymbol{\omega}(t) = \boldsymbol{\eta}(t_0)e^{-\alpha(t-t_0)} + \int_{t_0}^{t} \boldsymbol{\eta}(t_\tau)e^{-\alpha(t-t_\tau)}\mathrm{d}t_\tau \tag{39.23}$$

If the initial process noise is zero, Eq. (39.21) can be further reduced as

$$\boldsymbol{\omega}(t) = \int_{t_0}^{t} \boldsymbol{\eta}(t_\tau)e^{-\alpha(t-t_\tau)}\mathrm{d}t_\tau \tag{39.24}$$

Noticing that the mean square integral of $\boldsymbol{\eta}(\tau)\mathrm{e}^{-\alpha(t-\tau)}$ exists from 0 to t, the variance of process noise at time t can be calculated based on the Fubini's theorem,

$$\boldsymbol{Q}(t) = \lim_{\Delta\to\infty} \mathrm{E}\left(\left(\sum_{k=1}^{n} \boldsymbol{\eta}(\boldsymbol{u}_k)\mathrm{e}^{-\alpha(t-\boldsymbol{u}_k)}\Delta t_k\right)\overline{\left(\sum_{j=1}^{n} \boldsymbol{\eta}(\boldsymbol{v}_j)\mathrm{e}^{-\alpha\left(t-\boldsymbol{v}_j\right)}\Delta s_j\right)}^{\mathrm{T}}\right) \tag{39.25}$$

where $t_k \in [t_0, t]$; $\Delta t_k = t_k - t_{k-1}$; $\Delta s_j = s_j - s_{j-1}$; $\Delta = \max\limits_{\substack{1\le k\le n\\ 1\le j\le m}} \left\{\Delta t_k, \Delta s_j\right\}$; $\left(u_k, v_j\right) \in (t_{k-1}, t_k] \times (s_{k-1}, s_k]$. Then Eq. (39.25) can be further conducted as

$$\boldsymbol{Q}(t) = \int_{t_0}^{t}\int_{t_0}^{t} \mathrm{e}^{-\alpha(t-t_\tau)}\mathrm{e}^{-\alpha(t-s_\tau)}\mathrm{E}\left(\boldsymbol{\eta}(t_\tau)\boldsymbol{\eta}(s_\tau)^{\mathrm{T}}\right)\mathrm{d}t_\tau \tag{39.26}$$

Considering $\boldsymbol{Q}_{\boldsymbol{\eta}}$ as the variance of $\boldsymbol{\eta}(t)$, $\boldsymbol{Q}(t)$ is trivially derived by

$$\boldsymbol{Q}(t) = \frac{1}{2\alpha}\left(1 - e^{-2\alpha(t-t_0)}\right)\boldsymbol{Q}_{\eta} \tag{39.27}$$

In addition, we can similarly obtain the autocorrelation characteristic of $\boldsymbol{\omega}$

$$\mathrm{E}\left(\boldsymbol{\omega}(t)\boldsymbol{\omega}(s)^{\mathrm{T}}\right) = \frac{1}{2\alpha}\left(1 - e^{-2\alpha(\min(t,s)-t_0)}\right)\boldsymbol{Q}_{\eta} \tag{39.28}$$

Next we will derive the discrete-time case based on the equations above. The key issue is to solve $\boldsymbol{Q}_{\boldsymbol{w}_k}$ and $\boldsymbol{Q}_{\hat{\boldsymbol{x}}_{k-1}\boldsymbol{w}_k}$ for computation of Eqs. (39.20) and (39.21). Theoretically, $\boldsymbol{w}_k$ in discrete-time dynamic model should reflect the variations caused by the colored noise $\boldsymbol{\omega}$ accumulated from time t_{k-1} to t_k,

$$\begin{aligned}\boldsymbol{w}_k &= \int_{t_{k-1}}^{t_k} \boldsymbol{\Phi}_{k,\tau}\boldsymbol{G}\boldsymbol{\omega}(t_\tau)\mathrm{d}t_\tau \\ &= e^{At_k}\int_{t_{k-1}}^{t_k} e^{-At_\tau}\boldsymbol{G}\left(\int_{t_0}^{t_\tau}\boldsymbol{\eta}(t_\tau)e^{-\alpha(t_\tau-t_s)}\mathrm{d}t_s\right)\mathrm{d}t_\tau\end{aligned} \tag{39.29}$$

The corresponding expectation is

$$\mathrm{E}(\boldsymbol{w}_k) = \int_{t_{k-1}}^{t_k} \boldsymbol{\Phi}_{k,\tau}\boldsymbol{G}\mathrm{E}(\boldsymbol{\omega}(t))dt \tag{39.30}$$

Obviously, it is rather easy to prove $\mathrm{E}(\boldsymbol{w}_k) = 0_{m\times 1}$ thus $\boldsymbol{w}$ is still unbiased. Considering that $\boldsymbol{\Phi}_{k,\tau}\boldsymbol{G}\boldsymbol{\omega}(t_\tau)$ is mean-square integrable from t_{k-1} to t_k, the variance of $\boldsymbol{w}$ can be conducted as

$$\boldsymbol{Q}_{\boldsymbol{w}_k} = \int_{t_{k-1}}^{t_k} \boldsymbol{\Phi}_{k,\tau}dt_\tau \int_{t_{k-1}}^{t_k} \boldsymbol{G}\boldsymbol{Q}(t_s)\boldsymbol{G}^{\mathrm{T}}\boldsymbol{\Phi}_{k,s}^{\mathrm{T}}dt_s \tag{39.31}$$

To obtain $\boldsymbol{Q}_{\hat{\boldsymbol{x}}_{k-1}\boldsymbol{w}_k}$, we need to compute $\boldsymbol{Q}_{\boldsymbol{w}_k\boldsymbol{w}_{k-1}}$ first based on

$$\boldsymbol{Q}_{\boldsymbol{w}_k\boldsymbol{w}_{k-1}} = \mathrm{E}(\boldsymbol{w}_k\boldsymbol{w}_{k-1}) = \int_{t_{k-1}}^{t_k} \boldsymbol{\Phi}_{k,\tau}dt_\tau \int_{t_{k-2}}^{t_{k-1}} \boldsymbol{G}\boldsymbol{Q}(t_s)\boldsymbol{G}^{\mathrm{T}}\boldsymbol{\Phi}_{k,s}^{\mathrm{T}}dt_s \tag{39.32}$$

Insert $\boldsymbol{Q}_{\boldsymbol{w}_{k-1}\boldsymbol{w}_k}$ solved by Eqs. (39.32) into (39.21) and combine $\boldsymbol{Q}_{\boldsymbol{w}_k}$ solved by Eq. (39.31), thus SMIKF is refined through Eq. (39.19).

39.5 Computation Burden Discussions

Both SAKF and SMIKF formulae have been well-conducted in the presence of time-correlated process noise. Certainly, these methods are more complex compared with CKF. In this section, we will get insight into their computation burden. In order to comprehensively evaluate the computation burden aspect, CKF, SAKF and SMIKF are employed and analyzed in details. For more general and objective analysis, the state dimension and observation dimension are denoted as m and n respectively. The statistics of computation burdens for all schemes are presented in Tables 39.1 and 39.2. The inverse operation is the same for all schemes, for this reason we do not present the inverse operation in the Tables 39.1 and 39.2. To clearly show the computation cost, we draw the computation ratio figure (see Fig. 39.1) which indicates the computation burden of SAKF and SMIKF divided by that of CKF.

It can be seen from the figures that: (i) The computation cost is more sensitive to state dimension than observation dimension. In essence, this is due to the more computations involved in prediction step. It is therefore of importance to point out that all the state expansion methods will of course bring more computation burdens. In such the integrated navigation applications (e.g. INS related), the state dimension ranging from 15 to 30 is usually higher than observation dimension. (ii) Due to the state augmentation (double times of original state dimension), SAKF requires more than three times computation burden compared with SMIKF when state dimension is larger than observation dimension.

Table 39.1 Computation burdens for CKF and SMIKF

Operation	**CKF**	**SMIKF**	**MULT**	**ADD**
$(m, m) * (m, m)$	3	6	m^3	$(m-1)m^2$
$(m, m) * (m, 1)$	1	1	m^2	$(m-1)m$
$(m, m) + (m, m)$	2	4	0	m^2
$(n, 1) + (n, 1)$	1	1	0	n
$(m, 1) + (m, 1)$	1	1	0	m
$(n, m) * (m, 1)$	1	1	nm	$(m-1)n$
$(m, m) * (m, n)$	1	1	nm^2	$(m-1)mn$
$(m, m) * (m, 1)$	1	1	m^2	$(m-1)m$
$(n, m) * (m, m)$	1	1	nm^2	$(m-1)mn$
$(n, m) * (m, n)$	1	1	mn^2	$(m-1)n^2$
$(m, n) + (m, n)$	0	0	0	mn
$(n, n) + (n, n)$	1	1	0	n^2
$(m, n) * (n, m)$	1	1	nm^2	$(n-1)m^2$
$(m, n) * (n, n)$	1	1	mn^2	$(n-1)nm$
$(m, n) * (n, 1)$	1	1	mn	$(n-1)m$

Table 39.2 Computation burdens for SAKF

Operation	SAKF	MULT	ADD
$(2m, 2m) * (2m, 2m)$	3	$8m^3$	$(2m-1)4m^2$
$(2m, 2m) * (2m, 1)$	1	$4m^2$	$2(2m-1)m$
$(2m, 2m) + (2m, 2m)$	2	0	$4\ m^2$
$(n, 1) + (n, 1)$	1	0	n
$(2m, 1) + (2m, 1)$	1	0	$2m$
$(n, 2m) * (2m, 1)$	1	$2nm$	$(2m-1)n$
$(2m, 2m) * (2m, n)$	1	$4nm^2$	$2(2m-1)mn$
$(2m, 2m) * (2m, 1)$	1	$4m^2$	$2(2m-1)m$
$(n, 2m) * (2m, 2m)$	1	$4nm^2$	$2(2m-1)mn$
$(n, 2m) * (2m, n)$	1	$2mn^2$	$(2m-1)n^2$
$(2m, n) + (2m, n)$	0	0	$2mn$
$(n, n) + (n, n)$	1	0	n^2
$(n, n) * (n, 2m)$	0	$2mn^2$	$2(n-1)nm$
$(2m, n) * (n, 2m)$	1	$4nm^2$	$4(n-1)m^2$
$(2m, n) * (n, n)$	1	$2mn^2$	$2(n-1)nm$
$(2m, n) * (n, 1)$	1	$2mn$	$2(n-1)m$

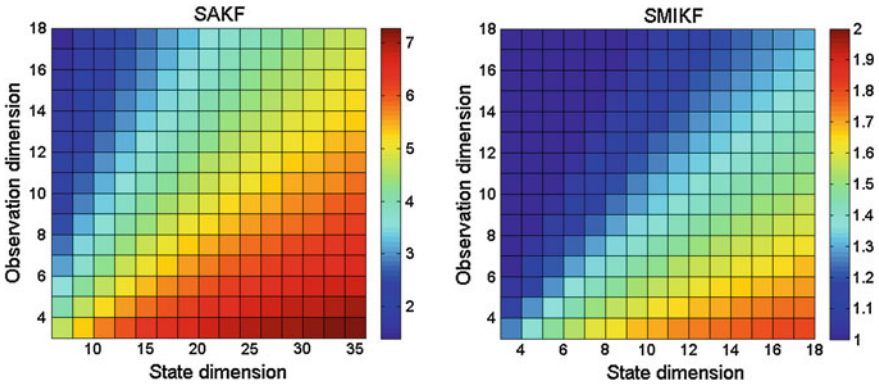

Fig. 39.1 Computation burden ratio for SAKF and SMIKF

39.6 Simulation Experiment

A simple moving trajectory is simulated with measurements sampling interval 1 s. The simulation lasts 200 s. The overall system model, i.e. continuous-time dynamic model and discrete-time observation model described as Eqs. (39.1) and (39.5) are specified by

$$\boldsymbol{x} = (X \quad Y \quad Z \quad V_X \quad V_Y \quad V_Z)^T,\ \boldsymbol{A} = \begin{pmatrix} 0 & 0 \\ 0 & 1 \end{pmatrix} \otimes \boldsymbol{I}_{3\times 3},\ \boldsymbol{G} = \begin{pmatrix} 0 \\ 1 \end{pmatrix} \otimes 1_{3\times 1},\ \boldsymbol{H} = \boldsymbol{I}_{6\times 6} \tag{39.33}$$

where $\boldsymbol{x}$ consists of six state parameters including three-dimensional position components (X, Y, Z) and three-dimensional velocity components (V_X, V_Y, V_Z); the transition matrix $\boldsymbol{A}$ indicates a CV dynamics; $\boldsymbol{I}$ is the identity matrix. The colored process noise in Eq. (39.1) is simulated by

$$\dot{\boldsymbol{\omega}}(t) = -0.1 \times \boldsymbol{\omega}(t) + \boldsymbol{\eta}(t), \quad \boldsymbol{\eta}(t) \sim \mathrm{N}(0_{3\times 1}, 4\boldsymbol{I}_{3\times 3}) \tag{39.34}$$

and the observation noises are WGN with

$$\boldsymbol{\varepsilon}_k \sim \mathrm{N}\left(0_{6\times 1}, \quad \begin{pmatrix} 0.25 & 0 \\ 0 & 1 \end{pmatrix} \otimes \boldsymbol{I}_{3\times 3}\right) \tag{39.35}$$

The colored process noises series are shown in Fig. 39.2 where we treat the noise generated with 0.1 s step as an approximate 'continuous-time' (compared with filtering step 1 s) process noise based on stochastic process theory [23]. The initial state variance is set as 1 m^2 and 1 m^2/s^2 for position and velocity (PV) respectively. Up to now, the overall system model is established. To demonstrate the efficiency of our proposed methods for dealing with colored process noise, four schemes i.e. CKF, SAKF, SMIKF and RSMIKF are computed for comparison purpose.

Hereinafter we will evaluate the performances of overall schemes. In order to clearly and reliably show the merits and drawbacks of these four schemes, 500 Monte Carlo (MC) runs are implemented for each scheme and the average results are shown under the root mean square errors (RMSE) criterion in Eq. (39.36)

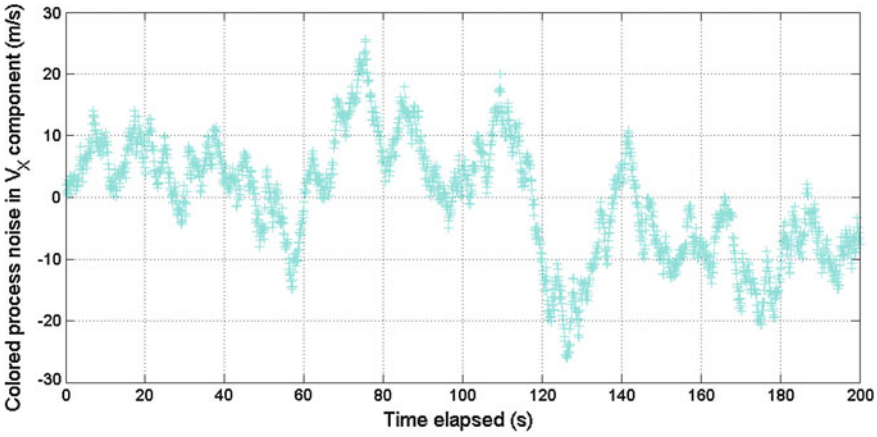

Fig. 39.2 Simulated colored process noise (approximate 'continuous-time' step: 0.1 s)

$$\mathrm{RMSE}(\boldsymbol{x}) = \frac{1}{p}\sum_{j=1}^{p}\left(\sqrt{\frac{\sum_{i=1}^{q}\left(\hat{\boldsymbol{x}}_i^j - \boldsymbol{x}_i^j\right)^2}{q}}\right) \tag{39.36}$$

where q and p are the epoch number and MC simulation times respectively; $\boldsymbol{x}$ and $\hat{\boldsymbol{x}}$ are the 'true' state and the corresponding estimate; the superscript of $\boldsymbol{x}$ denotes the jth MC run. Accordingly, the RMSE of position (denoted as P) and velocity (denoted as V) are calculated by Eqs. (39.37) and (39.38) respectively

$$\mathrm{RMSE}(P) = \sqrt{\mathrm{RMSE}(X)^2 + \mathrm{RMSE}(Y)^2 + \mathrm{RMSE}(Z)^2} \tag{39.37}$$

$$\mathrm{RMSE}(V) = \sqrt{\mathrm{RMSE}(V_X)^2 + \mathrm{RMSE}(V_Y)^2 + \mathrm{RMSE}(V_Z)^2} \tag{39.38}$$

Since trends of the simulation results are the same for all components, only X and V_X in state vector is shown and analyzed below. The filtering errors and RMSE results of four schemes are presented in Figs. 39.3, 39.4, 39.5, 39.6 and Table 39.3.

It can be seen from these figures and table that: (i) the CKF performs worst due to the unreasonable assumptions of WGN in such the time-correlated process noise contained system. (ii) By noise-whitening with state augmentation, the accuracy of SAKF is improved with about 16 and 5 % for PV respectively. (iii) As an alternative way, SMIKF outperforms SAKF due to the feedback of inaccurate noise estimate in SAKF. In other words, double times of state dimension dramatically decreases the model strength of SAKF, thus degrades the accuracy. This situation will be far from optimistic in real-time navigation due to lack of observation redundancy.

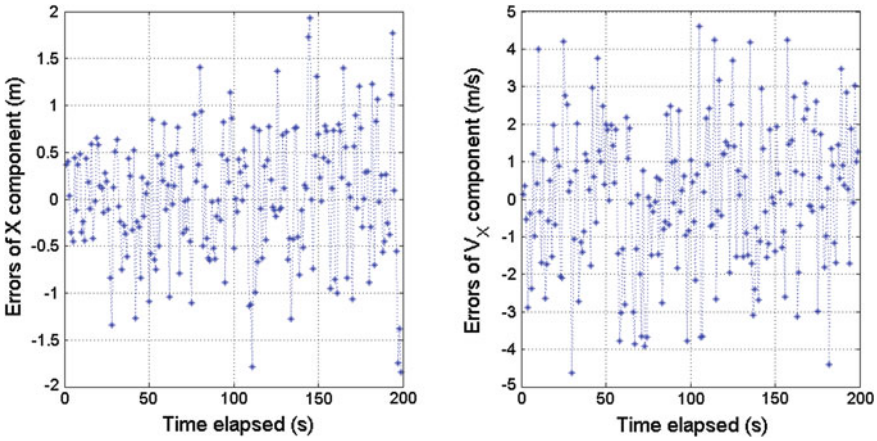

Fig. 39.3 Errors of CKF in X and V_X components

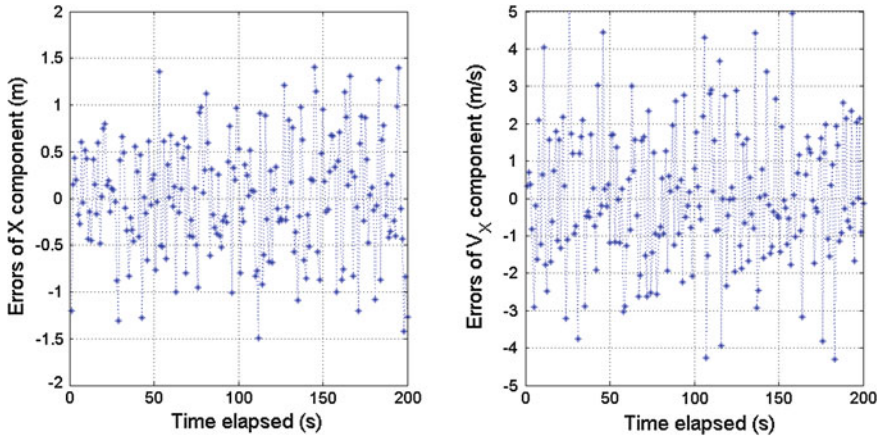

Fig. 39.4 Errors of SAKF in X and V_X components

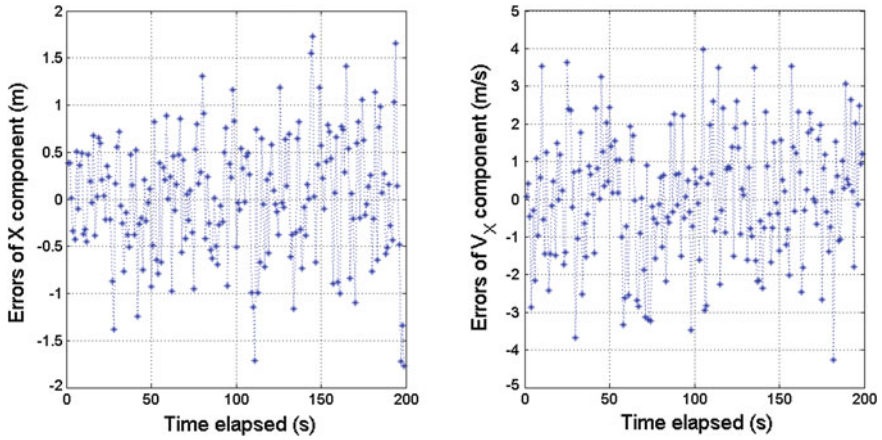

Fig. 39.5 Errors of SMIKF in X and V_X components

On the other hand, SMIKF processes the colored noise through its correct stochastic model and tend to adjust its filtering solution relying on observation information. (iv) In contrast to SMIKF, RSMIKF with the refinement by discrete-time stochastic model greatly enhances the accuracy and perform much better. The improvement reaches 32 and 47 % in PV respectively. It also indicates that discretizing process noise separating from the continuous-time dynamic model is not rigorous and sufficient in stochastic model establishment, thus leads to significant distinction between SMIKF and RSMIKF.

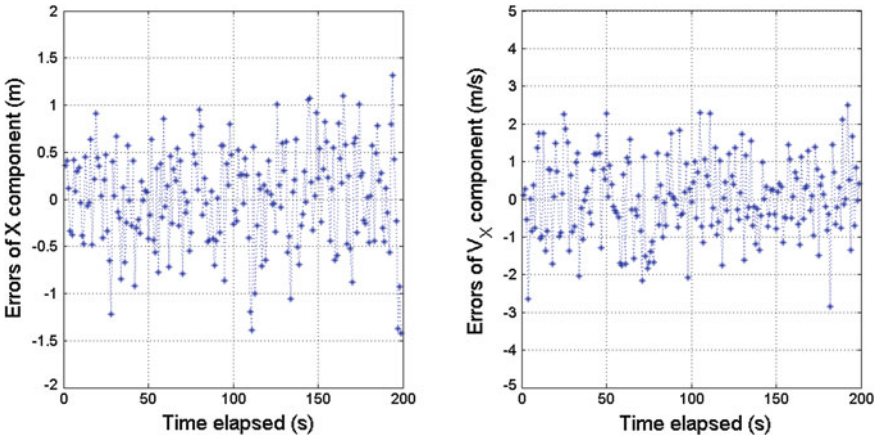

Fig. 39.6 Errors of RSMIKF in X and V_X components

Table 39.3 RMSE statistics of four schemes (unit: m for P; m/s for V)

Scheme	RMSE									
	X	Y	Z	P	Improvement of P	V_X	V_Y	V_Z	V	Improvement of V
CKF	0.674	0.864	0.706	1.304	N/A	1.942	1.508	2.429	3.508	N/A
SAKF	0.621	0.682	0.594	1.097	15.9 %	1.813	2.098	1.875	3.347	4.6 %
SMIKF	0.645	0.679	0.567	1.095	16.0 %	1.654	1.818	1.685	2.980	15.0 %
RSMIKF	0.525	0.536	0.470	0.879	32.6 %	1.050	1.090	1.079	1.859	47.0 %

39.7 Concluding Remarks

This paper comprehensively investigates state augmentation based KF (SAKF) and second moment information based KF (SMIKF) for dealing with time-correlated process noise. In essence, SAKF is a noise-whitening method while SMIKF directly compensates the variances through correct stochastic model. To precisely establish the stochastic model of discrete-time dynamic model, a refined SMIKF (RSMIKF) is rigorously derived from the continuous-time dynamic model. Simulation example is designed to verify our proposed method. The results show that time-correlated process noise dramatically degrades the accuracy of CKF. While both SMIKF and SAKF achieve more accurate and reliable solution than CKF. Generally SMIKF is superior to SAKF due to the feedback of inaccurate noise estimate in SAKF. Moreover, double times of state dimension dramatically decreases the model strength of SAKF, thus degrades the accuracy. Most importantly, the proposed RSMIKF is very simple and efficient in dealing with time-correlated process noise. If the correlation functions are perfectly known or established, RSMIKF will generate the optimal solution in the sense of minimum variance principle. For computation burden aspect, SMIKF is less time-consuming than SAKF and more suitable for navigation campaigns.

Acknowledgments This work is supported by the State Key Laboratory of Geodesy and Earth's Dynamics (SKLGED 2014-3-3-E), the Key Laboratory of Advanced Engineering Surveying of NASMG (TJES1306), the National Natural Science Fund of China (41304018), China Spark Program of Earthquake Science and Technology (Grant No.XH14036).

References

1. Parkinson BW, Spilker JJ (1996) Global positioning system: theory and application, vol 1 and 2. AIAA Publication, Washington D.C
2. Brown R, Hwang PYC (1997) Introduction to random signals and applied Kalman filtering. Wiley, New York
3. Zhou H, Kumar KSP (1984) A current statistical model and adaptive algorithm for estimating maneuvering targets. AIAA J Guidance Control Dyn 7(5):596–602
4. Zhou Z, Shen Y, Li B (2012) Stochastic model of GPS doppler: evaluation, modeling and performance. In: Proceedings of CSNC 2012, Springer, pp 395–406
5. Bar-Shalom Y, Campo L (1986) The effects of the common process noise on the two-sensor fused-track covariance. IEEE Trans Aerosp Electron Syst 22(6):803–805
6. Rogers SR (1987) Alpha-beta filter with correlated measurement noise. IEEE Trans Aerosp Electron Syst 23(4):592–594
7. Bryson AE, Johansen DE (1965) Linear filtering for time-varying systems using measurements containing colored noise. IEEE Trans Autom Control 10(1):4–10
8. Gazit R (1997) Digital tracking filters with high order correlated measurement noise. IEEE Trans Aerosp Electron Syst 33(1):171–177
9. Jia Y, Li JR (1998) Stochastic system with colored correlation between white noise and colored noise. Phys A Stat Mech Appl 252(3–4):417–427
10. Bryson AE, Henrikson LJ (1968) Estimation using sampled data containing sequentially correlated noise. J Spacecraft 5(6):662–665
11. Petovello MG, O'Keefe K, Lachapelle G, Cannon ME (2009) Consideration of time-correlated errors in a Kalman filter applicable to GNSS. J Geodesy 83(1):51–56
12. Rogers SR (1990) Continuous-time ECV and ECA track filters with colored measurement noise. IEEE Trans Aerosp Electron Syst 26(4):663–666
13. Wu W, Chang D (1996) Maneuvering target tracking with colored noise. IEEE Trans Aerosp Electron Syst 32(4):1312–1320
14. Godha S, Cannon ME (2007) GPS/MEMS-INS integrated system for navigation in urban areas. GPS Solutions 11(3):193–203
15. Titterton DH, Weston JL (2004) Strapdown inertial navigation technology (progress in astronautics and aeronautics series), 2nd edn. American Institute of Aeronautics & Ast
16. Yang Y, Cui X (2003) Influence functions of colored noises on kinematic positioning-taking the AR model of first class as an example. Acta Geodaetica Cartogr Sin 32(1):6–10
17. Geng Y, Wang J (2008) Adaptive estimation of multiple fading factors in Kalman filter for navigation applications. GPS Solutions 12(4):273–279
18. Mehra RK (1970) On the identification of variances and adaptive Kalman filtering. IEEE Trans Autom Control 15(2):175–184
19. Sage AP, Husa GW (1969) Adaptive filtering with unknown prior statistics. In: Proceedings of joint automatic control conference, Boulder, Colorado, pp 760–769
20. Yang Y, Xu T (2003) An adaptive Kalman Filter based on Sage windowing weights and variance components. J Navig 56(2):231–240

21. Yang Y, Gao W (2005) Comparison of adaptive factors in Kalman filter on navigation results. J Navig 58(3):471–478
22. Yang Y, Song L, Xu T (2002) Robust estimation for correlated observations based on bifactor equivalent weights. J Geodesy 76(6–7):353–358
23. Maybeck PS (1979) Stochastic Models, Estimation, and Control, vol 1. Academic Press, New York

Chapter 40
Prediction and Analysis of Chinese Earth Rotation Parameters Based on Robust Least-Squares and Autoregressive Model

Zhangzhen Sun, Tianhe Xu, Bing He and Gang Ren

Abstract Earth Rotation Parameters (ERP) are the necessary parameters to achieve mutual conversion of the celestial reference frame and earth reference frame. It is the requirements of national economic construction and national major strategic defense, and the needs of key frontier disciplines and production applications. In this paper, we take into account the consistency and stability of the Chinese ERP data, and the least-squares combination of Autoregressive (LS+AR) model and the Robust least-squares combination of Autoregressive (RLS+AR) model are proposed to use to predict different span of ERP based on Chinese ERP data, as the cycles and trends have the characteristic of time-varying in the data. The results show that, the RLS+AR model can reduce Influence of crude differential on forecast accuracy effectively, and then achieve the IERS prediction accuracy, and meet the need of national defense in time and space datum height consistency.

Keywords Earth rotation parameters · Time-varying · Robust · Least-squares · Autoregressive

Z. Sun (✉)
Institute of Space Science Shandong University, Weihai Shandong, China
e-mail: sunzhangzhen@126.com

T. Xu
State Key Laboratory of Geo-Information Engineering, Xi'an, Shanxi, China

T. Xu
Xian Research Institute of Surveying and Mapping, Xi'an, Shanxi, China

B. He
Shanghai Astronomical Observatory Chinese Academy of Sciences, Shanghai, China

B. He
University of Chinese Academy of Sciences, Beijing, China

G. Ren
Henan Provincial Architectural Institute Co., Ltd, Zhengzhou, Henan, China

J. Sun et al. (eds.), *China Satellite Navigation Conference (CSNC) 2015 Proceedings: Volume II*, Lecture Notes in Electrical Engineering 341,
DOI 10.1007/978-3-662-46635-3_40

40.1 Introduction

The Earth's rotation movement characterizes the situation of the whole earth movement, as well as the interaction between the Earth's various spheres of the Earth's core, mantle, crust and atmosphere [1]. It can be described by Earth Orientation Parameters (EOPs), which includes three parts: (1) the Nutation-precession parameters, (2) the Polar Motion (PM) parameters, (3) the Universal Time (UT1-UTC) or the Length of day (LOD). The PM and UT1-UTC or LOD are also called as Earth Rotation Parameters (ERP). ERP is the necessary parameters to achieve mutual conversion of the celestial reference frame and earth reference frame, and it is very important for high-precision space navigation and positioning. Modern measurement techniques such as VLBI, SLR, GPS and DORIS can provide people with high precision and high spatial and temporal resolution of Earth Orientation Parameters. Along with the requirements of national economic development and the major strategic defense, as well as the requires of the focus frontier and productivity application, we conducted the study to determine ERP independence in order to improve the measurement of ERP. And then, we have achieved a comprehensive ERP data by several space technologies combined with VLBI, SLR, GNSS and DORIS technology. However, due to the complexity of data processing, it is difficult to access to these parameters in real-time. In order to meet the needs of the space navigation and positioning, high-precision prediction for Earth Orientation Parameters is urgent.

At present, there are two major forecasting methods for ERP: linear and nonlinear models studied by many scholars. The linear models include: least square extrapolation (LS), combination of least square extrapolation and auto-regressive (LS+AR), combination of least square extrapolation and auto-covariance (LS+AC), etc. [2–7]. The nonlinear models include: Sequence of threshold auto-regressive model (TAR), Artificial Neural Network (ANN) [8–10], Fuzzy inference [11] and other methods. They have done a lot of work in the ERP prediction based on the IERS EOP data through the above methods, and achieved remarkable results. However, it's lack of theoretical foundation to predict ERP based on self-determination ERP (Chinese ERP) data, and it is to be further verified in the impaction on the predict accuracy of Chinese ERP data outliers. Based on this, we have analysis the consistency and stability in the Chinese ERP data, firstly. And then, fit the Chinese ERP data based on the Robust to remove or reduce the affection by the gross error/outliers, considering the characteristic of time-varying in the observational data of the ERP [12, 13], can intensify the impact of recent data and improve the prediction accuracy effectively. The results show that, the RLS+AR model can reduce the affection in the Chinese ERP data, and then obtain the equivalence prediction accuracy similar with depend on IERS EOP 08C04 data. That is to say, the Chinese ERP data has good stability and periodicity, and meet the needs of national defense in time and space datum height consistency.

40.2 Models

40.2.1 RLS Model

The robust weighted least squares can weaken/eliminate the influence of gross errors/outliers in the data effectively. An another weighted matrix added consider the closer the observational data is near to the prediction point, the greater the impact on the prediction is.

For the prediction of ERP, the first step is to remove the leap second from UT1-UTC to get UT1-TAI based on IERS Convention 2010 [14], and then remove the Earth's zonal harmonic tidal from UT1-TAI and LOD to generate the series of UT1R-TAI and LODR. The equation of removing tidal can be expressed as:

$$\begin{aligned} \delta \mathrm{UT1} &= \sum_{i=1}^{62} B_i \sin \xi_i + C_i \cos \xi_i \\ \delta \Delta &= \sum_{i=1}^{62} B_i^{'} \sin \xi_i + C_i^{'} \cos \xi_i \end{aligned} \tag{40.1}$$

where the meanings of various symbols in $\xi_i = \sum_{j=1}^{5} a_{ij}\alpha_j$ can refer to IERS Convention 2010.

After that the LS is used to fit the series of ERP considering the linear and periodic terms. For PM Chandler wobble, annual and semi-annual periodic terms are included. For LODR/UT1R-TAI the long-term of 18.6 and 9.3 years, annual, semi-annual and 1/3 annual periodic terms should be considered. The fitting equation of LS model can be expressed as:

$$\begin{aligned} \mathrm{f(t)} = \mathrm{a}_0 + a_1 t + B_1 \cos\left(\frac{2\pi t}{R_1}\right) + B_2 \sin\left(\frac{2\pi t}{R_1}\right) + C_1 \cos\left(\frac{2\pi t}{R_2}\right) \\ + \ C_2 \sin\left(\frac{2\pi t}{R_2}\right) + D_1 \cos\left(\frac{2\pi t}{R_3}\right) + D_2 \sin\left(\frac{2\pi t}{R_3}\right) + \ldots \end{aligned} \tag{40.2}$$

where a_0 is the constant term, a_1 is the linear term, B_i, C_i and D_i is the coefficients for periodic terms, R_i is the corresponding periodic, t is the time of UTC. The estimator by using the WLS for parameter solution can be written as:

$$X = \left(B^T P B\right)^{-1} B^T P L \tag{40.3}$$

where

$$\mathbf{X} = [\ a_0 \quad a_1 \quad B_1 \quad B_2 \quad C_1 \quad C_2 \quad D_1 \quad D_2 \quad \ldots\ ] \tag{40.4}$$

X is the estimated parameter vector; **B** is the coefficient matrix; **L** is observation vector of ERP series; **P** is the weight matrix. A diagonal matrix is considered for **P** in this paper.

The main principle for the choice of weight matrix is that the closer the data is near to the predicted value, the greater the weight is. Divide the basic of observation sequence to 10 equal parts, that is:

$$P = \begin{bmatrix} P_1 & & & \\ & P_2 & & \\ & & \ddots & \\ & & & P_{10} \end{bmatrix}^e \tag{40.5}$$

where $P_1, P_2, \ldots$ and P_{10} are the diagonal matrix with diagonal elements as $\frac{1}{10}, \frac{1}{9}, \ldots$ and 1, and e is the power.

and then add the robust matrix:

$$\bar{P}_t = \begin{cases} P_t & |\bar{v}_t| = \left|\frac{v_t}{\sigma}\right| \le c_0 \\ P_t \frac{c_0}{|\bar{v}_t|}\left(\frac{c_1 - |\bar{v}_t|}{c_1 - c_0}\right) & c_0 < |\bar{v}_t| \le c_1 \\ 0 & |\bar{v}_t| > c_1 \end{cases} \tag{40.6}$$

where, $\overline{P}_t$ is the robust weighted matrix; v_t is the observation residuals; σ is the mean square error of observation; $\bar{v}_t = \frac{v_t}{\sigma}$ is the standardized residuals of observation; $c_0,\ c_1$ is the const number, and $c_0 = 1.5,\ c_1 = 2.5$ in this paper.

40.2.2 AR Model

AR model is the description of the relationship between a random series $z_t (t = 1, 2, \ldots, N)$ before time t and the white noise of time t. Its expression can be written as following:

$$z_t = \sum_{i=1}^{p} \phi_i z_{t-i} + a_t \tag{40.7}$$

where $\phi_1, \phi_2, \ldots, \phi_p$ are the autoregressive coefficients, and a_t is the white noise with zero mean, p is the model order. The above equation denoted by AR (p) is well-known as the AR model of the order p.

The AR model requires the time series stationary random, which should meet the steady, normal and zero mean conditions. The key of using the AR model is how to determine the order p. Usually there are three methods for the determination of p, the final prediction error criterion, the information criterion and the delivery

function criterion. In practice, these 3 methods are almost equivalent. In this paper, the final prediction error criterion is adopted.

The final prediction error criterion can be expressed as:

$$\mathrm{FPE(p)} = P_M(n+p+1)/(n-p-1) \tag{40.8}$$

where

$$P_M = \frac{1}{n-p}\sum_{t=p+1}^{n}\left(z_t - \sum_{j=1}^{p}\phi_j z_{t-j}\right)^2 \tag{40.9}$$

The value p that minimums the FPE (p) is chosen as the order of AR model. The model coefficients $\phi_1, \phi_2, \ldots, \phi_p$ can be determined by solving the Yule-Walker equations.

40.2.3 Error Analysis

In order to evaluate the prediction accuracy, we use the mean absolute error (MAE) standards. It can be expressed as following:

$$E_i = P_i - O_i \tag{40.10}$$

$$MAE_j = \frac{1}{n}\sum_{i=1}^{n}(|E_i|) \tag{40.11}$$

where P_i is the predicted value of the i-th prediction, O_i is the corresponding observation value, E_i is real error (Assumed the observation value as true value), n is the total prediction number.

40.3 Calculation and Analysis

40.3.1 Data Description

In this paper, the time series EOP 08C04 file provided by the IERS and the Chinese ERP data self-determined are used for calculation and analysis (http://hpiers.obspm.fr/eoppc/eop/). The EOP 08C04 series contains from January 1962 (37665 MJD) to now. The PM, the LOD and the UT1-UTC et al. are included. The Chinese ERP data contains from January 4 1983 to February 15 2014. The sampling interval of these data is 1 day. The Chinese ERP is a combination and self-determined data, and which is depend on the VLBI, SLR, GNSS, DORIS technology (the

international Service Organization are: ILRS, IGS, IVS, IDS). The basic principles of its solution method is determined the terrestrial reference frame and ERP parameters simultaneously, which can eliminate inconsistencies between reference frame and ERP from the theoretical and practical feasibility. The results of solution is also has been tested and recognized in major projects. The main difference between the Chinese ERP data and IERS EOP 08C04 is: the Chinese ERP is determined by the terrestrial reference frame and ERP parameters simultaneously and IERS EOP 08C04 is computed alone. And this difference of those two data is better than 0.2 mas in wrms on polar motion and 0.02 ms in wrms on UT1-UTC and LOD, has reached the international advanced level.

40.3.2 Data Analysis

Due to the solution model, system difference of space technology, little observation data and low quality of observation, the gross error/outliers is exist in the determined ERP data based on VLBI, SLR, GNSS and DORIS, and then some larger error are exist in the comprehensive solutions. Now, we make the difference between the Chinese ERP data and IERS EOP 08C04 to test the consistency and accuracy.

From Fig. 40.1, we can see that it is has a large difference between the Chinese ERP data and IERS EOP 08C04 in early data, this is because the quality of observation in the years of 83–93 are worse the later. About 5 mas for PM and 2 ms for UT1-UTC, especially for LOD, there are too many error, this is because the EOP C04 is made smooth it handled in solving process and we not. It is good

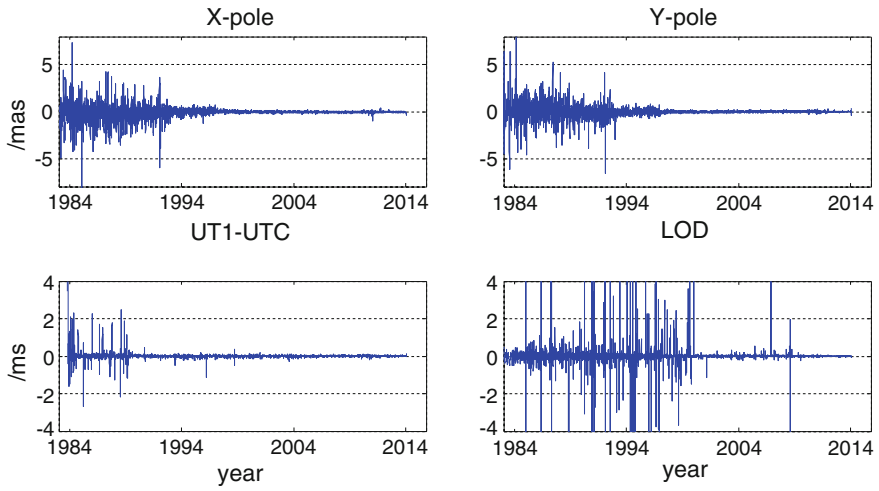

Fig. 40.1 Difference between the Chinese ERP data and IERS EOP 08C04

agreement in recent data, and there is little gross error in PM and UT1-UTC. In all, the Chinese ERP data meet the needs of national defense in time and space datum height consistency.

40.3.3 Data Processing

In order to test the prediction accuracy based on the Chinese ERP data meets the requirements or not, the same time of IERS EOP 08C04 series is used to predict, too. So 4 cases are conducted as following:

Case 1: Prediction of ERP based on LS+AR model and IERS EOP 08C04;
Case 2: Prediction of ERP based on LS+ARMA model and Chinese ERP data;
Case 3: Prediction of ERP based on WLS+AR model and IERS EOP 08C04;
Case 4: Prediction of ERP based on RLS+ARMA model and Chinese ERP data.

The case 3 is used the WLS+AR model which is because there is no the gross error in IERS EOP 08C04 series and have high accuracy. The basic sequence length of the polar motion components X and Y is chosen as 10-year, UT1-UTC as 12-year and LOD is as 18-year in order to improve prediction accuracy. Forecast accuracy statistics from January 1, 2003 to February 15, 2014, with the span of 1 to 360 days of the forecast are calculated and compared. The true error of 4 cases is shown in Figs. 40.2, 40.3, 40.4 and 40.5.

From Figs. 40.2, 40.3, 40.4 and 40.5, we can see that variation of the prediction error shows almost the same trends based on 4 cases in the PM and UT1-UTC between the Chinese ERP data and IERS EOP 08C04 series. But in LOD, the variation of the prediction error is too large, the reason may be that too many error

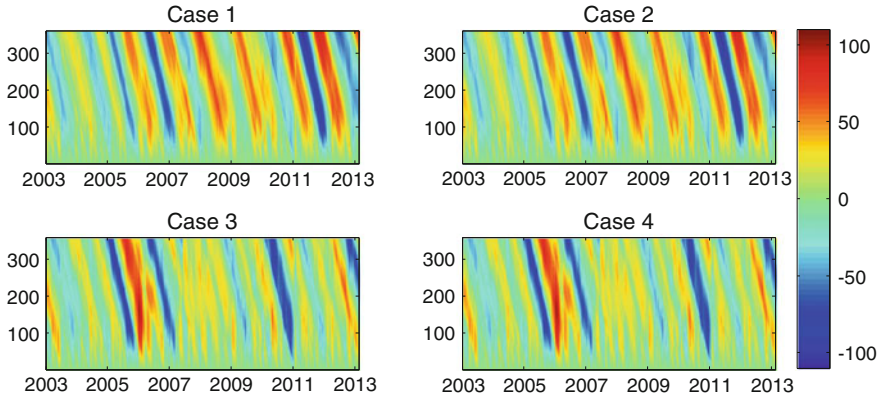

Fig. 40.2 Prediction errors for x-component of PM (unit: mas)

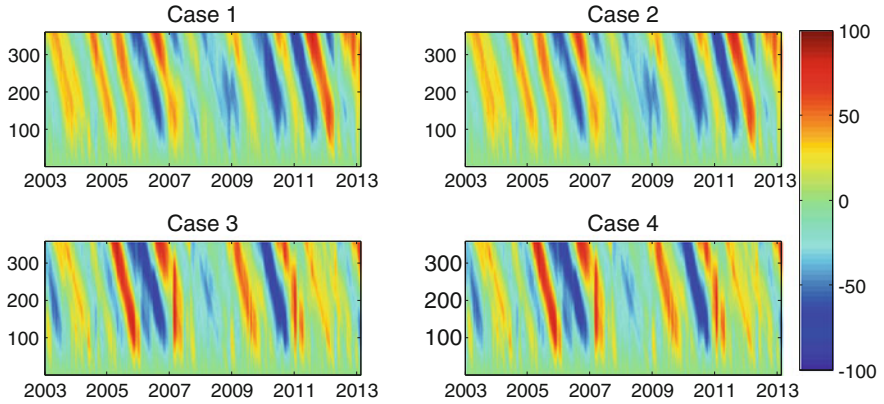

Fig. 40.3 Prediction errors for y-component of PM (unit: mas)

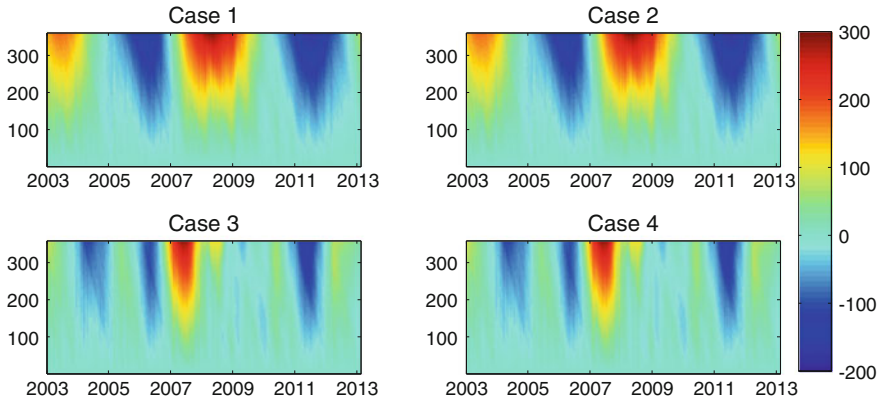

Fig. 40.4 Prediction errors for UT1-UTC (unit: ms)

in the LOD data, and changed the original term and cycles items. Figure 40.6 shows the MAE of 4 cases for different prediction span.

From Fig. 40.3, we can see that it is almost have the equal prediction accuracy in the PM and UT1-UTC based on the Chinese ERP data and IERS EOP 08C04 series. And the WLS+AR model and the RLS+AR model have higher prediction accuracy than LS+AR model for ERP, especially for PM x component and UT1-UTC. Fit the Chinese ERP data based on the Robust can remove or reduce the affection by the gross error in the Chinese ERP data, and then obtain the equivalence prediction accuracy similar with depend on IERS EOP 08C04 data. But in LOD, it is more bad in prediction accuracy than depend on IERS EOP 08C04 series, which can be found form the true prediction error, that is caused by too many error in LOD data, and regardless of the method of prediction model.

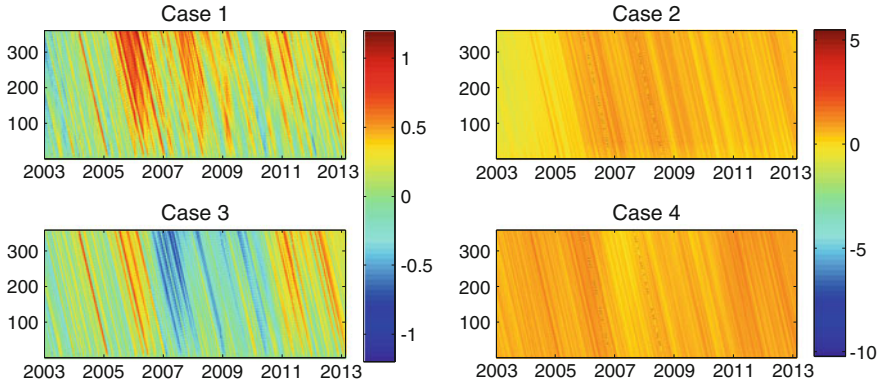

Fig. 40.5 Prediction errors for LOD (unit: ms)

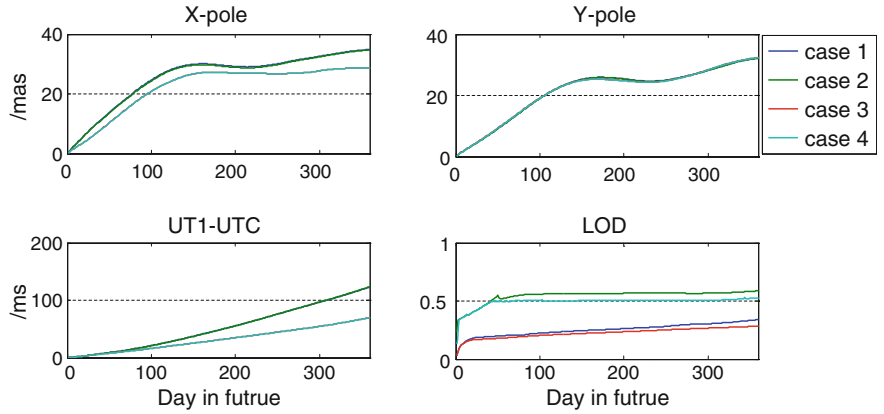

Fig. 40.6 MAE for different prediction span

40.4 Conclusions

The prediction ERP is the necessary parameters to achieve mutual conversion of the celestial reference frame and earth reference frame. The prediction and self-determined ERP data is the requirements of national economic development and the major strategic defense with the rapid construction of China's own navigation system "Beidou navigation and positioning system". We have analysis the consistency and stability between Chinese ERP data and the terrestrial reference frame and predict them in different span based on RLS+AR model. The results show that, the RLS+AR model can reduce the affection in the Chinese ERP data, and then obtain the equivalence prediction accuracy similar with depend on IERS EOP 08C04 data. That is to say, the Chinese ERP data has good stability and periodicity, and meet the needs of national defense in time and space datum height consistency.

Acknowledgments This work was supported by Natural Science Foundation of China (41174008) and the Open Foundation of State Key Laboratory of Geodesy and Earth's Dynamics (SKLGED2013-4-2-EZ) and State Key Laboratory of Astronautic and Dynamics (2014ADL-DW0101).

References

1. Zheng D, Yu N (1996) Earth rotation and it's relations to geophysical phenomena: the changes of length of the day. Adv Geophys 11(2):81–101 (In Chinese)
2. McCarthy DD, Luzum BJ (1991) Prediction of earth orientation. J Geodesy 65:18–21
3. Kosek W, Kalarus M, Niedzielski T (2008) Forecasting of the Earth orientation parameters—comparison of different algorithms. In: Capitaine N (ed) Proceedings of the journèes 2007, systèmes de référence spatio-temporels "The celestial reference frame for the future". Observatoire de Paris Systèmes de Référence Temps-Espace UMR8630/CNRS, Paris, France, pp 155–158
4. Kosek W (2010a) Future improvements in EOP prediction. In: Proceedings of the IAG 2009, Geodesy for planet earth, Buenos Aires, Argentina, Aug 31–Sept 4, 2009
5. Kosek W (2010b) Causes of prediction errors of pole coordinates data. In: Proceedings of the 6th Orlov's conference. The study of the earth as a planet by methods of geophysics, geodesy and astronomy, MAO NAS of Ukraine, Kiev, Ukraine, 22–24 June 2009, pp 96–103
6. Niedzielski T, Kosek W (2008) Prediction of UT1-UTC, LOD and AAM χ_3 by combination of least-squares and multivariate stochastic methods. J Geodesy 82:83–92
7. Kosek W, McCarthy DD, Luzum BJ (1998) Possible improvement of Earth orientation forecast using autocovariance prediction procedures. J Geodesy 72:189–199
8. Liao D, Wang Q, Zhou Y, Liao X, Huang C (2012) Long-term prediction of the earth orientation parameters by the artificial neural network technique. J Geodyn GEOD-1110:6
9. Schuh H, Ulrich M, Egger D et al (2002) Prediction of Earth orientation parameters by artificial neural networks. J Geodesy 76:247–258
10. Wang Q (2007). Studies on the prediction of Earth's variable rotation by Artificial Neural Networks. Shanghai Astronomical observatory, Chinese Academy of Sciences, Shanghai, China (In Chinese)
11. Akyilmaz O, Kutterer H (2004) Prediction of Earth rotation parameters by fuzzy inference systems. J Geodesy 78:82–93
12. Sun Z, Xu T (2012) Prediction of earth rotation parameters based on an improved weighted least-squares and AR model. Geodesy Geodyn 3(3):57–64
13. Sun Z, Xu T (2014) Prediction of polar motion based on combination of least-squares and autoregressive moving average. CSNC2014 2(25):303–311
14. McCarthy DD, Petit G (2010) IERS Conventions, America

Chapter 41
Research on the Selection Method of Triple Frequency Combination Based on the Beidou Satellite Navigation System

Rui Xue, Qingming Cao, Qiang Wei and Yanbo Sun

Abstract With the application of Chinese Beidou satellite navigation system more and more widely, its existing navigation accuracy and timeliness can not meet the requirements for use, how to improve the accuracy of the Beidou satellite navigation and positioning has gradually become a new hotspot. Existing main methods to improve navigation accuracy and timeliness are repair cycle slip, smooth pseudorange residuals and other methods, but they can only improve a single aspect of the error, can not simultaneously weaken the influence of multiple errors. However, triple frequency combination navigation can speed up the determination of integer ambiguity, weaken the ionospheric delay, reduce the observation noise, improve the precision of positioning effect is obvious. By a brief introduction of Beidou satellite navigation system to study conducted three frequency carrier phase combination method based on three frequencies have been published. While maintaining the ambiguity is an integer of the premise, by analyzing the ionospheric delay, observation noise and other factors affect on triple frequency combinations observations, based on the long-wavelength combination standard, weak ionospheric delay combination standard and weak observation noise combination standard, obtained a linear combination of good performance, effectively improve the navigation and positioning accuracy and timeliness. The results showed that: a combination of (1, 4, −5) and other combinations of observations can have longer wavelength while effectively weaken the ionospheric delay effects, significantly reduces the ambiguity initialization time, has certain reference value for the future development of the Beidou satellite navigation system.

Keywords Beidou satellite navigation system · Triple-frequency · Combination observation

R. Xue · Q. Cao (✉) · Q. Wei · Y. Sun
College of Information and Communication Engineering,
Harbin Engineering University, Harbin 150001, China
e-mail: cqm758@126.com

J. Sun et al. (eds.), *China Satellite Navigation Conference (CSNC) 2015 Proceedings: Volume II*, Lecture Notes in Electrical Engineering 341,
DOI 10.1007/978-3-662-46635-3_41

41.1 Introduction

Beidou satellite navigation system developed by China is a global satellite navigation system. It is composed of the space segment, ground segment and user segments. In the global scope of all-weather and all day for all types of users with high accuracy and high reliable positioning, navigation and time service, and with short message communication ability. Now already have area navigation, positioning and timing capabilities. Currently, three working band have been published, namely: B1 band (1559.052−1591.788 MHz), B2 band (1166.220−1217.37 MHz), B3 band (1250.618−1286.423 MHz). Beidou navigation system built to make China's own high-precision relative positioning becomes possible [1].

Since the Beidou system run so far, is widely used in various industries, but also in the application process found some problems, especially in the field that require high-precision positioning, existing navigation accuracy and speed still can not meet the use requirements, and from the references [2] shows that the Beidou system in terms of positioning accuracy than the GPS system has yet to be improved. How to improve the accuracy and real-time of navigation has become the key to solve the problem, and the integer ambiguity, cycle slips, ionospheric delay, tropospheric delay, receiver and satellite clock error, noise and multipath error and so can have an effect. Currently, various navigation systems often use double or triple frequency carrier phase smoothing pseudorange residuals of carrier phase, detection and repair cycle slips, carrier phase precision positioning and other methods to improve navigation and positioning accuracy. In 1996, scholar Ron Hatch first pointed out that if the use of three navigation frequency may get benefits, opens up the research direction of triple-frequency navigation signals in the application of high precision positioning and navigation aspects [3]. And later research also confirmed, triple-frequency navigation and positioning is better than the single or dual frequency navigation and positioning, mainly reflected in: triple-frequency is applied to ionospheric refraction error, can correct the higher-order terms; compared with dual-frequency combination observations, multi frequency combination observations showed more advantages in wavelength, ionospheric refraction errors and other aspects; in solving the ambiguity, the application of triple-frequency observations can use different combinations of the relationship between the wavelength and the observation error to resolve ambiguity quickly. Today, the Beidou system has B1/B2/B3 carrier frequencies, has reached the conditions of triple-frequency navigation.

According to triple-frequency combination observations application experience in the GPS system, this paper gives a general definition of the triple-frequency combination observations based on Beidou system, and discuss the observational error, and finally provides several useful groups of observations combination.

41.2 Main Factors Affecting the Positioning Accuracy

The three working bands' center frequency of Beidou satellite navigation system are denoted by f_1 = 1561.098 MHz, f_2 = 1207.14 MHz, f_3 = 1268.52 MHz [4], and the corresponding wavelength are λ_1 = 0.192 m, λ_2 = 0.248 m, λ_3 = 0.236 m.

In the multi-frequency carrier phase observations equation of the GNSS system [5], tropospheric delay generally refers to non-ionizing atmospheric refraction of electromagnetic wave; satellite clock error is the error between atomic clock time installed on the GPS satellite and GPS standard time; and multipath error is related with properties of the natural reflector close to the receiver, the antenna structure, and the satellite elevation angle. These errors cannot be significantly improved by combination observation, so in order to simplify the calculation, ignore tropospheric delay, satellite clock error, multipath error and other errors, only take the integer ambiguity N_i, ionospheric delay error I_i and observation noise σ_i of the B_i carrier in account, where $i = 1, 2, 3$. And the multi-frequency carrier phase observation equation is simplified as:

$$\varphi_i = \rho - \lambda_i N_i - I_i + \sigma_i \quad (i = 1,\ 2,\ 3) \tag{41.1}$$

where ρ represents the geometric distance between the satellite and the ground station. The combination observation is defined as:

$$\varphi_c = \alpha\varphi_1 + \beta\varphi_2 + \gamma\varphi_3 \tag{41.2}$$

According ionospheric delay definition, ionospheric delay for each carrier:

$$(V_{ion})_i = \left(40.3/f_i^2\right) \int_S N_e ds \quad (i = 1,\ 2,\ 3) \tag{41.3}$$

Which can be extrapolated, the relationship between each carrier ionosphere delay as follows:

$$I_2 = (f_1/f_2)^2 I_1 \qquad I_3 = (f_1/f_3)^2 I_1 \tag{41.4}$$

Ratio of each frequency is defined as:

$$\begin{aligned} m &= f_1/f_2 = 31/24 \\ n &= f_3/f_2 = 62/59 \\ p &= f_1/f_3 = 59/48 \end{aligned} \tag{41.5}$$

Well, take Eq. (41.1) and (41.4–41.5) into Eq. (41.2):

$$\varphi_c = (\alpha + \beta + \gamma)\rho - (\alpha\lambda_1 N_1 + \beta\lambda_2 N_2 + \gamma\lambda_3 N_3) - (\alpha + \beta m^2 + \gamma p^2) I_1 + \sigma_c \tag{41.6}$$

In order to make the combination observation does not affect the geometric distance, the need to make:

$$\alpha + \beta + \gamma = 1 \tag{41.7}$$

Assume:

$$\lambda N = \alpha\lambda_1 N_1 + \beta\lambda_2 N_2 + \gamma\lambda_3 N_3 \tag{41.8}$$

$$\eta = \alpha + \beta m^2 + \gamma p^2 \tag{41.9}$$

Take Eqs. (41.7–41.9) into Eq. (41.6):

$$\varphi_c = \rho - \lambda N - \eta I_1 + \sigma_c \tag{41.10}$$

Equation (41.10) gives the factors that influence the positioning accuracy of combined observations: integer ambiguity, ionospheric delay error and observation noise.

41.2.1 Integer Ambiguity

The size of the wavelength is crucial for determining the integer ambiguity, the longer the wavelength, the integer ambiguity determined more easily; on the contrary, for a combination observation with short-wavelength are difficult to determine the integer ambiguity.

By the formula (41.8) inferred:

$$N = \alpha\lambda_1 N_1/\lambda + \beta\lambda_2 N_2/\lambda + \gamma\lambda_3 N_3/\lambda \tag{41.11}$$

Assume:

$$i = \alpha\lambda_1/\lambda,\ j = \beta\lambda_2/\lambda,\ k = \gamma\lambda_3/\lambda \tag{41.12}$$

Then:

$$N = iN_1 + jN_2 + kN_3 \tag{41.13}$$

To make Ambiguity remains integer properties, requirements i, j, k are integers. Corresponding inferable:

$$\alpha = i\lambda/\lambda_1,\ \beta = j\lambda/\lambda_2,\ \gamma = k\lambda/\lambda_3 \tag{41.14}$$

The Eq. (41.14) into Eq. (41.7) can extrapolate that combination observation wavelength is:

$$\lambda = \lambda_1\lambda_2\lambda_3/(i\lambda_2\lambda_3 + j\lambda_1\lambda_3 + k\lambda_1\lambda_2) \tag{41.15}$$

Take formula $\lambda = c/f$, where c is the speed of light, into Eq. (41.15), we can get the frequency of combination observation:

$$f = if_1 + jf_2 + kf_3 \tag{41.16}$$

41.2.2 Ionospheric Delay Error

By Eq. (41.10) shows, the ionospheric delay of combination observation is expressed as:

$$I_c = \eta I_1 \tag{41.17}$$

For the processing of η, the Eq. (41.5) and (41.14) respectively into type (41.9), obtained:

$$\eta = \frac{i + (f_1/f_2)j + (f_1/f_3)k}{i + (f_2/f_1)j + (f_3/f_1)k} \tag{41.18}$$

The front of the frequency ratio into the above equation:

$$\eta = \frac{i + (31/24)j + (59/48)k}{i + (24/31)j + (48/59)k} \tag{41.19}$$

The above equation described, the combination coefficients of combined observations have a direct effect on the ionospheric delay.

41.2.3 Observation Noise

According to the error propagation law shows, the random noise (unit: rad) of combination observations can be expressed as:

$$\sigma_{\phi_c} = \sqrt{(i\sigma_{\phi_1})^2 + (j\sigma_{\phi_2})^2 + (k\sigma_{\phi_3})^2} \tag{41.20}$$

Which σ_{ϕ_1}, σ_{ϕ_2}, σ_{ϕ_3} representing the random measurement noise of carrier B1, B2, B3, mainly composed by the measuring phase error, if make:

$$\sigma_{\phi_1} = \sigma_{\phi_2} = \sigma_{\phi_3} = \sigma_{\phi_0} \tag{41.21}$$

Then the phase measurement noise of combination observations is expressed as:

$$\sigma_{\phi_c} = \sqrt{i^2 + j^2 + k^2}\sigma_{\phi_0} \tag{41.22}$$

Similarly, when unit is "m", set:

$$\sigma_1 = \sigma_2 = \sigma_3 = \sigma_0 \tag{41.23}$$

There is:

$$\sigma_c = \sqrt{\alpha^2 + \beta^2 + \gamma^2}\sigma_0 \tag{41.24}$$

By analyzing the Eqs. (41.22) and (41.24), it can be concluded: When unit is "rad", because i, j, k are integers, so the random measurement noise of combination observation is always greater than the single carrier's; and when "m" as a unit, random measurement noise of combination observation is less than the single carrier's may be present.

41.3 Selection Standards for Combination Observations Coefficient

Combination coefficient has a direct impact on the characteristic of combination observations. To select more targeted coefficient combination, so that the final result is conducive to determine the integer ambiguity, reducing the ionospheric delay and weaken the observation noise, specially formulated the following selection criteria:

(1) Combined observations to maintain ambiguity of integer;
(2) Combination observations have longer wavelengths;
(3) Combination observations have smaller ionospheric delay;
(4) Combination observations have smaller observation noise.

41.3.1 Long Wavelength Combination Standard

In order to ensure that the combined observations easier to identify integer ambiguity than a single carrier, we need to make the wavelength of combination observation greater than any single carrier wavelength. And among the three carriers of BeiDou System, B2 has the longest wavelength, combined Eq. (41.15), the wavelength of combination observation should meet:

$$\lambda = \frac{\lambda_1\lambda_2\lambda_3}{i\lambda_2\lambda_3 + j\lambda_1\lambda_3 + k\lambda_1\lambda_2} > \lambda_2 \tag{41.25}$$

After finishing:

$$\lambda_1\lambda_3 > i\lambda_2\lambda_3 + j\lambda_1\lambda_3 + k\lambda_1\lambda_2 > 0 \tag{41.26}$$

Equation (41.5) is deformed and get into the above equation:

$$1 - im - kn > j > -im - kn \tag{41.27}$$

Because of the need to ensure j is an integer and only one integer in the interval, the values can be obtained:

$$j = \lceil -im - kn \rceil \tag{41.28}$$

where, the symbol $\lceil \bullet \rceil$ represents positive direction rounding.

The Eq. (41.28) into Eq. (41.15), can obtain the combination observation wavelength expression which only associated with i and k:

$$\lambda = \lambda_2/(im + j + kn) = \lambda_2/(im + kn + \lceil -im - kn \rceil) \tag{41.29}$$

Because of m and n are integers ratio in above equation, so Eq. (41.29) with top integral function is a periodic function. Writing expressions:

$$im + kn + \lceil -im - kn \rceil = m(i + T_1) + n(k + T_2) + \lceil -m(i + T_1) - n(k + T_2) \rceil \tag{41.30}$$

where, T_1 and T_2 are cycle of i and k, and $T_1 = 24,\ T_2 = 59$. And by Eq. (41.22) and (41.24) shows that the size of the observation noise is proportional to the absolute value of the combination coefficients. In order to make the observation noise as low as possible, take:

$$i \in [-12, 12]\, k \in [-29, 30] \tag{41.31}$$

and i, j, k can not be 0 at the same time.

For more intuitive to express the size of the combination observation wavelength, define a parameter α_λ represents the wavelength ratio of observation combination and B2 carrier. The greater the parameters, that the longer wavelength combination observations.

$$\alpha_\lambda = \lambda/\lambda_2 = 1/(im + j + kn) \tag{41.32}$$

41.3.2 Weak Ionospheric Delay Combination Standard

By Eqs. (41.9) and (41.17) show:

$$I_c = (\alpha + \beta m^2 + \gamma p^2) I_1 \tag{41.33}$$

The Eq. (41.14) into above equation, obtained after finishing:

$$(I_c/\lambda)/(I_1/\lambda_1) = i + jm + kp \tag{41.34}$$

It can be inferred from the above equation, if want the ionospheric delay of combination observations becomes smaller, the absolute value of the ratio should be less than 1, that $|i + jm + kp| < 1$, finishing the absolute value:

$$(-1 - i - kp)/m < j < (1 - i - kp)/m \tag{41.35}$$

While the range $[(-1 - i - kp)/m, (1 - i - kp)/m]$ is processed to obtain:

$$1 < |(-1 - i - kp)/m - (1 - i - kp)/m| = 2/m \approx 1.5 < 2 \tag{41.36}$$

So integer j may have two values, namely:

$$j_1 = \lceil (-1 - i - kp)/m \rceil \tag{41.37}$$

$$j_2 = \lfloor (1 - i - kp)/m \rfloor \tag{41.38}$$

where, the symbol $\lfloor \bullet \rfloor$ represents negative direction rounding.

$$\lambda(i, j_1, k) = \lambda_2/(im + kn + j_1) \tag{41.39}$$

$$\lambda(i, j_2, k) = \lambda_2/(im + kn + j_2) \tag{41.40}$$

Different with Eqs. (41.29), (41.39) and (41.40) had no significant periodicity, and when $i = 28$, $k = -48$ or $i = -28$, $k = 48$, we can get $j_1 = j_2 = -24$, respectively, take the two sets of numbers into the Eq. (41.19) can obtain $\eta = 0$, that the ionospheric delay of combination observation is 0. Then take $i \in [-28, 28]$, $j \in [-24, 24]$, $k \in [-48, 48]$ as the scope, and i, j, k can not be 0 at same time. Combination observations within this range represent basically the characteristic of all combination observations, just search for qualifying combination coefficients within this range.

The same with long-wavelength combination standards, definitions ionospheric delay parameters α_{ion} to measure the degree of combination observations weaken ionospheric delay, which is the ionospheric delay's ratio of combination observation and carrier B1 phase observations. The smaller α_{ion}, compare with single carrier, combination observation to weaken the ionospheric delay effect is better. By Eqs. (41.17) and (41.19) shows that:

$$\alpha_{ion} = \frac{I_c}{I_1} = \eta = \frac{i + (31/24)j + (59/48)k}{i + (24/31)j + (48/59)k} \tag{41.41}$$

41.3.3 Weak Observation Noise Combination Standard

If we choose the Eq. (41.24) as the standard of screening combination observation, the demand should be met:

$$\sqrt{\alpha^2 + \beta^2 + \gamma^2} < 1 \tag{41.42}$$

The Eq. (41.14) into Eq. (41.24) to give:

$$\sigma_c = \lambda\sigma_0\sqrt{(i/\lambda_1)^2 + (j/\lambda_2)^2 + (k/\lambda_3)^2} \tag{41.43}$$

where, make $\sigma_0 = 0.005$ m [6].

Due to the combined coefficient of weak ionospheric delay observation combination without specific scope, the workload is huge, so the standard only as auxiliary references of the other two standards, and not individually listed specific combination observations.

41.4 Analysis the Results of Simulation

According to the selection standard for the combination observations coefficient, search on range, and list the combinations which meet the conditions. We can get long-wavelength combination observations and weak ionospheric delay combination observations.

41.4.1 Long Wavelength Combination Observations

Search in the scope mentioned above offer of the long wavelength combinations search criteria, after all the long wavelength combinations listed, pick ionospheric delay and observation noise are small combination observations, the results in Table 41.1.

Combinations listed in Table 41.1, the combinations of (−1, 5, 6), (0, 1, −1), (3, 13, −16) have longer wavelengths, but ionospheric delay slightly larger; combinations of (1, 4, −5), (2, 8, −10), (3, 11, −14), (4, 15, −19) all have longer

Table 41.1 Long-wavelength combination observations

i	j	k	λ(m)	λ/λ_2	α_{ion}	σ_c(m)
−1	−5	6	20.9468	84.46	−8.9631	0.4345
1	4	−5	6.3751	25.71	0.6521	0.2010
0	−1	1	4.8876	19.71	−1.5915	0.1423
3	13	−16	3.7597	15.16	2.3779	1.6340
2	8	−10	3.1876	12.85	0.6521	0.8631
3	11	−14	1.4811	5.97	−0.0278	0.5595
4	15	−19	1.2019	4.85	0.1004	0.6164
6	22	−28	0.7405	2.99	−0.0278	0.5595

Table 41.2 Weak ionospheric delay combination observations

i	j	K	λ(m)	λ/λ_2	α_{ion}	σ_c(m)
17	−16	3	0.0272	0.11	0.000058	0.0150
16	0	−13	0.0353	0.14	0.000297	0.0175
19	11	−27	0.0345	0.14	−0.000359	0.0274
21	−21	5	0.0218	0.09	−0.000499	0.0150
1	−16	16	0.1180	0.48	−0.000738	0.0550
15	16	−29	0.0505	0.20	0.000740	0.0400
24	−10	−9	0.0215	0.09	−0.000895	0.0145
13	−11	1	0.0362	0.15	0.000984	0.0145

wavelengths, while the ionospheric delay error and observation noise small, will be easy to quickly determine the integer ambiguity. Wherein the combination (1, 4, −5), (3, 11, −14) were excellent in all aspects.

41.4.2 Weak Ionospheric Delay Combination Observations

Get a large number of combination observations after the simulation, in order to greatly weaken the impact of ionospheric delay, weaken the meter-sized ionospheric delay to the millimeter-sized below, in the selection of the combination, select the combination $\alpha_{\text{ion}} < 0.001$, get a combination observations meet the conditions shown in Table 41.2.

Combinations listed in Table 41.2 were able to significantly weaken the ionosphere delay, and the observation noises are also centimeter-sized, has important implication for the integer ambiguity resolution and navigation positioning. Wherein the combination of (1, −16, 16) has reached more than 10 cm wavelength, and the observation noise characteristics is relatively good, recommended the use of.

41.5 Conclusions

Using triple frequency carrier phase observations combine the three carriers of the Beidou satellite navigation system, can get linear combination of long wavelength, weak ionospheric delay, low observation noise, which can accurately and quickly calculate the integer ambiguity of the combination observation, and effectively weaken the effect of ionospheric delay, it has important significance for improving the Beidou navigation positioning accuracy and real-time. This paper discusses the standard for the Beidou system selecting combination observations, what based on the wavelength, ionospheric delay and observation noise, and gives several groups of combination observations which have outstanding results in certain areas and the good performance in other areas. Such as combination (1, 4, −5), (3, 11, −14) beneficial ambiguity fixed, combinations (1, −16, 16) can greatly weaken ionospheric delay and so on. Provide a reference for the construction of Chinese Beidou satellite navigation system.

Acknowledgments Project supported by the National Natural Science Foundation of China (Grant No. 61403093), the National Natural Science Foundation of China (Grant No. 61371099), the Heilongjiang Province Foundation for Returnees (Grant No. LC2013C22), and the Project supported by the Fundamental Research Funds for the Central Universities of Ministry of Education of China (Grant No. HEUCF140807).

References

1. Zhang GM (2009) Discussing to feasibility of GNSS operation integrated with compass. GNSS World China 34(2):20–23
2. Xu JY (2013) Performance analysis of COMPASS/GPS differential positioning. In: CSNC 2013, Wuhan
3. Hatch R (1996) The promise of a third frequency. GPS World 7(5):55–58
4. Tang W, Deng C, Shi C et al (2014) Triple-frequency carrier ambiguity resolution for Beidou navigation satellite system. GPS Solutions 18(3):335–344
5. Liu ZJ, Zheng B, Liu WX (2012) Ou Gang analysis and comparison on algorithms of carrier phase smoothing pseudorange in three-frequency GNSS. Sci Surveying Mapp 37(6):15–18
6. Wang K, Rothacher M (2013) Ambiguity resolution for triple-frequency geometry-free and ionosphere-free combination tested with real data. J Geodesy 87(6):539–553

Chapter 42
A Baseline Ambiguity Resolution Using Un-combined and Un-differenced Model with Equality Constraint

Denghui Wang, Chengfa Gao, Shuguo Pan and Wang Gao

Abstract With the development of GNSS technology, the higher demand for calculation is put forward in the field of the whole network baseline solution. The conventional baseline solution is a three-step method, which is complex and relies on the success rate of ambiguity solution at each step. A modified strategy for baseline ambiguity resolution is proposed in the paper, using un-combined and un-differenced model. The equality constraint is also used to recover the integer property of ambiguities. By the constraint of the fixed ambiguities, the baseline solution could be obtained. The data sets from various lengths of baselines are conducted to investigate the performance of the UD strategy. Depending on the empirical fixed success rate and convergence time, the modified strategy has a better AR performance on the rising satellites and weakens the unknown coefficient of correlation between ambiguities.

Keywords Baseline solution · Un-combined and un-differenced model · Equality constraint · Fixed success rate

42.1 Introduction

RTK (real-time kinematic) is one of the most precise positioning technique with GNSS (global navigation satellite system). Users of RTK can easily obtain cm-level accuracy of user positions in real-time by obtaining correct integer DD carrier phase ambiguities [1]. In order to reduce the common error between user receiver and base station, such as the orbit error, the ionosphere and the troposphere et al., double-difference (DD) baseline solution is widely used in high precision

D. Wang (✉) · C. Gao · W. Gao
School of Transportation, Southeast University, 2 Sipailou, Nanjing 210096, China
e-mail: owenxun@gmail.com

S. Pan
School of Instrument Science and Engineering, Southeast University, 2 Sipailou, Nanjing 210096, China

J. Sun et al. (eds.), *China Satellite Navigation Conference (CSNC) 2015 Proceedings: Volume II*, Lecture Notes in Electrical Engineering 341,
DOI 10.1007/978-3-662-46635-3_42

positioning application. The satellite- and receiver-related clock biases and uncalibrated phase delays (UPDs) are also completely eliminated. For short baseline RTK, original observables L1, L2, P1 and P2 without linear combination (LC) are generally used to obtain the solutions. For conventional medium or long baseline post-processing, DD WL ambiguities are fixed first, followed by the determination of basic integer ambiguities based on the ionosphere-free model [2]. MW (Melbourne-Wübbena) wide-lane LC and ionosphere-free LCs are often utilized [3]. The atmospheric delay also needs to be estimated in the model to improve the DD ambiguity resolution (AR) performance over long baseline [4–6]. However, the effectiveness of RTK positioning is degraded as the baseline length increases, since the DD ambiguity resolution becomes increasingly unreliable to introduce the atmospheric errors [7]. The common tracking satellites need to be selected with independent baseline selection, data utilization efficiency is restricted compared the single receiver data processing method [3].

Techniques that were developed to overcome this shortcoming of baseline solution led to the introduction of Precise point positioning (PPP). Zumberge can provide centimeter or even millimeter positioning accuracy with a single dual-frequency receiver [8]. It usually takes about 30 min in order to obtain positions with accuracy better than 10 cm. The integer property of un-differenced (UD) ambiguities is deteriorated due to absorption of phase biases, and long convergence time must be guaranteed for the separation of uncalibrated phase delay (UPD) and integer ambiguities [9, 10]. There are several PPP integer ambiguity resolution methods to recover the integer property of ambiguity based on the regional CORS, including decoupled clock model [11], integer phase clock model [12] and single-difference (SD) between-satellites method [9]. Based on the advancements above, real-time PPP can also be improved by applying ambiguity resolution. In general, the extensive studies on PPP-RTK play a role to provide augmentation services to PPP users, thus achieving position solutions equivalent to the DD RTK method.

A modified method based on the un-differenced and un-combined (UC) model is proposed. In the data processing, the equality constraints are introduced in the filter to recover integer ambiguities and obtain cm-level accuracy of user positions. This paper is organized as follows. Section 42.2 introduces the UD model and the different equality constraints based on the baseline distance. Section 42.3 describes the results from various lengths of baselines. The empirical fixed success rate and the ratio of LAMBDA method are also shown to prove the effectiveness of the new method. The final section is a summary of the findings.

42.2 The Observation Equations

In this section, the original observations of both the reference station and the user sites are used to construct the observation vector. For simplifying the derivation of the un-differenced model and the equality constraint, only two stations are considered in the network processing. We firstly discussed the observation equations.

42.2.1 Un-Combined Observation Equations

The un-combined model is proposed by M.O. Keshin, A.Q. Le etc. at Delft University of Technology [13]. Four kinds of UD GNSS measurements are conducted to reflect the influence of the atmospheric changes. The code and phase observations from satellites to receiver k at frequency j are written as Eqs. (42.1) and (42.2).

$$P_{j,k}^{s} = \rho_k^s + c\delta t_k - c\delta t^s + T_k^s + \alpha_j I_k^s + d_{k,P_j} - d_{P_j}^s + \varepsilon_{k,others}^s + \varepsilon_{k,P_j}^s \tag{42.1}$$

$$\Phi_{j,k}^{s} = \rho_k^s + c\delta t_k - c\delta t^s + T_k^s - \alpha_j I_k^s + b_{k,\Phi_j} - b_{\Phi_j}^s + \varepsilon_{k,others}^s + \lambda_j N_j + \varepsilon_{k,\Phi_j}^s \tag{42.2}$$

where the symbol P denotes raw code observation, Φ is raw phase observation, ρ_k^s is the geometric range between satellite and receiver antenna phase center (m). δt_k and δt^s is the receiver and satellite clock offsets, respectively. T_k^s represents troposphere delay. I_k^s represents ionospheric delays, which is related to the signal frequency. α_i is the frequency scaling, set as: $\alpha_j = f_1^2 \big/ f_j^2$. d_{k,P_j}, $d_{P_j}^s$ are receiver and satellite code hardware biases. It's important to note that the bias is related to the frequency. $\varepsilon_{k,others}^s$ is the other error which could be modeled, including tidal correction, plate motions error, etc. $b_{\Phi_j}^s$ are receiver and satellite carrier phase fractional bases at different frequencies. λ_j is the carrier wavelength and N_j is carrier-phase ambiguity (cycle); ε_{k,P_j}^s, ε_{k,Φ_j}^s is phase multipath and phase noise.

For the purpose of simplifying the UD equations in the baseline solution, the unknown parameters can be divided into a temporal part and a non-temporal part. The temporal part consists of positional parameters of two stations, two zenith wet troposphere delay (ZWD), two receiver clock offsets, 2n-dimensional state vector of ionospheric slant delay and n-dimensional state vector of satellite clock offsets. The non-temporal part is composed of 4n-dimensional state vector of the original UD ambiguities. n represents the observable satellites number. The estimated original N_1 and N_2 ambiguities could be written as Eq. (42.3).

$$\lambda_j N_f' = \lambda_j N_j - \alpha_j \frac{f_2^2}{f_1^2 - f_2^2}(B_k - B^s) - b_{\Phi_j}^s + d_{P_{IF}}^s + b_{k,\Phi_j} - d_{k,P_{IF}} \tag{42.3}$$

B_k, B^s is receiver and satellite differential code bias (DCB) between $P1$ and $P2$, and $B_k = d_{k,P_2} - d_{k,P_1}$, $B^s = d_{P_2}^s - d_{P_1}^s$. $d_{P_{if}}^s$ is receiver and satellite differential code ionosphere-free bias [14]. It's important to note that the integer property of UD ambiguities is deteriorated due to absorption of phase and code biases and the precise satellite clock products would be added as the pseudo observation equations.

42.2.2 The Equality Constraint

In case of the receiver collect phase and code observations from n satellites at epoch i, the extended Kalman filter is written as Eq. (42.4).

$$\begin{cases} X_i = \Phi_{i,i-1}X_{i-1} + W_i, E(W_i) = 0, Cov(W_i) = Q_i \\ L_i = B_iX_i + V_i, E(V_i) = 0, Cov(V_i) = R_i, Cov(V, W) = 0 \\ C_iX_i + W_x = 0 \end{cases} \tag{42.4}$$

where X_i, X_{i-1} is the vector of unknown parameters, $\Phi_{i,i-1}$ is the state transfer matrix, L_i is the observation vector, B_i is the design matrix, C_i is the design matrix of the equality constraint and W_x represents the observation equality constraint.

The equality could be divided into two parts. Firstly, different from the PPP model, the high-precision coordinates of the reference stations is exactly known as the equality constraint. Secondly, the atmospheric delay could be used as the parameter of the constraint depending on the length of baselines. For short baseline RTK, the atmospheric delay between two stations could be regarded as equivalent parameter. It is noticed that the atmospheric constraint equation should consider the satellite-difference for the ionospheric estimated parameter, so that the receiver DCB could be eliminated. Using polynomial fit technique [15], the atmospheric constraint could else be used for mediate and long baselines.

With the addition of the equality constraint, the filtering results can be described as Eqs. (42.5) and (42.6).

$$\hat{X}_i = \bar{X}_i + Q_{\bar{X}_i}[B_i^T, C_i^T]\begin{bmatrix} B_iQ_{\bar{X}_i}B_i^T + Q_i & B_iQ_{\bar{X}_i}C_i^T \\ C_iQ_{\bar{X}_i}B_i^T & C_iQ_{\bar{X}_i}C_i^T \end{bmatrix}^{-1}\begin{bmatrix} L_i - B_i\bar{X}_i \\ W_x - C_i\bar{X}_i \end{bmatrix} \tag{42.5}$$

$$Q_{\hat{X}_i} = Q_{\bar{X}_i} - Q_{\bar{X}_i}[B_i^T, C_i^T]\begin{bmatrix} B_iQ_{\bar{X}_i}B_i^T + Q_i & B_iQ_{\bar{X}_i}C_i^T \\ C_iQ_{\bar{X}_i}B_i^T & C_iQ_{\bar{X}_i}C_i^T \end{bmatrix}^{-1}\begin{bmatrix} B_i \\ C_i \end{bmatrix}Q_{\bar{X}_i} \tag{42.6}$$

For the purpose of achieving the integer ambiguities of the UD data processing, the reference station is selected to define the initial datum. The DD ambiguity between the other station and the pivot station could be recovered to the integer property. The code and phase biases of satellites in the UD ambiguity are eliminated first by the between-station difference. And the code and phase biases related to the receiver are eliminated to recover the integer property by the between-satellite difference. By specifying an appropriate difference matrix, the vector of unknown parameters could be transformed to the combination of DD ambiguities and UD ambiguities.

In the UD data processing, the residual error has an obvious interference on the ambiguities. A linear combination matrix also need be used to improve the success rate of the DD ambiguities. The wide-lane ambiguities are obtained and fixed firstly as the known parameters.

$$\begin{aligned} C_{\underset{2(n-1)\times 2(n-1)}{linear}} &= \begin{bmatrix} I & -I \\ I & 0 \end{bmatrix}, \quad X_{nw,n1} = C_{linear} \times \begin{bmatrix} \hat{a}_{N_1} \\ \hat{a}_{N_2} \end{bmatrix} = \begin{bmatrix} \hat{a}_{N_w} \\ \hat{a}_{N_1} \end{bmatrix} \\ Q_{nw,n1} &= C_{linear} \begin{bmatrix} Q_{\hat{a}_{N_1}\hat{a}_{N_1}} & Q_{\hat{a}_{N_1}\hat{a}_{N_2}} \\ Q_{\hat{a}_{N_2}\hat{a}_{N_1}} & Q_{\hat{a}_{N_2}\hat{a}_{N_2}} \end{bmatrix} C_{linear}^{T} = \begin{bmatrix} Q_{\hat{a}_{N_w}\hat{a}_{N_w}} & Q_{\hat{a}_{N_w}\hat{a}_{N_1}} \\ Q_{\hat{a}_{N_1}\hat{a}_{N_w}} & Q_{\hat{a}_{N_1}\hat{a}_{N_1}} \end{bmatrix} \end{aligned} \tag{42.7}$$

The LAMBDA method would be used to guarantee the basic ambiguities, with the help of the reduction step to shrink the search space of an integer vector by a linear transformation and the skillful tree search procedure of the integer vector under ILS (integer least squares) condition. The transformer procedure could be described as Eq. (42.8).

$$\begin{aligned} \breve{a}_{N_1} &= \hat{a}_{N_1} - Q_{\hat{a}_{N_1}\hat{a}_{N_w}} Q_{\hat{a}_{N_w}\hat{a}_{N_w}}^{-1} (\hat{a}_{N_w} - \breve{a}_{N_w}) \\ Q_{\breve{a}_{N_1}\breve{a}_{N_1}} &= Q_{\hat{a}_{N_1}\hat{a}_{N_1}} - Q_{\hat{a}_{N_1}\hat{a}_{N_w}} Q_{\hat{a}_{N_w}\hat{a}_{N_w}}^{-1} Q_{\hat{a}_{N_w}\hat{a}_{N_1}} \end{aligned} \tag{42.8}$$

42.3 Test Results and Analysis

42.3.1 The Short Baseline Test

According to the above introduction, the equality constraint may have a different impact on the float baseline solution. A short baseline of 12.4 km is selected to validate the performances. In the section, three strategies are used and the detailed setting is shown in Table 42.1.

Table 42.1 The observation, the equality constraint and the estimable parameters

	The observation	The equality constraint	The number of estimable parameters
S1	UD and UC observations, the pseudo observations of satellite clock	None	7n + 10
			The coordinates of reference station and users (6), STEC (2n), ZWD (2), receiver and satellite clock offsets (n + 2), the ambiguities (4n)
S2	UD and UC observations, the pseudo observations of satellite clock	The coordinates of the reference stations, the ionospheric and tropospheric constraint	7n + 10
			The coordinates of reference station and users (6), STEC (2n), ZWD (2), receiver and satellite clock offsets (n + 2), the ambiguities (4n)
S3	DD ionosphere-free observations	None	n + 4
			The coordinates of users (3), ZWD (2), the ambiguities (n−1)

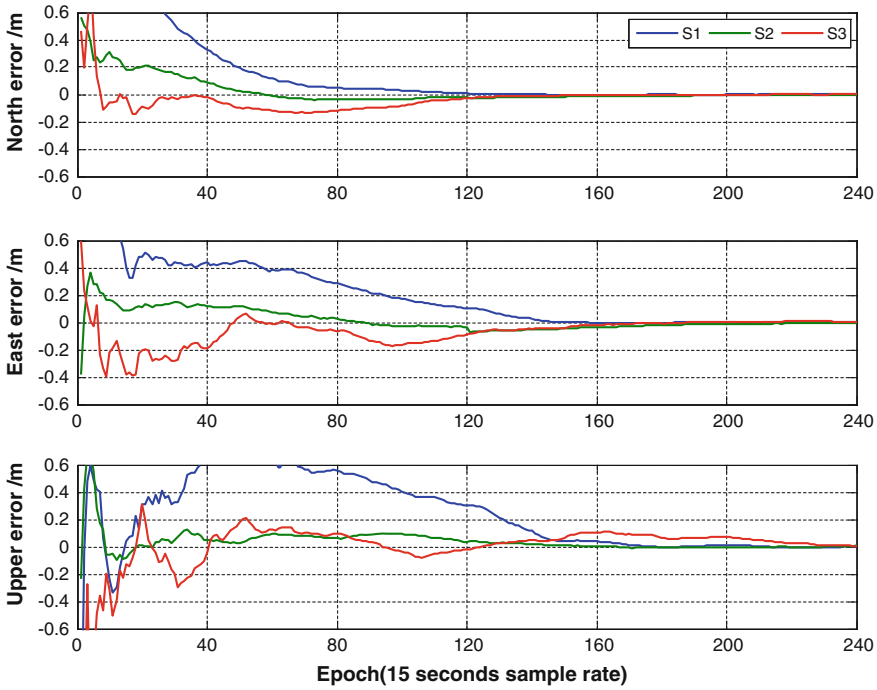

Fig. 42.1 The float positioning result on the *north*, *east* and *upper direction*

In the DD model, the zenith wet tropospheric delay of the two stations is estimated. The basic DD ambiguities are fixed by the combination of wide-lane ambiguities and ionosphere-free ambiguities. The MW linear combination is used to get the DD wide-lane ambiguities. Figure 42.1 shows the result with 12.4 km baseline by the simple implementation of three strategies. The plots indicate E/N/U components of the float solutions based on the Kalman filter.

It is can be seen in the comparison that the result with S2 method have a fastest convergence time on the three directions. Due to the ill-posed problem, this is the obvious fluctuate of S3 method at the initialization period. The equality constraints seem to have a real effect to improve the computational efficiency.

The bootstrapping success rate of ambiguities fixing is proposed by Teunissen [16]. It is invariant for the whole class of admissible ambiguity transformations. Based on the determinant of the ambiguity variance covariance matrix, the probability of correct integer rounding of three models is shown in Fig. 42.2.

In Fig. 42.2, it is obvious that the success rate has a relationship with a number of satellites tracked, number of observation epochs used, and amount of changing relative receiver-satellite geometry. More time is sacrificed to get 99.9 % credibility of AR with the S1 method. And S2 method is not sensitive to rising satellites. The ratio of the LAMBDA method also indicated the modified method (S2) could get a reliable result of the L1 and L2 ambiguity in a short time (Fig. 42.3).

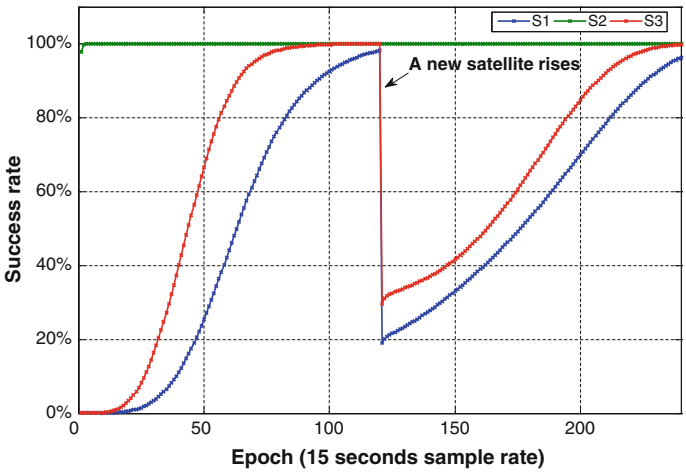

Fig. 42.2 The bootstrapping success rate of ambiguities fixing. A new satellite rises at the 120th epoch, results in the drop of the index. The success rate of S2 method is 97.8607 % at the first epoch and 99.9966 % at the 120th epoch

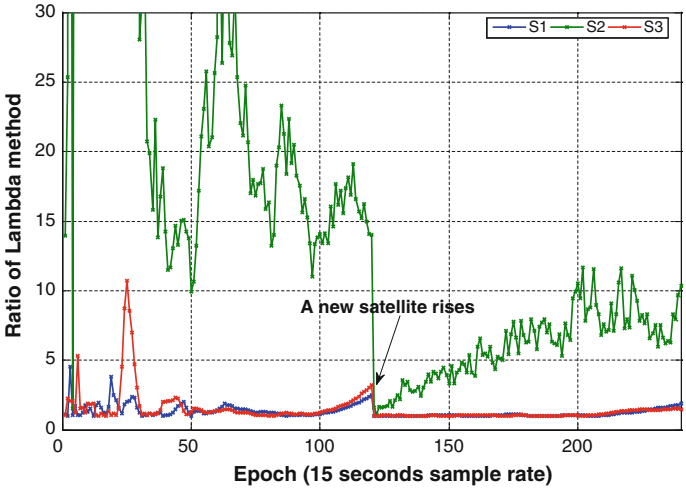

Fig. 42.3 The ratio of the LAMBDA method

The low fixing ratio of S1 and S3 seems mainly due to the satellites which are newly rising from the horizon. The carrier-phase ambiguities for such satellites usually need long convergence time after they firstly become visible and disturb the other ambiguity fixing by LAMBDA strategy under ILS condition, which assumes all of ambiguities are resolved together at the same time. By the addition of the equality constraint, the ambiguities vector and the covariance matrix would be changed, results in the improvement of the fixing ratio.

42.3.2 The Medium Baseline Test

More tests on the medium and long baseline have been done to certify that the above conclusion. A baseline of 157.8 km is selected to validate the performances. For the purpose of confirming the influence of the pseudo observations, the four data processing strategies are shown in Table 42.2. It is noted that the equality constraint is only the known coordinates of the reference stations due to the long baseline environment.

Figure 42.4 shows the E/N/U components of the float solutions by four strategies shown in Table 42.2.

UD strategies show better performance on the long baseline environment. The un-modelling residuals slow the DD process and reject the fixed solution because of biased. Due to the few constraints, the float solution of S1, S2 and S3 strategy have a similar convergence effect.

The surprising finding is that the success rate doesn't show up the same way compared with the float solution in Fig. 42.5. On the positive side, the constraints have a better influence on the improvement of the success rate.

The comparison can be seen obviously that the UD-UC method have a more credible contribution on the estimation of N1 float ambiguity bias in Fig. 42.6. The new method could get a reliable result of the L1 and L2 ambiguity in a short time. What is more, the UD-UC model also provides an alternative method for wide-lane ambiguity resolution.

Table 42.2 The observation, the equality constraint and the estimable parameters

	The observation	The equality constraint	The number of estimable parameters
S1	UD and UC observations	None	6n + 10
			The coordinates of reference station and users (6), STEC (2n), ZWD (2), receiver clock offsets (2), the ambiguities (4n)
S2	UD and UC observations, the pseudo observations of satellite clock	None	7n + 10
			The coordinates of reference station and users (6), STEC (2n), ZWD (2), receiver and satellite clock offsets (n + 2), the ambiguities (4n)
S3	UD and UC observations, the pseudo observations of satellite clock	The coordinates of the reference stations	7n + 10
			The coordinates of reference station and users (6), STEC (2n), ZWD (2), receiver and satellite clock offsets (n + 2), the ambiguities (4n)
S4	DD ionosphere-free observations	None	n + 4
			The coordinates of users (3), ZWD (2), the ambiguities (n − 1)

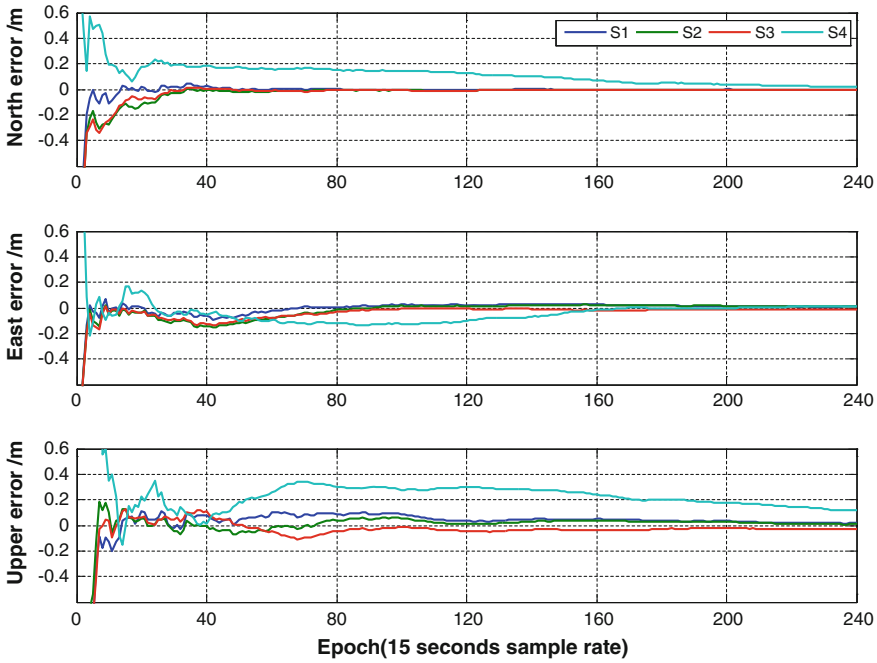

Fig. 42.4 The float positioning result of the baseline around 157.8 km in the *north*, *east* and *upper direction*

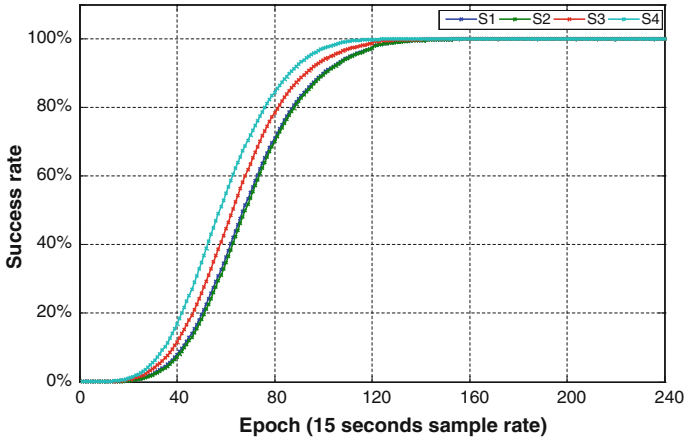

Fig. 42.5 The bootstrapping success rate of ambiguities fixing

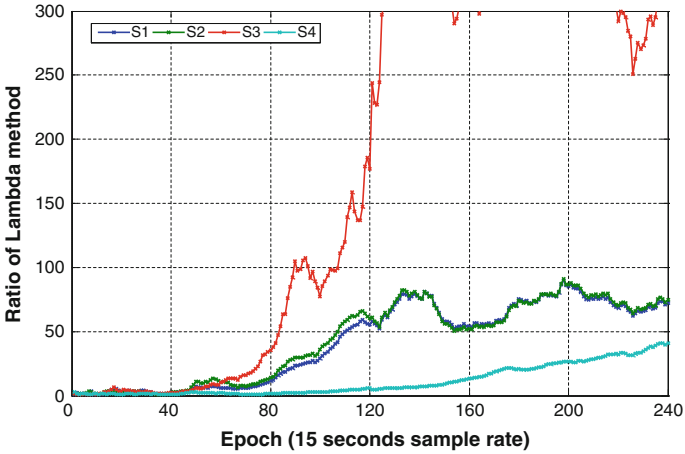

Fig. 42.6 The ratio of the LAMBDA method with different strategies

The four lines are shown in Fig. 42.7. It could be confirmed that the DD method has the minimum ADOP. With the addition of the equality constraint, the accuracy or the confidence interval of ambiguities could be improved. On the other hand, more time is sacrificed to get more credibility of AR with the addition of pseudo satellite clock measurements and unknown parameters.

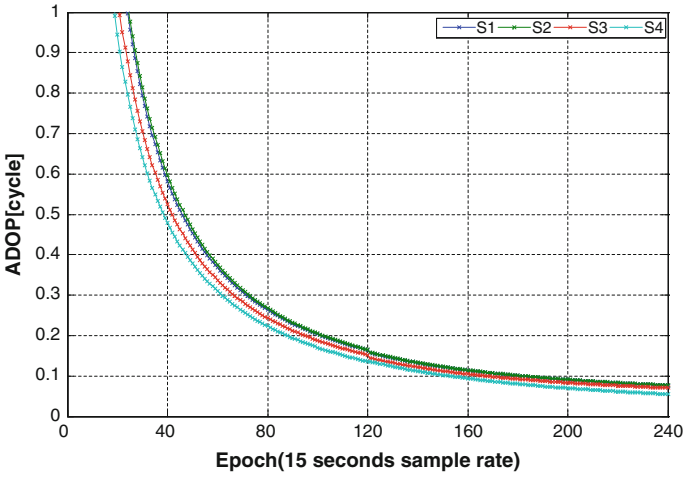

Fig. 42.7 ADOPs of four strategies

42.4 Conclusions

An alternative method is proposed in the application of the UD and UC model in the baseline ambiguity resolution. Based on the UD model, the common view of satellites is no need to avoid the loss of observation information. Besides, with the addition of equality constraint, the UD-UC model would be more effective to improve the convergence time and success rate of ambiguities fixing.

The following recommendations can be made based on the results: (1) the addition of equality constraints could improve the bootstrapping success rate; (2) Due to the more observation and less ill-posed problem, the UD-UC method with the constraints has a better AR performance on the baseline ambiguity resolution; (3) For simplifying the derivation, only two stations is considered in the filter, more station could be added to ensure better performance on the estimation of the ambiguities. The estimation of uncalibrated phase and code delay and the addition of the refined datum will be further researched in the future.

Acknowledgments This work is supported by the Key Projects in the National Science & Technology Pillar Program during the Twelfth Five-year Plan Period (No. 2012BAJ23B01). The authors are very grateful to the anonymous reviewers for their constructive comments and suggestions.

References

1. Hofmann-Wellenhof B, Lichtenegger H, Collins J (2001) Global positioning system: theory and practice, 5th revised edn. Springer Wien, New York, pp 192–196
2. Teunissen PJ (1995) The least-squares ambiguity decorrelation adjustment: a method for fast GPS integer ambiguity estimation. J Geodesy 70(1–2):65–82
3. Wübbena G, Schmitz M, Bagge A (2005) PPP-RTK: precise point positioning using state-space representation in RTK networks. In: Proceedings of ION GNSS, vol. 5, pp 13–16
4. Wielgosz P, Kashani I, Grejner-Brzezinska D (2005) Analysis of long-range network RTK during a severe ionospheric storm. J Geodesy 79(9):524–531
5. Takasu T, Yasuda A (2010) Kalman-filter-based integer ambiguity resolution strategy for long-baseline RTK with ionosphere and troposphere estimation. In: ION NTM
6. Li B, Verhagen S, Teunissen PJ (2014) Robustness of GNSS integer ambiguity resolution in the presence of atmospheric biases. GPS Solutions 18(2):283–296
7. Teunissen PJG, Kleusberg A, Teunissen PJG (1998) GPS for geodesy [M]. Springer, Berlin
8. Zumberge JF, Heflin MB, Jefferson DC, Watkins MM, Webb FH (1997) Precise point positioning for the efficient and robust analysis of GPS data from large networks. J Geophys Res 102:5005–5017
9. Ge M, Gendt G, Rothacher M, Shi C, Liu J (2008) Resolution of GPS carrier-phase ambiguities in precise point positioning (PPP) with daily observations. J Geodesy 82(7):389–399
10. Geng J, Teferle FN, Meng X, Dodson AH (2011) Towards PPP-RTK: ambiguity resolution in real-time precise point positioning. Adv Space Res 47(10):1664–1673
11. Laurichesse D, Mercier F, Berthias JP, Broca P, Cerri L (2008) Zero-difference ambiguity fixing for spaceborne GPS receivers. In: Proceedings of ION GNSS, pp 758–768

12. Collins P (2008) Isolating and estimating un differenced GPS integer ambiguities. In: Proceedings ION NTM, pp 720–732
13. Keshin MO, Le AQ, Marel H (2006) Single and dual-frequency precise point positioning: approaches and performance. In: Proceedings of the 3rd ESA workshop on satellite navigation user equipment technologies, NAVITEC 2006, 11–13 Dec, The Netherlands
14. Zhang B, Teunissen PJ, Odijk D (2011) A novel un-differenced PPP-RTK concept. J Navig 64 (S1):S180–S191
15. Li X (2012) Improving real-time PPP ambiguity resolution with ionospheric characteristic consideration. In: Proceedings of ION GNSS-12, institute of navigation, Nashville, Tennessee, 17–21 Sept
16. Teunissen PJ (1998) Success probability of integer GPS ambiguity rounding and bootstrapping. J Geodesy 72(10):606–612

Chapter 43
Using IGMAS/MGEX Ground Tracking Station Data to Solve the Global Beidou Satellite DCB Products

Junqiang Han, Qin Zhang, Guanwen Huang and Jin Wang

Abstract In view of BeiDou Satellite System (BDS) developed by China, DCB product is not yet mature, this paper presents some technique and methods to calculate BDS satellite and receiver DCB, then analysis the performance of results under different constraints. Besides, we first take use of the GPS data to validate the precision by using this method. Based on this, using BDS/GPS observation data received by International GNSS Monitoring and Assessment System (iGMAS) and The Multi-GNSS Experiment of IGS (MGEX) tracking stations calculated the differential code bias products of BDS satellite and receiver for more than 30 days. Finally, analyzed the stability and accuracy of the products, and assessed the performance of receiver made in China and foreign by DCB precision.

Keywords Beidou satellite system developed by china (BDS) · DCB

43.1 Introduction

Beidou Navigation Satellite System (BDS), which independently developed by China, is used to global satellite navigation. There are about 14 Beidou satellites are in orbit, and five of them are Geostationary Earth Orbit (GEO), five are Inclined Geosynchronous Satellite Orbit (IGSO) and four are Medium Earth Orbit (MEO). The BDS has 4 basically functionality, including positioning, navigation, communication (short message) and timing. It has provided service to the Asia Pacific

J. Han · Q. Zhang (✉) · G. Huang · J. Wang
College of Geology Engineering and Geomantic, Chang'an University, Xi'an, Shaanxi, China
e-mail: zhangqinle@263.net.cn

J. Han
e-mail: chd_hjq@126.com

G. Huang
National Key Laboratory of Geographic Information Engineering, Xi'an 710054, China

J. Sun et al. (eds.), *China Satellite Navigation Conference (CSNC) 2015 Proceedings: Volume II*, Lecture Notes in Electrical Engineering 341,
DOI 10.1007/978-3-662-46635-3_43

region. Different from GPS with a full constellation, the number of BDS and its distribution of sites very limited by series of politic or economic factors. Since this limitation, orbit measuring precision and position precision are correspondingly affected, atmospheric research will affected as well [1, 2].

The differential code bias (DCB) refers to an inter-frequency bias meaning the difference of instrumental delay between two different frequencies, which include satellite and site. It have been demonstrated that the maximum bias will achieve more than 10 ns [3], it will potentially lead to very impact on some Beidou application, such as positioning, ionospheric modeling. Presently, DCB products provided by the International GNSS Service (IGS) were widely approved as the relatively best level. The products comprehensively based on 4 different international ionospheric data analysis center's solution derived independently.

Currently, there are mainly about 3 methods for determining DCB: (1) DCB is estimated simultaneously with ionospheric total electron content modeling [4, 5]; (2) Two-steps to estimate Beidou satellite DCB [6]; and (3) DCB is determined as parameters after deducting the ionospheric delay [7, 8]. Although these 3 methods all can derive DCB parameters, the last one will be choose in this paper, not only for taking full use of Beidou satellite observation, but resolving time will be shorter than other 2 methods as well.

Besides timing group delays (TGD) in Broadcast ephemeris, there are no released official DCB products about satellites yet [9]. In view of this, taking receivers, that adopted by International GNSS Monitoring and Assessment Service (iGMAS) which are made in China, into account, an approach to estimate daily satellite DCB is validated by using iGMAS and MGEX observation data. Least squares were used to estimate DCB after eliminating ionospheric delay, then the performance of satellites and sites DCB are discussed respectively in these two aspects: site located and satellite constellation.

43.2 Mathematical Model

43.2.1 Observation Equation

For GPS satellites DCB, it always is estimated by using spherical harmonic model with imposing a zero-mean condition. BDS orbits are consists of GEO, IGSO and MEO, but the sites numbers is less than 100, while IGS has more than 180. If estimates BDS satellites DCB by the same strategy like IGS, the precision of DCB will not be the same with it in accuracy. In addition, the TGD parameters accuracy is demonstrated more than 10 ns, which could lead to at least 2.9 m error in positioning. To fill this gap, an alternative approach has been pursued. Firstly eliminate ionospheric delay by use the Global Ionosphere Map (GIM), then derive satellite DCB and receiver DCB by the combined satellite-plus-receiver DCB. Specific step as follow.

A single pseudorange observation $P_{i,r}^{s}$ and $\mathrm{P}_{\mathrm{j,r}}^{\mathrm{s}}$

$$P_{i,r}^{s} = \rho_{r}^{s} + c \cdot \delta t_{r} - c \cdot \delta t^{s} + c \cdot \tau_{i}^{s} + c \cdot \tau_{i}^{r} + \frac{40.28 \cdot TEC}{f_{i}^{2}} + d_{trop} + \varepsilon_{i} \tag{43.1}$$

$$P_{j,r}^{s} = \rho_{r}^{s} + c \cdot \delta t_{r} - c \cdot \delta t^{s} + c \cdot \tau_{j}^{s} + c \cdot \tau_{j}^{r} + \frac{40.28 \cdot TEC}{f_{j}^{2}} + d_{trop} + \varepsilon_{j} \tag{43.2}$$

Can be described by the sum of a geometric range ρ_{r}^{s}, receiver clock offsets δt_{r}, satellite clock offsets δt^{s}, total electron content TEC, tropospheric range delay d_{trop}, satellite additive bias τ_{i}^{s}, clock additive bias τ_{i}^{R}, other observation noise uncorrelated with frequency ε_{i}, light speed c and satellite frequency f.

Then the pseudorange difference can be derived from (43.1) and (43.2):

$$P_{i,j} = c\left(dcb_{i,j}^{s} + dcb_{i,j}^{r}\right) + \Delta I_{i,j} + \Delta\varepsilon_{i,j} \tag{43.3}$$

where $dcb_{i,j}^{s} = \tau_{i}^{s} - \tau_{j}^{s}$ is satellite DCB on the frequency i and j; $dcb_{i,j}^{r} = \tau_{i}^{r} - \tau_{j}^{r}$ is receiver DCB on the frequency i and j; $\Delta I = 40.28 \cdot \left(f_{j}^{2} - f_{i}^{2}\right) \cdot TEC \cdot \left(f_{i}^{2} f_{j}^{2}\right)^{-1}$ is ionospheric delay correlated with the frequency i and j.

It can be inferred that, ignoring multipath and noise, satellite DCB and receiver DCB can be described only by the difference pseudorange and the differential ionospheric path delay. The differential code bias equation can be described as follow:

$$dcb_{1,2}^{s} + dcb_{1,2}^{r} = \frac{1}{c}\left[P_{1,2} - \Delta I_{1,2}\right] \tag{43.4}$$

$$dcb_{1,3}^{s} + dcb_{1,3}^{r} = \frac{1}{c}\left[P_{1,3} - \Delta I_{1,3}\right] \tag{43.5}$$

If there are m receivers and n satellites, there will be $m + n$ parameters, the matrix equation can be derived as follow:

$$\begin{gathered} Ax = l \\ A = \begin{bmatrix} 1 & 0 & \cdots & 0 & 1 & 0 & \cdots & 0 \\ 1 & 0 & \cdots & 0 & 0 & 1 & \cdots & 0 \\ \vdots & \vdots & \ddots & 1 & \vdots & \vdots & \ddots & \\ 0 & 0 & \cdots & 1 & 0 & 0 & \cdots & 1 \end{bmatrix} \\ x = \begin{bmatrix} dcb^{1} & \cdots & dcb^{n} & dcb^{1} & \cdots & dcb^{m} \end{bmatrix} \\ l = \begin{bmatrix} l_{1} & \cdots & l_{r} \end{bmatrix}^{T} \end{gathered} \tag{43.6}$$

where $A_{r\times(m+n)}$ is Matrix coefficient, m is the number of receiver, n is satellite number, r is the number of observation, x is unknown parameters.

43.2.2 Constraint Condition

Since observation equation is lack of constraint condition and the correlations between equations existed, solving this problem requires additional constraint condition. The rank deficiency could be removed in two ways: (1) fixing a single receiver for satellite bias; (2) imposing a zero-mean condition for the validated satellite observed. While the latter is commonly applied within the IGS and likewise adopted in this study [6, 9]. The equation is as follow:

$$\begin{gathered} bx = l_{cstr} \\ b = [\, b_1 \quad b_2 \quad \cdots \quad b_n \quad 0 \quad 0 \quad \cdots \quad 0 \,] \end{gathered} \tag{43.7}$$

where n is satellites number. When a zero-mean condition is used $b_i(i = 1, \ldots, n) = 1$, $l_{cstr} = 0$ and then parameters can be carried out by using method of adjustment.

43.3 Solution Procedure

43.3.1 Calculating Model and Method

As we know, the signal of BDS satellites include $2I_{B1}$, $7I_{B2}$ and $6I_{B3}$, so the $DCB_{C2I\text{-}C7I}$ and $DCB_{C2I\text{-}C6I}$ will be discussed essentially in this paper, and $DCB_{C6I\text{-}C7I}$ can be derived by $DCB_{C2I\text{-}C7I} - DCB_{C2I\text{-}C6I}$. The main steps can be divided into four parts: preprocessing of observation data, ionospheric correction, establishing equation and parameters calculation. The specific process is as follow (Fig. 43.1).

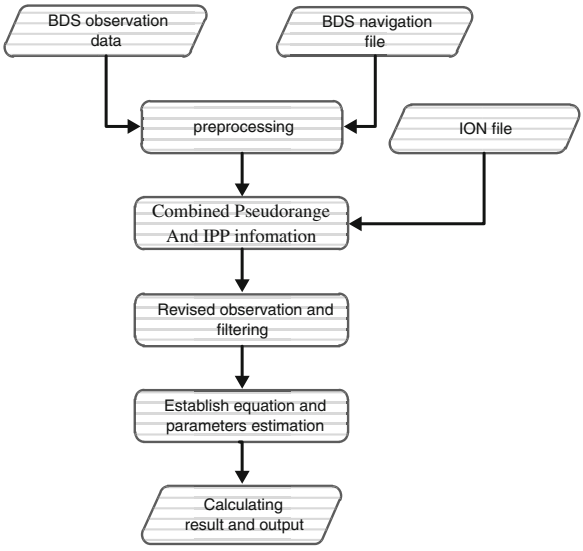

Fig. 43.1 Processing diagram of DCB parameters solving

Observation data received by iGMAS and MGEX tracking stations and GIM released by IGS must be prepared for program. Data preprocessing mainly carries on processing to the gross error, clock jump and cycle slip [10], and derive ionospheric pierce point information by using phase smoothing pseudorange; Then correct ionospheric delay according to the information; Finally establish equation and derive DCB parameters.

43.4 Exemplification

43.4.1 Validation of Strategy Based on GPS Data

Different GPS with a full constellation and tracking stations are faced with a wealth of restriction that make it is essential that the strategy in this pager must be demonstrated by using GPS data. The first test was performed in 286th day of 2014. 208 stations well-distributed globally were selected likewise the numbers IGS selected. Stations distribution is as shown in Fig. 43.2.

Using combined observation corrected by ionospheric solve GPS satellite $DCB_{C1P\text{-}C2W}$, and then the accuracy was compared with DCB products released by CODE. The bias are as follow (Fig. 43.3).

The strategy was approved by that the residual discrepancy is less than 0.1 ns. The mean residual is 6.25×10^{-5} ns. And the standard deviation is 0.085 ns. It can

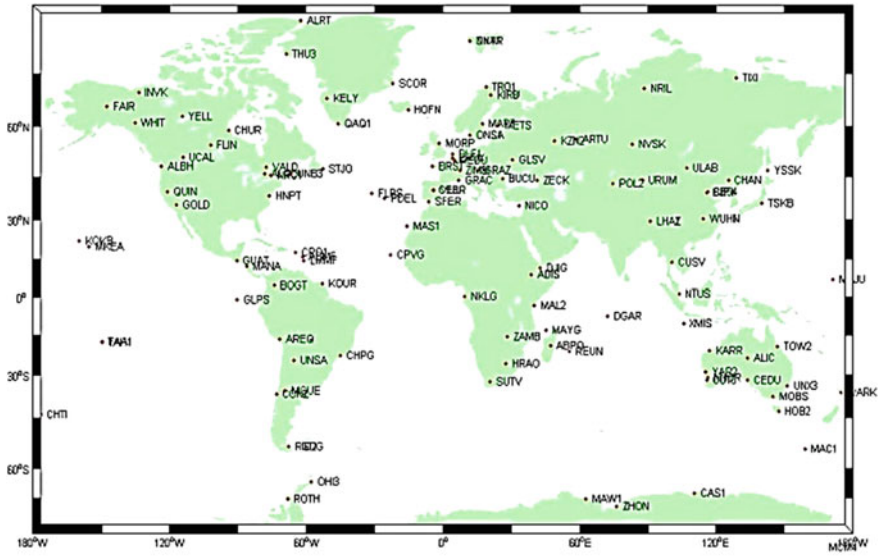

Fig. 43.2 IGS tracking station distribution

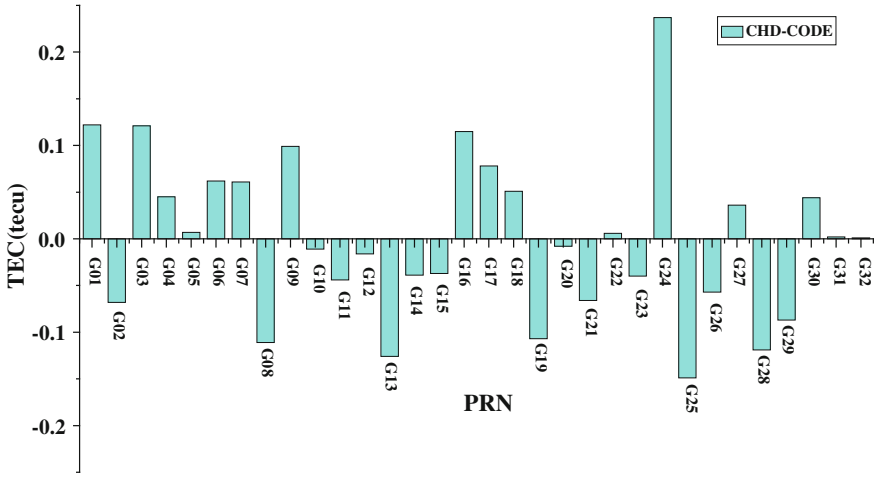

Fig. 43.3 Difference of GPS C1P-C2W DCBs determined in this study as compared to the monthly DCB products of CODC

be concluded that the method presented in this paper could assure the BDS satellites DCB products, especially in the font of that BDS satellites and tracking station does not realized the GPS level in some aspects.

43.4.2 DCB Results and Analysis Based on BDS Data

Due to the property of hardware, receivers who can track BDS signal are far more less than who can track GPS signal and all were established by iGMAS and MGEX. MGEX belong to IGS for dealing with GNSS navigation system, while iGMAS is established by Chinese government. In this paper, all receivers who can track BDS signal are statistic in the table as follow, including receiver observation types and numbers (Table 43.1).

Table 43.1 Receiver and observation types and numbers

Order	Type of receiver	Signal of BDS	Number
1	JAVAD TRE_G3TH DELTA	2I, 7I	16
2	SEPT ASTERX3	2I, 7I	1
3	SEPT POLARX4	2I, 7I	11
4	TRIMBLE NETR9	2I, 7I, 6I	34

43.4.2.1 DCB(C2I-C7I) of BDS Satellite

In this test, there are 80 stations are selected, including 62 MGEX stations and 18 iGMAS stations. Selection of BDS observation data is from 160th to 260th day in 2014. Using the method in this paper resolved 100 consecutive days $DCB_{C2I\text{-}C7I}$ of satellites and receivers. The results are as follows.

The BDS satellite $DCB_{C2I\text{-}C7I}$ shown in Fig. 43.4 is significantly smooth. The standard deviation index and classification according to constellation of results are show in Fig. 43.4 as well.

There are differences between constellations as shown in Fig. 43.4. The constellation of IGSO looks to be the best, and the maximum STD is 0.162 ns. The last is the constellation of GEO, the maximum value is 0.301 ns.

Analyzes for the reasons of results above are shown as follows:

(1) Affected directly by the equatorial anomaly, the precision of the ionosphere is poor, that also lead to the worse satellite DCB.
(2) As MEO is a full constellation, the data received less than 37 % [11], and the regional station can't track the signal round the clock so that the additional and valid observation data are limited correspondingly. The accuracy of MEO satellite DCB is affected as well.
(3) For IGSO constellation, not only tracking stations in service region could carry 24 h of continuous observation, but also the sites are well-distributed on both sides of the equator. This constellation is a kind of high efficiency of constellation [12]. Analyzing both from usage of data and distribution, the performance of IGSO is the best than two others constellation.

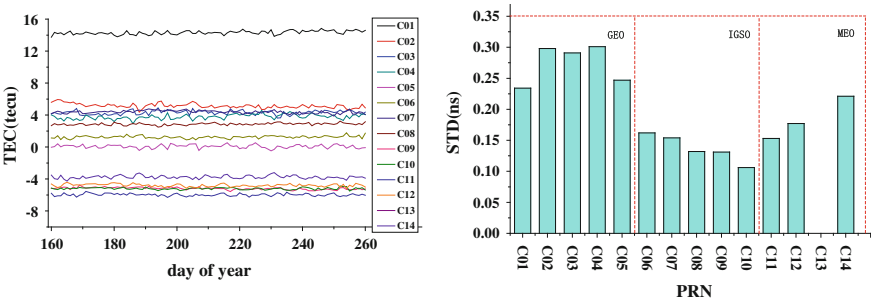

Fig. 43.4 Daily DCBs of BDS C2I-C7I estimated in this study and STD index of it from the 160th day to 260th day in year 2014

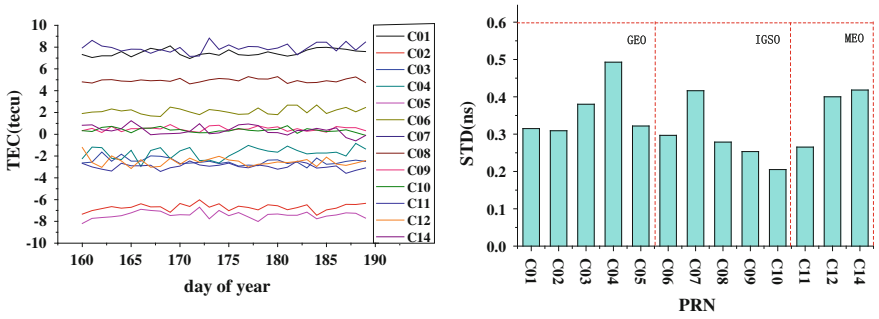

Fig. 43.5 Daily DCBs of BDS C2I-C6I estimated in this study and STD index of it from the 160th day to 189th day in year 2014

43.4.2.2 DCB(C2I-C6I) of BDS Satellite

In this test, selection of BDS observation data is from 160th to 189th day in 2014. Using the same method above, to resolve 30 consecutive days $DCB_{C2I\text{-}C6I}$ of satellite and receiver. The result is as follow (Fig. 43.5).

Besides C04, all of satellites STD index is within 0.5 ns, and the performance of IGSO is slightly better than the other two kinds of constellation. However, because of the quantity of observation of 6I signal, which there are only about 36, while that can receive 7I are 64, $DCB_{C2I\text{-}C6I}$ is not as better as $DCB_{C2I\text{-}C7I}$.

43.4.3 DCB(C2I-C7I) of BDS Receiver

DCB is the description of signal transmitted in signal generation and processing chain, it has a significantly relation with device itself. This paper choose the receiver from both domestic and foreign and derive its $DCB_{C2I\text{-}C7I}$, the results are as follow.

Range the results according to the ascending order as Fig. 43.6. It can be seen that the performance of foreign is mostly superior than that of domestic. In other words, domestic still has plenty of space to improve.

Since the directly relation between DCB and device, the same stations who use the same receiver Trimble-NETR9 are chose in next test for resolving $DCB_{C2I\text{-}C7I}$, the result is as follow (Fig. 43.7).

The average STD index of MGEX is 0.647 ns, the maximum is 1.717 ns, while the minimum is 0.211 ns. If dividing all the stations into two parts by 0.5 ns, the distribution is as follow.

As is shown in Fig. 43.8, the stations with poor precision are mostly distributed near equator, or in the back of sub-astral point of GEO or IGSO. In addition, there is a great difference between stations tracking BDS satellites signal. For example, stations in the back of GEO will never see GEO satellites, as well as IGSO. It is also

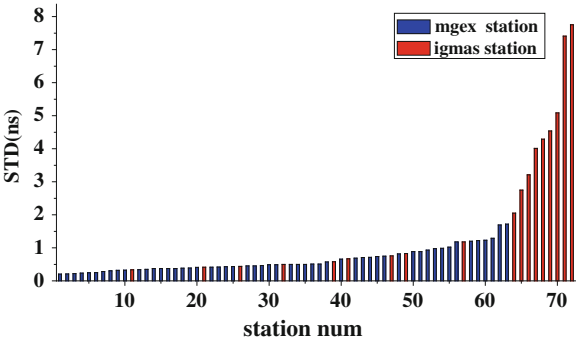

Fig. 43.6 STD of all site daily C2I-C7I DCBs estimated in this study from the 160th day to 260th day in year 2014

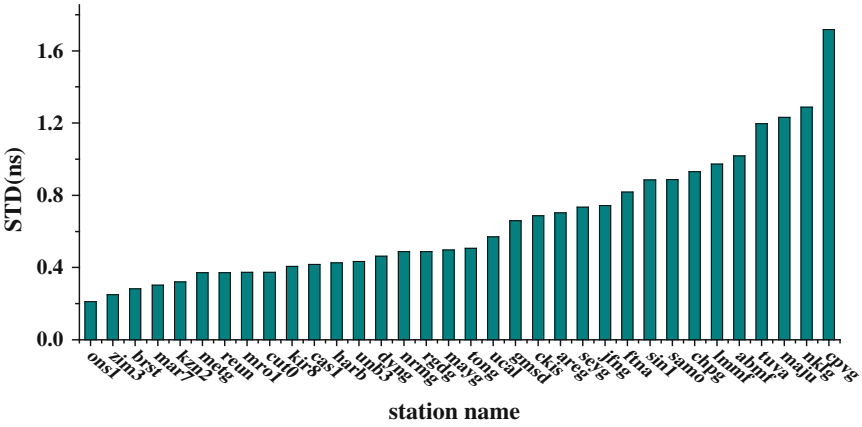

Fig. 43.7 STD of all site daily C2I-C7I DCBs, which used the same type of receiver, set into different position on earth

shown that stations located at the edge of land, such as CKIS, TONG, will have poor precision as well. That mainly account for the ionospheric accuracy affected by the station distribution.

Therefore, we can draw the following conclusions through the analysis above: when the tracking station located in the back of GEO or IGSO, the number of satellites who can be observed will be obviously reduced, and the accuracy will be affected directly. It is the same with the stations located at the edge of land or nearby equator. This may be highly influenced by the precision of GIM, which is consistent with accuracy of GEO satellite (For this paper is on high frequency DCB, the annual cycle of ionospheric effect by solar activity is neglected).

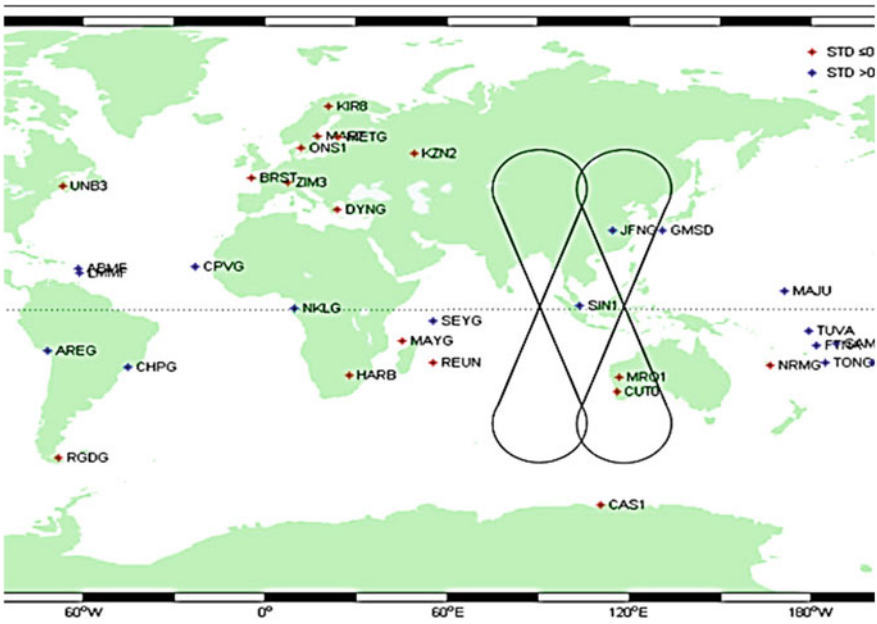

Fig. 43.8 The DCB STD distribution of MGEX station

43.5 Conclusion

A method base on MGEX/iGMAS observation data and GIM to provide highly frequency BDS satellite DCB products is present in this paper. Firstly, for determining the method, GPS satellite $DCB_{C1P\text{-}C2W}$ of were derived and compared with the product released by CODE. The STD index is 0.085 ns, which could obviously verify the accuracy and reliability of the method. Secondly, with the method, 100 consecutive days $DCB_{C2I\text{-}C7I}$ and 30 days $DCB_{C2I\text{-}C6I}$ of satellite were derived. The average STD index of $DCB_{C2I\text{-}C7I}$ and $DCB_{C2I\text{-}C6I}$ are 0.201 and 0.315 ns respectively. Among $DCB_{C2I\text{-}C7I}$, the IGSO satellite is 0.137 ns, the GEO satellite is 0.184 ns, the MEO satellite is 0.274 ns. It can be seen that the overall average accuracy of BDS satellite DCB resolved in this paper is within 0.3 ns. It also can be carried out that the accuracy of DCB will be affected by the constellation and station distribution. Furthermore, the comparison of receiver DCB shows that domestic receiver has larger space to promote.

Acknowledgments The data used for performance validation are downloaded from the Crustal Dynamics Data Information System (http://www.cddis.gsfc.nasa.gov), International GNSS Monitoring and Assessment System (GFZX0301040308), The project of National Natural Science Fund (41104019, 41104022 and 41304033), Project of Chinese Hydropower Engineering Consulting Group of science and technology (GW-KJ-2012-21), The authors would like to thank The open fundation of National Key Laboratory of Geographic Information Engineering (2013ADL-

DW0103),The open fund of Sate Key Laboratory of Geographic Information Engineering (SKLGIE 2013-Z-2-1) and Central University Research Funds (2014G1261051) for their support, and to the editor and anonymous referees for their valuable suggestions.

References

1. Yang Y (2010) Review on progress, contribution and challenges of Beidou satellite navigation system. Acta Geodaetica Cartogr Sin 39(1):1–6
2. Yang Y, Li J, Xu J et al (2011) Contribution of the compass satellite navigation system to global PNT users. Chin Sci Bull 56(26):2813–2819
3. Dai W, Jiao W, Jia X (2009) Application research for compass navigation satellite inter frequency bias correction terms. J Zhengzhou Inst Surv Mapp 26(5):367–369
4. Zhang HP, Shi C, Tang WM (2008) United solution to polynomial VTEC modeling and DCB analysis using ground-based GPS observations. Geo Inf Sci Wuhan Univ 33(8):805–809
5. Xiaolan W, Guanyi M (2014) Derivation of TEC and GPS hardware delay based on dual-frequency GPS observations. Chin J Space Sci 34(2):168–179 (in Chinese)
6. Li Z, Yuan Y, Li H, Ou J, Huo X (2012), Two-step method for the determination of the differential code biases of COMPASS satellites. J Geodesy 86(11):1059–1076
7. Nie W, Hu W, Pan S, Song Y (2014) Extract region ionosphere TEC using GPS dual-frequency data. Geo Inf Sci Wuhan Univ 39(9):1022–1027
8. Montenbruck O, Hauschild A, Steigenberger P (2014) Differential code bias estimation using multi-GNSS observations and global ionosphere maps. ION International Technical Meeting, San Diego
9. Fan JC, Wu XL, Li YX, Wei G (2013) COMPASS satellites DCB parameter accuracy assessment based on tri-frequency data. Chin Space Sci Tech 33(4):62–70
10. Li H, Huang G, Zhao M, Gong Y, Liu T (2012) Improvement of cycle slip detection in TurboEdit algorithm. J Time Freq 35(1):43–49
11. Xu Q (2001) Satellite constellation of local navigation system. Eng Surv Mapp 10(1):1–5
12. Liu G, Hao X, Chen X et al (2007) On constellation scheme of 2nd generation of China satellite navigation system for northward extending coverage range. J Geodesy Geodyn 27 (5):115–118

Chapter 44
BeiDou Satellite Navigation System (BDS) Real-Time Orbit Determination and Accuracy Analysis

Le Wang, Qin Zhang, Guanwen Huang, Rui Zhang and Xingyuan Yan

Abstract BeiDou Satellite Navigation System requires accurate real-time orbit products to support high precision real-time PNT services. Currently, BDS treats broadcast ephemeris as real-time orbits, whose precision is poor (at the level of meter). Based on characteristics of stations distribution and satellites constellations structure of BDS, this paper studies the method of real-time orbit determination, designs the corresponding calculative strategy, discusses and analyzes the accuracy and update rate of real-time orbits, draws the following conclusions: (1) when 6-h real-time orbits are extrapolated by 72-h observed orbits calculated by BDS regional network, the accuracy of GEO and IGSO/MEO satellite orbits is about 3 m and better than 2.5 m; while by 72-h observed orbits calculated by BDS global network, the accuracy of GEO and IGSO/MEO satellite orbits is better than 3 m and 30 cm respectively. (2) The accuracy of prediction orbits extrapolated by 24-h observed orbits calculated by BDS global network attenuates fast with the time period of the prediction increases. The average accuracy of 1-h prediction orbits of GEO and IGSO/MEO is better than 70 cm and about 40 cm, when the prediction duration is 6 h, the average accuracy of GEO and IGSO/MEO is about 120 and 60 cm respectively. Based on the current status and characteristics of BDS, using 3-day measured orbits to predict real-time orbits is the best strategy. With the improvement of stability and accuracy of the orbits calculated by single-day observational data, the high-frequency single-day prediction orbits with 1 h update rate are the better choice as real-time orbits.

Keywords BDS · Real-time orbit determination · Global · Regional · Time span

L. Wang (✉) · Q. Zhang (✉) · G. Huang · R. Zhang · X. Yan
College of Geology Engineering and Geomantic, Chang'an University, Xi'an, Shaanxi, China
e-mail: rexlele@163.com

Q. Zhang
e-mail: Zhangqinle@263.net.cn

G. Huang
National Key Laboratory of Geographic Information Engineering, Xi'an, China

J. Sun et al. (eds.), *China Satellite Navigation Conference (CSNC) 2015 Proceedings: Volume II*, Lecture Notes in Electrical Engineering 341,
DOI 10.1007/978-3-662-46635-3_44

44.1 Introduction

BeiDou Satellite Navigation System (BDS) plans to build a satellite constellation including 5 geostationary orbit satellites and 30 non-stationary orbit satellites, which will serve for global users around 2020 [1]. BeiDou Regional Satellite Navigation System began to provide services officially on December 27th, 2012. Currently, BDS has 14 satellites in orbit, including 5 Geostationary Orbit (GEO) satellites, 5 Inclined Geosynchronous Orbit (IGSO) satellites and 4 Medium Earth Orbit (MEO) satellites [2]. Its service area covers the entire Asia-Pacific region (Longitude 84°E–160°E, latitude 55°S–55°N). The ultimate goal of BeiDou Navigation Satellite System (BDS) is to provide high-quality navigation, positioning and timing services for users worldwide; precise satellite orbits are the foundation and key for navigation systems to provide services [3]. Presently, the Wide Area Augmentation Service has entered the practical stage. In order to meet high-precision real-time wide area augmentation services including Satellite Based Augmentation Systems (SBAS) and Ground Based Augmentation Systems (GBAS), the real-time orbit products of high update rate and high precision are needed.

Those days, the published real-time orbit of BDS is BeiDou broadcast ephemeris and the precision of that is unstable and poor. The accuracy of GEO satellites is about 10 m, IGSO/MEO satellites 3–5 m, which is far from satisfying the needs of real-time precision service users. For GPS, observed orbits of 40–45 h time span and global uniform distribution stations are more appropriate to extrapolate prediction orbits [4]. This paper designs three different orbit calculation schemes, compares and analyzes the prediction orbits accuracy of different time period; combines with the constellation structure and stations distribution of BeiDou Satellite Navigation System, analyzes the accuracy of the result and influence factors, chose 1-h prediction orbit as the real-time orbit, and proposes the proposal of BeiDou real-time orbits calculated strategy at this stage.

44.2 Mathematical Models

Currently, precise orbit determination techniques include dynamic orbit determination and kinematic orbit determination. Reasonable balancing information between geometry observations and dynamics by combining with dynamics and kinematic orbit determination will significantly improve the accuracy of satellite orbit determination [5]. The basic theory of satellite orbit determination is two-body problem [6]. In addition to two-body problem, satellites in orbit are also affected by several perturbation including conservative (non-spherical gravitational perturbation of the Earth, the Moon gravitational perturbations, gravitational perturbation sun, planets gravitational perturbation, the tidal perturbation, ocean tidal perturbation and perturbation of the Earth's rotation additional parameters, relativistic effects perturbation and so on.) and non-conservative forces (sunlight pressure perturbation, earthshine pressure perturbation, atmospheric drag and so on.) [7].

In addition to these perturbations of physical meanings, satellites in orbit need to take into account the experience perturbation, which can be defined as the perturbation force model error and not modeled perturbation [5].

Based on the above basic idea, the motion equation of satellites in orbit can be depicted as [8]:

$$\bar{a} = \bar{a}_{TB} + \bar{a}_{NS} + \bar{a}_{NB} + \bar{a}_{TD} + \bar{a}_{RL} + \bar{a}_{SR} + \bar{a}_{AL} + \bar{a}_{DG} + \bar{a}_{EM} \tag{44.1}$$

In the above equation, $\bar{a}_{\mathrm{TB}}$ is two-body problem force; $\bar{a}_{\mathrm{NS}}$ is non-spherical Earth gravitational; $\bar{a}_{\mathrm{NB}}$ is other planets' gravitational; $\bar{a}_{\mathrm{TD}}$ is Earth tides' gravitational; $\bar{a}_{\mathrm{RL}}$ is influence of relativistic effects on satellites; $\bar{a}_{\mathrm{SR}}$ is the satellite's pressure from solar radiation; $\bar{a}_{\mathrm{AL}}$ is the satellite's pressure from Earth's infrared radiation and reflection; $\bar{a}_{\mathrm{DG}}$ is resistance of the Earth's atmosphere; $\bar{a}_{\mathrm{EM}}$ is other empirical force.

Observational equations consisting of pseudorange and phase measurements are as follows [9]:

$$L_{i,k}^{p} = \rho_{k}^{p} + c \cdot dt_{k} - c \cdot dt^{p} - dion_{k,i,\emptyset}^{p} + \frac{c}{f_{i}} b_{i,k}^{p} + dtrop_{k}^{p} + dpath_{k,i,\emptyset}^{p} + \varepsilon_{k,i,\emptyset}^{p} \tag{44.2}$$

$$P_{i,k}^{p} = \rho_{k}^{p} + c \cdot dt_{k} - c \cdot dt^{p} + dion_{k,i,P}^{p} + dtrop_{k}^{p} + d\mathrm{path}_{k,i,P}^{p} + \varepsilon_{k,i,P}^{p} \tag{44.3}$$

In the above equations: $L_{i,k}^{p}$ are phase observations; $P_{i,k}^{p}$ are pseudorange observations; ρ_{k}^{p} is the distance between the station and satellite; b_{k}^{p} is ambiguity; *dtrop* is tropospheric delay; *dion* is the impact of the ionosphere; *d*path is multipath effect; ε is noise.

Brief orbit determination process is as follows: Firstly, get the initial orbits from the broadcast ephemeris and then integrating the equations; secondly, apply observations to correct errors and linearize observation equation; finally, establish normal equation, solve orbital parameters, and then get the corresponding orbit product.

Real-time orbits of navigation satellites are also called prediction orbits, which are mainly obtained by fitting the observed orbits, extrapolating observed orbits to obtain prediction orbits in the inertial frame and converting inertial coordinate system to Earth-fixed coordinate system. Specific mathematical models can refer to [8, 10].

44.3 BDS Real-Time Orbit Determination Methods

44.3.1 Data Source Description

Real-time orbit determination needs to use real-time or near real-time observational data, there are two formats of those data: real-time data streams and hourly or high frequency data files. Real-time data streams are decoded to obtain the observational

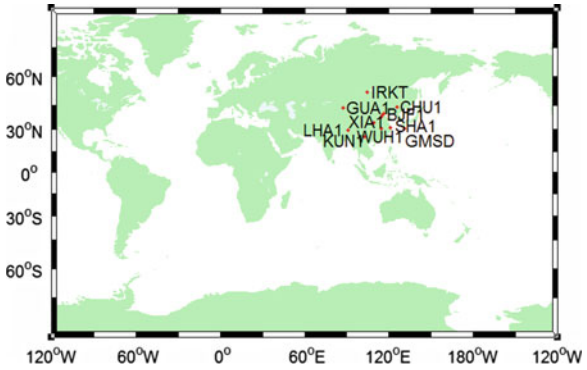

Fig. 44.1 The stations distribution of regional monitoring network

data, hourly or high frequency data files are read to obtain near real-time observational data. Real-time data streams are obtained from BeiDou Data Center of International GNSS Monitoring and Assessment Service (iGMAS); hourly or high frequency data files are obtained from BeiDou Data Center of iGMAS and Minneapolis Grain Exchange (MGEX) of CDDIS. In this paper, the data interface is real-time data streams and hourly or high frequency data files. When the data files existing delay, the data interface changes from hourly or high frequency data files to real-time data streams.

44.3.2 Requirement of Stations Number and Distribution

Currently, all stations of iGMAS and partly stations of MGEX provide multimode observation files containing BeiDou observational information. The examples of this paper firstly collect observational data from November 1st, 2014 to November 3rd, 2014, select 8 iGMAS stations and one MGEX station (GMSD) to compose Asian regional monitoring network (Fig. 44.1); select all iGMAS stations (excluding individual test stations) and 30 MGEX stations to compose global monitoring network (Fig. 44.2).

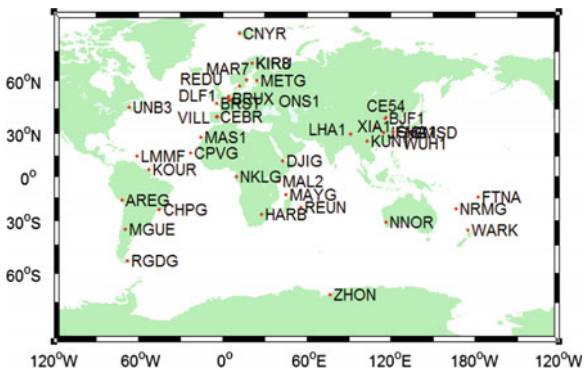

Fig. 44.2 The stations distribution of global monitoring network

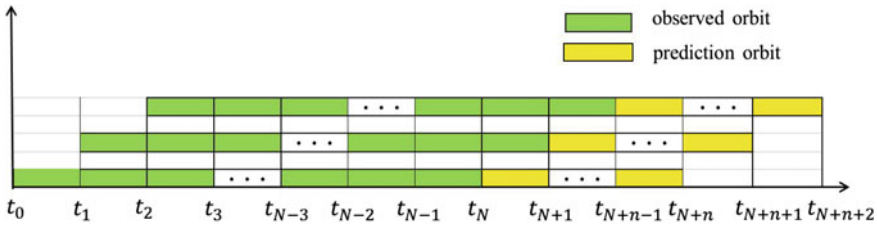

Fig. 44.3 The calculating method of sliding window

44.3.3 Calculation Process

In order to obtain a relatively smooth real-time satellite orbit product, this paper uses a sliding window method to calculate orbits [11]. Calculating method is as follows: using observations and table files of N hours before current time to calculate observed orbits, extrapolating n-hour prediction orbits by the observed orbits according to the models as real-time orbits. Calculation of data takes a sliding window method. Removing the observed data of the first arc segment after real-time orbits are calculated and adding the recent arc to process the next real-time orbits. Specific processes are shown in Fig. 44.3.

The calculation steps of BDS satellite precise real-time orbits determination are as follows: (1) obtain observational data; (2) observational data preprocessing, exclude gross errors and cycle slips; generate the initial orbit and orbit integration; (3) parameters estimation; (4) ambiguity fixing (optional); (5) residuals editor; (6) orbit integration; (7) orbit prediction. Detailed calculation process is shown in Fig. 44.4.

44.4 Results and Discussions

This paper designs the following three real-time orbit determination schemes:

Scheme 1: Select nine stations in Asian region from iGMAS and MGEX to establish BDS regional monitoring network (shown in Fig. 44.1 in Sect. 44.3). And calculate observed orbits applying 72-h observational data of BDS regional monitoring network and predict real-time orbits. (Prediction orbits are extrapolated by 72-h observed orbits calculated by BDS regional network.)

Scheme 2: Select 38 BeiDou monitoring stations from iGMAS and MGEX to establish BDS global monitoring network (shown in Fig. 44.2 in Sect. 44.3). And calculate observed orbits applying 72-h observational data of BDS global monitoring network and predict real-time orbits. (Prediction orbits are extrapolated by 72-h orbits calculated by BDS global network.)

Scheme 3: Select the same stations of Scheme 2, calculate observed orbits applying 24-h observational data of BDS global monitoring network and predict

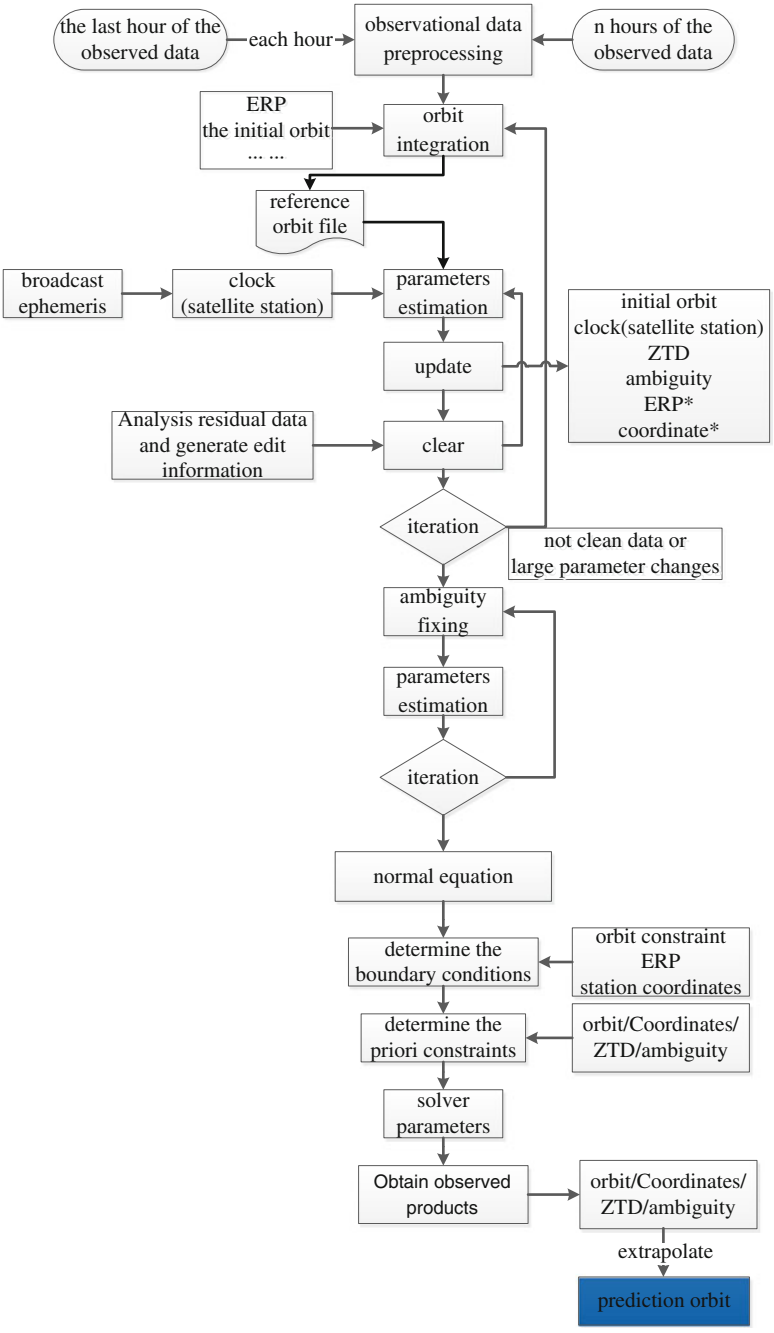

Fig. 44.4 The calculation process of real-time orbit determination

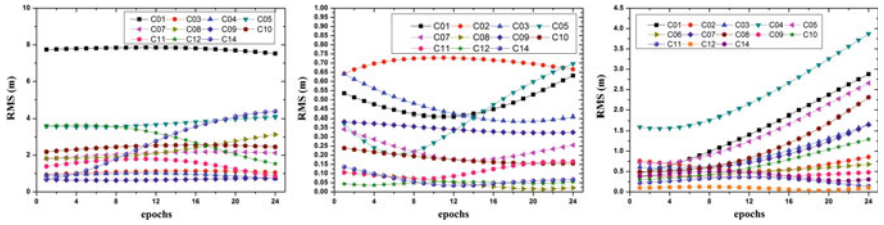

Fig. 44.5 The precision of 6-h prediction orbits of Scheme 1, 2 and 3

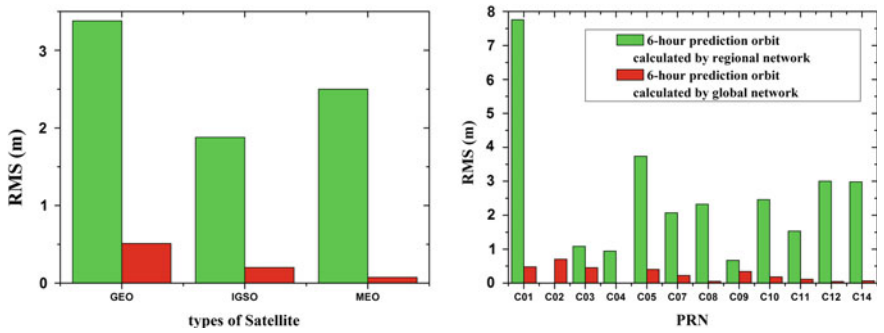

Fig. 44.6 The comparison of 6-h prediction orbits precision between Scheme 1 and 2

real-time orbits. (Prediction orbits are extrapolated by 24-h orbits calculated by BDS global network.)

This paper uses observational data from November 1st, 2014 to November 3rd, 2014, calculates BDS real-time orbits of three schemes, compares the results with BeiDou precise orbit products (gbm.sp3) calculated by Helmholtz-Centre Potsdam-German Research Centre for Geosciences (GFZ) and published by International GNSS Service (IGS), counts the precision of each BeiDou satellite every 15 min as shown in Fig. 44.5. Figure 44.6 shows the comparison of accuracy of 6-h prediction orbits between Scheme 1 and 2. Figure 44.7 shows the comparison of the average accuracy of 1 h prediction orbits and 6 h prediction orbits of Scheme 3.

As is shown of Fig. 44.5, the prediction orbits that are extrapolated by 72-h observational data of BDS global network are stable within 6 h of the prediction period, and the accuracy of which does not decrease significantly, due to that the amount of observational data of 3 days is large, and arcs of long time have a strong constrain for orbital model of integration, therefore the accuracy of prediction orbits decays slowly. Currently, the accuracy of BDS orbits is low and the section of the attenuation is not obvious. Compared Fig. 44.5, it reveals that the precision of prediction orbits extrapolated by single day observed orbits calculated by global network (Scheme 3) is significantly lower than which extrapolated by 3 days observed orbit calculated by global network (Scheme 2), and the precision of prediction orbits of Scheme 3 will obviously decrease over time. As is shown from

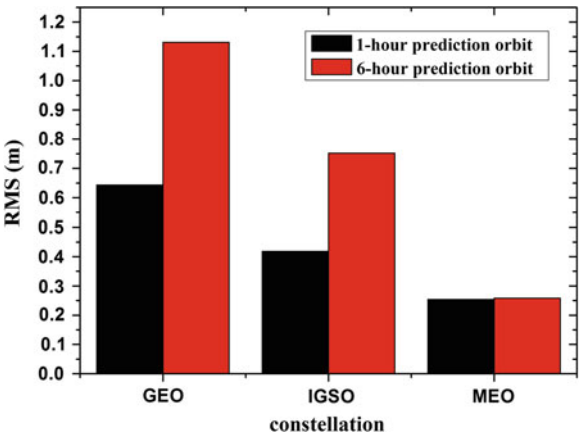

Fig. 44.7 The comparison of precision of prediction orbits with different time span of Scheme 3

the comparison of Fig. 44.6, the precision of prediction orbits extrapolated by 3 days observed orbits calculated by regional network (Scheme 1) is significantly lower than which by global network (Scheme 2). The reason is that the stations of Scheme 1 all distribute in Asia, having less continuous observation data, and regional stations distribution structure geometry is poor [12]. Based on these results above, BDS real-time orbit determination should choose the distribution structure of selected global network or regional encrypted network plus global network to improve the accuracy of real-time orbits.

The results of Fig. 44.7 shows the precision of 1-h prediction orbits of Scheme 3: GEO is 64 cm, IGSO is 42 cm, MEO is 25 cm, while the precision of 6-h prediction orbits of Scheme 3: GEO is 113 cm, IGSO is 75 cm, MEO is 26 cm, the precision reduced seriously along with the increase of prediction time. If the prediction orbits of the first hour are chosen as real-time orbits, the accuracy of real-time orbits of Scheme 3 is almost the same as that of Scheme 2. But there are great advantages of Scheme 3 using observational data of single day to Scheme 2 in terms of computation and timeliness.

In order to reveal the difference of prediction orbits between different constellations, the accuracy of 6-h prediction orbits extrapolated by single day observational orbits calculated by global network (Scheme 3) of GEO, IGSO and MEO was analyzed. Comparing the prediction orbits with BeiDou precise orbit products (gbm.sp3) calculated by GFZ, the accuracy of each BeiDou satellite was counted every 15 min as shown in Fig. 44.8.

As is shown in Fig. 44.8, the precision of prediction orbits of GEO and IGSO satellites induced quickly with the time period of prediction increases; the precision of prediction orbits of MEO is stable within 6 h. The mainly reason is that the stations receiving signal from MEO are too fewer to meet full coverage for MEO, as a result, the accuracy of MEO orbits precision is too low to reflect the relationship between accuracy and duration.

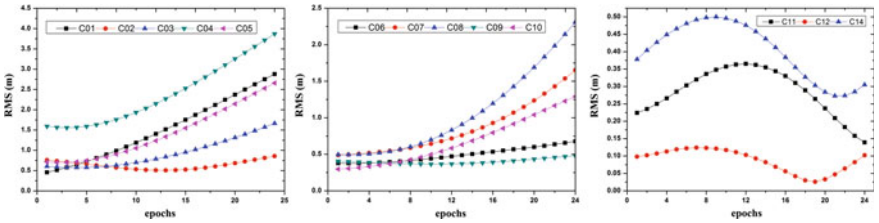

Fig. 44.8 The 6-h prediction orbits precision of GEO/IGSO/MEO

Table 44.1 BDS satellite real-time orbits average precision of long time

	RMS (m)			STD (m)		
	GEO	IGSO	MEO	GEO	IGSO	MEO
Scheme 1	3.04	1.46	2.28	0.15	0.20	0.30
Scheme 2	0.66	0.28	0.22	0.11	0.10	0.09
Scheme 3	1.22	0.78	0.32	0.32	0.10	0.11

In order to further verify the stability of real-time orbits of the three schemes in a long time, 28 segments of real-time orbits of the three schemes were calculated separately. RMS was obtained through comparing them with BeiDou precise orbit product (gbm.sp3) calculated by GFZ, STD also have statistical values. The accuracy of different schemes and constellations is shown in the following Table 44.1.

As presented in the above table, the accuracy of the current real-time orbits of GEO maintains at sub-meter level, IGSO/MEO about 30 cm, and long-time sequence is relatively stable.

Using the same stations and single day scheme to predict GPS orbits, the RMS is 0.29 m and the STD is 0.04 m. This precision is almost the same as Scheme 2.

44.5 Conclusions and Recommendations

Based on the observational data of BDS ground stations chosen from iGMAS and MGEX, this paper uses three schemes including 72-h data of regional network, 72-h data of global network and 24-h data of global network to calculate BDS real-time (prediction) orbit products. This paper compares and analyzes the result through three levels including the distribution of the stations, orbit fitting length and orbit prediction length. Results are summarized as follows:

(1) *The effect of the stations distribution* at the present stage, BDS uses global monitoring network to extrapolate 6 h prediction orbits, the precision of GEO is better than 70 cm, IGSO/MEO better than 30 cm, this results are better than using regional monitoring network significantly.

(2) *The effect of orbit fitting length* the accuracy of 6-h prediction orbits extrapolated by 72-h observed orbit calculated by global network is significantly higher than 6 h prediction orbits extrapolated by 24-h orbit calculated by global network.
(3) *The effect of orbit prediction length* the precision of prediction orbits extrapolated by single day observed orbit of GEO and IGSO satellites induced quickly with the length increase; with the few observational data, the precision of prediction orbits of MEO satellites is stable.

In summary, the proposal of researching BDS real-time orbit products at this stage is using the 72 h observed orbits calculated with data from the global network to extrapolate prediction orbits. If observational data of global network cannot be obtained, real-time orbits can be extrapolated by using observed orbits calculated by regional network with high update rate such as 1 h.

Acknowledgments Thanks for data support of iGMAS, MGEX, GFZ and IGS organizations. Thanks for the funding of National Natural Science Foundation of China (41104019, 41104022 and 41304033), Open Foundation of National Key Laboratory of Aerospace Dynamics (2013ADL-DW0103), Open Foundation of National Key Laboratory of Geographic Information Engineering (SKLGIE2013-Z-2-1), the construction, operation and maintenance of Analysis Center from the second generation navigation major subject, (GFZX0301040308) and Central University basic research funds (2014G1261051).

References

1. Yang Y (2011) Progress, contribution and challenges of compass/BeiDou satellite navigation system. Acta Geodaet Cartographica Sinaca 39(1):1–6
2. Yang Y, Li J, W Aibing et al (2014) Preliminary assessment of the navigation and positioning performance of BeiDou regional navigation satellite system. Sci China Earth Sci 44(1):72–81
3. Ge M, Liu J (1999) Real-time precise orbit determination for GPS satellite. J Wuhan Tech Univ Surv Mapp 24(1):32–35
4. Choi K et al (2013) Evaluation of GPS orbit prediction strategies for the IGS ultra-rapid products. GPS Solutions 17(3):403–412
5. Li M (2011) Research on multi-GNSS precise orbit determination theory and application. Wuhan University, Wuhan
6. Zhang Q, Li J et al (2005) GPS surveying principle and application. Science Press, Beijing
7. Liu L (2000) Orbit theory of spacecraft. National Defense Industry Press, Beijing
8. Li J (1995) Satellite precision orbit determination. Chin People's Liberation Army Publishing House, Beijing
9. Hofmann-Wellenhof B, Lichtenegger H, Wasle E (2009) GNSS—global navigation satellite systems GPS, GLONASS, galileo and more (trans: Cheng P, Cai Y, Wang J et al). Surveying and Mapping Press, Beijing
10. He S, Wu B, Chen J (2011) Orbit predictions for GPS satellites using IGS ephemeris. Ann Shanghai Obs Acad Sinica 32:25–34
11. Lou Y, Shi C, Ge M et al (2008) GPS real time orbit determination and initial results analysis. Geo Inf Sci Wuhan Univ 33(8):815–817
12. Shi C, Li M, Lou Y et al (2008) Near real-time orbit determination of navigation satellite using regional tracking network. Geo Inf Sci Wuhan Univ 33(7):697–700

Chapter 45
Periodic Oscillation Analysis of Gps Height Time Series Based on HHT

Xiaolei Wang, Qin Zhang, Lidu Zhao and Shuangcheng Zhang

Abstract This paper extracts the period of GPS elevation time series based on HHT algorithm. Firstly, the signal is decomposed by EMD. Taking the PBO fiducial stations, P061, P359, P059, P123, P067, P042 as the examples, the time series in elevation direction from 2008 to 2013 were decomposed into a finite number of intrinsic mode function, whose frequency was decreasing. Through the statistics, the result shows there are half of the month periodic oscillation graph, month periodic oscillation graph, double months periodic oscillation graph, annual periodic oscillation graph half of the annual periodic oscillation graph and annual periodic oscillation graph. Secondly, every component is transformed with Hilbert algorithm. Through the three-dimensional Hilbert spectrum in time-frequency energy space, the offshore stations' energy on the whole month and bi-monthly periodic oscillation is greater than the inland stations'. Finally, according to the different physical reasons to the elevation, this paper explores the causes of the different periodic oscillation.

Keywords Time series · Hilbert-Huang transform · Empirical mode decomposition · Hilbert spectrum

45.1 Introduction

High-precision time series of GPS site coordinate which consists of a sequence of high-precision position information, is come from the precise calculation of the site's continuous GPS observation. Through the analysis and study of the time series, we can obtain the information of period of GPS elevation, combining with the geographical environment, plate motion, earth oscillation cycle, etc. It is of great significance for geophysics. Zhang et al. [1] and Wang et al. [2] calculated

X. Wang · Q. Zhang (✉) · L. Zhao · S. Zhang
College of Geology Engineering and Geomantic, Chang'an University, Xi'an 710054, Shanxi, China
e-mail: chd_wxl@qq.com; zhangqinle@263.net.cn

J. Sun et al. (eds.), *China Satellite Navigation Conference (CSNC) 2015 Proceedings: Volume II*, Lecture Notes in Electrical Engineering 341,
DOI 10.1007/978-3-662-46635-3_45

non-tectonic crustal deformation caused by ocean tide loading, atmospheric mass loading, snow and soil moisture mass loading and non-tidal ocean mass loading and provided a reference for studying the crust tectonics movement in elevation direction. Fu et al. [3] analyzed the GPS time series in height component generated from continuously operating stations, which are globally distributed. Both annual and biannual vibrations of integrated expanding and contracting movement in the Earth were detected. Liu et al. [4] used the HHT method to decompose the time series of BJFS and BJSH in elevation of the GPS fiducial stations, and found the main components in time series of the both stations were a secular nonlinear trend, and semiannual signals. But corresponding relation between the elevation periodic signal and the physical reasons lack further study.

To dig the useful information contained in GPS time series, it need relevant methods for time series analysis. Hilbert-Huang transform (HHT) is a new technology for the analysis of the non-stationary signals, which consists of two successive parts, i.e., the empirical mode decomposition (EMD) and the Hilbert spectral analysis (HSA). Compared with wavelet method it is more straightforward, and not subject to the effects from the selection of certain wavelet function. It therefore can better extract and thus model the repeatability of the multipath errors, which is crucial in mitigating the errors [5]. For studying the phenomenon of oscillations of GPS elevation time sequences, this essay uses HHT method, power spectrum analysis and some common used analysis of time sequences, combining the geographical environment factor to discuss the physical reasons of causing the specific periodic oscillation.

45.2 EMD-HHT Algorithm

Spectrum analysis and EMD-HHT algorithm is the common analysis method in GPS time sequences. Whereby, Spectrum analysis method is aiming at analyzing the frequency domain of time sequences, which can extract the frequency and amplitude of time sequences and the IMF (IMF, Intrinsic Mode Function) components are decomposed by EMD method have distinct physical senses. The Hilbert spectra of all IMDs are grouped to get the Hilbert spectrum of the original signal. The Hilbert spectrum obtained by this way describes the non-stationary signal in the joint time-frequency-energy domain, and possesses high time-frequency resolution [5, 6]. Here is a brief introduction the EMD-HHT algorithm.

45.2.1 EMD Theory

EMD method can decompose the original signal into a finite number of intrinsic mode function (IMF), whose frequency is decreasing. An IMF is defined as a function that satisfies the following requirements: (1) In the whole data set, the

number of extrema and the number of zero-crossings must either be equal or differ at most by one. (2) At any point, the mean value of the envelope defined by the local maxima and the envelope defined by the local minima is zero.

The procedure of extracting an IMF is called sifting. The sifting process is as follows:

(1) Identify all the local extrema in the test data D(t). Connect all the local maxima by a cubic spline line as the upper envelope. Repeat the procedure for the local minima to produce the lower envelope. The upper and lower envelopes should cover all the data between them. Their mean is m1. The difference between the data and m1 is the first component $h_1(t)$;
(2) Ideally, h_1 should satisfy the definition of an IMF, since the construction of h_1 described above should have made it symmetric and having all maxima positive and all minima negative. After the first round of sifting, a crest may become a local maximum. New extrema generated in this way actually reveal the proper modes lost in the initial examination. In the subsequent sifting process, h_1 can only be treated as a proto IMF.
(3) In the next step, h_1 is treated as data: $h_1 - m_{11} = h_{11}$. After repeated sifting up to k times, h_1 becomes an IMF, that is: $h_1(k-1) - m_{1k} = h_{1k}$. Then, h_{1k} is designated as the first IMF component of the data: $c_1 = h_{1k}(t)$. Then C_2 and $C_3, \ldots, C_n$ can be got. The sifting process finally stops when the residue, becomes a monotonic function from which no more IMF can be extracted. From the above equations, we can induce that

$$D(t) = \sum_{i=1}^{n} C_i(t) + r_n(t) \tag{45.1}$$

r_n represent the trend of the signal; C_1 and $C_2, \ldots, C_n$ is the IMF which ordered from high to low frequency.

45.2.2 Hilbert Spectroscopy

The Hilbert transform of the signal IMF is given by:

$$H[C_i(t)] = \frac{1}{\pi} \int_{-\infty}^{\infty} A(\omega, t)dt \tag{45.2}$$

In the context of signal processing, the conjugate function interpretation of the Hilbert transform, discussed above, gives the analytic representation of a signal:

$$Z_i(t) = C_i(t) + jH[C_i(t)] = \alpha_i(t)e^{-i\varphi_i(t)} \tag{45.3}$$

For the narrowband model [above], the analytic representation is:

$$\alpha_i(t) = \sqrt{C_i(t) + H^2[C_i(t)]} \tag{45.4}$$

$$\varphi_i(t) = \arctan \frac{H[C_i(t)]}{C_i(t)} C_i(t) \tag{45.5}$$

Hilbert spectroscopy uses Hilbert transforms to analyze signals and get the time-frequency-energy domain. The meaning of Hilbert spectrum is to make amplitude represented as the function of instantaneous frequency and time, demonstrating that the amplitude changes with instantaneous frequency and time, showing the distribution of energy, especially revealing the energies (peak) corresponding instantaneous frequency and time; Moreover, it can make cycle analysis [5].

45.3 Analysis of Examples

45.3.1 Data Source

Choosing the PBO fiducial stations, the inland stations (P123, P042, P356) and the offshore stations (P067, P059, P061), as Fig. 45.1 shown. The time series in elevation from 2008 to 2013 are solved using the software GAMIT/GLOBK.

The Plate Boundary Observatory (PBO) is the geodetic component of EarthScope. PBO spans the North American continent, providing the detailed deformation data necessary to address a wide range of scientific goals at the forefront of tectonics and earthquake science. PBO provides stable data; regular construction and maintenance; wide scope of station distribution; high spatial resolution; new receiver devices, almost none replacement, avoiding the ladder mutations caused by devices replacement. P061, P356, P059 and P123, P067, P042 are respectively located in the North American coast and inland, which can compare the different appearance of coast and inland GPS stations in elevation.

At present, GAMIT/GLOBK is a widely-used baseline processing software of high precision, which has high accuracy, fast processing speed, high degree of automation. In the case of using precise ephemeris and high precise fixed initial point, the relative accuracy of resolving long baseline can reach about 10 mm, and the accuracy of resolving short baseline is better than 1 mm.

45.3.2 Physical Reasons

There are four main categories of the cause to the moving of GPS sites: the first is the variations of earth external gravitational field, including the solid Earth tides, pole tides and ocean tide loading; the second is the dynamic effect of the climate change, including the changes of atmospheric pressure, the surface non-tidal

Fig. 45.1 Stations map

variations, the thermal expansions of ground strata, the effects of wind, the variations of groundwater level; the third is the error of each models in GPS data processing; the sources of easy to cause large errors include the error of atmosphere models, the error of satellite orbits, the error of antenna phase center variation and multipath errors; the fourth is tectonic deformation, including plate motion, volcano, earthquake, postglacial rebound and fault movement. The former three categories affecting the vertical direction of the sites show the short cycle and long cycle effect. The short cycle, such as: a third day, half a day, a day, 2 weeks and so on; the long cycle, such as a month, 2 months, seasonality, half a year, a year, even a longer cycle. The latter one category often show the effect of change trend of vertical direction [1–3]. This essay mainly introduces that ocean tides and Earth tides affect the oscillations of elevation time sequences.

As we all know, ocean tides are under the lunisolar attraction, curst puts the elastic effect on the oceanic mass redistribution. The eight main tidal waves of ocean tides are semidiurnal tides or solar tides, so under the ideal observation state (observation uniformly distribution), single day resolving obtained by 24 h observation has averaged out the majority of semidiurnal tides or solar tides effects, the remaining are just the long cycle effects of the differences in tidal frequency and GPS satellite orbit frequency. Besides semidiurnal tides and solar tides, it also exist longer cycle tidal waves: (7.1 day), (9.2 day), (a half month), (1 month), (1 year, a half year), (many years), among which a half month, a month have a greatest influence of tidal waves

[7]. By the analysis above, concerning that: ocean tides influence the periodic oscillation of a whole month and bi-monthly in elevation direction.

Besides the above ocean tides, solid Earth tides can also result in the change of short and long cycles in the site vertical direction. Solid Earth tides are a visco-elastic deformation phenomenon that the solid earth produce, under the pressure of sun and the moon and other celestial tidal forces. Solid Earth tides include long period waves (half month waves, half year waves and anniversary waves), whole day waves, half day waves and third day waves; the largest amplitude is a half month wave [8]. In the following, the essay will make the further analysis of the various factors of the change of the elevation direction.

45.3.3 Example Results

Choosing the GPS fiducial stations, the inland stations (P123, P042, P356) and the offshore stations (P067, P059, P061), the time series in elevation direction from 2000 to 2006 are calculated as Fig. 45.2.

It can be seen from Fig. 45.2 that the original time series of every stations with amplitudes at about 20 cm, and the sequence is stable, less gross error and ladder mutations, guaranteeing for obtaining the correct EMD decomposition results in the next step.

Use EMD decomposition to obtain the intrinsic modal component with the time sequences, site P059 and P356 EMD result shown in Fig. 45.3a, b. Then, use

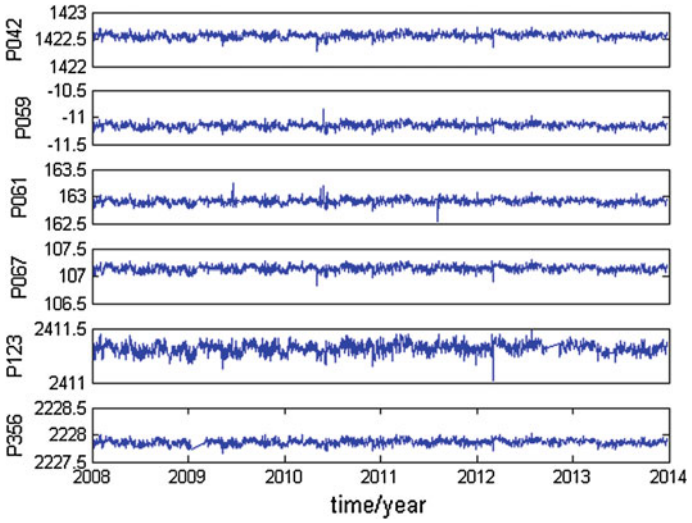

Fig. 45.2 Elevation original time series

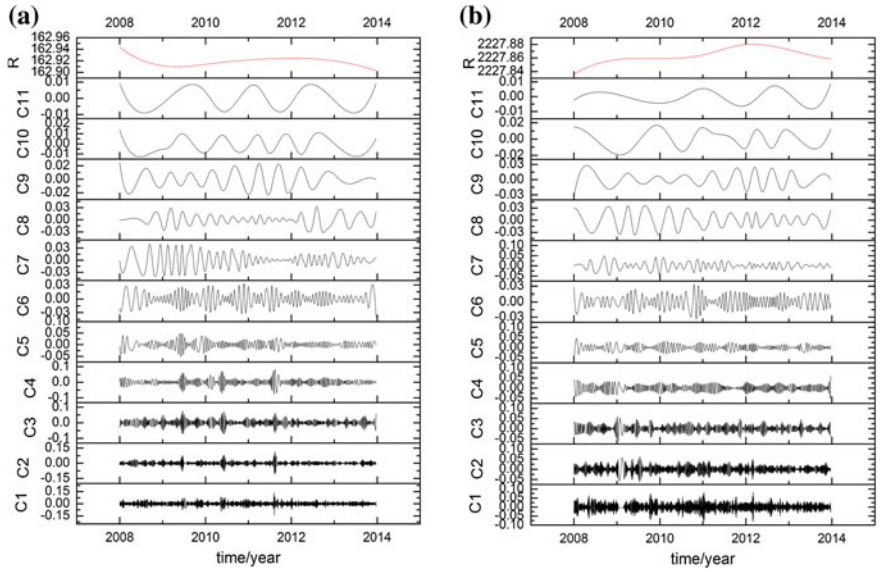

Fig. 45.3 P061 and P359 original series and IMF **a** P061 series and IMF **b** P359 series and IMF

original data of each site to make HTT spectrum analysis, detecting the original signal of high energy frequency habitat, as Fig. 45.4 show.

Figure 45.3 shows that elevation trend item of P061 was rising year by year, while trend item of P356 shows a downward trend. Offshore station P067 and P059 show the same trend as P061. Inland station P123 and P042 also shows the same downward trend as P356. This suggests that the offshore elevation may rise and the inland elevation subsidence year by year.

Figure 45.4. HHT spectrum shows the energy distribution. The greatest energy of offshore station P059 and P061 focuses in the monthly to bi-monthly cycle

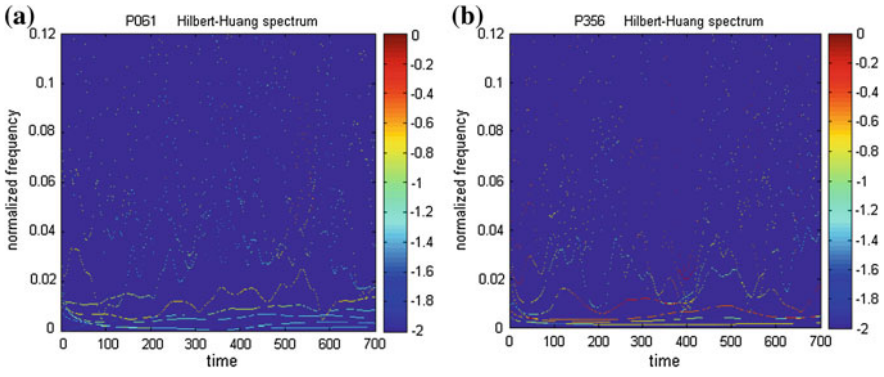

Fig. 45.4 HHT two-dimensional marginal spectrum **a** P061 HHT two-dimensional marginal spectrum **b** P356 HHT two-dimensional marginal spectrum

frequency (about 0.02), and the greater focuses in the semiannual cycle frequency (about 0.005). Offshore station P067 focuses the same energy in the semiannual cycle and the monthly to bi-monthly cycle. Inland station (P356, P123 and P042) shows the greater energy in semiannual cycle significantly. Inland and offshore stations all show the monthly to bi-monthly periodic oscillation. At the same time, the maximum energy of offshore station focuses in the monthly to bi-monthly cycle, and inland station focuses in the annual cycle. This suggests that the ocean tides make significant effect on offshore station in the monthly to bi-monthly periodic oscillation.

HHT method can only display energy on the frequency and can not analysis each IMF cycle information carefully. Therefore, Fourier spectrum analysis and statistics is done to each IMF (as Fig. 45.5 and Table 45.1 shown).

The Table 45.1 shows that GPS elevation time series of every stations with obvious semi-monthly, monthly, bi-monthly, semiannual, annual oscillatory motion. After analyzing Fig. 45.4. HHT two-dimensional marginal spectrum, the ocean tides making significant effect on offshore station in the monthly to bi-monthly periodic oscillation has been found. Table 45.1 corroborates this.

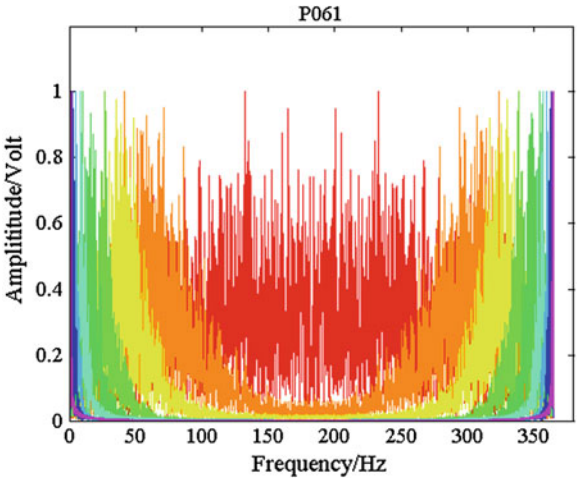

Fig. 45.5 IMF periodogram

Table 45.1 IMF periodic table

站名	半月 (天)	整月 (天)		2月 (天)	1季 (天)	半周年 (年)		周年 (年)	多年 (年)	
P059	13.61	52.51		70.63	146.29	0.49 年		0.94	1.6	2.24
P061	13.61	35.30	45.01	70.01	无	0.48	0.53	0.62	无	无
P067	13.61	19.25		69.40	91.02	0.49	0.53	1.10	1.6	2.24
P042	15.22	41.37		87.15	105.03	0.48		1.12	无	5.6
P123	13.61	22.88		70.67	120.41	0.49		1.02	1.6	无
P356	13.61	24.98	28.85	70.62	无	0.48		0.66	1.6	1.87

The hereinafter mainly analyzes the cause of semi-monthly, semiannual, annual oscillatory motion. To analyze semi-monthly and semiannual oscillation, through comparing the IMF of inland and offshore station in semi-monthly and semiannual cycle, this paper can explore the corresponding period of oscillation to different location. The paper will further contrast atmosphere pressure and the IMF of annual cycle to explore the influence of atmosphere pressure on time series of elevation.

Figure 45.6 shows semi-monthly oscillation of each station. Offshore station, P061, P058 and P067, has the average amplitude of 0.05, 0.045 and 0.025 respectively, greater than the amplitude of the inland station significantly. As is known to all, offshore station is affected more by the ocean tides than inland station, mainly due to semi-monthly cycle impact. In addition, Fig. 45.6 also shows that stations P061, P058, P067 have the annual oscillation but the inland station not. The ocean tide maybe makes apparent effect on offshore station in annual oscillation, but only play a small role in inland station.

Figure 45.7 shows that the maximum value of P123, P042, P356 and P067, P059, P061 on semiannual oscillatory motion is found in Apr–Jun and Dec–Jan with mean amplitude at about 0.016 m. After analyzing, the semiannual vibrations of integrated expanding and contracting movement in the Earth can be detected. Furthermore, the average amplitude of the inland stations (P123, P042, P356) with about 0.03, 0.04, 0.035 respectively, is bigger than the offshore stations (P067, P059, P061) with about 0.025, 0.025, 0.015. It may be that the ocean tide makes apparent effect on the offshore station making its show weaker amplitude in semiannual oscillatory motion than inland station.

Paper continues to study the physical reasons to the annual oscillation of the time series of elevation. It is known that atmosphere is the one cause for the seasonal vertical displacements of the Earth's crust. Under the effect of weather changing

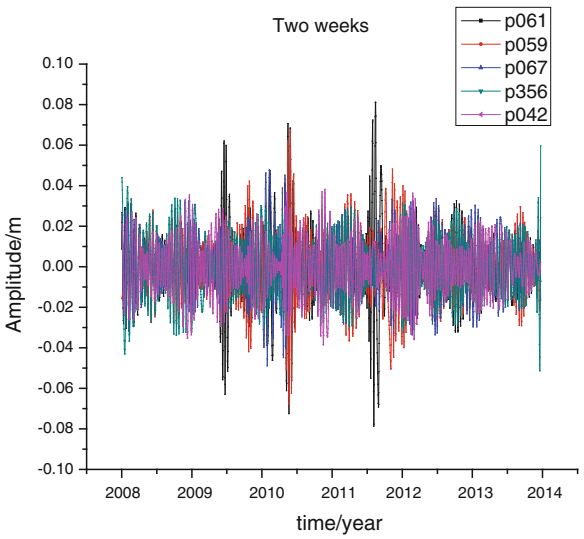

Fig. 45.6 Half of the month periodic oscillation graph

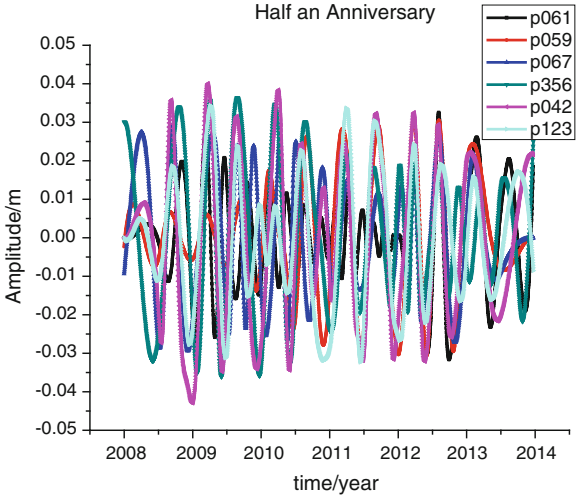

Fig. 45.7 Half of the annual periodic oscillation graph

and the Sun-Moon gravitation, atmospheric loading changes. Atmospheric loading effect includes the direct effect and indirect effect [9]. The deformation of station position is belong to the static deformation of elastic Earth.

In order to analyze the relationship between the pressure and the IMF of annual cycle, this pressure data of the station from the SOPAC (ftp://garner.ucsd.edu/archive/garner/met/) is acquired. The time resolution of MET pressure data is 5 min. Compare the pressure curve with the annual periodic oscillation curve, as shown in Fig. 45.8.

Figure 45.8 shows the inverse correlation between the IMF of annual cycle and the pressure. With the increasing of atmosphere pressure, elevation subsidence and with the decreasing of atmosphere pressure, the elevation uplifts. Slichter and

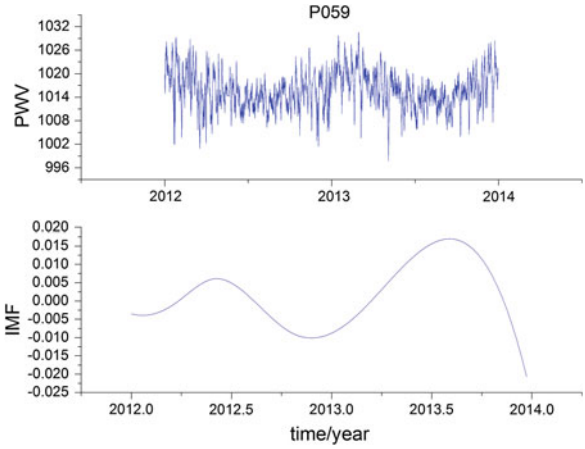

Fig. 45.8 The pressure curve and the anniversary of the oscillation curve comparison chart

Caputo (1960) studied the homogeneous elastic model of the earth crust, and they found that, when there were a migration of pressure rising with 50 hPa, the largest atmosphere displacement admittance is +0.195 mm/hPa. According to this theory, the elevation with negative changes in atmospheric pressure is reasonable.

According to the theory, when the pressure change with 30 hpa, the maximum displacement change should be 5 mm. But Fig. 45.8 shows the amplitude in 10 mm. This suggests that the atmospheric loading is not the only factor to the annual periodic. There are many other factors may cause annual cycle. The solid Earth tides, pole tides and ocean tide loading are all have annual tidal wave. The surface non-tidal variations and the variations of groundwater level can create an amplitude of station elevation in millimeter. The error of satellite orbits, the error of antenna phase center variation and multipath errors can also produce system error of annual oscillation.

45.4 Conclusion

This paper extracts the period of GPS elevation time series based on EMD-HHT algorithm, find the semi-monthly, monthly, bi-monthly, semiannual and annual periodic oscillation, analyzes the reasons of the physical combing with the Geography and climate factors, get the following conclusion:

1. In the semi-monthly oscillation of elevation time series, Offshore station and inland station all shows this oscillation. Amplitude of Offshore station is greater than the amplitude of the inland station significantly. It is can be due to the solid Earth tides and ocean tide loading.
2. In the monthly and bi-monthly oscillation of elevation time series, HHT spectrum shows the greatest energy of offshore station focuses in the monthly to bi-monthly cycle and inland station focuses in the semiannual cycle. It is can be due to the solid Earth tides and ocean tide loading.
3. In the semiannual and annual periodic oscillation of elevation time series, the semiannual vibrations of integrated expanding and contracting movement in the Earth and the semiannual tide can be detected, while the atmospheric loading is one of the physical cause of annual oscillation.

References

1. Zhang F et al (2002) Crustal vertical seasonal variation in China observed by GPS. Bull Surv Mapp 47(18):1370–1372
2. Wang M, Shen Z, Dong D (2005) Effects of tectonic crustal deformation on continuous GPS. 48 (5):1045–1052
3. Zhu W, Fuyang Y, Li Y (2003) Global elevation vibration and seasonal changes derived by the analysis of GPS height. Sci China (Series D) 33(5):470–471

4. Liu H, Wen H, Zhu G, Wang X (2013) Analysis of HHT in time series analysis for IGS fiducial stations. J Geodesy Geodyn 33(2):67–71
5. Shi C (2004) HHT transform and its application in structural analysis. Tongji University, China
6. Dai W et al (2006) EMD filter method and its application in GPS multipath. Acta Geodaetica et Cartographica Sinica 35(4):321–327
7. Yang D (2009) Tidal cyclical and its application in disaster prediction. Jilin University, China
8. Tian G et al (2005) Determination of long period gravity tide parameter at wuhan station. J Geodesy Geodyn 25(4):99–104
9. Luo S (2003) Study on the loading effects of the atmospheric pressure. Inst Geodesy Geophys

Chapter 46
Analysis of Ionosphere Modeling Accuracy Based on Multi-GNSS Data

Yongxing Zhu, Xiaolin Jia, Laiping Feng and Rengui Ruan

Abstract Satellite navigation has stepped into the era of multi-GNSS and multi-frequencies; it has brought new opportunities for ionosphere modeling. This paper studied the methods and principles of ionosphere modeling based on multi-GNSS, meanwhile developed the corresponding software. Experiments of ionosphere modeling, using 15 degree and 15 order spherical harmonics model, were carried out based on multi-GNSS observation data from day 210 to 216 at 2013. The results show that: the residual of the global ionosphere modeling is less than 3 TECU; the difference of STD is about 4 TECU, compared with the CODE's final product; the stability of DCB product is better than 0.4 ns for satellite, 0.8 ns for receiver.

Keywords Ionosphere modelling · Spherical harmonic model · Trigonometric model · Polynomial model · Accuracy analysis

46.1 Introduction

Ionosphere has great influence with human lives, the change of ionosphere also have a significant impact on weather forecasting, telecommunications, navigation, aviation, aerospace and so on. The temporal distribution and space variation of the ionosphere is mainly influenced by the earth movement, solar activity, geomagnetic field changes. Observation and prediction of ionosphere total electron content (TEC) has become an import topic [1–5]. In 1998 the IGS decided to offer ionosphere services for they realize that GPS is the important technical means to monitor ionosphere activity [6]. And now, the international GNSS Monitoring and

Y. Zhu (✉) · X. Jia · L. Feng
State Key Laboratory of Geo-Information Engineering, 710054 Xi'an, China
e-mail: chxyzyx_2008@126.com

R. Ruan
Xi'an Research Institute of Surveying and Mapping, 710054 Xi'an, China

J. Sun et al. (eds.), *China Satellite Navigation Conference (CSNC) 2015 Proceedings: Volume II*, Lecture Notes in Electrical Engineering 341,
DOI 10.1007/978-3-662-46635-3_46

Assessment System (IGMAS), which is led by Chinese, began to provide global ionosphere grid products.

Currently, there are lots of results about ionosphere modelling based on GPS (or GPS&GLONASS) observations data. In foreign countries, some units completed the construction of global ionosphere grid model (GIM) and afterwards to the IGS. The units contains the European Centre for Orbit Determination (CODE), Energy Mines and Resources Canada Centre (EMR), the Jet Propulsion Laboratory (JPL), the European Space Agency (ESA) and the University of Valencia, Spain Qahtani (UPC) [7–10]. In China, Institute of Geodesy and Geophysics, Wuhan University, Shanghai Astronomical Observatory and other units also complete ionosphere modelling and carried out fruitful results [2, 11, 12]. Among them, the ionosphere products offer by CODE is widely used by International GNSS user, because of high accuracy (2 $\sim$ 9 TECU), informative and complete studied [13, 14]. Nevertheless the precision of ionosphere provided by IGS is still limited in our country due to fewer domestic distribution, the uniform of ionosphere data and spatial distribution.

Beidou Navigation Satellite System (BDS) is the independent development global satellite navigation system of China, provided the position/velocity/time (PVT) services in Asia Pacific area by the end of 2012 and plan to cover the whole world in 2020 [15, 16]. BDS is the first system provide a complete three frequency observation data, users can take advantage of the rich observational information, conducting research about ionosphere modelling in the service region. On the one hand, a large number of domestic distribution BDS tracking station can provide ionosphere higher resolution, on the other hand, multi-frequency data fusion modelling can make full use of multi-frequency observations, increase extraction accuracy of ionosphere delay observation, by reasonable determine the weights. Based on this, this paper study the principles and methods of ionosphere modelling used by Multi-GNSS integration data, and independently developed the solver software, and then analysis the accuracy of the model.

46.2 Basic Principles and Methods

The multi-GNSS ionosphere modelling principles and data flow are as follow shown (Fig. 46.1).

Ionosphere Observations The accuracy of carrier phase measurement is two orders of magnitude than pseudo-range, but the carrier phase measurements affected by the integer ambiguity, and pseudo-range observations poor accuracy, so Ionosphere delay observations acquisition mainly carrier phase smoothing pseudorange.

Ionosphere Delay Extraction Because the refractive correction arising from ionosphere is square inversely proportional to the frequency, if the order terms effect of the ionosphere can be ignored, we can get ionization oblique path layer delay, frequency offset between the satellite and the receiver frequency deviation from the combination of dual-frequency pseudo-range data. The equation are as follow:

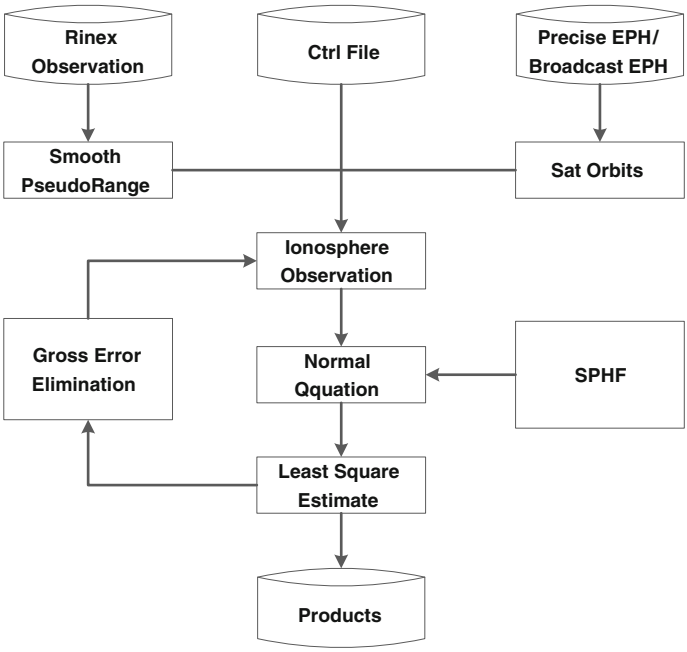

Fig. 46.1 The diagrams of basic principles and data flow

$$STEC + B_j + b^s + \varepsilon = \frac{f_1^2 f_2^2}{40.28(f_1^2 - f_2^2) \times 1.0\text{e}16}(\tilde{P}_2 - \tilde{P}_1) = \alpha_1(\tilde{P}_2 - \tilde{P}_1) \quad (46.1)$$

Among them, *STEC* are the puncture point oblique path of electronic content. B_j and b^s are the frequency deviation between the receiver and the satellite. ε are the combinations of multipath error and random noise combinations from the two frequency smoothed pseudo-range observables.

Projection Function In order to achieve the ionosphere modeling, we need to covert the slant total electron content (STEC) to the vertical total electron content (VTEC) using projection function. The commonly ionosphere projection functions are: Klobuchar proposed a projection function for ionosphere model for GPS broadcast ephemeris. Clynch proposed a projection function using the least squares fitting method for the Q factor. Ouji-kun proposed a segment projection function can fit the changes of the elevation angle. Schaer proposed the projection function that can amendments the single model MSLM and so on. Generally when the observation angle is greater than the height of 15–20°, the effect of various types of projection function is similar. This article selects the correction monolayer model projection function MSLM.

Ionosphere Modeling Usually we introduced single model to replace the entire ionosphere when study the ionization layer which assumes that all the free electrons are concentrated on an infinitely thin spherical layer at a height H. Scholars

proposed many ionosphere model based on GPS observations, including global models and regional models. The most basic and most important region ionosphere model is the polynomial model (POLY) the trigonometric model (GTSF) [17–19]. And the most important global model is the spherical harmonic model (SPHF).

Normal Equation Construction and Observation Weighting In order to reduces the computer resources and computing time for the multiplied of zero elements in the sparse matrix. The algorithm just consider the multiplication law only non-zero elements of the equation and use the methods of normal equation splice, building the equation in each epoch, and get the final normal equation. For observation weighting, assumed that the accuracy of the smooth pseudorange was fairly basic, for the same frequency combination of using elevation weighting; for different frequency combination data, using the coefficient value α_i of formula (46.1), set the weighting as μ_0^2/α_i^2, while μ_0 is the GPS $\tilde{P}_1\tilde{P}_2$ combination coefficient value $\alpha_{gpsp1p2}$.

Parameter Estimation The parameters include ionosphere model parameters and DCB parameters, mainly using the least squares method. In solving process using different frequency combinations to build normal equation, eliminate DCB parameters, getting the final normal equation, solving Ionosphere model parameters, then back on behalf solving the DCB parameters for different frequency combinations. Separation of the satellite and the receiver DCB, under the condition of the sum of all satellites DCB value is 0 (zero constraints) or set the DCB value of one satellite as 0.

46.3 Experiment and Analysis

In order to verify the accuracy of multi-GNSS ionosphere modeling, we chose 7 days of IGS data from day 210–216 in 2013 and partially MGEX station data for testing. Among them, the observation data of GPS and GLONASS is basically 250 station, the same as CODE. BDS observational data is from the cut0, dlf1, gmsd, jfng, mar7, reun and zim3 station in the MGEX system.

The ionosphere solving strategies: extract the ionosphere observations from the phase smoothed pseudorange, calculate the satellite coordinates from the broadcast ephemeris and the station coordinates previously obtained from Sinex file of IGS weekly products. Data sampling rate is 120 s, using the 15 degree and 15 order spherical harmonic models, solving a set of ionosphere coefficients each 2 h and 13 groups 1 day. Solving a set of DCB parameter each day. The combination data is the C1P2 and P1P2 for GPS, C1P2 and P1P2 for GLONASS and B1B2 and B1B3 for BDS. In the solving process the first step is to eliminate the DCB parameters then solving the DCB parameters for station and satellite for all combination. Among them, set the DCB value of first satellite of every combination observation as zero, when the satellite and the station DCB separated.

46.3.1 Ionosphere Accuracy

In order to evaluate the fitting accuracy of ionosphere modeling, this paper statistic the variance of difference (residual) at the puncture site between the model and observed values in seven consecutive days. The variance were 2.63 TECU, 2.93 TECU, 2.92 TECU, 2.94 TECU, 3.06 TECU, 2.76 TECU and 2.85 TECU, shown as follows (Fig. 46.2).

In order to further evaluate the outer ionosphere modeling accuracy, calculate 5°* 2.5° grid model values (VTEC) using the 212 and 213 two days data then statistics standard difference between the model and CODE final product. And the results are in the following figure (Fig. 46.3).

The above analysis shows:

(1) Ionosphere modeling residual is almost the same with measurement of the ionosphere delay observed quantity, the residual variance is less than 3 TECU;
(2) Compared with the final product provided by CODE, this paper implemented the ionosphere model product compared with the CODE final product, the variance of the residuals is about 4 TECU, with the same accuracy of the CODE final product accuracy.

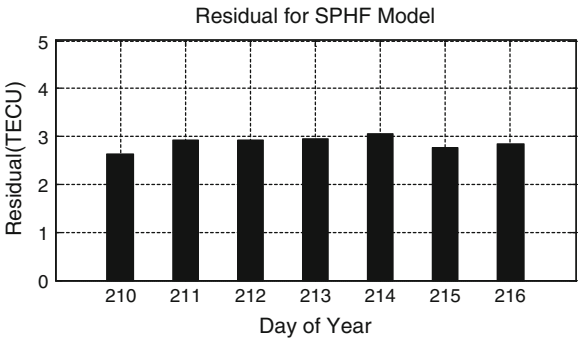

Fig. 46.2 Modeling residual using spherical harmonic model

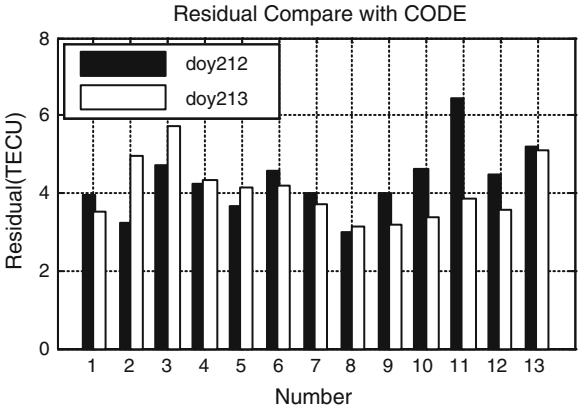

Fig. 46.3 Difference compared with CODE final product

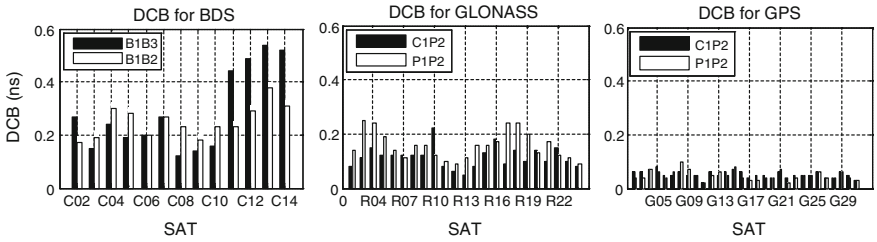

Fig. 46.4 DCB accuracy of satellites

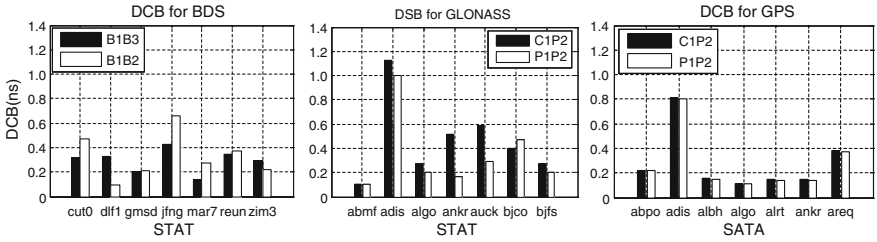

Fig. 46.5 DCB accuracy of stations

46.3.2 The Accuracy of DCB Parameters

The DCB is one of the main error sources of affecting the PVT services for users, and affecting the accuracy of ionosphere modeling. Numerous studies show that: the DCB parameters of satellites and receivers have stability and over time unchanged [7, 20]. The DCB values is not influenced by constraint conditions when separate the satellite and receiver [21]. In this paper, by constraint the DCB values of first satellite as zero to separate the DCB value of satellite and receiver. The daily accuracy of DCB is statistic as follows:

$$\text{accuracy} = \frac{\sum_{j=1}^{7}(x_j - \bar{X}_i)}{7}(i = 1, 2\ldots, N) \tag{46.2}$$

Among them, $\bar{X}_i$ is the i satellite or receiver mean DCB value of seven days. x_j is the i satellite or receiver DCB value at j day. N is the number of satellite or receivers involved in solving. In the paper, we counted the accuracy for all satellites and only seven stations in the order. Statistical results shown as follow (Figs. 46.4 and 46.5).

The analysis shows that:

(1) The accuracy of satellite DCB value for BDS's B1B2 combination and B1B3 combination are better than 0.4 ns, excepted the MEO is better than 0.8 ns, because MEO satellite observation less than other satellites. While the

accuracy of receiver DCB value for BDS's B1B2 combination and B1B3 combination are better than that 0.8 ns;

(2) The accuracy of satellite DCB value for GLONASS's C1P2 combination and P1P2 combination are better than 0.3 ns. While the accuracy of receiver DCB value for GLONASS's C1P2 combination and P1P2 combination are better than that 0.6 ns, except the adis station is better than 1.2 ns;

(3) The accuracy of satellite DCB value for GPS's C1P2 combination and P1P2 combination are better than 0.2 ns. While the accuracy of receiver DCB value for GPS's C1P2 combination and P1P2 combination are better than that 0.4 ns, except the adis station is better than 0.8 ns.

46.4 Conclusions

This paper studies the multi-GNSS ionosphere modeling theory and method, developed the ionosphere modeling software. Using seven continuous days' observation data, within the 210–216 day in 2013, test the ionosphere modeling accuracy. The results show that: the global ionosphere model residual is less than 3 TECU. The difference is about 4 TECU by comparing with the CODE final product. The precision of DCB value, better than 0.4 ns for satellites, better than 0.8 ns for receiver, the BDS calculation results of slightly less. This paper implements the integration of multi-GNSS and multi-frequency observation for ionosphere modeling, On the one hand, a large number of domestic distribution can provide ionosphere higher resolution, on the other hand, multi-frequency data fusion modelling can make full use of multi-frequency observations, increase extraction accuracy of ionosphere delay observation, by reasonable determine the weights.

Acknowledgments This study is supported by the National Natural Science Foundation of China (Grant No. 41204020; Grant No. 41074020).

References

1. Cai C, Gao J, Li Z (2006) Monitoring seasonal variations of ionospheric TEC using GPS measurements . Geomatics Inf Sci Wuhan Univ 31(5):451–453
2. Meng X, Gao Y (2004) Electric systems analysis. Higher Education Press, Beijing, pp 3–21
3. Yuan Y (2002) Study on theories and methods of correcting ionospheric delay and monitoring ionosphere based on GPS. Institute of Geodesy and Geophysics of the Chinese Academy of Sciences, Wuhan
4. Meng Y, An J et al (2011) Spatial distribution of antarctic ionosphere TEC based on GPS. Acta Geodaetica Cartogr Sin 40(1):37–40
5. Bhuyan PK, Borah RR (2007) TEC derived from GPS network in India and comparison with the IRI. Adv Space Res 39(5):830–840

6. Zhang X, Ren X et al (2014) Short-term TEC prediction of ionosphere based on ARIMA model. Acta Geodaetica Cartogr Sin 02:118–124
7. Li Z, Chen K, Liu et al (2007) Mathematical unification and method expansion of GNSS ionospheric delay model. Geomatics Inf Sci Wuhan Univ 08:699–703
8. Zhang H, Shi C et al (2008) United solution to polynomial VTEC modeling and DCB analysis using ground-based GPS observations. Geomatics Inf Sci Wuhan Univ 08:805–809
9. Schaer S (1999) Mapping and predicting the earth's ionosphere using the global positioning system. The University of Bern, Bern
10. Sardon E, Zarraoa N (1994) Estimation of the transmitter and receiver differential biases and the ionospheric total electron content from Global Positioning System observations. Radio Sci 29:577–586
11. Mannucci AJ, Wilson BD, Yuan DN et al (1998) A global mapping technique for GPS-derived ionospheric total electron content measurements. Radio Sci 33(3):565–582
12. Zhang H (2006) Study on GPS based China regional ionosphere monitoring and ionosphere delay correction. Shanghai Astronomical Observatory Chinese Academy of Sciences, Shanghai
13. Wan W, Ning B et al (2007) Nowcasting the ionospheric total electron content over China. Prog Geophys 04:1040–1045
14. Feltens J, Schaer S (1998) IGS products for the ionosphere. In: The IGS analysis centers workshop ES-OC
15. Feltens J (1999) IGS products for the ionosphere-one year of ionosphere working group activities. In: The IGS Analysis Center Workshop
16. Yang Y (2010) Review on progress, contribution and challenges of beidou satellite navigation system. Acta Geodaetica Cartogr Sin 39(1):1–6
17. Yang Y, Li J et al (2011) Contribution of the compass satellite navigation system to global PNT users. Chinese Sci Bull 56(21):1734–1740
18. Georgiadiou Y, Kleusberg A (1998) On the effects ionospheric delay on geodetic relative GPS positioning. Manuscripta Geodaetica 13(1):1–8
19. Georgiadiou Y (1994) Modeling the ionosphere for an active control network of GPS stations. Delft Geodetic Computing Centre, Delft
20. Yuan YB, OU JK (2004) A generalized trigonometric series function model for determining ionospheric delay. Prog Nat Sci 14(11):1010–1014
21. Yuan Y, Ou J (1999) The effects of Instrumental Bias in GPS observations on determining ionospheric delays and the methods of its calibration. Acta Geodaetica Cartogr Sin 02:19–23

Chapter 47
Precision Assessment of Broadcast Ionospheric Model of GNSS Based on Real Data of Base Station

Na Cheng, Xiao-lin Jia and Da-wei Sun

Abstract This paper proposes one method for precision assessment of broadcast ionospheric model of GNSS, performing by using real ionosperic delay as a reference based on base stations. It can decide the amount of ionospheric delay by base stations spread all over the world precisely, then statistic the precision of broadcast ionospheric model of GNSS station by station. As shown in results: the correction percent of broadcast ionospheric model of BDS/GPS/GAL normally is 60 % above, and the RMS is better than 2.0 m. In addition to, the correction percent of BDS is higher than GPS and Galileo, better than 75 % in China.

Keywords GNSS · Broadcast ionospheric model · Base station · Real ionospheric delay

47.1 Introduction

The ionospheric delay error affects the propagation of GNSS electromagnetic signals and it can't be ignored in navigating and positioning. For dual-frequency receivers, it can be effectively weakened by combining measurements; but for single-frequency receivers, we need to correct the error by using high-precision GNSS ionospheric model, which can decrease the influence of ionosphere delay [1–3].

Currently, the single-frequency users correct the delay error by receiving the broadcast ionospheric model parameters send by navigation system servers. GPS uses KLOBUCHAR 8-parameter ionospheric model as a global broadcast ionospheric delay correction model, the model parameters are updated [4] every day;

N. Cheng (✉) · D. Sun
School of Geology Engineering and Surveying, Chang'an University, Xi'an, Shanxi, China
e-mail: chn_chd@163.com

X. Jia
Xian Research Institute of Surveying and Mapping, Xi'an, Shanxi, China

J. Sun et al. (eds.), *China Satellite Navigation Conference (CSNC) 2015 Proceedings: Volume II*, Lecture Notes in Electrical Engineering 341,
DOI 10.1007/978-3-662-46635-3_47

being similar to GPS, BDS uses an improved KLOBUCHAR 8-parameter model as the regional ionospheric model, and updates every 2 h [5–7]; Galileo navigation system uses NeQuick model as a global broadcast ionospheric correction model, and send ionospheric correction coefficients to the users daily [8–10]; GLONASS does not broadcast any ionospheric correction parameters.

With the beginning of BDS providing formal operation services and the development of Galileo, the four satellite navigation systems have been activating in the field of satellite navigation of the world. China launched an international GNSS monitoring and assessment system (IGMAS). We can access the performance of one GNSS system precisely by tracking and monitoring the GNSS, and provide useful references and suggestions for worldwide users. The monitoring and assessment of broadcast ionospheric model is an important task of iGMAS, therefore, choosing a higher precision and a more reliable assessment benchmark and appropriate assessment method is particularly important. At present, the main method of assessing the precision of broadcast ionospheric model is using high precision GIM model provided by IGS (or CODE) as a reference [11]. As an analysis center of IGS, CODE offers global ionospheric grid products, the precision of those products is lower in China due to sparse IGS stations and they can not reflect the real ionosphere situation in China accurately. In addition, it needs to take account of time and other anomaly things, which would affect its reliability. Because of this, we establish the global ionospheric model datum based on real measured data which is regard as a reference and assess the precision of the broadcast ionospheric model.

47.2 Real Ionospheric Delay on Base Station

The key of determining the real ionospheric delay on base stations is the determination of DCB precisely. The generalized triangular series function (GTSF) is introduced to model the local ionospheric vertical TEC of each individual station based on a thin-layer approximation. Based on dual-frequency observations, we make use of it to model the ionospheric vertical TEC station by station, in order to achieve the separation between TEC and the inter-frequency difference. As well as, we get the total DCB of satellite and the receive, then separate them by taking a two-step method [12, 13].

47.2.1 Extracting TEC from GPS Data

We take GPS combination observations P4 to extract ionosphere TEC, the formula is expressed as follows:

$$P_{2j}^{i} - P_{1j}^{i} = \frac{40.28\left(f_1^2 - f_2^2\right)}{f_1^2 f_2^2} TEC + dq_j + dq^i \tag{47.1}$$

where, $dq_j = dq_{2j} - dq_{1j}$, $dq^i = dq_2^i - dq_1^i$ denotes the DCB of receiver and satellite.

Then:

$$TEC = 9.52437\left(P_{2j}^{i} - P_{1j}^{i} - q_j - q^i\right) \tag{47.2}$$

It is needed to use an ionospheric mapping function to achieve the conversion from slant path direction to the vertical. Ionospheric mapping function MSLM is defined by formula (47.3):

$$F(z) = \frac{STEC}{VTEC} = \frac{1}{\cos z} \tag{47.3}$$

where, z is satellite's zenith degree.

47.2.2 The Generalized Trigonometric Series Function Model

For GPS users at mid-latitudes, the zenith ionospheric TEC concentrated in a single station and local area roughly has the following daily various characteristics: it changes with the local time t in cosine in the day, usually maximum reached when t = 14 h; at night it changes smoothly and relatively little, t changes insignificantly over local time. According to the spatial changes of VTEC, the triangular series model is available as follows [14, 15]:

$$\begin{aligned} VTEC = A_1 + \sum_{i=1}^{N_2}\left\{A_{i+1}\varphi_m^i\right\} + \sum_{i=1}^{N_3} A_{i+N_2+1}h^i + \sum_{i=1,j=1}^{N_I,N_J}\left\{A_{i+N_2+N_3+1}\varphi_m^i h^j\right\} \\ + \sum_{i=1}^{N_4}\left\{A_{2i+N_2+N_3+N_{J-1}}\cos(i\cdot h) + A_{2i+N_2+N_3+N_J}\sin(i\cdot h)\right\} \end{aligned} \tag{47.4}$$

where, VTEC is the total ionospheric TEC in vertical at the IPP. A_i shows the unknown polynomial model coefficients. φ_m is the geomagnetic latitude, $h = 2\pi(t-14)/T$, $(T = 24\ h)$, t is local time at the IPP.

Combine formulas (47.2)–(47.4), we can get:

$$\begin{aligned} & A_1 + \sum_{i=1}^{N_2} \left\{ A_{i+1} \varphi_m^i \right\} + \sum_{i=1}^{N_3} A_{i+N_2+1} h^i + \sum_{i=1,j=1}^{N_I, N_J} \left\{ A_{i+N_2+N_3+1} \varphi_m^i h^j \right\} \\ & + \sum_{i=1}^{N_4} \left\{ A_{2i+N_2+N_3+N_{J-1}} \cos(i \cdot h) + A_{2i+N_2+N_3+N_J} \sin(i \cdot h) \right\} \\ & = 9.52437 \left(P_{2j}^i - P_{1j}^i - q_j - q^i \right) \cdot \cos z \end{aligned} \tag{47.5}$$

By using the high-precision dual-frequency GPS carrier phase smoothed pseudorange observables [2] and the least-square method we can accurately compute the given model coefficients, thus achieving the separation between TEC and the inter-frequency difference, then the quasi-stable adjustment method is used to separate the DCB of satellite and receiver and the DCB is precisely computed, at last with the DCB we may compute the real ionosphere delay at the base station.

47.3 Experiments Test and Analysis

We take the observations of 42 base stations distributed globally for 7 days, see Fig. 47.1. The time span is from August 6 to August 12 in 2014, the data sampling interval is 30 s, the cut-off angle is 25°. We use the GPS carrier phase smoothed pseudorange free-geometric combined observables, and with formulas from (47.2) to (47.5), we accurately compute the ionospheric delay of each base station, which can be as a reference of precision assessment of broadcast ionospheric model of GNSS. Figure 47.2 shows the global distribution of the base stations for day 222. We can see from the figure that the base stations are almost distributed in land of the whole world.

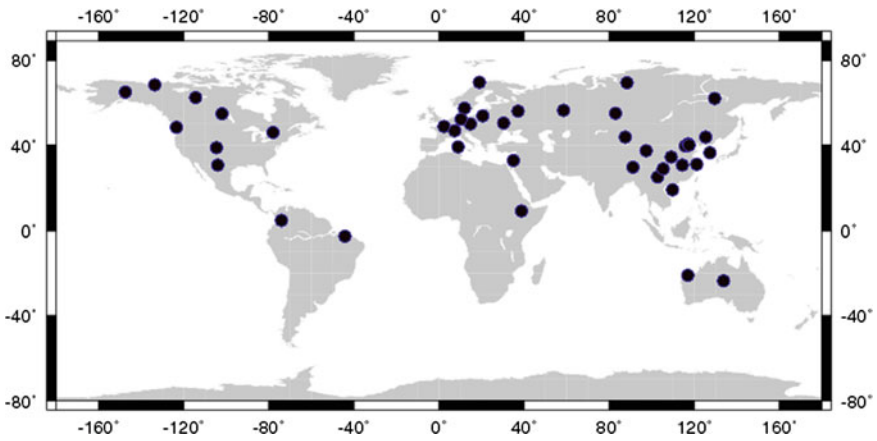

Fig. 47.1 GPS sites distribution

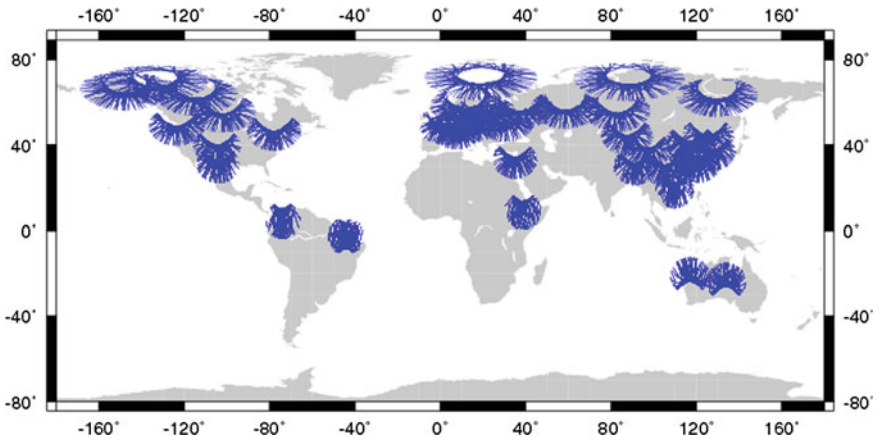

Fig. 47.2 IPPs distribution

47.3.1 Accuracy of Satellite DCB

The accuracy of ionosphere TEC computed by real data depends on the accuracy of DCB of satellite and receiver. The higher precision of DCB, the higher precision the ionospheric TEC extracted. In this paper, we analysis the precision of the computed DCB of satellites for 7 days with reference to the monthly average DCB supplied by CODE and final DCB product daily. Table 47.1 and Fig. 47.3 show the RMS of DCB computed by real data referenced to daily DCB of CODE. The results show that the computed DCB have a good consistency with the referenced DCB, and the accuracy is 0.1–0.15 ns.

47.3.2 Accuracy of Real Ionospheric Delay

We test the accuracy of real ionosphere delay with reference to the final ionosphere delay products of CODE. For this, we chose eight symbolic base stations (URUM, BJFS, LHAZ, ALIC, ALBH, PTBB, ZIMM, AMC2), three in China, two European stations, two North American stations, one in Australia, to statistic and analysis the average accuracy of real ionospheric delay relative to that of CODE for seven

Table 47.1 Precision of satellites' DCB

Accuracy	Day of year						
	218	219	220	221	222	223	224
RMS (ns)	0.12	0.15	0.12	0.14	0.13	0.15	0.13

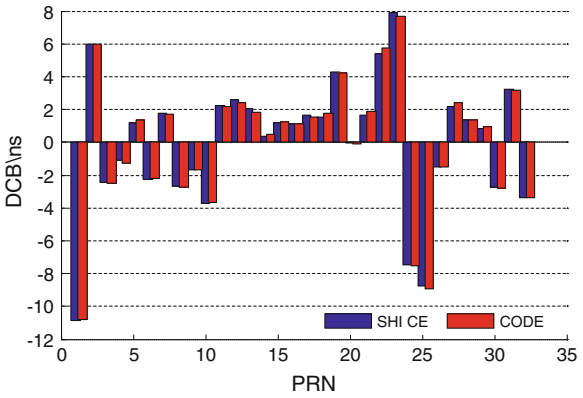

Fig. 47.3 Comparison of DCB between real data and CODE

consecutive days, statistical indicator is shown in formulas (47.6) and (47.7) [12], and the results are shown in the Table 47.2.

$$Mean = \frac{\sum_{n=1}^{N} \Delta_n}{N} STD = \sqrt{\frac{\sum_{n=1}^{N} (\Delta_n - Mean)^2}{N-1}} \tag{47.6}$$

$$RMS = \sqrt{\frac{\sum_{n=1}^{N} \Delta_n^2}{N}} \tag{47.7}$$

where, $\Delta_n = DR_{model,n} - DR_{ref,n}$, $DR_{model,n}$ is the real ionosphere delay, $DR_{ref,n}$ is the reference value, n is the number of satellites at one epoch, N is the number of epochs.

Table 47.2 shows that the RMS of real ionospheric delay relative to CODE is less than 0.4 m, STD is in 0.1–0.2 m, which is equivalent to 1–3 TECu. The real ionospheric delay has a better consistency with the CODE one. Therefore, we can conclude that the real ionosphere delay has a certain reliability and precision.

47.3.3 Precision Assessment of GNSS Broadcast Ionospheric Models

Due to the consistency and timely effectiveness of real ionosphere delay and CODE, we statistically analysis and access the accuracy of BDS/GPS/Galileo broadcast ionosphere delay model based on the above eight base stations and the correction accuracy of GNSS broadcast ionospheric model is shown in Table 47.3.

To assess the precision of broadcast ionospheric model, usually we take the following statistical methods:

Table 47.2 Precision of measured ionospheric delay on base stations

Station	Precision		
	RMS (m)	STD (m)	MEAN (m)
URUM	0.31	0.22	0.22
BJFS	0.18	0.17	−0.05
LHAZ	0.28	0.20	0.15
ALIC	0.19	0.17	0.07
ALBH	0.19	0.18	0.08
PTBB	0.17	0.12	0.11
ZIMM	0.15	0.12	0.08
AMC2	0.16	0.11	0.11

$$Correct = \sum_{k=1}^{n} (1 - \frac{|Model_k - Tec_k|}{Tec_k})/n \tag{47.8}$$

$$RMS = \sqrt{<(Model_k - Tec_k)^2>} \tag{47.9}$$

where $Model_k$ is the model value, Tec_k is real measured value.

As we can see from Table 47.3, the accuracy of BDS/GPS/Galileo broadcast ionospheric model corrected referenced to the real ionospheric model is generally in proportion of over 60 %, RMS is less than 2.0 m, the correction accuracy of BDS broadcast ionospheric models in China is better than GPS and Galileo with proportion of more than 75 %. BDS is a regional satellite navigation system and the correction accuracy in northern hemisphere is higher than that in the southern hemisphere; GPS KLOBUCHAR model and Galileo NeQuick model are global empirical ionospheric models, which can reflect the global average ionosphere well.

Table 47.3 Precision of BDS/GPS/GAL broadcast ionospheric models on base stations

Station	Pro					
	BDS		GPS		GAL	
	Correct	RMS	Correct	RMS	Correct	RMS
BJFS	0.81	0.92	0.72	1.25	0.76	1.01
URUM	0.80	0.93	0.77	1.14	0.67	1.50
LHAZ	0.75	1.36	0.72	1.83	0.79	1.18
ALIC	0.57	1.47	0.60	1.30	0.69	0.92
ALBH	–	–	0.77	0.66	0.67	1.05
AMC2	–	–	0.88	0.47	0.60	1.37
PTBB	–	–	0.84	0.58	0.68	1.14
ZIMM	–	–	0.84	0.66	0.70	1.14

47.4 Conclusion

By using the 42 base stations worldwide and the generalized trigonometric series function model, we reach the goal of receiving the DCB of satellites and receivers precisely and extracting the ionosphere delay in terms of one by one base station, and taking it as a reference to assess GNSS broadcast ionosphere delay level. The results show that the correct proportion of BDS/GPS/Galileo broadcast ionospheric models is generally above 60 %, RMS is less than 2.0 m, and the correction accuracy of BDS broadcast ionospheric models in China is better than GPS and Galileo with proportion of more than 75 %. In this test, by selecting 42 base stations to compare the computed DCB of satellites and receivers and real ionospheric delay with the ones of CODE, we can get that real ionosphere has a certain reliability and accuracy. Using it as a reference to assess the broadcast ionospheric model of GNSS can both make up the lock of CODE ionosphere products under special circumstances and meet the need of precision assessment of broadcast ionospheric model real-timely. The next step we will adjust the number of the base stations, increasing redundant observations, and further improve the accuracy of calculation. It can support the work of monitoring and assessment center of iGMAS on the precision assessment of broadcast ionospheric model of GNSS well.

References

1. Zhang Q, Li JQ (2005) GPS Measuring principle and application. Science Press, Beijing
2. Yuan YB (2002) Study on the theories and methods of correcting ionospheric delay and monitoring ionosphere based on GPS. Institute of Geodesy and Geophysics Chinese Academy of Sciences, Wuhan
3. Zhang HP (2006) Study on GPS based China regional ionosphere monitoring and ionospheric delay correction. Ph.D. Dissertation, Shanghai Astronomical Observatory, Chinese Academy of Sciences, Shanghai, China
4. Klobuchar J (1987) Ionospheric time delay algorithm for single frequency GPS users. IEEE Trans Aerosp Electron Syst 23(3):321–331
5. Huang YD, Wang MY, Han L et al (2006) The improved Klobuchar ionospheric model based on measurements of China. China Space Science Space Exploration Society of Professional Committee of the Nineteenth Conference, Ningbo
6. BeiDou Navigation Satellite System Signal in Space Interface Control Document. China Satellite Navigation Office, December 2012
7. Wu XL, Hu XG, Wang G (2012) Evaluation of COMPASS ionospheric model in GNSS positioning. Adv Space Res 51(6):959–968
8. Xie J, Zhang B, Hou B et al (2012) Simulation of NeQuick paramerters of Galileo satellite navigation system. Chin J Space Sci 32(6):881–886
9. Wang J, Dang YM, Xue SQ (2007) Application of a new ionospheric model-NeQuick in China. Sci Surv and Mapp 32(4):38–40
10. Bidaine B, Warnant R (2012) Assessment of the NeQuick model at mid-latitudes using GNSS TEC and ionosonde data. Adv Space Res 45:1122–1128
11. Gao WG, Su MD, Guo SR et al (2014) Testing and evaluation of signal in space accuracy for Beidou navigation satellite system (BDS). CSNC, Wuhan

12. Li ZS (2012) Study on the Mitigation of Ionospheric Delay and the Monitoring of Global Ionospheric TEC Based on GNSS/Compass. Institute of Geodesy and Geophysics Chinese Academy of Sciences, Wuhan
13. Li ZS, Yuan YB, Li H et al (2012) Two-step method for the determination of the differential code biases of COMPASS satellites. J Geodesy 86:1059–1076
14. Li ZS, Yuan YB, Huo XL et al (2012) The manual of GNSS ionospheric data processing software. Institute of Geodesy and Geophysics Chinese Academy of Sciences, Wuhan
15. Yuan YB, Ou JK (2004) A generalized trigonometric series function model for determining ionospheric delay. Prog Nat Sci 14:1010–1014

Chapter 48
The Characteristics Investigation of Ground-Based GPS/PWV During the "7.21" Extreme Rainfall Event in Beijing

Binyan Wang, Linna Zhao and Xuemei Bai

Abstract GPS/PWV data, combined with automatic station data in Beijing on 20–22 July 2012, the four partitions are analyzed, and the k-means clustering method is employed. The contract results of precipitation characteristics on the basis of four partitions show that (1) the trend of 1 h PWV has the almost same phase, during the rising and falling process corresponding to the start and end of precipitation. (2) The 1 hourly variable PWV is neither increase nor decrease before the precipitation, but 3 hourly variable PWV rises can reach more than 10 mm. The 3 hourly variable PWV is better indication of the intensity of rainfall and the precipitation area, with 3–5 h forecast precipitation for the warning instructions in the practice of forecasting. (3) The PWV of spatial distribution is consistent to the characteristics of precipitation movement from southwest to northeast and gradually increase, and precipitation has a maximum value in 3–4 h before precipitation starts. It has the certain significant instruction to predict future precipitation area and precipitation distribution in practice of forecasting.

Keywords GPS/PWV · Precipitation characteristics · Extreme rainfall · Clustering analysis

B. Wang (✉) · X. Bai
College of Atmospheric Sciences, Plateau Atmosphere and Environment Key Laboratory of Sichuan Province, Chengdu University of Information Technology, Chengdu, China
e-mail: w_byan@163.com

L. Zhao (✉)
State Key Laboratory of Severe Weather, Chinese Academy of Meteorological Sciences, Beijing, China
e-mail: zhaoln@cams.cma.gov.cn

J. Sun et al. (eds.), *China Satellite Navigation Conference (CSNC) 2015 Proceedings: Volume II*, Lecture Notes in Electrical Engineering 341,
DOI 10.1007/978-3-662-46635-3_48

48.1 Introduction

It is well known that the precipitation are little bite complicated processing and has uncertainties, its temporal and spatial distribution is related to the pattern of climate and weather closely. Different types of rainfall process, especially extreme precipitation events have different great impacts on all aspects of living and property [1]. This is caused mainly by the speeding up of urbanization extent of Metropolis. The intense of storm rainfall with short duration has become higher than that of suburb due to the diversification of the underlying surface of urban. Moreover, the increasing urban impermeable pavement areas result in the impeded drainage, and the water logging of urban. It brings serious destruction and enormous economic loses to the urban and the attention is rising on the storm rainfall events and secondary hazards [2].

Beijing area is located in the north part of the North China plain which has a complex terrain. The annual precipitation is about more than 500 mm [3]. The previous studies have showed that the precipitation generally has a trend of decrease since the 1950s over Beijing, but extremely rainfall event is increasing [4]. Due to the influence of terrain, the western of Beijing area that piedmont is easy to form rainfall, which significantly more than other regions. The in-homogeneity of spatial and temporal distribution of rainfall result in occurrence of the extreme local rainfall storm [5].

The extreme rainstorm outbreak on 21–22 July 2012 in Beijing area, that the torrential rain has long duration and strong intensity. It causes deaths of 79 people and loss of ten billion in economic, arousing great damage to social economy in Beijing. Up to now, many scholars have analyzed the rainstorm event by using conventional and unconventional meteorological observation data, such as automatic meteorological observation data, satellite, radar, wind profile data, as well as the NCEP reanalysis data, but research is less about the temporal and spatial distribution characteristics of the precipitation through other observation. The purpose of this paper is to catch some early warning indications of short-time drawing near of extremely heavy rain through investigating the GPS/PWV data combining with automatic meteorological rain gauge data of the extremely heavy rain, and also to provide an idea and method to explore prediction of extreme precipitation events.

48.2 Data and Methodology

The routine meteorological observation data is investigated, that is automatic rain gauge with 5 min interval during 00:00 BST 20 July to 23:55 BST 22 July 2012 over whole Beijing area (in Beijing Standard Time, hereafter). First of all, the Gamma distribution probability density function is employed to fit the spatial and temporal of precipitation distribution, then two parameters of the Gamma distribution probability density function and the percentile (that is 99th, 95th, 90th) of 1 hourly rainfall as partition clustering factors, the k-means clustering method is employed.

GPS/PWV is Perceptible Water Vapor (in mm) that all the water vapor in the air column zenith direction converted into liquid water in the water column height through Global Positioning System. The 1-hourly GPS/PWV data during 20–22 July in Beijing and surrounding is investigated. The data in Beijing and around 54 the International Global Navigation Satellite System (GNSS) Service station (IGS) is processed by special software.

48.3 Precipitation Process

The rainstorm process occurred on 10:00 BST 21 July to 2:00 BST 22 July 2012 in Beijing. The accumulated precipitation amount between 10 BST 21 July to 06 BST 22 July, as Fig. 48.1a shows, the large peak values of the spatial distribution mainly concentrate in the southwest of Beijing area, the maximum center of precipitation is located in Fangshan, upping to 330 mm/h which is more than historical records. The short-time strong rainfall frequency of intensity (Fig. 48.1b) shows clearly that it has lasted an average of 4–5 h on the whole process, even local area is more than 7 h. The intensity of precipitation process is so strong. The flash floods break out in mountainous of suburb and severe water logging occurred in urban consequently, causing serious influence on the life and property.

The Fig. 48.2 shows the time evolution of 1-hourly rainfall sequence in the Beijing area in order to further analyze the characteristics of extreme heavy rainfall at different stages. As shown in Fig. 48.2, it clearly presents two precipitation periods. The first stage of the precipitation is relatively gentle during 12:00 BST to 16:00 BST 21 July. It points out that warm air precipitation in front of frontal surface is leading, the second stage of the precipitation is dominant by frontal precipitation due to the cold front is reduced start at 17:00 BST 21 July and end at 19:00 BST 21 July. The precipitation of second stage is more severe heavy comparing to the first stage [6, 7].

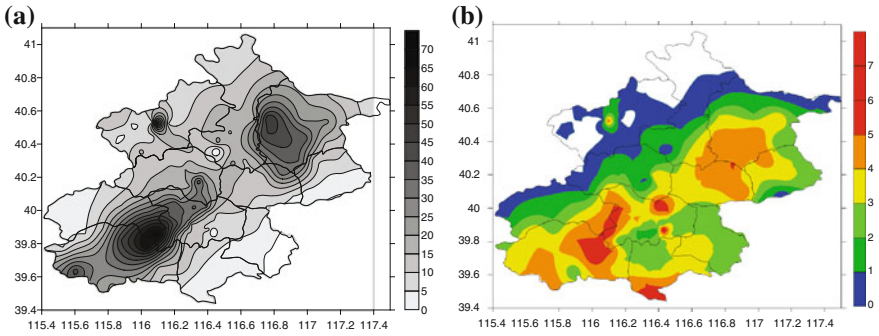

Fig. 48.1 The precipitation distribution during 10:00 BST 21 July to 06:00 BST 22 July 2012 over Beijing. **a** The accumulated precipitation (in mm), and **b** short-time strong rainfall frequency (≥20 mm/h)

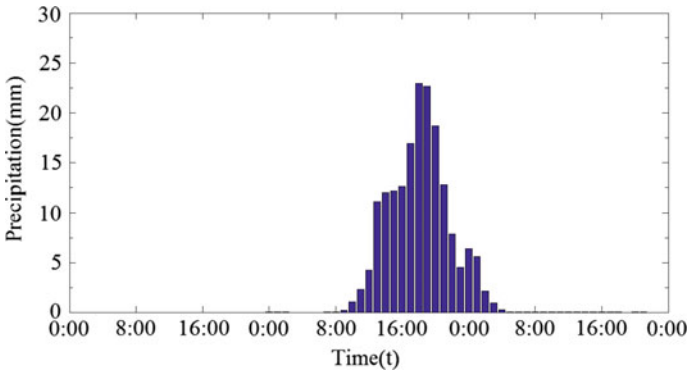

Fig. 48.2 Averaged hourly rainfall sequence of 166 rain gauges over Beijing (unit: mm)

48.4 Spatial Distribution of "7.21" Extreme Rainfall

The spatial distribution of rainfall is in-homogeneous, as indicated from the Fig. 48.1. Research has shown that Γ distribution probability density function has the very good capability about fitting the hourly rainfall distribution probability density [8]. Therefore, the Γ distribution function for observation site to get hourly precipitation probability density distribution, the partition based on two parameters of Γ distribution probability density function and percentile (90th, 95th, and 99th) by using k-means clustering method.

The results show that the partition is reasonable, it confirmed by either distinguish the greater value center of precipitation, or differentiate the type of underlying surface (Fig. 48.3). The four zones are: the 1st-zone including the northern and western part of Beijing; the 2nd-zone located in the northeast part of Beijing which is in the prevailing wind area; the 3rd-zone is the southwest part of Beijing, mainly

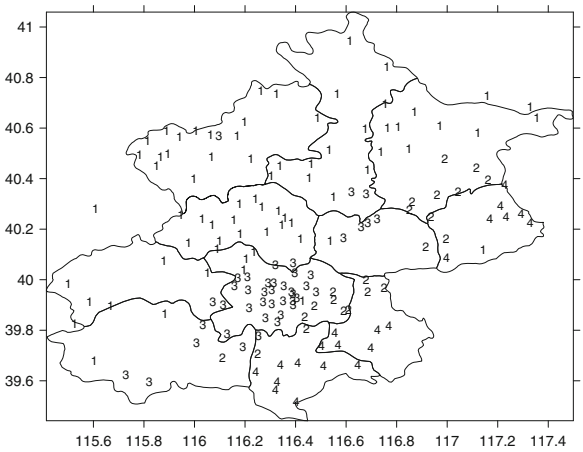

Fig. 48.3 ATW precipitation zones in Beijing area by using K-means clusters methods during 06:00 BST 21 to 23:55 BST 22 July, 2012

in urban area that is easily subjected by warm and moisture air; the 4th-zone mainly in the southeast part of Beijing area. The partition is consistent with the previous results based on four years of automatic rain gauge of Beijing area rainfall partition result [9]. The rationality of the partition provides a solid basis to analyze the process of the rainstorm in Beijing.

48.5 Correlation of Rainfall and GPS/PWV

In order to analyze the relationship between GPS/PWV data and rain gauge data, the representative station of four zones is analyzed, these IGS station are: Haidian Bei'an, Pinggu Beizhai, Fangshan Zhangfang, and Tongzhou Maju, respectively.

The basis of PWV value is high remaining about 50 mm before the start of the precipitation, Hourly PWV has the uniformity evolution with the rain gauge. From each representative IGS station in each area (Fig. 48.4), PWV value has an obvious rising trend, but the peak value of PWV is lagged behind that of rain gauge after the rainfall beginning 1–2 h later. PWV values of all IGS stations are reached in a high value when precipitation occurs; the value of PWV reaches more than 70 mm. It can be found that the maximum value of PWV is closed to the precipitation of corresponding IGS station (that is Zhangfang, Pinggu and Maju) than that of Bei'an (Fig. 48.4). The result shows that precipitation has high conversion efficiency. PWV values falls sharply to 30 mm, decreased by 50 mm after the precipitation, marking the end of precipitation. The result provides a hint to forecast the short-term and drawing near precipitation [10].

48.6 The Lag Correlation

Studies have shown that using hourly variable of GPS/PWV may well determine the intensity and area of precipitation [11]. In order to further obtain the relationship between the precipitation and the interval increment PWV at individual IGS station, the increment of PWV in 1 and 3 h interval are calculated according to the characteristics of the precipitation from southwest to northeast.

As Fig. 48.5 shows that 1 hourly interval increment of PWV is less fluctuation at Zhangfang station before the start of the first stage precipitation. From the beginning of precipitation to the start of the second stage, 1 hourly variable PWV has an obvious rising, can be upped to 10 mm/h. But 3 hourly variable PWV rises to 10 mm in the second precipitation process. At the same time, it can be found that the peak point of 3 hourly interval increment PWV is ahead of the peak of precipitation extreme at least 3 h during the first stage precipitation, while 4–5 h in advance during the second phase. After the precipitation, the variable PWV decreases rapidly.

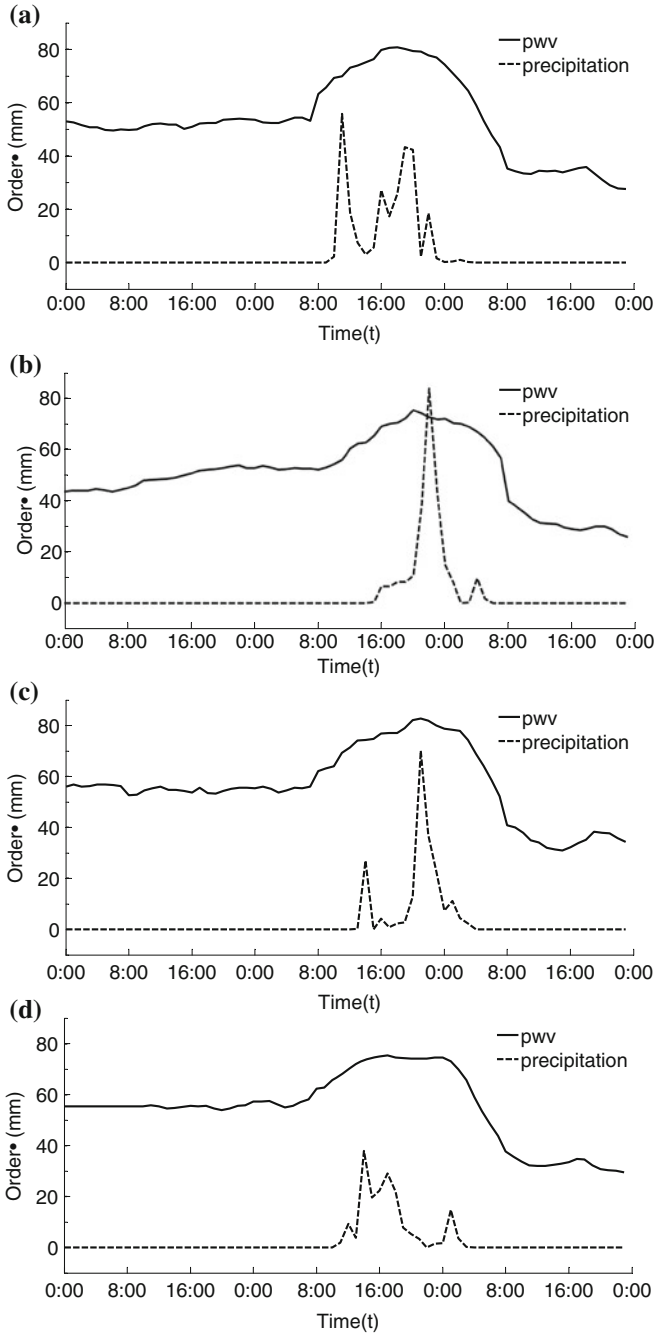

Fig. 48.4 Hourly precipitation and the PWV at representative stations. **a** Fangshan Zhangfang; **b** Pinggu Beizhai; **c** Tongzhou Maju; **d** Haidian Bei'an

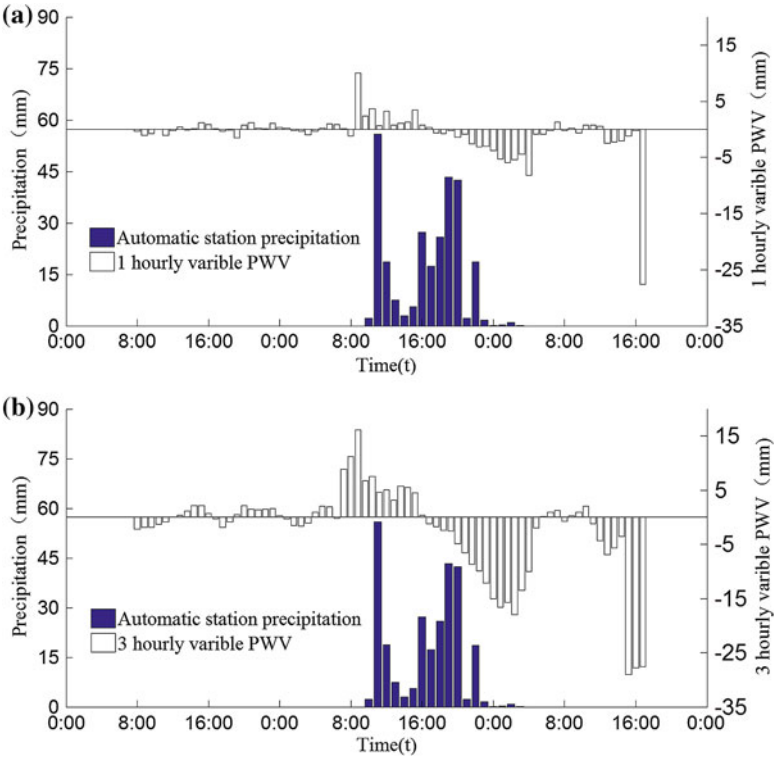

Fig. 48.5 Time series of 1-hourly precipitation (in mm), and **a** 1-hourly interval increment PWV, and **b** 3-hourly interval increment PWV at Zhangfang station, respectively

While for Beizhai (Fig. 48.6), precipitation is mainly belong to the second stage. 1 hourly variable PWV remains at a low value before the start of the second stage precipitation. The high value of PWV maintains a 3-4 h and reaching the peak in 5 mm/h rate, corresponding to the humidity conversion process of the arrival of the second precipitation stage during rainfall. And 3 hourly interval increment PWV increased 10 mm before the time that the precipitation amount reaches peak value. Meanwhile, we find that 3 hourly interval increment PWV of other IGS stations has the similar features (figures are omitted).

In order to investigate the relationship between the precipitation and hourly variable PWV quantitatively, the lag correlation analysis between the precipitation and 1-hourly or 3-hourly increment PWV is investigated respectively (Fig. 48.7). The precipitation is delay argument of lag correlation, if the correlation coefficient is greater than 0.0, then it shows that precipitation lags behind the hourly increment PWV.

As can be seen from Fig. 48.7a, the maximum of lag correlation coefficient between 1-hourly variable PWV and precipitation is 0.6 at the time 5 h before the beginning of precipitation, it hints that 1-hourly increment PWV has the warning instructions for the occurrence of precipitation in advance 5 h. Compared with the

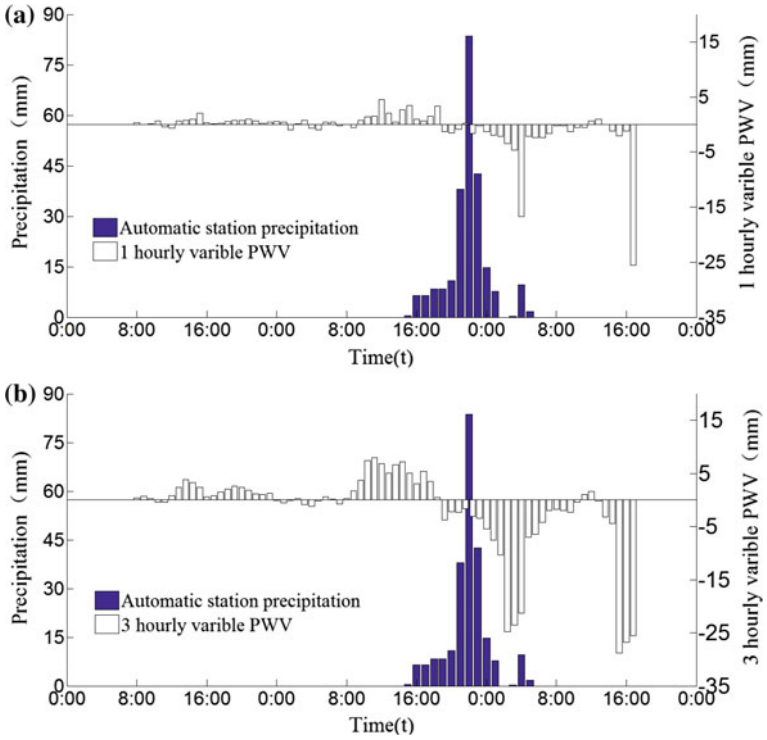

Fig. 48.6 Time series of 1-hourly precipitation (in mm), and **a** 1-hourly interval increment PWV, and **b** 3-hourly interval increment PWV at Beizhai station, respectively

1-hourly variable PWV, the 3-hourly variable PWV is more obvious on indicator significance because the correlation coefficient curve is more smooth, and the correlation coefficient through the significance test is more than that of the 1-hourly (Fig. 48.7b). It also can be found that the warning significance of the 3-hourly variable PWV is better than the 1-hourly variable PWV in Beizhai station (figure is omitted).

48.7 Distribution of GPS/PWV

In order to catch the spatial distribution of PWV, PWV distribution is analyzed at four moments according to the hints revealed from results of former sections, four moments include 10:00, 13:00, 14:00 and 18:00 21 July, respectively. Beijing area has been a high value of PWV center (Fig. 48.8a), mainly located in the southwest part of Beijing at 10:00. The big value center continuously expand eastward at 13:00 (Fig. 48.8b). Then the maximum PWV reaches to 75 mm, covering Middle East of Beijing at 14:00 (Fig. 48.8c). The great value further increases at 18:00, covering the entire Beijing area (Fig. 48.8d).

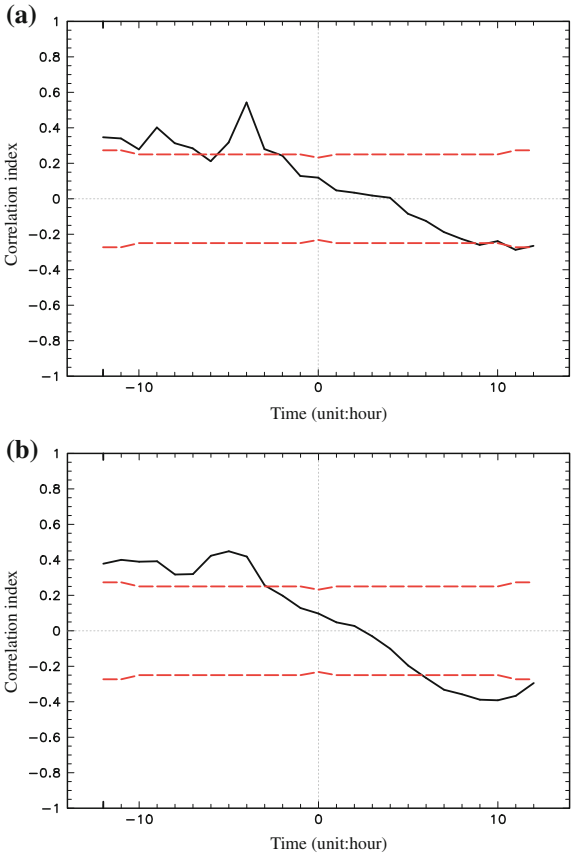

Fig. 48.7 The time series of lag correlation (*solid line*) of 1-hourly precipitation (in mm, *dash line* represents the significance of correlation), **a** 1-hourly increment PWV (in mm), and **b** 3-hourly increment PWV at Zhangfang station, respectively

To further analyze the spatial correlation between PWV and actual rainfall, Fig. 48.9 shows the corresponding moment of automatic station. Compared Fig. 48.8 with Fig. 48.9, it indicates that PWV spatial change has the basic trend consisted with actual rainfall expanding trend, reflecting the spatial correlation well.

48.8 Summary and Discussion

Based on GPS/PWV data, combined with automatic station data in Beijing on 20–22 July 2012 to analyze the "7.21" torrential rains in Beijing, and further research characteristic of PWV data in the time of the rainstorm, it shows that it has the indication of actual rainfall, especially for short-term and impending prediction, summarized as follows:

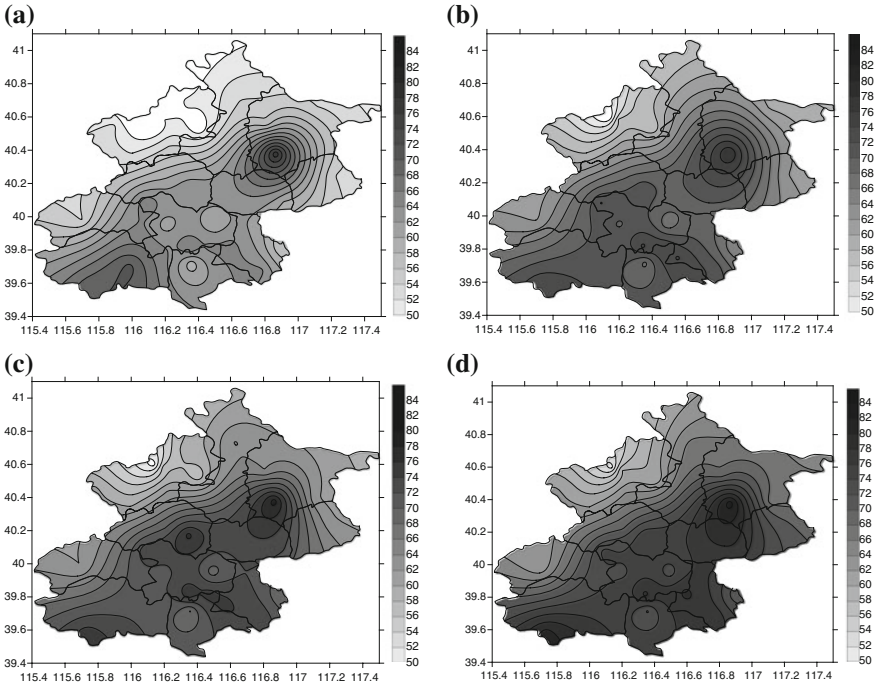

Fig. 48.8 The special distribution of GPS/PWV (in mm) over Beijing areas at **a** 10:00, **b** 13:00, **c** 14:00, and **d** 18:00 21 July 2012, respectively

1. The precipitation process is mainly divided into two phases: the first phase has a long duration, the warm area precipitation is dominant; the intensity of second stage is heavier. The greater value of 1 h precipitation mainly concentrates in the south-west of Beijing, and the average of short-time strong rainfall (≥20 mm/h) have lasted 4–5 h, local is more than 7 h.
2. The trend of 1 h PWV has the almost same phase, during the rising and falling process corresponding to the start and end of precipitation. When high value is basic matched, rainfall reaches the highest conversion efficiency. It also found that the appearing time of PWV maximum is behind for the great values of rainfall time lightly.
3. The lag correlation analysis between hourly variable PWV and rainfall shows that: the ability of 3 hourly variable PWV is better than 1 hourly variable PWV for the warning of rainfall, in advance for 3–5 h which provides a good basis and reference for prediction.
4. The PWV of spatial distribution is consistent to the characteristics of precipitation movement from southwest to northeast and gradually increase and precipitation have a maximum value in 3–4 h before precipitation start. It has the certain significant instruction to predict future precipitation area and precipitation distribution.

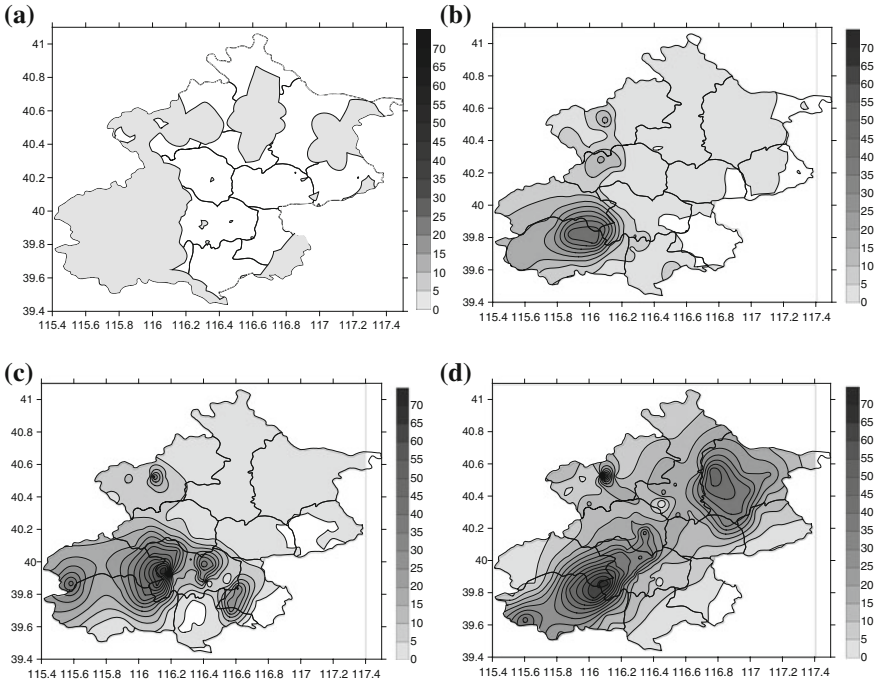

Fig. 48.9 The precipitation special distribution of ATW (in mm) over Beijing areas at **a** 10:00, **b** 13:00, **c** 14:00, and **d** 18:00 21 July 2012, respectively

To be sure, the analysis of PWV can provides the early warning meaningful instructions of the precipitation, making the warning time in advance for 3–5 h especially for the short forecast. But due to the complex of precipitation itself, forecast should also be combined with several of information, to make precipitation forecast objectively and quantitatively.

Acknowledgments The research is supported by the National Natural Science Foundation of China (The grant No. 41475044 and 91437104) and National Science and Technology Major Project of the Ministry of Science and Technology of China (The grant No. 2013ZX07304-001-1)

References

1. Kambezidis HD, Larissi IK, Nastos PT et al (2010) Spatial variability and trends of the rain intensity over Greece. Adv Geosci 26:65–69
2. Wu X, Wang X, Zeng X et al (2002) The effect of urbanization on short duration precipitation in Beijing. J Nanjing Inst Meteorol 23(1):68–72 (in Chinese)
3. Wang J, Zhang R, Wang Y (2012) Characteristics of precipitation in Beijing and the precipitation representative of Beijing weather observatory. J Appl Meteorol 23(3):265–273 (in Chinese)

4. Zhun L, Chen Y, Li L et al (2012) Analysis of precipitation variation trend in Beijing city from 1951 to 2009. Water Resources Prot 28(3):42–46 (in Chinese)
5. Sun J, Su W (2007) Beijing urban heat island effect of urban heat island on winter and summer precipitation in Beijing region. J Atmos Sci 31(2):311–320 (in Chinese)
6. Yu X (2012) Investigation of Beijing extreme flooding event on 21 July 2012. Meteorol Mon 38(11):1313–1329 (in Chinese)
7. Chen Y, Sun J, Xu J et al (2012) Analysis and thinking on the extremes of the 21 July 2012 torrential rain in Beijing part one: observation and thinking. Meteorol Mon 38(10):1255–1266 (in Chinese)
8. Tian F, Zheng Y, Mao D et al (2014) Study on probability distribution of warm season hourly rainfall with distribution. Meteorol Mon 40(7):787–795 (in Chinese)
9. Liu W, You H, Ren G et al (2014) AWS precipitation characteristics based on K-means clustering method in Beijing areas. Meteorol Mon 40(7):844–851 (in Chinese)
10. Li G, Li G, Lian Z et al (2007) Application ground-based GPS data rainfall in shijiazhuang. Meteorol Environ Sci 30(3):50–53 (in Chinese)
11. Xie N, Wang Y (2009) Analysis on a durative heavy rainfall in southwest based on GPS data of precipitation. Plateau Mt Meteorol Res 29(3):55–59 (in Chinese)

Chapter 49
Instantaneous and Controllable GNSS Integer Aperture Ambiguity Resolution with Difference Test

Jingyu Zhang, Meiping Wu and Kaidong Zhang

Abstract In the Global Navigation Satellite System (GNSS), integer ambiguity resolution (IAR) is critical to highly precise, fast positioning and attitude determination. The combination of ambiguity resolution and validation is usually named as integer aperture (IA) ambiguity resolution, which provides the foundation for the ambiguity validation. Based on the IA ambiguity resolution theory, fixed failure-rate (FFR) approach is proposed to realize the controlling of failure rate. Though fixed failure-rate approach can be applied for many acceptance tests, it is time-consuming and cannot be precisely realized in instantaneous scenario. In order to overcome these problems, this contribution will introduce an instantaneous and controllable (iCON) IA ambiguity resolution approach based on difference test for the first time. It has the following advantages: (1) It can independently compute the critical value by the required failure rate and GNSS model $\boldsymbol{Q}$ without external information such as look-up table; (2) It is instantaneous, and the stronger GNSS model, the better performance IA estimator will behave; (3) It can balance the instantaneous and precise quality control by adjusting the number of pull-in regions. The simulation experiment based on single and multi-frequencies, multi-GNSS systems verify the advantages of this approach. It completely solves the time consumption in precise quality control and has the same performance as the FFR approach based on Monte Carlo integral. It is available for instantaneous and precise GNSS applications, such as carrier phase based positioning, PPP-RTK, attitude determination, and will be a better choice the multi-frequency, multi-GNSS ambiguity resolution.

Keywords GNSS · IA aperture ambiguity resolution · Instantaneous · Controllable failure rate · Difference test

J. Zhang (✉) · M. Wu · K. Zhang
National University of Defense Technology, 410073 Changsha, China
e-mail: zjy8712@126.com

J. Sun et al. (eds.), *China Satellite Navigation Conference (CSNC) 2015 Proceedings: Volume II*, Lecture Notes in Electrical Engineering 341,
DOI 10.1007/978-3-662-46635-3_49

49.1 Introduction

In the rapid and high precision GNSS applications, IAR is a fundamental and difficult problem. Once the integer ambiguities are fixed, users can take advantage of the precise pseudo range data in positioning and navigation. Many GNSS models are developed for IAR applications. The principle of them can refer to [1, 2].

As the point of departure, most of GNSS models can be casted in the following conceptual frame of linear(ized) observation equations:

$$\mathbf{E}(\mathbf{y}) = \mathbf{A}\mathbf{a} + \mathbf{B}\mathbf{b}; \mathbf{D}(\mathbf{y}) = \mathbf{Q}_{\mathbf{yy}} \tag{49.1}$$

where $\mathbf{E}(\cdot)$ and $\mathbf{D}(\cdot)$ are the expectation and dispersion operators, and $\mathbf{y}$ the 'observed minus computed' single- or dual-frequency carrier phase or/and code observations. $\mathbf{Q}_{\mathbf{yy}}$ is the variance covariance (vc)-matrix of observations $\mathbf{y}$.

The procedure of IAR usually consists of four steps. In the first step, the integer constraint of ambiguities $\mathbf{a} \in \mathbb{Z}^{\mathbf{n}}$ is disregarded. The float solutions together with their vc-matrix are estimated based on least-square adjustment as $\begin{bmatrix} \hat{\mathbf{a}} \\ \hat{\mathbf{b}} \end{bmatrix}, \begin{bmatrix} \mathbf{Q}_{\hat{\mathbf{a}}\hat{\mathbf{a}}} & \mathbf{Q}_{\hat{\mathbf{a}}\hat{\mathbf{b}}} \\ \mathbf{Q}_{\hat{\mathbf{b}}\hat{\mathbf{a}}} & \mathbf{Q}_{\hat{\mathbf{b}}\hat{\mathbf{b}}} \end{bmatrix}$. Their estimation formulas are given as

$$\begin{aligned} \hat{\mathbf{a}} &= (\bar{\mathbf{A}}^{\mathbf{T}}\mathbf{Q}_{\mathbf{yy}}^{-1}\bar{\mathbf{A}})^{-1}\bar{\mathbf{A}}^{\mathbf{T}}\mathbf{Q}_{\mathbf{yy}}^{-1}\mathbf{y} \\ \hat{\mathbf{b}} &= (\mathbf{B}^{\mathbf{T}}\mathbf{Q}_{\mathbf{yy}}^{-1}\mathbf{B})^{-1}\mathbf{B}^{\mathbf{T}}\mathbf{Q}_{\mathbf{yy}}^{-1}(\mathbf{y} - \mathbf{A}\hat{\mathbf{a}}) \end{aligned} \tag{49.2}$$

where $\bar{\mathbf{A}} = \mathbf{P}_{\mathbf{B}}^{\perp}\mathbf{A}$, $\mathbf{P}_{\mathbf{B}}^{\perp} = \mathbf{I}_{\mathbf{m}} - \mathbf{P}_{\mathbf{B}}$ and $\mathbf{P}_{\mathbf{B}} = \mathbf{B}(\mathbf{B}^{\mathbf{T}}\mathbf{Q}_{\mathbf{yy}}^{-1}\mathbf{B})^{-1}\mathbf{B}^{\mathbf{T}}\mathbf{Q}_{\mathbf{yy}}^{-1}$. With the metric of $\mathbf{Q}_{\mathbf{yy}}$, $\mathbf{P}_{\mathbf{B}}$ is the projector that projects orthogonally onto the range space of B. Quality control steps, such as detection, identification and adaption of outliers are implemented in this step.

The second step takes into the previous integer constraint, and realizes the fixing process of float ambiguities. It can be described as a many-to-one mapping

$$\breve{\mathbf{a}} = \mathbf{S}(\hat{\mathbf{a}}),\ \mathbf{S} : \mathbf{R}^{\mathbf{n}} \to \mathbb{Z}^{\mathbf{n}} \tag{49.3}$$

The mapping process is realized by many integer estimators, such as integer rounding (IR), integer bootstrapping (IB), and integer least-square (ILS). Among them, ILS is the optimal one and can maximize the success rate of estimation [3]. Due to the influence of correlation between different ambiguities, the efficiency of integer estimators is often very low. In order to tackle this problem, LAMBDA method [4]; Teunissen [5–7] is introduced to improve the estimation efficiency and success rate [8].

After integer mapping, the third step is to test whether the fixed solutions should be accepted. This step is also called ambiguity validation and realized by many acceptance tests, including F-ratio test (FT) [9], R-ratio test (RT) [10], W-ratio test

(WT) [11], Difference test (DT) [12], Projector test (PT) [13]. Note that the function of testing is to exclude the suspected integers, and accept the most possible one, since most of times we do not know the correct ambiguity.

According to previous testing result, other parameters can be adjusted based on the estimated ambiguities in the last step

$$\breve{\mathbf{b}} = \hat{\mathbf{b}} - \mathbf{Q}_{\hat{\mathbf{b}}\hat{\mathbf{a}}}\mathbf{Q}_{\hat{\mathbf{a}}\hat{\mathbf{a}}}^{-1}(\hat{\mathbf{a}} - \breve{\mathbf{a}}) \tag{49.4}$$

where $\mathbf{Q}_{\hat{\mathbf{b}}\hat{\mathbf{a}}}$ is the vc-matrix between ambiguity vector and other parameters. After four steps, the carrier phase observations based on correctly fixed result will behave as the high precision range data.

In this contribution, we will focus on the third step. As is known, the combination of second step and third step is the so-called IA estimator. Be different from ILS estimator, there are three judgments after IA estimation: success, failure or undecided. The undecided part is formed by the intervals or holes between different aperture pull-in regions [14]. The benefit of IA estimators is that their failure rates and success rates can be adjusted by the controlling to critical values of acceptance tests. Since failure rate is the critical indicator for the performance of ambiguity resolution, In order to realize its controlling, FFR approach based on Monte Carlo integral is proposed by [15]. The IA estimation theory and FFR approach provide the ambiguity validation foundation and an initial solution to this problem. However, there still exist the following problems in this solution and the theory:

1. The critical values of IA estimators are determined by Monte Carlo integral with the GNSS models as input. Its precision depends on the simulation times. Hence, if we want to obtain a precise value, a large amount of simulation samples must be generated which is rather time-consuming. Since the pull-in regions of IA estimators are constructed by complicated geometries, most of the relations between critical value and success rate or failure rate are nonlinear. The computation for them cannot be realized analytically. The only choice is Monte Carlo integral, though we can improve the precision of Monte Carlo integral with more effective sampling methods, such as sample average approximation, importance sampling, stratified sampling [16], the contradiction between precision and time cost still hinders its application;
2. The practical way to apply the FFR approach is to create the look-up table for certain acceptance test. This work was firstly completed for RT in [17]. The look-up table is created based on numerous GNSS samples with FFR approach for local and global applications. It is constructed according to the number of satellites and failure rates and must satisfy the failure rate requirement for any GNSS samples for certain location. Hence, the choice of critical values in the table is chosen for the worst GNSS model with certain number of satellites. Essentially, the fixed failure-rate approach realized by look-up table actually constraints the failure rate within the user's requirement. Though this approach is applicable, it will be a huge workload for the global application and various acceptance tests;

3. At present, the research about the IA estimators and its application mainly focus on RT-IA estimator. Though properties of other IA estimator are investigated in [18, 19], the gaps between IA estimation theory and practice still have not been bridged. One of the difficult problems is the probability evaluation to IA estimators. Those popular estimators, such as RTIA, and optimal IA estimator, do not have analytical expression for the IA success rates and failure rates, which hinder the further investigation.

Fortunately, recent research about DT reveals the clue to resolve these problems. In [20], RT and DT are compared based on a large number of GNSS samples. Then in [21], the essence between their differences are revealed from geometry and mathematical analysis, which proves that DT is more suitable to the multi-frequency and multi-GNSS applications. According to the results in [22], the properties of DT-IA is derived and its analytical expression for success rate and failure rate are firstly given. This provides the necessary tools to realize the application of DT-IA estimator.

In this contribution, we will introduce an effective method to realize instantaneously controlling to the failure rate of DTIA estimator. This method takes full advantage of DT in strong GNSS scenarios. By using the relationship between ILS and IA probability evaluations of pull-in regions, the failure rate of DT-IA estimator can be effectively and instantaneously controlled by using the constraint of the presetting failure rate.

The whole contribution is organized as follows. In Sect. 49.2, we briefly review the previous research about DTIA estimator and present its corresponding properties. The analytical expressions for the success rates of ILS and DTIA estimators are presented. The probability ratio to connect both probability evaluations is defined and analyzed. Then the new controllable IA ambiguity resolution method is introduced in Sect. 49.3. Its principle is detailed presented. In order to verify the effectiveness of this method, simulation experiments based on multi-frequencies, multi-GNSS are implemented. The experiment results show that this method can instantaneously realize the controlling of failure rate within certain range, which has the same performance as FFR approach. The stronger GNSS model, the better instantaneity and the stronger capacity of quality control the iCON method will have.

49.2 Difference Test and Its Properties

49.2.1 Aperture Pull-in Regions Based on DT

The purpose of acceptance test is to exclude the suspected ambiguities. This is realized by the aperture pull-in region in geometry. If the float ambiguity falls into the aperture pull-in region, it will be more likely fixed to the corresponding integer

vector than those in integer pull-in region. Hence, it is a necessary quality control step. The overall definition of aperture pull-in region is given in [23]

$$\mathbf{\Omega_z} = \{\mathbf{x} \in \mathbb{R}^{\mathbf{n}}, \mathbf{z} \in \mathbb{Z}^{\mathbf{n}} | \mathbf{S}(\mathbf{x}) = \mathbf{z}, \gamma(\mathbf{x}) \leq \boldsymbol{\mu}\} \tag{49.5}$$

where $\boldsymbol{\gamma}(\cdot)$ is the acceptance testing function and $\boldsymbol{\mu}$ its critical value. Then the IA estimator is defined as

$$\bar{\mathbf{a}}_{\mathbf{IA}} = \begin{cases} \mathbf{z} \text{ if } \hat{\mathbf{a}} \in \mathbf{\Omega_z} \\ \hat{\mathbf{a}} \text{ if } \hat{\mathbf{a}} \notin \mathbf{\Omega_z} \end{cases} \tag{49.6}$$

The aperture pull-in regions satisfy the following properties

$$\begin{cases} \bigcup\limits_{\mathbf{z} \in \mathbb{Z}^{\mathbf{n}}} \mathbf{\Omega_z} = \mathbf{\Omega}, \ \mathbf{\Omega} \subset \mathbb{R}^{\mathbf{n}} \\ \mathbf{Int}(\mathbf{\Omega_u}) \cap \mathbf{Int}(\mathbf{\Omega_v}) = \emptyset, \ \mathbf{u} \neq \mathbf{v} \\ \mathbf{\Omega_z} = \mathbf{z} + \mathbf{\Omega}_0 \end{cases}$$

Thus the aperture pull-in regions $\mathbf{\Omega_z}$ are no overlapping subsets of $\mathbb{R}^{\mathbf{n}}$. The explicit expression of DT is given below

$$\left\| \hat{\mathbf{a}} - \breve{\mathbf{a}}_2 \right\|^2_{\mathbf{Q}_{\hat{\mathbf{a}}\hat{\mathbf{a}}}} - \left\| \hat{\mathbf{a}} - \breve{\mathbf{a}}_1 \right\|^2_{\mathbf{Q}_{\hat{\mathbf{a}}\hat{\mathbf{a}}}} \geq \boldsymbol{\mu}_{\mathbf{DT}} \tag{49.7}$$

with $\breve{\mathbf{a}}_1$ and $\breve{\mathbf{a}}_2$ the best and second best integer candidates, and $\boldsymbol{\mu}_{\mathbf{DT}}$ the critical value. The geometry of origin-center pull-in region for DTIA is

$$\begin{aligned} \Omega_{0,\mathbf{DTIA}} &= \{\hat{\mathbf{a}} \in \mathbb{R}^{\mathbf{n}} | \mathbf{S}(\hat{\mathbf{a}}) = 0, \|\hat{\mathbf{a}} - \mathbf{u}\|^2_{\mathbf{Q}_{\hat{\mathbf{a}}\hat{\mathbf{a}}}} - \|\hat{\mathbf{a}}\|^2_{\mathbf{Q}_{\hat{\mathbf{a}}\hat{\mathbf{a}}}} \geq \boldsymbol{\mu}_{\mathbf{DT}}\} \\ &= \{\hat{\mathbf{a}} \in \mathbb{R}^{\mathbf{n}} | \mathbf{S}(\hat{\mathbf{a}}) = 0, \frac{\mathbf{u}\mathbf{Q}^{-1}_{\hat{\mathbf{a}}\hat{\mathbf{a}}}\hat{\mathbf{a}}}{\|\mathbf{u}\|_{\mathbf{Q}_{\hat{\mathbf{a}}\hat{\mathbf{a}}}}} \geq \frac{\|\mathbf{u}\|^2_{\mathbf{Q}_{\hat{\mathbf{a}}\hat{\mathbf{a}}}} - \boldsymbol{\mu}_{\mathbf{DT}}}{2\|\mathbf{u}\|_{\mathbf{Q}_{\hat{\mathbf{a}}\hat{\mathbf{a}}}}}\} \end{aligned} \tag{49.8}$$

with $\mathbf{u} \in \mathbb{Z}^{\mathbf{n}} \backslash \{0\}$. It means that $\Omega_{0,\mathbf{DTIA}}$ are formed by intersecting half-spaces that are constrained by hyper-planes orthogonal to $\mathbf{u}$ and passing through the points $\frac{1}{2}(1 - \frac{\boldsymbol{\mu}_{\mathbf{DT}}}{\|\mathbf{u}\|^2_{\mathbf{Q}_{\hat{\mathbf{a}}\hat{\mathbf{a}}}}})\mathbf{u}$. The two-dimensional geometry construction of aperture pull-in region is demonstrated in Fig. 49.1. The two dimensional vc-matrix is $\begin{bmatrix} 0.0865 & -0.0364 \\ -0.0364 & 0.0847 \end{bmatrix}$.

49.2.2 Probability Evaluations of DTIA Estimator

In [22], the definition of DTIAB is firstly given, which can be seen as the generalized IA bootstrapping estimator. Its success rate is given as

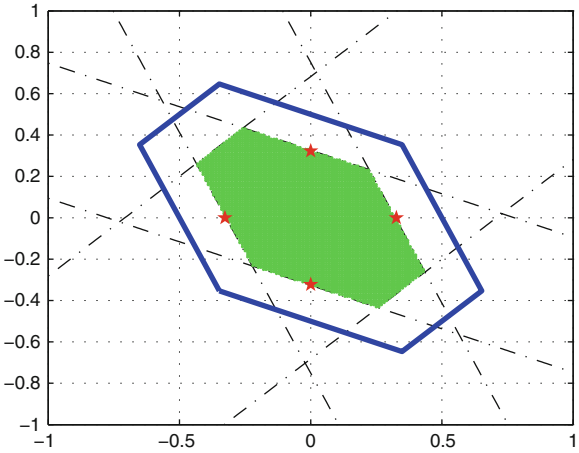

Fig. 49.1 Two-dimensional construction of DT aperture pull-in region with $\boldsymbol{\mu}_{\mathbf{DT}} = 5$. The red stars denote the intersecting points between pull-in regions and coordinate axes

$$\mathbf{P}_{\mathbf{s,DTIAB}} = \prod_{\mathbf{i}=1}^{\mathbf{n}} \left(2\boldsymbol{\Phi}\left(\frac{|\mathbf{x_i}|}{\boldsymbol{\sigma}_{\mathbf{i|I}}}\right) - 1 \right) \tag{49.9}$$

with $|\mathbf{x_i}|$ the intersecting points between DTIAB and coordinate axes and $\boldsymbol{\sigma}_{\mathbf{i|I}}$ the standard deviation from the LDL decomposition of $\mathbf{Q}_{\hat{\mathbf{z}}\hat{\mathbf{z}}}$, $\mathbf{Q}_{\hat{\mathbf{z}}\hat{\mathbf{z}}} = Z^{T}\mathbf{Q}_{\hat{\mathbf{a}}\hat{\mathbf{a}}}Z$, with Z the decorrelation matrix of $\mathbf{Q}_{\hat{\mathbf{a}}\hat{\mathbf{a}}}$. The analytical expression to compute $|\mathbf{x_i}|$ can be determined in decorrelated space when the GNSS model $\mathbf{Q}_{\hat{\mathbf{z}}\hat{\mathbf{z}}}$ and critical value $\boldsymbol{\mu}_{\mathbf{DT}}$ are given, just as shown below

$$\mathbf{x_i} = \frac{\|\mathbf{c_i}\|^2_{\mathbf{Q}_{\hat{\mathbf{z}}\hat{\mathbf{z}}}} - \boldsymbol{\mu}_{\mathbf{DT}}}{2\|\mathbf{c_i}\|^2_{\mathbf{Q}_{\hat{\mathbf{z}}\hat{\mathbf{z}}}}},\ \mathbf{i} = 1, 2, \ldots, \mathbf{n} \tag{49.10}$$

where $\mathbf{c_i}$ is the canonical vector with 1 at the i-th entry and 0 for other entries. Actually, DTIA and DTIAB have the same intersecting points between correct pull-in regions and coordinate axes. This means that the scaling ratios are the same for DTIA and DTIAB in the coordinate directions, which is consistent with the relationship between IB and ILS [22]. Hence, we can use the properties of DTIAB to approximate DTIA estimator after decorrelation step.

Based on the scaling ratios in different directions, the size of DT-IAB pull-in region can be derived as

$$\mathbf{V}_{\mathbf{DTIAB}} = \prod_{\mathbf{i}=1}^{\mathbf{n}} 2|\mathbf{x_i}| = \prod_{\mathbf{i}=1}^{\mathbf{n}} \left| 1 - \frac{\boldsymbol{\mu}_{\mathbf{DT}}}{\|\mathbf{c_i}\|^2_{\mathbf{Q}_{\hat{\mathbf{z}}\hat{\mathbf{z}}}}} \right| \tag{49.11}$$

There exists the maximization condition for computation of Eq. (49.11), and the proof is given in [22]. According to the formula (49.11), the size of DTIAB is variant and depends on $\boldsymbol{\mu}_{\mathbf{DT}}$ and $\mathbf{Q}_{\hat{\mathbf{a}}\hat{\mathbf{a}}}$, and the decorrelation step is helpful to improve the success rate of DTIAB.

Just as proven in [22], $\mathbf{P_{s,DTIAB}}$ can be seen as the lower bound for that of DTIA. Hence, we also can use it to approximate the success rate of DTIA. Its upper bound can be constrained by the scaling Euclidean ball based on ADOP. It is given below

$$\mathbf{P_{s,DTIA}} \leq \mathbf{P}(\boldsymbol{\chi}^2(\mathbf{n},0) \leq \frac{2\bar{\mathbf{x}}^2\mathbf{c_n}}{\mathbf{ADOP}^2}) \tag{49.12}$$

with $\bar{\mathbf{x}} = \frac{\sum_{\mathbf{i}=1}^{\mathbf{n}} |\mathbf{x_i}|}{\mathbf{n}}$, $\mathbf{c_n} = \frac{(\frac{\boldsymbol{\pi}}{2}\boldsymbol{\Gamma}(\frac{\boldsymbol{\pi}}{2}))^{\frac{\boldsymbol{\pi}}{2}}}{\boldsymbol{\pi}}$ and $\mathbf{ADOP} = \sqrt{|\mathbf{Q}_{\hat{\mathbf{z}}\hat{\mathbf{z}}}|^{\frac{1}{\mathbf{n}}}}$.

Actually this is a rather loose upper bound for DTIA estimator. A little sharper bound can be given, which is also based on ADOP and derived from the DTIAB

$$\mathbf{P_{s,DTIAB}} \leq \prod_{\mathbf{i}=1}^{\mathbf{n}} \left(2\boldsymbol{\Phi}(\frac{\boldsymbol{\beta}}{\mathbf{ADOP}}) - 1 \right) \tag{49.13}$$

with $\boldsymbol{\beta} = \sqrt[\mathbf{n}]{\prod_{\mathbf{i}=1}^{\mathbf{n}} |\mathbf{x_i}|}$. After enlarging twice by $\boldsymbol{\beta}$ and ADOP, the upper bound for DTIAB can be regarded as the upper bound of DTIA.

The effectiveness of these probability evaluations are verified in [22].

49.2.3 Probability Evaluations for Pull-in Regions of ILS and DTIA

In practice, the success rate is the probability evaluation to the correct or central pull-in region. It can provide the information about the GNSS model strength and reliability. Actually, probabilities of other pull-in regions are also important. They give us the reference for the design of ambiguity resolution. In this part, we will give the global analytical expressions for all pull-in regions, including ILS and DTIA pull-in regions.

Since DTIA can be seen as the generalized IALS which have different scaling ratios in different directions [22]. ILS can be seen as the special case for DTIA or IALS. Hence, we will take similar approach in the approximation of probability evaluations for both estimators.

The ILS probability evaluation for the correct integer vector can be approximated by

$$\mathbf{P_{s,ILS}} \approx \prod_{\mathbf{i}=1}^{\mathbf{n}} \left(2\boldsymbol{\Phi}(\frac{1}{2\boldsymbol{\sigma}_{\mathbf{i}|\mathbf{I}}}) - 1 \right) \tag{49.14}$$

This is the probability of central pull-in region. For the probabilities of other pull-in region, or the failing pull-in region, we have

$$\mathbf{P_{f,ILS}(i)} \approx \prod_{\mathbf{i}=1}^{\mathbf{n}} \left| \Phi\left(\frac{\mathbf{x_i}}{\boldsymbol{\sigma}_{\mathbf{i|I}}}\right) - \Phi\left(\frac{\mathbf{x_i}-1}{\boldsymbol{\sigma}_{\mathbf{i|I}}}\right) \right| \tag{49.15}$$

where $\mathbf{i}$ is the i-th integer candidate, $\mathbf{x_i} = \frac{1}{2} + \mathbf{z_i}, \mathbf{z_i} \in \mathbb{Z}$ is the intersecting element for each entry of integer vector.

Corresponding to the probabilities of ILS pull-in regions, the probabilities of the DTIA pull-in regions can also be derived

$$\mathbf{P_{f,DTIA}(i)} \approx \prod_{i=1}^{n} \left| \Phi\left(\frac{\mathbf{v_i}}{\boldsymbol{\sigma}_{\mathbf{i|I}}}\right) - \Phi\left(\frac{\mathbf{v_i}-2\mathbf{x_i}}{\boldsymbol{\sigma}_{\mathbf{i|I}}}\right) \right| \tag{49.16}$$

where $\mathbf{x_i}$ is given in (49.10) and $\mathbf{v_i} = \mathbf{x_i} + \mathbf{z_i}$.

In order to find the relationship between ILS and DTIA pull-in regions, here we give the definition to the ratio between probabilities of pull-in regions

$$\mathbf{R(i)} = \frac{\mathbf{P_{f,DTIA}(i)}}{\mathbf{P_{f,ILS}(i)}} \tag{49.17}$$

where $\mathbf{P_{f,DTIA}(i)}$ and $\mathbf{P_{f,ILS}(i)}$ are the i-th failure rate of the pull-in region, and calculated based on (49.16) and (49.15). Actually, $\mathbf{R(i)}$ is within the range [0, 1].

Based on the GNSS model matrix given in Figs. 49.1 and 49.2 gives the trend of probability ratios for different integer candidates.

Hence, the value of $\mathbf{R(i)}$ is basically a monotone decreasing function of different integer candidates. This is a useful property in approximation, which will be used in the computation of critical values for acceptance tests.

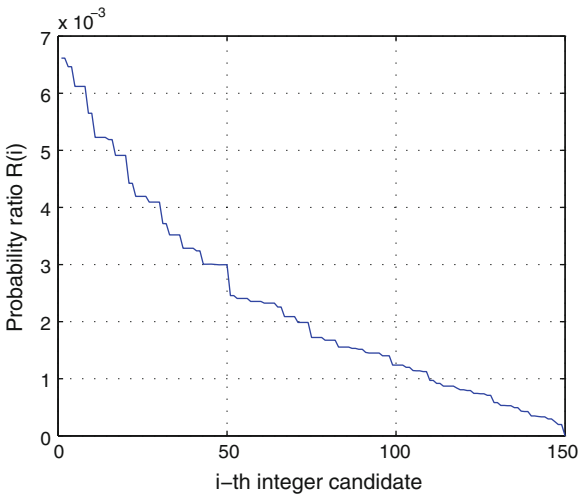

Fig. 49.2 The trend of probability ratio between ILS and DTIA probability of pull-in regions for different integer candidates

49.3 Instantaneous and Controllable IA Ambiguity Resolution

49.3.1 FFR Approach Based on Monte Carlo Integral

As the beginning of the discussion to tackle the IA ambiguity resolution, we will start from the review to Monte Carlo integral. The start point to use Monte Carlo integral is to resolve the problem of multivariate integral for irregular figures. Since the geometries of pull-in regions is not the regular shape, most of times we cannot directly compute their size. The computation of the probability evaluations for points falling into the pull-in regions are based on the multivariate integral for certain probability density function. One of the most direct and convenient approach is to implement Monte Carlo integral. It is firstly proposed by [24]. The procedures to determine the critical value of FFR IA estimator can be summarized into the following steps [19]:

1. Generate $\mathbf{N}$ float ambiguity samples which have normal distribution and conform to $\hat{\mathbf{a}}_\mathbf{i} \sim \mathbf{N}(0, \mathbf{Q}_{\hat{\mathbf{a}}\hat{\mathbf{a}}})$;
2. Set the fixed failure rate $\mathbf{P_f}$. Implement ambiguity resolution to each float ambiguities and compute the values of acceptance tests;
3. Based on the root finding method and pre-setting $\mathbf{P_f}$, determine the critical value $\boldsymbol{\mu}$ which satisfies the fixed failure rate so that $\mathbf{P_f}(\boldsymbol{\mu}) - \mathbf{P_f} = 0$;
4. Count the number of failing samples $\mathbf{N_f}$ and successful samples $\mathbf{N_s}$, then the failure rate and success rate can be determined $\mathbf{P_f} = \frac{\mathbf{N_f}}{\mathbf{N}}, \mathbf{P_s} = \frac{\mathbf{N_s}}{\mathbf{N}}$.

According to the principle of Monte Carlo integral, the precision of this method will improve as the increase of simulation times. An enough large number of samples can ensure the optimality of this method. However, though we can obtain the critical value which has enough precision, it is rather time-consuming and has limited reference value for the instantaneous application. Here we give the relationship between simulation samples and critical values in Fig. 49.3, which is based on the GNSS model matrix

$$\mathbf{Q} = \begin{bmatrix} 0.0865 & -0.0357 & 0.0421 \\ -0.0357 & 0.0847 & -0.0258 \\ 0.0421 & -0.0258 & 0.0797 \end{bmatrix}.$$

In Fig. 49.3, it is obvious that as the increase of simulation times, the variation of critical values keep steady. It proves that large simulation times can improve the precision of FFR approach. However, the huge time-consumption makes it almost unavailable in practice.

Even if the FFR approach is realized by look-up table, it is essentially to realize the controlling of failure rate below the certain failure. Strictly speaking, fixed failure rate cannot be realized.

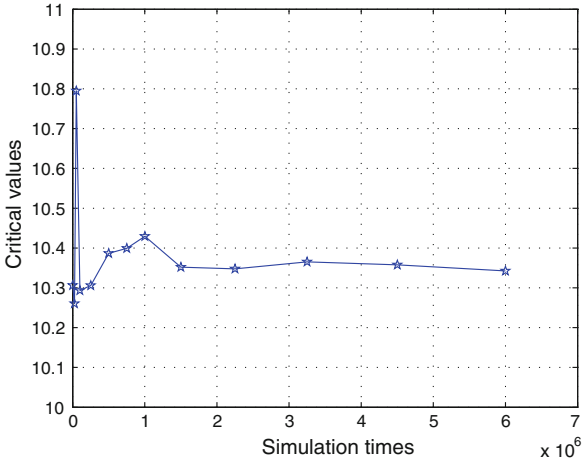

Fig. 49.3 Relationship between simulation times and corresponding critical values

In order to tackle this problem, we propose the **instantaneous and CONtrollable (iCON)** IA ambiguity resolution method. Based on its characteristics, we name it as iCON.

49.3.2 ICON IA Ambiguity Resolution

In order to overcome the disadvantages of Monte Carlo integral, the iCON method is proposed here. Its procedures are listed below

(1) Set the fixed failure rate and initial critical value as $\mathbf{P_f}$, $\boldsymbol{\mu}_0$ and $\mathbf{P}_0$. Calculate the probability evaluations for pull-in regions of ILS and determine the number of pull-in regions needed by the equation

$$\mathbf{P_{s,ILS}} + \sum_{\mathbf{i}=1}^{\mathbf{n}} \mathbf{P_{f,ILS}}(\mathbf{i}) = \mathbf{P}_0 \tag{49.18}$$

where $\mathbf{n}$ is the number of pull-in regions used below. $\mathbf{P}_0$ can be set as $1 - \mathbf{P_f}$ for the first time;

(2) Calculate the probabilities of $\mathbf{n}$ IA pull-in regions and the value of probability ratio in (49.17)

$$\mathbf{R}(\mathbf{n}) = \frac{\mathbf{P_{f,DTIA}}(\mathbf{n})}{\mathbf{P_{f,ILS}}(\mathbf{n})} \tag{49.19}$$

(3) According to the probability ratio in step 2, we can determine the critical value $\boldsymbol{\mu}_{\mathbf{DT}}$ for certain GNSS model by

$$\sum_{\mathbf{i}=1}^{\mathbf{n}} \mathbf{P}_{\mathbf{f},\mathbf{DTIA}}(\mathbf{i}, \boldsymbol{\mu}_{\mathbf{DT}}) + \mathbf{R}(\mathbf{n}) * \mathbf{P}_{\mathbf{f}} = \mathbf{P}_{\mathbf{f}} \tag{49.20}$$

In this method, two elements are the critical points. The first one is $\mathbf{P}_0$. The larger $\mathbf{P}_0$, the more pull-in regions needed in step 1 and 3. Since the resolution in step 3 is a recursive process, the most time-consumption for this method lies on this step. The other one is the GNSS model $\mathbf{Q}_{\hat{\mathbf{a}}\hat{\mathbf{a}}}$. Though it does not appear in previous equations, it determines the values of $\mathbf{P}_{\mathbf{s},\mathbf{ILS}}$, $\mathbf{P}_{\mathbf{f},\mathbf{ILS}}$, $\mathbf{P}_{\mathbf{f},\mathbf{DTIA}}$ and $\mathbf{R}(\mathbf{n})$. In other words, it indirectly influences the number of pull-in regions and time-consumption in this method. The stronger GNSS model, the less pull-in regions can be required and the less time the iCON method needed.

Equation (49.20) is the critical step to realize the controlling of failure rate. According to this equation, even if we can give precisely evaluation to $\mathbf{P}_{\mathbf{s},\mathbf{DTIA}}(\mathbf{i})$ and $\mathbf{P}_{\mathbf{s},\mathbf{ILS}}$, we still can constrain the range of approximation error in the left side by the constraining of $\mathbf{P}_{\mathbf{f}}$. It is because

$$\mathbf{R}(\mathbf{n}) * \mathbf{P}_{\mathbf{f}} < \mathbf{P}_{\mathbf{f}} \tag{49.21}$$

In the FFR approach, Eq. (49.20) should be written as

$$\sum_{\mathbf{i}=1}^{\infty} \mathbf{P}_{\mathbf{f},\mathbf{DTIA}}(\mathbf{i}, \boldsymbol{\mu}_{\mathbf{DT}}) = \mathbf{P}_{\mathbf{f}} \tag{49.22}$$

Equation (49.20) is essentially the approximation for the pull-in regions which can almost be neglected. At the same time

$$\sum_{\mathbf{i}=1}^{\mathbf{n}} \mathbf{P}_{\mathbf{f},\mathbf{DTIA}}(\mathbf{i}, \boldsymbol{\mu}_{\mathbf{DT}}) < \mathbf{P}_{\mathbf{f}} \tag{49.23}$$

Hence, the range of the controlled failure rate is $(0, 2\mathbf{P}_{\mathbf{f}})$. If we want to obtain the same failure rate range as Monte Carlo by iCON, we can apply $\frac{\mathbf{P}_{\mathbf{f}}}{2}$ into this approach.

49.4 Experiment Verification

In order to verify the performance of the iCON algorithm, we design the simulation experiment for a medium length baseline with the basic setting in Table 49.1. The $\mathbf{P}_{\mathbf{f}}$ in FFR approach and iCON are both chosen as 0.001. Here, the Monte Carlo simulation times is chosen as 50,000. The flow diagram of the simulation experiment is presented in Fig. 49.4.

Table 49.1 Simulation settings for GNSS models

Items	Settings
Systems	GPS, BeiDou, Galileo and their combinations
Frequency	L1, L2, L5, E1 (L1), E5a, E5b, B1, B2, B3
Time	July 12–13, 2014
Location	Changsha, China
Sampling intervals	300 s
Troposphere delay	ZTD estimated
STD[a] of ionosphere delay	0.01 m
STD of undifference observations	Code: 20 cm; phase: 2 mm

[a] STD means the standard deviation

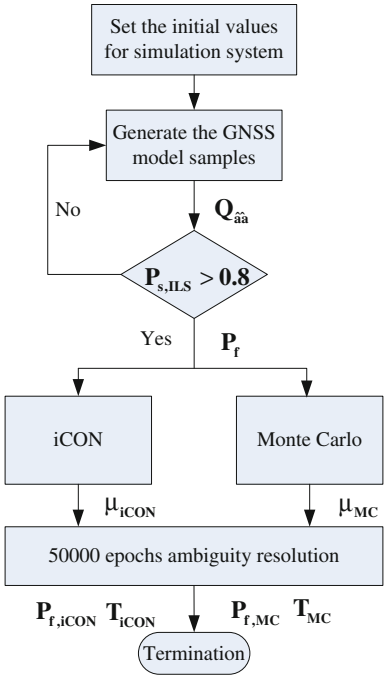

Fig. 49.4 The flow diagram for the simulation experiment

In Fig. 49.4, $\mathbf{P_{f,iCON}}, \mathbf{P_{f,MC}}, \boldsymbol{\mu}_{\mathbf{iCON}}, \boldsymbol{\mu}_{\mathbf{MC}}, \mathbf{T_{iCON}}$ and $\mathbf{T_{MC}}$ are the failure rates, critical values and time consumptions based on iCON and FFR approach.

Since if the model strength is weak, the IA success rates will be very low. It is not significant to analyse the GNSS samples whose success rates are very low. Hence, we set a threshold to do the comparison for GNSS model strength. If their ILS success rates are larger than 0.8, we will implement previous comparison.

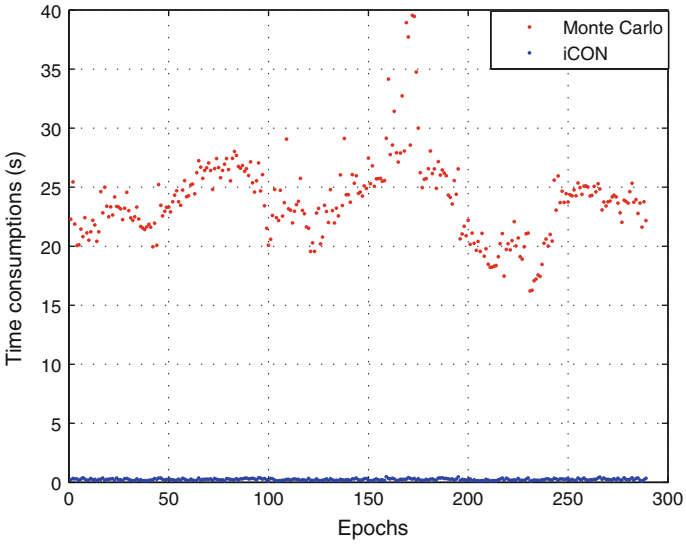

Fig. 49.5 The comparison of time consumptions between iCON and FFR approach within 1 day

Table 49.2 Statistics for FFR and iCON comparison

Items	Time[a] mean (s)	Time STD (s)	Pf[b] mean	Pf STD
Monte Carlo	23.860	3.3627	10e-4	2.108e-4
iCON	0.3309	0.0942	7.4e-4	2.083e-4

[a] Time means the time consumptions
[b] Pf means the failure rates

Here we give the comparison of time consumptions and failure rates for both methods based on 'GPS + BeiDou + Galieo'combination within 1 day in Figs. 49.4 and 49.5, whose statistics are summarized in Table 49.2.

According to Table 49.2, it is obvious that the iCON has rather shorter time consumptions in the computation of critical values, which can be realized instantaneously. Besides this, the controlling of failure rates is within the theoretical range. The controlling of iCON is also more precise than FFR approach. This comparison reveals one problem in FFR approach in Fig. 49.6. In order to keep its failure rate within the required range, its simulation times must be large enough, and the critical value should choose the worst GNSS scenario so that others can be satisfied. However, iCON method does not have these considerations. This proves that iCON is a better choice than the FFR approach based on Monte Carlo integral.

In order to explicitly demonstrate the relations between time consumptions and IA success rates of both methods, we generate more GNSS samples based on the settings in Table 49.1. Their experiment results are demonstrated in Figs. 49.7 and 49.8.

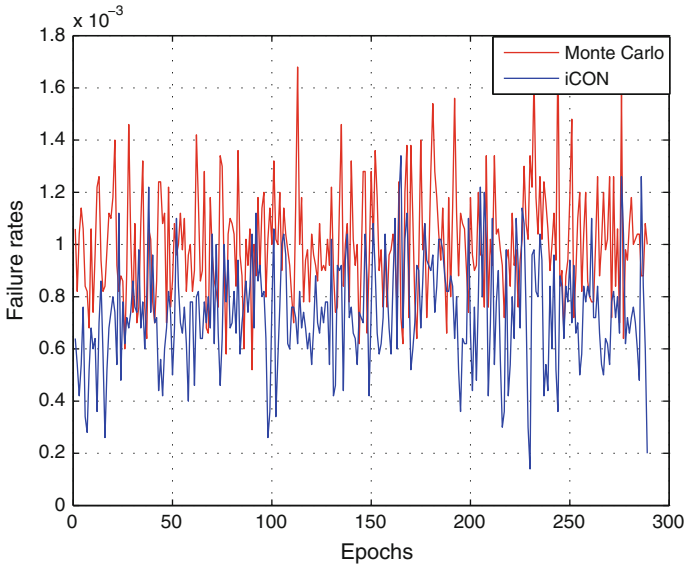

Fig. 49.6 The comparison of failure rates between iCON and FFR approach within 1 day

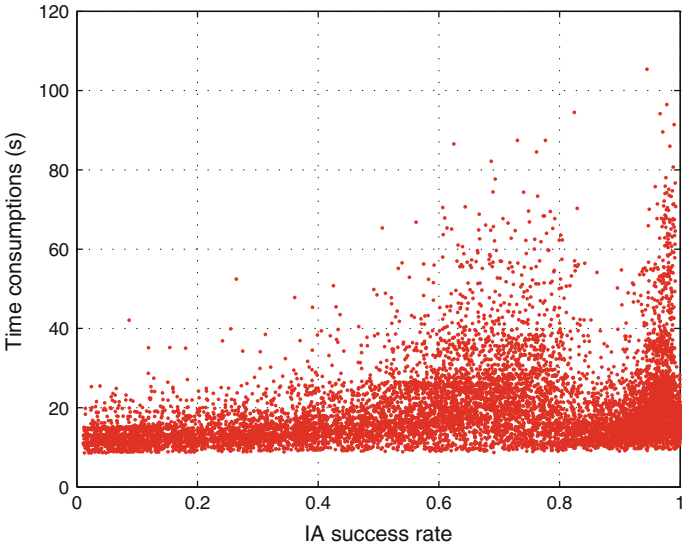

Fig. 49.7 Relations between IA success rates and time consumptions for Monte Carlo

According to Fig. 49.7, it is obvious that as the increase of IA success rate, the time consumptions will gradually increase. This is due to that FFR approach relies on the time cost of ambiguity resolution. The more dimension of ambiguity, the

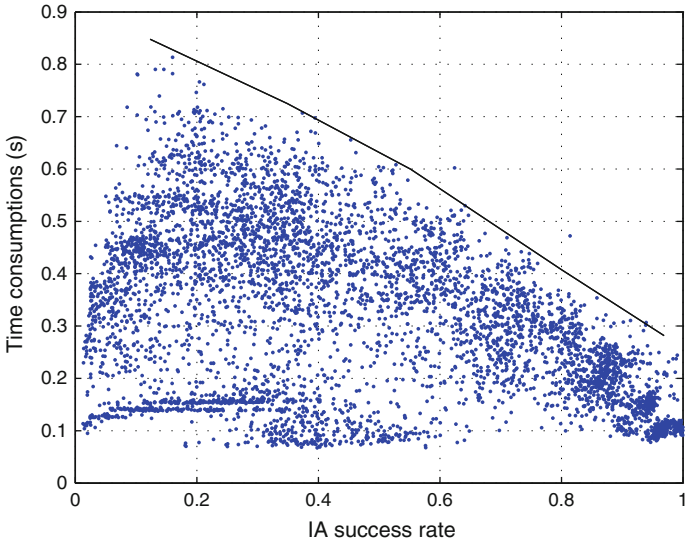

Fig. 49.8 Relations between IA success rates and time consumptions for iCON method

more time it will take in ambiguity resolution. Notice that there exist some gaps for the IA success (0.8, 0.9). This is due to the number of simulation samples. However, the maximizations of time consumptions increase as the GNSS models become strong. Besides this, the minimizations of the time consumptions basically keep constant. Since the strengthening of GNSS models can be realized by using several epochs in one estimation step. Then the dimension of GNSS model will keep constant and their time consumptions also do not change.

However, in Fig. 49.8 we can see that the time consumption gradually decreases as the increase of IA success rate. It means that the stronger model can decrease the number of pull-in regions needed, and then less time consumption of iCON method will be taken in the recursive process. Actually, the number of pull-in regions taken into consideration in the approximation process is no more than 300. The less time consumptions in iCON, the more pull-in regions can be added by enlarging $\mathbf{P}_0$ to increase the precision of failure rate controlling. Note that the increasing trend within (0, 0.1) is caused by the insufficient samples at that interval, since the ILS success rates of GNSS samples must be larger than 0.8.

49.5 Conclusions

Ambiguity validation is an important step to realize the quality control of ambiguity resolution. Its foundation is based on the IA ambiguity resolution theory and can be realized by many acceptance tests.

Due to the good properties of DT in previous research, this contribution firstly introduced the properties of DT. Then, the FFR approach based on Monte Carlo integral was introduced and analysed. Though the FFR approach can realize the controlling of failure rate, it is time-consuming and its precision relies on simulation times. In order to overcome these disadvantages, this contribution proposed the iCON method. This method can instantaneously compute the critical value of acceptance test based on pre-setting failure rate and constrain the failure rate within certain range. Both time consumptions and controlling of failure rate can be better than Monte Carlo integral. Besides this, as the GNSS models become strong, iCON will have better performance in time consumption and failure rate control. The simulation experiment based on single and multi-frequency, single and multi-GNSS combinations proves the effectiveness of this method. It will be a better choice in the instantaneous scenarios of next generation GNSS.

Furthermore, the iCON method can be used by any IA estimator whose success rate and failure rates have analytical expressions, such as the IAB, IALS and ellipsoid IA estimators. This will be the topic studied in the future.

Acknowledgements The research in this contribution is partly funded by the China Scholarship Council (CSC). The first author would like to thank the invitation and supports from Dr. Sandra Verhagen, and Prof. Peter Teunissen in Delft University of Technology, the Netherlands.

References

1. Leick A (2004) GPS satellite surveying. Wiley, New York
2. Misra P, Enge P (2006) Global positioning system: signals, measurements, and performance. Ganga-Jamuna Press, Lincoln
3. Teunissen PJG (1999) An optimality property of the integer least-squares estimator J Geod 73:587–593
4. De Jonge P, Tiberius CCJM (1996) The LAMBDA method for integer ambiguity estimation: implementation aspects. Publications of the Delft Computing Centre, LGR-Series
5. Teunissen PJG Least-squares estimation of the integer GPS ambiguities. In: Invited lecture, section IV theory and methodology, IAG general meeting, Beijing, China, 1993
6. Teunissen PJG (1995) The least-squares ambiguity decorrelation adjustment: a method for fast GPS integer ambiguity estimation. J Geod 70:65–82
7. Teunissen PJG (2010) Integer least-square theory for the GNSS compass. J Geod 84:433–447
8. Teunissen PJG (2000) The success rate and precision of GPS ambiguities. J Geod 74:321–326
9. Frei E, Beutler G (1990) Rapid static positioning based on the fast ambiguity resolution approach FARA: theory and first results. Manuscripta Geodaetica 15:325–356
10. Euler HJ, Schaffrin B (1991) On a measure for the discernibility between different ambiguity solutions in the static-kinematic GPS-mode. In: Kinematic systems in geodesy, surveying, and remote sensing. Springer, Heidelberg, pp 285–295
11. Wang J, Stewart MP, Tsakiri M (1998) A discrimination test procedure for ambiguity resolution on-the-fly. J Geod 72:644–653
12. Tiberius CCJM, De Jonge P (1995) Fast positioning using the LAMBDA method. Paper presented at the proceedings of the DSNS'95, Bergen, Norway
13. Han S (1997) Quality-control issues relating to instantaneous ambiguity resolution for real-time GPS kinematic positioning. J Geodesy 71:351–361

14. Teunissen PJG (2004) Integer aperture GNSS ambiguity resolution. Artificial Satellites 38:79–88
15. Verhagen S, Teunissen PJG (2006) New global navigation satellite system ambiguity resolution method compared to existing approaches. J Guid Cont Dyn 29:981–991
16. Rubinstein RY, Kroese DP (2011) Simulation and the Monte Carlo method. Wiley, New York
17. Verhagen S, Teunissen PJG (2012) The ratio test for future GNSS ambiguity resolution. GPS Solut Online(4):1–14
18. Li T, Wang J (2014) Analysis of the upper bounds for the integer ambiguity validation statistics. GPS Solut 18:85–94
19. Verhagen S (2005) The GNSS integer ambiguities: estimation and validation. Netherlands Geodetic Commission
20. Wang L, Verhagen S (2014) Ambiguity acceptance testing: a comparision of the ratio test and difference test. Paper presented at the CSNC 2014, Nanjing
21. Zhang J (2014) Acceptance test for future GNSS ambiguity resolution. GPS Solut (under review)
22. Zhang J, Wu M, Zhang B (2014) Integer aperture ambiguity resolution based on difference test. J Geod (under review)
23. Teuniseen PJG (2013) GNSS integer ambiguity validation: overview of theory and methods. In: Proceedings of the institute of navigation pacific PNT 2013. pp 673–684
24. Teunissen PJG (1998) On the integer normal distribution of the GPS ambiguities. Artif Satell 33:49–64

Chapter 50
Can BDS Improve Tsunami Early Warning in South China Sea?

Kejie Chen, Natalia Zamora, Andrey Babeyko and Maorong Ge

Abstract Currently, China is strengthening infrastructure construction in South China Sea (SCS) area, it is believed that in the near future, SCS territory will play an increasingly important role in political and economic exploitation as well as international cooperation issues. However, political and economical development plans must also consider possible impact of various natural hazards as well as strategies for damage minimization. In particular, the Manila subduction zone has been identified as a zone of potential tsunami hazard in the SCS region. Despite the fact, that no earthquake higher than Mw7.6 has occurred in this region during last years, events of higher magnitudes cannot be excluded which could expose SCS to the tsunami risk. Recently, development of a region-wide Tsunami Early Warning System (TEWS) was proposed. Traditional TEWS incorporates seismic network for detection of earthquakes and estimating their tsunamigenic potential combined with ocean-based observations for monitoring of wave propagation. After the striking Great Sumatra 2004 earthquake and tsunami, new technologies were introduced into the tsunami early warning. In particular, continuous GPS-arrays able to measure earthquake source parameters in almost real-time. Around the end of 2012, China has completed the constellation of the regional Beidou Navigation Satellite System (BDS), and this system is running operationally since that time. Nowadays, China government is reinforcing the application of BDS in scientific and engineering fields. Numerous studies have demonstrated that the precise positioning performance of BDS is equal in match against GPS in the Asian-Pacific region, which promisingly suggests BDS can be implemented to facilitate tsunami early warning in the South China Sea. In present study, we use numerical simulation technique to assess the potential of the BDS for the tsunami early warning in SCS. We suggest deployment of a real-time BDS coastal network at the Luzon Island. Such a network, if established, will effectively contribute to fast source inversion at the Manila trench and, hence, to more rapid and reliable tsunami early warning in the whole SCS region.

Keywords Tsunami early warning · China south sea · Beidou navigation system

K. Chen (✉) · N. Zamora · A. Babeyko · M. Ge
German Research Center for Geoscience, 14473 Potsdam, Germany
e-mail: kejie@gfz-potsdam.de

J. Sun et al. (eds.), *China Satellite Navigation Conference (CSNC) 2015 Proceedings: Volume II*, Lecture Notes in Electrical Engineering 341,
DOI 10.1007/978-3-662-46635-3_50

50.1 Introduction

The South China Sea (SCS), a marginal sea that is part of the Pacific Ocean, is one of the largest marginal seas along the continental margin of East Asia, covering an area around 3,500,000 km^2. The coastal population surge, the sharp increase of harbours and the exploration of mineral resources, together with the territorial dispute as well, have driven this region to play a more and more important role both in international political issues and economic aspects for China. Accompanying this development, central government of China is now strengthening infrastructure construction there.

Regional development strategies should consider risks and possible damages from various natural hazards including hurricanes, earthquakes and tsunamis as well as to prepare strategies and tools for hazard damage minimization. In particular, the Manila subduction zone (Fig. 50.1) has been identified as a zone of potential tsunami hazard in the SCS region ([5, 9, 11, 14, 16]). Numerical simulations suggest that a magnitude 8.0 or larger earthquake at the Manila trench may cause significant tsunami damage along the whole south-eastern coast of China, south-western Taiwan and west Philippines. In other words, if a tsunami breaks out, the SCS region may suffer a large-scale disaster.

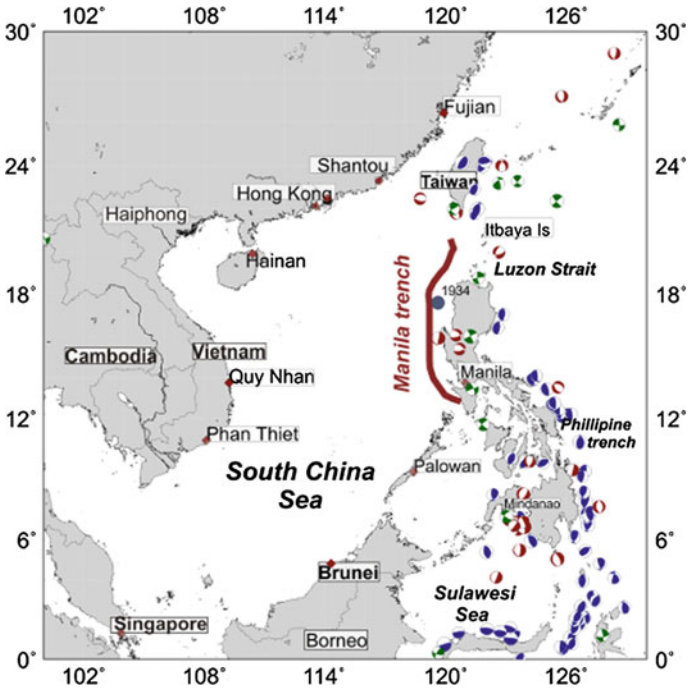

Fig. 50.1 Seismotectonic map of the Southern China Sea. Red thick line presents Manila trench of the seismogenic Manila subduction zone. Beachballs illustrate locations and focal mechanisms of historical earthquakes

To date, no real-time Tsunami Early Warning System (TEWS) is operational in the South China Sea. Liu et al. [11] used numerical simulation to evaluate possible tsunami impact and proposed development of a new TEWS in the SCS-region. Traditionally, TEWS incorporates seismic network for detection of earthquakes and estimating their tsunamigenic potential combined with ocean-based observations for monitoring of wave propagation and updating of tsunami forecasting [17]. In this scheme, deep ocean buoys are acoustically linked to their ocean-bottom units equipped with high-precision pressure sensors (tsunameter). This system can measure and transmit to the warning centre information about propagating tsunami waves in real-time. This information is, in turn, used to better constrain tsunami source parameters and, hence, update and improve tsunami forecasting along distant coasts. In their paper, Liu et al. [11] proposed a prototype for a tsunami early system in the Southern China Sea based on three tsunameters deployed 100–200 km east to the Manila trench. Placement of tsunameters close to the subduction zone should, on one hand, reduce tsunami forecasting time for the coasts under risk, but, on another hand, tsunami signal in the vicinity of epicenter may become strongly contaminated by seismic and acoustic noise. That, in turn, can degrade the reliability of forecasting.

Also traditional seismic methods have their limitations. For example, a distant tsunami could be revised as soon as the focal mechanism is identified. However, for large tsunamigenic earthquakes, broadband seismometers saturate near the source and, hence, magnitude estimation relies on teleseismic waves recorded much later at distant seismic stations, which, of course, devalues the time efficiency of tsunami forecasting. The latter may pose a problem for coastal segments located not too far from the epicentre.

Motivated by huge damages and losses after the Great Sumatra 2004 earthquake and tsunami, new technologies were introduced into the tsunami early warning aimed to provide faster and more reliable tsunami source inversion. The latter is especially important in the tsunami warning chain since its overall uncertainty is controlled by the uncertainty of source inversion. Recent progress in real-time GPS ground tracking accuracy, which now has reached cm-level, motivated first researches to propose incorporation of continuous real-time GPS-arrays into the tsunami early warning process [3, 15]. The main advantage of the RT-GPS lays by the fact that GPS-sensors do not saturate by strong ground motion and, thus, after RT-processing can deliver reliable values of ground displacements just in few minutes after an earthquake. Subsequent inversion of these displacements into source parameters provides necessary initial conditions for the tsunami forecasting.

Following this idea, GITEWS (German Indonesian Tsunami Early Warning System) became the first TEWS which implemented real-time GPS for tsunami early warning [2, 6]. Later on, after the Great Tohoku 2011 earthquake Ohta et al. [12] and Hoechner et al. [7] have once again demonstrated a very promising potential of the GPS-based tsunami early warning.

Around the end of 2012, China has completed the constellation of the regional Beidou Navigation Satellite System (BDS) and the system is running operationally since then. Numerous studies have demonstrated that precise positioning

performance of BDS is equal in match against GPS in the Asian-Pacific region [18], which promisingly suggests BDS can be competent for real-time tsunami source inversion in the SCS-region and, thus, become an important part of a regional TEWS.

This paper aims at assessment of RT-BDS to contribute to the tsunami early warning in Southern China Sea. In Sect. 50.2 we assess the real-time performance of BDS in the SCS-region and evaluate expected ground tracking accuracy (which is crucial for the reliable tsunami source inversion). In Sect. 50.3 we consider a numerical scenario encompassing a M8.0 earthquake along the northern segment of the Manila trench and corresponding tsunami propagation towards south-eastern coast of China. Our goal is to evaluate, if the expected RT-BDS ground tracking accuracy will be enough to "recognize" co-seismic displacements induced by the seismic rupture at the Luzon Island.

50.2 Potential of Retrieving Co-seismic Signal Using RT—BDS

To date, numerous approaches have been proposed to obtain co-seismic velocities, displacement waveforms and static displacements (see, e.g., [1, 4, 10, 12]) based on GPS observations. In general, these methods could be specified into two categories, i.e., relative positioning and single point positioning. For the former, Real Time Kinematic (RTK) positioning technology is among the best known and mature ones. It does not need precise satellite clock error products and most of the error budgets can be cancelled through double differencing between reference station and rover station, as a result, the mathematical model is relatively simple and easy to be conducted. Most importantly, integer-cycle phase ambiguities can be resolved to their correct integer values reliably because inter frequency bias is eliminated. However, it requires that the reference station being located outside the zone of deformation and that it does not move during the event, which is not always the case [12]. In contrast the single point positioning approach does not require such a reference station and is thus, in principle, more desirable. In this contribution, it was mainly employed. Nonetheless, one should keep in mind that for Precise Point Positioning (PPP) ambiguity resolution might fail and re-convergence periods, at least initially, can still be long. Fortunately, Variometric Approach for Displacements Analysis Stand-alone Engine (VADASE) [4] and Temporal Point Positioning (TPP) [10] are able to overcome this disadvantage.

To validate the performance of BDS in retrieving co-seismic signal, we selected two IGS Multi-GNSS Experiment (MGEX) stations in Asia-Pacific region which currently track BDS constellations and processed the observation data using VADASE and TPP algorithms, respectively. Details about the stations are listed in Table 50.1.

Table 50.1 Station details (from: http://igscb.jpl.nasa.gov/mgex/stations)

Site ID	Country	Lat	Lon	Height	Calibration	Satellite system
GMSD	Japan	30.56	131.02	142.647	ROBOT	GPS + GLO + BDS + GAL + QZSS
SIN1	Singapore	1.34	103.68	92.54	ROBOT	GPS + GLO + BDS + GAL + QZSS + SBAS

50.2.1 Performance of Velocity Determination from BDS

Velocity change of monitoring stations plays a very crucial role in detecting first co-seismic signals due to the fact that it is more sensitive than displacement varying. VADASE algorithm, which just uses broadcast ephemeris to retrieve velocity information with promising performance, potentially is able to be embedded to receiver hardware directly and have caught increasing attention.

GPS phase measurements can be described as:

$$\Phi_r^s = -u_r^s \cdot x - \delta t^s + \delta t_r + B^s - I_r^s + T_r^s + p_r^s + \varepsilon_r^s \tag{50.1}$$

Here, subscript r refers to a particular receiver and superscript s to a satellite, Φ_r^s is "Observed Minus Computed" (OMC) carrier phase observation of the receiver with respect to the satellite, u_r^s means unit vector from satellite s to receiver r, and it should be noted that if high-rate (≥ 1 Hz) observations are utilized, u_r^s is then all most the same for the two consecutive epochs. x is station coordinate, δt_r and δt^s are the receiver and the satellite clock errors; B^s is ambiguity; I_r^s and T_r^s are ionosphere and troposphere delay; p_r^s is the sum of other effects (e.g., relativistic effects, phase center variations, phase wind-up); ε_r^s is measurement noise.

Basic theory underlying VADASE [4] is in fact L_1 and L_2 ionosphere-free combination epoch differencing:

$$\begin{aligned} &\alpha[\lambda\Delta\Phi_r^s(t,\ t+1)]_{L_1} + \beta[\lambda\Delta\Phi_r^s(t,\ t+1)]_{L_2} \\ &= -\Delta u_r^s(t) \cdot x(t,\ t+1) + c(\Delta\delta t_r(t,\ t+1) - \Delta\delta t^s(t,\ t+1)) \\ &\quad + \Delta T_r^s(t, t+1) + \Delta p_r^s(t,\ t+1) + \Delta m_r^s(t,\ t+1) + \Delta\varepsilon_r^s(t,\ t+1) \end{aligned} \tag{50.2}$$

where $\alpha = f_{L_1}^2/(f_{L_1}^2 - f_{L_2}^2)$ and $\beta = -f_{L_2}^2/(f_{L_1}^2 - f_{L_2}^2)$, typical coefficients for ionosphere-free combination, Δ denotes difference operation; λ is the carrier phase wavelength; c is the speed of light. Since $x(\mathrm{t},\ \mathrm{t}+1)$ is station coordinate epoch difference, it can be treated as velocity.

Here we expand it to process GLONASS, and BDS observations. Multi-broadcast ephemeris was downloaded from MGEX website. Taking into account that even for megathrust earthquakes, the shaking time just lasts several minutes [7], we took 300 s in this contribution as window width to observe the feasibility of

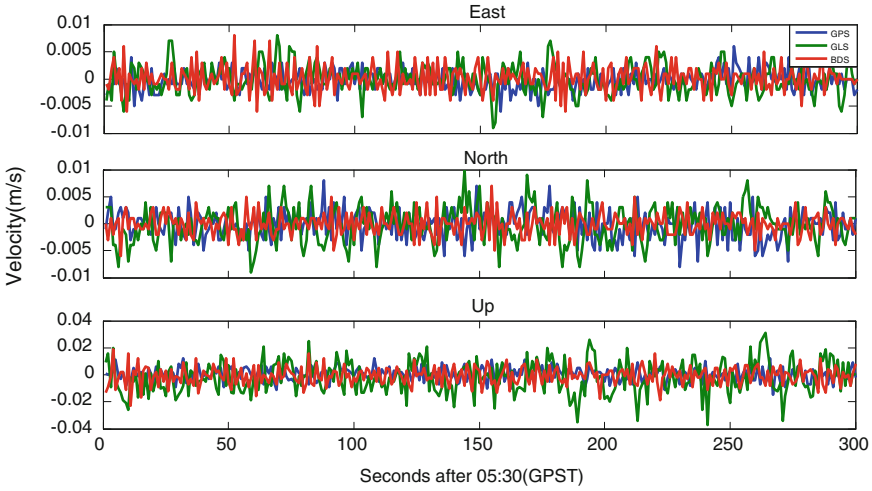

Fig. 50.2 Velocity estimation from GPS, GLONASS and BDS individually

Table 50.2 RMS of velocity (mm)

	East	North	Up
GPS	1.9	2.6	5.0
GLONASS	2.8	3.3	11.0
BDS	2.5	2.1	6.1

BDS in seismic velocity determination. Note that the data was recorded when no tectonic events broke, that's to say, instantaneous station velocity was zero, as a result, reliability and accuracy of VADASE could be assessed safely. For comparison, GPS and GLONASS observation data was processed at the same time. Error sources related to positioning were carefully dealt with models or treated as parameters to be solved. Resulting velocity time series from GPST 05:30 is shown in Fig. 50.2 as a demonstration.

Meanwhile, statistics information about velocity is also provided as shown in Table 50.2. Clearly, BDS has shown all most the same accuracy as GPS, both are better than GLONASS.

Mostly, to invert earthquake magnitude, co-seismic static displacements are needed. After integrating velocity into displacement, corresponding displacement waveforms were retrieved (see Fig. 50.3).

As expected, errors related to broadcast ephemeris demonstrate their effects in displacements more apparently than in velocity, a shift trend exists in displacement time series which devalues the application of VADASE for co-seismic displacement retrieving.

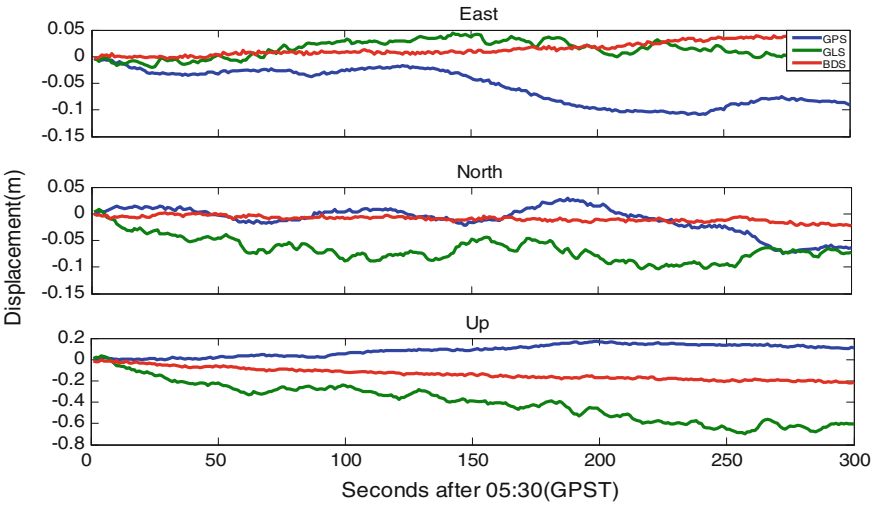

Fig. 50.3 Integration of velocity to displacement

50.2.2 Performance of BDS Temporal Point Positioning

To get reliable displacements, here we tested the performance of TPP by BDS. Similar to velocity estimation, GPS and GLONASS data were also processed for comparison, and results are depicted in Fig. 50.4. Precise orbit and clock were computed by PANDA and the strategies the same as Zhao et al. [18].

Statistics information of the displacements is summarized in Table 50.3.

Promisingly, displacement horizontal accuracy of BDS can reach 1.5 cm, the same level as GPS.

50.3 Can BDS Recognise a Strong Tsunamigenic Earthquake in Real Time? A Scenario Case for Luzon Island

Liu et al. [11] have designed and evaluated various scenarios of tsunami generation and propagation in the Southern China Sea. They have placed their tsunamigenic sources along the Manila subduction zone (Fig. 50.1) following recommendations by Kirby et al. [9]. All their scenarios have a magnitude of M8.0 and rupture different parts of the Manila trench, from north to south. In present study we do not need to consider all their scenarios or suggest any alternative sources. Our goal is to assess the capability of RT-BDS system to detect co-seismic displacements caused by earthquake rupture somewhere on the land. As we have noted before, measurement of co-seismic displacements is necessary for reliable tsunami source

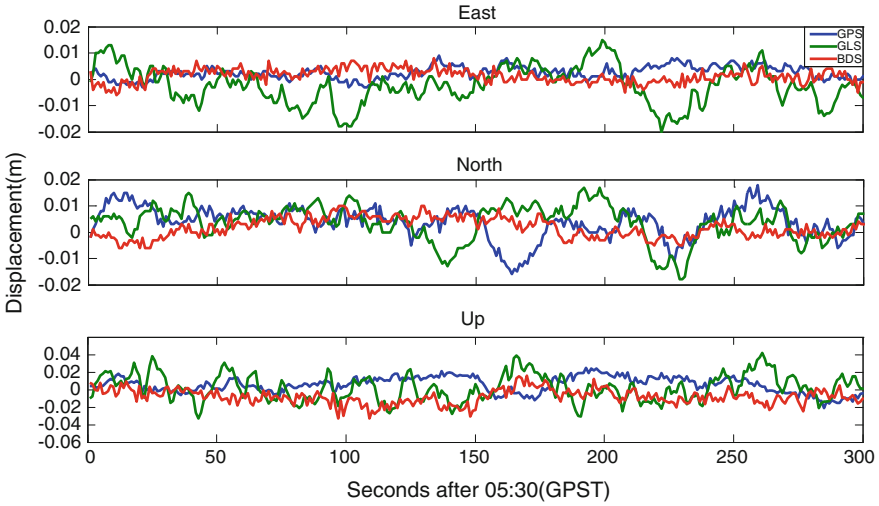

Fig. 50.4 Displacements retrieving by TPP using GPS, GLONASS and BDS data individually

Table 50.3 RMS of displacements (cm)

	East	North	Up
GPS	0.7	1.1	1.8
GLONASS	1.2	1.4	2.3
BDS	0.9	1.2	1.7

inversion and, consequently, forecasting. The closest land to the Manila trench is the Luzon Island of Philippines (Fig. 50.1).

Following these considerations, we have selected one rupture scenario from Liu et al. [11], namely, scenario called "E2". According to this scenario, earthquake with magnitude M8.0 ruptures the northern part of the Manila trench. Due to predominantly SW-NE orientation of the rupture, main tsunami energy is radiated towards the south-eastern coast of China, between the cities of Hong Kong and Shantou (see Fig. 50.5). Maximum expected tsunami wave heights reach 10 m at the west coast of the Luzon Island. At the south-west coast of Taiwan and south-east coast of China, tsunami wave heights may reach 1–2 m. For this scenario, tsunami simulation was performed with *easyWave* code (e.g., [7] which incorporates Okada's dislocation model [13] for source modelling and linear long-wave propagation algorithm for tsunami simulation [8].

While triggering devastating tsunami, earthquake rupture also causes significant horizontal displacements at the Luzon Island (Fig. 50.6). In particular, north-west part of the Luzon Island will experience NW-directed surface displacements larger than 10 cm. Displacements larger than 2 cm will be observed almost everywhere at Luzon. Please note, that according to our estimations from Sect. 50.2, real-time accuracy of BDS-derived ground horizontal displacements should be 1.5 cm. From

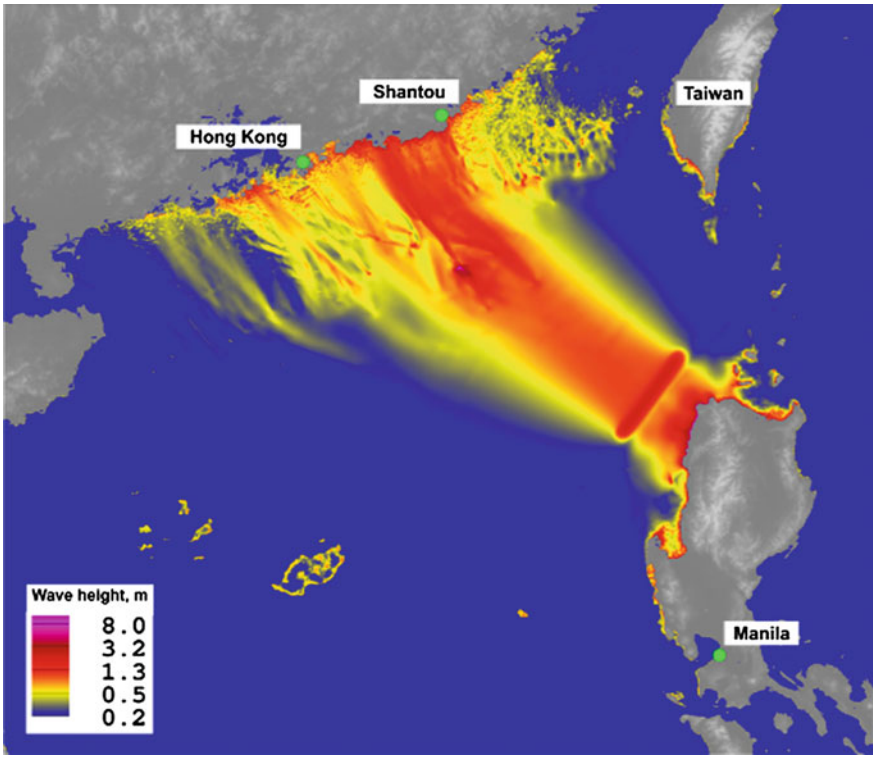

Fig. 50.5 Simulated maximum tsunami wave height for the M8.0 rupture along the northern part of the Manila trench (earthquake parameters are from [11], scenario E2). Note tsunami energy directivity pattern towards south-eastern coast of China

that we conclude that continuous BDS-network deployed at the western coast of the Luzon Island should be able to detect and measure in real-time co-seismic ground displacements, thus providing necessary conditions for fast source inversion and more reliable tsunami early warning in the Southern China Sea.

50.4 Summary

There is a persistent tsunami hazard in the Southern China Sea posed by probable M8.0 or larger earthquakes at the Manila subduction zone. This hazard requires establishment of a tsunami early warning system in the SCS region.

Proximity of the Manila trench to the Luzon Island provides favorable conditions for deployment of a GNSS (BDS) continuous ground-tracking network with real-time processing along the western coast of Luzon. Expected real-time displacement accuracy of such a network should be around 1.5 cm horizontally.

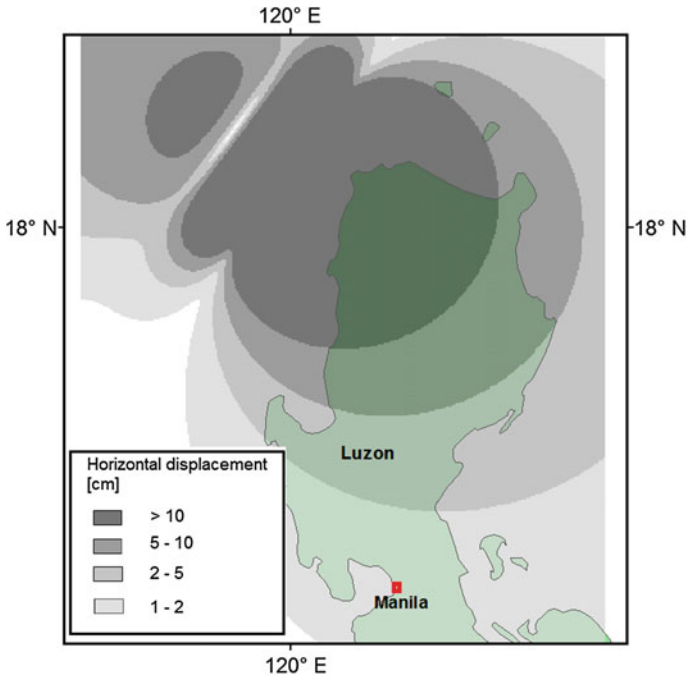

Fig. 50.6 Co-seismic horizontal surface dislocations due to the M8.0 rupture along the northern part of the Manila trench (compared with Fig. 50.5). Note the amplitude of dislocation: on most part of the Luzon Island it is significantly larger than the RT-BDS detection threshold of 1.5 cm

Tsunamigenic earthquakes with magnitudes M8.0 or higher, which pose high tsunami risk also for the south-east coast of China and Taiwan, will be securely detected and measured by such a network. Expected co-seismic displacements of 5–10 cm along the large part of the Luzon island are significantly larger than the "detection threshold" of the RT-BDS ground tracking network.

Thus, RT-BDS network along the west coast of Luzon will contribute significantly to the fast and reliable tsunami early warning in the Southern China Sea.

Acknowledgements K.C. is supported by China Scholarship Council (CSC) for his PhD study in Germany research Centre for Geoscience. N.Z. is supported by Helmholtz Association through the GeoSim program.

References

1. Allen RM, Ziv A (2011) Application of real-time GPS to earthquake early warning. Geophy Res Lett 38(16)
2. Babeyko AY, Hoechner A, Sobolev SV (2010) Source modeling and inversion with near real-time GPS: a GITEWS perspective for Indonesia. Nat Hazards Earth Syst Sci 10:1617–1627

3. Blewitt G, Kreemer C, Hammond WC, Plag HP, Stein S, Okal E (2006) Rapid determination of earthquake magnitude using GPS for tsunami warning systems. Geophy Res Lett 33(11)
4. Colosimo G, Crespi M, Mazzoni A (2011) Real-time GPS seismology with a stand—alone receiver: a preliminary feasibility demonstration. J Geophy Res: Solid Earth (1978–2012) 116 (B11)
5. Dao MH, Tkalich P, Chan ES, Megawati K (2009) Tsunami propagation scenarios in the South China Sea. J Asian Earth Sci 36(1):67–73
6. Falck C, Ramatschi M, Subarya C, Bartsch M, Merx A, Hoeberechts J, Schmidt G (2010) Near real-time GPS applications for tsunami early warning systems. Nat Hazards Earth Syst Sci 10:181–189. doi:10.5194/nhess-10-181-2010
7. Hoechner A, Ge M, Babeyko AY, Sobolev SV (2013) Instant tsunami early warning based on real-time GPS–Tohoku 2011 case study. Nat Hazards Earth Syst Sci 13(5):1285–1292
8. Imamura F, Goto C, Ogawa Y, Shuto N (1997) IUGG/IOC Time project, intergovernmental oceanographic commission (IOC) manuals and guides no 35, UNESCO
9. Kirby S et al (2006) In USGS tsunami sources workshop (2006): great earthquake tsunami sources: empiricism and beyond, April 21–22
10. Li X, Ge M, Guo B, Wickert J, Schuh H (2013) Temporal point positioning approach for real-time GNSS seismology using a single receiver. Geophy Res Lett 40(21):5677–5682
11. Liu PLF, Wang X, Salisbury AJ (2009) Tsunami hazard and early warning system in South China Sea. J Asian Earth Sci 36(1):2–12
12. Ohta Y, Kobayashi T, Tsushima H, Miura S, Hino R, Takasu T, Umino N (2012) Quasi real-time fault model estimation for near—field tsunami forecasting based on RTK—GPS analysis: application to the 2011 Tohoku—Oki earthquake (Mw 9.0). J Geophy Res: Solid Earth (1978–2012) 117(B2)
13. Okada Y (1985) Surface deformation due to shear and tensile faults in a half-space. Bull Seismol Soc Am 75:1135–1154
14. Okal EA, Synolakis CE, Kalligeris N (2011) Tsunami simulations for regional sources in the South China and adjoining seas. Pure Appl Geophys 168(6–7), 1153–1173
15. Sobolev SV, Babeyko AY, Wang R, Hoechner A, Galas R, Rothacher M, Subarya C (2007) Tsunami early warning using GPS-Shield arrays. J Geophy Res: Solid Earth (1978–2012) 112 (B8)
16. Suppasri A, Imamura F, Koshimura S (2012) Tsunami hazard and casualty estimation in a coastal area that neighbors the Indian Ocean and South China Sea. J Earthquake Tsunami 6 (02)
17. Titov V, Gonzalez F, Bernard E, Eble M, Mofjeld H, Newman J, Venturato A (2005) Real-time tsunami forecasting: challenges and solutions. Nat Hazards 35:41–58
18. Zhao Q, Guo J, Li M, Qu L, Hu Z, Shi C, Liu J (2013) Initial results of precise orbit and clock determination for COMPASS navigation satellite system. J Geodesy 87(5):475–486

Chapter 51
GTm_X: A New Version Global Weighted Mean Temperature Model

Peng Chen and Wanqiang Yao

Abstract The atmospheric weighted mean temperature (Tm) determines the calculation accuracy of perceptible water value. Recently, a variety of global Tm empirical formulas and models have been developed using different databases, which have defects of limited spatial resolution. To address this issue, we establish a high-resolution global Tm model, GTm_X, using global reanalysis data in 2011–2013 provided by the ECMWF. GTm_X achieves a global spatial resolution of 1° × 1°. Its accuracy is verified using 2011–2013 Tm data from 703 global radiosonde stations. GTm_X exhibits higher accuracy than Bevis's formula and other empirical models currently in use, including GTm_III, and GTm_N.

Keywords Weighted mean temperature · Spatial resolution · Calculation accuracy

51.1 Introduction

Water vapor is an important component of the Earth's atmosphere. GPS meteorology provides a new technical means to detect the Earth's atmosphere. The tropospheric zenith total delay (ZTD) can be accurately obtained from GPS observation data, whereas the zenith wet delay (ZWD) can be obtained by subtracting the zenith hydrostatic delay calculated using empirical model. The ZWD can be converted to atmospheric perceptible water value (PWV), one of the hot issues for current research in GPS meteorology. The relationship between PWV and ZWD is denoted as follows:

$$PWV = \Pi \cdot ZWD \tag{51.1}$$

P. Chen (✉) · W. Yao
College of Geomatics, Xi'an University of Science and Technology,
Xi'an 710054, China
e-mail: chenpeng0123@gmail.com

J. Sun et al. (eds.), *China Satellite Navigation Conference (CSNC) 2015 Proceedings: Volume II*, Lecture Notes in Electrical Engineering 341,
DOI 10.1007/978-3-662-46635-3_51

where Π is the water vapor conversion factor, expressed as:

$$\Pi = \frac{10^6}{\rho_w R_v \left[(k_3/T_m) + k_2' \right]} \tag{51.2}$$

where ρ_w is the density of liquid water, R_v is the gas constant of water vapor, k_2' and k_3 are atmospheric refractivity constants, and T_m is the atmospheric weighted mean temperature, a key variable to solve the conversion coefficient Π (Davis et al. [1]; Bevis et al. [2]). The calculation accuracy of Tm directly determines the accuracy of PWV (Wang et al. [3]).

Over the years, substantial research has been carried out on the calculation of Tm because of its importance in calculation of PWV process as well as the limitation of means for its direct access ([4], Ross et al. [5]; Li et al. [6]; Liu et al. [7]; Wang et al. [3, 8, 9]). Bevis et al. [10] used 8718 radiosonde records distributed within 27°–65°N in America to derive the linear relationship between Tm and ground surface temperature (Ts), i.e., Tm = 70.2 + 0.72 Ts. Later, this equation was revised by Bevis et al. (1995) as Tm = 85.63 + 0.668 Ts, based on an analysis of ~250,000 radiosonde profiles with a nearly global distribution. Boehm et al. [11] built a global pressure and temperature (GPT) model through which the pressure and temperature at any location on the Earth can be obtained from day of year (DOY) and three-dimensional coordinates. More recently, these calculations have been improved within a new combined model named GPT2, which provides pressure, temperature, lapse rate, water vapor pressure, and mapping function coefficients at any site on the Earth (Lagler et al. [12]).

Based on the GPT model, [13] used 2005–2009 radiosonde data from more than 100 stations to establish a global Tm model termed GWMT, which can derive Tm anywhere in the world from DOY, latitude, longitude, and altitude. Despite its higher accuracy, the GWMT model produces a large deviation in marine areas due to the lack of marine radiosonde stations. To address this issue, [14] presented the GTm_II model which realizes higher accuracy by supplementing Tm calculation in marine areas lacking radiosonde stations with Bevis's formula. Yao et al. [15] have used global 2° × 2.5° Tm grid data provided by the Global Geodetic Observing System (GGOS) to establish a new generation global Tm model, GTm_III, which considers semi-annual and diurnal variations in Tm. Moreover, [16] established a global Tm model, GTm_N, using NCEP reanalysis data in 2006–2011, which has similar accuracy as GTm_III.

GTm_III and GTm_N are two global Tm models established using GGOS and NCEP reanalysis data, respectively. Despite their high accuracy in both terrestrial and marine areas, GTm_III and GTm_N fit global Tm with a 9-order spherical harmonic model, resulting in relatively low spatial resolution (only ~20°) and failure to express minor Tm changes. To address this issue, we established a new high-accuracy high-resolution global Tm model using the European Center for Medium range Weather Forecasting (ECMWF) reanalysis data, in which Tm at each grid point are fitted independently using a set of parameters.

51.2 Model Establishment

The proposed global Tm model, GTm_X, was established based on 3-year 2011–2013 global profiles (4 times per day) for temperature, relative humidity, and geopotential from ERA-Interim [17], discretized at 37 pressure levels and 1° of latitude and longitude.

Tm corresponding to each pressure level of relative humidity, geopotential, and temperature was calculated from the bottom to the top. Here Tm of each level is the Tm from this level to the topmost level according to Eq. (51.3). We interpolated or extrapolated the Tm to the Earth's surface as needed. The topography is represented by a resampled 1° version of ETOPO5. Linear behavior was assumed for computing surface values of Tm. Tm corresponding to different pressure levels at each grid point was preprocessed to obtain the Tm lapse rate with height based on the Tm difference between adjacent levels. In this study, the Tm lapse rate was calculated using data from only 5 bottom levels from the ground.

Tm of each grid point at different levels was fitted with 8 coefficients according to Eq. (51.3), and 8 coefficients were obtained for each grid point: the average (a_0), annual variation coefficient (a_1, b_1), semi-annual variation coefficient (a_2, b_2), diurnal variation coefficient (a_3, b_3), and lapse rate (a_4).

$$\begin{aligned} Tm = a_0 &+ a_1 \cos\left(\frac{doy}{365.25}2\pi\right) + b_1 \sin\left(\frac{doy}{365.25}2\pi\right) \\ &+ a_2 \cos\left(\frac{doy}{365.25}4\pi\right) + b_2 \sin\left(\frac{doy}{365.25}4\pi\right) \\ &+ a_3 \cos\left(\frac{ut}{24}2\pi\right) + b_3 \sin\left(\frac{ut}{24}2\pi\right) + a_4 h \end{aligned} \tag{51.3}$$

The estimated values of all coefficients were saved in an external MATLAB matrix file (3.7 MB at 1° resolution), which must be loaded for every run of the GTm_X subroutine.

Tm at any position can be calculated using DOY, latitude, longitude, and altitude. First, 4 adjacent grid points were chosen around the desired point (latitude and longitude intervals are 1°, and height used is the height of the desired point); then, Tm of the 4 adjacent grid points was calculated using Eq. (51.3); finally, Tm values of the 4 grid points were averaged by distance weighing to obtain a desired Tm.

51.3 Accuracy Verification

A total of 1096 days (2011–2013) of Tm from 703 radiosonde stations were used as true values to verify the accuracy of Bevis's formula (using the measured values of Ts), GTm_III, GTm_N, and GTm_X.

Table 51.1 Statistics of differences in atmospheric weighted mean temperature obtained from 5 models compared with radiosonde data, 2011–2013 (in accordance with different days of year)

Models	Max (K)	Min (K)	Mean (K)
GTm_X	6.53	2.94	4.37
GTm_III	7.18	3.08	4.77
GTm_N	7.08	3.21	4.70
Bevis+True Ts	6.75	3.50	4.82

Table 51.1 shows the accuracy of 5 models with statistics based on DOY. GTm_X has smaller RMSE of Tm than the other models. The average RMSE of Tm from GTm_X is reduced by 0.4 and 0.37 K compared with those of GTm_III and GTm_N, respectively. The maximum and minimum RMSEs of Tm from GTm_X are also smaller than the extreme values of the other models. The results indicate that the Tm obtained from GTm_X is closest to radiosonde Tm.

Figure 51.1 shows the RMSE of Tm obtained from 5 models in accordance with DOY. The RMSE of Tm is within the range of 3–7 K, showing small differences among different models. GTm_X shows higher accuracy than the other models. There is a certain regularity between the RMSE of Tm and DOY. For example, the RMSE of Tm is generally larger in DOY 1–100 but smaller in DOY 200–250. During DOY 200–250, the northern hemisphere is in summer when Tm is more stable, accounting for the smaller RMSE of Tm.

Table 51.2 shows the accuracy indices of 5 models obtained at different latitudes. GTm_X exhibits better accuracy than the other 4 models. The average RMSE of Tm obtained from GTm_X is reduced by 0.36 K (8.76 %) and 0.41 K (9.86 %) compared with those of GTm_III and GTm_N, respectively.

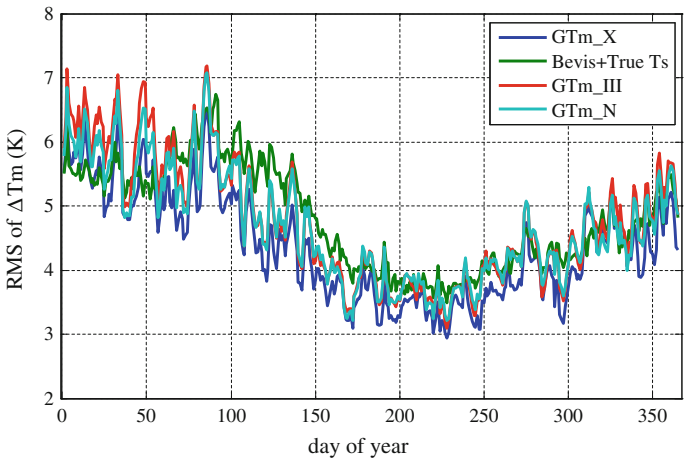

Fig. 51.1 The root mean square error (RMSE) of atmospheric weighted mean temperature (Tm) obtained from 5 models at different days of year tested with radiosonde data, 2011–2013

Table 51.2 Statistics of differences in atmospheric weighted mean temperature obtained from 5 models compared with radiosonde data, 2011–2013 (in accordance with different latitudes)

Models	Max (K)	Min (K)	Mean (K)
GTm_X	6.10	1.57	3.75
GTm_III	6.75	1.97	4.11
GTm_N	7.77	2.05	4.16
Bevis+True Ts	10.34	1.81	4.34

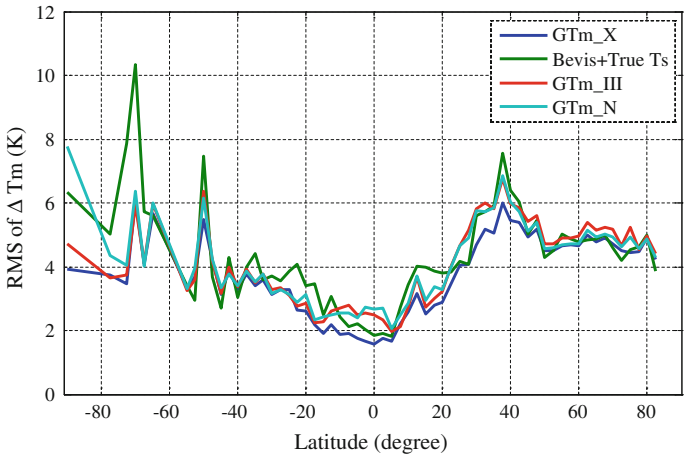

Fig. 51.2 The root mean square error (RMSE) of atmospheric weighted mean temperature (Tm) obtained from 5 models at different latitudes tested with radiosonde data, 2011–2013

Figure 51.2 shows the RMSE of Tm obtained from 5 models in relation to latitude. There is an evident regularity between the RMSE of Tm and latitude, with smaller RMSE of Tm in low latitudes than in middle and high latitudes. This phenomenon can be attributed to the generally higher temperature with smaller changes at low latitudes. In the southern hemisphere, the RMSE of Tm is higher south of 40°S than in other regions. In the northern hemisphere, the RMSE of Tm is significantly higher in 20°–50°N than in other regions.

Table 51.3 shows RMSE of Tm obtained from 5 models according to different radiosonde stations. GTm_X has smaller RMSE of Tm than the other models. Compared with data of GTm_III and GTm_N, the RMSE of Tm from GTm_X is reduced by 0.4 and 0.37 K, respectively.

Figure 51.3 given the RMSE of Tm obtained from 5 models tested with 703 global radiosonde stations. The accuracy of various models is higher in lower latitudes than in lower in middle and high latitudes. Significantly lower accuracy is observed in Northeast Asia and North America than in the other parts of the world.

Table 51.3 Statistics of differences in atmospheric weighted mean temperature obtained from 5 models compared with radiosonde data, 2011–2013 (in accordance with different radiosonde stations)

Models	Max (K)	Min (K)	Mean (K)
GTm_X	11.90	1.22	4.09
GTm_III	17.64	1.31	4.49
GTm_N	22.66	1.31	4.46
Bevis+True Ts	17.40	1.34	4.47

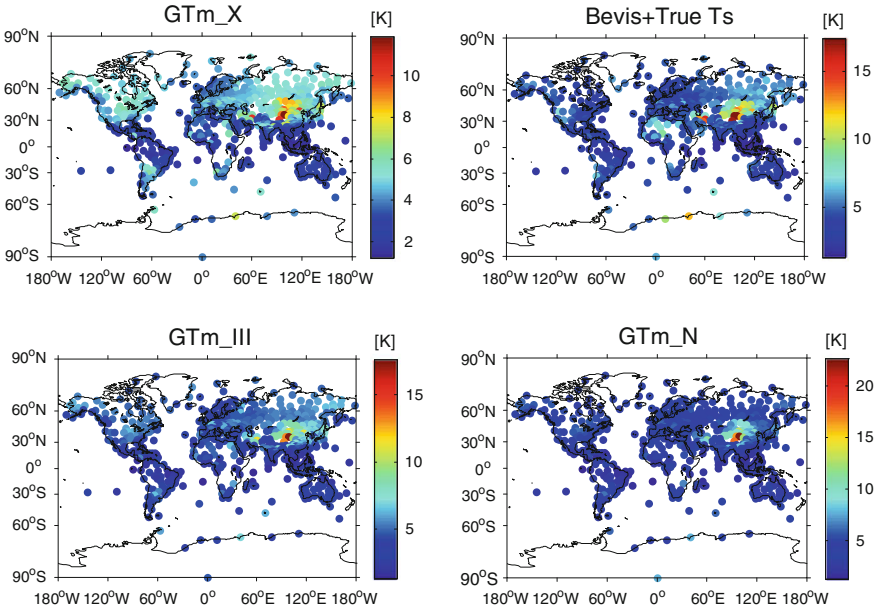

Fig. 51.3 The distributions of root mean square error (RMSE) of atmospheric weighted mean temperature (Tm) obtained from 5 models tested with radiosonde data, 2011–2013

51.4 Conclusions

This paper presents a new empirical global weighted mean temperature (Tm) model called GTm_X. The proposed model uses ECMWF reanalysis data at 1° × 1° pressure levels in 2011–2013 to estimate Tm at each grid point independently. It considers the annual, semi-annual, and diurnal variations and lapse rate of Tm with height. GTm_X is an improved version of the existing global Tm models with reduced horizontal resolution (1°) and it can describe fine variations in Tm within a small range. Verification analysis with radiosonde data shows that GTm_X has better accuracy than the existing global Tm models. This study provides a high-accuracy high-resolution Tm model especially suitable for ground-based GPS meteorology.

References

1. Davis JL, Herring TA, Shapiro II, Rogers AEE, Elgered G (1985) Geodesy by radio interferometry: effects of atmospheric modeling errors on estimates of baseline length. Radio Sci 20(6):1593–1607
2 Bevis M, Businger S, Herring TA, Rocken C, Anthes RA, Ware RH 1(992) GPS meteorology: remote sensing of atmosphericwater vapor using the global positioning system. J geophys Res [Atmos] (1984–2012) 97(D14):15787–15801
3. Wang J, Zhang L, Dai A (2005) Global estimates of watervapor-weighted mean temperature of the atmosphere for GPS applications. J geophys Res [Atmos] (1984–2012) 110(D21) doi: 10.1029/2005JD006215
4. Yu SJ, Liu LT (2009) Validation and analysis of the water-vaporweighted mean temperature from Tm-Ts relationship. Geomatics Inf Sci Wuhan Univ 34(6):741–744
5. Ross RJ, Rosenfeld S (1997) Estimating mean weighted temperature of the atmosphere for Global Positioning System applications. J geophys Res: [Atmos] (1984–2012) 102(D18) 21719–21730
6. Li JG, Mao JT (1999) The approach to remote sensing of water vapor based on GPS and linear regression Tm in eastern region of China. Acta Meteorol Sin 57(3):28–37.
7. Liu YX, Chen YQ, Liu JN (2000) Determination of weighted mean tropospheric temperature using ground meteorological measurement. J Wuhan Tech Univ Surv Map 25(5):400–404
8. Wang Y, Yang BY, Liu YP (2010) The study of the model about mean vapor pressure-weighted temperature of the atmosphere based on radiosonde. Sci Surv Map (2):112–113
9. Wang XY, Song LC, Dai, ZQ, Cao YC (2011) Feature analysis of weighted mean temperature Tm in Hong Kong. J Nanjing Univ Inform Sci Technol Nat Sci Edn 1 47–52
10. Bevis M, Businger S, Chiswell S (1995) Earth-based GPS meteorology: an overview, American Geophysical Union 1995 Fall Meeting (supplement), EOS. Trans Am geophys Un 76(46)
11. Böhm J, Heinkelmann R, Schuh H (2007) Short note: a global model of pressure and temperature for geodetic applications. J Geod 81(10):679–683
12. Lagler K, Schindelegger M, B¨ohm J, Kr´asn´a H, Nilsson T (2013) GPT2: empirical slant delay model for radio space geodetic techniques. Geophys Res Lett 40(6):1069–1073
13. Yao YB, Zhu S, Yue SQ (2012) A globally applicable, season-specific model for estimating the weighted mean temperature of the atmosphere. J Geod 86:1125–1135
14. Yao YB, Zhang B, Yue SQ, Xu CQ, Peng WF (2013) Global empirical model for mapping zenith wet delays onto precipitable water. J Geod 87:439–448
15. Yao Y, Xu C, Zhang B, Cao N (2014) GTm-III: a new global empirical model for mapping zenith wet delays onto precipitable water vapour. Geophys J Int 197(1):202–212
16. Chen P, Yao W, Zhu X (2014) Realization of global empirical model for mapping zenith wet delays onto precipitable water using NCEP re-analysis data. Geophys J Int 198(3):1748–1757
17. Dee DP, Uppala SM, Simmons AJ et al (2011) The ERA-Interim reanalysis: configuration and performance of the data assimilation system. Q J R Meteorol Soc 137:553–597

Chapter 52
Multi-GNSS PPP and PPP-RTK: Some GPS+BDS Results in Australia

Dennis Odijk, Baocheng Zhang and Peter J.G. Teunissen

Abstract As in the Asian-Pacific region BDS is operational next to GPS, satellite clocks (needed for Precise Point Positioning; PPP) and satellite phase hardware biases (needed for integer ambiguity resolution enabled PPP-RTK) have been estimated from a zero baseline in Perth, Australia, and applied to dual-frequency GPS+BDS data of a single GNSS receiver at a distance of 110 km from the zero baseline. Precise orbits were obtained from the IGS (GPS) and Wuhan University (BDS). It is shown that with GPS alone the PPP solution needs on average 1 h to converge to a level of a few decimetres, whereas with BDS alone this takes on average 2.5 h, which is due to the poorer geometry of the BDS satellites in Australia. With both GPS and BDS combined this convergence time is tremendously reduced to 30 min on average. With the satellite phase biases corrected, the precision of the GPS+BDS PPP-RTK solution is at the few centimetre level.

Keywords GNSS · GPS · BDS · PPP · PPP-RTK · Ambiguity resolution

52.1 Introduction

The technique of Precise Point Positioning (PPP) relies on the availability of satellite orbit, satellite clock and—in order to limit the convergence time of the solution—ionospheric products (together with the satellite differential code biases or DCBs). Based on a long observation time (multiple hours) the position accuracy of (static) PPP can reach the level of a few centimetres. This high accuracy is within quicker reach if the PPP user incorporates corrections on the satellite hardware

D. Odijk (✉) · B. Zhang · P.J.G. Teunissen
GNSS Research Centre, Curtin University, Perth, Australia
e-mail: d.odijk@curtin.edu.au

P.J.G. Teunissen
Department of Geosciences and Remote Sensing, Delft University of Technology, Delft, The Netherlands

J. Sun et al. (eds.), *China Satellite Navigation Conference (CSNC) 2015 Proceedings: Volume II*, Lecture Notes in Electrical Engineering 341,
DOI 10.1007/978-3-662-46635-3_52

phase biases. Using this satellite phase bias information the PPP user is able to resolve the phase ambiguities to integer values, allowing solving his position with high, centimetre precision after ambiguity resolution. Integer ambiguity resolution enabled PPP is also referred to as PPP-AR or PPP-RTK [1]. Although PPP-RTK requires less observation time than (standard) PPP to obtain the same precision level, both techniques suffer from the presence of the ionospheric delays in the observations, slowing down the convergence of the ambiguities before they can be reliably fixed to integers. Although the need for precise ionospheric corrections remains, PPP and PPP-RTK will enormously benefit from the availability of multiple Global Navigation Satellite System (GNSS) constellations. These additional constellations will bring an enormous increase in number of satellites and signals, as compared to one constellation, such as GPS, and will be very beneficial for the performance of positioning techniques, such as PPP, RTK and PPP-RTK.

In the Asian-Pacific region the Chinese BeiDou satellite System (BDS) is operational since 2012. This regional constellation consists of 5 Geostationary Earth Orbiting (GEO) satellites, 5 Inclined Geo-Synchronous Orbiting (IGSO) satellites, as well as 4 Medium Earth Orbiting (MEO) satellites. Full global operational capability of BDS is expected by 2020. An example of the ground tracks of the BDS satellites (as observed from a receiver at Curtin University in Australia) is depicted in Fig. 52.1. Results of PPP based on real data of the BDS combined with GPS and other constellations are presented in several publications, among others [2–4], while relative positioning results (RTK; short and long baselines) are presented in, among others, [2, 5, 6]. In this chapter we will present results of PPP as well as PPP-RTK based on BDS+GPS data collected near Perth in Western Australia. This chapter is set up as follows. Section 52.2 presents the observation models underlying PPP and PPP-RTK. Section 52.3 shows results of both positioning techniques, for GPS alone, BDS alone, as well as GPS+BDS combined. Finally, Sect. 52.4 presents the conclusions.

52.2 PPP and PPP-RTK Models

The between-satellite differenced, linearized GNSS code and carrier-phase observation equations on frequency j read, for receiver r and satellite pair $p-s$ [1]:

$$\begin{aligned} E(p_{r,j}^{ps}) &= \rho_r^{ps} - c(dt^{ps} + d_j^{ps}) + \mu_j \imath_r^{ps} \\ E(\phi_{r,j}^{ps}) &= \rho_r^{ps} - c(dt^{ps} + \delta_j^{ps}) - \mu_j \imath_r^{ps} + \lambda_j z_{r,j}^{ps} \end{aligned} \tag{52.1}$$

Here $E(\bullet)$ denotes the expectation, p the code and ϕ the phase observables (both expressed in meter), ρ the receiver-satellite range combined with the tropospheric delay (in meter), c the speed of light (meter/second), dt the satellite clock error (in second), d the satellite code bias (in second), δ the satellite phase bias (in second), $\imath$ the ionospheric delay (in meter), $\mu_j = \lambda_j^2/\lambda_1^2$ the frequency-dependent

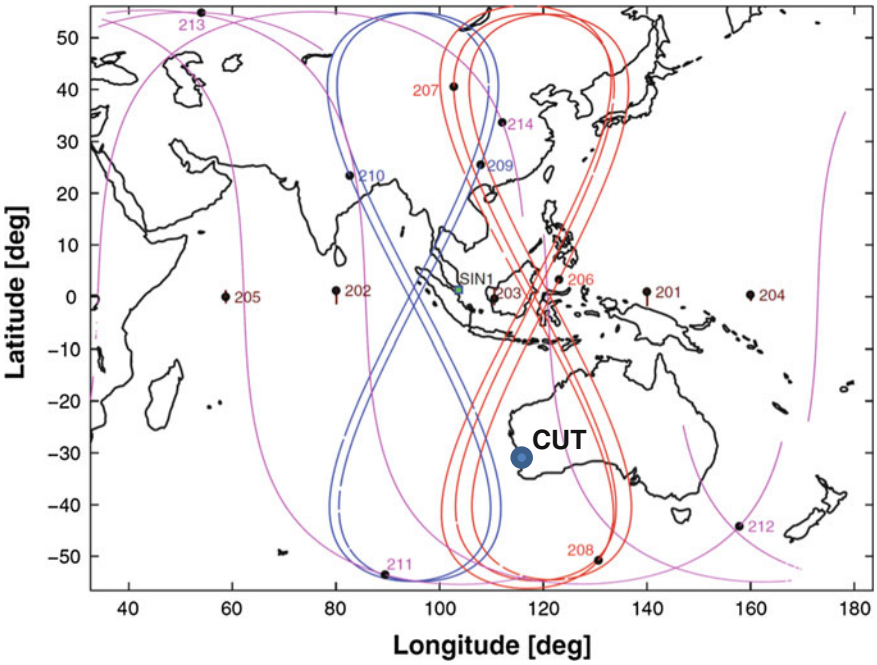

Fig. 52.1 Example of the ground tracks of the BDS satellites as observed from station CUT (Curtin University) in Perth, Australia. The 5 GEO satellites are (almost) stationary above the equator, whereas the 5 IGSO satellites follow an '8' shaped ground track

ionospheric coefficient with λ_j the wavelength (in meter), and z the integer carrier-phase ambiguity (in cycle). Due to the between-satellite differencing any receiver-specific parameters are eliminated.

In case of PPP and PPP-RTK the above observation equations are linearized with respect to the unknown receiver position. For this the satellite positions are needed, which in case of GPS are provided by the International GNSS Service in the form of precise IGS orbits [7]. For BDS the precise WUM orbits provided by Wuhan University [8] are used. Both these orbit products are given in the same reference frame (IGS08), so there is no need to transform them to a common reference frame. In addition to these precise satellite orbits, both PPP and PPP-RTK rely on the availability of precise satellite clocks. These are provided as *ionosphere-free* satellite clocks, which are interpreted as [1]:

$$d\tilde{t}^{ps} = dt^{ps} + d_j^{ps} + \frac{\mu_j}{\mu_2 - \mu_1} DCB^{ps}, \quad j = 1,\ 2 \tag{52.2}$$

Here the ionosphere-free clock is denoted using a tilde on top, as to distinguish it from the true satellite clock. Note that $DCB^{ps} = d_1^{ps} - d_2^{ps}$ denotes the Differential Code Bias, i.e. the difference between the satellite code biases on two frequencies,

which is pre-multiplied by the ionosphere-free coefficient $\frac{\mu_j}{\mu_2-\mu_1}$. In case of GPS the ionosphere-free clock products are based on the L1 and L2 frequencies (i.e. the P1 and P2 code), for which these coefficients are $\frac{\mu_1}{\mu_2-\mu_1} = 1.546$ and $\frac{\mu_2}{\mu_2-\mu_1} = 2.546$. For BDS the coefficients are based on the B1 and B2 frequencies, for which they read $\frac{\mu_1}{\mu_2-\mu_1} = 1.487$ and $\frac{\mu_2}{\mu_2-\mu_1} = 2.487$.

Correcting the code and phase observations for the above clock products yields the following dual-frequency ($j = 1,\ 2$) observation equations for PPP:

$$\begin{aligned} E(p_{r,j}^{ps} + c\tilde{dt}^{ps}) &= \rho_r^{ps} + \mu_j \underbrace{(\imath_r^{ps} + \frac{1}{\mu_2-\mu_1} cDCB^{ps})}_{\tilde{\imath}_r^{ps}} \\ E(\phi_{r,j}^{ps} + c\tilde{dt}^{ps}) &= \rho_r^{ps} - \mu_j \underbrace{(\imath_r^{ps} + \frac{1}{\mu_2-\mu_1} cDCB^{ps})}_{\tilde{\imath}_r^{ps}} + \lambda_j \underbrace{[z_{r,j}^{ps} - \frac{c}{\lambda_j}(\delta_j^{ps} - d_j^{ps} - \frac{2\mu_j}{\mu_2-\mu_1} DCB^{ps})]}_{\tilde{z}_{r,j}^{ps}} \end{aligned} \tag{52.3}$$

To solve for the receiver position, the above observation equations are linearized. It is remarked that, besides the satellite clocks, the observations are also corrected for errors due to troposphere, phase windup, relativity, tides, ocean loading, etc. In addition, if in case of GPS the C/A code data are used, a correction needs to be applied for the C/A-P1 code bias. If needed, a zenith tropospheric delay (ZTD) is modelled as unknown parameter. In this chapter it is assumed that the observations are *not* corrected for ionospheric delays. As consequence, the ionospheric delays are unknown parameters of the model, which get biased by the DCBs coming from the clock product. This means that the ionospheric delay biased by the DCB, denoted as $\tilde{\imath}_r^{ps}$ becomes an additional estimable parameter in the observation model. This parameter could be eliminated by taking the ionosphere-free observation combination, however in this chapter we solve for the *uncombined* observation equations. In addition to this ionospheric parameter, the corrected phase observation equation has another estimable parameter, which is the phase ambiguity, denoted as $\tilde{z}_{r,j}^{ps}$, which not only consists of the true ambiguity, but is biased by a combination of satellite phase and code biases. Because these phase and code biases cannot be separated from the ambiguity $z_{r,j}^{ps}$, integer ambiguity resolution is not possible. This is the well-known situation for standard PPP.

The information that is missing in order to resolve the ambiguities as integer, are satellite phase biases. Like the satellite clocks, these cannot be provided as *unbiased* phase biases, but only biased by other terms. In this chapter we assume them to be provided having the following interpretation [1]:

$$\tilde{\delta}_j^{ps} = \delta_j^{ps} - d_j^{ps} - \frac{2\mu_j}{\mu_2-\mu_1} DCB^{ps} - \frac{\lambda_j}{c} z_{1,j}^{ps}, \quad j = 1,\ 2 \tag{52.4}$$

It can be seen that the first three terms in this expression exactly correspond to the bias term in the estimable PPP ambiguity in (52.3). However, there is an

additional term, i.e. $z_{1,j}^{ps}$, which is the between-satellite differenced ambiguity of the *pivot receiver* (denoted using subscript 1) in the reference network that is providing the satellite phase bias product. Correcting the phase observations for these satellite phase biases yields the following (PPP-RTK) observation equations ($j = 1,\ 2$):

$$\begin{aligned} E(p_{r,j}^{ps} + c\tilde{dt}^{ps}) &= \rho_r^{ps} + \mu_j \underbrace{(\iota_r^{ps} + \frac{1}{\mu_2 - \mu_1} cDCB^{ps})}_{\tilde{\iota}_r^{ps}} \\ E(\phi_{r,j}^{ps} + c\tilde{dt}^{ps} + c\tilde{\delta}_j^{ps}) &= \rho_r^{ps} - \mu_j \underbrace{(\iota_r^{ps} + \frac{1}{\mu_2 - \mu_1} cDCB^{ps})}_{\tilde{\iota}_r^{ps}} + \lambda_j \underbrace{(z_{r,j}^{ps} - z_{1,j}^{ps})}_{\tilde{z}_{r,j}^{ps}} \end{aligned} \tag{52.5}$$

Because of the satellite phase bias correction, the estimable ambiguity parameter $\tilde{z}_{r,j}^{ps}$ now only consists of integer ambiguity terms. In fact, it is estimable as a *double-differenced* ambiguity, with respect to the network's pivot receiver, and therefore automatically estimable as an integer. Thus, although the corrected observation equations for PPP in (52.3) and PPP-RTK in (52.5) will result in exactly identical models, the phase corrections and therefore the interpretation of the estimable ambiguities are *completely different*. The PPP-RTK model is usually solved in *three steps*, with the first step the ambiguity-float solution. The positioning solution of this first step is identical to the standard PPP solution. In the second step, the integer ambiguities are resolved by means of the standard LAMBDA method [9], whereas in the third step these ambiguities are held fixed (ambiguity-fixed).

In case GPS and BDS data are processed together, the code/phase observation equations of both constellations are solved together, having the receiver position (plus optionally ZTD) as common parameters. As GPS and BDS do not have identical frequencies, it is not needed to parameterize *inter-system biases* as additional parameters. This means that for each constellation a constellation-specific pivot satellite should be selected, in order to perform the between-satellite differencing.

52.3 Some PPP and PPP-RTK Results for GPS and BDS

In this section we present results for PPP as well as PPP-RTK based on real GPS+BDS data. This is done for the multi-GNSS Septentrio PolaRx4 receiver set up in New Norcia (NNOR), Australia, which is part of the *Multi-GNSS Experiment* (MGEX) network. As satellite phase biases for BDS data are not yet produced on a global level, the satellite clocks as well as satellite phase biases for both GPS and BDS that are needed to perform PPP and PPP-RTK are estimated from a *zero baseline* setup at Curtin University in Perth, Australia tracking data of both constellations.

The zero baseline is formed by two multi-GNSS Trimble NetR9 receivers (i.e. CUT0 and CUT2), connected to one common antenna. Figure 52.2 (left) depicts a map of a part of Western Australia showing the locations of CUT0/CUT2 and NNOR. The distance between CUT0/CUT2 and NNOR is about 110 km. The GNSS data that are used were collected during the full day of 14 December 2013. Table 52.1 presents some information on the data collected.

The GPS and BDS satellite clock and phase biases determined by the zero baseline CUT0/CUT2 are in a next step applied to correct the data of NNOR. In addition, as these corrections are determined by Trimble receivers, while the receiver in NNOR is of another type (Septentrio), the BDS phase data corresponding to the GEO satellites are corrected by 0.5 cycle to account for the *Inter-Satellite-Type Biases* that are known to occur between the GEO and the IGSO/MEO BDS satellites in case of mixed (Septentrio-Trimble) receiver combinations [10].

Figure 52.3 (left) shows the number of GPS and BDS satellites that are tracked above the selected 15° cut-off elevation. It can be seen that the number of satellites varies between 4 and 10 during the day, whereas the number of BDS satellites varies between 6 and 10. The combined number of satellites varies between 10 and 19. Although the number of BDS satellites is comparable to the number of GPS satellites, their geometry is generally less favorable for positioning in Australia, as can be seen from their PDOP values in Fig. 52.3 (right). During the day the BDS

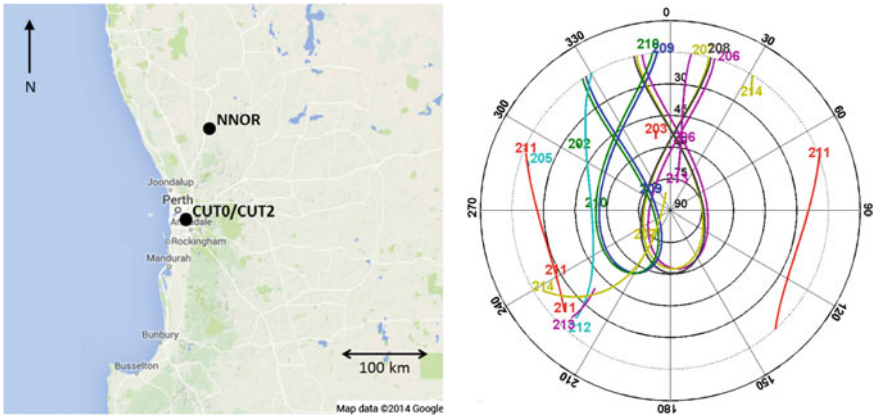

Fig. 52.2 Map showing the locations of the multi-GNSS stations CUT0/CUT2 and NNOR in Western Australia (*left*) versus sky plot of the tracked BDS satellites in NNOR on 14 December 2013 (*right*)

Table 52.1 Some information on the GPS+BDS data used

Date	14 December 2013, 0:00–24:00 GPS time
Cut-off elevation	15°
Observables	GPS L1+L2; BDS B1+B2
Precise orbits	IGS (GPS); WUM (BDS)

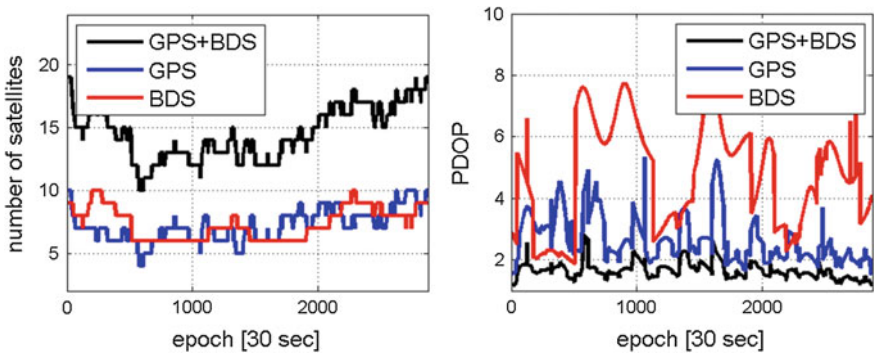

Fig. 52.3 Number of GPS and BDS satellites and combined tracked in NNOR on 14 December 2013 (*left*) versus PDOP values for this day, based on GPS-only, BDS-only and GPS+BDS (*right*)

PDOPs are much larger than for GPS, apart from a period during the beginning of the day. The worse BDS geometry can also be inferred from Fig. 52.2 (right), which shows a sky plot of the BDS satellites that are tracked at NNOR during the day. It can be seen that there is almost no satellite coverage in the East direction. However, one has to take into account that the BDS constellation is not yet final, as there will be many more MEO satellites launched the coming years.

Concerning integer ambiguity resolution in case of PPP-RTK, we decided *not* to resolve the ambiguities of the BDS GEO satellites, but to keep them *float* instead. This decision, which was also taken in [5], is motivated by the fact that the receiver-satellite geometry for these (almost) stationary satellites is barely changing and therefore it is very difficult to resolve these ambiguities using a model that includes ionospheric parameters as well. Other reasons for not including the GEO satellites in the ambiguity resolution are that the quality of its orbits is worse than of the other satellites and multipath effects are not averaged out over time [11].

As precise coordinates are available for the NNOR receiver, these will be used as ground-truth to assess the position errors obtained with PPP and PPP-RTK. To assess the performance of the PPP-RTK integer ambiguity resolution, the ratio test with a fixed failure rate of 0.001 [12] is executed to assess whether the integer solution obtained with LAMBDA can be accepted with sufficient confidence. In addition, a ground-truth for the integer ambiguities is computed as well, by solving the full day of data in a Kalman filter, keeping the ambiguities constant in time. This ground-truth solution is used to compute for every epoch of the day the time that is needed to obtain this correct integer solution, i.e. the ambiguity convergence time, also known as the *time-to-fix-the-ambiguities* (TTFA).

Figure 52.4 shows the TTFA during the day, for three cases: (i) GPS-only, (ii) BDS-only and (iii) GPS+BDS. The TTFAs in Fig. 52.4 (left) are computed using a Kalman filter that introduces a receiver position for every epoch that is not connected in time ("kinematic" mode), whereas the TTFAs in Fig. 52.4 (right) are based on positions that are kept constant in time ("static" mode).

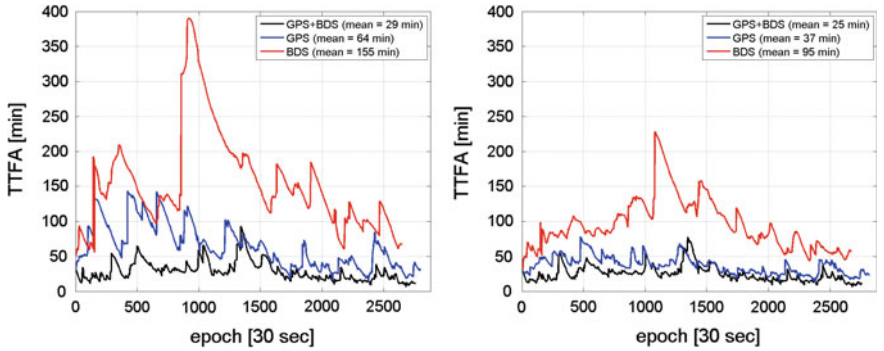

Fig. 52.4 Time-to-Fix-the-Ambiguities (TTFA) for single-receiver integer ambiguity resolution of receiver NNOR, based on GPS+BDS, GPS-only as well as BDS-only, solving the receiver position in *kinematic* mode (*left*) and in *static* mode (*right*)

With respect to the results in Fig. 52.4, the TTFAs are significantly worse for BDS in standalone mode as compared to GPS alone, which is due to the relatively low number of BDS ambiguities that are resolved (as the GEO ambiguities are kept float), in combination with a poor BDS geometry (see Fig. 52.3, right). Despite this,

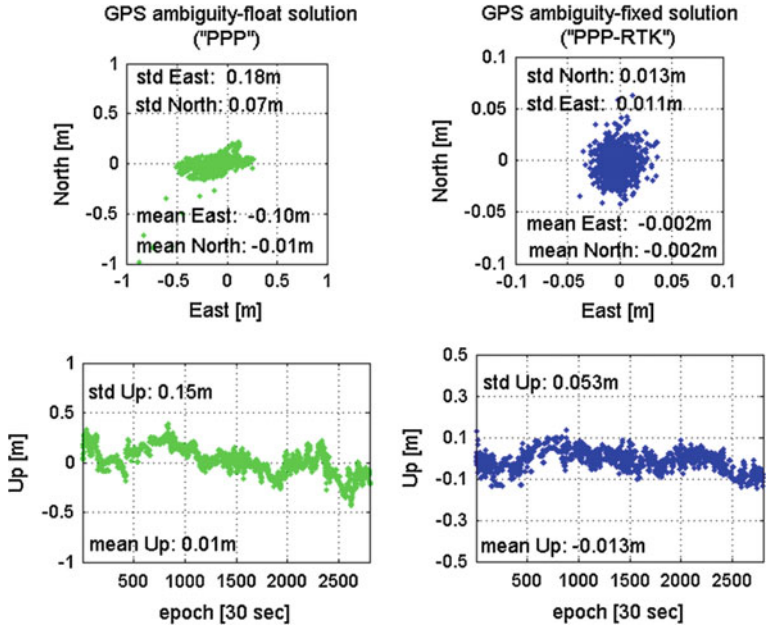

Fig. 52.5 Horizontal position scatter (*top*) and vertical position time series (*bottom*) for station NNOR based on GPS only data: ambiguity-float (*left*) versus ambiguity-fixed (*right*)

the combination of BDS with GPS turns out to be very favorable: in kinematic mode the TTFA of GPS+BDS (29 min) is still only half the time of GPS alone (64 min). Although this effect is less pronounced in static mode (GPS alone: 37 min vs. GPS+BDS: 25 min), there is still gain in combining the two constellations.

Based on the TTFAs, Figs. 52.5, 52.6 and 52.7 show the horizontal scatters as well as the vertical time series of the position errors of NNOR, estimated in the kinematic mode. Shown are the positions based on the ambiguities held float, as well as held fixed (after integer ambiguity resolution), and since these scatters and time series are based on the same number of epochs (i.e. the TTFA), they are directly comparable. The ambiguity-float positions can be considered as standard PPP results, whereas their ambiguity-fixed counterparts represent results of PPP-RTK. Based on an average TTFA of 64 min for GPS only, the float horizontal precision is at the level of a few decimeters, whereas after ambiguity fixing this is at the 1 cm level horizontally and 5 cm vertically. In case of BDS alone, the float horizontal precision is comparable to GPS, however the BDS positioning results are based on a much larger average TTFA than for GPS, benefitting the float results. The BDS-only fixed results are based on the instantaneous BDS geometry and almost a factor 3 worse than of GPS, up to a standard deviation of 12 cm in height.

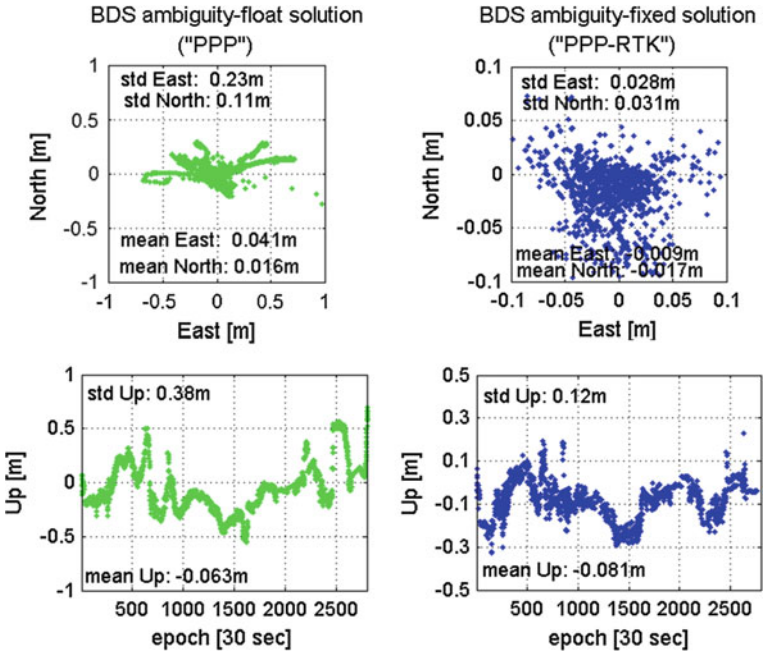

Fig. 52.6 Horizontal position scatter (*top*) and vertical position time series (*bottom*) for station NNOR based on BDS only data: ambiguity-float (*left*) versus ambiguity-fixed (*right*)

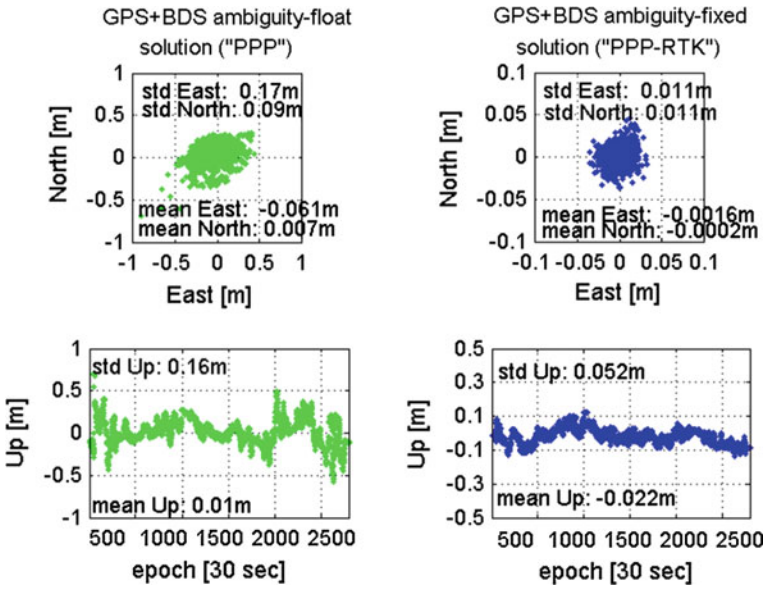

Fig. 52.7 Horizontal position scatter (*top*) and vertical position time series (*bottom*) for station NNOR based on GPS+BDS data: ambiguity-float (*left*) versus ambiguity-fixed (*right*)

The positioning results for GPS+BDS combined are very similar to that of GPS only. One has however to realize that the ambiguity-float solution is based on a much shorter average TTFA, which is 29 min for GPS+BDS, versus 64 min for GPS alone.

52.4 Conclusions

Standard PPP and integer ambiguity resolution enabled PPP (PPP-RTK) will benefit in presence of new GNSSs, as more observations of more satellites will significantly strengthen the underlying positioning models. This benefit is mainly felt in a decrease of convergence time or time-to-fix-the-ambiguities (TTFA) when observations of multiple constellations are combined. In this chapter it has been demonstrated that combining dual-frequency GPS with dual-frequency BDS data for a single receiver Australia, where BDS is regionally operational, the TTFA for PPP-RTK ambiguity resolution is reduced from 64 min in case of GPS only to 29 min for GPS+BDS. The resulting precision based on the fixed ambiguities is at the 1 cm level for the horizontal position components and 5 cm in vertical direction.

Acknowledgments This work has been done in the context of the Positioning Program Project 1.01 "New carrier phase processing strategies for achieving precise and reliable multi-satellite, multi-frequency GNSS/RNSS positioning in Australia" of the Cooperative Research Centre for Spatial Information (CRC-SI). The third author is the recipient of an Australian Research Council (ARC) Federation Fellowship (project number FF0883188). Mr. Robert Odolinski is acknowledged for creating Fig. 52.1.

References

1. Odijk D, Teunissen PJG, Zhang B (2012) Single-frequency integer ambiguity resolution enabled GPS precise point positioning. J Surv Eng 138:193–202
2. Shi C, Zhao Q, Li M, Tang W, Hu Z, Lou Y, Zhang H, Niu X, Liu J (2012) Precise orbit determination of BeiDou satellites with precise positioning. Sci China Earth Sci 55(7):1079–1086
3. Li M, Qu L, Zhao Q, Guo J, Su X, Li X (2014) Precise point positioning with the BeiDou navigation satellite system. Sensors 14:927–943
4. Tegedor J, Ovstedal O, Vigen E (2014) Precise orbit determination and point positioning using GPS, Glonass, Galileo and BeiDou. J Geodetic Sci 4:65–73
5. Odolinski R, Teunissen PJG, Odijk D (2015) Combined GPS+BDS for short to long baseline RTK positioning. Published in the mean time. Measurement Science and Technology. doi:10.1088/0957-0233/26/4/045801
6. Wang M, Cai H, Pan Z (2015) BDS/GPS relative positioning for long baseline with undifferenced observations. Adv Space Res 55:113–124
7. Dow JM, Neilan RE, Rizos C (2009) The International GNSS Service in a changing landscape of Global Navigation Satellite Systems. J Geodesy 83:191–198
8. Zhao Q, Guo J, Li M, Qu L, Hu Z, Shi C, Liu J (2013) Initial results of precise orbit and clock determination for COMPASS navigation satellite system. J Geodesy 87(5):475–486
9. Teunissen PJG (1995) The least-squares ambiguity decorrelation adjustment: a method for fast GPS integer estimation. J Geodesy 70:65–82
10. Nadarajah N, Teunissen PJG, Sleewaegen JM, Montenbruck O (2014) The mixed-receiver BeiDou inter-satellite-type bias and its impact on RTK positioning. GPS Solutions. doi:10.1007/s10291-014-0392-6
11. Wang G, de Jong K, Zhao Q, Hu Z, Guo J (2015) Multipath analysis of code measurements for BeiDou geostationary satellites. GPS Solutions 19:129–139
12. Verhagen S, Teunissen PJG (2013) The ratio test for future GNSS ambiguity resolution. GPS Solutions 17:535–548